Research Topics

Wave propagation in complex environments, volume II

Edited by
Leilei Chen, Pei Li, Elena Atroshchenko and
Yilin Qu

Published in
Frontiers in Physics

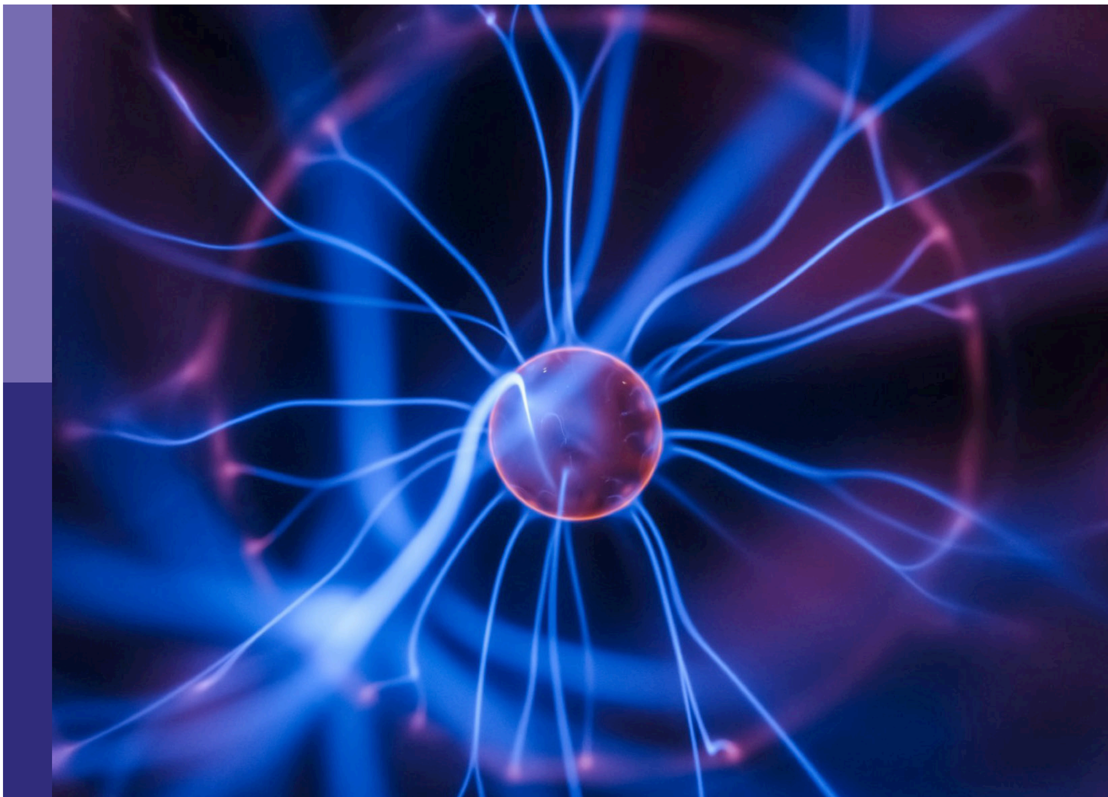

ISSN 1664-8714
ISBN 978-2-8325-6816-3
DOI 10.3389/978-2-8325-6816-3

Generative AI statement
Any alternative text (Alt text) provided alongside figures in the articles in this ebook has been generated by Frontiers with the support of artificial intelligence and reasonable efforts have been made to ensure accuracy, including review by the authors wherever possible. If you identify any issues, please contact us.

About Frontiers

Frontiers is more than just an open access publisher of scholarly articles: it is a pioneering approach to the world of academia, radically improving the way scholarly research is managed. The grand vision of Frontiers is a world where all people have an equal opportunity to seek, share and generate knowledge. Frontiers provides immediate and permanent online open access to all its publications, but this alone is not enough to realize our grand goals.

Frontiers journal series

The Frontiers journal series is a multi-tier and interdisciplinary set of open-access, online journals, promising a paradigm shift from the current review, selection and dissemination processes in academic publishing. All Frontiers journals are driven by researchers for researchers; therefore, they constitute a service to the scholarly community. At the same time, the *Frontiers journal series* operates on a revolutionary invention, the tiered publishing system, initially addressing specific communities of scholars, and gradually climbing up to broader public understanding, thus serving the interests of the lay society, too.

Dedication to quality

Each Frontiers article is a landmark of the highest quality, thanks to genuinely collaborative interactions between authors and review editors, who include some of the world's best academicians. Research must be certified by peers before entering a stream of knowledge that may eventually reach the public - and shape society; therefore, Frontiers only applies the most rigorous and unbiased reviews. Frontiers revolutionizes research publishing by freely delivering the most outstanding research, evaluated with no bias from both the academic and social point of view. By applying the most advanced information technologies, Frontiers is catapulting scholarly publishing into a new generation.

What are Frontiers Research Topics?

Frontiers Research Topics are very popular trademarks of the *Frontiers journals series*: they are collections of at least ten articles, all centered on a particular subject. With their unique mix of varied contributions from Original Research to Review Articles, Frontiers Research Topics unify the most influential researchers, the latest key findings and historical advances in a hot research area.

Find out more on how to host your own Frontiers Research Topic or contribute to one as an author by contacting the Frontiers editorial office: frontiersin.org/about/contact

Wave propagation in complex environments, volume II

Topic editors
Leilei Chen — Huanghuai University, China
Pei Li — University of Southern Denmark, Denmark
Elena Atroshchenko — University of New South Wales, Australia
Yilin Qu — Northwestern Polytechnical University, China

Citation
Chen, L., Li, P., Atroshchenko, E., Qu, Y., eds. (2025). *Wave propagation in complex environments, volume II*. Lausanne: Frontiers Media SA.
doi: 10.3389/978-2-8325-6816-3

Table of contents

Frontiers in Physics

TYPE Original Research
PUBLISHED 08 October 2024
DOI 10.3389/fphy.2024.1452876

EDITED BY
Leilei Chen,
Huanghuai University, China

REVIEWED BY
Kui Liu,
Harbin Institute of Technology, China
Ang Zhao,
Shanghai Civil Aviation College, China

*CORRESPONDENCE
Shujie Jiang,
✉ jiangshujie@cardc.cn
Yuxiang Liang,
✉ ngjhlyx@163.com

RECEIVED 21 June 2024
ACCEPTED 04 September 2024
PUBLISHED 08 October 2024

CITATION
Jiang S, Liang Y, Cheng Y and Gao L (2024) Research on the prediction method of wing structure noise based on the combination of conditional generative adversarial neural network and numerical methods.
Front. Phys. 12:1452876.
doi: 10.3389/fphy.2024.1452876

Research on the prediction method of wing structure noise based on the combination of conditional generative adversarial neural network and numerical methods

Shujie Jiang[1]*, Yuxiang Liang[1]*, Yu Cheng[1] and Lingyu Gao[1,2]

[1]State Key Laboratory of Aerodynamics, Mianyang, Sichuan, China, [2]School of Aeronautics and Astronautics, Shanghai Jiao Tong University, Shanghai, China

This paper presents a technique for predicting noise generated by airfoil structures that combines deep learning techniques with traditional numerical methods. In traditional numerical methods, accurately predicting the noise of airfoil structures requires significant computational resources, making it challenging to perform low-noise optimization design for these structures. To expedite the prediction process, this study introduces Conditional Generative Adversarial Networks (CGAN). By replacing the generator and discriminator of CGAN with traditional regression neural network models, the suitability of CGAN for regression prediction is ensured. In this study, the data computation was accelerated by expanding the kernel function in the traditional boundary element method using a Taylor series. Based on the resulting data, an alternative predictive model for wing structure noise was developed by integrating Conditional Generative Adversarial Networks (CGAN). Finally, the effectiveness and feasibility of the proposed method are demonstrated through three case studies.

KEYWORDS

airfoil structure, CGAN, boundary element, aeroacoustic noise, computational fluid dynamics

1 Introduction

The propeller is usually an open (non-enclosed) rotating mechanical device with multiple blades, and it has a history of nearly a century as an aviation propulsion system [1, 2]. As early as the 1940s, propellers were widely used in various types of aircraft, and the development of propeller technology has always been closely linked to the development of aircraft. Propeller engines are still widely used in military and civilian aircraft today, mainly due to their excellent fuel economy [3]. However, the propulsion speed of propellers significantly decreases under high subsonic conditions, resulting in relatively low cruising speeds for propeller-driven aircraft. Later, the concept of contra-rotating propeller engines was proposed. The contra-rotating propeller engine is a conceptually different aviation engine related to the turboprop engine and turbofan engine, and it is also referred to as a propeller fan engine, advanced turboprop engine, un ducted fan, or ultra-high bypass ratio turbofan engine [4, 5]. The design objective is to balance the efficiency and fuel economy of turboprop engines with the cruising speed and performance of turbofan engines [6–8], filling the speed gap between conventional turboprop engines and turbofan engines. It effectively addresses the contradiction between the cruising speed and propulsive efficiency of conventional turboprop engines and turbofan engines, and it is the direction of development for the propulsion systems of future medium-sized transport aircraft [9].

Compared to the 1980s, although modern contra-rotating propellers have made significant advances in aerodynamic design [10], noise optimization techniques, and manufacturing processes, according to NASA's research, contra-rotating propeller engines still have a noise level that is more than 10 dB higher than that of ducted fan engines [11]. Therefore, aerodynamic and noise optimization design remains a key technical issue in the development of contra-rotating propellers [12]. However, due to the complex aerodynamic disturbances such as viscous wake interference, potential flow field interference, and propeller tip vortex interference between the two rows of propellers, the aerodynamic noise mechanism is more complicated [13–15]. Therefore, noise prediction and acoustic optimization design of propeller engines have become one of the key technologies in propeller design [16].

As the main component of propeller noise, accurate prediction of the noise generated by airfoils can guide the optimization design of propellers. Currently, in addition to using engineering estimation methods based on empirical theories, common methods for predicting airfoil vibration noise mainly rely on numerical calculation methods [17]. Engineering estimation methods typically use semi-theoretical and semi-empirical formulas combined with structural sound radiation theory and measured data. Engineering estimation methods are convenient and fast, but they are mainly applicable to specific structures or their similar models. Numerical simulation methods mainly rely on finite element methods (FEM) [18], boundary element methods (BEM) [19–21], and computational aeroacoustic methods (CAA) [22]. Among them, CAA methods combine computational fluid dynamics (CFD) simulations and the FW-H analogy method, which can simultaneously obtain the near-field flow distribution of the structure and the far-field acoustic characteristics, making it one of the reliable methods. However, in the pre-processing stage of CAA calculations, it is necessary to establish a very detailed model in the computer, which requires a significant amount of time and leads to a longer prediction process. Therefore, developing efficient aerodynamic noise prediction methods by combining deep learning methods can significantly reduce the computational cost of aerodynamic noise [23, 24]. This is of great importance for guiding the optimization design of low-noise propellers.

In light of the reflect on mentioned, the objective of this study is to propose a new method for analyzing the uncertainty of piezoelectric and flexoelectric characteristics using Conditional Generative Adversarial Networks (CGAN), which is a machine learning (ML) technique [25–27]. CGAN has emerged as a significant advancement in the field of ML, allowing for the generation of high-quality predictions and opening up new possibilities for data-driven creativity and problem-solving [28]. Generative Adversarial Networks (GANs) [29] revolutionized image generation [30]. However, GANs are limited in controlling the output of the generated network. For example, when dealing with the MINIST dataset consisting of handwritten digits from 0 to 9, GANs may generate any number as output without predictability. This lack of control hinders the practicality of GANs in real-world scenarios [31–33].

To address this issue, Conditional Generative Adversarial Networks (CGANs) are introduced. CGANs include a conditional variable that allows for control over the behavior of the generator network, constraining the output to a user-specified distribution and improving stability [34]. Adversarial training in CGANs not only enables the generation of accurate and realistic images but also helps in learning the relationships between data [35]. CGANs have found applications in various domains, including image synthesis for generating new images with specific attributes [36, 37], data augmentation to enhance the performance of ML models, style transfer for applying the style of one image to another, and text-to-image synthesis based on textual descriptions. Moreover, there have been several variations introduced in different fields, such as DCGAN [38] and DAGAN [39], among others [40, 41].

This paper primarily focuses on combining CGAN with traditional numerical simulation methods to predict the vibration noise of airfoil structures [42], reducing the cumbersome calculations involved in numerical methods and speeding up the prediction process of airfoil structure noise [43]. Figure 1 illustrates the process of establishing a surrogate model using CGAN.

2 Conditional generation adversarial neural network theory

2.1 Generate adversarial neural networks

Generative Adversarial Networks (GAN) are an innovative technology that combines deep learning with probability theory. It consists of two competing neural networks that have the ability to learn independently and aims to learn and mimic the distribution of real data through unsupervised learning [44, 45]. The basic structure of GAN includes a generator and a discriminator, which compete against each other during the iterative training process. The objective is to make the generated data resemble the characteristics of real data as much as possible [46]. The generator is responsible for creating data that can deceive the discriminator by making it appear close to authentic data, the discriminator aims to distinguish between genuine and synthesized data. In this process, both sides continuously learn and self-optimize, aiming to reach the Nash equilibrium point in game theory, where the generated data is indistinguishable from real data. The flowchart of the GAN process is shown in Figure 2.

The input to the generator model G is random noise z, and its output is a sample that resembles the distribution of real data. On the other hand, the input to the discriminator model D is either real data x or samples generated by G, denoted as G(z) [47]. When the input is x, the discriminator D outputs 1, and when the input is G(z), the discriminator D outputs 0. The abilities of G and D improve during the iterative training process and eventually reach an equilibrium state where D cannot distinguish between the two types of input data, indicating that the generator G has successfully approximated

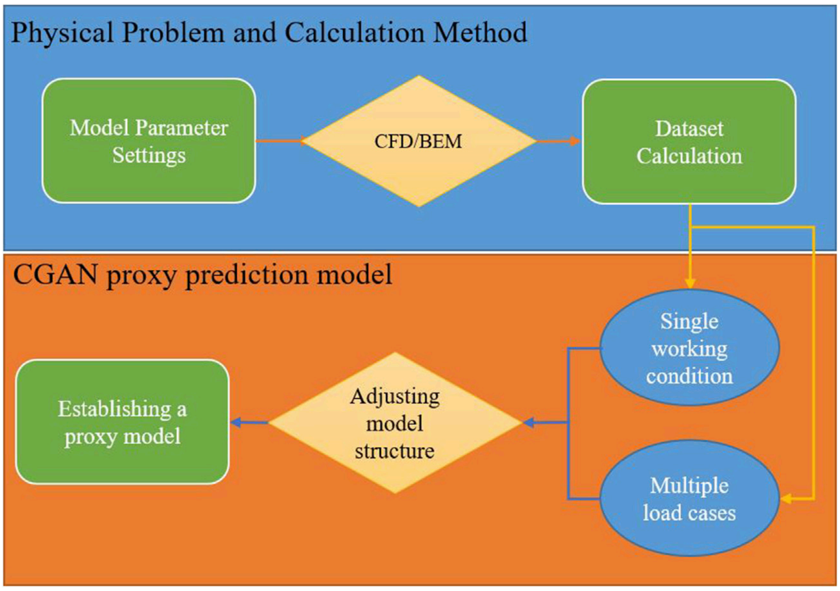

FIGURE 1
Process of establishing a proxy prediction model for predicting wing structure noise.

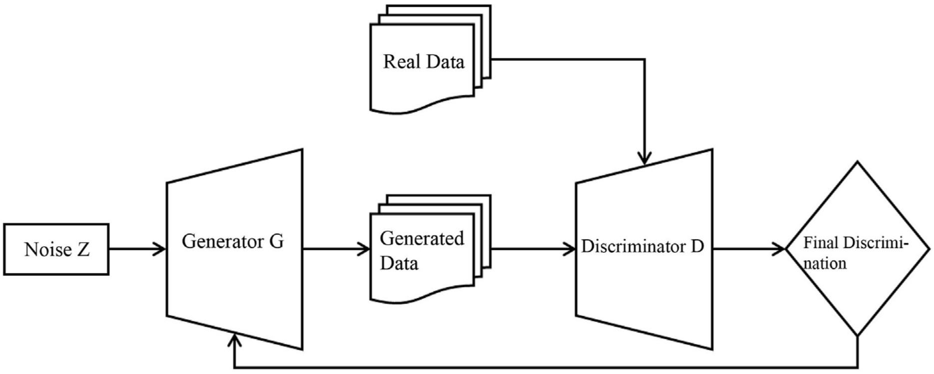

FIGURE 2
GAN process structure diagram.

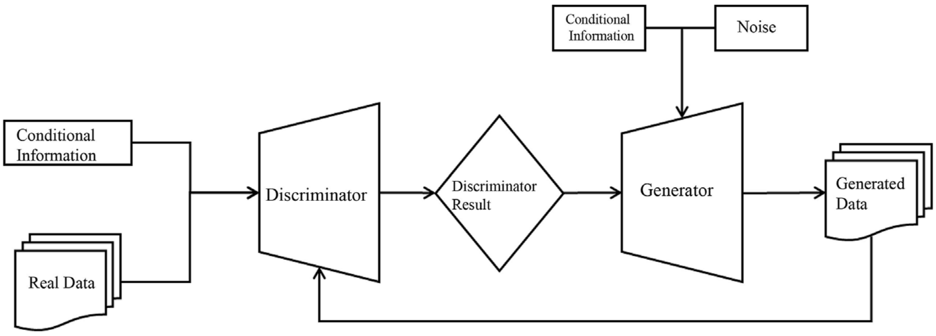

FIGURE 3
CGAN training flowchart.

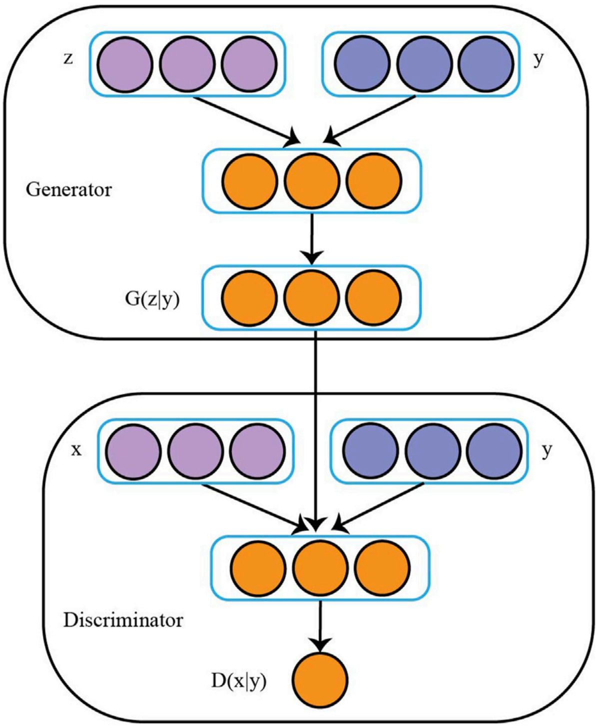

FIGURE 4
Schematic diagram of CGAN structure: Generator *G* and Discriminator *D*.

the distribution of real data [48]. The loss of GAN is closely related to the losses of G and D. The loss function of GAN is represented by Equation 1.

$$\min_{G}\max_{D} V(D,G) = E_{x\ P_{data}(x)}[\log D(x)] + E_{z\ P_z(z)}[\log(1 - D(G(z)))] \tag{1}$$

Both $P_{data}(\cdot)$ and $P_z(\cdot)$ represent the distribution of real data and noise data, respectively. In the training of GAN, the generator G is first fixed, and the discriminator D is trained with the main objective of improving D's ability to discriminate between the two sources of data [49]. Then, the discriminator model is fixed, and the generator model is trained to generate data that can deceive the discriminator as much as possible. The introduction of GAN has provided more possibilities for the development of deep learning, receiving extensive attention from scholars worldwide at that time. However, GAN also has its limitations, such as asynchronous training of the generator and discriminator, low accuracy of generated data, high variability in generated data, and difficulty in reaching an equilibrium state. These issues restrict the application of GAN in various fields, especially in practical engineering scenarios where many problems cannot be directly solved by formulas. To address these issues, researchers have proposed derivative models such as CGAN, which incorporates conditional information into the GAN framework, transforming the originally unsupervised learning GAN into a supervised learning approach. This provides a direction for data generation in GAN and greatly expands its application areas. Many subsequent variants of GAN have been inspired by CGAN. Therefore, in this study, we have decided to use CGAN for noise data prediction. The following sections will provide a detailed introduction to CGAN.

2.2 Conditional generation adversarial neural network

Conditional Generative Adversarial Networks (CGANs), developed by Mirza [13] introduce conditional variables into the model, which constrain the process of data generation and enable targeted generation of desired data. This model introduces conditional variables into the network architecture to guide the data generation process and achieve targeted generation of specific data. The CGAN architecture is similar to the original GAN [49], but with the addition of extra conditional variables, denoted as y, in both the generator G and discriminator D. This modification allows CGAN to operate as a controlled and supervised network model. The objective function of CGAN is presented in Equation 2, which

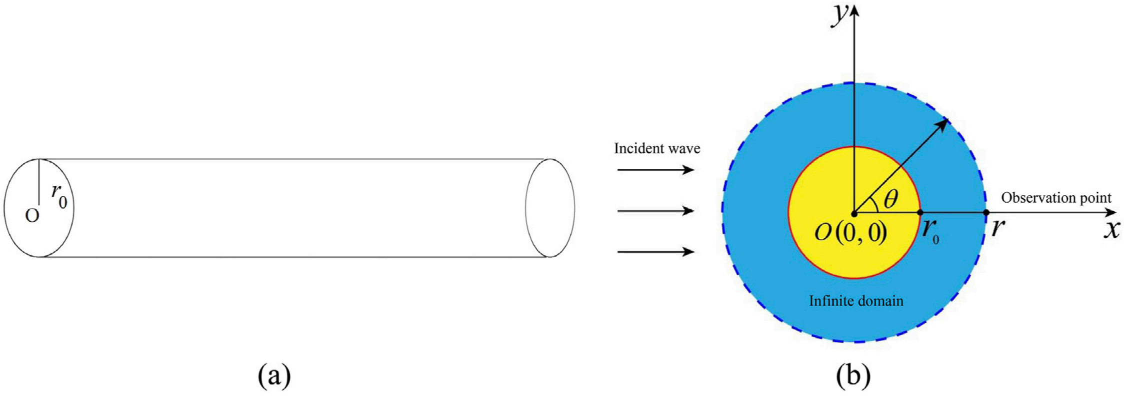

FIGURE 5
(A) Tubular structure; **(B)** Section diagram.

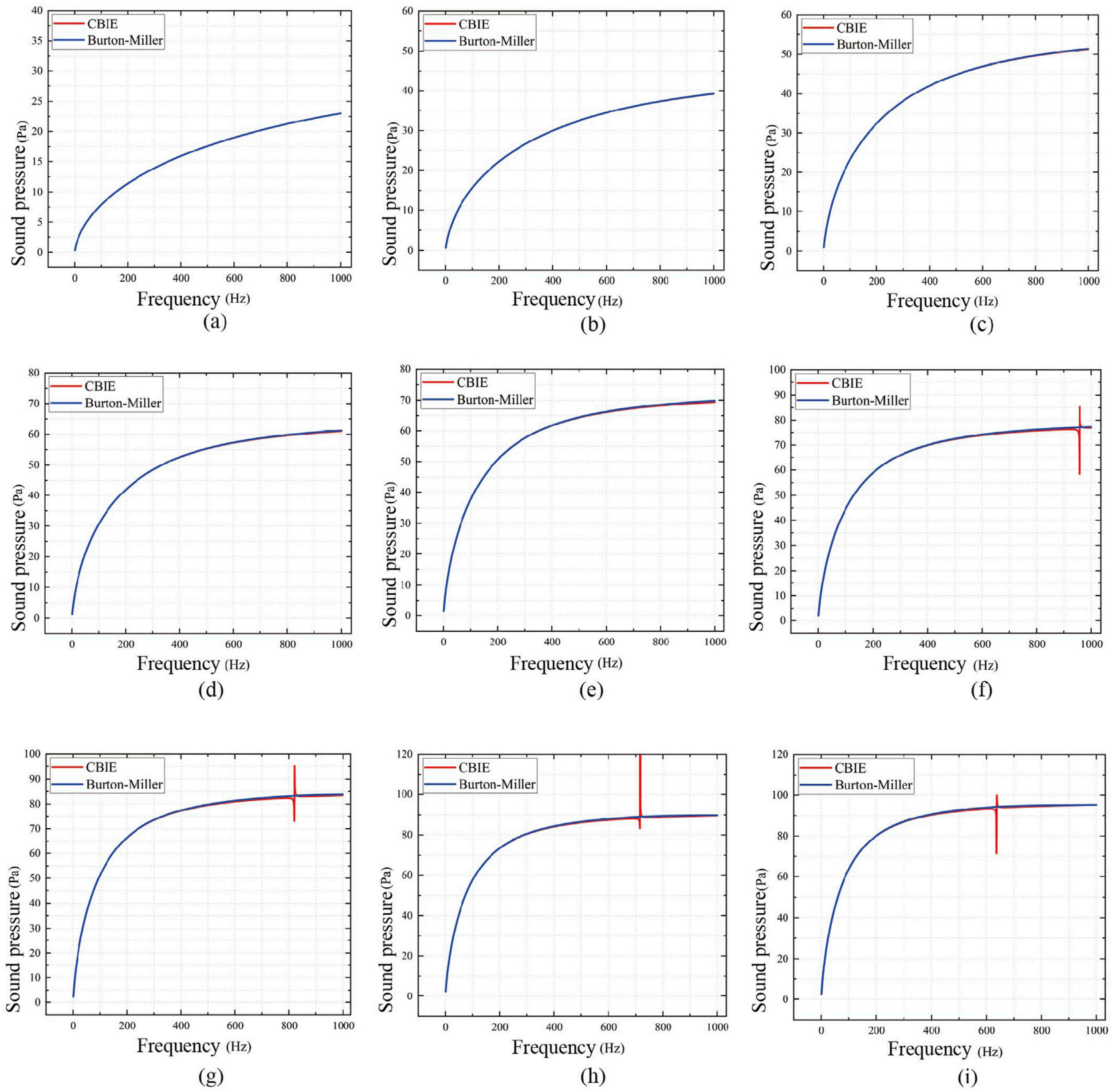

FIGURE 6
r_0 = 100,200, CBIE and Burton-Miller method for sound pressure calculation at 900 mm **(A–I)**.

incorporates conditional probabilities to form a constrained maximin function.

$$\min_G \max_D V(D,G) = E_{x\sim P_{\text{data}}(x)}[\log D(x|y)] + E_{z\sim P_z(z)}[\log(1-D(G(z|y)))] \quad (2)$$

Figure 3 presents the CGAN model, which is built upon the core concept of Nash equilibrium derived from game theory. It mainly consists of two network structures, G and D, which can be regarded as players in the game. G's function is to learn data distribution features from real data as much as possible, and then generate false data that may confuse the discriminator. The primary role of the discriminator is to effectively differentiate between real and generated data, thereby accurately determining the source of the data. To outperform each other, both the generator and discriminator must continuously enhance and optimize their abilities. This iterative process of improvement and optimization in CGAN aims to achieve a Nash equilibrium between the two components. For the generation model G, its input is random noise z and corresponding conditional information y, and its output is generated sample similar to real data distribution. The discriminator model D is designed to take real data x, corresponding conditional information y, and generated sample $G(y,z)$ as inputs. It assigns an output of 1 or 0, depending on whether the input is real data or a generated sample, respectively. Its main function is a dichotomous test. The mutual game optimization process of generator G and

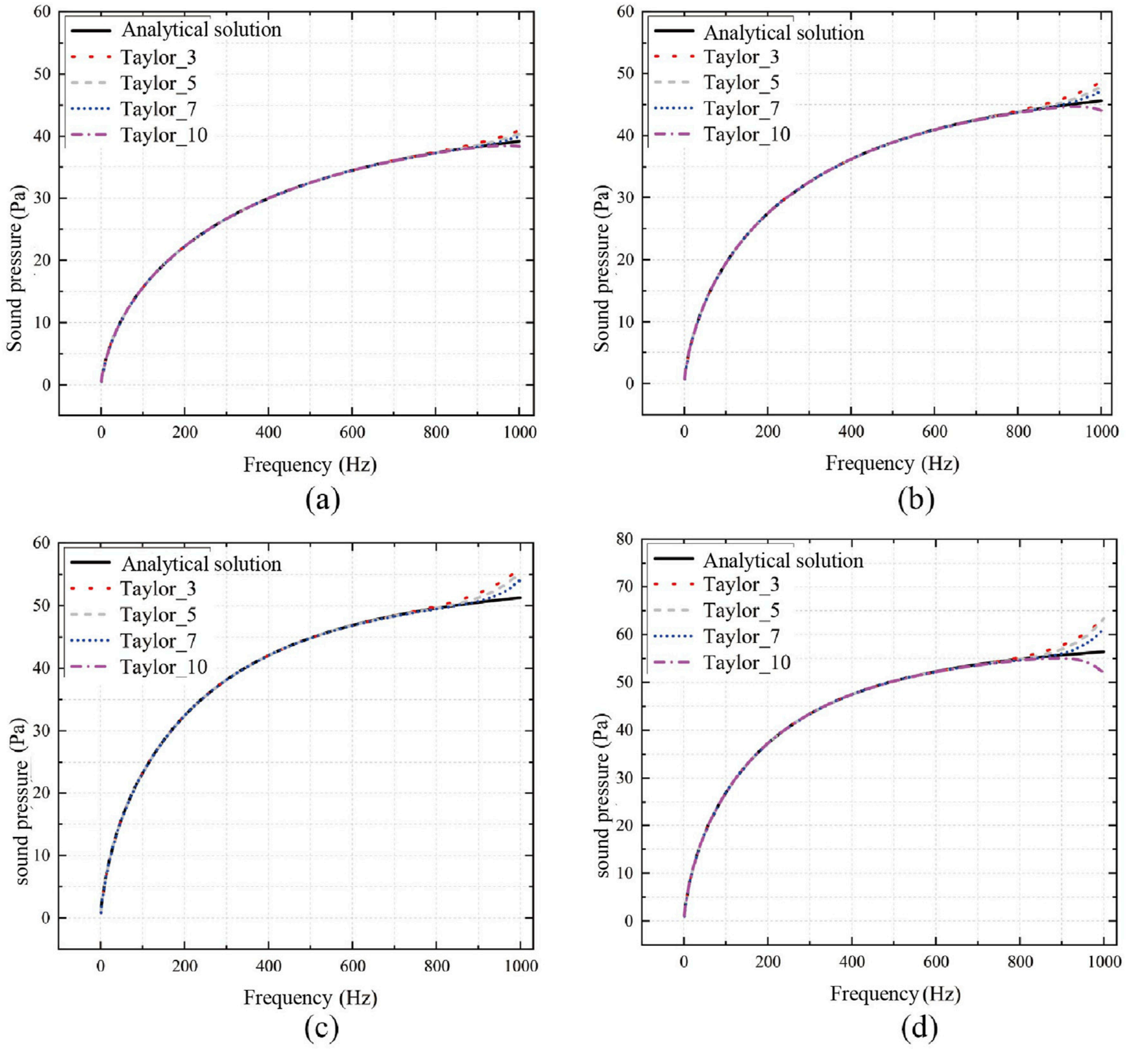

FIGURE 7
Sound pressure calculation results of Taylor's expansion method and analytical solutions for tubular structures. **(A)**: r_0 = 200 mm; **(B)** r_0 = 250 mm; **(C)** r_0 = 300 mm; **(D)** r_0 = 350 mm.

discriminator *D* makes the ability of *D* and *G* continuously improve and finally reach an equilibrium state, that is, discriminator *D* can no longer distinguish between the two types of input data. The training of CGAN is a process of *D* and *G* alternating repeatedly, so its loss function is closely related to the loss function of *D* and *G*, which can be expressed as Equation 3:

$$L(G,D) = E_{x,y,P_{data}(x,y)}[\log D(x,y)] + E_{y,p_y(y),z,p_z(z)}[\log(1 - D(G(y,z),y))] \tag{3}$$

where $P_{data}(x,y)$ represents the distribution of input data, $D(.)$ and $G(.)$ represent the output of *D* and *G* respectively, z is random noise. The loss function for *D* and *G* is written as Equation 5:

$$L_D = -E_{x,y,p_{data}(x,y)}[\log D(x,y)] - E_{z,p_z,y,p_y(z,y)}[\log(1 - D(G(z,y),y))] \tag{4}$$

$$L_G = E_{z,p_z,y,p_y(z,y)}[\log(1 - D(G(z,y)),y)] \tag{5}$$

where $\tilde{u} \gg$ u, and when the prediction accuracy of the neural network is high enough. The optimal result of the predicted value can be considered as the optimization result of the original problem.

After the introduction of conditional variables y, the discriminator and generator in CGAN are responsible for distinguishing between real and generated data under the given condition and generating corresponding data, respectively. Figure 4 illustrates the training process of CGAN, where both the generator G and discriminator D take into account the additional information y as inputs.

3 Acoustic boundary element method

First, the common Burton-Miller-based equation of boundary integral is employed to accurately evaluate the sound pressure field at broadband frequencies, as follows

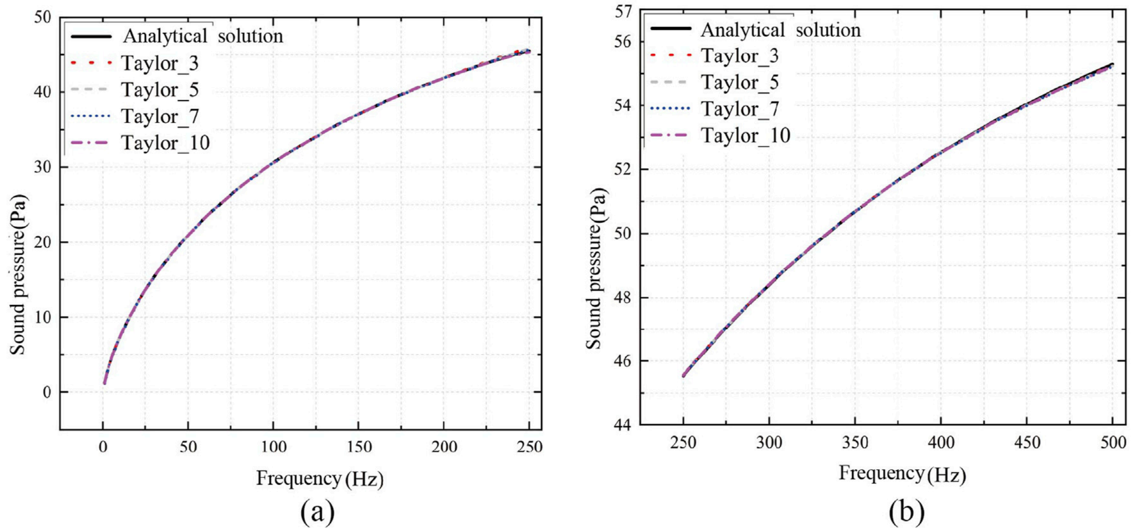

FIGURE 8
Sound pressure calculation results of Taylor's expansion method and analytical solution at [1,500]Hz when r_0 = 400 mm. **(A)** Frequency at [0,250]; **(B)** Frequency at [250,500].

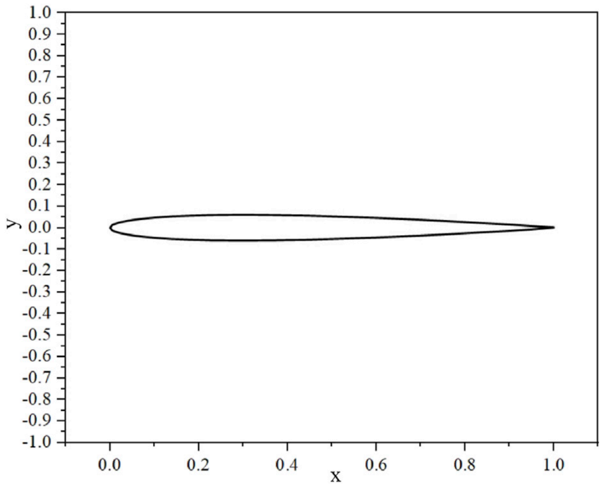

FIGURE 9
NACA0012 airfoil structure diagram.

$$C(\mathbf{x})\left(p(\mathbf{x})+\alpha q(\mathbf{x})\right)+\int_S F(\mathbf{x},\mathbf{y})p(\mathbf{y})\mathrm{d}S(\mathbf{y})+\alpha\int_S H(\mathbf{x},\mathbf{y})p(\mathbf{y})\mathrm{d}S(\mathbf{y})$$
$$=\int_S G(\mathbf{x},\mathbf{y})q(\mathbf{y})\mathrm{d}S(\mathbf{y})+\alpha\int_S K(\mathbf{x},\mathbf{y})q(\mathbf{y})\mathrm{d}S(\mathbf{y})$$
$$+\left[p_{\text{inc}}(\mathbf{x})+\alpha\frac{\partial p_{\text{inc}}(\mathbf{x})}{\partial n(\mathbf{x})}\right]$$

where α represents the coupling parameter: defined as $\alpha = \mathrm{i}/k$ where $k > 1$ and $\alpha = \mathrm{i}$ in other cases. The symbol k represents the wave number, where $k = c/\omega$, with ω being the angular frequency and c being the speed of sound. When the point of source $\mathbf{x}$ is located on a border that is smooth S, $C(\mathbf{x}) = 1/2$, the sound pressure is indicated by $p(\mathbf{x})$, $p(\mathbf{y})$ represents the sound pressure at the field point $\mathbf{y}$, while $q(\mathbf{y})$ represents its normal derivative. $p_{\text{inc}}(\mathbf{x})$ represents the plane wave's incident acoustic pressure. The function of Green $G(\mathbf{x},\mathbf{y})$ and the equation given in Equation 6 and its corresponding derivative are defined as follows.

$$\begin{cases} G(\mathbf{x},\mathbf{y}) = \dfrac{\mathrm{i}}{4}H_0^{(1)}(kr) \\ F(\mathbf{x},\mathbf{y}) = \dfrac{\partial G(\mathbf{x},\mathbf{y})}{\partial n(\mathbf{y})} = -\dfrac{\mathrm{i}k}{4}H_1^{(1)}(kr)\dfrac{\partial r}{\partial n(\mathbf{y})} \\ K(\mathbf{x},\mathbf{y}) = \dfrac{\partial G(\mathbf{x},\mathbf{y})}{\partial n(\mathbf{x})} = -\dfrac{\mathrm{i}k}{4}H_1^{(1)}(kr)\dfrac{\partial r}{\partial n(\mathbf{x})} \\ H(\mathbf{x},\mathbf{y}) = \dfrac{\partial^2 G(\mathbf{x},\mathbf{y})}{\partial n(\mathbf{x})\partial n(\mathbf{y})} = \dfrac{\mathrm{i}k}{4r}H_1^{(1)}(kr)n_j(\mathbf{x})n_j(\mathbf{y}) \\ \qquad\qquad -\dfrac{\mathrm{i}k^2}{4}H_2^{(1)}(kr)\dfrac{\partial r}{\partial n(\mathbf{x})}\dfrac{\partial r}{\partial n(\mathbf{y})} \end{cases} \tag{6}$$

where $H_n^{(1)}(kr)$ represents the nth order Hankel function of the first kind for the Green's function $G(x,y)$, $\mathrm{i} = \sqrt{-1}$, $r = |\mathbf{x}-\mathbf{y}|$ represents the distance between the source and field points, n_j is the Cartesian component of $n(\mathbf{x})$ or $n(\mathbf{y})$ and $\partial r/\partial n = r_{,j}n_j$.

The boundary of the structure's surface is discretized using constant elements. Subsequently, after gathering all the collocation points (nodes) at the center of each element, Equation 6 is reformulated in matrix form as follows.

$$\mathbf{Hp} = \mathbf{Gq} + \mathbf{p}_{\text{inc}} \tag{7}$$

In the above equation, H and G represent the coefficient matrices utilized in the BEM. These matrices are characterized by their high density and non-symmetry, and they also exhibit frequency-dependent variations. The vectors p and q are denoted by $\mathbf{p}$ and $\mathbf{q}$ respectively, and $\mathbf{p}_{\text{inc}}$ represents the incident wave vector. Taking into account the impedance boundary condition $q(\mathbf{x}) = \mathrm{i}k\beta(\mathbf{x})p(\mathbf{x})$, Equation 7 can be rewritten as

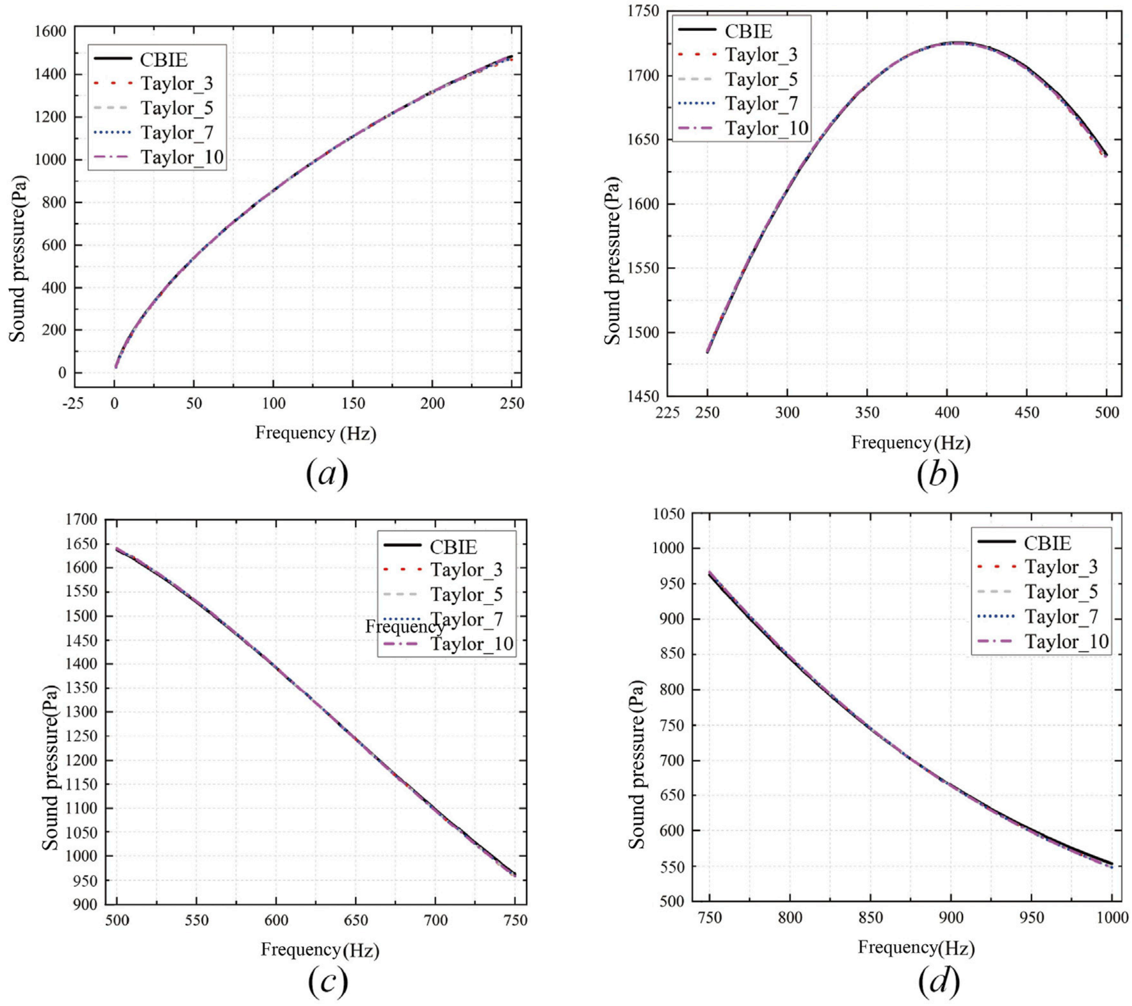

FIGURE 10
Frequency segmentation simulation results [**(A–D)**: 1–1000 Hz].

TABLE 1 Network structure and training parameter setting of CGAN.

Network structure	Number of hidden layers	Loss function	Activation function	Optimizer	Learning rate
Generator	3	Mean Squared Error	Sigmoid	Adam	0.0002
Discriminator	3	Mean Squared Error	Sigmoid	Adam	0.0002

$$\mathbf{p} = \mathbf{p}_{\text{inc}} \tag{8}$$

in which the diagonal matrix **B** can be expressed as Equation 9.

$$\mathbf{B} = \mathrm{i}k\begin{bmatrix} \beta_1 & \cdots & 0 \\ \vdots & \ddots & \vdots \\ 0 & \cdots & \beta_n \end{bmatrix} \tag{9}$$

where the normalized acoustic impedance value of the ith element is represented by β_i. Incorporating the external sound field, the sound pressure $\mathbf{p}_f$ can be represented as Equation 10.

$$\mathbf{p}_f = -\left[\mathbf{H}_f - \mathbf{G}_f\mathbf{B}\right]\mathbf{p} + \mathbf{p}_f^{\text{inc}} \tag{10}$$

where akin to the coefficient matrix in Equation 7, $\mathbf{H}_f$ and $\mathbf{G}_f$ stand for the coefficient matrices corresponding to field points $\mathbf{y}$ situated in the external acoustic domain. The Taylor expansion of the n-th order Hankel function of the first kind at the frequency $z_0 = k_0 r$ is given by

$$H_n^{(1)}(z) = \sum_{m=0}^{\infty} \frac{(z - z_0 r)^m}{m!}\left[H_n^{(1)}(z)\right]_{z=z_0}^{(m)} \tag{11}$$

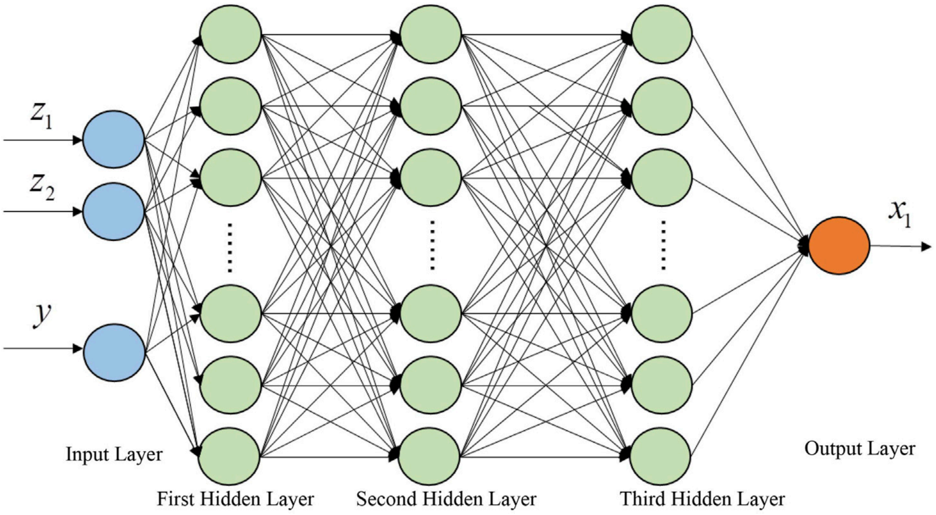

FIGURE 11
Network architecture of CGAN's generator.

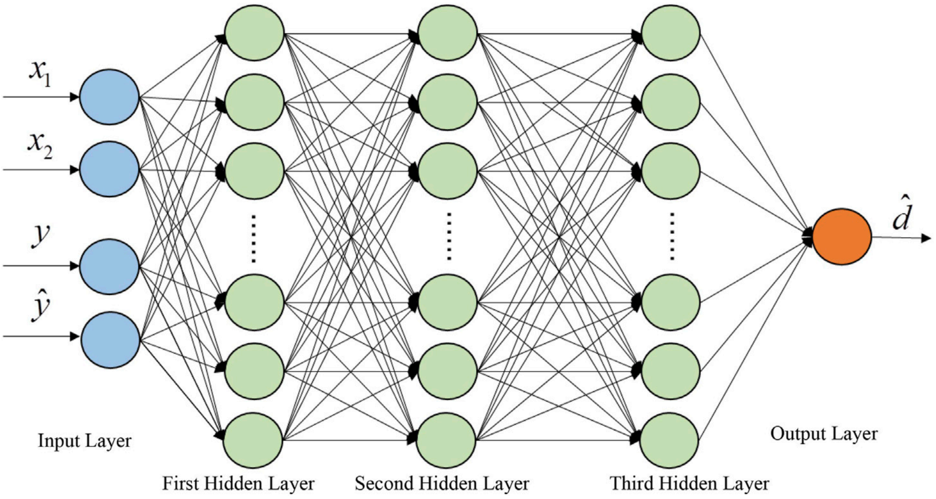

FIGURE 12
Network architecture of CGAN's discriminator.

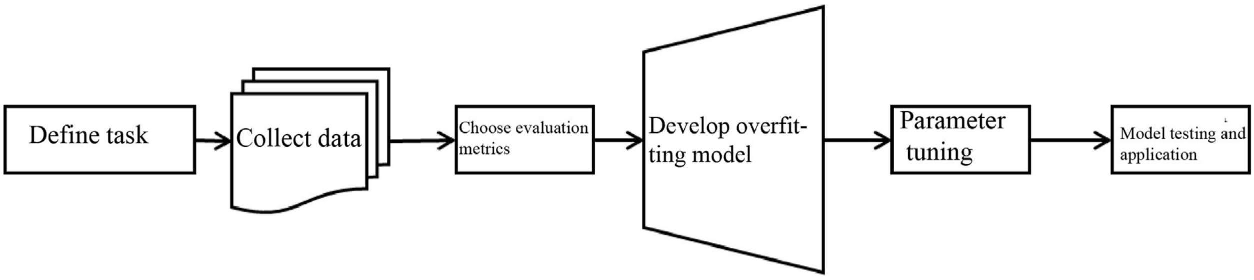

FIGURE 13
General modeling flowchart of machine learning.

TABLE 2 Development environment parameters table.

Operating system	Development framework	Programming language	Memory (GB)	GPU
Windows Server 2019	Tensorflow-GPU 2.6.0	Python	32	NVIDIA GeForce RTX 4090

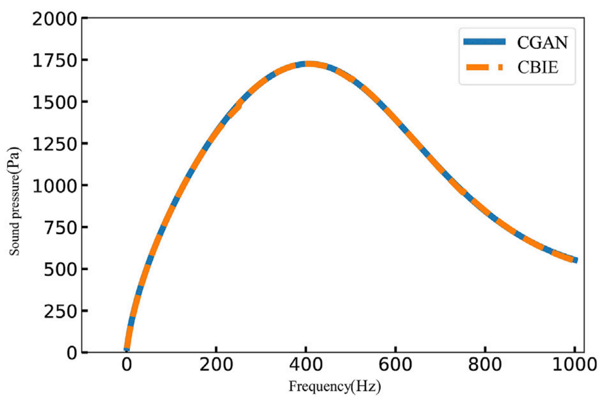

FIGURE 14
Prediction results of CGAN on the CBIE dataset for airfoil structure.

in which $[H_n^{(1)}(z)]_{z=z_0}^m = \frac{\mathrm{d}^m H_n^{(1)}(z)}{\mathrm{d}z^m}|_{z=z_0}$. Replacing z and z_0 with kr and $k_0 r$ respectively, we obtain the Taylor series expansion of the kernel function in Equation 6. As deriving an explicit expression for the m-th derivative of the n-th order Hankel function is highly intricate, this paper uses the recursive form as in Equation 12.

$$\frac{\mathrm{d}H_n^{(1)}(z)}{\mathrm{d}z} = \frac{n}{z}H_n^{(1)}(z) - H_{n+1}^{(1)}(z) \tag{12}$$

Through successive differentiations with respect to the variable z, we derive the recursive expression for the m-th derivative of the n-th order Hankel function.

$$\left[H_n^{(1)}(z)\right]^{(m)} = \sum_{i=1}^{m}\left[H_n^{(1)}(z)\right]^{(m-i)}\frac{(-1)^{i+1}(m-1)!}{z^i(m-i)!} - \left[H_{n+1}^{(1)}(z)\right]^{(m-1)} \tag{13}$$

Next, by substituting Equation 13 into Equation 11, we derive the expansion of $H_n^{(1)}(kr)$ at point k_0.

Combining Equations 6, 11, we can derive the expansion of the integral in Equation 4 at the point $\mathbf{y}$ as follows

$$\begin{aligned}
&\int_S F(\mathbf{x},\mathbf{y})p(\mathbf{y})\mathrm{d}S(\mathbf{y}) = \sum_{m=0}^{\infty}\frac{(k-k_0)^m}{m!}I_1^m \\
&\int_S G(\mathbf{x},\mathbf{y})q(\mathbf{y})\mathrm{d}S(\mathbf{y}) = \sum_{m=0}^{\infty}\frac{(k-k_0)^m}{m!}kI_2^m \\
&\alpha\int_S H(\mathbf{x},\mathbf{y})p(\mathbf{y})\mathrm{d}S(\mathbf{y}) = \sum_{m=0}^{\infty}\frac{(k-k_0)^m}{m!}\left(kI_3^m + k^2 I_4^m\right) \\
&\alpha\int_S K(\mathbf{x},\mathbf{y})q(\mathbf{y})\mathrm{d}S(\mathbf{y}) = \sum_{m=0}^{\infty}\frac{(k-k_0)^m}{m!}k^2 I_5^m
\end{aligned} \tag{14}$$

where

$$\begin{aligned}
I_1^m &= -\int_S \frac{\mathrm{i}r^{m-1}}{4}\left[zH_1^{(1)}(z)\right]_{z=k_0 r}^{(m)}\frac{\partial r}{\partial n(\mathbf{y})}p(\mathbf{y})\mathrm{d}S(\mathbf{y}) \\
I_2^m &= -\int_S \frac{\beta_i r^m}{4}\left[H_0^{(1)}(z)\right]_{z=k_0 r}^{(m)}p(\mathbf{y})\mathrm{d}S(\mathbf{y}) \\
I_3^m &= \int_S \frac{\alpha\mathrm{i}r^{m-1}}{4}\left[H_1^{(1)}(z)\right]_{z=k_0 r}^{(m)}n_j(\mathbf{x})n_j(\mathbf{y})p(\mathbf{y})\mathrm{d}S(\mathbf{y}) \\
I_4^m &= \int_S \frac{\alpha\mathrm{i}r^m}{4}\left[H_2^{(1)}(z)\right]_{z=k_0 r}^{(m)}\frac{\partial r}{\partial n(\mathbf{x})}\frac{\partial r}{\partial n(\mathbf{y})}p(\mathbf{y})\mathrm{d}S(\mathbf{y}) \\
I_5^m &= \int_S \frac{\alpha\beta_i r^m}{4}\left[H_1^{(1)}(z)\right]_{z=k_0 r}^{(m)}\frac{\partial r}{\partial n(\mathbf{y})}p(\mathbf{y})\mathrm{d}S(\mathbf{y})
\end{aligned} \tag{15}$$

In the integral I_1^m, the m-th derivative of the function $zH_1^{(1)}(z)$ is represented as Equation 16.

$$\left[(z)H_1^{(1)}(z)\right]^{(m)} = m\left[H_1^{(1)}(z)\right]^{(m-1)} + z\left[H_1^{(1)}(z)\right]^{(m)} \tag{16}$$

Substituting Equations 14, 15 into Equation 6 with impedance boundary conditions, we derive the following expression.

$$\begin{aligned}
C(\mathbf{x})p(\mathbf{x})\left(1+\alpha\mathrm{i}k\beta(\mathbf{x})\right) + \sum_{m=0}^{\infty}\frac{(k-k_0)^m}{m!}\left[I_1^m + k\left(-I_2^m + I_3^m\right) + k^2\left(I_4^m - I_5^m\right)\right] \\
= \left[p_{\mathrm{inc}}(x) + \alpha\frac{\partial p_{\mathrm{inc}}(x)}{\partial n(\mathbf{x})}\right]
\end{aligned} \tag{17}$$

Due to the presence of singularity in the kernel function and its normal derivative in Equation 6, not only is the behavior of this equation affected but it also has an impact on other associated expressions. Consequently, the boundary integrals involving a series of expansions in Equation 15 also exhibit singularity. Standard integration methods are insufficient to solve these singular integrals. Instead, techniques such as Cauchy principal value and Hadamard finite part integral must be employed to handle them.

To discretize Equation 17, the collocation method can be utilized along with constant elements. This results in the following expression.

$$\mathbf{Cp} + k\bar{\mathbf{C}}p + \sum_{m=0}^{\infty}\frac{(k-k_0)^m}{m!}\left[\mathbf{I}_1^m + k\mathbf{I}_2^m + k^2\mathbf{I}_3^m\right]\mathbf{p} = \mathbf{P}_{inc} \tag{18}$$

where C matrix can be expressed in the form of Equation 19.

$$\mathbf{C} = \begin{bmatrix} C_1 & & \mathbf{0} \\ & \ddots & \\ \mathbf{0} & & C_N \end{bmatrix} \quad \text{and} \quad \bar{\mathbf{C}} = \alpha\mathrm{i}\begin{bmatrix} \beta_1 C_1 & & \mathbf{0} \\ & \ddots & \\ \mathbf{0} & & \beta_N C_N \end{bmatrix} \tag{19}$$

Let matrices $\tilde{\mathbf{I}}_1^m$ and $\tilde{\mathbf{I}}_2^m$ be defined as Equation 20.

$$\tilde{\mathbf{I}}_1^m = \begin{cases} \mathbf{C} + \mathbf{I}_1^0, & m = 0 \\ \mathbf{I}_1^m, & m \neq 0 \end{cases} \quad \text{and} \quad \tilde{\mathbf{I}}_2^m = \begin{cases} \bar{\mathbf{C}} + \mathbf{I}_2^0, & m = 0 \\ \mathbf{I}_2^m, & m \neq 0 \end{cases} \tag{20}$$

Then, by setting $\mathbf{I}_3^m = \tilde{\mathbf{I}}_3^m$, Equation 18 can be redefined as Equation 21.

$$\left[\sum_{m=0}^{M}\frac{(k-k_0)^m}{m!}\left(\tilde{\mathbf{I}}_1^m + k\tilde{\mathbf{I}}_2^m + k^2\tilde{\mathbf{I}}_3^m\right)\right]\mathbf{p} = \tilde{\mathbf{P}}_{inc} \tag{21}$$

This expression includes only the initial M terms of the Taylor expansion. Since matrices $\tilde{\mathbf{I}}_1^m$, $\tilde{\mathbf{I}}_2^m$, and $\tilde{\mathbf{I}}_3^m$ are not influenced by

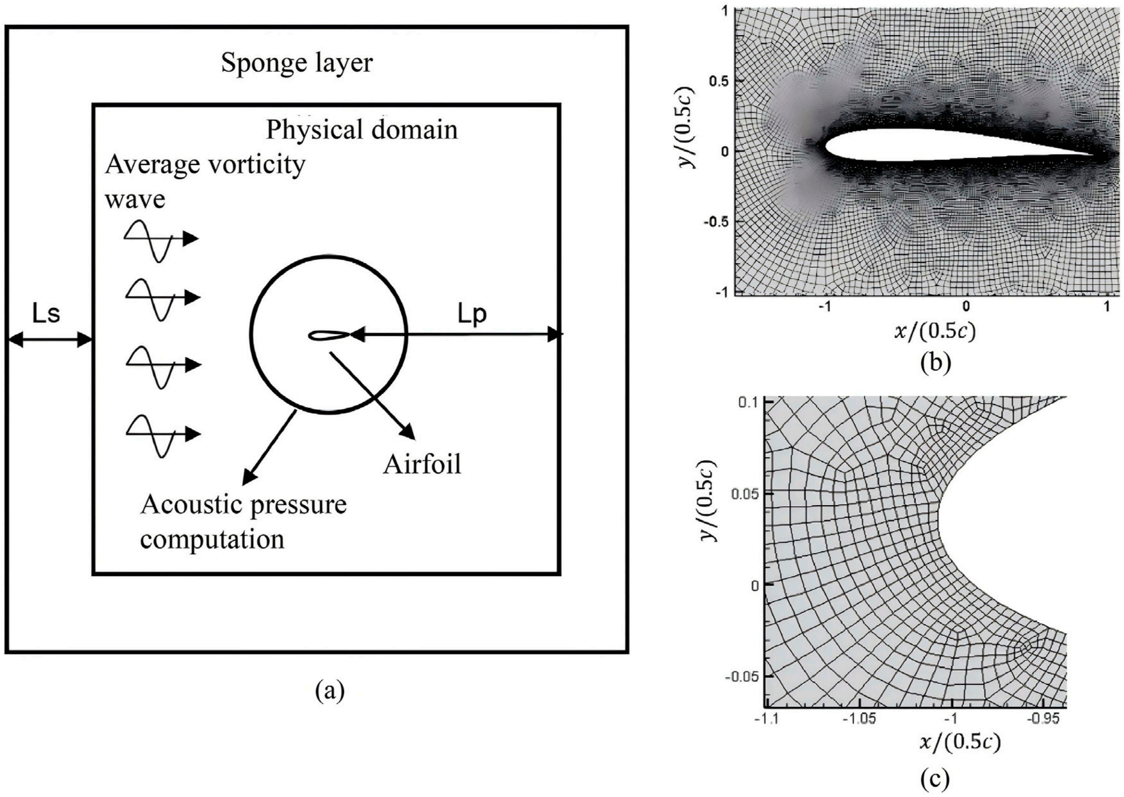

FIGURE 15
Examples of two-dimensional meshes used in current research. **(A)** Sketch the computational domain. **(B)** The grid near the wings. **(C)** Enlarged view near the leading edge.

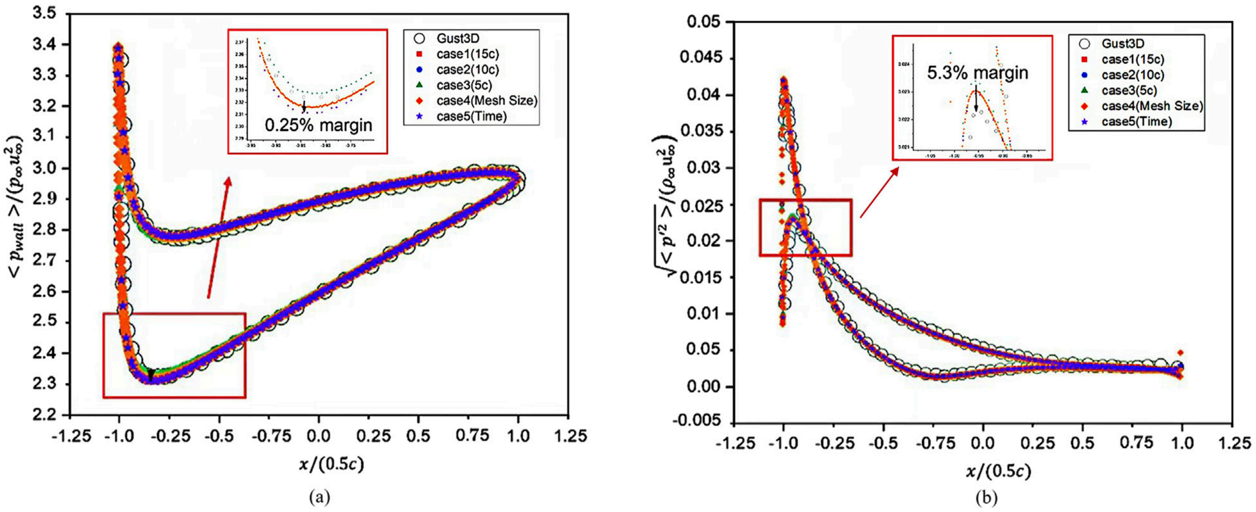

FIGURE 16
(A) average pressure distribution on the airfoil surface and **(B)** RMS pressure on the airfoil surface.

frequency, they can be computed just once for wideband acoustic analysis. This helps to eliminate the significant computational cost associated with repeatedly calculating Equation 8 for different frequencies.

4 Numerical examples

In this section, the validation of the previously proposed methods was conducted [50]. First, the BEM method was

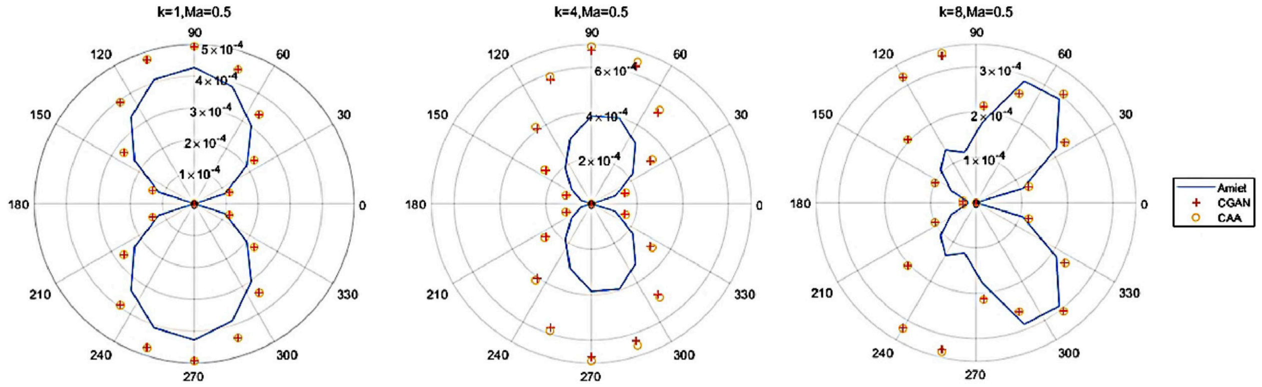

FIGURE 17
Comparison of far-field sound pressure prediction results when wave number k = 1,4,8 and Mach number Ma = 0.5.

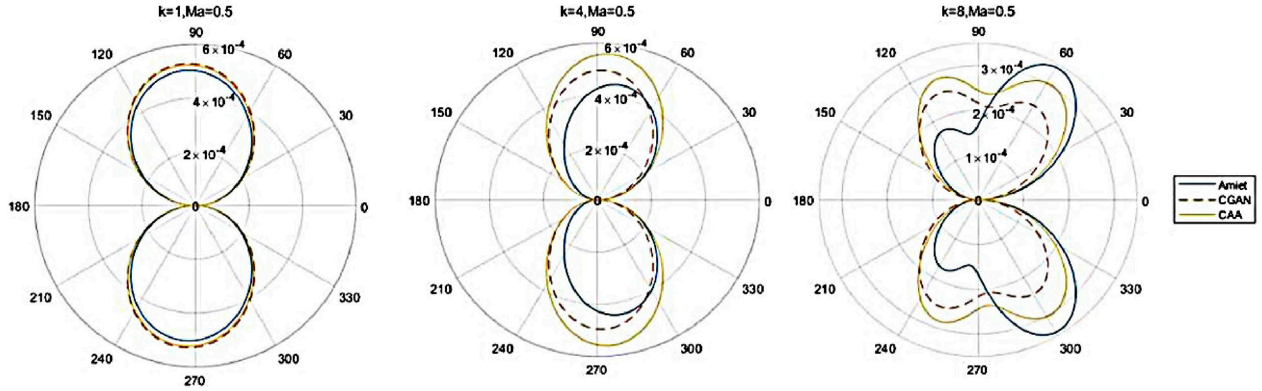

FIGURE 18
Comparison of prediction results of CGAN on sound pressure data under unknown working conditions.

verified, followed by the establishment of the BEM-CGAN wing noise surrogate prediction model based on BEM data integrated with CGAN. Additionally [51–53], the CAA-CGAN model validation was performed, along with the prediction of a propeller wake model.

4.1 The wing structural vibration and noise prediction model based on BEM-CGAN

First, consider the two-dimensional acoustic field calculation model of the tubular structure as shown in Figure 5. Let r_0 be the radius of the cylindrical shell. In the acoustic field calculation, a normal velocity $v_0 = 9.6\times 10^{-5}$m/s is provided, which is generated by the internal pressure of the pipe wall. The boundary condition is set at the observation point r (2 m, 0 m).

The 2D cylindrical shell surface is uniformly discretized into 100 constant elements. When the pipe radius r0 is set to 100, 150, 200 . . . , 900 mm, and the frequency f ranges from 0 to 1000 Hz (with a step size of 1 Hz), Figure 6 presents the frequency response curves of sound pressure amplitudes computed using the conventional boundary element method (referred to as CBIE) and the Burton-Miller method. From Figure 6, several conclusions can be drawn: as the pipe radius increases, the sound pressure at the observation location also increases. The results obtained using the CBIE method and the Burton-Miller method are essentially the same. However, when the radius $r_0 \geq 600$mm, the CBIE method exhibits false peak issues, while the Burton-Miller method can effectively resolve this problem.

The comparison between the Taylor expansion method and the analytical solution is shown in Figure 7. The acoustic pressure results for different pipe structure radii r_0 were obtained using the Taylor expansion-based boundary element method in the frequency range of [1, 1,000] Hz with a frequency step size of 1 Hz.

From Figure 7, it is evident that as the number of terms in the Taylor expansion increases, the numerical solution approaches the analytical solution more closely. Notably, there are substantial disparities in the boundaries of the frequency range, primarily because the fixed frequency expansion point is positioned in the middle of the frequency range. The numerical results become increasingly inaccurate as one moves farther away from the fixed frequency expansion point. To validate this hypothesis, simulations were conducted for the radius r_0 = 400 mm with frequency ranges of

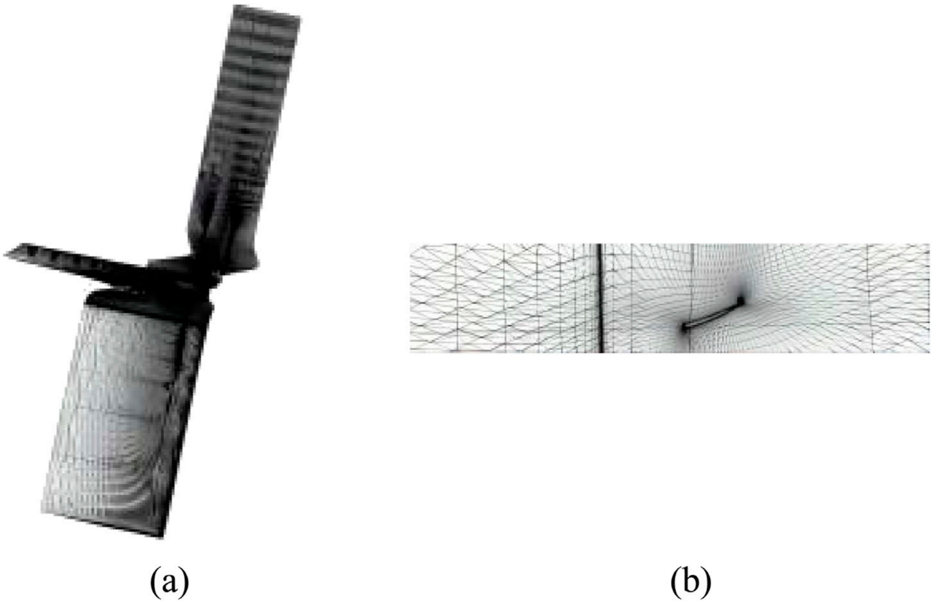

FIGURE 19
Schematic Diagram of the Contra-Rotating Propeller Grid Model and Local View of the Rear Blade: **(A)** Regarding the mesh model of a propeller; **(B)** Regarding the local image of a propeller's trailing blade.

TABLE 3 Input and output variables of CGAN under single operating conditions.

Input variables	Output variables	Hidden layer settings	Learning rate
x, y	V	66,89,105,154,121,87,65	0.0002

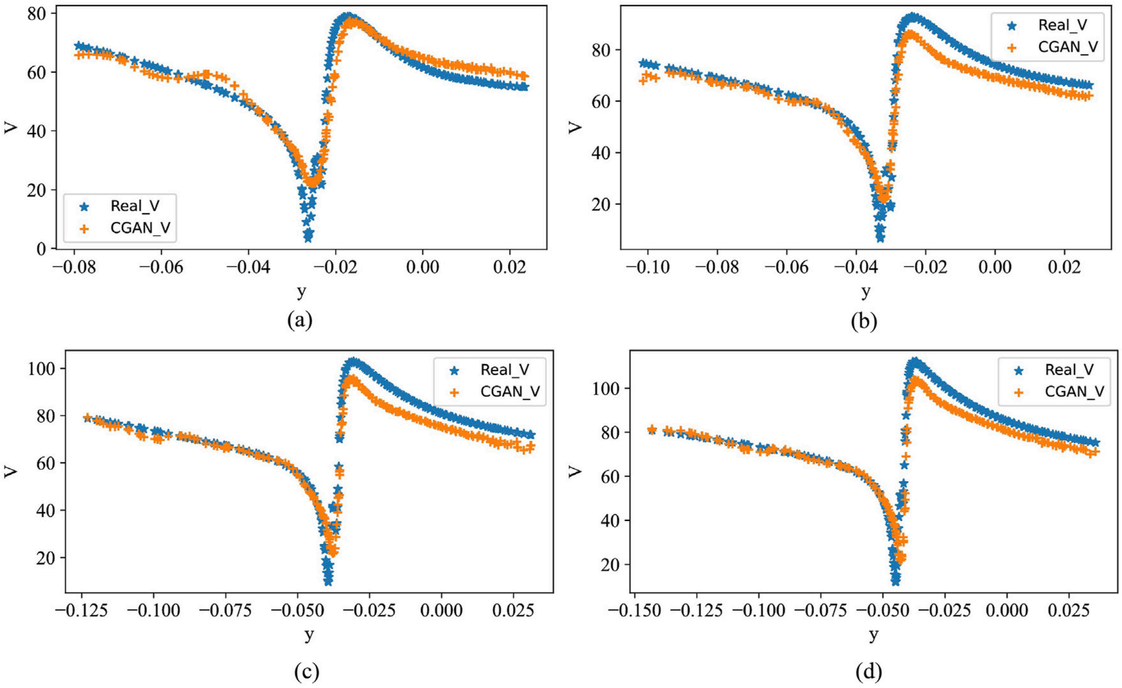

FIGURE 20
The velocity distribution on the tangent line of the leading edge of the rear blade of a counter rotating propeller (wind speed:30 m/s,rotational speed:2500 *r*/min). **(A)** Cross-Section 1; **(B)** Cross-Section 2; **(C)** Cross-Section 3; **(D)** Cross-Section 4.

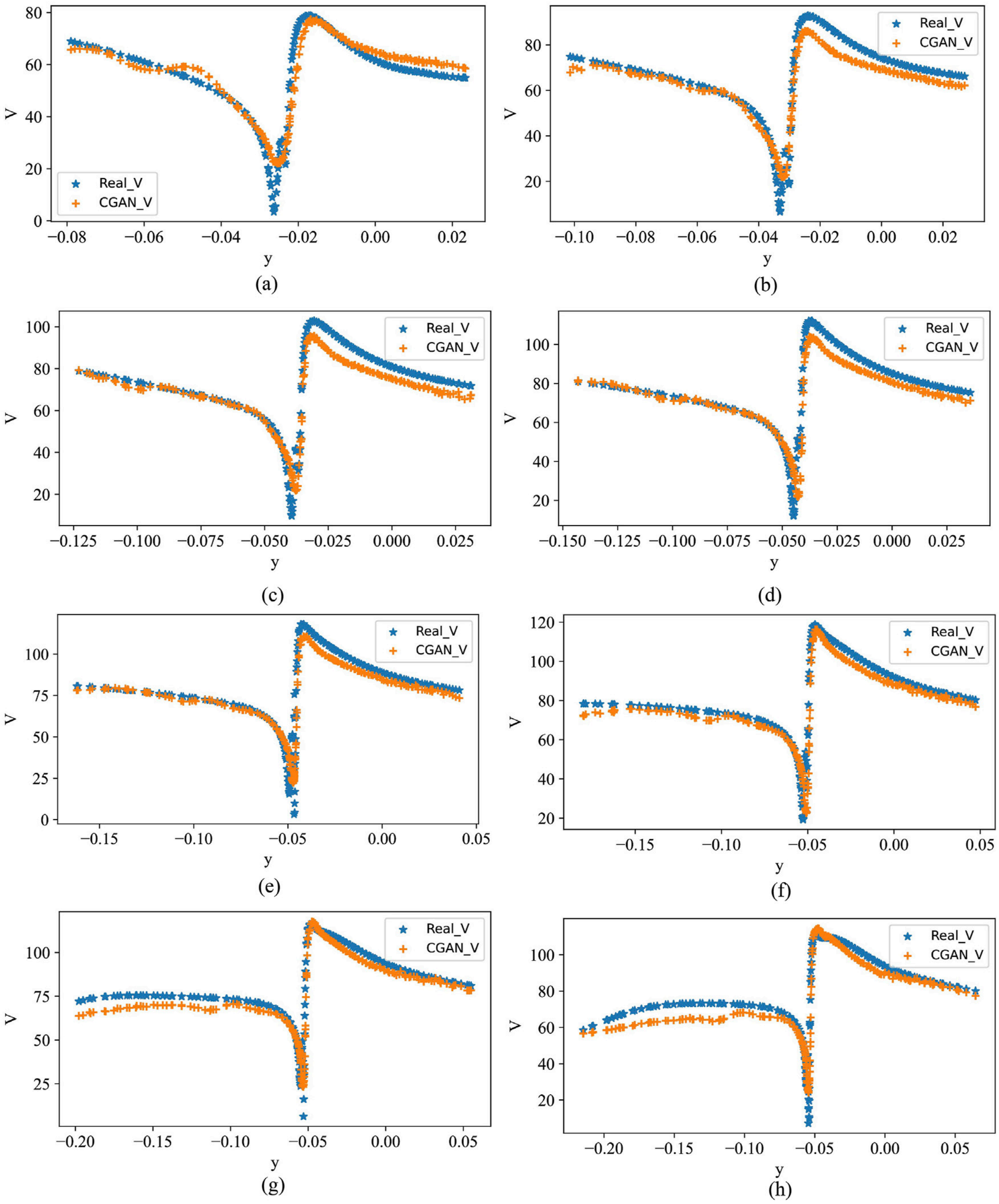

FIGURE 21
Prediction results of CGAN on a test set with wind speed of 50 *m/s* and rotational speed of 5,500 *r/min*. **(A)** Cross-Section 1; **(B)** Cross-Section 2; **(C)** Cross-Section 3; **(D)** Cross-Section 4; **(E)** Cross-Section 5; **(F)** Cross-Section 6; **(G)** Cross-Section 7; **(H)** Cross-Section 8.

[1, 250] Hz and [250, 500] Hz. Figure 8 presents the simulated results.

So far, the numerical methods used in this study have been validated. Next, these methods will be applied to simulate the airfoil structure, providing sample data for the construction of the BEM-CGAN model. The airfoil model used in this study is the NACA0012 airfoil, and its structure is shown in Figure 9.

The sound pressure in the frequency range of [1–1,000] Hz, the first approach utilized is the CBIE method together with the fast sweeping method, both of which rely on Taylor expansion. This frequency band is further divided into [1–250], [250–500], [500–750], and [750–1,000]. Then, these two methods are used for simulation, and the results are shown in Figure 10.

Based on Figure 10, it can be observed that as the frequency band decreases, the error between the results obtained from the fast sweeping method based on Taylor expansion and the CBIE method decreases. Therefore, we can conclude that as the frequency band becomes smaller, the results obtained from the

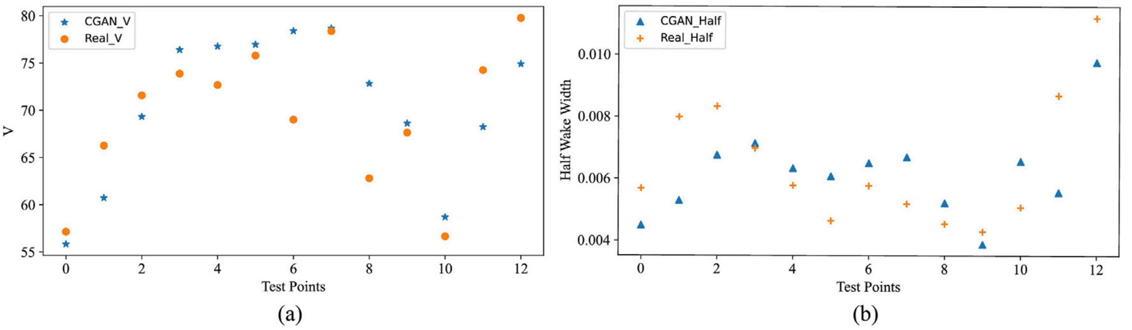

FIGURE 22
Comparison between CGAN's predicted results on the test set and the actual results: **(A)** The speed prediction results of CGAN; **(B)** Prediction results of half wake width for CGAN.

fast sweeping method based on Taylor expansion become closer to the true solution. At this point, the obtained samples can serve as the foundation for training the CGAN model. Next, let's analyze the modeling and prediction results of the CGAN model using the airfoil structure in the [1–1,000] Hz frequency range as an example. For the noise prediction problem of the airfoil, the discriminator and generator of the CGAN can be viewed as regression models. Therefore, the Mean Squared Error (MSE) function is selected as the loss function, and the Sigmoid function is chosen as the activation function. The capability of the generator and discriminator should approach a balance, and the representation has a relatively small parameter dimension. Thus, both the generator and discriminator adopt fully connected neural networks with three hidden layers. The network structure configuration for the CGAN model is presented in Table 1, and the schematic diagram of the network structure is shown in Figures 11, 12. The general modeling flowchart of machine learning is shown in Figure 13.

In Figure 11, z_1 and z_2 represent the random vectors input to the generator. y represents the label information, where in this case it corresponds to the frequency information. x_1 represents the generated data, which is the sound pressure at the observation points. In the discriminator, x_2 represents the real data, apologies for the confusion. In the discriminator, $\hat{y}$ represents the label information, specifically the frequency information. $\hat{d}$ represents the judgment result of the discriminator's output layer, indicating the discriminator's classification of the input as real or fake. x_2 represents the real data. The machine learning modeling in this study was conducted on a desktop workstation with the following specifications: Windows Server 2019 as the operating system, 32 GB of memory, an NVIDIA GeForce RTX 4090 GPU, TensorFlow-GPU 2.6.0 as the development framework, and Python as the programming language. The detailed contents can be found in Table 2. After setting the CGAN parameters, the sound pressure data of the wing structure calculated by CBIE in the frequency range of [1, 1,000] Hz was used as the dataset and input into CGAN for training. The testing dataset was also set to be the same as the training dataset to validate the applicability of CGAN. The predicted results are shown in Figure 14. From the figure, it can be seen that the predictions of CGAN align well with CBIE itself, indicating a good agreement. Subsequently, the next step of testing was performed by extracting 3/4 of the data from the CBIE dataset as the training set and the remaining 1/4 of the data as the testing set to evaluate the generalization performance of the CGAN model. Supplementary Figure 1 illustrates the performance of CGAN on the testing set. From the figure, it can be observed that the predicted results of CGAN on the testing set exhibit a good consistency with CBIE itself, demonstrating that CGAN can be applied in the field of regression prediction. These results validate the effectiveness and generalization capability of the CGAN model in predicting the sound pressure data of the wing structure.

4.2 Interference noise prediction model for wing vortex with CAA-CGAN

In the next step, the data obtained from simulating the structural vortex interference noise of the wing using computational aeroacoustics (CGAA) method is combined with CGAN to establish a proxy prediction model called CAA-CGAN [12]. The NACA0012 airfoil is chosen as the reference airfoil, having a thickness of 0.12c, degree of deflection 0.02c, and an angle of attack $a = 2^{\circ}$, where c represents the chord length of the airfoil. k is a wave number vector and ε is a small parameter, satisfy $\varepsilon \ll 1$. The model and grid are shown in Figure 15.

For wind speed with wave numbers $k_1 = k_2 = 1$, Figure 16 presents the average wall pressure P_{wall} and root-mean-square and compares them with the benchmark reference values provided by [54].

Based on the observation from the graph, we believe that the data obtained from CAA calculations is accurate and effective, making it suitable for training data in the subsequent CGAN modeling. Next, we will proceed with the establishment of the CAA-CGAN model. The configuration information is set as follows: for wave numbers k = 1,4,8, Ma = 0.1, 0.2, . . . , 0.7, and the far-field angles of the airfoil are considered as conditional information. The output data will be the calculated sound pressure from the CAA.

First, the generalization prediction ability of CGAN under a single operating condition is tested. The Mach number (Ma) and far-field azimuth are used as conditional information, and the far-field sound pressure data is considered as the data to be generated. For each operating condition, the dataset is divided into a 9:1 ratio for training and testing. The CGAN is used to learn and predict the CAA dataset, and the outcomes are then contrasted with the forecasts made by the Amiet theory. Figure 17 shows the far-field sound pressure results at different wave numbers for a Mach number of 0.5, on a circular region with a radius of $4c$.

After conducting the generalization testing, we extend the predictive model to predict the far-field sound pressure data under unknown operating conditions. The specific procedure is as follows: we extract the data from the training set at wave numbers $k = 1$, 4, 8, and Mach number $Ma = 0.5$, and use it as the test set. We evaluate the accuracy of the CAA-CGAN predictive model when predicting far-field sound pressure data under unknown operating conditions. Figure 18 presents a comparison of the predictive results from CGAN, CAA, and the predictions based on Amiet theory.

From the graph, it can be observed that the predictive results from CGAN align well with the data from CAA, and the accuracy is stronger compared to the results obtained from Amiet theory.

4.3 Regarding the prediction of the velocity profile of a propeller wake

Finally, we validate the model using an example of a propeller wake. The model structure, as shown in Figure 19A, divided the domain into 12 million grids. RANS algorithm was employed in the simulation using Numeca software. The detailed diagram of the model is presented in Figure 19B. Firstly, we verified the effectiveness of CGAN in predicting the flow field data of a propeller under a single operating condition. Then, we considered using CGAN to predict the velocity distribution and key parameters of the propeller wake under multiple operating conditions. In this example, the main operating condition information considered was the wind speed and propeller rotation speed.

Firstly, under fixed wind speed and rotation speed conditions, the three-dimensional flow field of the propeller wake was divided into 13 planes. The velocity distribution at the trailing edge of the rear propeller blade was extracted. CGAN was used for the adaptability test of predicting the velocity distribution and semi-wake width of the propeller wake. The input and output parameters of CGAN are shown in Table 3.

Secondly, we verify the applicability of CGAN by testing it on the training dataset itself. The data from the cases with a wind speed of 30 m/s and a rotation speed of 2,500 r/min are selected as the overall dataset. A portion of the wind speed distribution data from these cases is chosen as the training and testing sets. After 2,000 iterations of training, the predictive results of CGAN are shown in Figure 20.

Testing on the dataset under a single operating condition indicates that CGAN has the potential to be applied to such problems. Therefore, further exploration of CGAN's generalization performance is needed.

From a practical perspective, what we often need is complete data for any operating condition, rather than partial data for specific conditions. Therefore, both the wind speed and velocity will be used as input variables, while other settings will be similar to before. Following the previous applicability test, the next step is to directly perform generalization testing. After multiple rounds of debugging, the number of hidden layers in CGAN has been increased to 10. The overall dataset consists of 27 sets of data under varying wind speeds and rotation speeds. The data with a wind speed of 50 m/s and a rotation speed of 5,500 r/min are selected as the testing set, and the results after 20,000 iterations of training are shown in Figure 21.

Figure 21 shows the velocity distribution along the tangential plane at 10 cross-sections of the propeller's leading edge under the experimental conditions, yielding fairly accurate results. Additionally, we also predicted the velocity loss and half-wake width at a wind speed of 30 m/s and rotational speed of 4,800 rpm. The predicted results by the CGAN are shown in Figure 22.

In Figure 22A shows the summary prediction results of the CGAN for velocity, while Figure 22B shows the summary results for the half-wake width. The half-wake width data was obtained through simple calculations on the initial data. The horizontal axis represents the test points corresponding to 13 cross-sections under this operating condition.

It is worth mentioning that when using CGAN to establish a surrogate prediction model, the generator of CGAN has an important parameter: the noise vector. In previous applications for image generation, this vector often had dozens or even hundreds of dimensions to ensure the richness of generated images. However, in the present study, a high-dimensional noise vector would not only lead to some generated data deviating from the desired results, but also significantly increase the complexity of the network structure in order to meet the accuracy requirements.

5 Conclusion

This study combines three numerical methods with Conditional Generative Adversarial Networks (CGANs) to establish a surrogate modeling approach for predicting the noise of airfoil structures. The main findings are as follows:

1. The combination of BEM, CAA, CFD, and CGANs has been explored to investigate the applicability of CGANs to this type of problem.
2. The surrogate prediction model established through CGANs reduces significant computation time, aiding in speeding up the optimization and design process of airfoil structures.
3. Modifying certain structures of CGANs proves beneficial for handling regression problems in this research.

However, this approach has some limitations. It may struggle to achieve ideal prediction results when the data dimension is too high or when there is poor correlation between the data, rendering the predictions unreliable. To address these limitations, our future research will focus on developing more efficient numerical algorithms. Additionally, exploring advanced deep learning techniques to improve the accuracy of the surrogate model. By doing so, we aim to overcome these challenges and enhance the reliability and accuracy of the surrogate prediction model.

Data availability statement

The original contributions presented in the study are included in the article/Supplementary Material, further inquiries can be directed to the corresponding authors.

Author contributions

SJ: Writing–review and editing, Writing–original draft. YL: Writing–review and editing, Writing–original draft. YC: Writing–original draft. LG: Writing–original draft.

Funding

The author(s) declare that financial support was received for the research, authorship, and/or publication of this article. This research was supported by the State Key Laboratory of Aerodynamics (Grant No. SKLA2022KFKT007), and the Laboratory of Aerodynamic Noise Control (Grant No. ANCL 20230306).

Conflict of interest

The authors declare that the research was conducted in the absence of any commercial or financial relationships that could be construed as a potential conflict of interest.

Publisher's note

Supplementary material

The Supplementary Material for this article can be found online at: https://www.frontiersin.org/articles/10.3389/fphy.2024.1452876/full#supplementary-material

SUPPLEMENTARY FIGURE 1
Comparison of CGAN's prediction results on the test set with CBIE results.

References

1. Hubbard HH. Sound from dual-rotating and multiple single-rotating propellers. *Tech Rep* (1948).

2. Parry AB. *Theoretical prediction of counter-rotating propeller noise*. University of Leeds (1988). Ph.D. thesis.

3. Qu Y, Zhou Z, Chen L, Lian H, Li X, Hu Z, et al. Uncertainty quantification of vibro-acoustic coupling problems for robotic manta ray models based on deep learning. *Ocean Eng* (2024) 299:117388. doi:10.1016/j.oceaneng.2024.117388

4. Marburg S, Schneider S. Performance of iterative solvers for acoustic problems. Part I. Solvers and effect of diagonal preconditioning. *Eng Anal Boundary Elem* (2003) 27: 727–50. Special issue on Acoustics. doi:10.1016/S0955-7997(03)00025-0

5. Marburg S, Hardtke H-J. Shape optimization of a vehicle hat-shelf: improving acoustic properties for different load cases by maximizing first eigenfrequency. *Comput and Structures* (2001) 79:1943–57. doi:10.1016/S0045-7949(01)00107-9

6. Kostas K, Ginnis A, Politis C, Kaklis P. Ship-hull shape optimization with a T-spline based BEM—isogeometric solver. *Computer Methods Appl Mech Eng* (2015) 284:611–22. Isogeometric Analysis Special Issue. doi:10.1016/j.cma.2014.10.030

7. Lian H, Wu P. The shape optimization of underground caverns based on strain energy criterion via explicit interface tracking methods. *Int J Adv Eng Sci Appl Mathematics* (2020) 12:183–92. doi:10.1007/s12572-020-00281-7

8. Li S, Trevelyan J, Wu Z, Lian H, Wang D, Zhang W. An adaptive SVD-Krylov reduced order model for surrogate based structural shape optimization through isogeometric boundary element method. *Computer Methods Appl Mech Eng* (2019) 349:312–38. doi:10.1016/j.cma.2019.02.023

9. Liu Z, Bian P, Qu Y, Huang W, Chen L, Chen J, et al. A galerkin approach for analysing coupling effects in the piezoelectric semiconducting beams. *Eur J Mechanics-A/Solids* (2024) 103:105145. doi:10.1016/j.euromechsol.2023.105145

10. Lian H, Kerfriden P, Bordas S. Implementation of regularized isogeometric boundary element methods for gradient-based shape optimization in two-dimensional linear elasticity. *Int J Numer Methods Eng* (2016) 106:972–1017. doi:10.1002/nme.5149

11. Jin Y, Hou L, Lu Z, Chen Y. Crack fault diagnosis and location method for a dual-disk hollow shaft rotor system based on the radial basis function network and pattern recognition neural network. *Chin J Mech Eng* (2023) 36:35. doi:10.1186/s10033-023-00856-y

12. Cao G, Yu B, Chen L, Yao W. Isogeometric dual reciprocity bem for solving non-fourier transient heat transfer problems in fgms with uncertainty analysis. *Int J Heat Mass Transfer* (2023) 203:123783. doi:10.1016/j.ijheatmasstransfer.2022.123783

13. Carazo A, Roger M, Omais M. Analytical prediction of wake-interaction noise in counter-rotating open rotors. In: 17th AIAA/CEAS aeroacoustics conference (32nd AIAA aeroacoustics conference) (2011). p. 2758.

14. Kingan M, Self R. Counter-rotation propeller tip vortex interaction noise. In: 15th AIAA/CEAS Aeroacoustics Conference (30th AIAA Aeroacoustics Conference) (2009). p. 3135.

15. Roger M, Schram C, Moreau S. On open-rotor blade-vortex interaction noise. In: 18th AIAA/CEAS Aeroacoustics Conference (33rd AIAA Aeroacoustics Conference) (2012). p. 2216.

16. Envia E. Open rotor aeroacoustic modelling. In: 15th International Conference on Fluid Flow Technologies (CMFF"12) (2012). E-18485.

17. Jin Y, Hou L, Zhong S, Yi H, Chen Y. Invertible koopman network and its application in data-driven modeling for dynamic systems. *Mech Syst Signal Process* (2023) 200:110604. doi:10.1016/j.ymssp.2023.110604

18. Chen L, Lian H, Pei Q, Meng Z, Jiang S, Dong H, et al. Fem-bem analysis of acoustic interaction with submerged thin-shell structures under seabed reflection conditions. *Ocean Eng* (2024) 309:118554. doi:10.1016/j.oceaneng.2024.118554

19. Chen L, Lian H, Xu Y, Li S, Liu Z, Atroshchenko E, et al. Generalized isogeometric boundary element method for uncertainty analysis of time-harmonic wave propagation in infinite domains. *Appl Math Model* (2023) 114:360–78. doi:10.1016/j.apm.2022.09.030

20. Lu C, Chen L, Luo J, Chen H. Acoustic shape optimization based on isogeometric boundary element method with subdivision surfaces. *Eng Anal Boundary Elem* (2023) 146:951–65. doi:10.1016/j.enganabound.2022.11.010

21. Chen L, Lian H, Natarajan S, Zhao W, Chen X, Bordas S. Multi-frequency acoustic topology optimization of sound-absorption materials with isogeometric boundary element methods accelerated by frequency-decoupling and model order reduction techniques. *Computer Methods Appl Mech Eng* (2022) 395:114997. doi:10.1016/j.cma.2022.114997

22. Li H, Chen L, Zhi G, Meng L, Lian H, Liu Z, et al. A direct fe2 method for concurrent multilevel modeling of piezoelectric materials and structures. *Computer Methods Appl Mech Eng* (2024) 420:116696. doi:10.1016/j.cma.2023.116696

23. Ling J, Kurzawski A, Templeton J. Reynolds averaged turbulence modelling using deep neural networks with embedded invariance. *J Fluid Mech* (2016) 807:155–66. doi:10.1017/jfm.2016.615

24. Tracey BD, Duraisamy K, Alonso JJ. A machine learning strategy to assist turbulence model development. In: *F53rd AIAA aerospace sciences meeting* (2015). p. 1287.

25. LeCun Y, Bengio Y, Hinton G. Deep learning. *nature* (2015) 521:436–44. doi:10.1038/nature14539

26. Oishi A, Yagawa G. Computational mechanics enhanced by deep learning. *Computer Methods Appl Mech Eng* (2017) 327:327–51. doi:10.1016/j.cma.2017.08.040

27. Papadrakakis M, Lagaros ND. Reliability-based structural optimization using neural networks and Monte Carlo simulation. *Computer Methods Appl Mech Eng* (2002) 191:3491–507. doi:10.1016/s0045-7825(02)00287-6

28. Chen L, Lian H, Liu Z, Chen H, Atroshchenko E, Bordas S. Structural shape optimization of three dimensional acoustic problems with isogeometric boundary element methods. *Computer Methods Appl Mech Eng* (2019) 355:926–51. doi:10.1016/j.cma.2019.06.012

29. Samaniego E, Anitescu C, Goswami S, Nguyen-Thanh VM, Guo H, Hamdia K, et al. An energy approach to the solution of partial differential equations in computational mechanics via machine learning: concepts, implementation and applications. *Computer Methods Appl Mech Eng* (2020) 362:112790. doi:10.1016/j.cma.2019.112790

30. Lee DD, Pham P, Largman Y, Ng A. Advances in neural information processing systems 22. *Tech Rep* (2009).

31. Zhang J, Zhang W, Zhu J, Xia L. Integrated layout design of multi-component systems using XFEM and analytical sensitivity analysis. *Computer Methods Appl Mech Eng* (2012) 245-246:75–89. doi:10.1016/j.cma.2012.06.022

32. Dühring MB, Jensen JS, Sigmund O. Acoustic design by topology optimization. *J Sound Vibration* (2008) 317:557–75. doi:10.1016/j.jsv.2008.03.042

33. Chen L, Lu C, Lian H, Liu Z, Zhao W, Li S, et al. Acoustic topology optimization of sound absorbing materials directly from subdivision surfaces with isogeometric boundary element methods. *Computer Methods Appl Mech Eng* (2020) 362:112806. doi:10.1016/j.cma.2019.112806

34. Shen X, Du C, Jiang S, Zhang P, Chen L. Multivariate uncertainty analysis of fracture problems through model order reduction accelerated sbfem. *Appl Math Model* (2024) 125:218–40. doi:10.1016/j.apm.2023.08.040

35. Radford A, Metz L, Chintala S. Unsupervised representation learning with deep convolutional generative adversarial networks. arXiv preprint arXiv:1511.06434 (2015).

36. Creswell A, White T, Dumoulin V, Arulkumaran K, Sengupta B, Bharath AA. Generative adversarial networks: an overview. *IEEE Signal Processing Magazine* (2018) 35:53–65. doi:10.1109/msp.2017.2765202

37. Zhang H, Xu T, Li H, Zhang S, Wang X, Huang X, et al. Stackgan++: realistic image synthesis with stacked generative adversarial networks. *IEEE Trans pattern Anal machine intelligence* (2018) 41:1947–62. doi:10.1109/tpami.2018.2856256

38. Antoniou A, Storkey A, Edwards H. *Data augmentation generative adversarial networks*. arXiv preprint arXiv:1711.04340 (2017).

39. Liu Y, Zhang J, Zhao T, Wang Z, Wang Z. Reconstruction of the meso-scale concrete model using a deep convolutional generative adversarial network (dcgan). *Construction Building Mater* (2023) 370:130704. doi:10.1016/j.conbuildmat.2023.130704

40. Zhu J-Y, Park T, Isola P, Efros AA. Unpaired image-to-image translation using cycle-consistent adversarial networks. In: Proceedings of the IEEE international conference on computer vision (2017). p. 2223–32.

41. Jain P, Kar P. Non-convex optimization for machine learning. *Foundations Trends® Machine Learn* (2017) 10:142–336. doi:10.1561/2200000058

42. Mirza M, Osindero S. Conditional generative adversarial nets. *arXiv preprint arXiv:1411.1784* (2014).

43. Zhang S, Yu B, Chen L. Non-iterative reconstruction of time-domain sound pressure and rapid prediction of large-scale sound field based on ig-drbem and pod-rbf. *J Sound Vibration* (2024) 573:118226. doi:10.1016/j.jsv.2023.118226

44. Chen L, Lian H, Dong H, Yu P, Jiang S, Bordas S. Broadband topology optimization of three-dimensional structural-acoustic interaction with reduced order isogeometric fem/bem. *J Comput Phys* (2024) 509:113051. doi:10.1016/j.jcp.2024.113051

45. Shen X, Du C, Jiang S, Sun L, Chen L. Enhancing deep neural networks for multivariate uncertainty analysis of cracked structures by pod-rbf. *Theor Appl Fracture Mech* (2023) 125:103925. doi:10.1016/j.tafmec.2023.103925

46. Burton A, Miller G. The application of integral equation methods to the numerical solution of some exterior boundary-value problems. *Proc R Soc Lond A. Math Phys Sci* (1971) 323:201–210.

47. Schittkowski K, Zillober C, Zotemantel R. Numerical comparison of nonlinear programming algorithms for structural optimization. *Struct Optimization* (1994) 7:1–19. doi:10.1007/BF01742498

48. Storn R, Price K. Differential evolution—a simple and efficient heuristic for global optimization over continuous spaces. *J Glob Optimization* (1997) 11:341–59. doi:10.1023/A:1008202821328

49. Svanberg K. The method of moving asymptotes-A a new method for structural optimization. *Int J Numer Methods Eng* (1987) 24:359–73. doi:10.1002/nme.1620240207

50. Marburg S. Developments in structural-acoustic optimization for passive noise control. *Arch Comput Methods Eng* (2002) 9:291–370. doi:10.1007/BF03041465

51. Chen L, Wang Z, Lian H, Ma Y, Meng Z, Li P, et al. Reduced order isogeometric boundary element methods for cad-integrated shape optimization in electromagnetic scattering. *Computer Methods Appl Mech Eng* (2024) 419:116654. doi:10.1016/j.cma.2023.116654

52. Chen L, Zhao J, Lian H, Yu B, Atroshchenko E, Li P. A bem broadband topology optimization strategy based on taylor expansion and soar method—application to 2d acoustic scattering problems. *Int J Numer Methods Eng* (2023) 124:5151–82. doi:10.1002/nme.7345

53. Chen L, Cheng R, Li S, Lian H, Zheng C, Bordas S. A sample-efficient deep learning method for multivariate uncertainty qualification of acoustic–vibration interaction problems. *Computer Methods Appl Mech Eng* (2022) 393:114784. doi:10.1016/j.cma.2022.114784

54. Wang X-Y, Himansu A, Chang S-C, Jorgenson PC. Computation of a single airfoil gust response and gust-cascade interaction using the ce/se method. In: *Fourth computational aeroacoustics (CAA) workshop on benchmark problems* (2004).

Frontiers in Physics

TYPE Original Research
PUBLISHED 12 November 2024
DOI 10.3389/fphy.2024.1468327

OPEN ACCESS

EDITED BY
Leilei Chen,
Huanghuai University, China

REVIEWED BY
Lu Meng,
Taiyuan University of Technology, China
Kui Liu,
Harbin Institute of Technology, China
Paolo Mercorelli,
Leuphana University Lüneburg, Germany

*CORRESPONDENCE
Kuanyao Zhao,
✉ ky.zhao@huanghuai.edu.cn

RECEIVED 21 July 2024
ACCEPTED 09 October 2024
PUBLISHED 12 November 2024

CITATION
Xu Y, Wang J, Yang S, Lei G and Zhao K (2024) Acoustic analysis of a three-dimensional cylindrical shell model under electromagnetic vibration.
Front. Phys. 12:1468327.
doi: 10.3389/fphy.2024.1468327

Acoustic analysis of a three-dimensional cylindrical shell model under electromagnetic vibration

Yanming Xu[1], Jiachen Wang[1], Sen Yang[1,2], Guang Lei[1,2] and Kuanyao Zhao[1]*

[1]Henan International Joint Laboratory of Structural Mechanics and Computational Simulation, College of Architectural and Civil Engineering, Huanghuai University, Zhumadian, China, [2]College of Architecture and Civil Engineering, Xinyang Normal University, Xinyang, China

This paper presents the acoustic analysis of a three-dimensional cylindrical shell model under electromagnetic vibration, a critical factor affecting the performance of electric motors in various applications such as automotive, aerospace, and industrial systems. The study provides a multidisciplinary approach that integrates electromagnetics, structural vibration, and acoustics, solved using the fast multipole boundary element method (FMBEM). The results summarize the validation of the analytical models and numerical simulations, offering insights into effective vibration reduction methods. The conclusions indicate that the 3-D numerical analysis using FMBEM aligns well with the analytical solution for the sound pressure in the exterior acoustic domain of the cylindrical shell model. The paper contributes valuable insights for the design of low-noise motors and the control of electromagnetic vibration and noise in electric motors.

KEYWORDS

electromagnetic vibration, acoustic analysis, electric motors, fast multipole boundary element method, permanent magnet synchronous motors

1 Introduction

The performance of electric motors, especially in applications such as automotive, aerospace, and industrial systems, is heavily influenced by their electromagnetic vibration and noise. These aspects not only affect the operational efficiency but also the comfort and reliability of motor-driven systems. With the rapid development of electric vehicles and advanced industrial automation, there is an increasing demand for motors that are efficient, compact, and silent. Therefore, the accurate prediction and control of their electromagnetic vibration and noise have become paramount. A significant body of research has been dedicated to understanding and mitigating the sources of electromagnetic vibration and noise in permanent magnet synchronous motors (PMSMs) and other types of electric motors.

Studies by Ballo et al. [1] and Xing et al. [2, 3] have focused on developing simplified analytical models and numerical prediction models to forecast the noise and vibration in PMSMs at the design stage. The influence of electromagnetic forces on motor vibration [4, 5] has also been a central theme. Strategies to mitigate vibrations and noise have been explored [6, 7]. Experimental studies by Torregrossa et al. [8] and Zhao et al. [9] have validated theoretical models and numerical simulations, providing insights into the effectiveness of various vibration reduction methods. The detection and analysis of oscillations in rail vehicle systems has been significantly advanced [10–12], particularly focusing on pantograph control, which not only improved the understanding of signal processing in this context but also provided practical solutions for real-time applications, enhancing the safety and efficiency of rail transportation. A multidisciplinary approach by Chai et al. [13] and Wu et al. [14], combining electromagnetics, structural mechanics, and acoustics, has been employed to provide a comprehensive understanding of motor behavior. The dynamic behavior of the rotor and the acoustic performance of the entire motor system have been examined [15, 16]. Optimization studies by Mendizabal et al. [17] have provided guidelines for designing low-noise motors. Certain studies have focused on specific aspects such as the effects of laminations [18], axial forces [19], and the application of amorphous alloys in stators [20], offering specialized insights into motor design.

The finite element method (FEM) has been extensively employed by Mao et al. [21] and Wang et al. [22] to predict acoustics, fracture mechanics, electromagnetics, and vibrations. Additionally, [23, 24] investigated the natural frequencies of motor components. However, there are several problems with FEM when modeling infinite domains. The boundary element method (BEM) has been used to tackle potential problems because it offers good accuracy and easy mesh construction. Particularly for exterior acoustic problems, the Sommerfeld radiation condition at infinity is rapidly satisfied [25]. The boundary integral problem has been quantitatively solved using the Galerkin approach for BEM implementation [26, 27].

In order to directly resolve the equation system, the conventional boundary element method (CBEM) produces a dense and non-symmetric coefficient matrix that takes a long time to compute. The fast multipole method (FMM) [28–30], the fast direct solver [31, 32], and the adaptive cross approximation approach [33] are only a few of the methods that have been employed to expedite the resolution of the integral issue. Architects and designers are increasingly considering changing the structural geometry to reduce noise. There is much potential for radiated noise reduction with this structural-acoustic optimization [34–36]. FEM and BEM may be employed with some computer-aided engineering (CAE) software. However, contemporary CAE requires that the models produced by CAD software be converted into simulation-ready models as part of the preprocessing phase. The transfer of geometric model data by the CAE results in geometry errors. One proposed approach to this problem [12, 37] is to combine BEM with geometric modeling and numerical simulation using isogeometric analysis (IGA) [38–40]. IGABEM has been employed to tackle an extensive variety of problems, including elastic mechanics [41], potential problems [42–46], heat transfer problems [47], wave propagation [48–53], fracture mechanics [54], electromagnetics [55–60], and structural optimization [61–66].

In this study, the acoustic analysis under electromagnetic vibration is solved using the fast multipole boundary element method (FMBEM). With regard to the advantages of FMBEM over CBEM, please refer to Chen et al. [67].

2 Analytical solution of sound pressure in a cylindrical shell model for external acoustic analysis

A cylindrical shell with radius a and infinite length is the subject of the investigation. Consider a region of length l in the model where the cylindrical shell vibrates and outside of which there are no displacements of the cylindrical shell. The acoustic vibration coupling is not taken into account while analyzing the sound field. The region outside the cylindrical shell when $r > a$ is the acoustical analysis domain. The model is presented in Figure 1.

Assuming a known radial displacement w in Equation 1:

$$w(z,\theta,t) = W_m \gamma_m(z)\cos(n\theta)e^{-\mathrm{j}\omega t}, \tag{1}$$

where $\gamma_m(z)$ is the modal function in the axial direction, $\cos(n\theta)$ is the modal function in the circumferential direction, W_m is the amplitude, and j is the imaginary unit. After that, the time term $e^{-\mathrm{j}\omega t}$ is omitted from the calculation in the frequency domain.

Equation 1 is derived for time t in order to obtain the velocity expression, as shown in Equation 2.

$$\dot{w}(z,\theta) = -\mathrm{j}\omega W_m \gamma_m(z)\cos(n\theta). \tag{2}$$

The sound field in the domain must follow Equation 3 after being excited by the displacement in Equation 1.

$$p(r,z,\theta) = P(r)\gamma_m(z)\cos(n\theta). \tag{3}$$

A Fourier transform of Equations 1, 3 in the z direction yields Equations 4, 5.

$$\tilde{w}(k_z,\theta,t) = W_m \tilde{\gamma}_m(k_z)\cos(n\theta), \tag{4}$$

$$\tilde{p}(r,k_z,\theta) = P(r)\tilde{\gamma}_m(k_z)\cos(n\theta), \tag{5}$$

in which $k_z = \omega/c_z$ is the wave number, and we have Equation 6.

$$\tilde{\gamma}_m(k_z) = \int_{-\infty}^{\infty} \gamma_m(z)e^{-\mathrm{j}k_z z}\mathrm{d}z. \tag{6}$$

In the cylindrical coordinate system, the acoustic Helmholtz equation has the form shown in Equation 7.

$$\frac{\partial^2 p}{\partial r^2} + \frac{1}{r}\frac{\partial p}{\partial r} + \frac{1}{r^2}\frac{\partial^2 p}{\partial \theta^2} + \frac{\partial^2 p}{\partial z^2} + k_f^2 p = 0, \tag{7}$$

where the wave number $k_f = \omega/c_f$.

A Fourier transform of Equation 7 in the z direction yields Equation 8.

$$\frac{\partial^2 \tilde{p}}{\partial r^2} + \frac{1}{r}\frac{\partial \tilde{p}}{\partial r} + \left[k_f^2 - k_z^2 - \left(\frac{n}{r}\right)^2\right]\tilde{p} = 0. \tag{8}$$

Substituting Equation 5 into Equation 8 yields Equation 9.

$$\left\{\frac{\partial^2 P(r)}{\partial r^2} + \frac{1}{r}\frac{\partial P(r)}{\partial r} + \left[k_f^2 - k_z^2 - \left(\frac{n}{r}\right)^2\right]P(r)\right\}\tilde{\gamma}_m(k_z)\cos(n\theta) = 0. \tag{9}$$

We need Equation 10 to make Equation 9 constant.

$$\frac{\partial^2 P(r)}{\partial r^2} + \frac{1}{r}\frac{\partial P(r)}{\partial r} + \left[k_f^2 - k_z^2 - \left(\frac{n}{r}\right)^2\right]P(r) = 0. \tag{10}$$

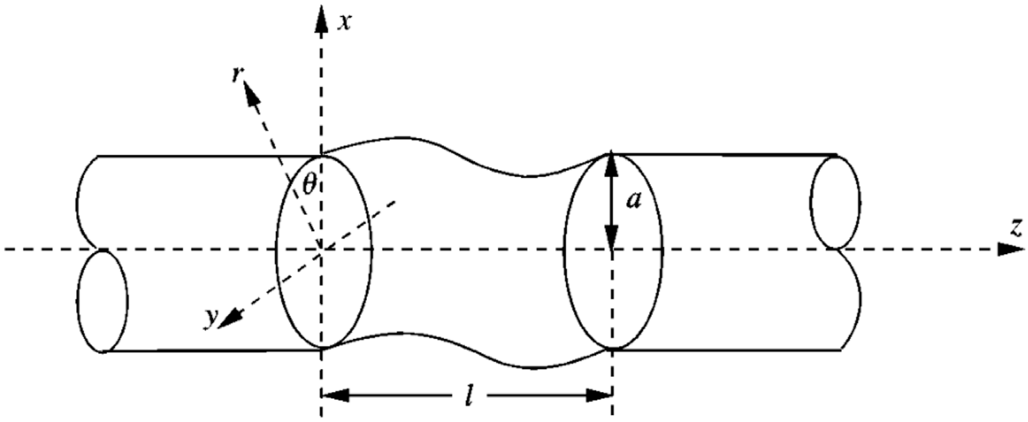

FIGURE 1
Cylindrical shell model for the acoustical analysis.

The homogeneous equation shown in Equation 10 is a Bessel equation with the solution in Equation 11.

$$P(r) = AJ_n(k_r r) + BY_n(k_r r), \quad k_r = \left(k_f^2 - k_z^2\right)^{1/2}. \tag{11}$$

When $r \to \infty$, the radiation field tends to be in the form of a plane wave, as shown in Equation 12.

$$P(r) \to Ae^{\mathrm{j}k_r r - \mathrm{j}\omega t} = A\left(\cos(k_r r) + \mathrm{j}\sin(k_r r)\right)e^{-\mathrm{j}\omega t}. \tag{12}$$

Furthermore, based on the approximation of two classes of Bessel functions at infinity in Equation 13,

$$\lim_{k_r r\to\infty} J_n(k_r r) \to \sqrt{\frac{2}{\pi k_r r}}\cos\left(k_r r - \frac{2n+1}{4}\pi\right), \quad \lim_{k_r r\to\infty} Y_n(k_r r) \to \sqrt{\frac{2}{\pi k_r r}}\sin\left(k_r r - \frac{2n+1}{4}\pi\right). \tag{13}$$

$B = \mathrm{j}A$ is needed to satisfy the infinity condition. Then, we have Equation 14.

$$P(r) = A\left[J_n(k_r r) + \mathrm{j}Y_n(k_r r)\right] = AH_n^{(1)}(k_r r), \tag{14}$$

where $H_n^{(1)}$ denotes the Hankel functions of the n-th order first kind.

The continuity conditions shown in Equation 15 must be satisfied at the interface:

$$-\frac{1}{\mathrm{j}\omega\rho_f}\left.\frac{\partial p}{\partial r}\right|_{r=a} = \dot{w}|_{r=a}. \tag{15}$$

Performing a Fourier inverse transform of Equation 15, we have Equation 16.

$$\frac{\partial\tilde{p}}{\partial r} = -\omega^2\rho_f\tilde{w}. \tag{16}$$

Substituting Equations 4, 5 into Equation 16 yields Equation 17.

$$A = -\frac{\omega^2\rho_f W_m}{k_r H_n^{(1)'}(k_r a)}, \tag{17}$$

and then, we have Equation 18.

$$\tilde{p} = -\frac{\omega^2\rho_f H_n^{(1)}(k_r r)}{k_r H_n^{(1)'}(k_r a)}\tilde{y}_m(k_z)W_m\cos(n\theta). \tag{18}$$

Performing a Fourier inverse transform of Equation 18, we finally obtain an analytical solution for the sound pressure at any point in the exterior acoustic domain for the cylindrical shell model, as shown in Equation 19.

$$p(r,z,\theta) = -\frac{\omega^2\rho_f}{2\pi}\left[\int_{-\infty}^{\infty}\frac{H_n^{(1)}(k_r r)}{k_r H_n^{(1)'}(k_r a)}\tilde{y}_m(k_z)e^{\mathrm{j}k_z z}\mathrm{d}k_z\right]W_m\cos(n\theta). \tag{19}$$

Note that $r > a$.

3 Numerical analysis of sound pressure in three-dimensional external acoustic analysis

Consider the Helmholtz governing equation in time-harmonic acoustic analysis, as shown in Equation 20.

$$\nabla^2 p(\mathbf{x}) + k^2 p(\mathbf{x}) = 0, \quad \forall\mathbf{x}\in\Omega, \tag{20}$$

where ∇^2 is the Laplace operator, $p(\mathbf{x})$ is the sound pressure at field point $\mathbf{x}$, $k = \omega/c$ is the wave number, ω is the angular frequency of the incoming wave, c is the sound speed in the domain Ω, and Ω is the domain for acoustic analysis. In the frequency domain, the time-dependent component $e^{-\mathrm{j}\omega t}$ can be excluded from the computation.

Applying Green's second theorem to the Helmholtz equation yields the following integral equation, as shown in Equation 21.

$$p(\mathbf{x}) + \int_\Gamma\frac{\partial G(\mathbf{x},\mathbf{y})}{\partial\mathbf{n}(\mathbf{y})}p(\mathbf{y})\mathrm{d}\Gamma(\mathbf{y}) = \int_\Gamma G(\mathbf{x},\mathbf{y})q(\mathbf{y})\mathrm{d}\Gamma(\mathbf{y}) + p^{\mathrm{inc}}(\mathbf{x}), \quad \mathbf{y}\in\Gamma, \tag{21}$$

where $\Gamma = \partial\Omega$ is the border of the domain Ω, $\mathbf{y}$ is the sound source point on the boundary Γ, $\mathbf{x}$ is the field point affected by the sound source $\mathbf{y}$, $G(\mathbf{x},\mathbf{y})$ is the Green's function, $\mathbf{n}(\mathbf{y})$ is the outward unit normal vector at point $\mathbf{y}$, $\partial()/\partial\mathbf{n} = \nabla()\cdot\mathbf{n}$ is the exterior derivative, p^{inc} is the sound pressure of the incident wave, and $q(\mathbf{y})$ is the outward flux at point $\mathbf{y}$. $q(\mathbf{y})$ satisfies the Neumann boundary condition, as shown in Equation 22.

$$q(\mathbf{y}) = \frac{\partial p(\mathbf{y})}{\partial \mathbf{n}(\mathbf{y})} = \mathrm{j}\rho\omega v_f(\mathbf{y}), \tag{22}$$

where ρ is the density of the medium in which the sound wave propagates, and $v_f(\mathbf{y})$ is the normal velocity at point $\mathbf{y}$.

To obtain the unknown sound pressure on the boundary Γ, the field point $\mathbf{x}$ may converge to the boundary, and thus, the Kirchhoff–Helmholtz conventional boundary integral equation (CBIE) is obtained from Equation 21, as shown in Equation 23.

$$\begin{aligned} c(\mathbf{x})p(\mathbf{x}) + \int_\Gamma \frac{\partial G(\mathbf{x},\mathbf{y})}{\partial \mathbf{n}(\mathbf{y})} p(\mathbf{y})\mathrm{d}\Gamma(\mathbf{y}) \\ = \int_\Gamma G(\mathbf{x},\mathbf{y})q(\mathbf{y})\mathrm{d}\Gamma(\mathbf{y}) + p^{\mathrm{inc}}(\mathbf{x}), \quad \mathbf{x},\mathbf{y} \in \Gamma. \end{aligned} \tag{23}$$

The normal derivative boundary integral equation (NDBIE) of Equation 23 is given by Equation 24.

$$\begin{aligned} c(\mathbf{x})q(\mathbf{x}) + \int_\Gamma \frac{\partial^2 G(\mathbf{x},\mathbf{y})}{\partial \mathbf{n}(\mathbf{y})\partial \mathbf{n}(\mathbf{x})} p(\mathbf{y})\mathrm{d}\Gamma(\mathbf{y}) \\ = \int_\Gamma \frac{\partial G(\mathbf{x},\mathbf{y})}{\partial \mathbf{n}(\mathbf{x})} q(\mathbf{y})\mathrm{d}\Gamma(\mathbf{y}) + \frac{\partial p^{\mathrm{inc}}(\mathbf{x})}{\partial \mathbf{n}(\mathbf{x})}, \quad \mathbf{x},\mathbf{y} \in \Gamma. \end{aligned} \tag{24}$$

In Equations 23, 24, $c(\mathbf{x}) = 1/2$ when the boundary around point $\mathbf{x}$ is smooth.

Applying only CBIE or NDBIE leads to non-uniqueness of the solution to the exterior sound field analysis, which can be solved by linearly combining CBIE and NDBIE. This is called the Burton–Miller method [68], as shown in Equation 25.

$$\begin{aligned} & c(\mathbf{x})p(\mathbf{x}) + \alpha c(\mathbf{x})q(\mathbf{x}) + \int_\Gamma \frac{\partial G(\mathbf{x},\mathbf{y})}{\partial \mathbf{n}(\mathbf{y})} p(\mathbf{y})\mathrm{d}\Gamma(\mathbf{y}) \\ & + \alpha \int_\Gamma \frac{\partial^2 G(\mathbf{x},\mathbf{y})}{\partial \mathbf{n}(\mathbf{y})\partial \mathbf{n}(\mathbf{x})} p(\mathbf{y})\mathrm{d}\Gamma(\mathbf{y}) \\ & = \int_\Gamma G(\mathbf{x},\mathbf{y})q(\mathbf{y})\mathrm{d}\Gamma(\mathbf{y}) + \alpha \int_\Gamma \frac{\partial G(\mathbf{x},\mathbf{y})}{\partial \mathbf{n}(\mathbf{x})} q(\mathbf{y})\mathrm{d}\Gamma(\mathbf{y}) + p^{\mathrm{inc}}(\mathbf{x}) \\ & + \alpha \frac{\partial p^{\mathrm{inc}}(\mathbf{x})}{\partial \mathbf{n}(\mathbf{x})}, \quad \mathbf{x},\mathbf{y} \in \Gamma, \end{aligned} \tag{25}$$

in which α is the coupling coefficient, and we have Equation 26.

$$\alpha = \begin{cases} \mathrm{j}, & k < 1, \\ -\dfrac{\mathrm{j}}{k}, & k \geq 1. \end{cases} \tag{26}$$

In Equation 25, for 2-D acoustic analysis, we have Equation 27.

$$\begin{aligned} G(\mathbf{x},\mathbf{y}) &= \frac{\mathrm{j}}{4} H_0^{(1)}(kr), \\ \frac{\partial G(\mathbf{x},\mathbf{y})}{\partial \mathbf{n}(\mathbf{x})} &= -\frac{\mathrm{j}k}{4} H_1^{(1)}(kr) \frac{\partial r}{\partial \mathbf{n}(\mathbf{x})}, \\ \frac{\partial^2 G(\mathbf{x},\mathbf{y})}{\partial \mathbf{n}(\mathbf{y})\partial \mathbf{n}(\mathbf{x})} &= \frac{\mathrm{j}k^2}{4} H_2^{(1)}(kr) \frac{\partial r}{\partial \mathbf{n}(\mathbf{y})} \frac{\partial r}{\partial \mathbf{n}(\mathbf{x})} + \frac{\mathrm{j}k}{4r} H_1^{(1)}(kr) n_i(\mathbf{y}) n_i(\mathbf{x}), \end{aligned} \tag{27}$$

and for the 3-D acoustic problem, we have Equation 28.

$$\begin{aligned} G(\mathbf{x},\mathbf{y}) &= \frac{\mathrm{e}^{\mathrm{j}kr}}{4\pi r}, \\ \frac{\partial G(\mathbf{x},\mathbf{y})}{\partial \mathbf{n}(\mathbf{x})} &= -\frac{\mathrm{e}^{\mathrm{j}kr}}{4\pi r^2}(1 - \mathrm{j}kr) \frac{\partial r}{\partial \mathbf{n}(\mathbf{x})}, \\ \frac{\partial^2 G(\mathbf{x},\mathbf{y})}{\partial \mathbf{n}(\mathbf{y})\partial \mathbf{n}(\mathbf{x})} &= \frac{\mathrm{e}^{\mathrm{j}kr}}{4\pi r^3}\left[(3 - 3\mathrm{j}kr - k^2r^2)\frac{\partial r}{\partial \mathbf{n}(\mathbf{y})}\frac{\partial r}{\partial \mathbf{n}(\mathbf{x})} + (1 - \mathrm{j}kr) n_i(\mathbf{y}) n_i(\mathbf{x})\right], \end{aligned} \tag{28}$$

where $H_n^{(1)}$ is the Hankel function of n-th order first kind, r is the distance between point $\mathbf{x}$ and $\mathbf{y}$, $r = |\mathbf{x} - \mathbf{y}|$, and n_i is the component of the coordinate.

In Equation 25, discretizing the boundary Γ yields the linear equations shown in Equation 29.

$$\mathbf{Hp} = \mathbf{Gq} + \mathbf{p_i}, \tag{29}$$

where $\mathbf{p_i}$ is the nodal pressure from p^{inc}.

The sound pressure at point $\mathbf{x}$ could be obtained by solving Equation 29.

4 Numerical example

In this part, we will calculate the sound pressure at some certain location using the analytical equation (Equation 19) and numerical analysis (using BEM), respectively. Both are implemented using our in-house Fortran code. The algorithm is crafted using the Fortran 90 programming language and compiled with the combination of Visual Studio 2022 and Intel® oneAPI 2022 toolkit. It is executed on a PC with an Intel(R) Xeon(R) Bronze 3204 CPU @ 1.90 GHz and complemented by 128.0 GB of RAM. In this part, the coordinates of the points are described using the cylindrical coordinate system in Equation 19.

Consider the cylindrical shell model shown in Figure 1. The cylindrical shell of radius $a = 0.5$ m and length $l = 0.4$ m is closed at both ends for the three-dimensional (3-D) numerical analysis. Consider Equation 1. Let the vibration of the cylindrical shell be uniformly distributed in the axial direction; that is, let $\gamma_m = 1$. Let the amplitude of the vibration $W_m = 2.24 \times 10^{-8}$ m, the frequency $f = \omega/2\pi = [100, 1{,}000]$ Hz, and the order of the circumferential vibration order be $n = 0$.

The cylindrical shell model is meshed with quadrilateral elements. Figures 2A, B gives the meshing scheme with element number of 2112 and 8320, separately. Figure 3 provides the numerical solutions of the sound pressure at $(\sqrt{2}/2,\ 0.0,\ \pi/4)$ — (0.5, 0.5, 0.0) in the cartesian coordinates for the meshing schemes in Figure 2, where the center of the cylindrical shell is at (0.0, 0.0, 0.0). The comparison in Figure 3 is crucial, as it tests the sensitivity of the numerical solution to the mesh density. A fine mesh provides a more accurate representation of the continuous problem but at a higher computational cost. Conversely, a coarse mesh reduces computational demand but may lead to inaccuracies. The two mesh schemes have 2,112 and 8,320 elements, respectively. The agreement between these two schemes suggests that the coarser mesh (2,112 elements) is sufficiently refined for the problem at hand, capturing the essential features of the sound pressure distribution without the excessive computational cost associated with a very fine mesh. Good agreement between the two mesh schemes indicates that the numerical solution has converged to a value that accurately represents the sound pressure at the specified point. This convergence is a critical aspect of numerical methods, ensuring that the solution is reliable and independent of the discretization. The consistency of results from different mesh densities also serves as an indirect validation of the FMBEM approach. It demonstrates that the method is capable of providing accurate results even with relatively coarse meshes, which is particularly beneficial for complex geometries and larger models where fine meshing becomes

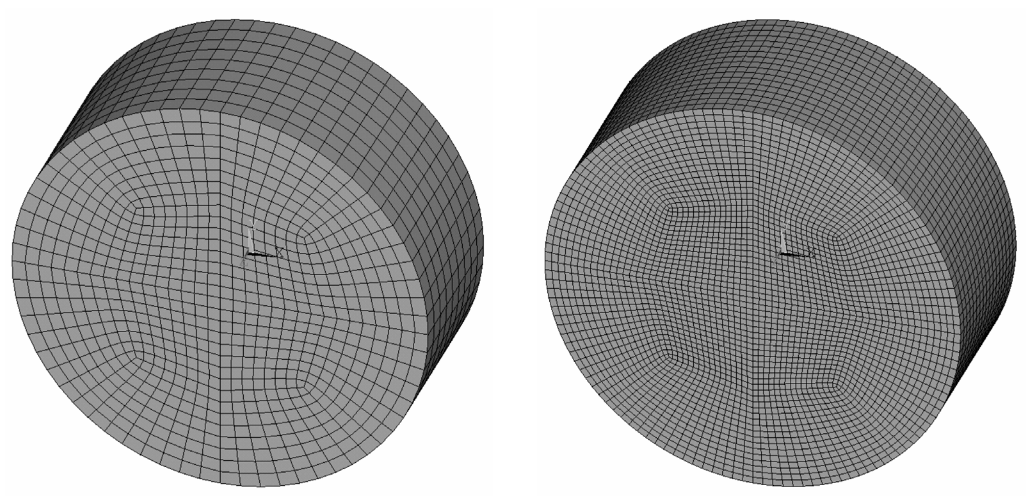

a. Model meshing. Element number 2112.

b. Model meshing. Element number 8320.

FIGURE 2
Meshing scheme for the cylindrical shell model with closed ends. Radius a = 0.5 m and length l = 0.4 m. **(A)** Model meshing. Number of elements = 2,112. **(B)** Model meshing. Number of elements = 8,320.

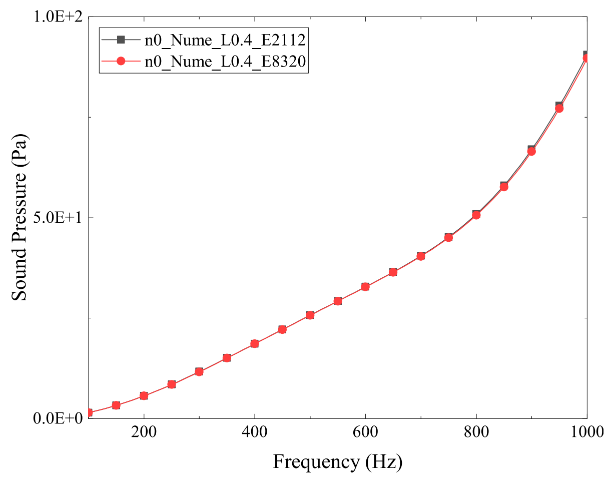

FIGURE 3
Numerical results of sound pressure at ($\sqrt{2}/2$, 0.0, $\pi/4$). Circumferential vibration order n = 0, length l = 0.4 m; number of elements = 2,112 vs. 8,320.

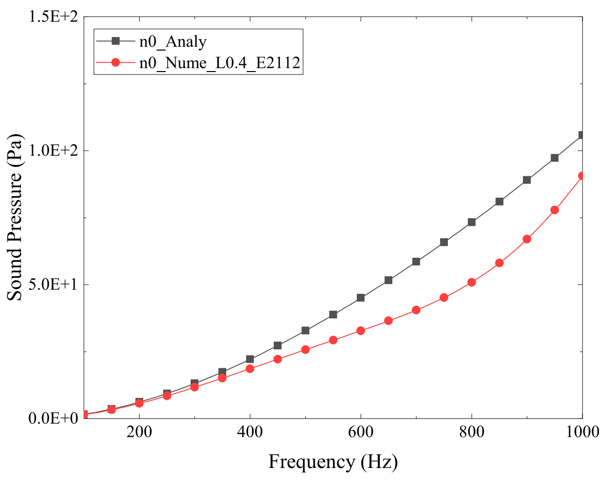

FIGURE 4
Numerical vs. analytical results of sound pressure at ($\sqrt{2}/2$, 0.0, $\pi/4$) for a cylindrical shell model of length l = 0.4 m. Circumferential vibration order n = 0.

impractical. Based on this, we will select the element size configuration shown in Figure 2A for the cylindrical shell model with radius a = 0.5 m and length $l \geq$ 0.4 m in the subsequent analysis.

Consider the model presented in Figure 1. The cylindrical shell model for analytical analysis is of infinite length, in which only a segment of length l vibrates. This infinite-length cylindrical shell is considered as the boundary of the exterior acoustic domain, meaning that the acoustic analysis does not take into account the interior region of the cylindrical shell. However, during the 3-D numerical analysis, the boundary of the exterior acoustic domain is not a cylindrical shell of infinite length but a shell of length l with closed ends, which causes the space outside the l-length segment in the infinitely long cylindrical shell to be involved in the acoustic analysis. Thus, computing errors are introduced. For the cylindrical shell model with a radius of 0.5 m and a length of 0.4 m, the analytical and 3-D numerical solutions for the sound pressure at ($\sqrt{2}/2$, 0.0, $\pi/4$) are provided in Figure 4. The two curves do not fit well, as we have predicted. This discrepancy is expected and can be attributed to several factors. The analytical model assumes an infinite length for the cylindrical shell, which simplifies the boundary conditions but deviates from the actual finite length used in the numerical model. The numerical model includes the effects of the shell's finite length, which introduces additional

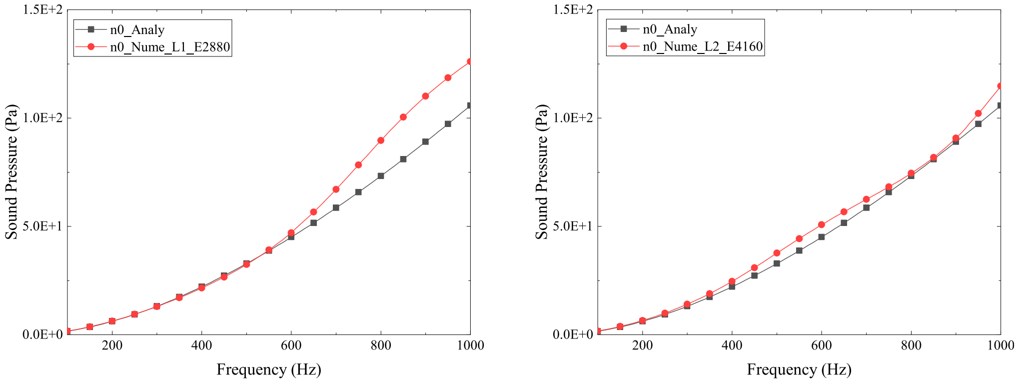

a. Length l = 1 m, element number2880 **b.** Length l = 2 m, element number 4160.

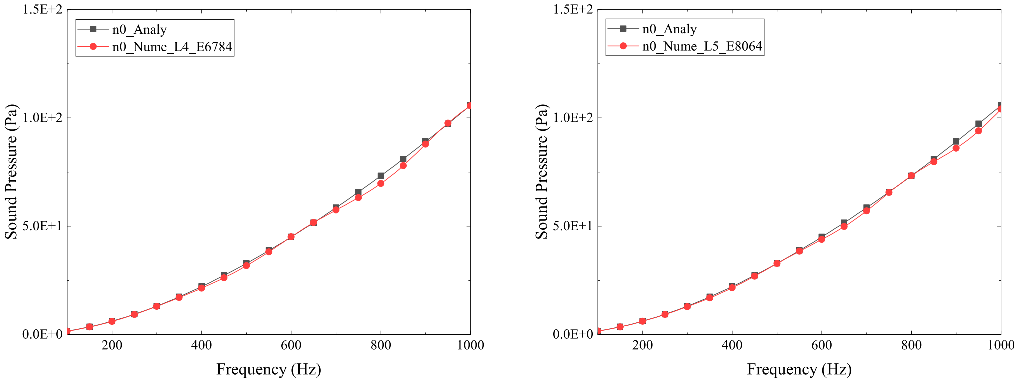

c. Length l = 4 m, element number 6784. **d.** Length l = 5 m, element number 8064.

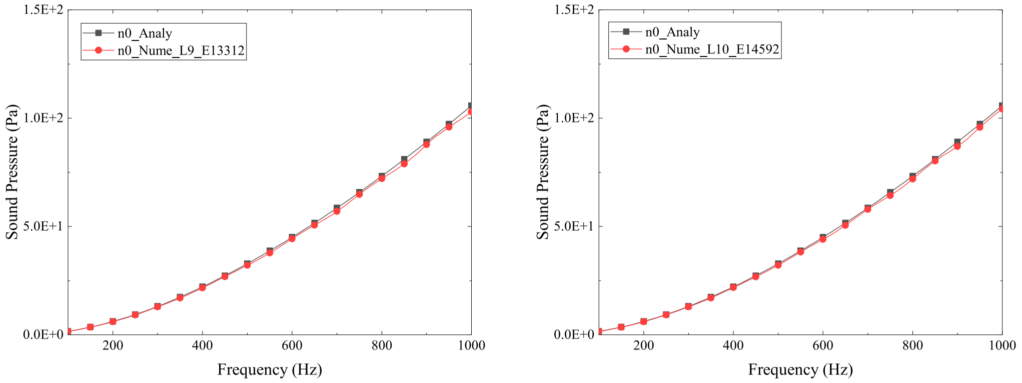

e. Length l = 9 m, element number 13312. **f.** Length l = 10 m, element number 14592.

FIGURE 5
Numerical vs. analytical results of sound pressure at ($\sqrt{2}/2$, 0.0, $\pi/4$) for cylindrical shell models of different lengths. Circumferential vibration order $n = 0$. **(A)** Length $l = 1$ m, number of elements = 2,880. **(B)** Length $l = 2$ m, number of elements = 4,160. **(C)** Length $l = 4$ m, number of elements = 6,784. **(D)** Length $l = 5$ m, number of elements = 8,064. **(E)** Length $l = 9$ m, number of elements = 13,312. **(F)** Length $l = 10$ m, number of elements = 14,592.

complexities not fully captured by the analytical model's assumptions. The discrepancy highlights the limitations of analytical models when they are based on simplified assumptions that may not fully represent the physical system's complexity. The comparison underscores the importance of validating analytical models with numerical simulations, especially when the models are used for design and optimization in engineering applications. The results suggest that the model configuration, particularly the length of the cylindrical shell, significantly affects the accuracy of the sound pressure predictions. This insight is crucial for selecting appropriate model parameters in both theoretical and numerical studies. The choice between analytical and numerical methods should be guided by the specific requirements of the problem, including the need for accuracy, computational resources, and the complexity of the model.

To reduce the computational errors resulting from the axial external space of the cylindrical shell, we attempt to lengthen the shell model with closed ends in the 3-D numerical analysis. For

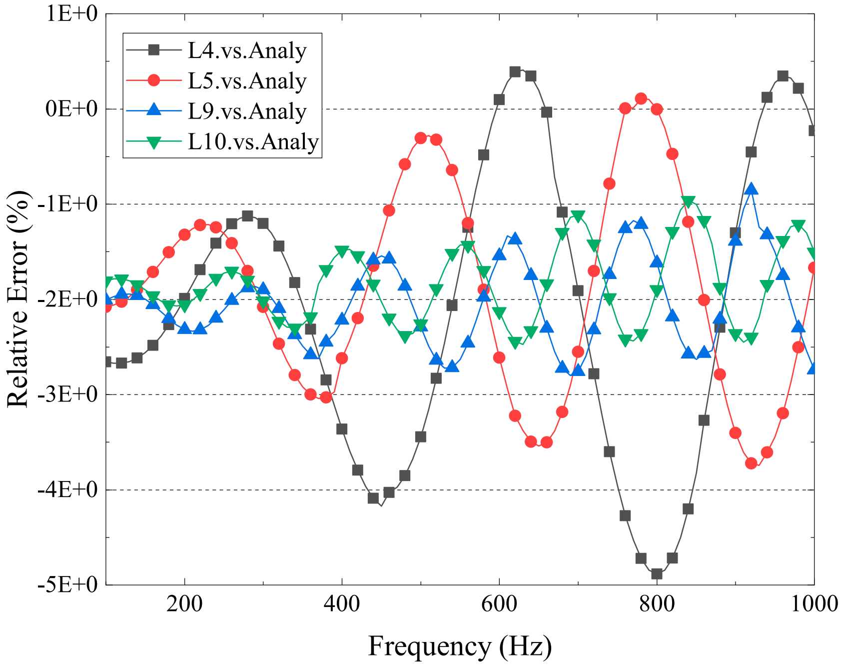

FIGURE 6
Relative error, numerical results vs. analytical results. Circumferential vibration order $n = 0$, length $l = 4$ m, 5 m, 9 m, and 10 m.

models of various lengths, the numerical results are compared with the analytical solution to determine an appropriate model configuration. Figure 5 gives the sound pressure at ($\sqrt{2}/2$, 0.0, $\pi/4$) for cylindrical shell models of different lengths. The circumferential vibration order $n = 0$. Figures 5A–F show that the 3-D numerical result agrees well with the analytical solution when the length $l \geq 4$ m. The analytical model assumes an infinite length for the cylindrical shell, which simplifies the boundary conditions but deviates from the actual finite length used in the numerical model. The numerical model includes the effects of the shell's finite length, which introduces additional complexities not fully captured by the analytical model's assumptions. The discrepancy between the analytical and numerical solutions for shorter shells highlights the limitations of analytical models when they are based on simplified assumptions that may not fully represent the physical system's complexity. The comparison underscores the importance of validating analytical models with numerical simulations, especially when the models are used for design and optimization in engineering applications.

The data in Figures 5C–F, 6 give the relative error of the 3-D numerical solution to the analytical result. Similar characteristics are displayed by the four curves, namely, a rising relative error between the analytical and numerical solutions with increasing frequency, indicating that higher frequencies are more challenging to model accurately. This could be due to the higher spatial and temporal resolution required for capturing the dynamics of higher-frequency waves. For the cylindrical shell model of length $l = 4$ m, the relative error range is (−5%, 1%); for the model of $l = 5$ m, it is (−4%, 1%); and for the models of $l = 9$ m and $l = 10$ m, it is about (−3%, −1%). The relative error decreases, and the computational accuracy generally improves as the model lengthens. The present shell model has a radius of 0.5 m. The model length is 10 times the radius when $l = 5$ m and 20 times the radius when $l = 10$ m. The results suggest that the length of the model plays a critical role in the accuracy of numerical simulations. The analytical model assumes an infinite length for simplicity, but the numerical model must account for the finite length, which introduces additional complexities. The findings indicate that a model length of at least 10 times the radius is necessary for accurate uncoupling analysis. Although increasing the model length improves accuracy, it also increases the computational cost in terms of memory usage and processing time. Therefore, a balance must be struck between accuracy and computational efficiency, which is achieved when the model length is approximately 10 times the radius. In our future work, acceleration algorithms may be employed to speed up the calculation.

Consider the cylindrical shell model shown in Figure 1. The cylindrical shell is closed at both ends for the 3-D numerical analysis. The radius $a = 0.5$ m. The length $l = 5$ m or $l = 10$ m for the 3-D numerical analysis. Consider Equation 1. Let $\gamma_m = 1$, the amplitude of the vibration $W_m = 2.24 \times 10^{-8}$ m, and the frequency $f = \omega/2\pi = [100, 1{,}000]$ Hz. The analytical and 3-D numerical solutions for the sound pressure at ($\sqrt{2}/2$, 0.0, $\pi/4$) for different circumferential vibration orders n are given in Figure 7. Figures 7A–F show that the 3-D numerical result agrees well with the analytical solution when the circumferential vibration order $n = 1$, 3, or 4. The data in Figures 7A, 8 provide, as an example, the relative error between the 3-D numerical result and the analytical solution.

Figure 7 shows that for n = 2, 6, and 10, the analytical solution goes to zero, and the numerical solution is less than 3.0E−12, which might be thought of as tending toward zero in numerical analysis. Note that the sound pressure at ($\sqrt{2}/2$, 0.0, $\pi/4$) is calculated in

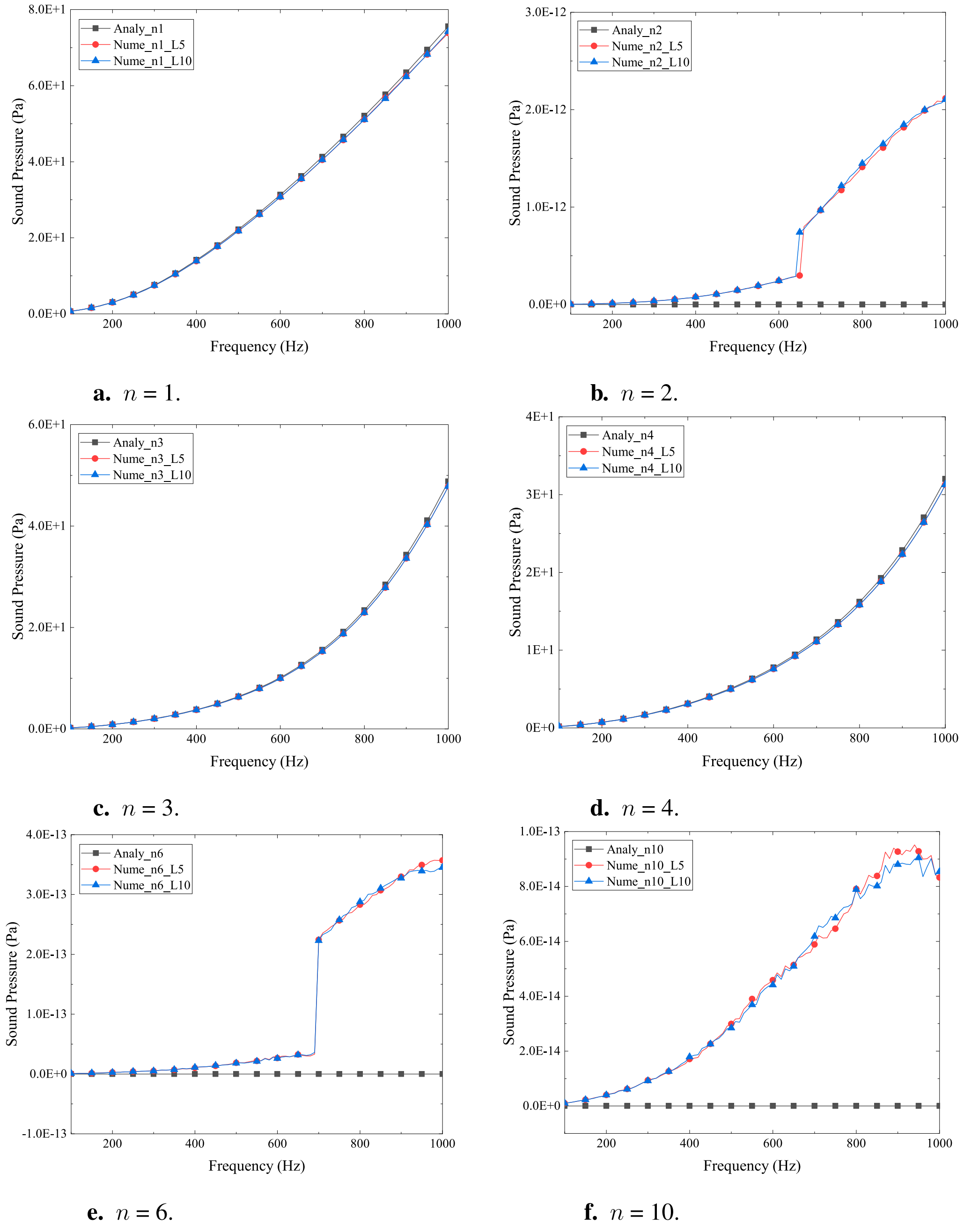

a. $n = 1$.

b. $n = 2$.

c. $n = 3$.

d. $n = 4$.

e. $n = 6$.

f. $n = 10$.

FIGURE 7
Sound pressure at $(\sqrt{2}/2, 0.0, \pi/4)$ and the circumferential vibration order n varies. Numerical results vs. analytical result, in which L5 is length $l = 5$ m, and L10 is length $l = 10$ m. **(A)** $n = 1$. **(B)** $n = 2$. **(C)** $n = 3$. **(D)** $n = 4$. **(E)** $n = 6$. **(F)** $n = 10$.

Figure 7. Consider Equation 19. When $\theta = \pi/4$ and $n = 2$, 6, or 10, $\cos(n\theta) = 0$, meaning that the sound pressure $p(r, z, \theta) = 0$ in Equation 19, which coincides with Figures 7B, E, F.

The agreement between analytical and numerical results for certain modes validates the theoretical model's assumptions and the mathematical formulations that describe the sound pressure distribution. This is crucial for the reliability of predictions made using these models in practical applications. The results highlight the importance of considering different vibration modes in the analysis. The theoretical model predicts different behaviors for different modes, and the numerical simulations confirm these predictions, emphasizing the need for accurate modeling of vibration modes in the design and analysis of electric motors. The findings provide valuable insights for the design and optimization of electric motors, particularly in controlling the vibration modes that contribute to noise. Understanding which modes contribute to the sound pressure can guide the design of motor components to minimize noise emissions. The choice between analytical and numerical methods should be guided by the specific requirements of the problem, including the need for accuracy, computational resources, and the complexity of the model. The agreement between the two methods for certain

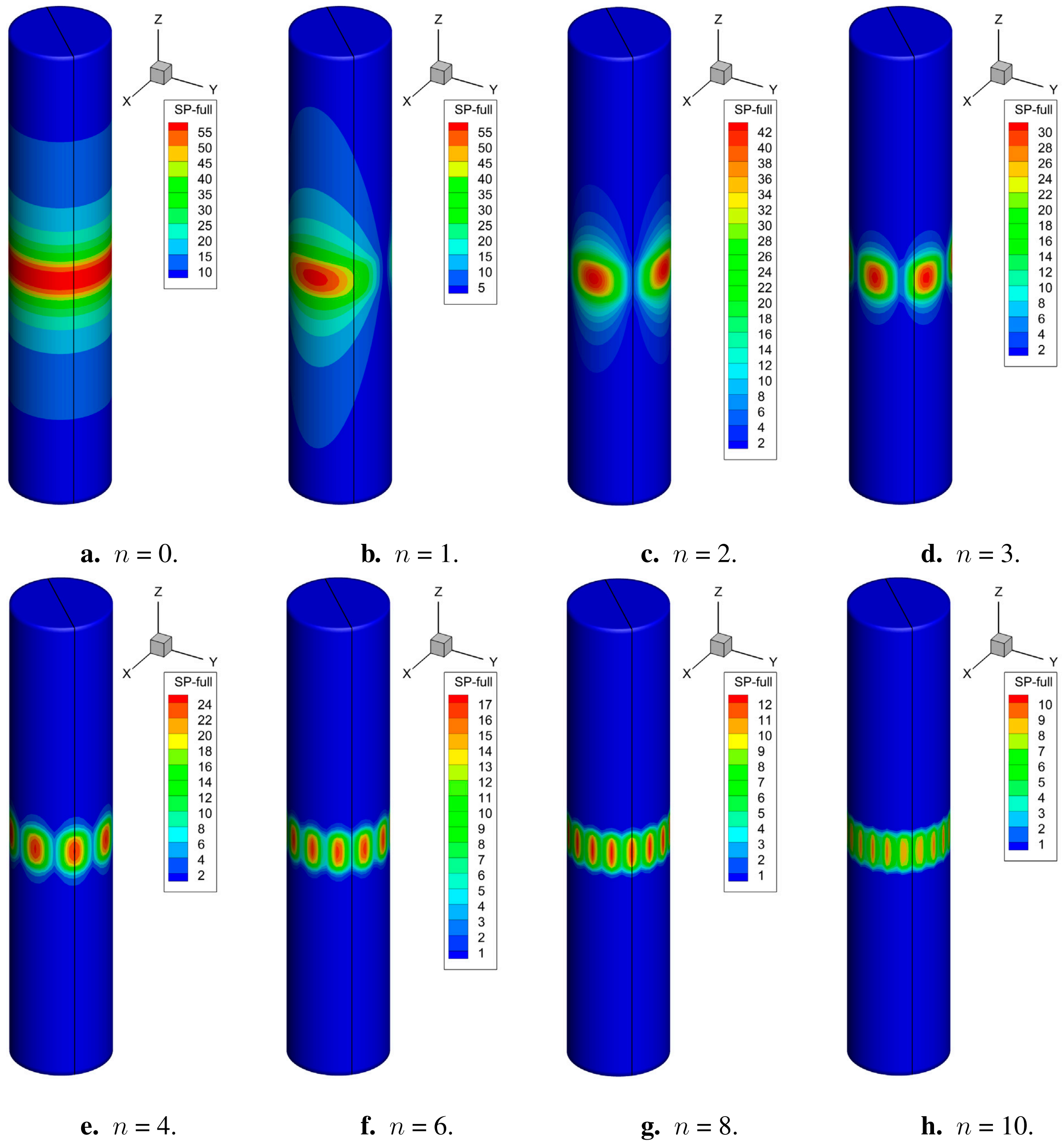

a. $n = 0$. **b.** $n = 1$. **c.** $n = 2$. **d.** $n = 3$.

e. $n = 4$. **f.** $n = 6$. **g.** $n = 8$. **h.** $n = 10$.

FIGURE 8
Numerical results. Sound pressure on the cylindrical shell with a length of 5 m. Frequency f = 500 Hz. Circumferential vibration order n varies. The black line represents the section for $\theta = pi/4$. **(A)** $n = 0$. **(B)** $n = 1$. **(C)** $n = 2$. **(D)** $n = 3$. **(E)** $n = 4$. **(F)** $n = 6$. **(G)** $n = 8$. **(H)** $n = 10$.

modes suggests that, under these conditions, either method could be reliably used.

For the closed cylindrical shell model with a length of 5 m, Figures 8A–H provide the numerical sound pressure on the structure surface for various circumferential vibration orders, in which the frequency $f = 500$ Hz. The black line in the figure represents the section for $\theta = \pi/4$. In Equation 19, when $\theta = 0$, $\cos(n\theta) = 1$, and the sound pressure $p(r, z, \theta)$ reaches its maximum. This is in accordance with Figure 8I. Furthermore, in Equation 19, when $n = 0$, $\cos(n\theta) = 1$, indicating that the sound pressure $p(r, z, \theta)$ is constant along the cylindrical shell's circumferential direction. This finding aligns with Figure 8A. Still in Equation 19, when $\theta = \pi/4$ and $n = 2$, 6, or 10, $\cos(n\theta) = 0$, indicating that the sound pressure $p(r, z, \theta) = 0$. This conclusion is consistent with Figures 8C, F, H. Remaining in Equation 19, when $\theta = \pi/4$ and $n = 4$ or 8, $\mathrm{abs}(\cos(n\theta)) = 1$, indicating that the sound pressure $p(r, z, \theta)$ is maximized. This is in accordance with Figures 8E, G. These results demonstrate good agreement between the results of our 3-D numerical analysis and the analytical solution. The agreement between the numerical results and the analytical predictions validates the analytical model's accuracy in predicting the sound pressure distribution on the cylindrical shell under different vibration modes. This is essential for the model's reliability in practical applications. The results highlight the importance of considering different vibration modes in the analysis. Each mode affects the sound pressure distribution, which is crucial for noise control and motor design.

5 Conclusion

This study concludes that the 3-D numerical analysis using FMBEM aligns well with the analytical solution for the sound pressure in the exterior acoustic domain of a cylindrical shell model, particularly when the model length is sufficient relative to its radius. The investigation reveals that computational accuracy improves as the model lengthens, suggesting a model length of at least 10 times the radius for accurate uncoupling analysis. The findings provide valuable insights for the design of low-noise motors and contribute to the understanding of electromagnetic vibration and noise control in electric motors.

Data availability statement

The original contributions presented in the study are included in the article/supplementary material; further inquiries can be directed to the corresponding author.

Author contributions

YX: conceptualization, investigation, methodology, project administration, and writing–original draft. JW: formal analysis, resources, supervision, and writing–review and editing. SY: data curation, validation, and writing–original draft. GL: software, visualization, and writing–review and editing. KZ: funding acquisition, validation, and writing–review and editing

Funding

The author(s) declare that financial support was received for the research, authorship, and/or publication of this article. The author(s) were sponsored by the Henan Provincial Key R&D and Promotion Project under Grant No. 232102220033, the National Natural Science Foundation of China under Grant No. 42207200, the Natural Science Foundation of Henan under Grant No. 222300420498, the Zhumadian 2023 Major Science and Technology Special Project under Grant No. ZMDSZDZX2023002, and the Postgraduate Education Reform and Quality Improvement Project of Henan Province under Grant No. YJS2023JD52.

Conflict of interest

The authors declare that the research was conducted in the absence of any commercial or financial relationships that could be construed as a potential conflict of interest.

Publisher's note

References

1. Ballo F, Gobbi M, Mastinu G, Palazzetti R. Noise and vibration of permanent magnet synchronous electric motors: a simplified analytical model. *IEEE Trans Transportation Electrification* (2023) 9:2486–96. doi:10.1109/TTE.2022.3209917

2. Xing Z, Wang X, Zhao W, Sun L, Niu N. Calculation method for natural frequencies of stator of permanent magnet synchronous motors based on three-dimensional elastic theory. *IEEE Trans Energy Convers* (2021) 36:755–66. doi:10.1109/TEC.2020.3030042

3. Xing Z, Wang X, Zhao W. Fast calculation of electromagnetic vibration of surface-mounted pmsm considering teeth saturation and tangential electromagnetic force. *IEEE Trans Ind Electronics* (2024) 71:316–26. doi:10.1109/TIE.2023.3243298

4. Zhu S, Zhao W, Ji J, Liu G, Mao Y, Liu T. Investigation of bread-loaf magnet on vibration performance in fscw pmsm considering force modulation effect. *IEEE Trans Transportation Electrification* (2021) 7:1379–89. doi:10.1109/TTE.2020.3035180

5. Hong J, Wang S, Sun Y, Sun X, Cao H. Piecewise stagger poles with continuous skew edge for vibration reduction in surface-mounted pm synchronous machines. *IEEE Trans Ind Electronics* (2021) 68:8498–506. doi:10.1109/TIE.2020.3013535

6. Lin F, Zuo SG, Deng WZ, Wu SL. Reduction of vibration and acoustic noise in permanent magnet synchronous motor by optimizing magnetic forces. *J Sound Vibration* (2018) 429:193–205. doi:10.1016/j.jsv.2018.05.018

7. Hu S, Zuo S, Wu H, Liu M. An analytical method for calculating the natural frequencies of a motor considering orthotropic material parameters. *IEEE Trans Ind Electronics* (2019) 66:7520–8. doi:10.1109/TIE.2018.2883194

8. Torregrossa D, Peyraut F, Fahimi B, M'Boua J, Miraoui A. Multiphysics finite-element modeling for vibration and acoustic analysis of permanent magnet synchronous machine. *IEEE Trans Energy Convers* (2011) 26:490–500. doi:10.1109/TEC.2010.2080681

9. Zhao J, Wang Z, Liu H, Ning F, Hong X, Du J, et al. Modal analysis and structure optimization of permanent magnet synchronous motor. *IEEE Access* (2020) 8:151856–65. doi:10.1109/ACCESS.2020.3017679

10. Mercorelli P. Denoising and harmonic detection using nonorthogonal wavelet packets in industrial applications. *J Syst Sci Complexity* (2007) 20:325–43. doi:10.1007/s11424-007-9028-z

11. Mercorelli P. Detection of oscillations with application in the pantograph control. *Recent Patents Electr Eng* (2011) 4:71–7. doi:10.2174/1874476111104010071

12. Mercorelli P. A denoising procedure using wavelet packets for instantaneous detection of pantograph oscillations. *Mech Syst Signal Process* (2013) 35:137–49. doi:10.1016/j.ymssp.2012.09.001

13. Chai F, Li Y, Pei Y, Li Z. Accurate modelling and modal analysis of stator system in permanent magnet synchronous motor with concentrated winding for vibration prediction. *IET Electric Power Appl* (2018) 12:1225–32. doi:10.1049/iet-epa.2017.0813

14. Wu Z, Fan Y, Chen H, Wang X, Lee CHT. Electromagnetic force and vibration study of dual-stator consequent-pole hybrid excitation motor for electric vehicles. *IEEE Trans Vehicular Technology* (2021) 70:4377–88. doi:10.1109/TVT.2021.3075461

15. Park S, Kim W, Kim SI. A numerical prediction model for vibration and noise of axial flux motors. *IEEE Trans Ind Electronics* (2014) 61:5757–62. doi:10.1109/TIE.2014.2300034

16. Čorović S, Miljavec D. Modal analysis and rotor-dynamics of an interior permanent magnet synchronous motor: an experimental and theoretical study. *Appl Sci* (2020) 10:5881. doi:10.3390/app10175881

17. Mendizabal M, McCloskey A, Poza J, Zarate S, Iriondo J, Irazu L. Optimum slot and pole design for vibration reduction in permanent magnet synchronous motors. *Appl Sci* (2021) 11:4849. doi:10.3390/app11114849

18. Wang H, Williams K. Effects of laminations on the vibrational behaviour of electrical machine stators. *J Sound Vibration* (1997) 202:703–15. doi:10.1006/jsvi.1996.0845

19. Deng W, Zuo S. Axial force and vibroacoustic analysis of external-rotor axial-flux motors. *IEEE Trans Ind Electronics* (2018) 65:2018–30. doi:10.1109/TIE.2017.2739697

20. Xu X, Han Q, Qin Z, Chu F. Analytical methods for the radial electromagnetic vibration of stator in permanent magnet motors with an amorphous alloy core. *Mech Syst Signal Process* (2020) 145:106909. doi:10.1016/j.ymssp.2020.106909

21. Mao Y, Zhao W, Zhu S, Chen Q, Ji J. Vibration investigation of spoke-type pm machine with asymmetric rotor considering modulation effect of stator teeth. *IEEE Trans Ind Electronics* (2021) 68:9092–103. doi:10.1109/TIE.2020.3022530

22. Wang S, Hong J, Sun Y, Cao H. Mechanical and magnetic pivot roles of tooth in vibration of electrical machines. *IEEE Trans Energy Convers* (2021) 36:139–48. doi:10.1109/TEC.2020.3007802

23. Xing Z, Wang X, Zhao W, Wang F. Calculation of stator natural frequencies of electrical machines considering complex boundary conditions. *IEEE Trans Industry Appl* (2022) 58:7079–87. doi:10.1109/TIA.2022.3191301

24. Zhao G, Sun L, Niu N, Wang X, Xing Z. Analysis of vibration characteristics of stators of electrical machines under actual boundary. *Mech Syst Signal Process* (2023) 185:109778. doi:10.1016/j.ymssp.2022.109778

25. Sommerfeld A. Partial differential equations in physics. Academic Press (1949). v-vi. doi:10.1016/B978-0-12-654658-3.50003-3

26. Engleder OSS. Stabilized boundary element methods for exterior Helmholtz problems. *Numerische Mathematik* (2008) 110:145–60. doi:10.1007/s00211-008-0161-y

27. Chen L, Zhang Y, Lian H, Atroshchenko E, Ding C, Bordas S. Seamless integration of computer-aided geometric modeling and acoustic simulation: isogeometric boundary element methods based on catmull-clark subdivision surfaces. *Adv Eng Softw* (2020) 149:102879. doi:10.1016/j.advengsoft.2020.102879

28. Greengard L, Rokhlin V. A fast algorithm for particle simulations. *J Comput Phys* (1987) 73:325–48. doi:10.1016/0021-9991(87)90140-9

29. Coifman R, Rokhlin V, Wandzura S. The fast multipole method for the wave equation: a pedestrian prescription. *IEEE Antennas Propagation Mag* (1993) 35:7–12. doi:10.1109/74.250128

30. Rokhlin V. Diagonal forms of translation operators for the Helmholtz equation in three dimensions. *Appl Comput Harmonic Anal* (1993) 1:82–93. doi:10.1006/acha.1993.1006

31. Martinsson P, Rokhlin V. A fast direct solver for boundary integral equations in two dimensions. *J Comput Phys* (2005) 205:1–23. doi:10.1016/j.jcp.2004.10.033

32. Martinsson P, Rokhlin V. A fast direct solver for scattering problems involving elongated structures. *J Comput Phys* (2007) 221:288–302. doi:10.1016/j.jcp.2006.06.037

33. Bebendorf SMR. Adaptive low-rank approximation of collocation matrices. *Computing* (2003) 70:1–24. doi:10.1007/s00607-002-1469-6

34. Kim NH, Dong J. Shape sensitivity analysis of sequential structural-acoustic problems using FEM and BEM. *J Sound Vibration* (2006) 290:192–208. doi:10.1016/j.jsv.2005.03.013

35. Chen L, Zhao J, Lian H, Yu B, Atroshchenko E, Li P. A BEM broadband topology optimization strategy based on Taylor expansion and SOAR method-Application to 2D acoustic scattering problems. *Int J Numer Methods Eng* (2023) 124:5151–82. doi:10.1002/nme.7345

36. Qu Y, Zhou Z, Chen L, Lian H, Li X, Hu Z, et al. Uncertainty quantification of vibro-acoustic coupling problems for robotic manta ray models based on deep learning. *Ocean Eng* (2024) 299:117388. doi:10.1016/j.oceaneng.2024.117388

37. Simpson R, Bordas S, Trevelyan J, Rabczuk T. A two-dimensional isogeometric boundary element method for elastostatic analysis. *Computer Methods Appl Mech Eng* (2012) 209-212:87–100. doi:10.1016/j.cma.2011.08.008

38. Hughes T, Cottrell J, Bazilevs Y. Isogeometric analysis: CAD, finite elements, NURBS, exact geometry and mesh refinement. *Computer Methods Appl Mech Eng* (2005) 194:4135–95. doi:10.1016/j.cma.2004.10.008

39. Chen L, Lu C, Lian H, Liu Z, Zhao W, Li S, et al. Acoustic topology optimization of sound absorbing materials directly from subdivision surfaces with isogeometric boundary element methods. *Computer Methods Appl Mech Eng* (2020) 362:112806. doi:10.1016/j.cma.2019.112806

40. Shen X, Du C, Jiang S, Sun L, Chen L. Enhancing deep neural networks for multivariate uncertainty analysis of cracked structures by POD-RBF. *Theor Appl Fracture Mech* (2023) 125:103925. doi:10.1016/j.tafmec.2023.103925

41. Scott M, Simpson R, Evans J, Lipton S, Bordas S, Hughes T, et al. Isogeometric boundary element analysis using unstructured T-splines. *Computer Methods Appl Mech Eng* (2013) 254:197–221. doi:10.1016/j.cma.2012.11.001

42. Takahashi T, Matsumoto T. An application of fast multipole method to isogeometric boundary element method for Laplace equation in two dimensions. *Eng Anal Boundary Elem* (2012) 36:1766–75. doi:10.1016/j.enganabound.2012.06.004

43. Chen L, Cheng R, Li S, Lian H, Zheng C, Bordas S. A sample-efficient deep learning method for multivariate uncertainty qualification of acoustic-vibration interaction problems. *Computer Methods Appl Mech Eng* (2022) 393:114784. doi:10.1016/j.cma.2022.114784

44. Zhang S, Yu B, Chen L. Non-iterative reconstruction of time-domain sound pressure and rapid prediction of large-scale sound field based on ig-drbem and pod-rbf. *J Sound Vibration* (2024) 573:118226. doi:10.1016/j.jsv.2023.118226

45. Chen L, Lian H, Dong HW, Yu P, Jiang S, Bordas SP. Broadband topology optimization of three-dimensional structural-acoustic interaction with reduced order isogeometric FEM/BEM. *J Comput Phys* (2024) 509:113051. doi:10.1016/j.jcp.2024.113051

46. Chen L, Lian H, Pei Q, Meng Z, Jiang S, Dong HW, et al. FEM-BEM analysis of acoustic interaction with submerged thin-shell structures under seabed reflection conditions. *Ocean Eng* (2024) 309:118554. doi:10.1016/j.oceaneng.2024.118554

47. Cao G, Yu B, Chen L, Yao W. Isogeometric dual reciprocity bem for solving non-fourier transient heat transfer problems in fgms with uncertainty analysis. *Int J Heat Mass Transfer* (2023) 203:123783. doi:10.1016/j.ijheatmasstransfer.2022.123783

48. Ginnis A, Kostas K, Politis C, Kaklis P, Belibassakis K, Gerostathis T, et al. Isogeometric boundary-element analysis for the wave-resistance problem using T-splines. *Computer Methods Appl Mech Eng* (2014) 279:425–39. doi:10.1016/j.cma.2014.07.001

49. Zhang G, He Z, Qin J, Hong J. Magnetically tunable bandgaps in phononic crystal nanobeams incorporating microstructure and flexoelectric effects. *Appl Math Model* (2022) 111:554–66. doi:10.1016/j.apm.2022.07.005

50. Zhang G, He Z, Gao XL, Zhou H. Band gaps in a periodic electro-elastic composite beam structure incorporating microstructure and flexoelectric effects. *Archive Appl Mech* (2023) 93:245–60. doi:10.1007/s00419-021-02088-9

51. Chen L, Lian H, Xu Y, Li S, Liu Z, Atroshchenko E, et al. Generalized isogeometric boundary element method for uncertainty analysis of time-harmonic wave propagation in infinite domains. *Appl Math Model* (2023) 114:360–78. doi:10.1016/j.apm.2022.09.030

52. Zhang G, Gao X, Wang S, Hong J. Bandgap and its defect band analysis of flexoelectric effect in phononic crystal plates. *Eur J Mechanics-A/Solids* (2024) 104:105192. doi:10.1016/j.euromechsol.2023.105192

53. Zhang G, He Z, Wang S, Hong J, Cong Y, Gu S. Elastic foundation-introduced defective phononic crystals for tunable energy harvesting. *Mech Mater* (2024) 191:104909. doi:10.1016/j.mechmat.2024.104909

54. Shen X, Du C, Jiang S, Zhang P, Chen L. Multivariate uncertainty analysis of fracture problems through model order reduction accelerated SBFEM. *Appl Math Model* (2024) 125:218–40. doi:10.1016/j.apm.2023.08.040

55. Simpson R, Liu Z, Vázquez R, Evans J. An isogeometric boundary element method for electromagnetic scattering with compatible B-spline discretizations. *J Comput Phys* (2018) 362:264–89. doi:10.1016/j.jcp.2018.01.025

56. Qu Y, Jin F, Yang J. Temperature effects on mobile charges in thermopiezoelectric semiconductor plates. *Int J Appl Mech* (2021) 13:2150037. doi:10.1142/s175882512150037x

57. Xu Y, Li H, Chen L, Zhao J, Zhang X. Monte Carlo based isogeometric stochastic finite element method for uncertainty quantization in vibration analysis of piezoelectric materials. *Mathematics* (2022) 10:1840. doi:10.3390/math10111840

58. Qu Y, Zhang G, Gao X, Jin F. A new model for thermally induced redistributions of free carriers in centrosymmetric flexoelectric semiconductor beams. *Mech Mater* (2022) 171:104328. doi:10.1016/j.mechmat.2022.104328

59. Chen L, Wang Z, Lian H, Ma Y, Meng Z, Li P, et al. Reduced order isogeometric boundary element methods for CAD-integrated shape optimization in electromagnetic scattering. *Computer Methods Appl Mech Eng* (2024) 419:116654. doi:10.1016/j.cma.2023.116654

60. Li H, Chen L, Zhi G, Meng L, Lian H, Liu Z, et al. A direct fe2 method for concurrent multilevel modeling of piezoelectric materials and structures. *Computer Methods Appl Mech Eng* (2024) 420:116696. doi:10.1016/j.cma.2023.116696

61. Chen L, Liu C, Zhao W, Liu L. An isogeometric approach of two dimensional acoustic design sensitivity analysis and topology optimization analysis for absorbing material distribution. *Computer Methods Appl Mech Eng* (2018) 336:507–32. doi:10.1016/j.cma.2018.03.025

62. Xu G, Li M, Mourrain B, Rabczuk T, Xu J, Bordas SP. Constructing IGA-suitable planar parameterization from complex CAD boundary by domain partition and global/local optimization. *Computer Methods Appl Mech Eng* (2018) 328:175–200. doi:10.1016/j.cma.2017.08.052

63. Li S, Trevelyan J, Wu Z, Lian H, Wang D, Zhang W. An adaptive SVD-Krylov reduced order model for surrogate based structural shape optimization through

isogeometric boundary element method. *Computer Methods Appl Mech Eng* (2019) 349: 312–38. doi:10.1016/j.cma.2019.02.023

64. Chen L, Lian H, Liu Z, Chen H, Atroshchenko E, Bordas S. Structural shape optimization of three dimensional acoustic problems with isogeometric boundary element methods. *Computer Methods Appl Mech Eng* (2019) 355:926–51. doi:10.1016/j.cma.2019.06.012

65. Chen L, Lian H, Natarajan S, Zhao W, Chen X, Bordas S. Multi-frequency acoustic topology optimization of sound-absorption materials with isogeometric boundary element methods accelerated by frequency-decoupling and model order reduction techniques. *Computer Methods Appl Mech Eng* (2022) 395:114997. doi:10.1016/j.cma.2022.114997

66. Lu C, Chen L, Luo J, Chen H. Acoustic shape optimization based on isogeometric boundary element method with subdivision surfaces. *Eng Anal Boundary Elem* (2023) 146:951–65. doi:10.1016/j.enganabound.2022.11.010

67. Chen L, Lian H, Liu Z, Gong Y, Zheng C, Bordas S. Bi-material topology optimization for fully coupled structural-acoustic systems with isogeometric FEM-BEM. *Eng Anal Boundary Elem* (2022) 135:182–95. doi:10.1016/j.enganabound.2021.11.005

68. Burton AJ, Miller GF. The application of integral equation methods to the numerical solution of some exterior boundary-value problems. *Proc R Soc Lond* (1971) 323:201–10. doi:10.1098/rspa.1971.0097

Frontiers in Physics

TYPE Original Research
PUBLISHED 04 December 2024
DOI 10.3389/fphy.2024.1490012

OPEN ACCESS

EDITED BY
Leilei Chen,
Huanghuai University, China

REVIEWED BY
Arun Y. Patil,
Manipal Institute of Technology
Bengaluru, India
Ang Zhao,
Shanghai Civil Aviation College, China

*CORRESPONDENCE
Qidan Xiao,
xiaoqidan253@163.com

RECEIVED 02 September 2024
ACCEPTED 15 November 2024
PUBLISHED 04 December 2024

CITATION
Xiao Q, Deng H, Gao B and Zhao J (2024) Design and thermal performance analysis of self-insulation concrete compound blocks. *Front. Phys.* 12:1490012.
doi: 10.3389/fphy.2024.1490012

Design and thermal performance analysis of self-insulation concrete compound blocks

Qidan Xiao[1,2]*, Hui Deng[1,2], Bo Gao[1,2] and Jun Zhao[3]

[1]College of Architecture and Civil Engineering, Xinyang Normal University, Xinyang, China, [2]Henan New Environmentally-Friendly Civil Engineering Materials Engineering Research Center, Xinyang Normal University, Xinyang, China, [3]School of Water Conservancy and Civil Engineering, Zhengzhou University, Zhengzhou, China

More than 60% of energy losses occur through the building envelope. Exterior wall insulation technology is widely used for wall insulation, but it is prone to cracking, falling off, and causing fires. Self-insulation concrete compound blocks (SIB) have attracted considerable attention in recent years for meeting building energy efficiency standards without the need for external insulation treatment. In this study, the shale ceramsite concrete (SCC) was prepared as the base material for the blocks through the orthogonal test and range analysis. In accordance with the insulation requirements of residential building walls, 12 types of self-insulation concrete compound blocks (SIB) were designed. The heat transfer process of these blocks was simulated and analyzed using Ansys Workbench, enabling a comparison of the thermal conductivity effects resulting from different hole distribution schemes in the insulation blocks. The simulated values were compared with the theoretical calculations, and the simulated results were in good agreement with the theoretical calculations. The results showed that TZ-12 exhibited the optimal hole configuration with a heat transfer coefficient of 0.5 W/(m^2·K), which was 38.3% lower than that of the external insulation block TZ-9. Additionally, TZ-12 demonstrated the average compressive strength of 8.28 MPa and the minimum compressive strength of 7.45 MPa, meeting the requirements for MU7.5 strength grade and also satisfying the requirement of not less than MU5.0 when self-insulation blocks were used for external walls. The simulated heat flux rate of the self-insulation concrete compound block wall (SIBW) was 15.4 W, and its heat transfer coefficient was 0.56 W/(m^2·K), which was 29.1% lower than that of the external thermal insulation wall (ETIW), meeting the design standard for achieving the 65% energy saving in residential buildings situated in regions with hot summers and cold winters.

KEYWORDS

self-insulation concrete compound blocks, ANSYS workbench, heat transfer coefficient, optimization design, energy saving

1 Introduction

The building sector was responsible for 45.5% of China's overall energy consumption in 2020, with more than 60% of energy loss occurring through the building envelope [1, 2]. Therefore, the energy consumption in buildings can be effectively reduced by focusing on enhancing the thermal insulation and energy-saving capabilities of the outer wall [3, 4]. External insulation technology is widely used for wall insulation but has two inevitable defects: firstly, the lifespan of building insulation materials differs from that of the structure, making them prone to cracking and falling off; secondly, fire hazards cannot be avoided [5, 6]. Self-insulation concrete compound blocks (SIB) have garnered significant attention due to their unique composition of concrete and thermal insulation materials [7]. This construction material eliminates the need for external insulation treatments while still meeting building energy conservation standards [8, 9].

The mechanical properties requirements can still be met by incorporating insulation material, thereby optimizing the thermal conductivity of the blocks [10, 11]. Jiao et al. [12] conducted a study on the optimal combination and resultant characteristics of hollow blocks made from alkali-activated slag ceramsite concrete, which exhibited a compressive strength of up to MU15. The study conducted by Osman et al. [13] demonstrated that the recently developed ceramist concrete blocks effectively meet the criteria for insulation blocks in extremely cold areas, contributing to energy conservation efforts. Xie et al. [14] reported that the thermal resistance coefficient of the recycled concrete hollow block containing Sludge ceramsite was measured to be 0.884 (m^2·K)/W. Al-Tarbi et al. [15] investigated the compliance of the recently developed blocks (composed of perlite, vermiculite, scoria, and polystyrene) with the non-load-bearing compressive strength requirement specified in ASTMC129. Al-Tamimi et al. [16] incorporated perlite into a recently developed concrete block at a proportion of 30% to enhance its thermal efficiency. The addition of perlite resulted in a significant reduction in the thermal conductivity of the block, with a value of 0.309 W/(m·K), indicating a substantial decrease by 33% compared to the control block that lacked any insulating materials.

Topcu and Iskdag [17] utilized perlite as a means to manufacture clay blocks with enhanced resistance to heat. The introduction of 30% perlite replacement resulted in a significant reduction of approximately 52% in thermal conductivity, compared to the control block. Liu et al. [18] conducted a comprehensive experimental analysis on the insulation performance of recycled concrete blocks made from construction and demolition waste. According to Jaafar et al. [19], the utilization of broken bricks and concrete slurry waste in partition walls made of concrete blocks could potentially enhance their ability to withstand high temperatures, thereby offering an added value application. According to the study conducted by Zhao et al. [20], it was observed that concrete blocks manufactured using 100% recycled concrete aggregates exhibited a compressive strength of 11.1 MPa after a curing period of 28 days. Al-Awsh et al. [21] studied utilizing volcanic scoria as the primary material for constructing walls can significantly enhance thermal resistance, resulting in an impressive increase of approximately 279% compared to traditional concrete blocks.

By integrating holes optimization into numerical simulation techniques, it is possible to further improve the thermal conductivity of the bricks [22–24]. Al-Tamimi et al. [25] employed the ABAQUS software to ascertain the most favorable hole configuration for concrete bricks, aiming to enhance wall thermal resistance and subsequently decrease electricity consumption. Al-Awsh et al. [26] utilized rectangular cavities arranged in three rows to minimize the effective thermal conductivity. They also verified their findings by employing a three-dimensional model developed through the ANSYS-Fluent software program. According to the study conducted by Cuce et al. [27], it was found that the 5-row hollow design demonstrated superior thermal resistance and lightness compared to the 3-row and 4-row configurations. Shuai et al. [28] found that H-shaped interlocking insulation blocks exhibited superior thermal performance compared to crossed-shaped ones. Notably, the most significant enhancement in block's thermal performance was achieved through a reduction in the thermal conductivity of concrete materials.

According to the study conducted by Ouakarrouch et al. [29], it was observed that an augmentation in both the width and quantity of cavities results in a notable reduction in heat dissipation and an elevation in thermal insulation. Blanco et al. [30] demonstrated that numerical analysis provides a reliable estimation of the thermal performance of walls, which aligns well with experimental results obtained using a guarded hot-box apparatus. Li et al. [31] investigated the impact of various combinations and configurations of holes on thermal conductivity, revealing a complex relationship between hole quantity, arrangement, and thermal conductivity. Bi-chao et al. [32] studied that enhancing the thermal insulation characteristic of the block can be achieved by increasing the number of hole rows in the air layer, while maintaining a certain hole rate. Sutcu et al. [33] demonstrated the effective application of DOE-SM techniques in conjunction with finite element modeling for optimizing the overall heat transfer coefficient.

In the context of the current building energy-saving goal, developing higher-performance SIB to meet the standards for energy-saving design and market demand has become a significant challenge in the industry. This paper designed a new type of SIB specifically for residential buildings located in areas with hot summers and cold winters. The heat transfer process of blocks was simulated and analyzed using Ansys Workbench, enabling a comparison of the thermal conductivity effects resulting from different hole distribution schemes in the insulation blocks. Finally, an optimal design scheme was obtained to meet the 65% energy saving standard in hot summer and cold winter regions, providing theoretical guidance for the development of high-performance SIB and promoting its popularization and application.

2 Preparation for shale ceramsite concrete

Compared to conventional concrete, ceramic lightweight aggregate concrete possesses characteristics such as low bulk density, thermal insulation, and heat preservation [34, 35]. These properties enable a reduction in the dead weight of building structural elements by approximately 20%–25%. However, the utilization rate of lightweight aggregate concrete in building structure engineering remains low due to challenges in achieving sufficient structural strength and harsh construction conditions. The shale ceramite exhibits exceptional strength, making it an ideal material for the production of lightweight aggregate concrete [36]. Consequently, this study undertook the design and preparation of shale ceramsite concrete (SCC) to ensure both the desired lightweight characteristics of prefabricated building components and their structural performance.

TABLE 1 Main parameters of shale ceramsite.

Cylinder compressive strength (MPa)	Stacking density (kg/m^3)	Apparent density (kg/m^3)	Aggregate size (mm)	Water absorption rate at 1 h (%)
4.2	768	1,430	5–20	3

2.1 Materials

The test utilized Tongli brand PO42.5 common Portland cement as the primary binder. Natural river sand, with an accumulation density of 1,450 kg/m^3 and an apparent density of 2,710 kg/m^3, was employed as the lightweight aggregate. Grade 800 shale ceramsite, characterized by its main parameters outlined in Table 1, served as the coarse aggregate material. Class I fly ash, having a density of 2,100 kg/m^3, was incorporated for this experimental study. A polycarboxylic acid water reducer was employed in this investigation with a water reduction efficiency of approximately 32%. For thermal insulation purposes, hydrophobic perlite insulation board exhibiting a thermal conductivity value of 0.051 W/m·K was implemented.

2.2 Mix proportion design

A comprehensive experiment is one in which all possible combinations of factor levels are tested. This experimental design offers the advantage of providing extensive information, but it also has the drawback of requiring a large number of experiments and consuming significant resources. The orthogonal test employed in this study is a design method used to investigate multiple factors and levels. It selects representative points from the comprehensive test based on orthogonality, making it an efficient, rapid, and cost-effective experimental design method [37].

The fundamental tool for designing orthogonal experiments is the orthogonal table, a mathematical table based on the principles of equilibrium distribution and combinatorial mathematics. By utilizing the orthogonal table, experiments can be designed to possess balanced dispersion characteristics. According to JGJ/T12-2019 [38], shale ceramsite concrete (SCC) with LC30 strength was designed using the loose volume method. Sixteen orthogonal tests were conducted based on four factors and four levels, as shown in Table 2. Test factor A represents the sand rate, test factor B represents the water-cement ratio, test factor C represents the fly ash substitution rate, and test factor D represents the dosage of water reducing agent.

In this research, the compressive strength and flexural tensile strength were chosen as control factors to primarily examine their impact on the compressive strength and flexural tensile strength of concrete samples. The experimental design is presented in Table 3. The evaluation of compressive strength and flexural tensile strength for the test blocks was conducted following GB/T50081-2019 [39]. The dimensions of the test blocks utilized for evaluating compressive strength were 100 mm × 100 mm × 100 mm, while for evaluating flexural tensile strength, they were 100 mm × 100 mm × 400 mm in size. The compressive strength and flexural strength of the specimens were tested using WAW-3000 universal testing machine. The test process is shown in Supplementary Figure S1 (supplementary figure at the end of the article).

The compressive strength of the test blocks shall be calculated according to the following formula 1:

$$f_{cc} = \frac{F}{A} \tag{1}$$

Where: f_{cc} is the compressive strength of the test blocks, F is the failure load of the specimen, A is the bearing surface of the specimen.

The flexural tensile strength of the test blocks should be calculated according to the following formula 2:

$$f_f = \frac{Fl}{b\hbar^2} \tag{2}$$

Where: f_{cc} is the flexural tensile strength of the test blocks, F is the failure load of the specimen, l is the span between supports, b is the section width of the specimen, $\hbar$ is the height of the specimen section.

2.3 Range analysis

The outcomes of the orthogonal experiment conducted on SCC are presented in Table 4 following testing and data processing.

The range analysis, also referred to as intuitive analysis, is an intuitive and widely employed analytical method in the examination of results from orthogonal test design. $\overline{K}$ represents the mean value of the sum of experimental indices corresponding to identical levels within a specific column of factors. The magnitude of $\overline{K}$ can be used to determine the optimal level and optimal combination for a particular column of factors. R denotes the range of a factor within a column, which is essentially the difference between the maximum and minimum values of $\overline{K}$ in that column. The magnitude of R can be utilized to assess the primary and secondary order of influence exerted by test factors on test indexes.

The compressive strength test data of the SCC was subjected to range analysis. The results in Table 5 demonstrated that the range values (R) for the four test factors A, B, C, and D were higher than those of the control group (E), indicating compliance with orthogonal test error requirements. By comparing primary and secondary factors, it was evident that sand rate exerted the most significant influence on compressive strength of the SCC, followed by fly ash substitution rate, dosage of water-reducing agent, and water-cement ratio. Notably, both sand rate and fly ash substitution rate exhibited a substantial impact on compressive strength of the SCC. The optimal levels determined were as follows: sand rate at 50%, water-cement ratio at 0.3, fly ash substitution rate at 20%, and dosage of water-reducing agent at 0.25%. In other words, $A_3B_2C_3D_3$ represented the optimal combination for achieving maximum compressive strength.

TABLE 2 The orthogonal table consists of four factors and four levels.

Test number	Factor			
	Sand rate (A) %	Water-cement ratio (B)	Fly ash substitution rate (C) %	Dosage of water reducing agent (D) %
1	A_1(30)	B_1(0.28)	C_1(0)	D_1(0.15)
2	A_1(30)	B_2(0.30)	C_2(10)	D_2(0.20)
3	A_1(30)	B_3(0.32)	C_3(20)	D_3(0.25)
4	A_1(30)	B_4(0.34)	C_4(30)	D_4(0.30)
5	A_2(40)	B_1(0.28)	C_2(10)	D_3(0.25)
6	A_2(40)	B_2(0.30)	C_1(0)	D_4(0.30)
7	A_2(40)	B_3(0.32)	C_4(30)	D_1(0.15)
8	A_2(40)	B_4(0.34)	C_3(20)	D_2(0.20)
9	A_3(50)	B_1(0.28)	C_3(20)	D_4(0.30)
10	A_3(50)	B_2(0.30)	C_4(30)	D_3(0.25)
11	A_3(50)	B_3(0.32)	C_1(0)	D_2(0.20)
12	A_3(50)	B_4(0.34)	C_2(10)	D_1(0.15)
13	A_4(60)	B_1(0.28)	C_4(30)	D_2(0.20)
14	A_4(60)	B_2(0.30)	C_3(20)	D_1(0.15)
15	A_4(60)	B_3(0.32)	C_2(10)	D_4(0.30)
16	A_4(60)	B_4(0.34)	C_1(0)	D_3(0.25)

It could be seen from Table 5 that with the increase of sand rate (A), the compressive strength of SCC first increased and then decreased. When the sand rate was 50%, the compressive strength of SCC reached the maximum, which was 48.46 MPa. The reason was that the strength of shale ceramite was lower than that of cement stone, and it was prone to failure first under loading and compression conditions. The smaller the content of shale pottery was, the larger the sand rate was, and the higher the strength of the concrete was. However, when the sand rate exceeded the reasonable sand rate, the gradability of SCC became worse, which easily led to poor compactness and low compressive strength.

The proper replacement of cement with fly ash (C) was beneficial to improve the compressive performance of SCC. In the later curing stage, fly ash could react with cement twice to produce hydrated calcium silicate gel. Moreover, the particle size of fly ash was much smaller than the particle size of cement in the pores of shale ceramite. The pores between cement could be filled with fly ash particles, which improved the overall compacting degree of concrete and its strength. However, if the replacement rate of fly ash was too large, the strength of concrete would also be insufficient due to too little cement content. Therefore, with the increase of the replacement rate of fly ash, the compressive strength of SCC would increase first and then decrease. When the replacement rate of fly ash was 20%, the compressive strength of SCC reached the maximum of 47.14 MPa. It was about 13.29% higher than that when the substitution rate of fly ash was 0.

The compressive strength of SCC increased with the increase of the dosage of water reducing agent (D), and the fluctuation of compressive strength was not obvious when the dosage of water reducing agent increased from 0.2% to 0.3%. This was because the water reducing agent could play a certain dispersion effect. With the increase of the dosage of water reducing agent, the concrete could maintain good flow performance under low water consumption. Thus, the compressive strength of shale concrete could be improved. The characteristics of ceramsite in SCC were different from the stones of ordinary concrete. The ceramsite was pre-wet for 1 h before use, so that the ceramsite reached the saturation state, and the water curing concrete would be released in the later period, so the water-cement ratio (C) changed within a certain range, and the impact on concrete was not very large.

The flexural tensile strength test data of the SCC was subjected to range analysis. The results in Table 6 demonstrated that the range values (R) for the four test factors A, B, C, and D were higher than those of the control group (E), indicating compliance with orthogonal test error requirements. By comparing primary and secondary factors, it was concluded that sand rate exerted the

TABLE 3 Mixing proportions for shale ceramsite concrete.

Test number	Concrete (kg/m^3)	Fly ash (kg/m^3)	Water (kg/m^3)	Ceramsite (kg/m^3)	Sand (kg/m^3)	Water reducing agent (kg/m^3)
1	400	0	112	645.12	522	0.6
2	360	40	120	645.12	522	0.8
3	320	80	128	645.12	522	1
4	280	120	136	645.12	522	1.2
5	360	40	112	552.96	696	1
6	400	0	120	552.96	696	1.2
7	280	120	128	552.96	696	0.6
8	320	80	136	552.96	696	0.8
9	320	80	112	460.8	870	1.2
10	280	120	120	460.8	870	1
11	400	0	128	460.8	870	0.8
12	360	40	136	460.8	870	0.6
13	280	120	112	368.64	1,044	0.8
14	320	80	120	368.64	1,044	0.6
15	360	40	128	368.64	1,044	1.2
16	400	0	136	368.64	1,044	1

most significant influence on the flexural tensile strength of SCC, followed by fly ash substitution rate, water-reducing agent mixing amount, and water-cement ratio. The optimal levels determined were as follows: sand rate at 50%, water-cement ratio at 0.3, fly ash substitution rate at 20%, and dosage of water-reducing agent at 0.25%. Therefore, based on these findings, $A_3B_2C_3D_3$ represented the optimal combination for achieving maximum flexural tensile strength. Table 6 showed that the flexural strength variation pattern was almost consistent with the compressive strength variation pattern.

The optimal combination for compressive strength, as determined by range analysis, was $A_3B_2C_3D_3$. Similarly, the optimal combination for flexural tensile strength also corresponded to $A_3B_2C_3D_3$. However, since this ideal combination was not included in the orthogonal table, we conducted a separate test on $A_3B_2C_3D_3$ and measured its thermal conductivity for further investigation. Several 300 mm × 300 mm × 50 mm specimens were prepared, and the thermal conductivity of SCC was tested using DR-3030 double plate thermal conductivity tester. The test process is shown in Supplementary Figure S2 (supplementary figure at the end of the article). The results of this test are presented in Table 7. The compressive strength of the optimal combination ($A_3B_2C_3D_3$) was 52.03 MPa, which was 1.2% higher than that of the optimal blocks in the other 16 groups. The flexural tensile strength of the optimal combination ($A_3B_2C_3D_3$) was 5.13 MPa, which was 1.9% higher than that of the optimal blocks in the other 16 groups. It was verified that $A_3B_2C_3D_3$ is the combination with the optimal mechanical properties. The thermal conductivity of SCC ($A_3B_2C_3D_3$) was 0.8314 W/(m·K). It was prepared as the base material of the blocks.

3 Optimization design and thermal performance analysis of holes

3.1 Evaluation index

The heat transfer coefficient pertains to the rate at which heat is transferred per unit area within a given time, under steady-state conditions, when there is a temperature difference of one unit between the air on either side of the building envelope. The magnitude of the heat transfer coefficient serves as an indicator for evaluating the thermal insulation performance of the wall, which is inversely proportional to building energy consumption. In this paper, numerical simulation methods are used to simulate the average surface temperature of the block under steady-state heat transfer conditions. Subsequently, the block's heat flux density is

TABLE 4 Results of orthogonal tests on shale ceramsite concrete.

Test number	Combination of factors	Dry apparent density (kg/m^3)	Compression strength (MPa)	Flexural tensile strength (MPa)
1	$A_1B_1C_1D_1$	1822.26	38.09	3.59
2	$A_1B_2C_2D_2$	1789.14	44.23	4.34
3	$A_1B_3C_3D_3$	1761.71	45.58	4.48
4	$A_1B_4C_4D_4$	1738.78	43.17	3.5
5	$A_2B_1C_2D_3$	1845.78	46.86	4.59
6	$A_2B_2C_1D_4$	1830.08	44.25	4.25
7	$A_2B_3C_4D_1$	1818.36	45.28	4.43
8	$A_2B_4C_3D_2$	1855.12	48.07	4.67
9	$A_3B_1C_3D_4$	1905.95	51.4	5.03
10	$A_3B_2C_4D_3$	1892.38	50.57	4.94
11	$A_3B_3C_1D_2$	1916.75	45.31	4.51
12	$A_3B_4C_2D_1$	1896.36	46.54	4.55
13	$A_4B_1C_4D_2$	1960.36	43.21	4.22
14	$A_4B_2C_3D_1$	1926.86	43.5	4.14
15	$A_4B_3C_2D_4$	1935.93	42.09	3.66
16	$A_4B_4C_1D_3$	1937.36	38.77	3.77

TABLE 5 The range analysis of compressive strength. (Unit: MPa).

Range values	A (%)	B	C (%)	D (%)	E
$\overline{K}_1$	42.77	44.89	41.61	43.35	44.71
$\overline{K}_2$	46.12	45.64	44.93	45.21	44.92
$\overline{K}_3$	48.46	44.57	47.14	45.45	44.90
$\overline{K}_4$	41.89	44.14	45.56	45.23	44.71
R	6.56	1.50	5.53	2.09	0.22
A>C >D >B >E					

TABLE 6 The range analysis of flexural tensile strength. (Unit: MPa).

Range values	A (%)	B	C (%)	D (%)	E
$\overline{K}_1$	3.98	4.36	4.03	4.18	4.22
$\overline{K}_2$	4.49	4.42	4.29	4.44	4.39
$\overline{K}_3$	4.76	4.27	4.58	4.45	4.38
$\overline{K}_4$	3.95	4.12	4.27	4.11	4.19
R	0.81	0.30	0.55	0.34	0.21
A>C >D >B >E					

calculated using Formula 3.

$$q = h\left(t_s - t_f\right) \tag{3}$$

Where: q is the surface heat flux density of the block perpendicular to the heat transfer direction, t_s is the surface temperature of the block, t_f is the surface environmental temperature of the block, and h is the heat transfer coefficient of the indoor and external surface.

Then the heat transfer coefficient of the block is calculated based on Formula 4:

$$K = \frac{q}{\Delta t} \tag{4}$$

Where: K is the heat transfer coefficient of the block, and Δt is the temperature difference of the environment on both sides of the block.

The heat transfer resistance is a physical quantity that measures the thermal impedance of the building envelope, which is the

TABLE 7 Results of the test for $A_3B_2C_3D_3$.

Serial number	Dry apparent density (kg/m^3)	Compression strength (MPa)	Flexural tensile strength (MPa)	Thermal conductivity (W/(m·K))
17	1909.36	52.03	5.13	0.8314

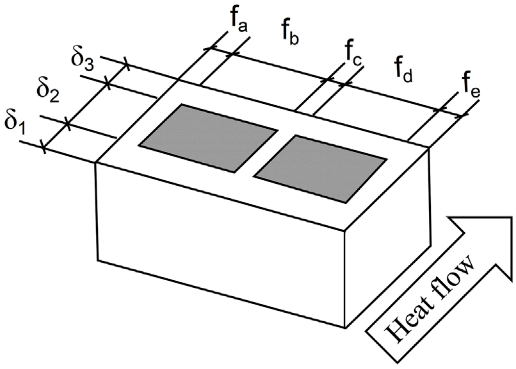

FIGURE 1
The schematic of the average thermal resistance calculation.

TABLE 8 Mesh optimization.

Element order	Hot surface temperature (K)				
	2 mm	3 mm	10 mm	15 mm	20 mm
Linear	297.38	297.38	297.37	297.36	297.35
Quadratic	297.38	297.38	297.38	297.37	297.37

reciprocal of the heat transfer coefficient. According to GB50176-2016 [40], the thermal resistance, heat transfer resistance, and heat transfer coefficient of the blocks are calculated theoretically.

The calculation formula for the heat resistance of a single material layer is shown in (5):

$$R = \frac{\delta}{\lambda} \tag{5}$$

Where: R is the thermal resistance of the material layer, δ is the thickness of the material layer, and λ is the thermal conductivity of the material.

The calculation formula for the thermal resistance of the multi-layer building envelope is shown in (6):

$$R = R_1 + R_2 + \cdots\cdots + R_n \tag{6}$$

Where: $R_1 + R_2 + \cdots\cdots + R_n$ is the thermal resistance of each layer of material.

The schematic of the average thermal resistance calculation is shown in Figure 1. The calculation of the thermal resistance for the composite envelope can be determined using the formula provided below:

$$\overline{R} = \frac{R_{ou} + R_{ol}}{2} - (R_i + R_e) \tag{7}$$

$$R_{ou} = \frac{1}{\frac{f_a}{R_{oua}} + \frac{f_b}{R_{oub}} + \cdots\cdots + \frac{f_q}{R_{ouq}}} \tag{8}$$

$$R_{ol} = R_i + R_1 + R_2 + \cdots\cdots + R_j + \cdots\cdots + R_n + R_e \tag{9}$$

$$R_j = \frac{1}{\frac{f_a}{R_{aj}} + \frac{f_b}{R_{bj}} + \cdots\cdots + \frac{f_q}{R_{qj}}} \tag{10}$$

Where: $\overline{R}$ is the thermal resistance of the heterogeneous composite building envelope, R_i is the heat transfer resistance of the inner surface, R_e is the heat transfer resistance of the external surface, $f_a, f_b, \cdots\cdots f_q$ is the percentage of the area of each part in the parallel direction of the heat flux in the total area, $R_{oua}, R_{oub}, \cdots\cdots R_{ouq}$ is the heat transfer resistance of each part parallel to the heat flux, $R_{aj}, R_{bj}, \cdots\cdots R_{qj}$ is the thermal resistance of each part of the j layer perpendicular to the heat flux.

The calculation of the heat transfer resistance for the flat wall of the envelope shall be based on Formula 11:

$$R_o = R_i + R + R_e \tag{11}$$

Where: R_o is the heat transfer resistance of the flat wall of the envelope.

The heat transfer coefficient of the flat wall of the envelope shall be calculated according to Formula 12:

$$K = \frac{1}{R_O} \tag{12}$$

Where: K is the heat transfer coefficient of the flat wall of the envelope.

3.2 Calibration parameters

According to the specifications outlined in JG/T407-2013 [41] regarding blocks dimensions, the length of the SIB is either 390 mm or 290 mm, with a width of 190 mm, 240 mm, or 280 mm, and a height of 190 mm. Other specifications and sizes are subject to mutual agreement between suppliers and consumers. To meet energy-saving requirements in regions characterized by hot summers and cold winters while considering existing research findings, the final block specification had been determined as 390 mm × 240 mm × 190 mm.

The concrete substrate and insulation material were assumed to be homogeneous, isotropic media with constant thermal properties.

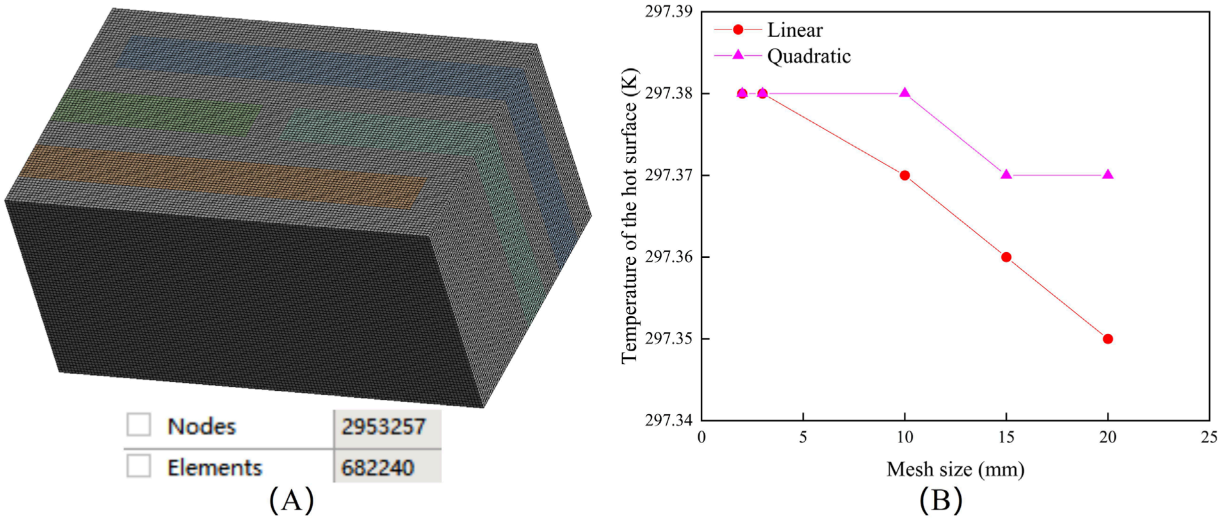

FIGURE 2
Block model: **(A)** 3 mm mesh size for TZ-12. **(B)** Mesh optimization curve.

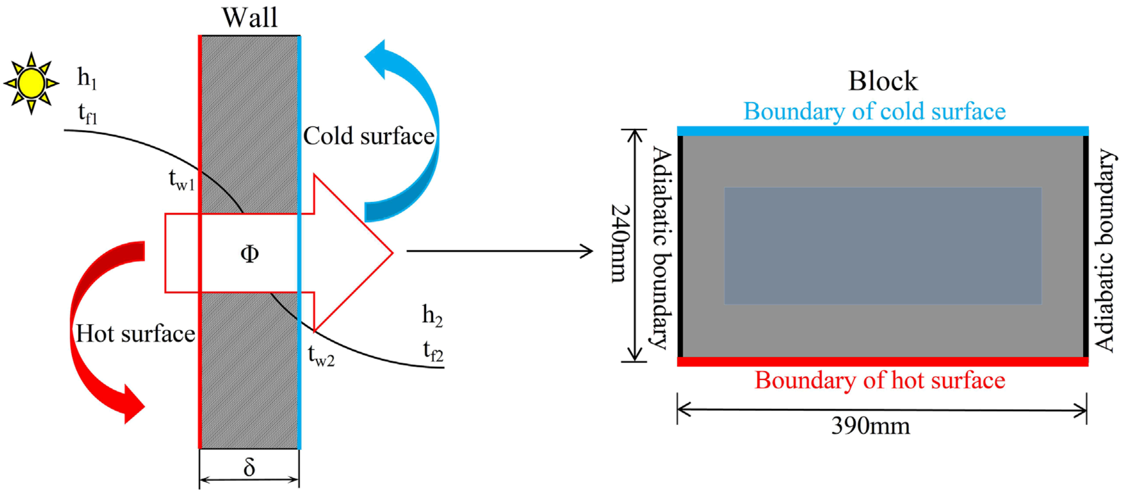

FIGURE 3
The heat transfer process of wall and setting of the block boundary conditions.

The thermal conductivity of the SCC was 0.8314 W/(m·K), while that of the perlite insulation board was 0.051 W/(m·K). Due to the difficulty in determining the thermal conductivity of air, this study converted the corresponding thermal resistance of an air layer's thickness into its equivalent thermal conductivity value for analysis purposes. For vertical air interlayers thicker than 40 mm, their thermal conductivity was considered as 0.222 W/(m·K) [42].

Since the geometric models were relatively regular, hexahedral elements were used for meshing. The element was made from"Solid 279", a 20-node element model. The element was suitable for thermal analysis of various materials and structures, including metals, plastics, composites, etc. Its flexibility made it the preferred element type in steady-state thermal analysis [43, 44].

The entire analysis relied on the grid-type approach used in this paper. The convergence criterion used a combination of H-type and P-type methods, focusing on the investigation of element size and element order [45, 46]. In the preliminary simulation, the finite element results differed greatly due to the different model geometries, so the mesh-independent simulation was carried out for the most complex hollow block (TZ-12), and the results are shown in Table 8. Both H-type and P-type methods met the convergence conditions in the model, as shown in Figure 2. In order to save time and reduce errors, the optimal mesh size of 3 mm was selected for simulation. The Element Order was set to Quadratic. The second-order element provided higher spatial resolution and enabled more accurate simulation of temperature gradients and

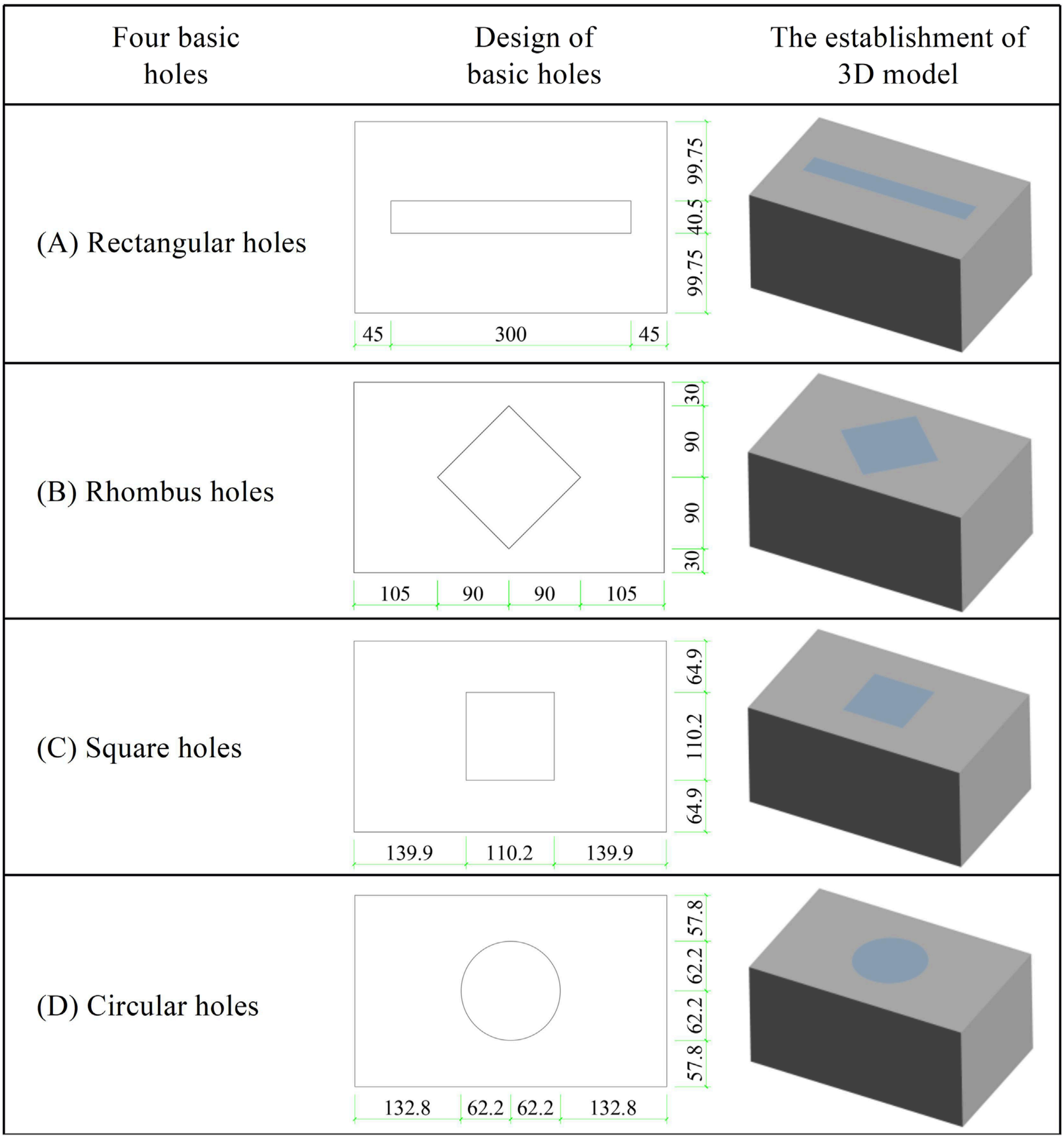

FIGURE 4
The design of the basic hole for the block and establishment of 3D model. (Unit: mm). **(A)** Rectangular holes, **(B)** Rhombus holes, **(C)** Square holes, **(D)** Circular holes.

heat flow distributions. The entire model had 682,240 elements and 2,953,257 nodes, as shown in Figure 2 [47, 48].

There were three common types of boundary conditions for steady-state heat transfer: (1) Constant boundary temperature; (2) Constant heat flux density at the boundary; (3) Known surface heat transfer coefficient on an object's boundary with known fluid temperature surrounding it.

The heat transfer problem in engineering could be simplified to a one-dimensional scenario due to the significantly smaller thickness compared to the length and width perpendicular to the direction of heat transfer. It was assumed that the thermal conductivity of air and concrete, used in simulations, remains constant within a specific temperature range. Furthermore, it was considered that both ambient temperatures at the low and high ends of the block remain unchanged.

The heat transfer process between the two fluids is depicted in Figure 3. In this study, we adopted the third type of boundary condition for steady-state heat transfer, designating the hot surface

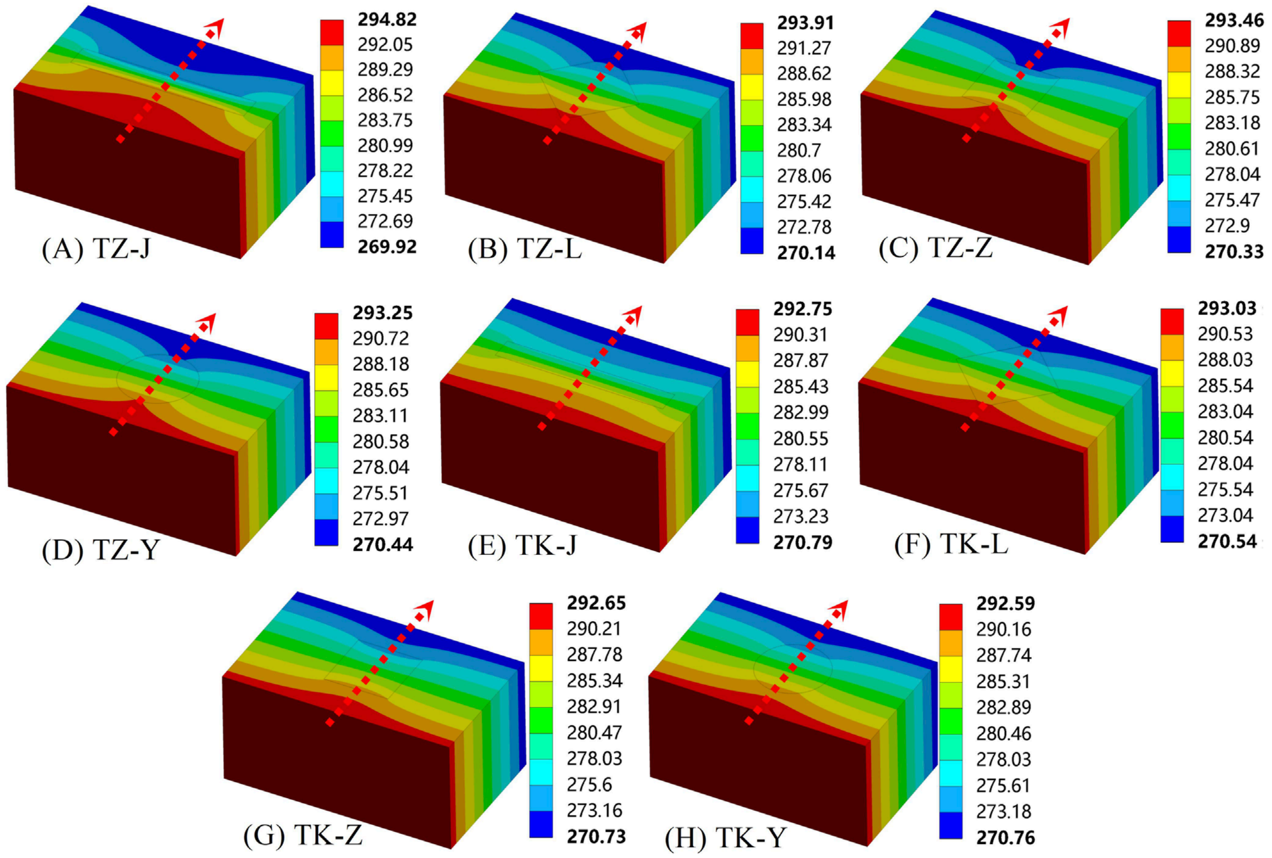

FIGURE 5
The cloud map of the temperature distribution for the basic hole block. (Unit: K). **(A)** TZ-J, **(B)** TZ-L, **(C)** TZ-Z, **(D)** TZ-Y, **(E)** TK-J, **(F)** TK-L, **(G)** TK-Z, **(H)** TK-Y.

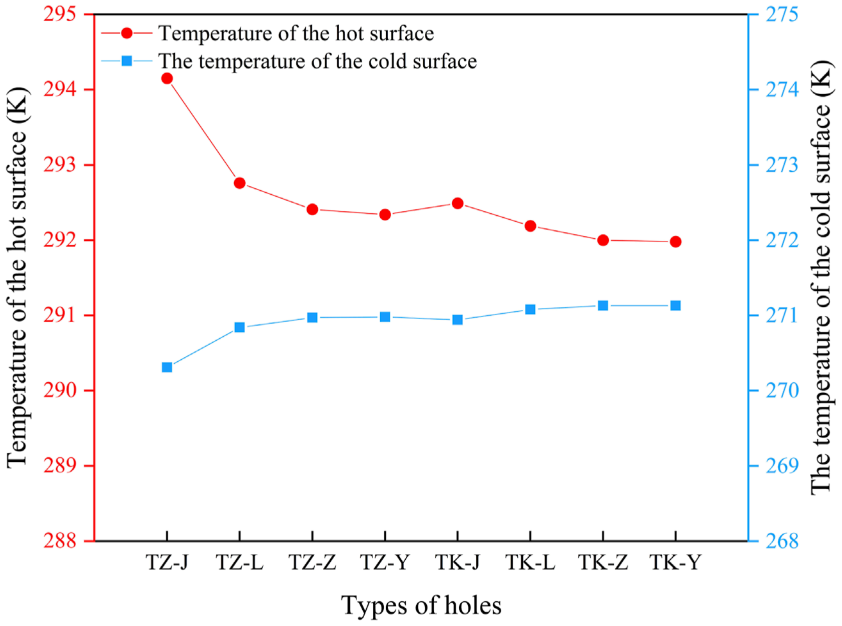

FIGURE 6
The simulated surface temperature of the basic hole block.

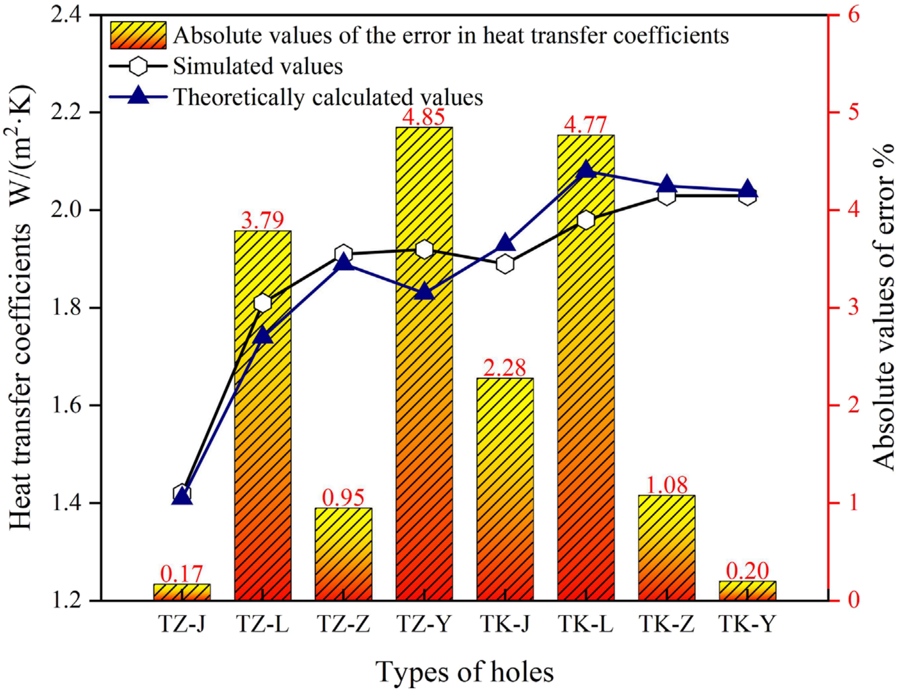

FIGURE 7
The error analysis of the heat transfer coefficient for the basic hole block.

and cold surface as the outer surfaces in the vertical direction of heat transfer. Following GB50176-2016 guidelines, convection conditions were applied on both sides, with a hot convection heat transfer coefficient (h_1) set to 8.7 W/(m^2·K) at an ambient temperature of 299.15 K (26°C); and a cold convection heat transfer coefficient (h_2) set to 23.0 W/(m^2·K) at an ambient temperature of 268.42 K (−4.73°C). (The values were obtained by referring to the average indoor temperature in summer and the average outdoor temperature in winter in Xinyang City, China.)The block boundary conditions are illustrated in Figure 3, where convective loads were imposed on two surfaces along the thickness direction of the block model while four walls along its height and width directions were designated as adiabatic conditions. The ambient temperature and convective heat transfer coefficients on both sides of the block remained unchanged to ensure a steady-state heat transfer process.

3.3 Basic hole types

The design incorporated four basic hole types, namely, rectangular, rhombus, square, and circular holes. Figure 4 illustrates the design of the basic hole for the block. To eliminated interference from other factors, a single hole with the hole rate of 13% was employed. The 3D model is created using the DesignModeler module, as depicted in Figure 4.

The cloud map in Figure 5 showed the temperature distribution for the basic hole block, where TZ referred to the block with a perlite insulation board filled inside, and TK referred to the block with an air interlayer inside. From the temperature cloud maps of the four TZ blocks, it was evident that TZ-J had the most effective heat flow blocking capability. Similarly, based on the temperature cloud maps of the 4 TK blocks, it was apparent that TK-J exhibits superior heat flow blocking performance. Notably, TZ-J demonstrated a significantly better heat flow blocking effect compared to TK-J. Therefore, rectangular holes exhibited the highest level of effectiveness in blocking heat flow, and blocks filled with perlite insulation boards provided better insulation than air interlayer blocks. The order of insulation effectiveness for the blocks was as follows: rectangular holes < rhombus holes < square holes < circular holes.

Based on the numerical simulation results obtained from ANSYS Workbench, the hot surface temperature and cold surface temperature of the block were determined. The simulated surface temperature of the basic hole block was illustrated in Figure 6. Heat flux within the block was transferred from the hot surface to the cold surface. A higher temperature on the hot surface or a lower temperature on the cold surface indicated a more effective insulation performance of the block. As depicted in Figure 6, it could be observed that for basic hole blocks, TZ-J exhibited superior insulation effect compared to TZ-L, TZ-Z, and TZ-Y; similarly, TK-J demonstrated better insulation effect than TK-L, TK-Z, and TK-Y. Specifically, TZ-J had a 0.57% higher temperature than that of TK-J's hot surface while being 0.23% cooler than that of TK-J's hot surface; thus confirming that rectangular holes filled with perlite insulation board contribute to enhanced insulation effectiveness.

The error analysis of the heat transfer coefficient for the basic hole block is shown in Figure 7. To ensure the credibility of the simulation, theoretical calculations were conducted to determine the heat transfer coefficient of four different types of basic hole blocks, as

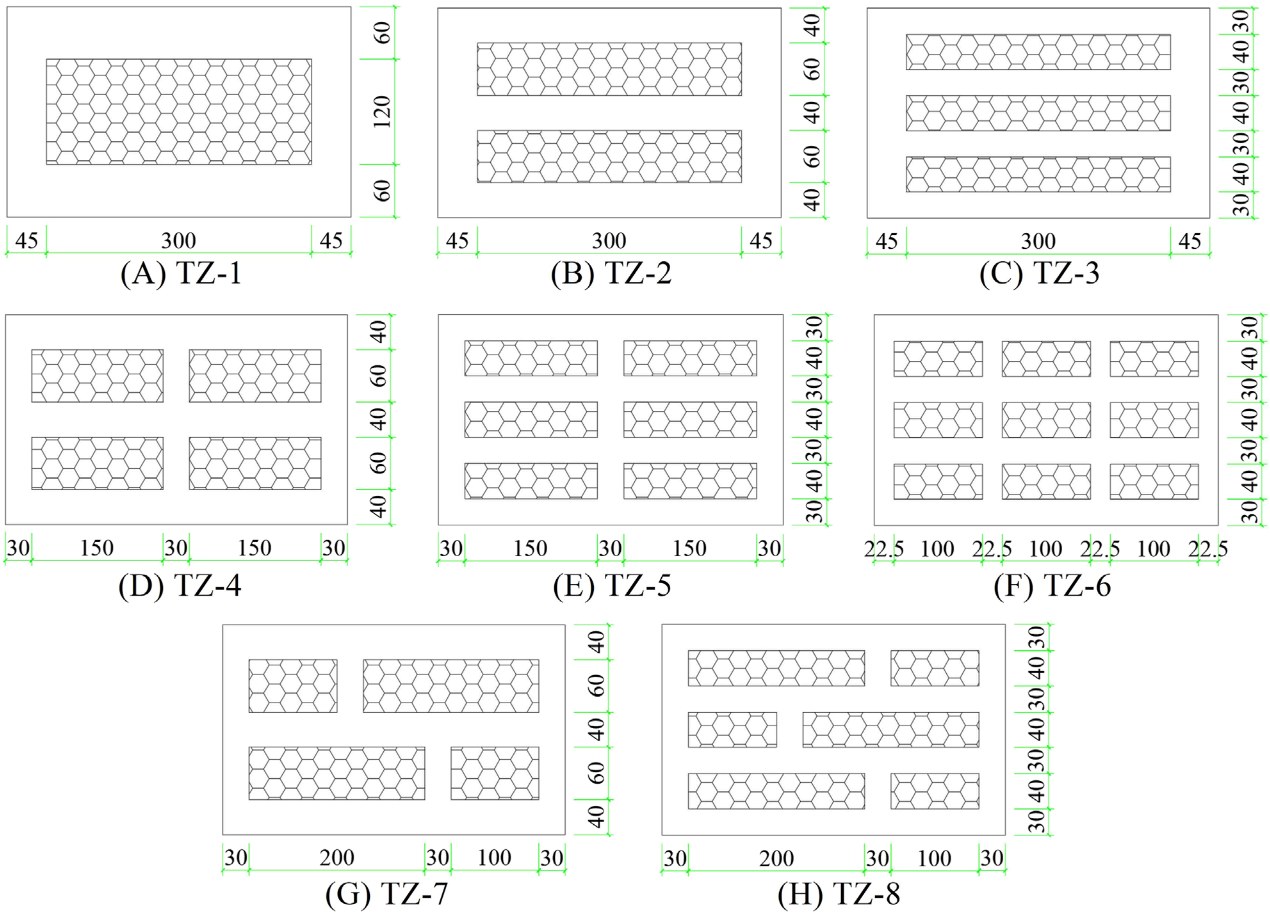

FIGURE 8
Design of the perlite block holes. (Unit: mm). **(A)** TZ-1, **(B)** TZ-2, **(C)** TZ-3, **(D)** TZ-4, **(E)** TZ-1, **(F)** TZ-6, **(G)** TZ-7, **(H)** TZ-8.

per Equations 5–12. By comparing the theoretical calculations with the simulated values, it was found that the error between the two values of different hole blocks was less than 5%, which confirmed the high accuracy of the numerical simulation method adopted in this study.

3.4 Design of holes and analysis of thermal performance

In conclusion, eight hole-schemes for perlite blocks using rectangular holes had been designed with the hole rate of 38.5%. The design of the perlite block holes is illustrated in Figure 8.

The distribution of heat flux density for the perlite block is visually represented in Figure 9. It can be observed from Figure 9 that the SCC displayed a comparatively elevated heat flux, while the perlite insulation board exhibited a relatively reduced heat flux. This was because of the high thermal conductivity of SCC, which allowed most of the heat flux to be transferred through the concrete. Additionally, there were direct transfers of heat flux from the hot side to cold side on both left and right sides of the block, forming a heat bridge and resulting in high heat flux density for all eight types of perlite blocks.

The simulated results of the heat flux density and heat transfer coefficient for the perlite block are shown in Figure 10. The study found that: Compared with the simulated results of TZ-1, TZ-2, and TZ-3, it was observed that the heat flux and heat transfer coefficient of the block gradually decreased with an increase in the number of rows of holes. Furthermore, when comparing the simulated results of TZ-3, TZ-5, and TZ-6, it was discovered that as the number of columns of holes increased, there was a greater number of direct heat transfer channels from the hot side to the cold side. Consequently, both the heat flux and heat transfer coefficient of the blocks increased gradually. Additionally, by comparing the simulated results between TZ-4 and TZ-7 as well as between TZ-5 and TZ-8 respectively, it was determined that staggered holes could enhance insulation performance.

3.5 Optimal design

In summary, the row of holes, the column of holes, and the staggered arrangement could improve the heat transfer performance of the block. It was necessary to further optimize the hole design because there was still a certain gap with the energy-saving target of 65% due to direct heat transfer from the hot side to the cold side

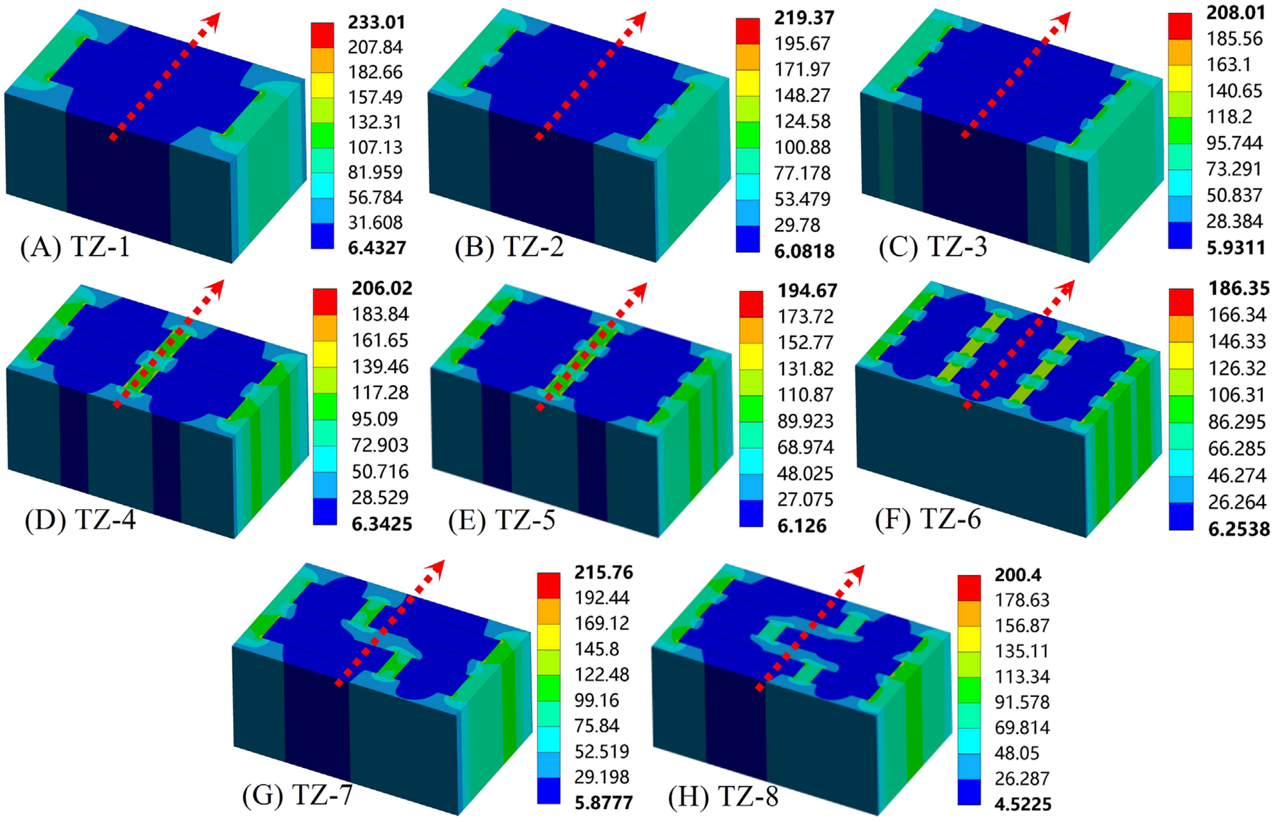

FIGURE 9
The cloud map of the heat flux density distribution for the perlite block. (Unit: W/m^2). **(A)** TZ-1, **(B)** TZ-2, **(C)** TZ-3, **(D)** TZ-4, **(E)** TZ-1, **(F)** TZ-6, **(G)** TZ-7, **(H)** TZ-8.

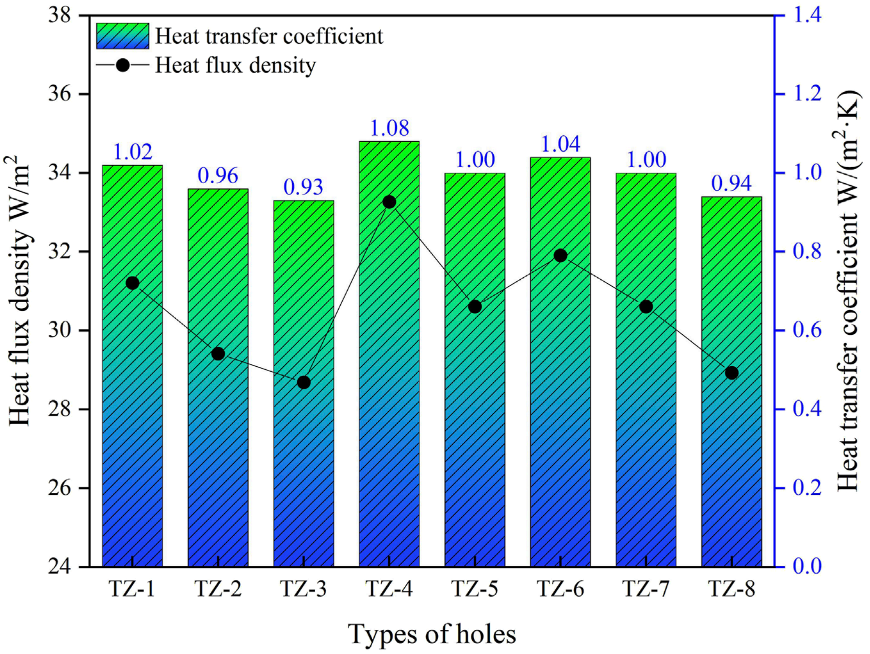

FIGURE 10
The simulated results of the heat flux density and heat transfer coefficient.

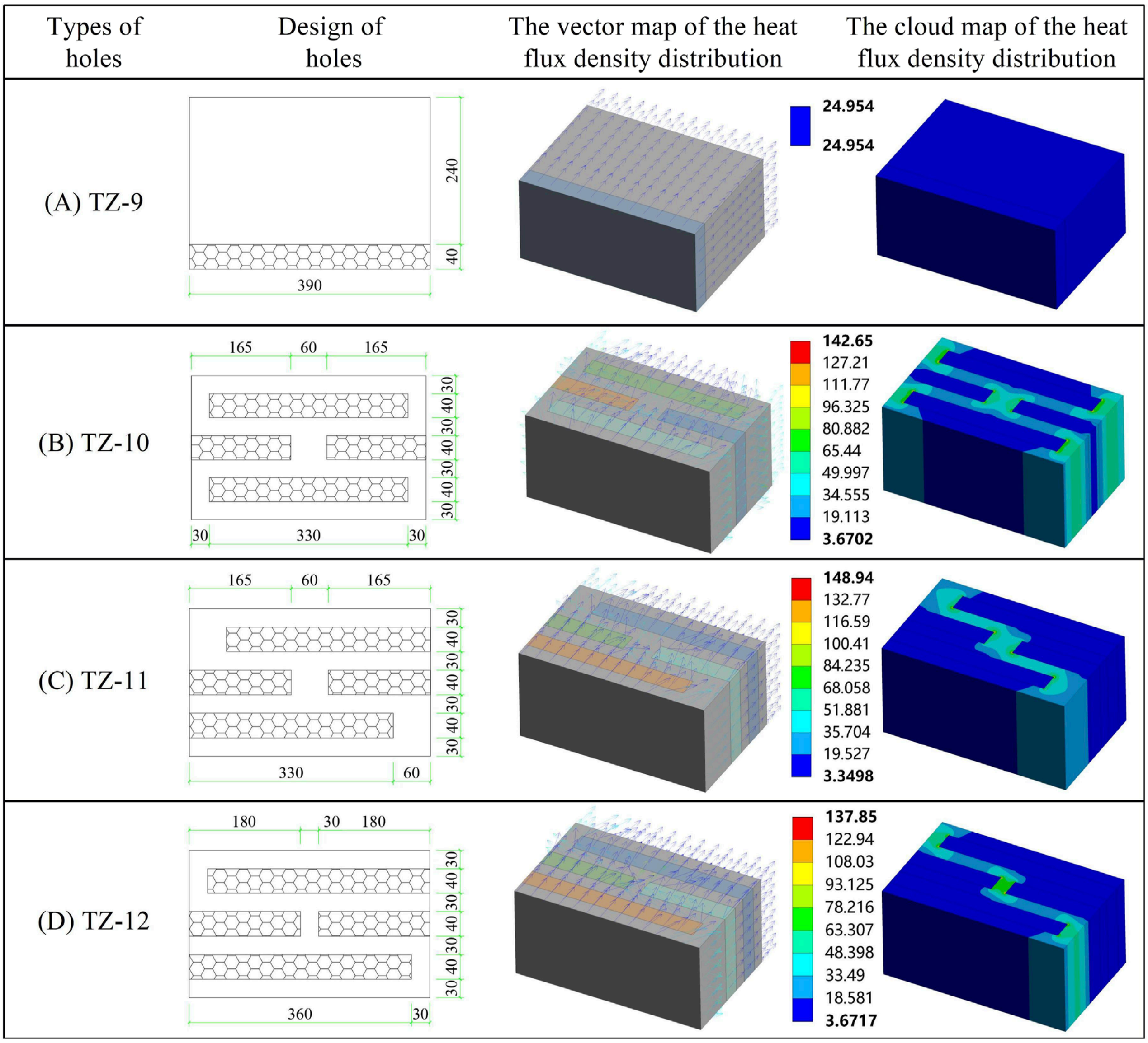

FIGURE 11
Optimal design of holes and simulated result (Unit: mm and W/m^2). **(A)** TZ-9, **(B)** TZ-10, **(C)** TZ-11, **(D)** TZ-12.

at the left and right sides of the block, forming a thermal bridge. The optimized hole design is shown in Figure 11. For subsequent comparative analysis, TZ-14 was a simulated block with a 40 mm thick perlite external insulation board. From Figure 11 of heat flux cloud map for the optimized block, it could be observed that these optimized holes effectively prevented edge heat bridges and extend the path for heat flux.

The simulated results of heat transfer coefficient for the block are shown in Figure 12. The study found that: (1) According to the simulated results, the heat transfer coefficients of optimized TZ-10, TZ-11, and TZ-12 were better than those of TZ-9. The optimal hole among them was TZ-12, with a heat transfer coefficient of 0.5 W/(m^2·K), which was 38.3% lower than that of the external insulation block TZ-9. (2) The hole rate of TZ-10 and TZ-11 was 42.31%, and the total width of the middle and external heat transfer channels was 60 mm. By comparing the simulated results of TZ-10 and TZ-11, it could be observed that the heat transfer coefficient of the blocks decreased as the number of external heat transfer channels reduced. (3) Comparing the simulated results of TZ-11 and TZ-12, it could be seen that the heat transfer coefficient of the blocks decreased as the width of the heat transfer channel decreased.

3.6 Error analysis

The error analysis of the heat transfer coefficient for the blocks is presented in Table 9. In order to ensure the credibility of the simulation, theoretical calculations were performed to determine the heat transfer coefficient of twelve different types of blocks using Equations 5–12. By comparing these theoretical calculations with

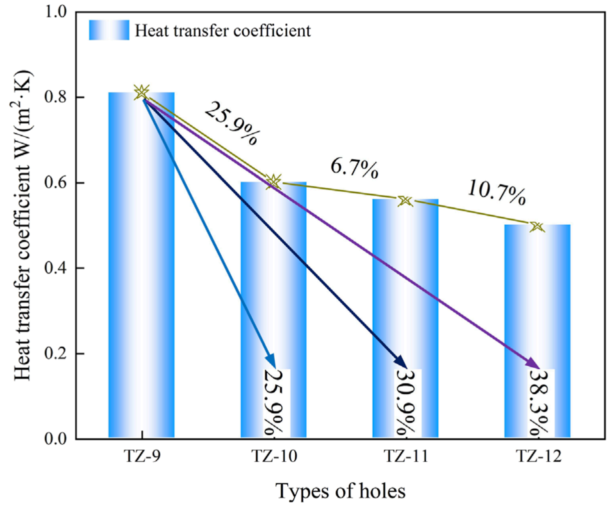

FIGURE 12
The simulated results of heat transfer coefficient for the block.

the simulated values, it was observed that the discrepancy between the two values for different hole blocks was less than 10%, thus confirming the high accuracy of the numerical simulation method employed in this study [49].

3.7 Compressive strength test

The wooden molds required for the test were fabricated in this study, according to the detailed dimensions of the TZ-12 shown in Figure 11. The mold produced is shown in Figures 13A. The pouring was done using the optimal mix ratio of SCC from Table 7, and the results are shown in Figures 13B, with 5 blocks prepared for each group. Following the relevant provisions of GB/T4111-2013 [50], the compressive strength test of blocks was carried out using the YAW-2000 pressure testing machine, as depicted in Figures 13C.

The compressive strength (P) of the SIB was calculated according to the code, and the result is accurate to 0.01 MPa. The calculation formula is shown in (13). Finally, we obtained the average compressive strength and minimum compressive strength of each group of blocks.

$$P = \frac{F}{LB} \tag{13}$$

Where: P is the compressive strength of the blocks, F is the maximum failure load of the blocks, L is the length of the bearing surface, and B is the width of the bearing surface.

The proportion of perlite insulation board in TZ-12 was 46.15%. The average compressive strength of TZ-12 was 8.28 MPa, and the minimum compressive strength was 7.45 MPa. Its strength grade met the requirements of MU7.5, and also satisfied the requirement of not less than MU5.0 when self-insulation blocks were used for external walls.

4 Thermal performance analysis of self-insulation wall

4.1 Model building

The structural entity made of SIB with masonry mortar is called the self-insulation concrete compound block masonry (SIBM), and the structural entity made of the SIBM with plaster mortar is called the self-insulation concrete compound block wall (SIBW). JGJ/T323-2014 [51] provides relevant requirements for masonry mortar and ash joints: for the masonry of SIB, when thermal performance is required, the thermal conductivity of special masonry mortar shall not be greater than 0.2 W/(m·K); plastering should be layered, and the total thickness should be 15–20 mm; the horizontal ash joint thickness and vertical ash joint width of SIBW should be 8–12 mm.

The physical model of SIBW was established based on the aforementioned standard regulations. Figures 14A illustrates the physical model of SIBW, with dimensions of 1.6 m × 1.6 m × 0.28 m. The substrate had a thickness of 240 mm, while the masonry ash joints and internal/external plastering had thicknesses of 10 mm and 20 mm respectively. The primary structure for SIBW consisted of TZ-17, while inorganic insulation mortar (with a thermal conductivity of 0.18 W/(m·K)) was utilized for masonry mortar and ordinary cement mortar (with a thermal conductivity of 0.93 W/(m·K)) was employed for plastering purposes.

The external thermal insulation wall (ETIW) consists of the substrate and the external thermal insulation composite system. The external thermal insulation composite system generally includes an insulation layer, a protective layer, and fixing materials, which collectively refer to non-load-bearing insulation structures fixed on the exterior surface of the outer wall.

In order to compare the thermal performance of the SIBW and the common the ETIW, the thermal performance of the ordinary the ETIW with the same material was also simulated. The physical model of the ordinary the ETIW is shown in Figures 14B. The simplified model had dimensions of 1.6 m × 1.6 m × 0.32 m, with a substrate thickness of 240 mm, insulation layer thickness of 40 mm, masonry ash joint thickness of 10 mm, and internal and external plastering thicknesses of 20 mm. The substrate consisted of shale ceramsite concrete solid masonry blocks (with a thermal conductivity of 0.8314 W/(m·K)); the external insulation material used perlite insulation boards (with a thermal conductivity of 0.051 W/(m·K)); both masonry mortar and plaster mortar were made from ordinary cement mortar (with a thermal conductivity of 0.93 W/(m·K)).

4.2 Thermal performance

The indoor ambient temperature was set to 299.15 K (26°C) according to GB50176-2016, with a convection heat transfer coefficient (h_1) of the heat surface set at 8.7 W/(m^2·K). The outdoor ambient temperature was set to 268.42 K (−4.73°C), and the convection heat transfer coefficient (h_2) of the cold surface was set at 23.0 W/(m^2·K). (The values were obtained by referring to the average indoor temperature in summer and the average outdoor temperature in winter in Xinyang City, China.)

TABLE 9 The error analysis of the heat transfer coefficient. [Unit: W/(m^2·K)].

Types of holes	Simulated values W/(m^2·K)	Theoretically calculated values W/(m^2·K)	Absolute value of error (%)
TZ-1	1.02	0.98	4.1
TZ-2	0.96	0.98	2.0
TZ-3	0.93	0.98	5.1
TZ-4	1.08	0.98	9.3
TZ-5	1.00	0.98	2.0
TZ-6	1.04	0.98	6.1
TZ-7	1.00	0.92	8.7
TZ-8	0.94	0.91	3.3
TZ-9	0.81	0.82	1.2
TZ-10	0.62	0.64	3.1
TZ-11	0.56	0.61	8.2
TZ-12	0.50	0.52	3.8

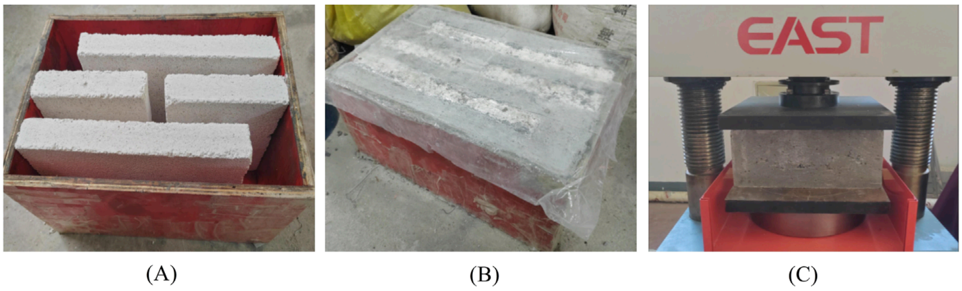

FIGURE 13
Experimental procedure of compressive strength for blocks: **(A)** The mold making. **(B)** Pouring of blocks. **(C)** Test of compressive strength.

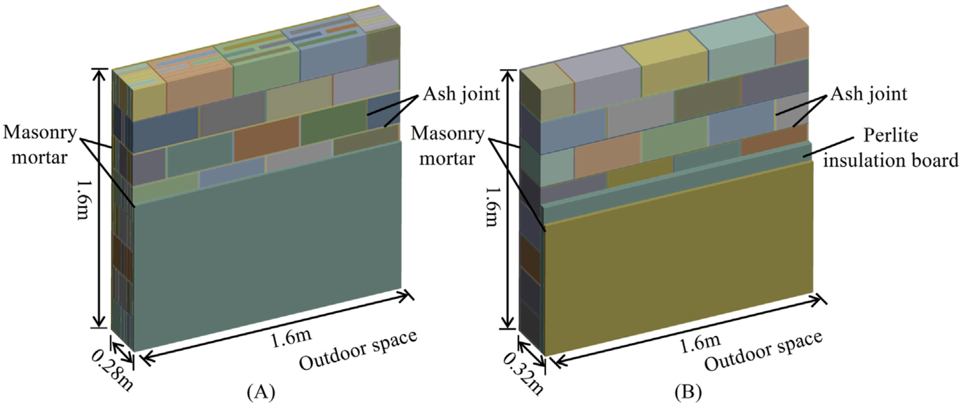

FIGURE 14
The physical model of wall: **(A)** The physical model of the SIBW. **(B)** The Physical model of the ETIW. (The Masonry mortar and Perlite insulation board in this diagram are shown in cross-section).

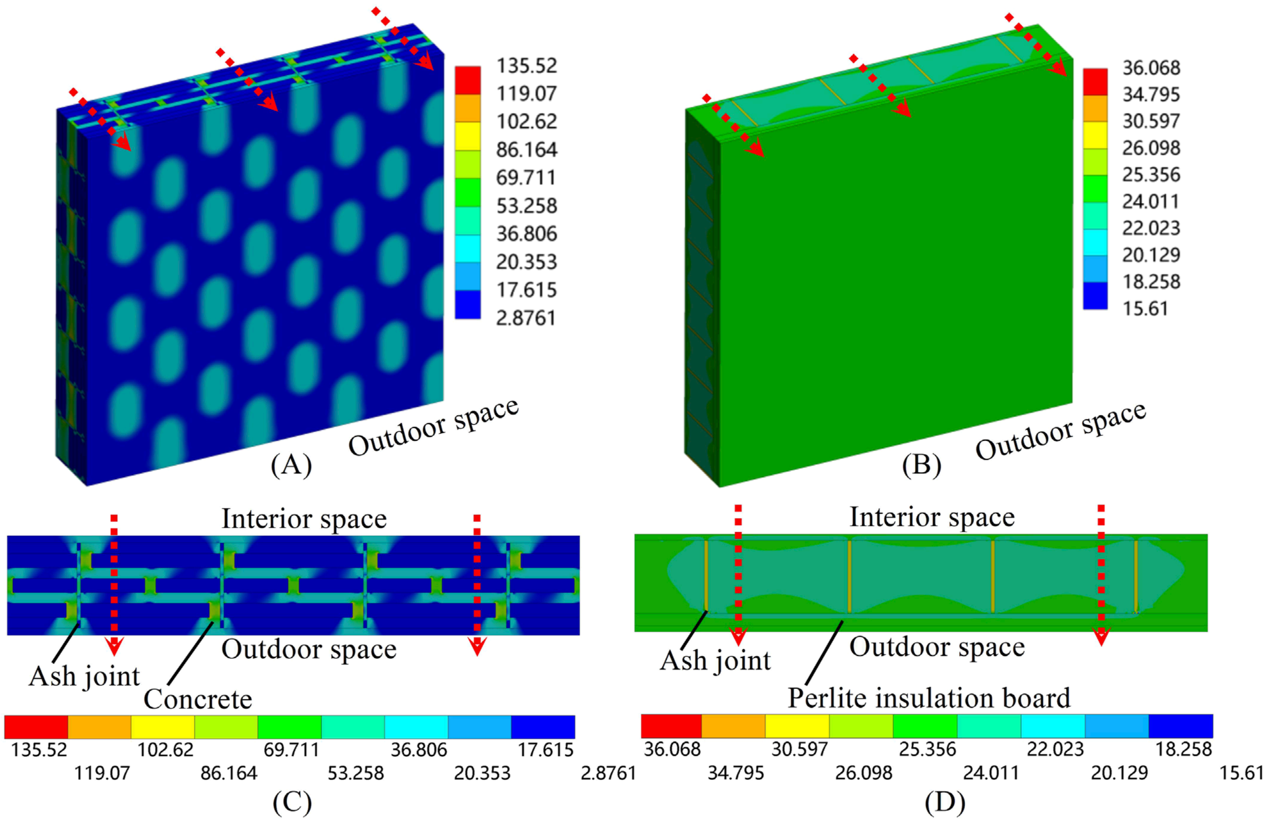

FIGURE 15
The heat flux density of the wall: **(A)** The cloud map of the heat flux density distribution for the SIBW. **(B)** The cloud map of the heat flux density distribution of the ETIW. **(C)** The cloud map of the heat flux density distribution on the top surface for the SIBW. **(D)** The cloud map of the heat flux density distribution on the top surface for the ETIW. (The direction of the arrow is the direction of the heat flow. Unit: W/m^2).

The numerical simulation of the steady-state heat transfer for the SIBW was conducted. Figures 15A shows the cloud map of the 3D heat flux density distribution of the SIBW, and Figures 15C shows the cloud map of the heat flux density distribution on the top surface of the SIBW. According to Figures 15A, C, the heat flux density at the concrete substrate was highest, while it was lowest at the insulation material. Due to using inorganic thermal insulation mortar with low thermal conductivity for masonry mortar, there was no significant thermal bridge effect in masonry ash joints. The simulated heat flux rate on the wall surface was 15.4 W, and its heat transfer coefficient was 0.56 W/(m^2·K), which meets the design standard for achieving a 65% energy saving in residential buildings situated in regions with hot summers and cold winters.

The numerical simulation of the steady-state heat transfer for the ETIW was conducted. Figures 15B shows the cloud map of the 3D heat flux density distribution of the ETIW, and Figures 15D shows the cloud map of the heat flux density distribution on the top surface of the ETIW. According to Figures 15B–D, the heat flux density at the masonry mortar was the largest and the solid ceramsite concrete blocks was minimal. The simulation showed that the heat flux rate on the wall surface was 24.12 W, and its heat transfer coefficient was 0.79 W/(m^2·K). When the heat was transferred to the perlite insulation board on the outside of the wall, the heat flux density was evenly distributed, indicating that the external insulation system can better block the heat bridge effect produced at the ash joints. However, it did not meet the design standard of 65% energy saving in residential buildings situated in regions with hot summers and cold winters.

To sum up, it could be observed that under the same substrate thickness and insulation material for both walls, the heat transfer coefficient of the SIBW was lower, being 29.1% lower than that of the ETIW. This was because the SIBW was the insulation material filled in the hole of the SIB, which could use the insulation material with high thermal resistance to the greatest extent without increasing the thickness of the wall. The thickness of the insulation material for the ETIW often determined the heat transfer coefficient of the wall, which not only reduced the economy of the external insulation system but also increased construction difficulty.

5 Conclusion

In this study, the shale ceramsite concrete (SCC) was prepared as the base material for the blocks through the orthogonal test and range analysis. Subsequently, the influence of different hole type distribution schemes on the thermal performance of self-insulation blocks (SIB) was studied using the Steady-State module of Ansys Workbench. The following conclusions could be drawn:

(1) The orthogonal test employed in this study was a design method used to investigate multiple factors and levels. It selected representative points from the comprehensive test based on orthogonality, making it an efficient, rapid, and cost-effective experimental design method. Through orthogonal test and range analysis, the results showed that:
   - i. The compressive strength of the optimal combination ($A_3B_2C_3D_3$) was 52.03 MPa, which was 1.2% higher than that of the optimal blocks in the other 16 groups. The flexural tensile strength of the optimal combination ($A_3B_2C_3D_3$) was 5.13 MPa, which was 1.9% higher than that of the optimal blocks in the other 16 groups. It was verified that $A_3B_2C_3D_3$ is the combination with the optimal mechanical properties.
   - ii. The thermal conductivity of SCC ($A_3B_2C_3D_3$) was 0.8314 W/(m·K). It was prepared as the base material of the blocks.

(2) The influence of different hole type distribution schemes on the thermal performance of self-insulation blocks (SIB) was studied using the Steady-State module of Ansys Workbench. The results showed that:
   - i. The heat transfer coefficient of blocks gradually decreased with an increase in the number of rows of holes, while the heat transfer coefficient of blocks gradually increased with an increase in the number of columns of holes.
   - ii. The staggered holes could improve insulation performance.
   - iii. The heat transfer coefficient of the blocks decreased with a reduction in the number of external heat transfer channels and a decrease in the width of the heat transfer channel.

(3) By comparing these theoretical calculations with the simulated values, it was observed that the discrepancy between the two values for different hole blocks was less than 10%, thus confirming the high accuracy of the numerical simulation method employed in this study. According to the simulated results of heat transfer coefficient for the block, it was determined that:
   - i. TZ-12 exhibited the optimal hole configuration with a heat transfer coefficient of 0.5 W/(m^2·K), which was 38.3% lower than that of the external insulation block TZ-9.
   - ii. Additionally, TZ-12 demonstrated the average compressive strength of 8.28 MPa and the minimum compressive strength of 7.45 MPa, meeting the requirements for MU7.5 strength grade and also satisfying the requirement of not less than MU5.0 when self-insulation blocks were used for external walls.
   - iii. The simulated heat flux rate of the SIBW was 15.4 W, and its heat transfer coefficient was 0.56 W/(m^2·K), which was 29.1% lower than that of the ETIW, meeting the design standard for achieving the 65% energy saving in residential buildings situated in regions with hot summers and cold winters.

Data availability statement

The raw data supporting the conclusions of this article will be made available by the authors, without undue reservation.

Author contributions

QX: Conceptualization, Data curation, Formal Analysis, Funding acquisition, Investigation, Methodology, Project administration, Resources, Software, Supervision, Validation, Visualization, Writing–original draft, Writing–review and editing. HD: Conceptualization, Data curation, Formal Analysis, Funding acquisition, Investigation, Methodology, Project administration, Resources, Writing–original draft, Writing–review and editing. BG: Data curation, Formal Analysis, Funding acquisition, Methodology, Project administration, Resources, Writing–original draft. JZ: Investigation, Methodology, Resources, Software, Supervision, Validation, Visualization, Writing–review and editing.

Funding

The author(s) declare that financial support was received for the research, authorship, and/or publication of this article. This research was sponsored by the Training Scheme for Young Backbone Teachers in Colleges and Universities in Henan Province, No. 2019-163; the Excellent Teaching Case Project of Professional Degree Postgraduates in Henan Province (2022-115); the Scientific Research Foundation of Graduate School of Xinyang Normal University (2024KYJJ107); Special Projects of Key R and D and Promotion in Xinyang City (20220055); and Key Scientific and Technological Projects in Henan Province (232102320196).

Conflict of interest

The authors declare that the research was conducted in the absence of any commercial or financial relationships that could be construed as a potential conflict of interest.

Publisher's note

Supplementary material

The Supplementary Material for this article can be found online at: https://www.frontiersin.org/articles/10.3389/fphy.2024.1490012/full#supplementary-material

SUPPLEMENTARY FIGURE S1
Test blocks: **(A)** Test blocks making. **(B)** Test of compressive strength. **(C)** Test of flexural tensile strength.

SUPPLEMENTARY FIGURE S2
The thermal conductivity of shale ceramsite concrete: **(A)** Test blocks making. **(B)** Test of thermal conductivity. **(C)** DR-3030 double plate thermal conductivity tester.

References

1. Li H, Li Y, Wang Z, Shao S, Deng G, Xue H, et al. Integrated building envelope performance evaluation method towards nearly zero energy buildings based on operation data. *Energy and Buildings* (2022) 268:112219. doi:10.1016/j.enbuild.2022.112219

2. Guo Y-Y. Revisiting the building energy consumption in China: insights from a large-scale national survey. *Energy Sustainable Development* (2022) 68:76–93. doi:10.1016/j.esd.2022.03.005

3. Dai J, Wang J, Bart D, Gao W. The impact of building enclosure type and building orientation on indoor thermal comfort —A case study of Kashgar in China. *Case Stud Therm Eng* (2023) 49:103291. doi:10.1016/j.csite.2023.103291

4. Hu S, Zhang Y, Yang Z, Yan D, Jiang Y. Challenges and opportunities for carbon neutrality in China's building sector—modelling and data. *Building Simulation* (2022) 15:1899–921. doi:10.1007/s12273-022-0912-1

5. Kumar D, Alam M, Zou PXW, Sanjayan JG, Memon RA. Comparative analysis of building insulation material properties and performance. *Renew Sustainable Energy Rev* (2020) 131:110038. doi:10.1016/j.rser.2020.110038

6. Yang Y, Chen S. Thermal insulation solutions for opaque envelope of low-energy buildings: a systematic review of methods and applications. *Renew Sustainable Energy Rev* (2022) 167:112738. doi:10.1016/j.rser.2022.112738

7. Lin H, Feng X, Zhang P, Han Y. Technical and economic analysis on self-insulation schemes of 65 percent energy efficiency for residential buildings in hot summer and cold winter zone. *Appl Mech Mater* (2012) 178–181:209–12. doi:10.4028/www.scientific.net/AMM.178-181.209

8. Ding X, Liu F, Yuan X, Hao J. Experimental study on the shear performance of recycled concrete self-insulating block walls. *J Mater Civil Eng* (2021) 33:04020456. doi:10.1061/(ASCE)MT.19435533.0003554

9. Abdelmoneim Elamin Mohamad A-B, Chen Z. Experimental and numerical analysis of the compressive and shear behavior for a new type of self-Insulating concrete masonry system. *Appl Sci* (2016) 6:245. doi:10.3390/app6090245

10. Sassine E, Cherif Y, Dgheim J, Antczak E. Experimental and numerical thermal assessment of Lebanese traditional hollow blocks. *Int J Thermophys* (2020) 41:47. doi:10.1007/s10765-020-02626-7

11. Zukowski M, Haese G. Experimental and numerical investigation of a hollow brick filled with perlite insulation. *Energy and Buildings* (2010) 42:1402–8. doi:10.1016/j.enbuild.2010.03.009

12. Jiao Z, Wang Y, Zheng W, Huang W, Zhou X. Use of industrial waste slag in alkali-activated slag ceramsite concrete hollow blocks. *Appl Sci* (2018) 8:2358. doi:10.3390/app8122358

13. Osman BH, Chen Z, Carroll A, Abuserriya A. Optimisation and design of new energy-saving concrete self-insulation block. *Gradevinar* (2024) 76:119–37. doi:10.14256/JCE.3821.2023

14. Xie J, Zhao J, Wang J, Huang P, Liu J. Investigation of the high-temperature resistance of sludge ceramsite concrete with recycled fine aggregates and GGBS and its application in hollow blocks. *J Building Eng* (2021) 34:101954. doi:10.1016/j.jobe.2020.101954

15. Al-Tarbi SM, Baghabra Al-Amoudi OS, Al-Osta MA, Al-Awsh WA, Shameem M, Sharif Zami M. Development of energy-efficient hollow concrete blocks using perlite, vermiculite, volcanic scoria, and expanded polystyrene. *Construction Building Mater* (2023) 371:130723. doi:10.1016/j.conbuildmat.2023.130723

16. Al-Tamimi AS, Baghabra Al-Amoudi OS, Al-Osta MA, Ali MR, Ahmad A. Effect of insulation materials and cavity layout on heat transfer of concrete masonry hollow blocks. *Construction Building Mater* (2020) 254:119300. doi:10.1016/j.conbuildmat.2020.119300

17. Topcu IB, Iskdag B. Manufacture of high heat conductivity resistant clay bricks containing perlite. *Building Environ* (2007) 42:3540–6. doi:10.1016/j.buildenv.2006.10.016

18. Liu D, Qiao L, Li G. Experimental performance measures of recycled insulation concrete blocks from construction and demolition waste. *J Renew Mater* (2022) 10:1675–91. doi:10.32604/jrm.2022.018397

19. Jaafar AS, Abbas ZK, Allawi AA. Studying sustainable concrete block efficiency production: a review. *J Eng* (2023) 29:134–49. doi:10.31026/j.eng.2023.09.10

20. Zhao Z, Courard L, Groslambert S, Jehin T, Leonard A, Xiao J. Use of recycled concrete aggregates from precast block for the production of new building blocks: an industrial scale study. *Resour Conservation and Recycling* (2020) 157:104786. doi:10.1016/j.resconrec.2020.104786

21. Al-Awsh WA, Baghabra Al-Amoudi OS, Al-Osta MA, Ahmad A, Saleh TA. Experimental assessment of the thermal and mechanical performance of insulated concrete blocks. *J Clean Prod* (2021) 283:124624. doi:10.1016/j.jclepro.2020.124624

22. Chen L, Wang Z, Lian H, Ma Y, Meng Z, Li P, et al. Reduced order isogeometric boundary element methods for CAD-integrated shape optimization in electromagnetic scattering. *Computer Methods Appl Mech Eng* (2024) 419:116654. doi:10.1016/j.cma.2023.116654

23. Martinez M, Huygen N, Sanders J, Atamturktur S. Thermo-fluid dynamic analysis of concrete masonry units via experimental testing and numerical modeling. *J Building Eng* (2018) 19:80–90. doi:10.1016/j.jobe.2018.04.029

24. Cao G, Yu B, Chen L, Yao W. Isogeometric dual reciprocity BEM for solving non-Fourier transient heat transfer problems in FGMs with uncertainty analysis. *Int J Heat Mass Transfer* (2023) 203:123783. doi:10.1016/j.ijheatmasstransfer.2022.123783

25. Al-Tamimi AS, Al-Osta MA, Al-Amoudi OSB, Ben-Mansour R. Effect of geometry of holes on heat transfer of concrete masonry bricks using numerical analysis. *Arabian J Sci Eng* (2017) 42:3733–49. doi:10.1007/s13369-017-2482-6

26. Al-Awsh WA, Qasem NAA, Baghabra Al-Amoudi OS, Al-Osta MA. Experimental and numerical investigation on innovative masonry walls for industrial and residential buildings. *Appl Energy* (2020) 276:115496. doi:10.1016/j.apenergy.2020.115496

27. Cuce E, Cuce PM, Besir AB. Improving thermal resistance of lightweight concrete hollow bricks: a numerical optimisation research for a typical masonry unit. *J Energy Syst* (2020) 4:121–44. doi:10.30521/jes.775961

28. Shuai L, Zhang J, Song J, Chi D, Chen Z. Numerical thermal assessment and theoretical analysis of horizontal-hole interlock composite insulation blocks. *Heliyon* (2024) 10:e26490. doi:10.1016/j.heliyon.2024.e26490

29. Ouakarrouch M, Laaroussi N, Garoum M, Hajji A. Thermal performances assessment and improvement of hollow concrete blocks commonly used in Morocco: experimental and numerical approach. *J Therm Sci Eng Appl* (2022) 14:101005. doi:10.1115/1.4054077

30. Blanco JM, Frometa YG, Madrid M, Cuadrado J. Thermal performance assessment of walls made of three types of sustainable concrete blocks by means of FEM and validated through an extensive measurement campaign. *Sustainability* (2021) 13:386. doi:10.3390/su13010386

31. Li LP, Wu ZG, Li ZY, He YL, Tao WQ. Numerical thermal optimization of the configuration of multi-holed clay bricks used for constructing building walls by the finite volume method. *Int J Heat Mass Transfer* (2008) 51:3669–82. doi:10.1016/j.ijheatmasstransfer.2007.06.008

32. Bi-chao Y, Zhou H. Thermal performance analysis of concrete small hollow block. *Mater Sci Eng* (2019) 556:012041. doi:10.1088/1757-899X/556/1/012041

33. Sutcu M, Coz Diaz JJdel, Alvarez Rabanal FP, Gencel O, Akkurt S. Thermal performance optimization of hollow clay bricks made up of paper waste. *Energy and Buildings* (2014) 75:96–108. doi:10.1016/j.enbuild.2014.02.006

34. Fan L, Zhang Z, Yu Y, Li P, Cosgrove T. Effect of elevated curing temperature on ceramsite concrete performance. *Construction Building Mater* (2017) 153:423–9. doi:10.1016/j.conbuildmat.2017.07.050

35. Wu X, Wang S, Yang J, Zhu S, Kodama J. Mechanical properties and dynamic constitutive relation of lightweight shale ceramsite concrete. *Eur J Environ Civil Eng* (2020) 26:2898–912. doi:10.1080/19648189.2020.1782772

36. Wu X, Wang S, Yang J, Zhao J, Chang X. Damage characteristics and constitutive model of lightweight shale ceramsite concrete under static-dynamic loading. *Eng Fracture Mech* (2022) 259:108137. doi:10.1016/j.engfracmech.2021.108137

37. Xu C, Deng X. Study on preparation of ceramsite from shale slag and its application. *Mater Sci Eng* (2020) 744:012026. doi:10.1088/1757-899X/744/1/012026

38. *JGJ/T12-2019: technical standard for application of lightweight aggregate concrete*. Architecture and Building Press Beijing, China. (2019).

39. *GB/T50081-2019:Standard for test methods of concrete physical and mechanical properties*. Architecture and Building Press Beijing, China. (2019).

40. *GB50176-2016:Code for thermal design of civil buildings*. Architecture and Building Press Beijing, China. (2016).

41. *JG/T407-2013: self-insulation concrete compound blocks*. Architecture and Building Press Beijing, China. (2013).

42. GB55015-2021:General code for energy efficiency and renewable energy application in buildings. (2021).

43. Yavagal PS, Kulkarni PA, Patil NM, Salimath NS, Patil AY, Savadi RS, et al. Cleaner production of edible straw as replacement for thermoset plastic. *Mater Today* (2020) 32:492–7. doi:10.1016/j.matpr.2020.02.667

44. Patil AY, Banapurmath NR, Yaradoddi JS, Kotturshettar BB, Shettar AS, Basavaraj GD, et al. Experimental and simulation studies on waste vegetable peels as bio-composite fillers for light duty applications. *Arabian J Sci Eng* (2019) 44:7895–907. doi:10.1007/s13369-019-03951-2

45. Patil AY, Hegde C, Savanur G, Kanakmood SM, Contractor AM, Shirashyad VB, et al. Biomimicking nature-inspired design structures—an experimental and simulation approach using additive manufacturing. *Biomimetics* (2022) 7:186. doi:10.3390/biomimetics7040186

46. Mysore THM, Patil AY, Raju GU, Banapurmath NR, Bhovi PM, Afzal A, et al. Investigation of mechanical and physical properties of big sheep horn as an alternative biomaterial for structural applications. *Materials* (2021) 14:4039. doi:10.3390/ma14144039

47. Patil VS, Banoo F, Kurahatti RV, Patil AY, Raju GU, Afzal A, et al. A study of sound pressure level (SPL) inside the truck cabin for new acoustic materials: an experimental and FEA approach. *Alexandria Eng J* (2021) 60:5949–76. doi:10.1016/j.aej.2021.03.074

48. Dhaduti SC, Sarganachari SG, Patil AY, Khan TMY. Prediction of injection molding parameters for symmetric spur gear. *J Mol Model* (2020) 26:302. doi:10.1007/s00894-020-04560-9

49. Nimbagal V, Banapurmath NR, Sajjan AM, Patil AY, Ganachari SV. Studies on hybrid bio-nanocomposites for structural applications. *J Mater Eng Perform* (2021) 30:6461–80. doi:10.1007/s11665-021-05843-9

50. *GBT4111-2013: test method for concrete block and brick*. Architecture and Building Press Beijing, China. (2013).

51. *JGJT323-2014: technical specification for application of self-insulation concrete compound block walls*. Architecture and Building Press Beijing, China. (2014).

frontiers | Frontiers in Physics

TYPE Original Research
PUBLISHED 05 December 2024
DOI 10.3389/fphy.2024.1464716

OPEN ACCESS

EDITED BY
Leilei Chen,
Huanghuai University, China

REVIEWED BY
Xudong Li,
Chinese Academy of Sciences (CAS), China
Jing Fang,
Dalian Maritime University, China
Lu Meng,
Taiyuan University of Science and Technology, China

*CORRESPONDENCE
Xinbo Jiang,
✉ jiangxinbo2002@usc.edu.cn
Jing Du,
✉ jdstarry@aliun.com

RECEIVED 15 July 2024
ACCEPTED 18 November 2024
PUBLISHED 05 December 2024

CITATION
Zhong S, Jiang X, Du J and Liu J (2024) A reduced-order boundary element method for two-dimensional acoustic scattering.
Front. Phys. 12:1464716.
doi: 10.3389/fphy.2024.1464716

A reduced-order boundary element method for two-dimensional acoustic scattering

Senhao Zhong[1,2], Xinbo Jiang[1]*, Jing Du[3]* and Jie Liu[4]

[1]Solux College of Architecture and Design, University of South China, Hengyang, China, [2]College of Mining Engineering, Taiyuan University of Technology, Taiyuan, China, [3]Center for Strategic Assessment and Consulting, Academy of Military Science, Beijing, China, [4]Computer Engineering Department, Taiyuan Institute of Technology, Taiyuan, China

This study presents a novel method for wideband acoustic analysis using the Boundary Element Method (BEM), addressing significant computational challenges. Traditional BEM requires repetitive computations across different frequencies due to the frequency-dependent system matrix, resulting in high computational costs. To overcome this, the Hankel function is expanded into a Taylor series, enabling the separation of frequency-dependent and frequency-independent components in the boundary integral equations. This results in a frequency-independent system matrix, improving computational efficiency. Additionally, the method addresses the issue of full-rank, asymmetric coefficient matrices in BEM, which complicate the solution of system equations over wide frequency ranges, particularly for large-scale problems. A Reduced-Order Model (ROM) is developed using the Second-Order Arnoldi (SOAR) method, which retains the key characteristics of the original Full-Order Model (FOM). The singularity elimination technique is employed to directly compute the strong singular and super-singular integrals in the acoustic equations. Numerical examples demonstrate the accuracy and efficiency of the proposed approach, showing its potential for large-scale applications in noise control and acoustic design, where fast and precise analysis is crucial.

KEYWORDS

boundary element method, SOAR, Taylor expansion, sound barrier, acoustic scattering

1 Introduction

In the acoustics domain, simulating and analyzing the propagation of sound waves through complex structures is essential. Frequency sweep calculations play a pivotal role in understanding sound wave behavior across various frequencies, crucial for designing effective acoustic barriers and noise reduction devices. Traditional methods for these calculations often utilize the finite element method (FEM) or the boundary element method (BEM). It is common knowledge that BEM is frequently utilized to address acoustic issues because of its superior accuracy and simplicity in mesh creation [1–4]. For external acoustic problems, it naturally satisfies the Sommerfeld radiation condition at infinity [5–9]. Conventional sound pressure calculations are typically optimized for specific frequencies, limiting their applicability across a broader frequency spectrum. To address this limitation, broadband analysis is introduced to provide results over a wider range of frequencies [10]. Nevertheless, in broadband analysis, the frequency band within a given range is segmented, and the coefficient matrix along with the boundary elements system equation is recalculated at every distinct frequency point. This procedure results in substantial computational expense. This study presents an efficient approach for rapid frequency sweep calculations in broadband acoustics.

When performing broadband acoustic analysis with the BEM, the frequency dependence of the $H_n^{(1)}(kr)$ results in coefficient matrices that change with frequency [11, 12]. Consequently, for large-scale issues, the approach is particularly time-consuming because the boundary element system equations must be recalculated for every discrete frequency point. Researchers came up with a number of techniques to speed up the broadband analysis computational process to address this problem [13–16]. A three-dimensional (3D) axisymmetric multifrequency acoustic analysis technique called the Linear Frequency Interpolation Technique (FIT) was proposed by Vanhille et al. [17]. In this approach, the second-order isoparametric segment of the Helmholtz Integral Equation (HIE) is discretized. Despite its effectiveness, FIT requires substantial storage capacity. Li [18] addressed the issue by separating the frequency terms from the damping function through power series expansions of sine and cosine functions into algebraic polynomials, which significantly reduced computational time for multifrequency problems. Similarly, Zhang et al. [19] tackled multifrequency issues using BEM and incorporated series expansion techniques in their calculations, which offer high accuracy and computational efficiency [20]. The advantages of using series expansion are precision and computational economy [21–23]. In this study, the frequency-related and frequency-unrelated components of the product function in the Boundary Integral Equations (BIE) are separated using a Taylor series expansion.

In the realm of acoustic computations using the BEM, coefficient matrices exhibit characteristics of being asymmetric, full-rank, and dense [24, 25]. These attributes contribute to diminished computational efficiency, particularly evident in scenarios involving large-scale problems [26, 27]. Model Order Reduction (MOR) emerges as a viable solution to this challenge [28–31]. Among the most prominent MOR techniques [32] is Proper Orthogonal Decomposition (POD) [33, 34]. However, the quality of the simplified model is not guaranteed, as it depends on the representativeness of the snapshots (or primary frequencies) selected during the POD process [35]. The second-order Arnoldi (SOAR) algorithm for two-dimensional (2D) linear systems, which was introduced by Bai et al. [36, 37], has garnered interest from numerous scholars. The full-order model (FOM) gets mapped onto the projection space. SOAR facilitates the acquisition of an orthogonal basis within the projection space and the construction of a Reduced-Order Model (ROM) that preserves the characteristics of the initial model. Furthermore, the SOAR method finds extensive application in structural acoustic analysis, second-order dynamical system modeling [19], and quadratic eigenvalue problems [37, 38].

Singular Helmholtz boundary integral equations may fail to yield unique solutions when applied to exterior boundary value problems. To address this issue, two primary approaches have been proposed [39–42]. The Combined Helmholtz Integral Equation Formula (CHIEF), cited in Ref. [43], effectively addresses this issue by introducing additional HIE within the internal domain [44, 45]. The resulting overdetermined system of equations can be solved using the method of least squares. However, determining the optimal number and placement of internal points, particularly for issues of high frequency, remains challenging. The Burton-Miller method [46] presents another useful strategy for handling non-unique solutions, offering a linear formulation of the Classical Boundary Integral Equation (CBIE) and its associated Normal Derivative Boundary Integral Equation (NDBIE). If the boundary is nonsmooth, NDBIE becomes hypersingular, requiring special numerical treatment. This study utilizes Cauchy principal value integrals and Hadamard finite part integrals for handling singular integrals.

To enable the application of the Boundary Element Method (BEM) in 2D acoustic computations across a wide frequency range, this study proposes the following enhancements:

- Frequency-dependence elimination for the 2D acoustic state boundary integral equation using Taylor series expansion.
- A ROM of a 2D acoustic state system based on SOAR is proposed.
- The singularity elimination technique is suggested for accurately resolving the singularities in the boundary integrals present in the Taylor series expansion formulation.

This article has the following structure. Section 2 details the BEM formulation for acoustic state analysis. Section 3 elaborates on the BEM formulation with Taylor series expansion for acoustic state analysis. MOR built on the adaptive SOAR method is employed in Section 4 to speed up the BEM computation for 2D broadband acoustic situations. The treatment of singular integrals in kernel function border integrals is described in Section 5. Section 6 includes multiple numerical instances that verify the effectiveness of the proposed algorithm. Finally, conclusions and further discussions are drawn in Section 7.

2 BEM formulations for acoustic state analysis

The Helmholtz half-space problem can be represented by the following BIE and normal derivative boundary integral equation (HBIE).

$$C(\mathbf{x})p(\mathbf{x}) + \int_S F(\mathbf{x},\mathbf{y})p(\mathbf{y})\,\mathrm{d}S(\mathbf{y}) = \int_S G(\mathbf{x},\mathbf{y})q(\mathbf{y})\,\mathrm{d}S(\mathbf{y}) + p_{\text{inc}}(\mathbf{x}) \tag{1}$$

and

$$C(\mathbf{x})q(\mathbf{x}) + \int_S H(\mathbf{x},\mathbf{y})p(\mathbf{y})\,\mathrm{d}S(\mathbf{y}) = \int_S K(\mathbf{x},\mathbf{y})q(\mathbf{y})\,\mathrm{d}S(\mathbf{y}) + \frac{\partial p_{\text{inc}}(\mathbf{x})}{\partial n(\mathbf{x})} \tag{2}$$

where $\mathbf{y}$ signifies the field point, $\mathbf{x}$ denotes the source point, and q is the normal derivative of the sound pressure p: $q(\mathbf{x}) = \partial p(\mathbf{x})/\partial n(\mathbf{x})$. When $\mathbf{x}$ is located on a border that is smooth S, $C(\mathbf{x}) = 1/2$. Acoustic pressure incident at position $\mathbf{x}$ is given by p_{inc}. The function of Green $G(\mathbf{x},\mathbf{y})$ and its derivatives in Equation 1 and Equation 2 are presented as follows, which can be expressed in Equation 3.

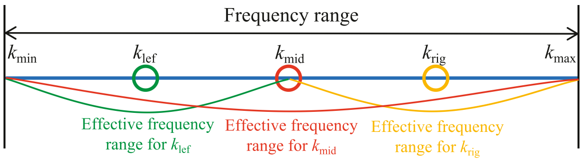

FIGURE 1
Calculate the frequency band.

$$\begin{cases} G(\mathbf{x},\mathbf{y}) = \dfrac{\mathrm{i}}{4} H_0^{(1)}(kr) \\ F(\mathbf{x},\mathbf{y}) = \dfrac{\partial G(\mathbf{x},\mathbf{y})}{\partial n(\mathbf{y})} = -\dfrac{\mathrm{i}k}{4} H_1^{(1)}(kr) \dfrac{\partial r}{\partial n(\mathbf{y})} \\ K(\mathbf{x},\mathbf{y}) = \dfrac{\partial G(\mathbf{x},\mathbf{y})}{\partial n(\mathbf{x})} = -\dfrac{\mathrm{i}k}{4} H_1^{(1)}(kr) \dfrac{\partial r}{\partial n(\mathbf{x})} \\ H(\mathbf{x},\mathbf{y}) = \dfrac{\partial^2 G(\mathbf{x},\mathbf{y})}{\partial n(\mathbf{x}) \partial n(\mathbf{y})} = \dfrac{\mathrm{i}k}{4r} H_1^{(1)}(kr) n_j(\mathbf{x}) n_j(\mathbf{y}) - \dfrac{\mathrm{i}k^2}{4} H_2^{(1)}(kr) \dfrac{\partial r}{\partial n(\mathbf{x})} \dfrac{\partial r}{\partial n(\mathbf{y})} \end{cases} \tag{3}$$

where the nth order first kind Hankel function is indicated by $H_n^{(1)}$, k denotes by the wave number, $\mathrm{i} = \sqrt{-1}$, n_j is the Cartesian component of $n(\mathbf{x})$ or $n(\mathbf{y})$ and the distance between the field and source locations is represented by the formula $r = |\mathbf{x} - \mathbf{y}|$.

For exterior acoustic problems, using either Equation 1 or Equation 2 alone can lead to non-uniqueness of the solution at certain imaginary frequencies. According to the Burton-Miller idea, a linear combination of Equation 1 and Equation 2 can effectively resolve this issue. The Burton-Miller formulation is expressed as follows [46].

$$C(\mathbf{x})[p(\mathbf{x}) + \alpha q(\mathbf{x})] + \int_S [F(\mathbf{x},\mathbf{y}) + \alpha H(\mathbf{x},\mathbf{y})] p(\mathbf{y}) \, \mathrm{d}S(\mathbf{y}) = \int_S [G(\mathbf{x},\mathbf{y}) + \alpha K(\mathbf{x},\mathbf{y})] q(\mathbf{y}) \, \mathrm{d}S(\mathbf{y}) + p_{\text{inc}}(\mathbf{x}) + \alpha \frac{\partial p_{\text{inc}}(\mathbf{x})}{\partial n(\mathbf{x})} \tag{4}$$

in which α represents the coupling parameter: defined as $\alpha = \mathrm{i}/k$ where $k > 1$ and $\alpha = \mathrm{i}$ in other cases.

By discretizing the structural boundary into several elements using constant elements and introducing the coefficient matrix, Equation 4 can be reformulated as follows

$$\mathbf{Hp} - \mathbf{Gq} = \mathbf{p}_f^{inc} \tag{5}$$

where $\mathbf{H}$ and $\mathbf{G}$ $\in \mathbb{C}^{N \times N}$ (N indicates the quantity of degrees of freedom.) are the coefficient matrices. They are asymmetric, fully populated, and frequency-related. The column vectors $\mathbf{p}$ and $\mathbf{q}$, respectively, represent the sound pressure and the acoustic flux at the collocation locations. $\mathbf{p}_f^{inc}$ is the vector of the incident wave.

To determine the sound pressure values at the boundary surface nodes, Equation 5 needs to be solved. Subsequently, the sound pressure can be computed at any point within the acoustic domain by using Equation 4 with $\alpha = 0$ and $C(\mathbf{x}) = 1$.

Its sound pressure, $\mathbf{p}_f$, can be written as follows if the computation takes into account the external acoustic field.

$$\mathbf{p}_f = -\left| \mathbf{H}_f \mathbf{p} - \mathbf{G}_f \mathbf{q} \right| + \mathbf{p}_f^{inc} \tag{6}$$

where the matrices $\mathbf{H}_f$ and $\mathbf{G}_f$ as well as the vector $\mathbf{p}_f$ are similar to those in Equation 5, except that the source point $\mathbf{x}$ is outside the structure domain. And $\mathbf{H}_f$ and $\mathbf{G}_f$ $\in \mathbb{C}^{\tilde{N} \times N}$ ($\tilde{N}$ indicates the quantity of degrees of freedom.)

3 Frequency sweep analysis for acoustic state

In broadband acoustic analysis using BEM, the frequency-dependent coefficient matrices result in time-consuming repetitive computations and repeated solutions of the system equations, posing challenges for practical engineering applications. This frequency dependence arises because the underlying solution is inherently frequency-related. To address this issue, the frequency dependence of the coefficient matrix is eliminated by applying the Taylor series theorem.

The Taylor series expansion of $H_n^{(1)}(kr)$ [47] is given by

$$H_n^{(1)}(kr) = \sum_{m=0}^{\infty} \frac{(kr - k_0 r)^m}{m!} \left[H_n^{(1)}(kr) \right]_{kr=k_0 r}^{(m)} \tag{7}$$

where k_0 is a fixed frequency expansion point. As seen in Figure 1, the fixed expansion point in this paper is the midway point of the frequency band.

Considering an incident wave traveling along the ℓ-axis, the Taylor series expansion of the term related to $p_{\text{inc}}(\mathbf{x})$ in Equation 4 can be expressed as follows

$$p_{\text{inc}}(\mathbf{x}) + \alpha \frac{\partial p_{\text{inc}}(\mathbf{x})}{\partial n(\mathbf{x})} = e^{\mathrm{i}k x_\ell} \left(1 + \alpha \mathrm{i}k \frac{\partial x_\ell}{\partial n(\mathbf{x})} \right) \tag{8}$$

where $\mathbf{x}_\ell$ denotes the ℓ-axis coordinate of the source point, with ℓ being either x or y.

The terms of incident wave in Equation 8 are Taylor series expanded into

$$e^{\mathrm{i}kr} = e^{\mathrm{i}k_0 r} \sum_{m=0}^{\infty} \frac{(\mathrm{i}r)^m (k - k_0)^m}{m!} \tag{9}$$

The expansion expression for the integral of the kernel functions is obtained by combining Equation 7 and Equation 4.

$$\begin{gathered} \int_S G(\mathbf{x},\mathbf{y}) q(\mathbf{y}) \, \mathrm{d}S(\mathbf{y}) = \sum_{m=0}^{\infty} \frac{(k - k_0)^m}{m!} I_g^m \\ \int_S F(\mathbf{x},\mathbf{y}) p(\mathbf{y}) \, \mathrm{d}S(\mathbf{y}) = \sum_{m=0}^{\infty} \frac{(k - k_0)^m}{m!} I_f^m \\ \int_S \alpha K(\mathbf{x},\mathbf{y}) q(\mathbf{y}) \, \mathrm{d}S(\mathbf{y}) = \sum_{m=0}^{\infty} \frac{(k - k_0)^m}{m!} k I_k^m \\ \int_S \alpha H(\mathbf{x},\mathbf{y}) p(\mathbf{y}) \, \mathrm{d}S(\mathbf{y}) = \sum_{m=0}^{\infty} \frac{(k - k_0)^m}{m!} \left[k I_{h1}^m + k^2 I_{h2}^m \right] \end{gathered} \tag{10}$$

where

$$\begin{aligned} I_g^m &= \int_S \frac{\mathrm{i}r^m}{4} \left[H_0^{(1)}(kr) \right]_{kr=k_0 r}^{(m)} q(\mathbf{y}) \, \mathrm{d}S(\mathbf{y}) \\ I_f^m &= -\int_S \frac{\mathrm{i}r^{m-1}}{4} \left[(kr) H_1^{(1)}(kr) \right]_{kr=k_0 r}^{(m)} \frac{\partial r}{\partial n(\mathbf{y})} p(\mathbf{y}) \, \mathrm{d}S(\mathbf{y}) \\ I_k^m &= -\int_S \frac{\alpha \mathrm{i}r^m}{4} \left[H_1^{(1)}(kr) \right]_{kr=k_0 r}^{(m)} \frac{\partial r}{\partial n(\mathbf{x})} q(\mathbf{y}) \, \mathrm{d}S(\mathbf{y}) \\ I_{h1}^m &= \int_S \frac{\alpha \mathrm{i}r^{m-1}}{4} \left[H_1^{(1)}(kr) \right]_{kr=k_0 r}^{(m)} n_j(\mathbf{x}) n_j(\mathbf{y}) p(\mathbf{y}) \, \mathrm{d}S(\mathbf{y}) \\ I_{h2}^m &= -\int_S \frac{\alpha \mathrm{i}r^m}{4} \left[H_2^{(1)}(kr) \right]_{kr=k_0 r}^{(m)} \frac{\partial r}{\partial n(\mathbf{x})} \frac{\partial r}{\partial n(\mathbf{y})} p(\mathbf{y}) \, \mathrm{d}S(\mathbf{y}) \end{aligned} \tag{11}$$

where

$$\left[(kr)H_1^{(1)}(kr)\right]^{(m)} = m\left[H_1^{(1)}(kr)\right]^{(m-1)} + (kr)\left[H_1^{(1)}(kr)\right]^{(m)} \tag{12}$$

By combining Equation 12 and Equation 9, an expression related to the incident wave in Equation 4 is obtained.

$$\tilde{p}_{\text{inc}} = \sum_{\bar{m}=0}^{\infty} \frac{(k-k_0)^{\bar{m}}}{\bar{m}!}\left[\tilde{P}^{\bar{m}}_{\text{inc},1} + k\tilde{P}^{\bar{m}}_{\text{inc},2}\right] \tag{13}$$

where the respective components can be expressed as Equation 14.

$$\begin{aligned} \tilde{P}^{\bar{m}}_{\text{inc},1} &= e^{\mathrm{i}k_0x_\ell}(\mathrm{i}x_\ell)^{\bar{m}} \\ \tilde{P}^{\bar{m}}_{\text{inc},2} &= e^{\mathrm{i}k_0x_\ell}(\mathrm{i}x_\ell)^{\bar{m}}(\alpha\mathrm{i})\frac{\partial x_\ell}{\partial n(\mathbf{x})} \end{aligned} \tag{14}$$

A new formulation of Equation 4 is given below by substituting Equation 10 and Equation 13 into Equation 4.

$$\begin{aligned} &C(\mathbf{x})\,p(\mathbf{x}) + \alpha C(\mathbf{x})\,q(\mathbf{x}) + \sum_{m=0}^{\infty}\frac{(k-k_0)^m}{m!}\left[\left(I_f^m - I_g^m\right) + k\left(I_{h1}^m - I_k^m\right)\right) + k^2 I_{h2}^m\right] \\ &= \sum_{\bar{m}=0}^{\infty}\frac{(k-k_0)^{\bar{m}}}{\bar{m}!}\left[\tilde{P}^{\bar{m}}_{\text{inc},1} + k\tilde{P}^{\bar{m}}_{\text{inc},2}\right] \end{aligned} \tag{15}$$

By discretizing Equation 15 using constant elements, the following matrix expression is derived.

$$\begin{aligned} &\sum_{m=0}^{\infty}\frac{(k-k_0)^m}{m!}\left\{\left[\mathbf{I}_{p1}^m + k\mathbf{I}_{p2}^m + k^2\mathbf{I}_{p3}^m\right]\tilde{\mathbf{p}} - \left[\mathbf{I}_{q1}^m + k\mathbf{I}_{q2}^m\right]\tilde{\mathbf{q}}\right\} \\ &\quad = \sum_{\bar{m}=0}^{\infty}\frac{(k-k_0)^{\bar{m}}}{\bar{m}!}\left[\tilde{\mathbf{P}}^{\bar{m}}_{\text{inc},1} + k\tilde{\mathbf{P}}^{\bar{m}}_{\text{inc},2}\right] \end{aligned} \tag{16}$$

Due to the linearization of the BEM system, the solutions $\tilde{\mathbf{p}}$ and $\tilde{\mathbf{q}}$ in Equation 16 with truncation term $\bar{M}$ can be expressed as Equation 17 and Equation 18.

$$\tilde{\mathbf{p}} = \sum_{\bar{m}=0}^{\bar{M}}\frac{(k-k_0)^{\bar{m}}}{\bar{m}!}\tilde{\mathbf{p}}_1^{\bar{m}} + \sum_{\bar{m}=0}^{M}\frac{k(k-k_0)^{\bar{m}}}{\bar{m}!}\tilde{\mathbf{p}}_2^{\bar{m}} \tag{17}$$

and

$$\tilde{\mathbf{q}} = \sum_{\bar{m}=0}^{\bar{M}}\frac{(k-k_0)^{\bar{m}}}{\bar{m}!}\tilde{\mathbf{q}}_1^{\bar{m}} + \sum_{\bar{m}=0}^{M}\frac{k(k-k_0)^{\bar{m}}}{\bar{m}!}\tilde{\mathbf{q}}_2^{\bar{m}} \tag{18}$$

where the respective solutions of the following system equations are $\tilde{\mathbf{p}}_1^{\bar{m}}$, $\tilde{\mathbf{p}}_2^{\bar{m}}$, $\tilde{\mathbf{q}}_1^{\bar{m}}$ and $\tilde{\mathbf{q}}_2^{\bar{m}}$.

$$\sum_{m=0}^{\infty}\frac{(k-k_0)^m}{m!}\left\{\left[\mathbf{I}_{p1}^m + k\mathbf{I}_{p2}^m + k^2\mathbf{I}_{p3}^m\right]\tilde{\mathbf{p}}_j^{\bar{m}} - \left[\mathbf{I}_{q1}^m + k\mathbf{I}_{q2}^m\right]\tilde{\mathbf{q}}_j^{\bar{m}}\right\} = \tilde{\mathbf{P}}^{\bar{m}}_{\text{inc,j}} \quad j = 1,2 \tag{19}$$

The coefficient matrices $\mathbf{I}_{p1}^m$, $\mathbf{I}_{p2}^m$, $\mathbf{I}_{p3}^m$, $\mathbf{I}_{q1}^m$ and $\mathbf{I}_{q2}^m$ $\in \mathbb{C}^{N\times N}$ in Equation 19 are frequency unrelated. Thus, it only needs to be solved once for wide-frequency acoustic problems, eliminating the need for repetitive calculations of coefficient matrices in BEM systems. However, there is another disadvantage of this method, which is that it is still very difficult to solve the equations directly using GMRES for large problems with multiple frequencies because the coefficient matrices are full-rank and asymmetric and the truncation terms require high storage capacity ($O(5(M+1)N^2)$). It is evident from observation that Equation 19 is the second-order system equation concerning frequency. An efficient SOAR method is presented in [48] to accelerate the broadband solution of Equation 19.

4 Dimension reduction of BEM system for acoustic state analysis

In this section, an effective SOAR method is proposed to expedite the solution of the coefficient matrix by reducing the dimensionality of the 2D system. This projection technique is predicated on the Krylov subspace of second order. By using the method, a system with an equivalent second-order structure but with a diminished state space dimension is created. In Equation 19, the frequency-independent coefficients $\mathbf{I}_{p1}^m$, $\mathbf{I}_{p2}^m$, $\mathbf{I}_{p3}^m$, $\mathbf{I}_{q1}^m$ and $\mathbf{I}_{q2}^m$ are utilized to construct the frequency-unrelated orthogonal basis iteratively, implementing the SOAR algorithm.

In this work, the scattering of an incident wave by a rigid structural surface is considered. The vectors $\mathbf{q}$ in Equation 5 vanish because the particle velocity on the surface of the structure is zero. Thus, Equation 19 can be rewritten as

$$\sum_{m=0}^{\infty}\frac{(k-k_0)^m}{m!}\left[\mathbf{I}_{p1}^m + k\mathbf{I}_{p2}^m + k^2\mathbf{I}_{p3}^m\right]\tilde{\mathbf{p}}_j^{\bar{m}} = \tilde{\mathbf{P}}^{\bar{m}}_{\text{inc},j} \quad j = 1,2 \tag{20}$$

When $m = 0$, the coefficients in Equation 19 are utilized to create frequency-independent orthogonal bases, then Equation 19 is re-expressed as

$$\left(\mathbf{I}_{p1}^0 + k\mathbf{I}_{p2}^0 + k^2\mathbf{I}_{p3}^0\right)\tilde{\mathbf{p}}_j^{\bar{m}} = \tilde{\mathbf{P}}^{\bar{m}}_{\text{inc},j} \quad j = 1,2 \tag{21}$$

It should be noted that Equation 21 is not an approximation of the original system equation; rather, it is used for the construction of the orthogonal basis. Equation 21, approximated around a chosen expansion point k_0, can be expressed as Equation 22.

$$\left[\mathbf{I}_{p5}^0 + (k-k_0)\mathbf{I}_{p4}^0 + (k-k_0)^2\mathbf{I}_{p3}^0\right]\tilde{\mathbf{p}}_j^{\bar{m}} = \tilde{\mathbf{P}}^{\bar{m}}_{\text{inc},j} \quad j = 1,2 \tag{22}$$

where $\mathbf{I}_{p5}^0 = k_0^2\mathbf{I}_{p3}^0 + k_0\mathbf{I}_{p2}^0 + \mathbf{I}_{p1}^0$ and $\mathbf{I}_{p4}^0 = 2k_0\mathbf{I}_{p3}^0 + \mathbf{I}_{p2}^0$.

Following the SOAR method procedure outlined in Ref. [48], a sequence of frequency-independent orthogonal bases $\mathbf{Q}_j^{\bar{m}}$ was constructed in the second-order Krylov subspace $\mathcal{G}_n(\mathbf{A},\mathbf{B};\mathbf{r}_0)$ using the coefficients from Equation 19, where $n \ll N$ as shown in Equation 23.

$$\operatorname{span}\left\{\mathbf{Q}_j^{\bar{m}}\right\} = \mathcal{G}_n(\mathbf{A},\mathbf{B};\mathbf{r}_0) = \operatorname{span}\{\mathbf{r}_0,\mathbf{r}_1,\mathbf{r}_2,\ldots,\mathbf{r}_{n-1}\} \tag{23}$$

where the respective quantities are shown in Equation 24.

$$\begin{cases} \mathbf{A} = -\left(\mathbf{I}_{p5}^0\right)^{-1}\mathbf{I}_{p4}^0 \\ \mathbf{B} = -\left(\mathbf{I}_{p5}^0\right)^{-1}\mathbf{I}_{p3}^0 \\ \mathbf{r}_0 = \left(\mathbf{I}_{p5}^0\right)^{-1}\tilde{\mathbf{P}}^{\bar{m}}_{\text{inc},j} \\ \mathbf{r}_1 = \mathbf{A}\mathbf{r}_0 \\ \mathbf{r}_\ell = \mathbf{A}\mathbf{r}_{\ell-1} + \mathbf{B}\mathbf{r}_{\ell-2} \qquad \text{for} \quad \ell \geq 2 \end{cases} \tag{24}$$

To define a reduced system equation of the initial Equation 20, the projection subspace is constructed by spanning a sequence of nonzero columns of $\mathbf{Q}_j^{\bar{m}}$. Equation 20 is reformulated as Equation 25.

$$\tilde{\mathbf{p}}_j^{\bar{m}} = \left[\sum_{m=0}^{M}\frac{(k-k_0)^m}{m!}\left(\mathbf{I}_{p1}^m + k\mathbf{I}_{p2}^m + k^2\mathbf{I}_{p3}^m\right)\right]^{-1}\tilde{\mathbf{P}}^{\bar{m}}_{\text{inc},j} \quad j = 1,2 \tag{25}$$

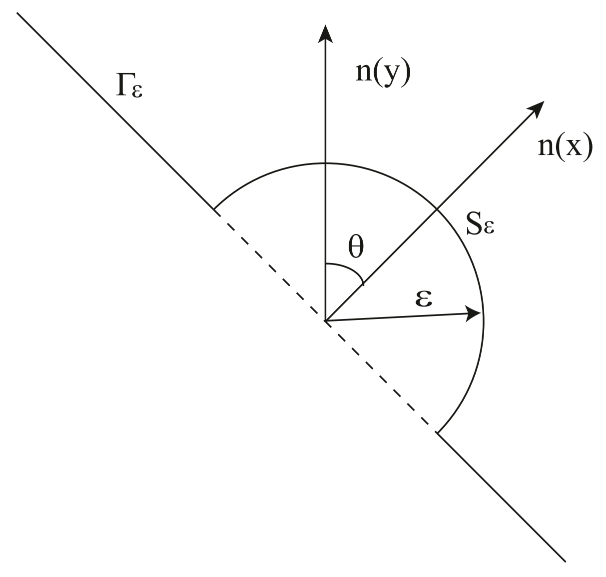

FIGURE 2
The constant element $S_{\mathbf{x}}$ is connected to an infinitesimal semicircle. Normal derivatives at source points **x** and field points **y** are represented by the notations $n(\mathbf{x})$ and $n(\mathbf{y})$, respectively.

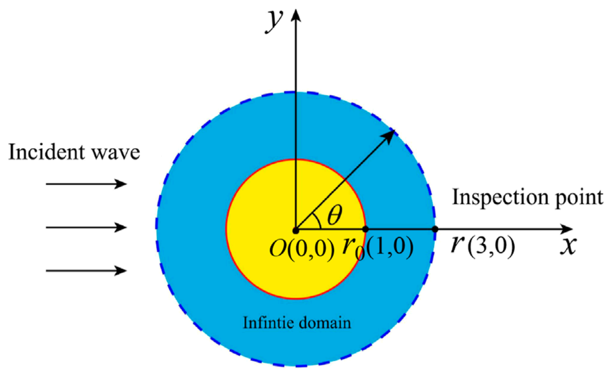

FIGURE 3
The infinite cylinder serves as the design domain for sound scattering.

Subsequently, the simplified system equation at the expansion point k_0 can be stated as Equation 26.

$$\mathbf{b}_j^{\bar{m}} = \left[\sum_{m=0}^{M} \frac{(k-k_0)^m}{m!} \left(\mathbf{I}_{p1}^{m,n} + k\mathbf{I}_{p2}^{m,n} + k^2 \mathbf{I}_{p3}^{m,n} \right) \right]^{-1} \left[\mathbf{Q}_j^{\bar{m}} \right]^{\mathrm{T}} \tilde{\mathbf{P}}_{\mathrm{inc},j}^{\bar{m}} \quad j = 1,2 \tag{26}$$

where the coefficient matrix is shown in Equation 27.

$$\begin{cases} \mathbf{I}_{p1}^{m,n} = \left[\mathbf{Q}_j^{\bar{m}} \right]^{\mathrm{T}} \mathbf{I}_{p1}^{m} \mathbf{Q}_j^{\bar{m}} \\ \mathbf{I}_{p2}^{m,n} = \left[\mathbf{Q}_j^{\bar{m}} \right]^{\mathrm{T}} \mathbf{I}_{p2}^{m} \mathbf{Q}_j^{\bar{m}} \\ \mathbf{I}_{p3}^{m,n} = \left[\mathbf{Q}_j^{\bar{m}} \right]^{\mathrm{T}} \mathbf{I}_{p3}^{m} \mathbf{Q}_j^{\bar{m}} \end{cases} \tag{27}$$

The relation between the solution of FOM and ROM is expressed as

$$\tilde{\mathbf{p}}_j^{\bar{m}} = \mathbf{Q}_j^{\bar{m}} \mathbf{b}_j^{\bar{m}} \tag{28}$$

$\tilde{\mathbf{p}}_j^{\bar{m}}$ is the nth order Padé-type approximation of $\tilde{\mathbf{P}}_{\mathrm{inc},j}^{\bar{m}}$ about the fixed expansion point k_0, as shown in Equation 29.

$$\tilde{\mathbf{p}}_j^{\bar{m}} = \tilde{\mathbf{P}}_{\mathrm{inc,j}}^{\bar{m}} + O\left((k-k_0)^n \right) \tag{29}$$

In the ROM, $\mathbf{I}_{p1}^{m,n}$, $\mathbf{I}_{p2}^{m,n}$ and $\mathbf{I}_{p3}^{m,n}$ are $n \times n$ matrices where $n \ll N$. This significantly reduced storage requirements and improved computational efficiency. At the collocation points on the structural surface, the sound pressure can be obtained using Equation 28. Afterward, at any point within the acoustic domain, Equation 6 can be used to get the sound pressure value.

5 Singular integral in BEM

The boundary integral of the kernel function in Equation 11 can be expressed as the sum of singular and non-singular terms.

$$\int_S f(\mathbf{y})\,\mathrm{d}S(\mathbf{y}) = \underbrace{\int_{S \backslash S_{\mathbf{x}}} f(\mathbf{y})\,\mathrm{d}S(\mathbf{y})}_{non-singular} + \underbrace{\int_{S_{\mathbf{x}}} f(\mathbf{y})\,\mathrm{d}S(\mathbf{y})}_{singular} \tag{30}$$

where $S_{\mathbf{x}}$ is the element that contains the source point **x**. $S \backslash S_{\mathbf{x}}$ denotes the boundary S that does not contain $S_{\mathbf{x}}$. Since the integral does not exhibit singularity on the boundary $S \backslash S_{\mathbf{x}}$, Gauss quadrature can be employed for its solution. However, the integral over the boundary $S_{\mathbf{x}}$ is singular and must be processed to do a numerical calculation.

The steps for handling singular integrals are as follows:

1. Suppose there is a singular function $\hat{f}(\mathbf{x})$. First, perform a singular order analysis on the integrand to obtain a simple function $\hat{f}_0(\mathbf{x})$ that shares the same order of singularity.
2. Then, split the integral of the singular function into two parts: one part is the integrand minus the simple function $\hat{f}(\mathbf{x}) - \hat{f}_0(\mathbf{x})$, and the other part is the integral of the simple function $\hat{f}_0(\mathbf{x})$. Since $\hat{f}(\mathbf{x}) - \hat{f}_0(\mathbf{x})$ is non-singular, it can be directly computed using Gaussian-Legendre quadrature. Although $\hat{f}_0(\mathbf{x})$ retains its singularity, its simple form allows for accurate integral results through various methods, such as integration by parts, the Cauchy principal value, and the Hadamard finite part integral.
3. Finally, adding these two parts yields the accurate integral value of the original singular function $\hat{f}(\mathbf{x})$.

In this study, singular integrals are handled using the Cauchy principal value and the Hadamard finite part integral methods. With reference to Figure 2, let S_ε represent a semicircle of radius ε, and Γ_ε represent $S_{\mathbf{x}} \backslash S_\varepsilon$. Equation 30 can be used to rewrite the singular integral term in Equation 31.

$$\int_{S_{\mathbf{x}}} f(\mathbf{y})\,\mathrm{d}S(\mathbf{y}) = \underbrace{\lim_{\varepsilon \to 0} \int_{\Gamma_\varepsilon} [f(\mathbf{y}) - D(\mathbf{y})]\,\mathrm{d}S(\mathbf{y})}_{\text{nonsingular}} + \underbrace{\lim_{\varepsilon \to 0} \int_{S_\varepsilon} f(\mathbf{y})\,\mathrm{d}S(\mathbf{y})}_{\text{singular}} + \underbrace{\lim_{\varepsilon \to 0} \int_{\Gamma_\varepsilon} D(\mathbf{y})\,\mathrm{d}S(\mathbf{y})}_{\text{singular}} \tag{31}$$

When $\mathbf{y} \in S_{\mathbf{x}}$, then $\frac{\partial r}{\partial n(\mathbf{x})} = \frac{\partial r}{\partial n(\mathbf{y})} = 0$, hence I_f^m, I_k^m and I_{h2}^m are all zero. Therefore, the singular integrals in Equation 11 are present only in I_g^m and I_{h1}^m.

To facilitate the derivation of singular integrals, the singular terms of I_g^m and I_{h1}^m are denoted as f_g^m and f_{h1}^m respectively.

$$\begin{aligned} f_g^m &= r^m \left[H_0^{(1)}(kr) \right]_{kr=k_0 r}^{(m)} \\ f_{h1}^m &= r^{m-1} \left[H_1^{(1)}(kr) \right]_{kr=k_0 r}^{(m)} \end{aligned} \tag{32}$$

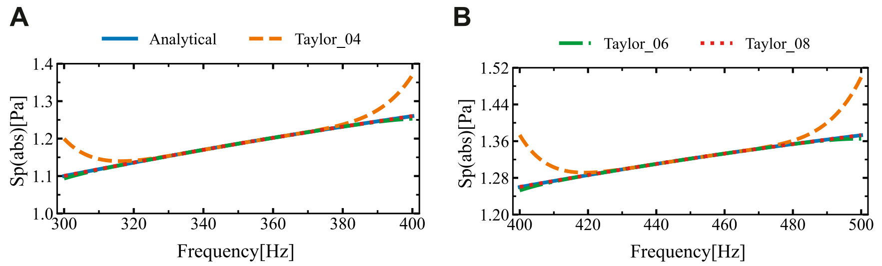

FIGURE 4
The sound pressure amplitudes at the computational point located at (3 m, 0 m) in two different frequency ranges were obtained using the analytical solution and SOAR Accelerated Taylor Extension-based BEM: **(A)**. f = (300,400) Hz, **(B)**. f = (400,500) Hz.

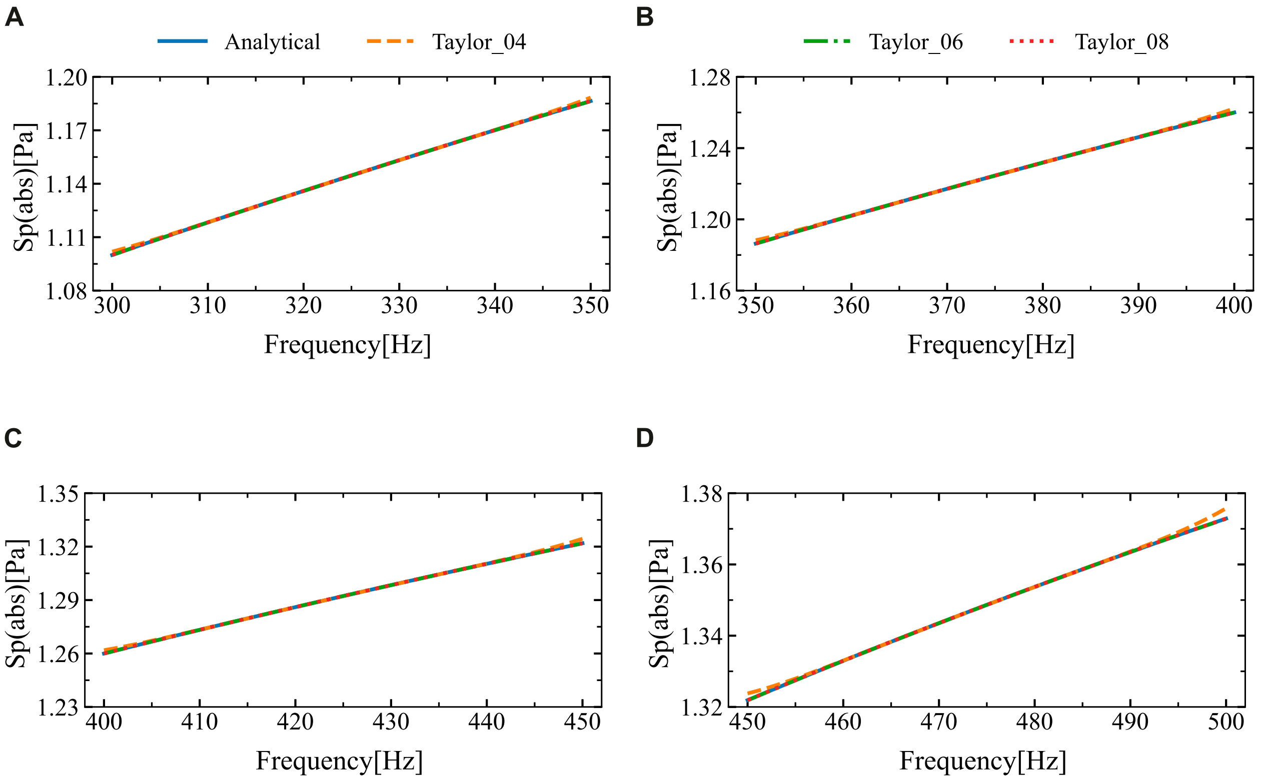

FIGURE 5
The sound pressure amplitudes at the computational point located at (3 m, 0 m) in four different frequency ranges were obtained using the analytical solution and SOAR Accelerated Taylor Extension-based BEM: **(A)**. f = (300,350) Hz, **(B)**. f = (350,400) Hz, **(C)**. f = (400,450) Hz, **(D)**. f = (450,500) Hz.

Based on Equation 31 and Equation 32, the integrals I_g^m and I_{h1}^m in $S_{\mathbf{x}}$ can be restated as

$$\begin{aligned} \int_{S_{\mathbf{x}}} f_g^m \mathrm{d}S(\mathbf{y}) &= \underbrace{\lim_{\varepsilon\to 0}\int_{\Gamma_\varepsilon}\left[f_g^m - D_g^m\right]\mathrm{d}S(\mathbf{y})}_{\text{nonsinglar}} + \underbrace{\lim_{\varepsilon\to 0}\int_{S_\varepsilon} f_g^m \mathrm{d}S(\mathbf{y})}_{g_0^m} + \underbrace{\lim_{\varepsilon\to 0}\int_{\Gamma_\varepsilon} D_g^m \mathrm{d}S(\mathbf{y})}_{d_0^m} \\ \int_{S_{\mathbf{x}}} f_{h1}^m \mathrm{d}S(\mathbf{y}) &= \underbrace{\lim_{\varepsilon\to 0}\int_{\Gamma_\varepsilon}\left[f_{h1}^m - D_{h1}^m\right]\mathrm{d}S(\mathbf{y})}_{\text{nonsinglar}} + \underbrace{\lim_{\varepsilon\to 0}\int_{S_\varepsilon} f_{h1}^m \mathrm{d}S(\mathbf{y})}_{g_1^m} + \underbrace{\lim_{\varepsilon\to 0}\int_{\Gamma_\varepsilon} D_{h1}^m \mathrm{d}S(\mathbf{y})}_{d_1^m} \end{aligned} \tag{33}$$

where $n_j(\mathbf{x})n_j(\mathbf{y}) = 1$ and $dr = d\mathrm{S}(\mathbf{y})$ in $S_{\mathbf{x}}$. The non-singular terms in Equation 33 are computed using Gaussian quadrature. The singular part of $H_0^{(1)}(kr)$ is $2\mathrm{i}\ln(kr)/\pi$ and that of $H_1^{(1)}(kr)$ is $2\mathrm{i}/(-\pi kr) + \mathrm{i}(kr)\ln(kr)/\pi$ Thus, their m-th derivatives are represented as Equations 34, 35.

$$D_g^m = \begin{cases} \dfrac{2\mathrm{i}}{\pi}\ln(k_0 r), & m = 0 \\ O(r^0), & m \neq 0 \end{cases} \tag{34}$$

and

$$D_{h1}^m = \begin{cases} -\dfrac{2\mathrm{i}}{\pi}k_0^{-1}r^{-2} + \dfrac{\mathrm{i}k_0}{\pi}\ln(k_0 r), & m = 0 \\ \dfrac{2\mathrm{i}}{\pi}k_0^{-2}r^{-2} + \dfrac{\mathrm{i}}{\pi}\ln(k_0 r), & m = 1 \\ -\dfrac{2\mathrm{i}}{\pi}(-1)^m k_0^{-(m+1)}r^{-2}m!, & m \geq 2 \end{cases} \tag{35}$$

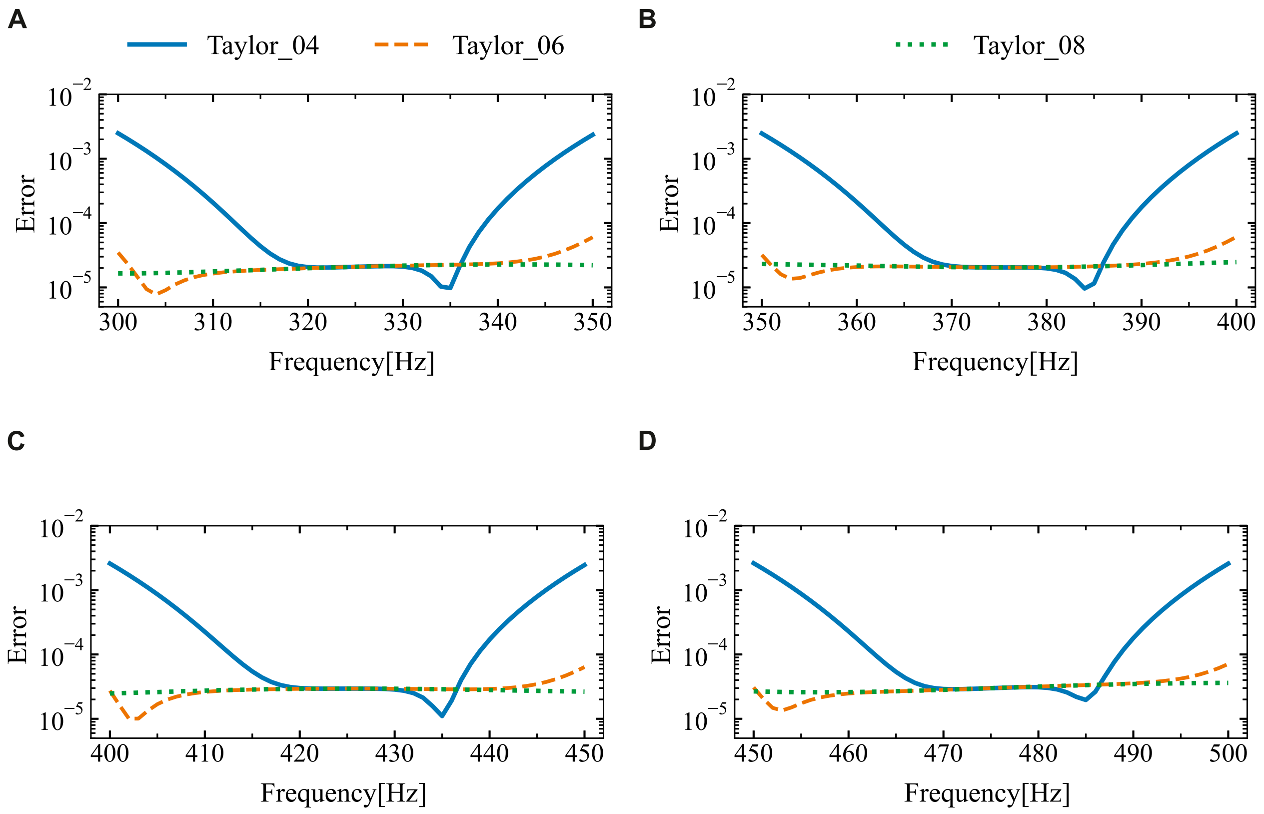

FIGURE 6
The relative error of the sound pressure at the point of calculation (3 m, 0 m) for different expansion terms was derived through the utilization of the analytical solution and SOAR Accelerated Taylor Extension-based BEM: **(A)**. f = (300,350) Hz, **(B)**. f = (350,400) Hz, **(C)**. f = (400,450) Hz, **(D)**. f = (450,500) Hz.

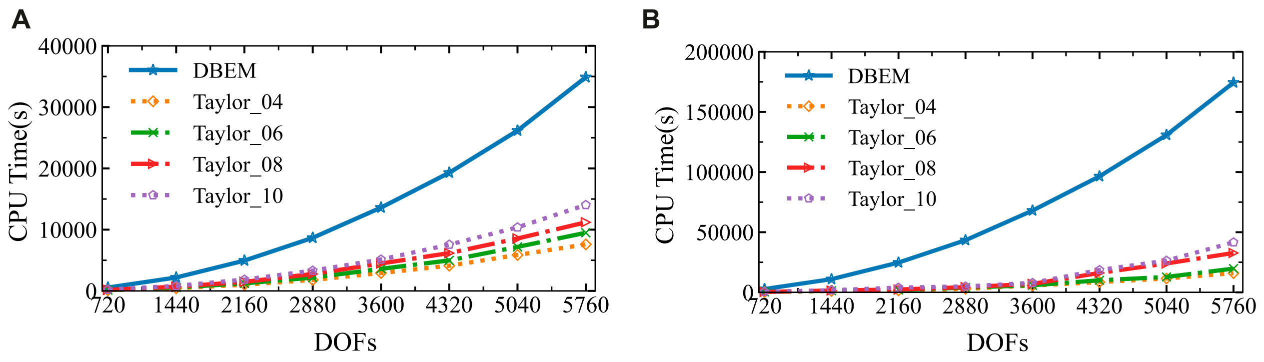

FIGURE 7
The sound pressure amplitudes at the computational point located at (3 m, 0 m) in two different frequency ranges were obtained using the analytical solution and SOAR Accelerated Taylor Extension-based BEM: **(A)**. Frequency step length = 0.5 Hz., **(B)**. Frequency step length = 0.1 Hz.

By substituting Equation 34 into the first equation of Equation 33, the two singular terms g_0^0 and d_0^0 in Equation 33 can be expressed as Equation 36.

$$\begin{aligned} g_0^0 &= 0 \\ d_0^0 &= \frac{2\mathrm{i}L}{\pi}\left[\ln\left(k_0 L/2\right) - 1\right] \end{aligned} \tag{36}$$

where L is the length of the element.

Similarly, by substituting Equation 34 into the second equation of Equation 33, the expressions for g_1^m and d_1^m are obtained.

$$g_1^m = \lim_{\varepsilon \to 0}\left[\frac{4\mathrm{i}}{\pi}(-1)^m k_0^{-(m+1)} m! \frac{1}{\varepsilon}\right] \tag{37}$$

and

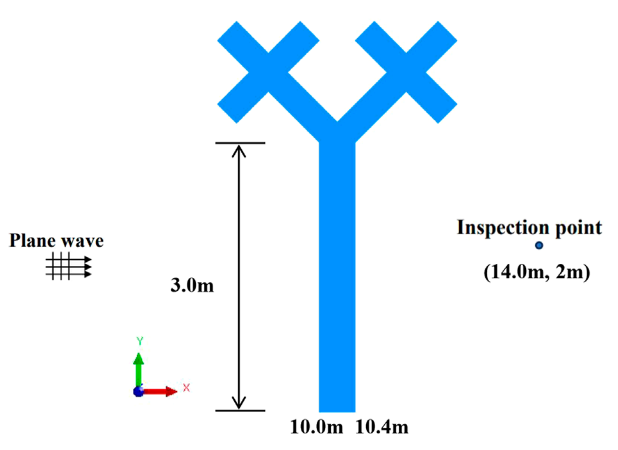

FIGURE 8
The design domain of the tree-shaped sound barrier model.

$$d_1^m = \begin{cases} \dfrac{8\mathrm{i}}{\pi k_0 L} + \dfrac{\mathrm{i}k_0 L}{\pi}\left[\ln\left(k_0 L/2\right) - 1\right] - \lim\limits_{\varepsilon \to 0} \dfrac{4\mathrm{i}}{\pi k_0 \varepsilon} & m = 0 \\ \dfrac{-8\mathrm{i}}{\pi {k_0}^2 L} + \dfrac{\mathrm{i}L}{\pi}\left[\ln\left(k_0 L/2\right) - 1\right] + \lim\limits_{\varepsilon \to 0} \dfrac{4\mathrm{i}}{\pi {k_0}^2 \varepsilon} & m = 1 \\ \dfrac{8\mathrm{i}}{\pi L}(-1)^m k_0^{-(m+1)} m! - \lim\limits_{\varepsilon \to 0}\left[\dfrac{4\mathrm{i}}{\pi}(-1)^m k_0^{-(m+1)} m! \dfrac{1}{\varepsilon}\right] & m \geq 2 \end{cases} \tag{38}$$

By combining Equation 37 and Equation 38, the expression for the singular integral is derived as Equation 39.

$$g_1^m + d_1^m = \begin{cases} \dfrac{8\mathrm{i}}{\pi k_0 L} + \dfrac{\mathrm{i}k_0 L}{\pi}\left[\ln\left(k_0 L/2\right) - 1\right] & m = 0 \\ \dfrac{-8\mathrm{i}}{\pi {k_0}^2 L} + \dfrac{\mathrm{i}L}{\pi}\left[\ln\left(k_0 L/2\right) - 1\right] & m = 1 \\ \dfrac{8\mathrm{i}}{\pi L}(-1)^m k_0^{-(m+1)} m! & m \geq 2 \end{cases} \tag{39}$$

6 Numerical example

Three computational examples are presented in this section to evaluate the performance of the proposed algorithm. The research employed the Fortran 90 programming language to conduct numerical simulations. 64 GB of RAM and an Intel (R) Core (TM) i9-10900H Central Processing Unit (CPU) were installed on a desktop computer to perform calculations.

In the simulations, some common parameters are as follows: an incident wave with an amplitude of $p_0 = 1$ propagating in the positive x-axis direction, expressed as $\mathbf{p}_{\mathrm{inc}} = p_0 e^{ikr\cos\theta}$. The medium for the acoustic wave is air, with a density of 1.21 kg/m^3 and a speed of 343 m/s.

6.1 Acoustic scattering by an infinitely rigid cylinder

The acoustic scattering from a cylinder can be reduced to a two-dimensional problem by assuming that a plane wave beam acts on an infinitely rigid cylinder (see Figure 3). And a plane wave follows the positive x-axis of propagation. The cylinder is centered at (0 m, 0 m) with a radius of 1 m, and the circumference is discretized using 720 constant boundary elements. Additionally, the coordinates of the calculation point are (3 m, 0 m) (see Figure 3).

The problem of acoustic scattering by an infinitely rigid cylinder has the analytical solution, which is represented as Equation 40 [49].

$$p(r,\theta) = -\sum_{n=0}^{\infty} \varepsilon_n \mathrm{i}^n \frac{nJ_n(kr_0) - kr_0 J_{n+1}(kr_0)}{nH_n^{(1)}(kr_0) - kr_0 H_{n+1}^{(1)}(kr_0)} H_n^{(1)}(kr)\cos(n\theta) \tag{40}$$

In the above equation, $\varepsilon_0 = 1$ for $n = 0$, and $\varepsilon_n = 2$ otherwise, where ε_n represents the Neumann symbols. The expansion consists of 50 terms, and at the detection point, $\theta = 0$.

The relative error between the numerical result computed and the analytical solution is evaluated, as shown in Equation 41, to ensure that the proposed approach is accurate.

$$e^{\Gamma} = \left(\sum_{i=1}^{N} |p_n(\mathbf{x}_i) - p_e(\mathbf{x}_i)|^2\right)^{1/2} \Big/ \left(\sum_{i=1}^{N} |p_e(\mathbf{x}_i)|^2\right)^{1/2} \tag{41}$$

where $\mathbf{x}_i$ denotes the computational points within the domain, the numerical solution for sound pressure is represented by $p_n(\mathbf{x}_i)$, and the analytical solution for sound pressure is denoted by $p_e(\mathbf{x}_i)$. The number of computed points, $N = 720$, is evenly distributed along the perimeter of the circle shown in Figure 3, which has a radius of r = 3 m.

Figure 4 shows the sound pressure amplitude at the computed location (3 m, 0 m) obtained using the proposed algorithm. The analytical solution and this outcome are contrasted. Numerical simulations considered two distinct intervals (300, 400) Hz and (400, 500) Hz. In the frequency interval (f_{lef}, f_{rig}), the fixed expansion point is the midpoint frequency $(f_{lef}, f_{rig})/2$. "Taylor_03", "Taylor_06", and "Taylor_08" denote the retention of the first 3, 6, and 8 terms of the Taylor expansion, respectively. The ROM attainments by the SOAR approach have an order of 10.

Figure 4 demonstrates that the sound pressure amplitude values derived from various Taylor series terms of the proposed algorithm are comparatively consistent with the analytical solution. Due to the fixed expansion point being the midpoint of the frequency interval, significant differences occur at the two ends of each frequency interval. In order to minimize the disparity between the analytical and numerical solutions, we subdivided the frequency intervals (300, 400) Hz and (400, 500) Hz into four sub-intervals each, and then recalculated the numerical simulations.

Figure 5 presents the results of the analytical and numerical solutions for the four sub-intervals after subdivision. It is evident that the numerical solutions match the analytical solutions very closely. Figure 6 shows the relative errors between them. Based on the observations, it can be inferred that the relative error is sufficiently minimal and exhibits little fluctuation when six or more expansion terms are used.

Figure 7 illustrates how long it takes to compute the point sound pressure amplitude using both the conventional boundary element method (DBEM) and the proposed approach. The

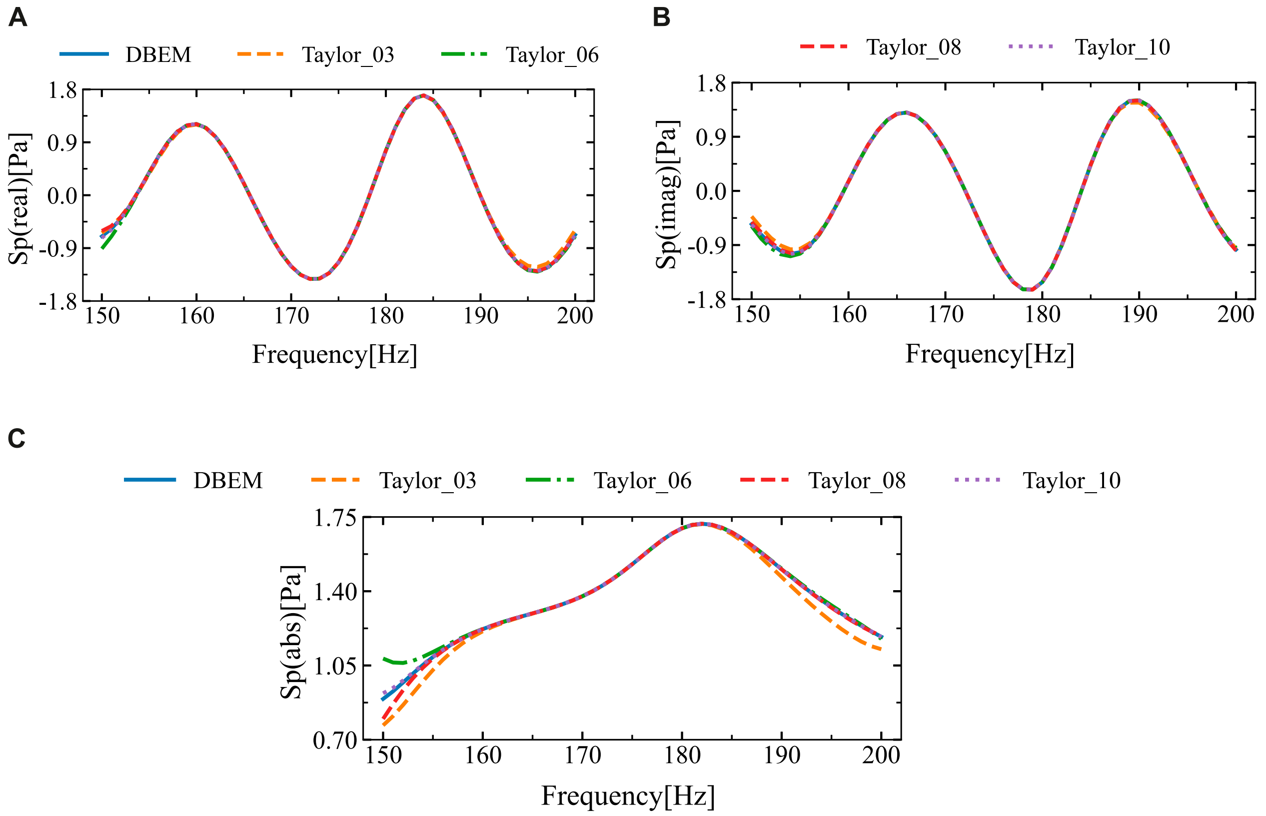

FIGURE 9
The sound pressure findings at a computing position (14 m, 2 m) that were acquired using DBEM and SOAR Accelerated Taylor Extension-based BEM: **(A)**. Real part, **(B)**. Imaginary part, **(C)**. Sound pressure amplitude.

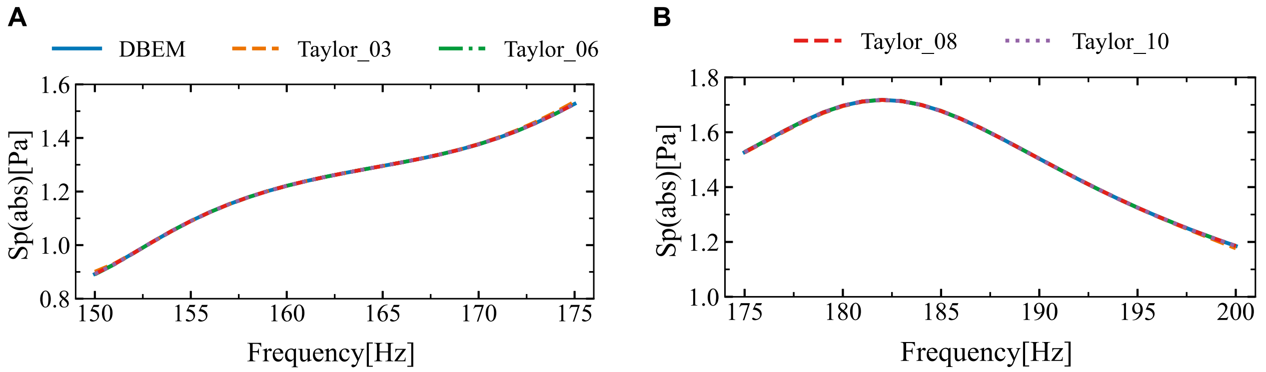

FIGURE 10
At a point of computation (14 m, 2 m), the sound pressure amplitude were acquired using DBEM and SOAR Accelerated Taylor Extension-based BEM: **(A)**. f = (150,175) Hz, **(B)**. f = (175,200) Hz.

frequency sweep range is (300, 400) Hz, with the number of frequency sweeps set to 200 and 1,000, respectively. The ROM attainments by the SOAR approach have an order of 10. It can be observed that for wide-frequency sweep calculations, when compared to the DBEM, the proposed method takes a lot shorter amounts of time. Moreover, the more frequency sweeps performed, the greater the time savings, indicating higher efficiency. Based on the above analysis, six terms for the Taylor series expansion are advised in computational simulations to minimize CPU time.

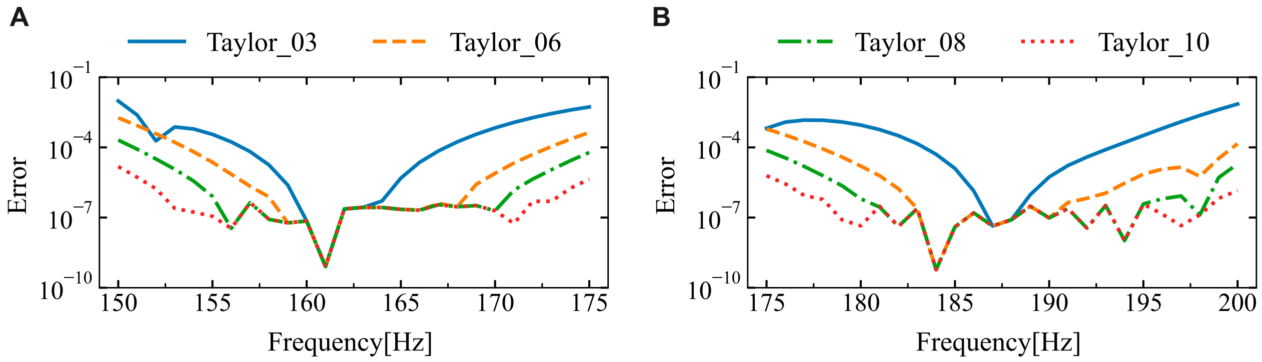

FIGURE 11
The relative error of the sound pressure at the point of calculation (14 m, 2 m) for different expansion terms was derived through the utilization of the DBEM and SOAR Accelerated Taylor Extension-based BEM: **(A)**. f = (150,175) Hz, **(B)**. f = (175,200) Hz.

TABLE 1 Sound pressure values and relative errors for different taylor expansion terms.

Frequency	DBEM	Taylor_03		Taylor_06		Taylor_08		Taylor_10	
		$\lvert Sp\rvert$	ε_r	$\lvert Sp\rvert$	ε_r	$\lvert Sp\rvert$	ε_r	$\lvert Sp\rvert$	ε_r
150	0.89217	0.90074	9×10^{-3}	0.89053	1×10^{-3}	0.89235	2×10^{-4}	0.89215	2×10^{-5}
155	1.08997	1.08959	3×10^{-4}	1.08995	2×10^{-5}	1.08998	9×10^{-6}	1.08998	9×10^{-6}
160	1.22135	1.22131	3×10^{-5}	1.22132	3×10^{-5}	1.22137	2×10^{-5}	1.22136	8×10^{-6}
165	1.29554	1.29557	2×10^{-5}	1.29556	2×10^{-5}	1.29555	9×10^{-6}	1.29555	8×10^{-6}
170	1.37634	1.37727	7×10^{-4}	1.37632	1×10^{-5}	1.37633	7×10^{-6}	1.37633	7×10^{-6}
175	1.52724	1.53539	5×10^{-3}	1.52657	4×10^{-4}	1.52733	6×10^{-5}	1.52723	7×10^{-6}
180	1.69679	1.69526	9×10^{-4}	1.69681	1×10^{-5}	1.69678	6×10^{-6}	1.69678	6×10^{-6}
185	1.67760	1.67758	1×10^{-5}	1.67759	6×10^{-6}	1.67759	6×10^{-6}	1.67759	6×10^{-6}
190	1.50347	1.50345	1×10^{-5}	1.50346	7×10^{-6}	1.50346	7×10^{-6}	1.50346	7×10^{-6}
195	1.32502	1.32549	4×10^{-4}	1.32500	2×10^{-5}	1.32501	8×10^{-6}	1.32501	8×10^{-6}
200	1.18539	1.17692	7×10^{-3}	1.18556	1×10^{-4}	1.18536	3×10^{-5}	1.18538	8×10^{-6}

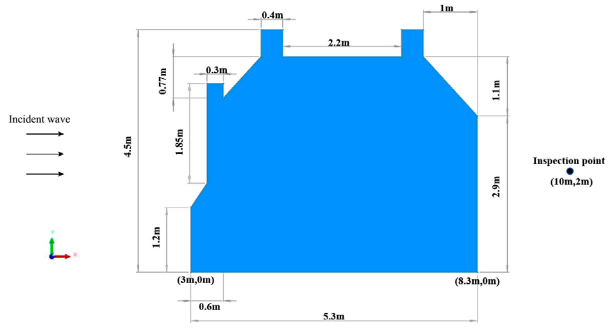

FIGURE 12
Acoustic scattering design domain for two-dimensional room.

6.2 Acoustic scattering by tree-shaped sound barriers

Traffic noise is a major source of environmental noise in urban areas, significantly impacting health and quality of life. The use of sound barriers can mitigate the effects of traffic noise on both the environment and human health.

Figure 8 depicts a tree-shaped sound barrier model, where the model boundary is discretized into 868 scattered points by constant elements. The remaining parameters for the tree-shaped sound barrier model are as follows: the trunk and four branches of the tree-shaped sound barrier are each 0.5 m in length and 0.3 m in width. The base of the trunk measures 0.8 m in length and 0.3 m in width. A Tree-shaped sound barrier scatters a plane wave that is traveling along the positive *x*-axis with an amplitude of $p_0 = 1$. The observation point is located at (14 m, 2 m).

Figure 9 depicts the amplitude, imaginary part and real part of the sound pressure at the observation point, obtained using the traditional boundary element method and different Taylor series expansion terms of the proposed algorithm. The figure shows that as the number of Taylor expansion terms increases, the sound pressure results obtained by the proposed approach converge. Due to the fixed frequency expansion point being located at the midpoint of the frequency range, discrepancies appear at the ends of the interval, whereas other regions show good agreement. The frequency band of (150, 200) Hz is split into two sub-intervals, and numerical simulations are conducted separately for each sub-interval. The simulation results are shown in Figure 10. From Figure 10, it can be concluded that the results obtained with different Taylor expansion terms are in high agreement with those obtained using the DBEM.

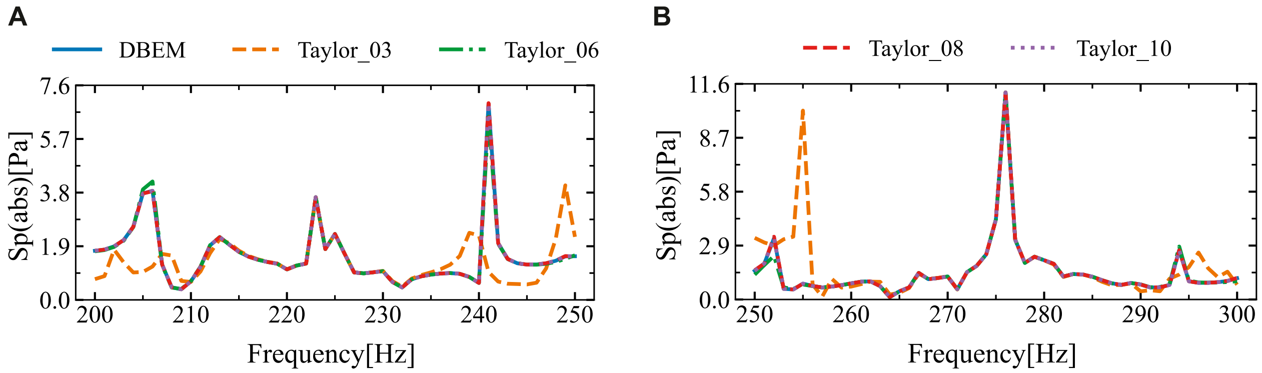

FIGURE 13
The sound pressure amplitudes at the computational point located at (10 m, 2 m) in four different frequency ranges were obtained using the DBEM and SOAR Accelerated Taylor Extension-based BEM: **(A)**. f = (200,250) Hz, **(B)**. f = (250,300) Hz.

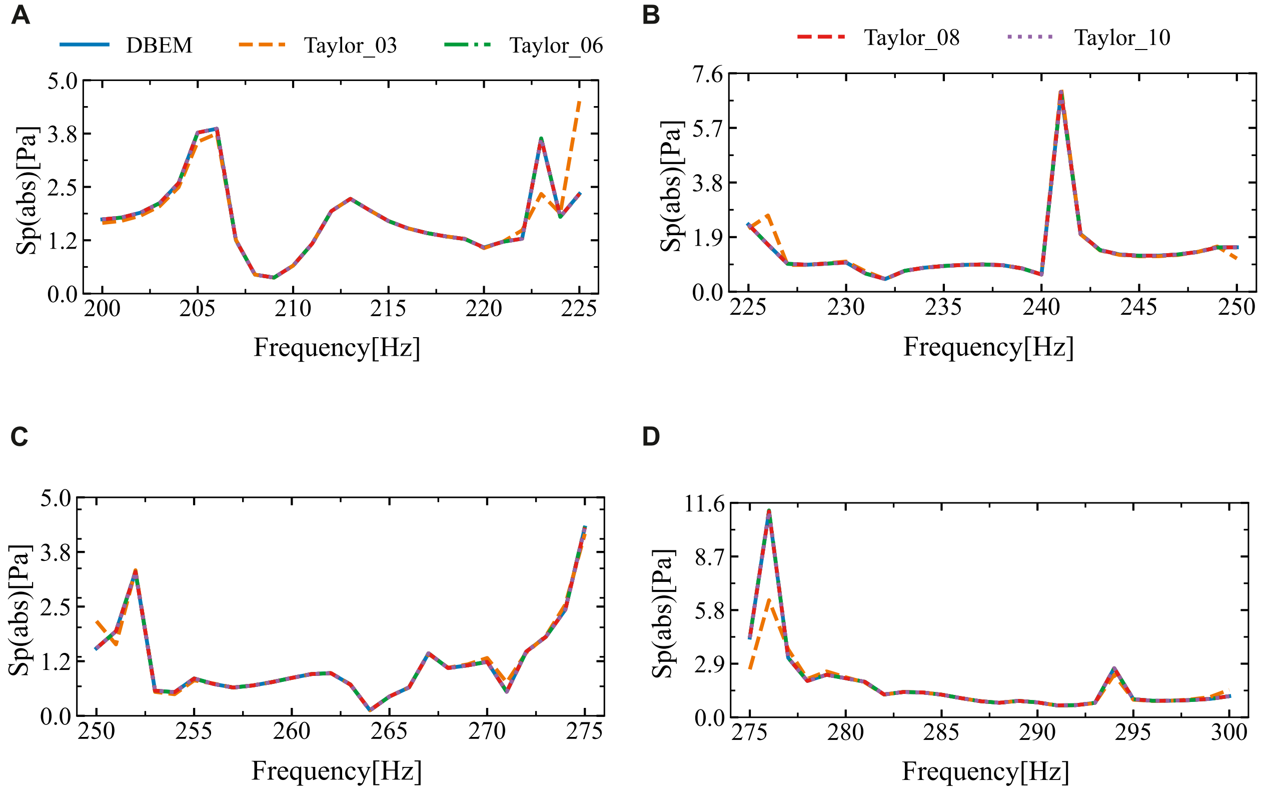

FIGURE 14
The sound pressure amplitudes at the computational point located at (10 m, 2 m) in four different frequency ranges were obtained using the DBEM and SOAR Accelerated Taylor Extension-based BEM: **(A)**. f = (200,225) Hz, **(B)**. f = (225,250) Hz, **(C)**. f = (250,275) Hz, **(D)**. f = (275,300) Hz.

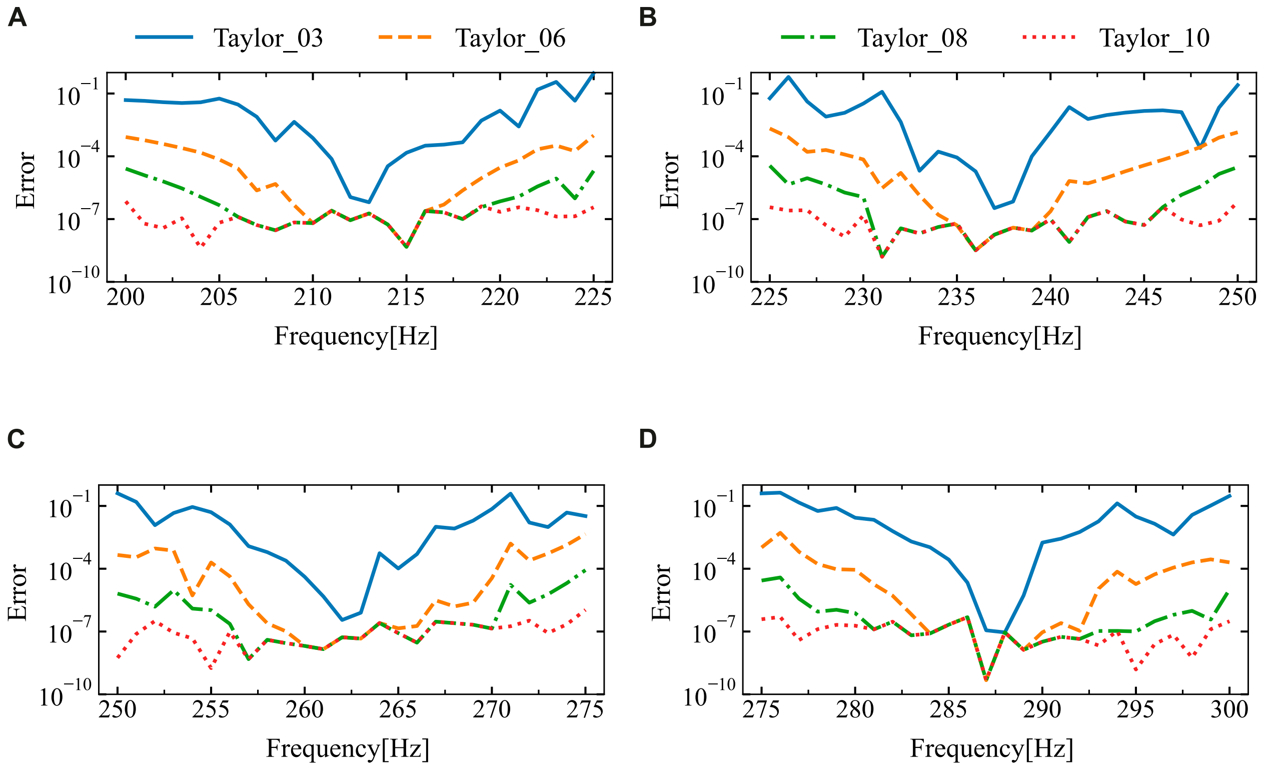

FIGURE 15
The relative error of the sound pressure at the point of calculation (10 m, 2 m) for different expansion terms was derived through the utilization of the DBEM and SOAR Accelerated Taylor Extension-based BEM: **(A)**. f = (200,225) Hz, **(B)**. f = (225,250) Hz, **(C)**. f = (250,275) Hz, **(D)**. f = (275,300) Hz.

Figure 11 presents the relative error between the results at the calculation points for different expansion terms and those from the traditional boundary element method. The figure indicates that if there are six or more Taylor expansion terms, the relative error remains consistently low and stable. Table 1 displays the sound pressure amplitudes at various frequency points obtained through two different algorithms, along with the relative errors between them.

6.3 Acoustic scattering by room

This section demonstrates the calculation of sound pressure amplitudes at observation points within a two-dimensional room. Both the BEM and the Taylor series expansion-based BEM accelerated by the SOAR algorithm are employed. The results from these methods are then compared and analyzed. As depicted in Figure 12, the two-dimensional room model measures 4.5 m in height and 5.3 m in width. The boundary is divided into 994 discrete points using constant elements. A wave with an amplitude of 1, traveling in the positive x-direction, is scattered by the room. The observation point is situated at (10 m,2 m).

The frequency range scanned in Figure 13 spans from 200 Hz to 250 Hz and from 250 Hz to 300 Hz. Figure 13 indicates that the sound pressure amplitudes obtained by both methods exhibit good agreement within the intervals of (210, 235) Hz and (260, 290) Hz, but show significant discrepancies at the ends of these intervals. The discrepancy arises because the frequencies used for calculations within each frequency sweep interval are centered on the midpoint of the interval. Consequently, the further a frequency is from the midpoint, the greater the error in the calculated result. To enhance accuracy and diminish errors, the intervals (200, 250) Hz and (250, 300) Hz are subdivided into four sub-intervals each. Within each sub-interval, calculations are performed using the midpoint frequency. The outcomes are illustrated in Figure 14. Figure 14 indicates a high level of agreement between the results obtained by the two algorithms, this suggests that narrowing the intervals to enhance the precision of the algorithm proposed is effective.

Figure 15 illustrates the errors between the two algorithms. It is evident that with six or more terms in the Taylor series expansion, the error remains stable and within an acceptable range. Table 2 presents the sound pressure amplitudes and corresponding relative errors at different frequency points.

By comparing the three cases, it is evident that the frequency sweep range is significantly reduced in more complex models. This indicates that the complexity of the model affects the accuracy of the proposed algorithm. However, precise calculations can still be achieved by narrowing the frequency sweep range.

TABLE 2 Sound pressure values and relative errors for different taylor expansion terms.

Frequency	DBEM	Taylor_03		Taylor_06		Taylor_08		Taylor_10	
		$\lvert Sp\rvert$	ε_r	$\lvert Sp\rvert$	ε_r	$\lvert Sp\rvert$	ε_r	$\lvert Sp\rvert$	ε_r
200	1.73971	1.65520	5×10^{-2}	1.73826	8×10^{-4}	1.73975	3×10^{-5}	1.73971	7×10^{-7}
205	3.77269	3.55690	6×10^{-2}	3.77243	7×10^{-5}	3.77270	5×10^{-7}	3.77269	7×10^{-8}
210	0.65607	0.65559	7×10^{-4}	0.65607	6×10^{-8}	0.65607	6×10^{-8}	0.65607	6×10^{-8}
215	1.69961	1.69936	1×10^{-4}	1.69961	5×10^{-9}	1.69961	5×10^{-9}	1.69961	5×10^{-9}
220	1.08095	1.06445	2×10^{-2}	1.08098	3×10^{-5}	1.08095	7×10^{-7}	1.08095	2×10^{-7}
225	2.33577	2.19804	6×10^{-2}	2.33345	1×10^{-3}	2.33582	2×10^{-5}	2.33577	4×10^{-7}
230	1.01752	1.05120	3×10^{-2}	1.01745	7×10^{-5}	1.01753	1×10^{-6}	1.01753	1×10^{-7}
235	0.89543	0.89551	9×10^{-5}	0.89543	5×10^{-8}	0.89543	6×10^{-8}	0.89543	6×10^{-8}
240	0.59929	0.60016	1×10^{-3}	0.59929	2×10^{-7}	0.59929	1×10^{-7}	0.59929	1×10^{-7}
245	1.25059	1.23222	1×10^{-2}	1.25055	4×10^{-5}	1.25059	5×10^{-8}	1.25059	5×10^{-8}
250	1.54559	1.15591	2×10^{-1}	1.54341	1×10^{-3}	1.54564	3×10^{-5}	1.54559	7×10^{-7}
255	0.85390	0.81109	5×10^{-2}	0.85373	2×10^{-4}	0.85390	1×10^{-6}	0.85390	2×10^{-9}
260	0.86751	0.86747	4×10^{-5}	0.86751	2×10^{-8}	0.86751	2×10^{-8}	0.86751	2×10^{-8}
265	0.44207	0.44203	1×10^{-4}	0.44207	1×10^{-7}	0.44207	8×10^{-8}	0.44207	8×10^{-8}
270	1.23592	1.32387	7×10^{-2}	1.23587	4×10^{-5}	1.23592	1×10^{-7}	1.23592	8×10^{-7}
275	4.30881	4.16733	3×10^{-2}	4.32828	5×10^{-3}	4.30844	9×10^{-5}	4.30882	1×10^{-6}
280	2.11202	2.16971	3×10^{-2}	2.11221	9×10^{-5}	2.11202	8×10^{-7}	2.11202	2×10^{-7}
285	1.22514	1.22547	3×10^{-4}	1.22514	2×10^{-7}	1.22514	2×10^{-7}	1.22514	2×10^{-7}
290	0.80695	0.80552	2×10^{-3}	0.80695	9×10^{-8}	0.80695	3×10^{-8}	0.80695	3×10^{-8}
295	0.97933	0.94893	3×10^{-2}	0.97935	2×10^{-5}	0.97933	1×10^{-7}	0.97933	2×10^{-9}
300	1.14332	1.48699	3×10^{-1}	1.14355	2×10^{-4}	1.14333	1×10^{-5}	1.14332	3×10^{-7}

7 Conclusion

This paper employs the BEM to compute sound pressure for frequency scanning analysis. It introduces an efficient computational approach, which includes:

1. The Taylor expansion method decomposes the integral of boundary elements into frequency-related and frequency-unrelated terms, thus eliminating the frequency dependence in the coefficient matrix.
2. By reducing the order of the original system model through the application of the SOAR method, the computational performance for solving large-scale problems was improved.

The algorithm proposed in this paper has potential applications in various engineering fields. For example, in the design of sound barriers, it can be used to quickly assess the acoustic performance of different design options, thereby optimizing the design process. In noise control engineering, this method can be employed to simulate and analyze noise propagation in complex environments, enhancing the effectiveness of noise control measures. We believe that these applications highlight the practical significance of our research and its potential to contribute to real-world engineering challenges. Future work will involve applying the proposed algorithm to problems involving broadband sensitivity scanning and topology optimization.

Data availability statement

The original contributions presented in the study are included in the article/supplementary material, further inquiries can be directed to the corresponding authors.

Author contributions

SZ: Conceptualization, Software, Writing–original draft. XJ: Methodology, Software, Writing–review and editing. JD: Conceptualization, Data curation, Writing–review and editing. JL: Data curation, Methodology, Software, Writing–review and editing.

Funding

The author(s) declare that no financial support was received for the research, authorship, and/or publication of this article.

Conflict of interest

The authors declare that the research was conducted in the absence of any commercial or financial relationships that could be construed as a potential conflict of interest.

Publisher's note

References

1. Marburg S. Six boundary elements per wavelength: is that enough? *J Comput Acoust* (2002) 10:25–51. doi:10.1142/s0218396x02001401

2. Marburg S, Schneider S. Influence of element types on numeric error for acoustic boundary elements. *J Comput Acoust* (2003) 11:363–86. doi:10.1142/s0218396x03001985

3. Qu Y, Zhou Z, Chen L, Lian H, Li X, Hu Z, et al. Uncertainty quantification of vibro-acoustic coupling problems for robotic manta ray models based on deep learning. *Ocean Eng* (2024) 299:117388. doi:10.1016/j.oceaneng.2024.117388

4. Chen L, Lian H, Liu Z, Gong Y, Zheng C, Bordas S. Bi-material topology optimization for fully coupled structural-acoustic systems with isogeometric fem–bem. *Eng Anal Boundary Elem* (2022) 135:182–95. doi:10.1016/j.enganabound.2021.11.005

5. Chen L, Lian H, Liu Z, Chen H, Atroshchenko E, Bordas SPA. Structural shape optimization of three dimensional acoustic problems with isogeometric boundary element methods. *Comput Methods Appl Mech Eng* (2019) 355:926–51. doi:10.1016/j.cma.2019.06.012

6. Sommerfeld A. *Partial differential equations in physics*. Academic Press (1949).

7. Chen L, Huo R, Lian H, Yu B, Zhang M, Natarajan S, et al. Uncertainty quantification of 3d acoustic shape sensitivities with generalized nth-order perturbation boundary element methods. *Comput Methods Appl Mech Eng* (2025) 433:117464. doi:10.1016/j.cma.2024.117464

8. Preuss S, Gurbuz C, Jelich C, Baydoun SK, Marburg S. Recent advances in acoustic boundary element methods. *J Theor Comput Acoust* (2022) 30:2240002. doi:10.1142/s2591728522400023

9. Chen L, Lian H, Pei Q, Meng Z, Jiang S, Dong H-W, et al. Fem-bem analysis of acoustic interaction with submerged thin-shell structures under seabed reflection conditions. *Ocean Eng* (2024) 309:118554. doi:10.1016/j.oceaneng.2024.118554

10. Sobolev A. Wide-band sound-absorbing structures for aircraft engine ducts. *Acoust Phys* (2000) 46:466–73. doi:10.1134/1.29911

11. Wang Z, Zhao Z, Liu Z, Huang Q. A method for multi-frequency calculation of boundary integral equation in acoustics based on series expansion. *Appl Acoust* (2009) 70:459–68. doi:10.1016/j.apacoust.2008.05.005

12. Chen L, Zhao J, Lian H, Yu B, Atroshchenko E, Li P. A bem broadband topology optimization strategy based on taylor expansion and soar method—application to 2d acoustic scattering problems. *Int J Numer Methods Eng* (2023) 124:5151–82. doi:10.1002/nme.7345

13. Wu T, Li W, Seybert A. An efficient boundary element algorithm for multi-frequency acoustical analysis. *The J Acoust Soc America* (1993) 94:447–52. doi:10.1121/1.407056

14. Kirkup SM, Henwood DJ. Methods for speeding up the boundary element solution of acoustic radiation problems. *J Vibration Acoust* (1992) 114:374–80. doi:10.1115/1.2930272

15. Marburg S, Schneider S. Performance of iterative solvers for acoustic problems. part i. solvers and effect of diagonal preconditioning. *Eng Anal Boundary Elem* (2003) 27:727–50. doi:10.1016/s0955-7997(03)00025-0

16. Gao Z, Li Z, Liu Y. A time-domain boundary element method using a kernel-function library for 3d acoustic problems. *Eng Anal Boundary Elem* (2024) 161:103–12. doi:10.1016/j.enganabound.2024.01.001

17. Vanhille C, Lavie A. An efficient tool for multi-frequency analysis in acoustic scattering or radiation by boundary element method. *Acta Acustica United Acustica* (1998) 84:884–93.

18. Li S. An efficient technique for multi-frequency acoustic analysis by boundary element method. *J Sound Vibration* (2005) 283:971–80. doi:10.1016/j.jsv.2004.05.027

19. Zhang Q, Mao Y, Qi D, Gu Y. An improved series expansion method to accelerate the multi-frequency acoustic radiation prediction. *J Comput Acoust* (2015) 23:1450015. doi:10.1142/s0218396x14500155

20. Poungthong P, Giacomin A, Kolitawong C. Series expansion for normal stress differences in large-amplitude oscillatory shear flow from oldroyd 8-constant framework. *Phys Fluids* (2020) 32:023107. doi:10.1063/1.5143566

21. Chen L, Lian H, Xu Y, Li S, Liu Z, Atroshchenko E, et al. Generalized isogeometric boundary element method for uncertainty analysis of time-harmonic wave propagation in infinite domains. *Appl Math Model* (2023) 114:360–78. doi:10.1016/j.apm.2022.09.030

22. Cao G, Yu B, Chen L, Yao W. Isogeometric dual reciprocity bem for solving non-fourier transient heat transfer problems in fgms with uncertainty analysis. *Int J Heat Mass Transfer* (2023) 203:123783. doi:10.1016/j.ijheatmasstransfer.2022.123783

23. Liu Z, Bian P-L, Qu Y, Huang W, Chen L, Chen J A galerkin approach for analysing coupling effects in the piezoelectric semiconducting beams. *Eur J Mechanics-A/Solids* (2024) 103:105145. doi:10.1016/j.euromechsol.2023.105145

24. Li R, Liu Y, Ye W. A fast direct boundary element method for 3d acoustic problems based on hierarchical matrices. *Eng Anal Boundary Elem* (2023) 147:171–80. doi:10.1016/j.enganabound.2022.11.035

25. Chen L, Liu L, Zhao W, Liu C. An isogeometric approach of two dimensional acoustic design sensitivity analysis and topology optimization analysis for absorbing material distribution. *Comput Methods Appl Mech Eng* (2018) 336:507–32. doi:10.1016/j.cma.2018.03.025

26. Li Q, Sigmund O, Jensen JS, Aage N. Reduced-order methods for dynamic problems in topology optimization: a comparative study. *Comput Methods Appl Mech Eng* (2021) 387:114149. doi:10.1016/j.cma.2021.114149

27. Chen L, Lu C, Lian H, Liu Z, Zhao W, Li S, et al. Acoustic topology optimization of sound absorbing materials directly from subdivision surfaces with isogeometric boundary element methods. *Comput Methods Appl Mech Eng* (2020) 362:112806. doi:10.1016/j.cma.2019.112806

28. Chen L, Wang Z, Lian H, Ma Y, Meng Z, Li P, et al. Reduced order isogeometric boundary element methods for cad-integrated shape optimization in electromagnetic scattering. *Comput Methods Appl Mech Eng* (2024) 419:116654. doi:10.1016/j.cma.2023.116654

29. Chen L, Lian H, Dong H-W, Yu P, Jiang S, Bordas SPA. Broadband topology optimization of three-dimensional structural-acoustic interaction with reduced order isogeometric fem/bem. *J Comput Phys* (2024) 509:113051. doi:10.1016/j.jcp.2024.113051

30. Bai Z. Krylov subspace techniques for reduced-order modeling of large-scale dynamical systems. *Appl Numer Math* (2002) 43:9–44. doi:10.1016/s0168-9274(02)00116-2

31. Shen X, Du C, Jiang S, Zhang P, Chen L. Multivariate uncertainty analysis of fracture problems through model order reduction accelerated sbfem. *Appl Math Model* (2024) 125:218–40. doi:10.1016/j.apm.2023.08.040

32. Chatterjee A. An introduction to the proper orthogonal decomposition. *Curr Sci* (2000) 808–17.

33. Pearson K. One lines and planes of closest fit to systems of points in space. *Philosophical Mag* (1901) 2:559–72. doi:10.1080/14786440109462720

34. Chen L, Cheng R, Li S, Lian H, Zheng C, Bordas SPA. A sample-efficient deep learning method for multivariate uncertainty qualification of acoustic–vibration interaction problems. *Comput Methods Appl Mech Eng* (2022) 393:114784. doi:10.1016/j.cma.2022.114784

35. Chinesta F, Ladevèze P. Separated representations and pgd-based model reduction. *Int Centre Mech Siences, Courses Lectures* (2014) 554:24.

36. Bai Z-j., Su Y-f. *Second-order krylov subspace and arnoldi procedure*, 8. Springer: Journal of Shanghai University (English Edition (2004) p. 378–90. doi:10.1007/s11741-004-0048-9

37. Bai Z, Su Y. Soar: a second-order arnoldi method for the solution of the quadratic eigenvalue problem. *SIAM J Matrix Anal Appl* (2005) 26:640–59. doi:10.1137/s0895479803438523

38. Yang C. Solving large-scale eigenvalue problems in scidac applications. *J Phys Conf Ser* (2005) 16:425–34. doi:10.1088/1742-6596/16/1/058

39. Zhang Y, Gong Y, Gao X. Calculation of 2d nearly singular integrals over high-order geometry elements using the sinh transformation. *Eng Anal Boundary Elem* (2015) 60:144–53. doi:10.1016/j.enganabound.2014.12.006

40. Marburg S. The burton and miller method: unlocking another mystery of its coupling parameter. *J Comput Acoust* (2016) 24:1550016. doi:10.1142/s0218396x15500162

41. Gong Y, Trevelyan J, Hattori G, Dong C. Hybrid nearly singular integration for isogeometric boundary element analysis of coatings and other thin 2d structures. *Comput Methods Appl Mech Eng* (2019) 346:642–73. doi:10.1016/j.cma.2018.12.019

42. Liu H, Wang F, Qiu L, Chi C. Acoustic simulation using singular boundary method based on loop subdivision surfaces: a seamless integration of cad and cae. *Eng Anal Boundary Elem* (2024) 158:97–106. doi:10.1016/j.enganabound.2023.10.022

43. Schenck HA. Improved integral formulation for acoustic radiation problems. *The J Acoust Soc America* (1968) 44:41–58. doi:10.1121/1.1911085

44. Chen J-T, Chen I, Chen K. Treatment of rank deficiency in acoustics using svd. *J Comput Acoust* (2006) 14:157–83. doi:10.1142/s0218396x06002998

45. Chen L, Lian H, Natarajan S, Zhao W, Chen X, Bordas S. Multi-frequency acoustic topology optimization of sound-absorption materials with isogeometric boundary element methods accelerated by frequency-decoupling and model order reduction techniques. *Comput Methods Appl Mech Eng* (2022) 395:114997. doi:10.1016/j.cma.2022.114997

46. Burton A, Miller G. The application of integral equation methods to the numerical solution of some exterior boundary-value problems. *Proc R Soc Lond A. Math Phys Sci* (1971) 323:201–10. doi:10.1098/rspa.1971.0097

47. Zhou H, Liu Y, Wang J. Optimizing orthogonal-octahedron finite-difference scheme for 3d acoustic wave modeling by combination of taylor-series expansion and remez exchange method. *Exploration Geophys* (2021) 52:335–55. doi:10.1080/08123985.2020.1826890

48. Bai Z, Su Y. Dimension reduction of large-scale second-order dynamical systems via a second-order arnoldi method. *SIAM J Scientific Comput* (2005) 26:1692–709. doi:10.1137/040605552

49. Junger MC, Feit D *Sound, structures, and their interaction*, 225. Cambridge, MA: MIT press (1986).

frontiers | Frontiers in Physics

TYPE Original Research
PUBLISHED 11 December 2024
DOI 10.3389/fphy.2024.1494394

EDITED BY
Yilin Qu,
Northwestern Polytechnical University, China

REVIEWED BY
Lei Wang,
Beihang University, China
Liang Shihua,
Guangdong University of Technology, China
Wei Huang,
Chongqing University of Science and Technology, China

*CORRESPONDENCE
Xibin Li,
✉ ytulxb@zafu.edu.cn

RECEIVED 10 September 2024
ACCEPTED 22 November 2024
PUBLISHED 11 December 2024

CITATION
Zhao H and Li X (2024) Torsional vibration of a static drill-rooted nodular pile embedded in elastic media.
Front. Phys. 12:1494394.
doi: 10.3389/fphy.2024.1494394

Torsional vibration of a static drill-rooted nodular pile embedded in elastic media

Hui Zhao[1] and Xibin Li[2]*

[1]Hangzhou Transportation Investment and Construction Management Group Co., Ltd., Hangzhou, China, [2]College of Landscape Architecture, Zhejiang A & F University, Hangzhou, China

This study examines the vibration characteristics of static drill-rooted nodular (SDRN) piles in elastic soils under time-harmonic torsional loads via an analytical approach. SDRN piles, which are characterized by uniformly distributed nodes and enhanced surrounding cemented soil, are able to increase the vertical bearing capacity of piles in soft soils. Piles are modelled using elastic rod theory, while surrounding soils are separated into two sublayers along radial direction: a core zone made up of cemented soil and an outer semi-infinite natural soil layer. An analytical method is proposed to solve the problem after formulating the wave equations for pile and radial soil layer. This methodology rigorously considers the continuity of twist angle and shear stress across the interface of the pile and radial soil layers. The simulation of nodes in the SDRN pile involves discretizing the pile-soil system and applying the principle of impedance function recursion to accurately compute the torsional stiffness at the top of the pile. Developed results are validated against the existing benchmarks for a cylindrical pile in elastic soil. Detailed numerical examples are carried out to assess the effect of major factors on the torsional impedance of the pile. For improved comprehension in engineering applications, the impedance function is applied to derive the twist angle of the rigid foundation, with the amplitude-frequency response expressed in a closed form. Results indicate that the vibration behavior of the piles is significantly influenced by the inner radius, outer radius, the dimension of the node, the radial width of the cemented soil and the damping ratio of the radial soil layer. The developed solution offers valuable insights for the optimization design of SDRN piles under dynamic torsional loads.

KEYWORDS

static drill-rooted nodular pile, torsional vibration, rigid foundation, cemented soil, wave propagation

1 Introduction

Pile foundations are crucial for supporting large-scale structures like high-rise buildings [1], offshore bridges [2], and ocean platforms [3]. Therefore, understanding their response to complex dynamic loads is essential. While pile foundations are generally subjected to static and dynamic vertical and horizontal loads, wind and machine-induced vibrations can cause torsional loads that significantly affect their dynamic performance [4–6]. Accordingly, assessing the impact of dynamic torsional loads is vital to ensure the stability and safety of pile foundations. To address this, researchers have proposed various methods to investigate torsional vibration characteristics of piles.

Cai et al. [7] performed a comprehensive study on the torsional vibration of elastic piles in a uniform poroelastic medium. Based on this fundamental research, Chen et al. [8] introduced the concept of transverse isotropy to examine the vibration characteristics of piles embedded in saturated soils under transient loading. Their study emphasized the impact of soil transverse isotropy and the pile slenderness ratio on the vibration characteristics of the piles. Subsequent research further illustrated the effects of soil properties on end-bearing piles [9, 10] and pipe piles [11, 12]. Given the inherently layered and vertically non-uniform nature of soil profiles, Zou et al. [13] explored the mechanical behavior of single piles in a two-layer vertically non-uniform subgrade and subjected to axial-torsional combined loads. Liu and Zhang [14] expanded upon these findings by investigating the transient torsional vibration behavior of heterogeneous piles in multi-layered poroelastic media, with a focus on the influence of typical pile defects. To advance this field of study, Li et al. [15], Zhang and Pan [16] assessed the influences of construction disturbances on the surrounding soil, analyzing the impact of radial inhomogeneity induced by such disturbances on the vibration behavior of piles in layered media. Further research has addressed open-ended pipe piles [17–19], examining the effects of construction-induced inhomogeneity in radial direction on the torsional impedance of piles. Additionally, studies have investigated the impact of pile end soil [20] and variation in cross-sectional dimensions [21] on the torsional response of piles. Typically, these investigations model soil as a composite material composed of pore water and soil particles. However, this assumption does not always hold true in practical applications, particularly in surface or shallow soils where unsaturated conditions are prevalent. Unsaturated soils, characterized by incomplete pore saturation, exhibit markedly different mechanical behaviors compared to their saturated counterparts. Research concerning unsaturated soils primarily focused on the effects of transverse isotropy [22, 23], radial inhomogeneity [24, 25], vertical inhomogeneity of soil [25, 26], and pile end soil [27]. Despite the significant influence of torsional loads on pile performance, this factor has not been received adequate consideration in studies of nodular piles.

In soft soil regions, traditional piles, such as cast-in-situ and precast piles often face challenges such as low skin friction and construction-related defects in the pile body. To address these problems, static drill-rooted nodular (SDRN) piles, an innovative foundation type initially developed in Japan, have been increasingly used in engineering practice [28, 29]. As for SDRN pile, the prefabricated nodular pile is embedded into cemented soil via static drilling, effectively overcoming the limitations of conventional pile installation techniques and providing a more efficient, cost-effective scheme. Due to the construction similarities, SDRN piles are often evaluated in comparison to cast-in-situ piles. Research by Zhou et al. [30–33] has demonstrated, through extensive field studies and finite element simulations, that SDRN piles exhibit significantly superior skin friction and compressive bearing capacity compared to cast-in-situ piles, making them particularly advantageous for use in soft soil conditions. Li et al. [34] estimated the vibration characteristics of SDRN piles in layered soil profiles and under vertical loads, affirming the substantial benefits of SDRN piles in mitigating vertical deformation and vibration relative to cast-in-situ piles. Additionally, Wu et al. [35] investigated the impact of various cross-sectional geometries on vertical vibration. Despite considerable research on the performance of SDRN piles under vertical loads [36–38], the effects of torsional loads on SDRN piles remain underexplored.

The literature review above reveals that studies on the dynamic performance of SDRN piles under torsional loading are limited. Therefore, this article aims to examine the torsional vibration characteristics of SDRN piles in elastic soils using an analytical method. It should be pointed out that the analytical solutions presented here provides engineers with a precise, convenient, and efficient tool for quickly assessing the performance of SDRN piles. Specifically, it allows for the evaluation of factors such as pile inner and outer radii, node width, vertical node spacing, and variations in properties of the surrounding cemented soil on the overall performance of SDRN piles. The layout is as follows: Section 2 establishes the mathematical model. Section 3 derives the analytical solutions for the dynamic response problem. Numerical examples and the corresponding analysis and discussion are presented in Section 4. Section 5 applies the present solution into the vibration characteristic of pile-supported foundation. The main conclusions are summarized in Section 6.

2 Mathematical model

As depicted in Figure 1A, a SDRN pile in elastic soil, undergoing a time-harmonic torque is considered. This study considers the hardening surrounding cemented soil, a radially semi-infinite natural soil deposit and the nodular pile itself, but neglects the effect of the soil within the SDRN pile. Given the large slenderness ratio of the pile, it is approximated as an elastic rod with a fixed inner radius r_{in} and a series of equally spaced, enlarged nodes (see Figure 1B). The external (outer) radius of pile is r_0 at non-noded sections, while the maximum external radius at nodes is r_{oumax}. The vertical spacing between two adjacent nodes is l_b, and the radial protrusion thickness and length at each node are w_b. Based on the node distribution, the pile-soil interaction model is divided into N segments (elements), numbered sequentially from the bottom upward. Each segment has equal thickness in both the pile section and the surrounding soil section. The thickness and the radius of segment i are denoted by h_i and r_i, respectively. For node sections, sufficient segmentation is required to simulate the continuous variation in the pile's outer radius. The soil around the pile is split into two distinct zones: (1) the inner zone, composed of cemented soil, extends to a distance r_c from the pile's centroid, and (2) the outer zone, consisting of radially semi-infinite natural soil, lies beyond the cemented soil layer.

Previous studies [16, 39] have shown that neglecting the gradient of shear stress $\sigma_{\theta z}$ along the z-axis (i.e., assuming a plane strain model) has a minimal effect on the dynamic impedance of the pile. Therefore, following the plane strain assumption, the wave equation for any soil layer under torsional load is given by [39].

$$u_{\theta,rr}(r,t) + r^{-1}u_{\theta,r}(r,t) - r^{-2}u_{\theta}(r,t) = \frac{\rho_s}{G_s}u_{\theta,tt}(r,t) \tag{1}$$

where the subscript, "j" denotes the partial derivative to the variable j $(j = r, t)$; $u_\theta(r,t)$, G_s and ρ_s represents the tangential displacement, shear modulus and density of the soil, respectively.

The dynamic equilibrium equation for an elastic pile under torsional load is given by

$$G_p I_p \phi_{,zz}(z,t) + 2\pi r^2 \tau(z,t) = \rho_p I_p \phi_{,tt}(z,t) \tag{2}$$

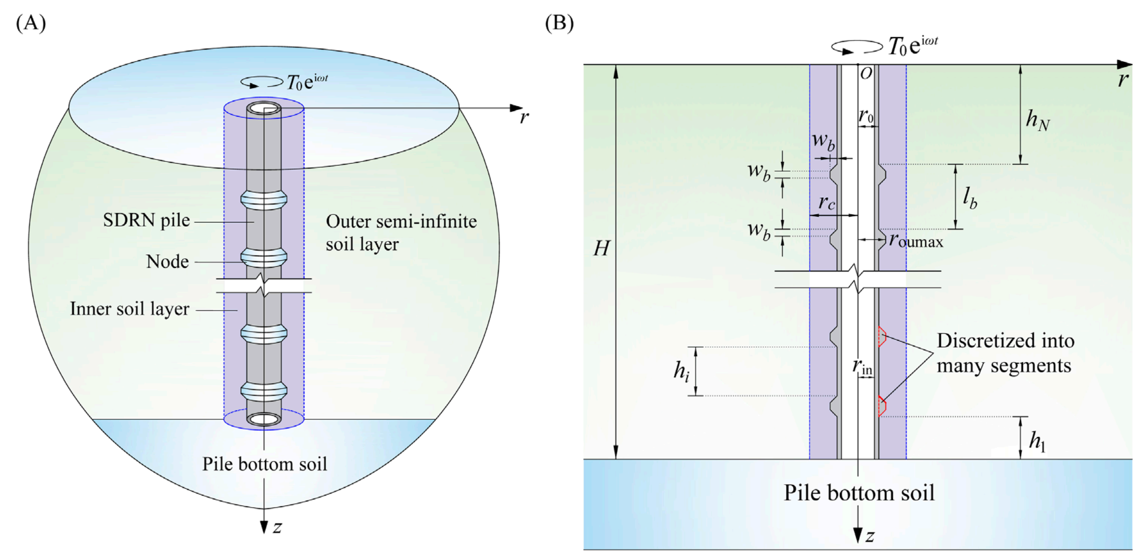

FIGURE 1
Diagram of a SDRN pile in elastic soil undergoing a time-harmonic torsional load: **(A)** 3D model; **(B)** section plan.

where $\phi(z, t)$, G_p, ρ_p and I_p represent the twist angle, shear modulus, density and polar moment of inertia of the pile, respectively; $\tau(z, t)$ denotes the tangential shear stress applied by the soil around the pile.

The boundary condition for the outer natural soil deposit can be specified as

$$u_{\theta ij}(r \to \infty, t) = 0, (j = 2) \tag{3}$$

where the subscript ij represents the component in the j-th (where j = 1, 2) radial region corresponding to the i-th (where i = 1-N) pile segment; Specifically, $j = 1$ and $j = 2$ refer to the inner and outer radial zones, respectively; In the subsequent sections, the subscript ij will maintain this definition, unless specified otherwise.

The boundary conditions at top and bottom of the i-th (i = 1-N) pile element are

$$\phi_{i,z}(z = 0, t) = -\frac{T_i(t)}{G_{pi}I_{pi}} \tag{4}$$

$$\phi_{i,z}(z = h_i, t) + \frac{\phi_i(z = h_i, t)\Theta_i}{G_{pi}I_{pi}} = 0 \tag{5}$$

where $I_{pi} = 0.5\pi(r_i^4 - r_{\text{in}}^4)$; $\phi_i\ (z,\ t)$ denotes the twist angle in the i-th pile element; Θ_i represents the complex impedance at the lower end of the i-th pile element; $T_i(t)$ represents the torque exerted on the top of the i-th pile element; For the N-th pile element (i.e., the top element), $T_N(t) = T_0(t)$ holds; When i = 1, the impedance from the pile bottom soil is $\Theta_1 = 16G_{su}\left(r_0^3 - r_{\text{in}}^3\right)/3$ as described by Li et al. [17].

The continuity conditions at $r = r_c$ can be given by

$$u_{\theta i2}(r = r_c, t) = u_{\theta i1}(r = r_c, t) \tag{6}$$

$$\tau_{r\theta i2}(r = r_c, t) = \tau_{r\theta i1}(r = r_c, t) \tag{7}$$

The continuity conditions at $r = r_i$ can be formulated as

$$u_{\theta ij}(r = r_i, t) = \phi_i(z, t)r_i \tag{8}$$

$$\tau_i(z, t) = \tau_{r\theta i}(r = r_i, t) = G_{si}[u_{\theta i1,r}(r_i, t) - r^{-1}u_{\theta i1}(r_i, t)] \tag{9}$$

3 Solutions

The time-harmonic solution of Equation 1 can be given by

$$u_\theta(r) = AK_1(qr) + BI_1(qr) \tag{10}$$

where $q = \mathrm{i}\omega(\rho_s/G_s)^{0.5}$; $\mathrm{i}=(-1)^{0.5}$; ω is the angular frequency.

Substituting the boundary condition from Equation 3 into Equation 10, it follows that $B = 0$. Consequently, the field quantities in the natural soil deposit corresponding to the i-th element can be given by

$$u_{\theta i2}(r) = A_{i2}K_1(q_{i2}r) \tag{11a}$$

$$\tau_{r\theta i2}(r) = -A_{i2}G_{si2}q_{i2}K_2(q_{i2}r) \tag{11b}$$

where $q_{i2} = \mathrm{i}\omega(\rho_{si2}/G_{si2})^{0.5}$.

The field quantities in the cemented soil layer can be formulated as

$$u_{\theta i1}(r) = A_{i1}K_1(q_{i1}r) + B_{i1}I_1(q_{i1}r) \tag{12a}$$

$$\tau_{r\theta i1}(r) = -A_{i1}G_{si1}q_{i1}K_2(q_{i1}r) + B_{i1}G_{si1}q_{i1}I_2(q_{i1}r) \tag{12b}$$

where $q_{i1} = \mathrm{i}\omega(\rho_{si1}/G_{si1})^{0.5}$.

Substituting Equations 11, 12 into continuity conditions given by Equations 6, 7 results in

$$B_{i1} = \kappa_{i1}A_{i1} \tag{13}$$

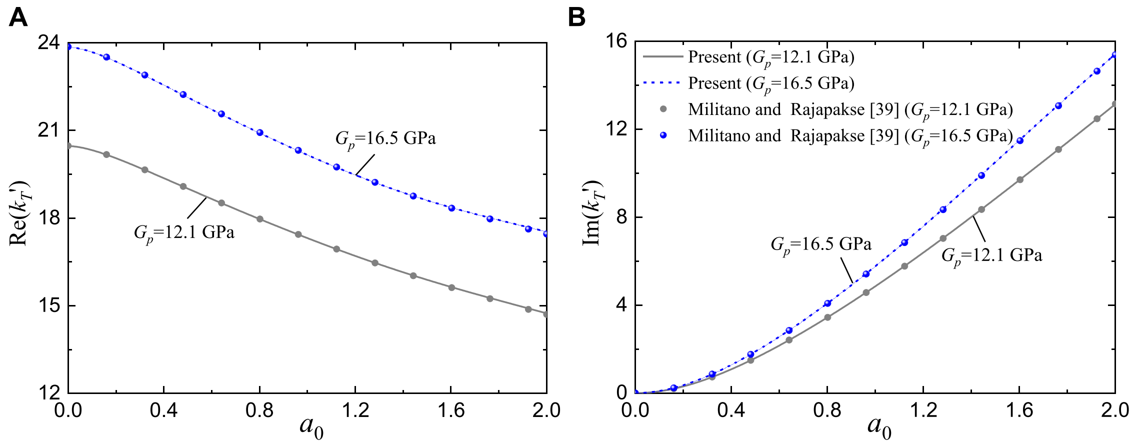

FIGURE 2
Comparison of torsional impedance results for an elastic cylindrical pile in homogeneous soil with those from existing solutions: **(A)** Real part; **(B)** Imaginary part.

TABLE 1 Properties in SDRN pile and composite soil layers.

G_p (MPa)	ρ_p (kg/m^3)	r_0 (m)	r_{in} (m)	r_{oumax} (m)	r_c (m)	w_b (m)	H (m)
16,500	2,500	0.3	0.19	0.4	0.19	0.1	10

ρ_{s1} (kg/m^3)	G_{s1} (MPa)	ρ_{s2} (kg/m^3)	G_{s2} (MPa)	β_{s1}	β_{s2}	ρ_{su} (kg/m^3)	G_{su} (MPa)
1,900	200	1,800	20	0.05	0.05	1,800	20

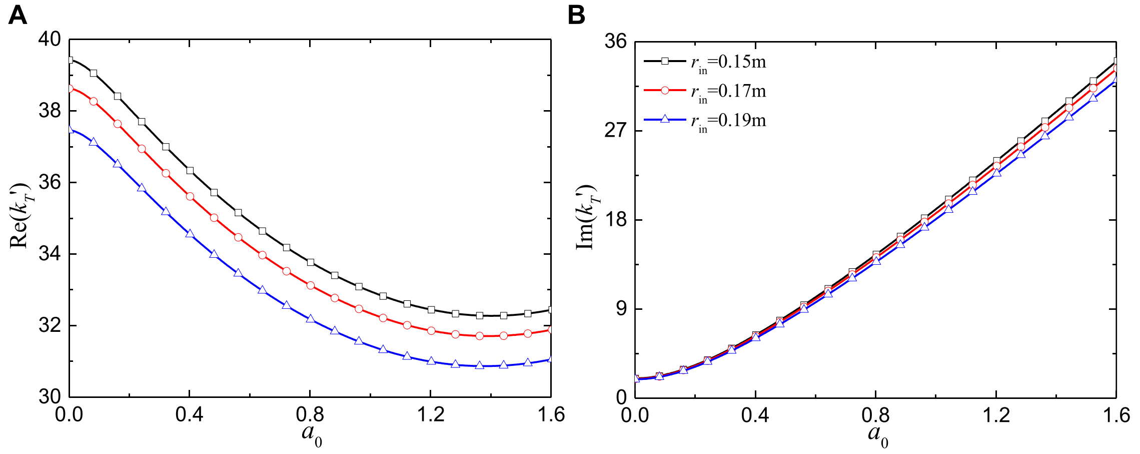

FIGURE 3
Torsional impedance for an elastic pile in elastic soil vs. excitation frequency for various inner radii: **(A)** Real part; **(B)** Imaginary part.

where

$$\kappa_{i1} = \frac{G_{si1} q_{i1} K_2(q_{i1} r_c) K_1(q_{i2} r_c) - G_{si2} q_{i2} K_2(q_{i2} r_c) K_1(q_{i1} r_c)}{G_{si1} q_{i1} I_2(q_{i1} r_c) K_1(q_{i2} r_c) + G_{si2} q_{i2} K_2(q_{i2} r_c) I_1(q_{i1} r_c)} \tag{14}$$

Making use of Equation 13, Equation 12 can be rewritten as

$$u_{\theta i1}(r) = A_{i1} K_1(q_{i1} r) + \kappa_{i1} A_{i1} I_1(q_{i1} r) \tag{15a}$$

$$\tau_{r\theta i1}(r) = -A_{i1} G_{si1} q_{i1} K_2(q_{i1} r) + \kappa_{i1} A_{i1} G_{si1} q_{i1} I_2(q_{i1} r) \tag{15b}$$

In the case of a time-harmonic load, Equation 2 can be reformulated as (for i-th element)

$$G_{pi} I_{pi} \frac{\mathrm{d}^2 \phi_i(z)}{\mathrm{d}z^2} + 2\pi r_i^2 \tau_i(z) = -\rho_{pi} I_{pi} \omega^2 \phi_i(z) \tag{16}$$

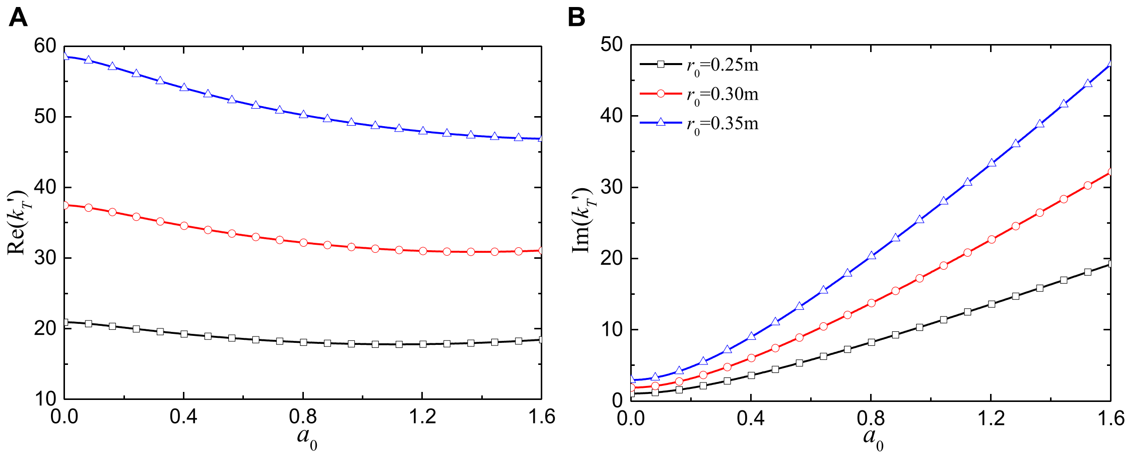

FIGURE 4
Torsional impedance for an elastic pile in elastic soil vs. excitation frequency for various outer radii: **(A)** Real part; **(B)** Imaginary part.

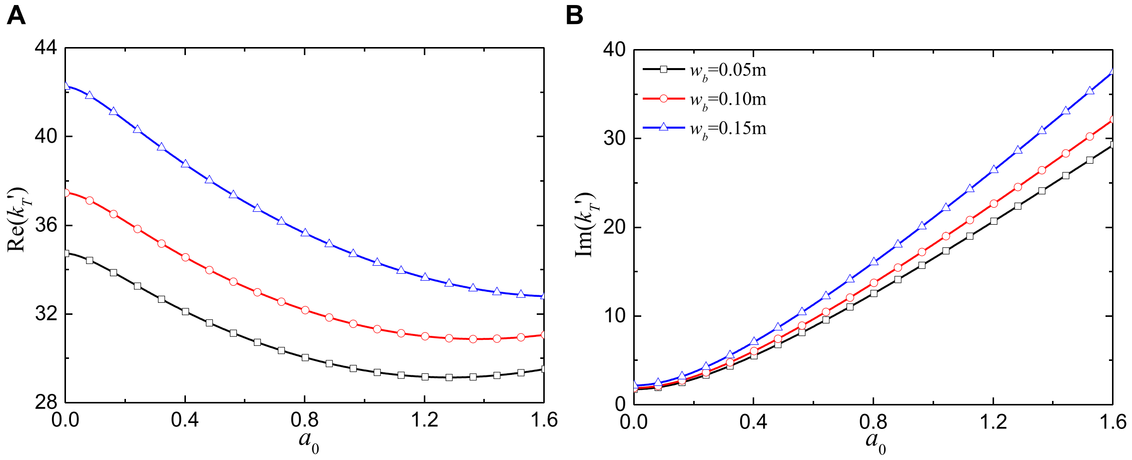

FIGURE 5
Torsional impedance for an elastic pile in elastic soil vs. excitation frequency for different node widths: **(A)** Real part; **(B)** Imaginary part.

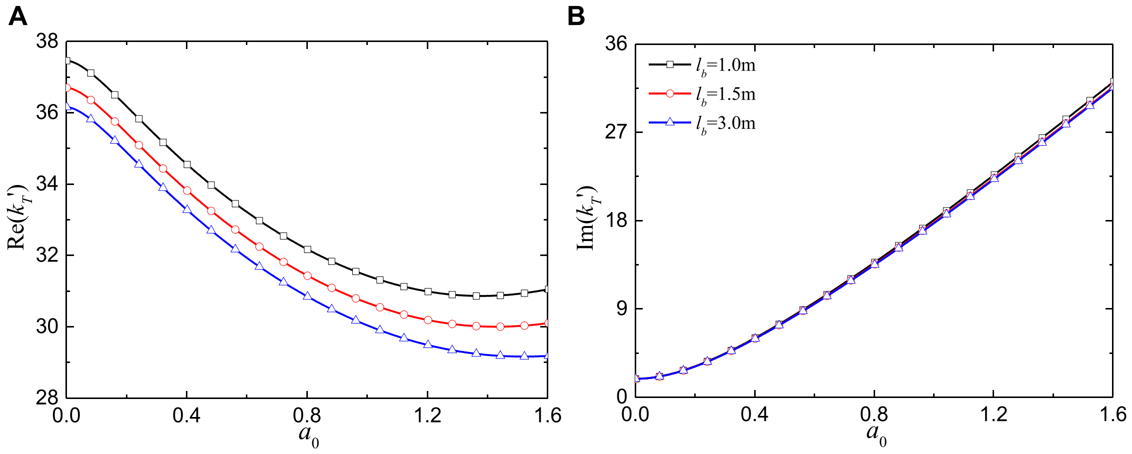

FIGURE 6
Torsional impedance for an elastic pile in elastic soil vs. excitation frequency for different vertical spacings of nodes: **(A)** Real part; **(B)** Imaginary part.

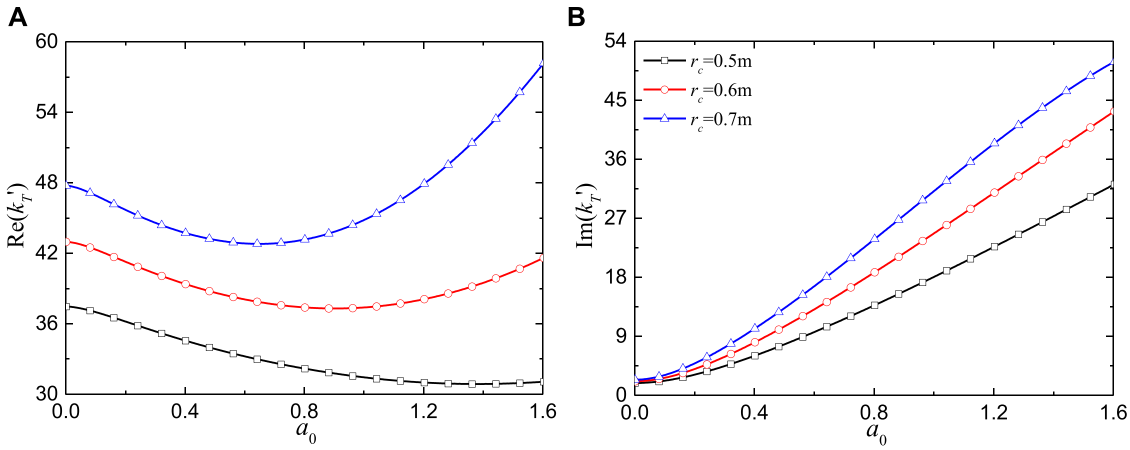

FIGURE 7
Torsional impedance for an elastic pile in elastic soil vs. excitation frequency for different radial widths of cemented soil: **(A)** Real part; **(B)** Imaginary part.

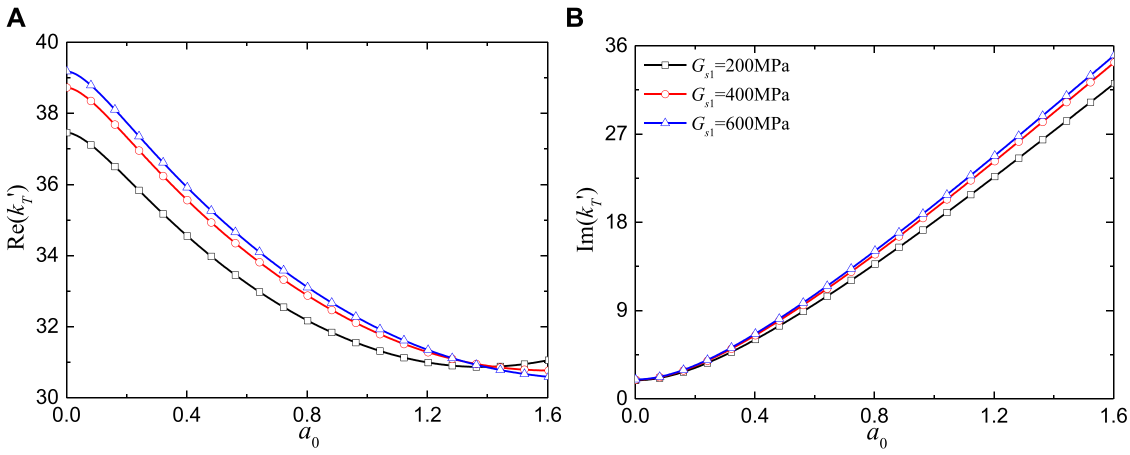

FIGURE 8
Torsional impedance for an elastic pile in elastic soil vs. excitation frequency for different shear modulus of cemented soil: **(A)** Real part; **(B)** Imaginary part.

Combining Equations 8, 9, 15, 16 yields

$$\frac{\mathrm{d}^2\phi_i(z)}{\mathrm{d}z^2} + \gamma_i^2\phi_i(z) = 0 \tag{17}$$

where

$$\gamma_i^2 = \left(\delta_{i1} + \rho_{pi}I_{pi}\omega^2\right)/\left(G_{pi}I_{pi}\right) \tag{18}$$

$$\delta_{i1} = \frac{2\pi r_i^3 G_{si1} q_{i1}\left[-K_2(q_{i1}r_i) + \kappa_{i1}I_2(q_{i1}r_i)\right]}{K_1(q_{i1}r_i) + \kappa_{i1}I_1(q_{i1}r_i)} \tag{19}$$

The solution of Equation 17 can be expressed as

$$\phi_i(z) = C_i\cos(\gamma_i z) + D_i\sin(\gamma_i z) \tag{20}$$

Combining Equation 5 and Equation 20 results in

$$D_i = \eta_i C_i \tag{21}$$

where

$$\eta_i = \frac{\overline{\gamma}_i\sin(\overline{\gamma}_i) - \overline{\Theta}_i\cos(\overline{\gamma}_i)}{\overline{\gamma}_i\cos(\overline{\gamma}_i) + \overline{\Theta}_i\sin(\overline{\gamma}_i)};\quad \overline{\Theta}_i = \frac{\Theta_i h_i}{G_{pi}I_{pi}};\quad \overline{\gamma}_i = \gamma_i h_i \tag{22}$$

Substituting Equation 20, 21 into Equation 4 yields

$$k_{Ti} = \frac{T_i}{\phi_i(z=0)} = -G_{pi}I_{pi}\gamma_i\eta_i \tag{23}$$

where k_{Ti} denotes the top-end torsional impedance of the i-th pile element.

The principle of impedance function recursion has been effectively used in past studies to address the vibration behavior of piles in layered soils [40]. According to this principle, the torque and twist angle at the interface between adjacent pile elements are continuous, meaning that the torsional impedance at the interface (i.e., torque/twist angle) is also continuous. That is to say, the impedance at the top of the i-th element is equal to

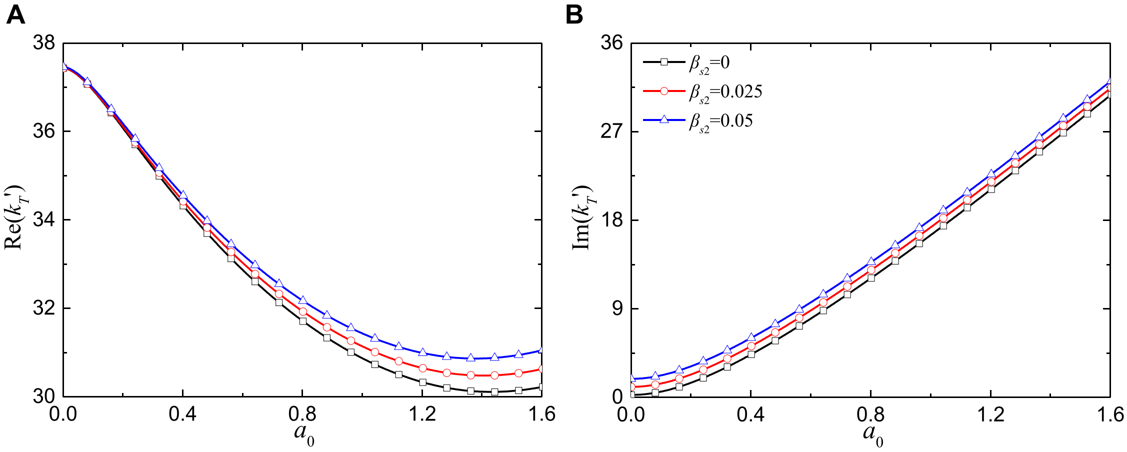

FIGURE 9
Torsional impedance for an elastic cylindrical pile in elastic soil vs. excitation frequency for different damping ratios of outer soil layer: **(A)** Real part; **(B)** Imaginary part.

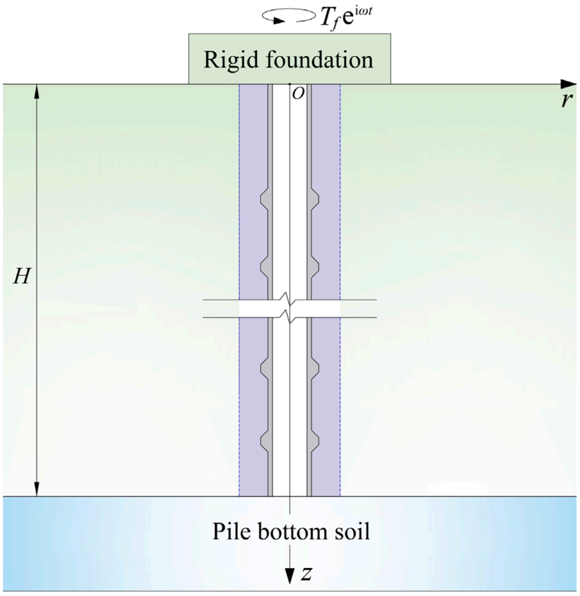

FIGURE 10
Dynamic interaction between a rigid foundation and supported SDRN pile.

the impedance at the bottom of (i+1)-th element (i.e., $k_{Ti} = \Theta_{i+1}$). Hence based on Equation 23, the torsional impedance function at the top end of the pile can be determined via a step-by-step recursion from the first element to the N-th element, which can be written as follows

$$k_{TN} = -G_{pN} I_{pN} \gamma_N \eta_N \tag{24}$$

Following Militano and Rajapakse [39], the normalized torsional impedance can be defined as

$$k_T' = -\frac{3 G_{pN} I_{pN} \gamma_N \eta_N}{16 G_0 r_{0r}^3} \tag{25}$$

where k_T' denotes the normalized torsional impedance at the pile top; G_0 and r_{0r} denote the reference shear modulus and radius, respectively.

4 Numerical results and discussion

First, to confirm the correctness of the developed model, a comparison is made with the analytical results from Militano and Rajapakse [39]. For this comparison, the SDRN pile is reduced a solid cylindrical rod and the surrounding soil is assumed to be a uniform elastic material. The used parameters are ρ_p = 2,500 kg/m^3, G_p = 12.1 or 16.5 GPa, r_0 = 0.3 m, r_{in} = 0 m, r_{oumax} = 0.3 m, r_c = 0.5 m, H = 10 m, w_b = 0 m, $\rho_{s1} = \rho_{s2}$ = 1800 kg/m^3, $G_{s1} = G_{s2} = G_{su} = G_{s0}$ = 20 MPa, $\beta_{s1} = \beta_{s2}$ = 0. For analysis purposes, the normalized frequence is defined as $a_0 = \omega r_{0r} (\rho_0/G_0)^{0.5}$, in which reference density ρ_0 = 1800 kg/m^3 and G_0 = 20 MPa. In Figure 2, Re ( ) and Im ( ) denote respectively the real and imaginary components of the torsional impedance. Figure 2 demonstrates that an increase in excitation frequency leads to a decrease in real stiffness (real part) and an increase in damping (imaginary part). Additionally, the torsional impedance in the current solution corresponds well with those in the existing solution.

After verifying the present solution, the effect of key parameters on the torsional impedance at the pile top is examined here. To account for soil damping, G_{sj} is replaced by G_{sj} (1+2iβ_{sj}), where β_{sj} denotes the damping ratio. Unless specified differently, the properties for SDRN pile and composite soil layers are outlined in Table 1. Additionally, each node is divided into 10 elements to simulate the continuous variation of cross-sectional dimension (see Figure 1B), where the length of the first pile segment h_1 fixed at 0.425 m.

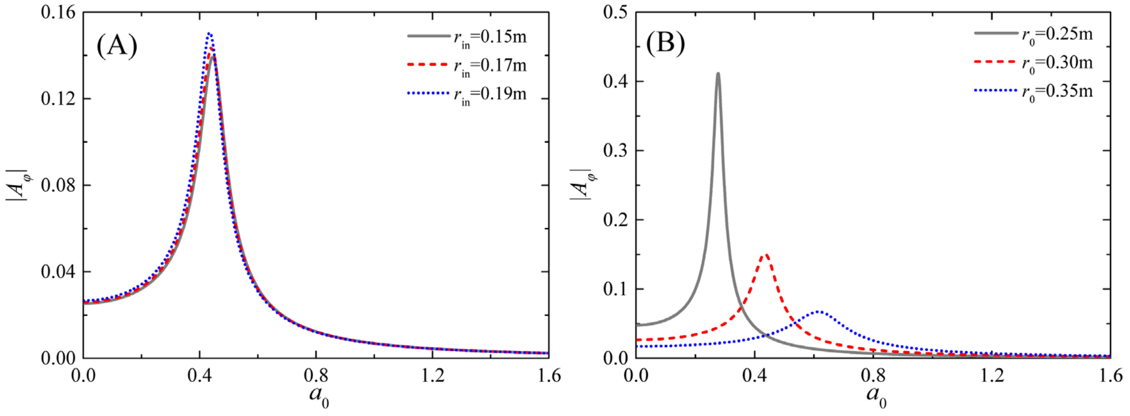

FIGURE 11
Variation of the normalized twist angle amplitude with excitation frequencies for different inner radii in **(A)** and outer radii in **(B)**.

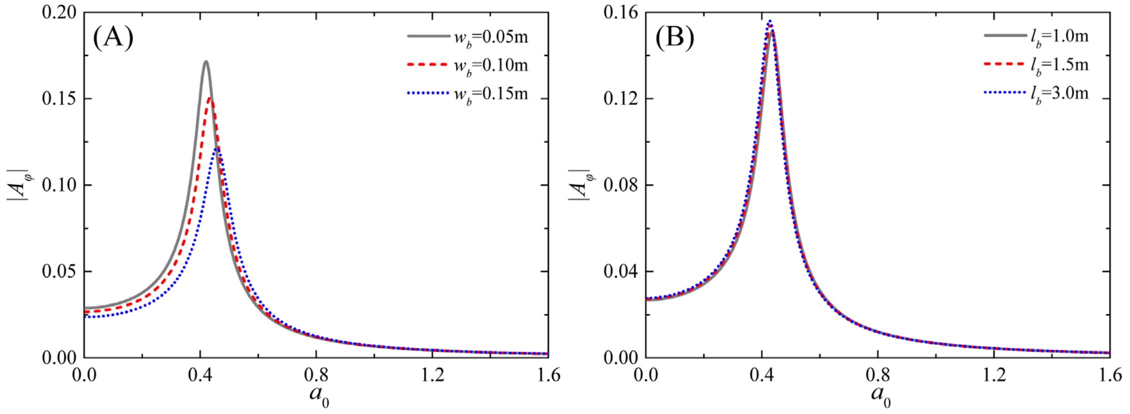

FIGURE 12
Variation of the normalized twist angle amplitude with excitation frequencies for different node widths in **(A)** and vertical spacings of nodes in **(B)**.

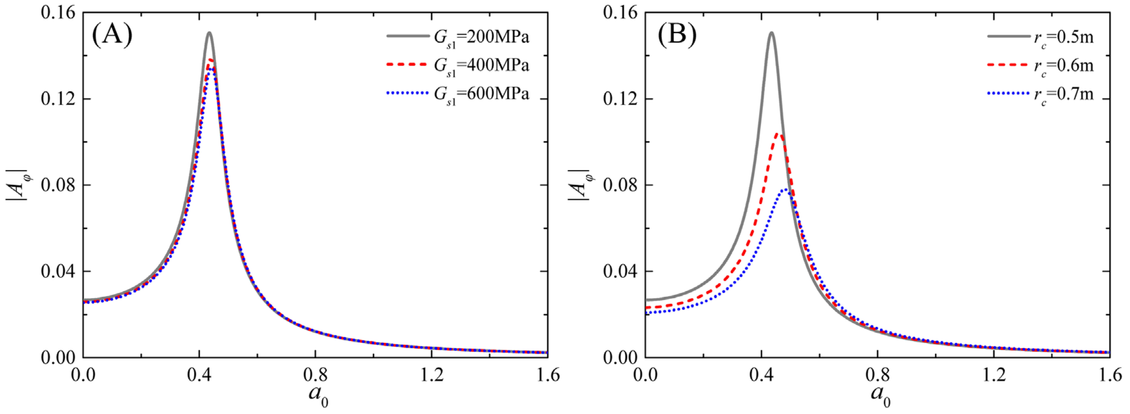

FIGURE 13
Variation of the normalized twist angle amplitude with excitation frequencies for different shear moduli in **(A)** and radial widths in **(B)** of cemented soil.

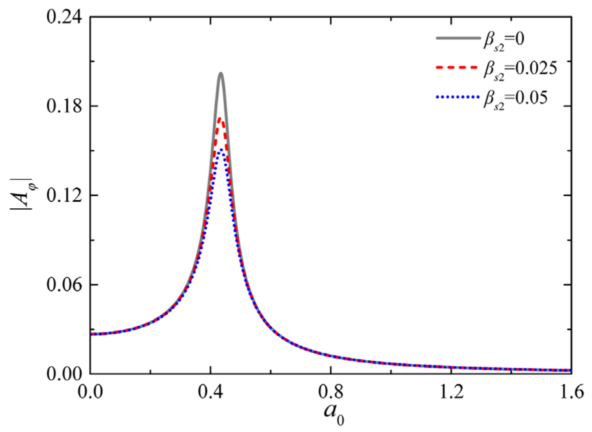

FIGURE 14
Variation of the normalized twist angle amplitude with excitation frequencies for different damping ratios of outer soil layer.

Figure 3 depicts the impact of inner radius (r_{in}) of the SDRN pile on the torsional impedance across different frequencies. The real stiffness initially decreases with an increase in frequency, then begins to increase at higher frequencies. In contrast, the imaginary part consistently increases as frequency rises. Moreover, both the real and imaginary parts decrease as r_{in} increases, indicating that the thinner wall ($t_w = r_0 - r_{\text{in}}$) reduces the stiffness and damping of the pile, thereby decreasing its torsional resistance. This behavior is mainly attributed to the fact that a larger r_{in} decreases the polar moment of inertia of the pile, thereby reducing its dynamic resistance.

Figure 4 demonstrates the impact of outer radius (r_0) of the SDRN pile on the torsional impedance at various frequencies. For consistency, the radial width of cemented soil ($r_c - r_0$) is fixed at 0.2 m. As shown in Figure 4, r_0 has a greater impact on the torsional impedance than the inner radius. Both the real and imaginary components increase significantly as r_0 increases.

The effects of the node width (w_b) and vertical spacing (l_b) on the torsional impedance at different frequencies are presented in Figures 5, 6. It should be noted that for a fixed pile length, a smaller l_b corresponds to a greater number of nodes along the pile body. Figure 5 shows that increasing w_b leads to a rise in both the real and imaginary parts, revealing that a larger node width enhances the torsional resistance of the pile. This improvement is due to the increases in the polar moment of inertia at the node location, which enhances the dynamic resistance. It is evident from Figure 6 that the real part decreases as l_b increases, while the imaginary part is insensitive to l_b.

Figures 7, 8 describe the effects of the radial width and shear modulus of cemented soil on the torsional impedance at different frequencies. The radial width is represented by the outer radius of the cemented soil, with a larger r_c corresponding to a broader enhanced range. According to Figure 7, increasing the radial width leads to an increase in both the real and imaginary parts. In comparison, the effect of the shear modulus G_{s1} is relatively smaller. As depicted in Figure 8, the components of torsional impedance increase as G_{s1} increases, although the rate of increase slows down as G_{s1} continues to rise. This suggests that enhancing the radial width of the cemented soil is more effective than increasing the shear modulus in improving the torsional impedance of the pile.

Figure 9 describes the effect of the damping ratio of the outer soil layer on the torsional impedance for different frequencies. The focus here is to present the impact of the damping ratio of the outer natural soil layer due to minor effect of damping ratio of the inner soil. As shown in Figure 9, at lower frequencies, the damping ratio has little effect on the real part. However, at higher frequencies, the torsional impedance increases with increasing damping ratio.

5 Application to pile-supported rigid foundation

When a pile-supported rigid foundation is subjected to dynamic torsional loads (see Figure 10), the dynamic equilibrium of the foundation is defined by the equation given below

$$I_f \frac{\mathrm{d}^2\varphi(t)}{\mathrm{d}t^2} + \frac{\mathrm{d}\varphi(t)}{\mathrm{d}t} + k_f \varphi(t) = T_f(t) \tag{26}$$

where I_f and $\varphi(t)$ represent the mass moment of inertia and angle of rotation of the foundation, respectively; k_f and c_f denote the stiffness and equivalent damping coefficient of the supported pile; $T_f(t)$ denotes the external time-dependent torsional load.

To obtain the solution for the foundation, Equation 24 can be reformulated as

$$k_{TN} = k_f + \mathrm{i}\omega c_f \tag{27}$$

Assuming a time-harmonic external load on the foundation and making use of Equation 27, the solution to Equation 26 can be given by

$$\varphi = T_f / \left(k_f - I_f \omega^2 + \mathrm{i}\omega c_f\right) \tag{28}$$

Making use of Equation 28, the normalized twist angle amplitude can be formulated as

$$\left|A_\varphi\right| = \left|\frac{16 G_0 r_0^3 \varphi}{3 T_f}\right| = \frac{16 G_0 r_0^3}{3\sqrt{\left(k_f - I_f\omega^2\right)^2 + \left(\omega c_f\right)^2}} \tag{29}$$

The following parts discuss the impact of key parameters on the twist angle amplitude, with the parameters listed in Table 1. To clearly observe the changing trends in resonant frequency and amplitude, we use the module of the twist angle amplitude instead of the real and imaginary part. In the analysis, I_f is fixed at 4,144 kg m^2. Figure 11 illustrates the effect of inner radius (r_{in}) and outer radius (r_0) of the SDRN pile on the twist angle amplitude at varying frequencies. The data in Figure 11A indicate that the twist angle amplitude initially ascends with frequency, reaches a peak, and then gradually approaches zero. The resonant peak shows obvious increase with an increase in r_{in}, while the resonant frequency slightly decreases as r_{in} increases. As shown in the Figure 11B, r_0 has a greater effect on the twist angle amplitude than the inner radius. The twist angle amplitude increases significantly as r_0 decreases. Furthermore, the resonant frequency increases markedly with an increase in r_0. This indicates that increasing the outer radius can substantially alter the natural frequency and reduce the twist angle of the whole system.

Figure 12 describes the effect of the node width (w_b) and vertical spacing (l_b) of the nodes on the twist angle amplitude for different frequencies. As observed in Figure 12A, the twist angle amplitude decreases significantly with an increase in w_b, revealing that a larger node width enhances the dynamic torsional resistance of the system. Besides, the resonant frequency rises with increasing w_b. Therefore, it can be concluded that increasing the node dimension is an effective strategy for improving the vibration behavior of the system in engineering practice. It can be observed in Figure 12B that contrary to expectations, the vertical spacing of the nodes has a relatively small impact on the twist angle amplitude. Additionally, the resonant peak shows a slight increase with increasing l_b.

Figure 13 describes the impact of the shear modulus and radial width of cemented soil on the twist angle amplitude at different frequencies. As observed in Figure 13A, the resonant peak decreases as G_{s1} increases, while the resonant frequency increases with higher G_{s1}. At high frequencies, the influence of G_{s1} becomes negligible. The impact of r_c is more pronounced than of the shear modulus of the cemented soil. The resonant peak significantly decreases as r_c increases, while the resonant frequency shows the opposite trend (see Figure 13B).

Figure 14 shows the effect of the damping ratio in the outer soil layer on the twist angle amplitude for different frequencies. The twist angle amplitude is notably affected by the damping ratio. The twist angle amplitude decreases substantially with increasing damping ratio, indicating that materials with a higher damping ratio are more effective in reducing vibrations.

6 Conclusion

A closed-form solution is developed to address the time-harmonic torsional vibration of a SDRN pile embedded in elastic soils. The wave equations corresponding to the pile and surrounding soils are initially established. In the case of a time-harmonic load, the general solutions for the composite soil layers are derived. The pile and soil are partitioned into multiple elements, and interface continuity conditions of the pile and soil for each element are applied to derive the torsional impedance at the top end of each pile element. Using the principle of impedance function recursion, the torsional impedance of the pile and the twist angle amplitude are ultimately determined. The correctness of the proposed solution is meticulously checked, and detailed numerical analysis is conducted. The key findings are outlined as follows:

(1) Increasing the inner radius of the pile significantly reduces the torsional impedance of the pile and enhances the resonant peak of the system. In contrast, enlarging the outer radius markedly improves the torsional impedance of the pile, reduces the twist angle amplitude and raises the resonant frequency.

(2) Expanding the node width substantially increases the torsional impedance of the pile, reduces the twist angle amplitude and raises the resonant frequency, thereby improving the dynamic torsional resistance of the system. In contrast, variations in the vertical spacing of nodes have a relatively minor impact on the dynamic performance of the pile foundation.

(3) The radial width and shear modulus of the cemented soil are crucial in determining the dynamic characteristics of the system. Increasing the radial width of the cemented soil effectively increases the torsional impedance of the pile, attenuates both the resonant peak and frequency, thereby significantly enhancing the deformation resistance of the system. Moreover, enhancing the radial width of the cemented soil is more effective than increasing the shear modulus in improving the deformation resistance of the system.

(4) The damping ratio of the outer natural soil deposit is crucial for the dynamic response of the system. Increasing the damping ratio in the natural soil substantially improves the torsional impedance of the pile and reduces the twist angle amplitude, thereby effectively mitigating vibrations. These findings provide a solid theoretical foundation for optimizing SDRN pile designs.

Data availability statement

The original contributions presented in the study are included in the article/supplementary material, further inquiries can be directed to the corresponding author.

Author contributions

HZ: Formal Analysis, Software, Validation, Writing–original draft. XL: Conceptualization, Funding acquisition, Project administration, Supervision, Writing–review and editing.

Funding

The author(s) declare that financial support was received for the research, authorship, and/or publication of this article. This work is funded by the National Natural Science Foundation of China (Grant No. 52478371).

Conflict of interest

Author HZ was employed by Hangzhou Transportation Investment and Construction Management Group Co., Ltd.

The remaining author declares that the research was conducted in the absence of any commercial or financial relationships that could be construed as a potential conflict of interest.

Publisher’s note

References

1. Tipsunavee T, Arangjelovski G, Jongpradist P. Numerical analysis on effects of soil improvement on pile forces on existing high-rise building. *Buildings* (2023) 13(6):1523. doi:10.3390/buildings13061523

2. An-Jie W, Wan-Li Y. Numerical study of pile group effect on the hydrodynamic force on a pile of sea-crossing bridges during earthquakes. *Ocean Eng* (2020) 199:106999. doi:10.1016/j.oceaneng.2020.106999

3. Fabo C, Ben H, Peng G, Xiangming G, Yong Z, Weijiang C. Effect of installation platform on bearing capacity of an offshore monopile foundation. *Front Phys* (2022) 9:809581. doi:10.3389/fphy.2021.809581

4. Gupta BK. A hybrid formulation for torsional dynamic response of pile foundations in a layered soil deposits. *Comput Geotech* (2024) 168:106115. doi:10.1016/j.compgeo.2024.106115

5. Luan L, Zheng C, Kouretzis G, Ding X. Dynamic analysis of pile groups subjected to horizontal loads considering coupled pile-to-pile interaction. *Comput Geotech* (2020) 117:103276. doi:10.1016/j.compgeo.2019.103276

6. Liu X, El Naggar MH, Wang K, Wu W. Dynamic soil resistance to vertical vibration of pipe pile. *Ocean Eng* (2021) 220:108381. doi:10.1016/j.oceaneng.2020.108381

7. Cai Y, Chen G, Xu C, Wu D. Torsional response of pile embedded in a poroelastic medium. *Soil Dyn Earthq Eng* (2006) 26(12):1143–8. doi:10.1016/j.soildyn.2005.10.009

8. Chen G, Cai Y, Liu F, Sun H. Dynamic response of a pile in a transversely isotropic saturated soil to transient torsional loading. *Comput Geotech* (2008) 35(2):165–72. doi:10.1016/j.compgeo.2007.05.009

9. Wang K, Zhang Z, Leo CJ, Xie K. Dynamic torsional response of an end bearing pile in saturated poroelastic medium. *Comput Geotech* (2008) 35(3):450–8. doi:10.1016/j.compgeo.2007.06.013

10. Wang K, Zhang Z, Leo CJ, Xie K. Dynamic torsional response of an end bearing pile in transversely isotropic saturated soil. *J Sound Vib* (2009) 327(3-5):440–53. doi:10.1016/j.jsv.2009.06.017

11. Zheng C, Liu H, Ding X, Lv Y. Torsional dynamic response of a large-diameter pipe pile in viscoelastic saturated soil. *Int J Numer Anal Methods Geomech* (2014) 38(16):1724–43. doi:10.1002/nag.2279

12. Zheng C, Hua J, Ding X. Torsional vibration of a pipe pile in transversely isotropic saturated soil. *Earthq Eng Eng Vib* (2016) 15(3):509–17. doi:10.1007/s11803-016-0340-2

13. Zou X, Du H, Zhou M, Zhou X. Analysis of a single pile under vertical and torsional combined loads in two-layered nonhomogeneous soil. *Int J Geomech* (2019) 19(6):04019054. doi:10.1061/(ASCE)GM.1943-5622.0001429

14. Liu K, Zhang Z. Dynamic response of an inhomogeneous elastic pile in a multilayered saturated soil to transient torsional load. *Math Probl Eng* (2021) 2021(1):1–13. doi:10.1155/2021/5528237

15. Li X, Zhang Z, Sheng J. Exact solution for the torsional vibration of an elastic pile in a radially inhomogeneous saturated soil. *J Math* (2021) 2021(1):1–12. doi:10.1155/2021/6644057

16. Zhang Z, Pan E. Dynamic torsional response of an elastic pile in a radially inhomogeneous soil. *Soil Dyn Earthq Eng* (2017) 99:35–43. doi:10.1016/j.soildyn.2017.04.020

17. Li Z, Gao Y. Influence of the inner soil on the torsional vibration of a pipe pile considering the construction disturbance. *Acta Geotech* (2021) 16(11):3647–65. doi:10.1007/s11440-021-01298-3

18. Li Z, Pan Y, Gao Y, El Naggar MH, Wang K. Torsional vibration of open-ended pipe piles in saturated soil considering the construction disturbance. *Ocean Eng* (2023) 267:113253. doi:10.1016/j.oceaneng.2022.113253

19. Sun M, Peng MQ, Chen Z, Zhao S, Li W, Chen F, et al. Dynamic torsional vibration of a pipe pile in radial heterogeneous transversely isotropic saturated soil. *J Eng Mech* (2024) 150(10):04024068. doi:10.1061/JENMDT.EMENG-7668

20. Wu W, Liu H, El Naggar MH, Mei G, Jiang G. Torsional dynamic response of a pile embedded in layered soil based on the fictitious soil pile model. *Comput Geotech* (2016) 80:190–8. doi:10.1016/j.compgeo.2016.06.013

21. Vega-Posada CA, Areiza-Hurtado M. Analysis of torsionally loaded non-uniform circular piles in multi-layered non-homogeneous elastic soils. *Eng Struct* (2022) 260:114205. doi:10.1016/j.engstruct.2022.114205

22. Ma W, Wang B, Zhou S, Leong EC, Wang C. Torsional dynamic response of an end-bearing pile in homogeneous unsaturated transversely isotropic soil. *Ocean Eng* (2024) 299:117241. doi:10.1016/j.oceaneng.2024.117241

23. Ma W, Shan Y, Xiang K, Wang B, Zhou S. Torsional dynamic response of a pipe pile in homogeneous unsaturated soils. *Comput Geotech* (2022) 143:104607. doi:10.1016/j.compgeo.2021.104607

24. Ma W, Shan Y, Wang B, Zhou S, Wang C, Wang B, et al. Torsional dynamic response of a pipe pile embedded in unsaturated poroelastic transversely isotropic soil. *Ocean Eng* (2024) 310:118574. doi:10.1016/j.oceaneng.2024.118574

25. Li Z, Zhao C, Xi Y, Jin N, Gao Y. Torsional vibration of a pile in unsaturated soil considering the construction disturbance. *Comput Geotech* (2024) 172:106409. doi:10.1016/j.compgeo.2024.106409

26. Ma W, Shan Y, Wang B, Zhou S, Wang C. Analytical solution for torsional vibration of an end-bearing pile in nonhomogeneous unsaturated soil. *J Build Eng* (2022) 57:104863. doi:10.1016/j.jobe.2022.104863

27. Li Z, Zhao C, Gao Y, Wu W, Wang K, Zhang Z. Torsional vibration of a floating pile in radially inhomogeneous unsaturated soil based on the fictitious unsaturated soil pile model. *Soil Dyn Earthq Eng* (2024) 183:108812. doi:10.1016/j.soildyn.2024.108812

28. Honda T, Hirai Y, Sato E. Uplift capacity of belled and multi-belled piles in dense sand. *Soils Found* (2011) 51(3):483–96. doi:10.3208/sandf.51.483

29. Horiguchi T, Karkee MB. Load tests on bored PHC nodular piles in different ground conditions and the bearing capacity based on simple soil parameters. *AIJ J Technol Des* (1995) 1(1):89–94. doi:10.3130/aijt.1.89

30. Zhou JJ, Wang KH, Gong XN, Zhang RH. Bearing capacity and load transfer mechanism of a static drill rooted nodular pile in soft soil areas. *J Zhejiang Univ Sci* (2013) A(14):705–19. doi:10.1631/jzus.a1300139

31. Zhou JJ, Gong XN, Wang KH, Zhang RH. A field study on the behavior of static drill rooted nodular piles with caps under compression. *J Zhejiang Univ Sci* (2015) A(16):951–63. doi:10.1631/jzus.a1500168

32. Zhou JJ, Gong XN, Wang KH, Zhang RH, Yan TL. A model test on the behavior of a static drill rooted nodular pile under compression. *Mar Georesour Geotech* (2016) 34(3):293–301. doi:10.1080/1064119X.2015.1012313

33. Zhou JJ, Gong XN, Wang KH, Zhang RH, Yan JJ. Testing and modeling the behavior of pre-bored grouting planted piles under compression and tension. *Acta Geotech* (2017) 12:1061–75. doi:10.1007/s11440-017-0540-6

34. Li ZY, Wang KH, Wu WB, Leo CJ. Longitudinal dynamic impedance of a static drill rooted nodular pile embedded in layered soil. Mar. *Georesour Geotech* (2018) 36(3):253–63. doi:10.1080/1064119X.2016.1214194

35. Wu JT, Wang KH, Liu X. Effect of a nodular segment on the dynamic response of a tubular pile subjected to longitudinal vibration. *Acta Geotech* (2020) 15:2925–40. doi:10.1007/s11440-020-00930-y

36. Guo J, Dai GL. Study on vertical bearing capacity calculation method of the static drill rooted nodular piles. *Spec Struct* (2019) 36(05):44–50. (In Chinese). doi:10.19786/j.tzjg.2019.05.007

37. Wang KH, Xiao S, Gao L, Wu JT. Vertical dynamic response of a static drill rooted nodular pile. *J Vib Shock* (2019) 38(15):49–56+86. (In Chinese). doi:10.13465/j.cnki.jvs.2019.15.007

38. Liu QY, Zhou JJ, Gong XN, Zhang RH, Huang S. Numerical simulation of bearing performance of prestressed nodular pile in soft soil area. *J Hunan Univ Nat Sci* (2023) 50(03):235. (In Chinese). doi:10.16339/j.cnki.hdxbzkb.2023048

39. Militano G, Rajapakse R. Dynamic response of a pile in a multi-layered soil to transient torsional and axial loading. *Geotechnique* (1999) 49(1):91–109. doi:10.1680/geot.1999.49.1.91

40. Zhang Z, Zhou J, Wang K, Li Q, Liu K. Dynamic response of an inhomogeneous viscoelastic pile in a multilayered soil to transient axial loading. *Math Probl Eng* (2015) 2015(1):1–13. doi:10.1155/2015/495253

Frontiers in Physics

TYPE Original Research
PUBLISHED 07 January 2025
DOI 10.3389/fphy.2024.1475622

OPEN ACCESS

EDITED BY
Yilin Qu,
Northwestern Polytechnical University, China

REVIEWED BY
Yousef Azizi,
Independent Researcher, Zanjan, Iran
Guilherme Jurkevicz Delben,
Federal University of Santa Catarina, Brazil

*CORRESPONDENCE
Mingyang Wang,
✉ w2022241616@163.com

RECEIVED 04 August 2024
ACCEPTED 10 December 2024
PUBLISHED 07 January 2025

CITATION
Gao C, Wang M, Sima Y and Yuan Z (2025) Double array system identification research based on LSTM neural network.
Front. Phys. 12:1475622.
doi: 10.3389/fphy.2024.1475622

Double array system identification research based on LSTM neural network

Chunhua Gao, Mingyang Wang*, Yifei Sima and Zihan Yuan

College of Architecture and Civil Engineering, Xinyang Normal University, Xinyang, Henan, China

The earthquake simulation shaking table array is an important experimental equipment with a wide range of applications in the field of earthquake engineering. To efficiently address the complex nonlinear problems associated with earthquake simulation shaking array systems, this paper proposes the identification of the earthquake simulation shaking array system using the Long Short-Term Memory (LSTM) algorithm. A dual array system model with flexible specimen connections is established, and this system is identified using the LSTM neural network. The LSTM neural network was validated for identifying the dual array closed-loop system of the earthquake simulation shaking table by using three natural waves and one artificial wave. The results demonstrated that the similarity between the predicted output and the theoretical output of the network identified by LSTM exceeded 0.999. This indicates that the algorithm can accurately reproduce the characteristics of the shaking table itself and shows good performance in time series prediction and data mining. References for earthquake simulation shaking array system experiments are provided.

KEYWORDS

system identification, dual array, LSTM neural network, shaking table, deep learning

1 Introduction

The earthquake simulation shaking table is a key laboratory tool for studying and evaluating the seismic resistance of structures. It generates horizontal, vertical, and multidimensional accelerations through a driven platform, simulating the impact of seismic waves on buildings and other structures [1]. The earthquake simulation shaking table array comprises multiple independent earthquake simulation shaking tables that work together to simulate more realistic and complex ground motions. Each table can also be controlled independently to achieve more accurate earthquake wave simulations [2]. Due to factors such as high investment, expensive maintenance and experimental costs, and long construction periods, it is clearly unreasonable to infinitely increase the size and scale of shaking table. Additionally, due to similarity ratios, simply enlarging the shaking table cannot fully meet the requirements. For large-span structures such as bridges, pipelines, aqueducts, and transmission lines, combining multiple small shaking table arrays can be used for testing. The construction and research of shaking table array systems are becoming a trend in both domestic and international research. Gao Chunhua [3] conducted a survey and comparative analysis of various algorithms for domestic shaking tables, summarized the construction forms and loading methods of

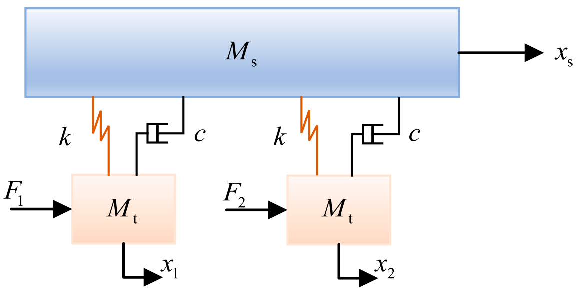

FIGURE 1
The mechanical model of two-array flexible connection of specimens.

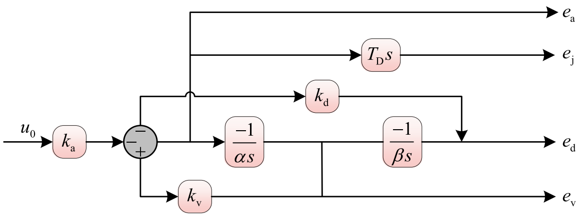

FIGURE 2
Multi-parameter generator schematic diagram.

shaking table substructure tests, as well as the construction and control technical difficulties of shaking table array systems. Ji Jinbao [4, 5] et al. summarized and introduced the functions and characteristics of the shaking table array control system using the nine sub array of Beijing University of Technology as an example, and conducted large-span spatial structure model tests using the equipment. They pointed out the issues and areas that need improvement in using the shaking table array system and explored the relevant research and development of control technology for multi-shaking table array systems. Tao Dehuai [6] conducted a dynamic analysis of the foundation of a dual-array earthquake simulation shaking table and found that the impact of shaking on the foundation remained essentially unchanged under different load conditions. Guan Guangfeng [7] et al. conducted a detailed analysis of different control strategies for a dual array shaking table system and verified the effectiveness of the array system controller through experiments.

The nonlinear influence of shaking table system has always existed in earthquake simulation shaking table test, and has seriously affected its reproduction accuracy and waveform reproduction ability [8, 9]. For more complex shaking table array systems, due to the simultaneous operation of a large number of actuators, the existing control methods cannot meet the requirements for system stability and synchronization [10]. This means that more advanced intelligent control algorithms are needed. As a type of intelligent algorithm, neural network algorithms have good adaptive and generalization abilities, can model and handle nonlinear problems [11–13], and perform well in the control of seismic simulation shaking tables. Gao Chunhua [14, 15] et al. carried out parameter optimization and parameter identification for seismic simulation shaker by intelligent control algorithm, and simulation results showed that the intelligent control algorithm could optimize control parameters, identify multiple parameters, and improve the control effect of the shaker. Yu Shipin [16] et al. used a BP neural network to optimize the control instructions so that the control peak and valley values reached the expected values. Byung Kwan Oh [17] et al. proposed a new model for earthquake response prediction of buildings based on the correlation between ground motion and structure using neural networks. They verified the effectiveness of the proposed neural network model by studying its response prediction performance. A. Zeroual [18] et al. proposed an artificial neural network model, applied it to the prediction of the safety factor for a new earth dam dataset, and compared the predicted results with the stability calculation results of different limit equilibrium slopes. The comparison proved that the prediction ability of the artificial neural network model for the safety factor is satisfactory. Long Short-Term Memory network (LSTM) is a special type of recurrent neural network (RNN) that efficiently processes and predicts sequence data by introducing gating mechanisms. LSTM is designed to solve the problem of gradient vanishing or gradient explosion encountered by traditional RNNs when processing long

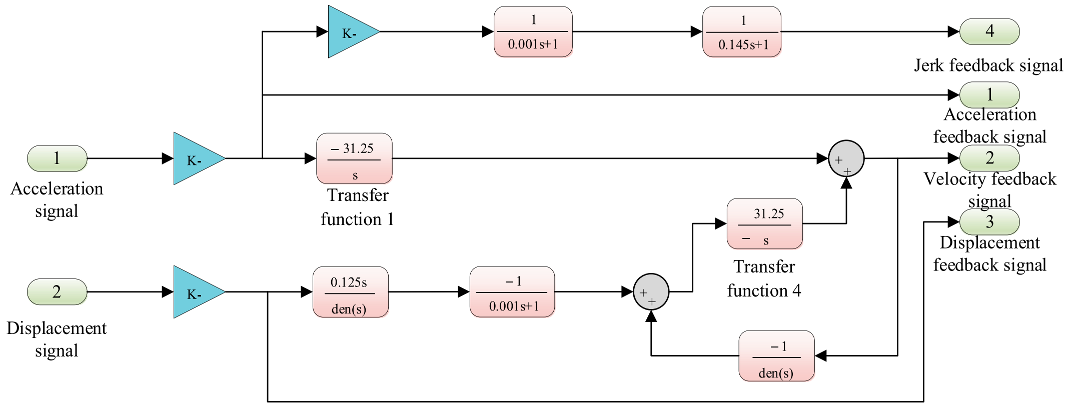

FIGURE 3
Multi-parameter speed synthesizer simulation model.

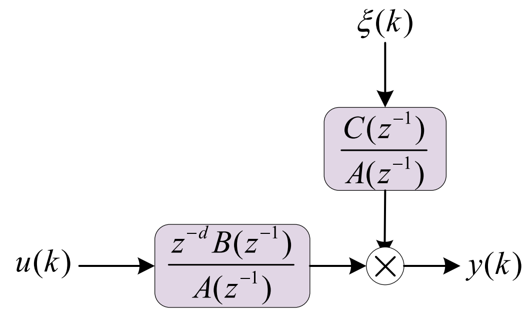

FIGURE 4
Single input single output CAR model.

sequences of data [19]. LSTM can learn long-term dependencies, which is difficult for traditional RNNs to achieve. It is easy to integrate into network structures and is suitable for various time series prediction tasks. Compared with other methods for solving long series problems (such as bidirectional RNNs), LSTM requires fewer parameters. Zhang Wenpeng [20] et al. proposed a three-parameter control parameter tuning algorithm for shakers based on LSTM and adopted the gradient descent method for offline tuning of control parameters. This was combined with the original parameters of the control system for real machine verification. The results showed that the proposed tuning method can achieve better results than manual tuning, and the tuning process is completed offline by the system model without real machine operation, offering advantages of high efficiency and good effect. Ruiyang Zhang [21] et al. proposed two long short-term memory (LSTM) network schemes aimed at data-driven structural seismic response modeling. The verification results show that the proposed LSTM network is a promising, reliable, and computationally efficient method for nonlinear structural response prediction. It has great potential in the reliability assessment of seismic vulnerability analysis of buildings.

System identification is the process of analyzing the input and output data of a system to obtain the mathematical model or dynamic characteristics of the system. This process includes determining the transfer function, state-space model, or other mathematical descriptions of the system. Effective system identification is the key to realize high performance control of shaking table [22, 23]. Zhan Pengyun [24] et al. used the least squares method to identify the model parameters of the shaking table model for seismic simulation. The research shows that the identified model can well reproduce the characteristics of the shaking table system itself, and the least squares identification method can be used to identify the hydraulic and control systems of the shaking table for seismic simulation. Ji Jinbao [25] et al. trained and tested a constructed LSTM network model based on the shaking table system model. The test results show that the LSTM network can reproduce the characteristics of a single-axis open-loop system and can be used as the control object for system simulation and algorithm testing. Febina Christudas [26] et al. utilized input-output data of long short-term memory recurrent neural networks (LSTM-RNN) to model real-time CTS. Compared with empirical models, the LSTM-RNN model achieved better modeling results. Wei Guo [27] et al. developed a physics-guided long short-term memory (PhyLSTM) network for system identification of shaking tables. After detailed hyperparameter testing, the performance of the PhyLSTM model significantly outperformed that of traditional transfer function models.

Based on the above analysis, this paper designs a system identification scheme for a dual-array seismic simulation shaking table based on LSTM neural networks. The LSTM is used to identify the multi-parameter control closed-loop system of the dual array. By comparing the predicted results after neural network training with theoretical results, the feasibility and high research value of this identification scheme are verified.

2 Shaking table two-array system modeling

2.1 Two array system with flexible connection of specimens

For the two-array system, the forces acting on the shaking table platform include not only the actuator forces and the interaction forces between the specimen and the platform but also the additional forces generated due to the asynchronous movement of the two sub-shaking tables. Taking the dual-array system with a flexible connection of the specimen as an example, Figure 1 shows a schematic diagram of the mechanical model of the dual-array system with the specimen.

The mass of the specimen in the system is M_s, the mass of the shaking table is M_t, k is the stiffness coefficient of the connection of the two sub-tables, c is the damping coefficient; The outputs

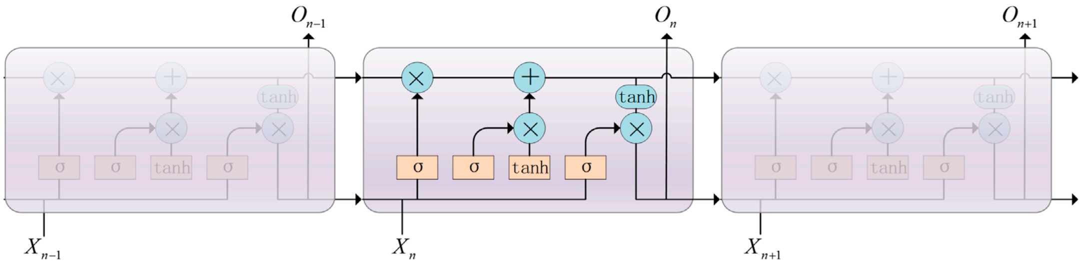

FIGURE 5
LSTM structure diagram.

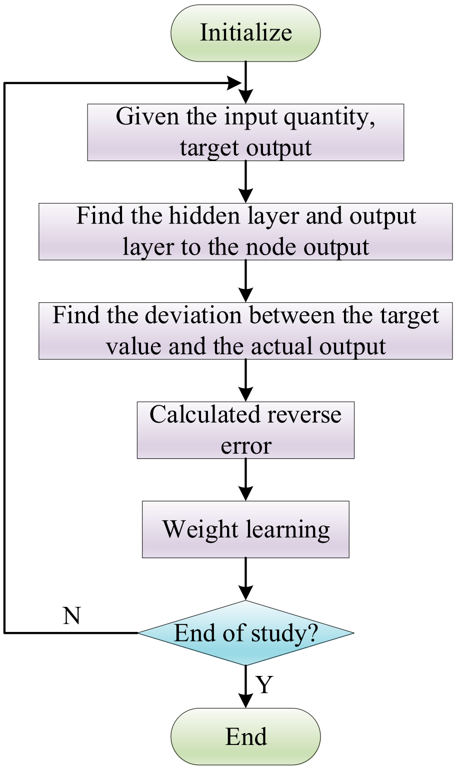

FIGURE 6
LSTM network identification flowchart.

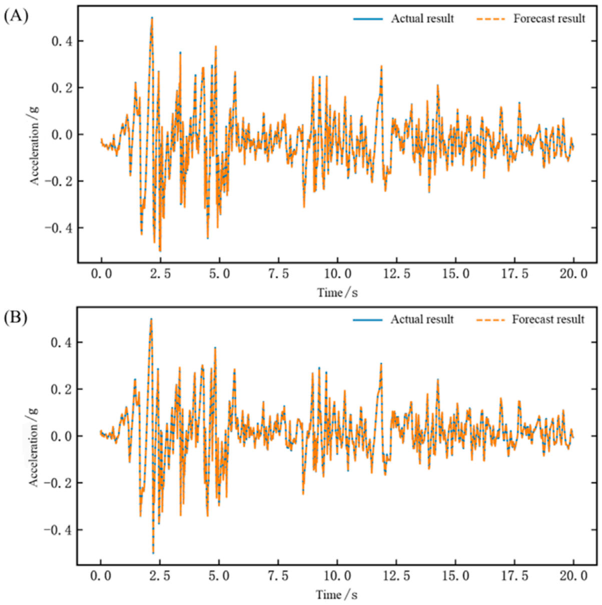

FIGURE 7
Time domain waveform chart of network training for the dual-array system identification **(A)** Shaking table 1 training results comparison **(B)** Shaking table 2 training results comparison.

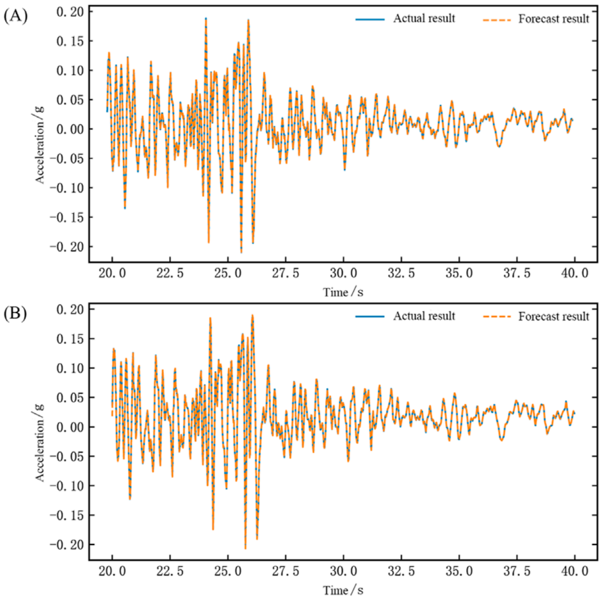

FIGURE 8
Time domain waveform chart of network testing for the dual-array system identification (EL Centro wave) **(A)** Comparison chart of results for Shaking Table 1 **(B)** Comparison chart of results for Shaking Table 2.

of the two shaker exciter are F_1 and F_2 respectively, and the displacements of the two tables are x_1 and x_2 respectively. Assuming the displacement of the specimen is x_s, the force balance Equation 1 of the two-array system can be obtained:

$$\begin{cases} M_s s^2 x_s + (cs+k)(x_s - x_1) + (cs+k)(x_s - x_2) = 0 \\ M_t s^2 x_1 + (cs+k)(x_1 - x_s) = F_1 \\ M_t s^2 x_2 + (cs+k)(x_2 - x_s) = F_2 \end{cases} \tag{1}$$

The acceleration response of the two sub-stations can be obtained as follows:

$$\begin{cases} s^2 x_1 = \dfrac{F_1 + \frac{(cs+k)^2}{M_s s^2+2cs+2k} x_2}{M_t + \frac{cs+k}{s^2} - \frac{(cs+k)^2}{(M_s s^2+2cs+2k)s^2}} \\ s^2 x_2 = \dfrac{F_2 + \frac{(cs+k)^2}{M_s s^2+2cs+2k} x_1}{M_t + \frac{cs+k}{s^2} - \frac{(cs+k)^2}{(M_s s^2+2cs+2k)s^2}} \end{cases} \tag{2}$$

There is a coupling between the two expressions in Equation 2, in other words, the displacement x_1 of shaker 1 depends not only on the parameters of the shaker itself, but also on the displacement x_2 of shaker 2. Next, because the output of the exciter meets Equation 3:

$$\begin{cases} A_p p_{L1} = F_1 \\ A_p p_{L2} = F_2 \end{cases} \tag{3}$$

Without loss of generality, it is assumed that the parameters of the two sub-shaker exciters are the same. In addition, p_{L1} and p_{L2} are used to represent the load pressure of the two shakers, Q_{L1} and Q_{L2} are the total oil flow of the two shakers, and E_1 and E_2 are respectively the control signals of the two shakers. Then, the hydraulic continuity

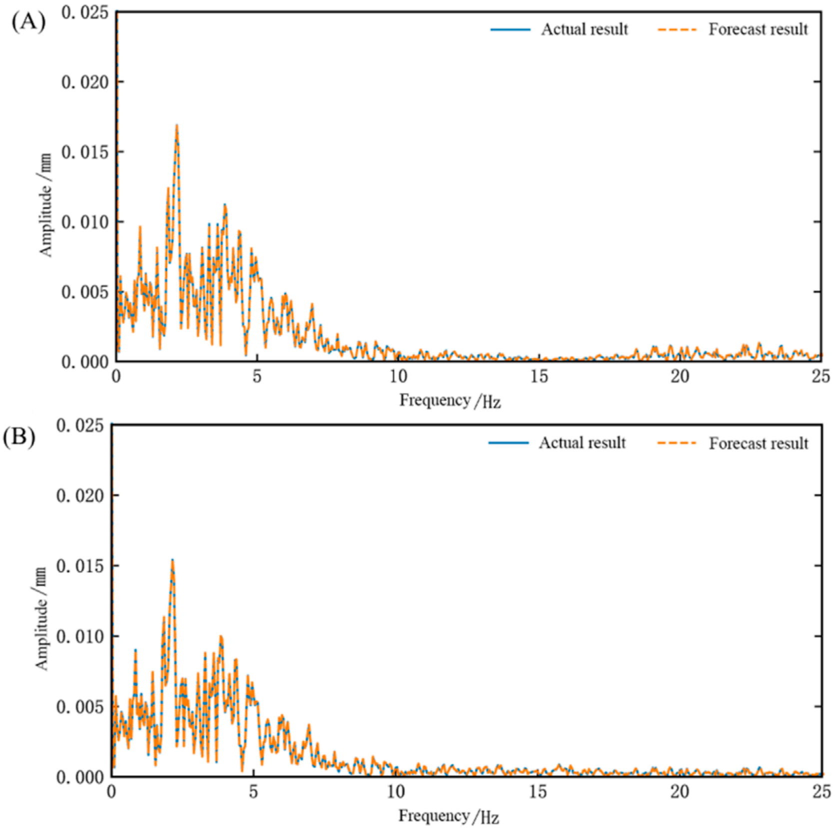

FIGURE 9
Frequency domain waveform chart of network testing for the dual-array system identification (EL Centro wave) **(A)** Comparison chart of results for Shaking Table 1 **(B)** Comparison chart of results for Shaking Table 2.

Equations 4, 5 can be obtained:

$$\begin{cases} Q_{L1} = k_q E_1 - K_c p_{L1} \\ Q_{L2} = k_q E_2 - K_c p_{L2} \end{cases} \tag{4}$$

$$\begin{cases} Q_{L1} = A_p s x_1 + \dfrac{V}{4\beta} s p_{L1} + C_c p_{L1} \\ Q_{L2} = A_p s x_2 + \dfrac{V}{4\beta} s p_{L2} + C_c p_{L2} \end{cases} \tag{5}$$

After simplification, we obtain:

$$\begin{cases} A_p p_{L1} = \dfrac{1}{G_1}\left(\dfrac{k_q E_1}{A_p} - s x_1\right) = F_1 \\ A_p p_{L2} = \dfrac{1}{G_1}\left(\dfrac{k_q E_2}{A_p} - s x_2\right) = F_2 \end{cases} \tag{6}$$

Where Equation 7 is:

$$G_1 = \frac{V}{4\beta A_p^2} s + \frac{K_c + C_c}{A_p^2} \tag{7}$$

After substituting Equation 6 into Equation 2, the two-array open-loop system model is obtained as follows:

$$\begin{cases} \left[(M_t s^2 + cs + k)G_1 + s - \dfrac{G_1 (cs+k)^2}{(M_s s^2 + 2cs + 2k)}\right] \\ x_1 - \dfrac{G_1 (cs+k)^2}{(M_s s^2 + 2cs + 2k)} x_2 = \dfrac{k_q E_1}{A_p} \\ \left[(M_t s^2 + cs + k)G_1 + s - \dfrac{G_1 (cs+k)^2}{(M_s s^2 + 2cs + 2k)}\right] \\ x_2 - \dfrac{G_1 (cs+k)^2}{(M_s s^2 + 2cs + 2k)} x_1 = \dfrac{k_q E_2}{A_p} \end{cases} \tag{8}$$

2.2 Modeling of two-array closed-loop system with multi-parameter control

Building on Section 2.1, a control system is introduced that considers the second-order characteristics of the servo valve and sensor. Additionally, based on the three-parameter control system, the acceleration derivative, which yields the jerk, is introduced. The multi-parameter generator and multi-parameter velocity synthesizer are shown in Figures 2, 3. The introduction of jerk feedforward and jerk feedback forms a multi-parameter control closed-loop system.

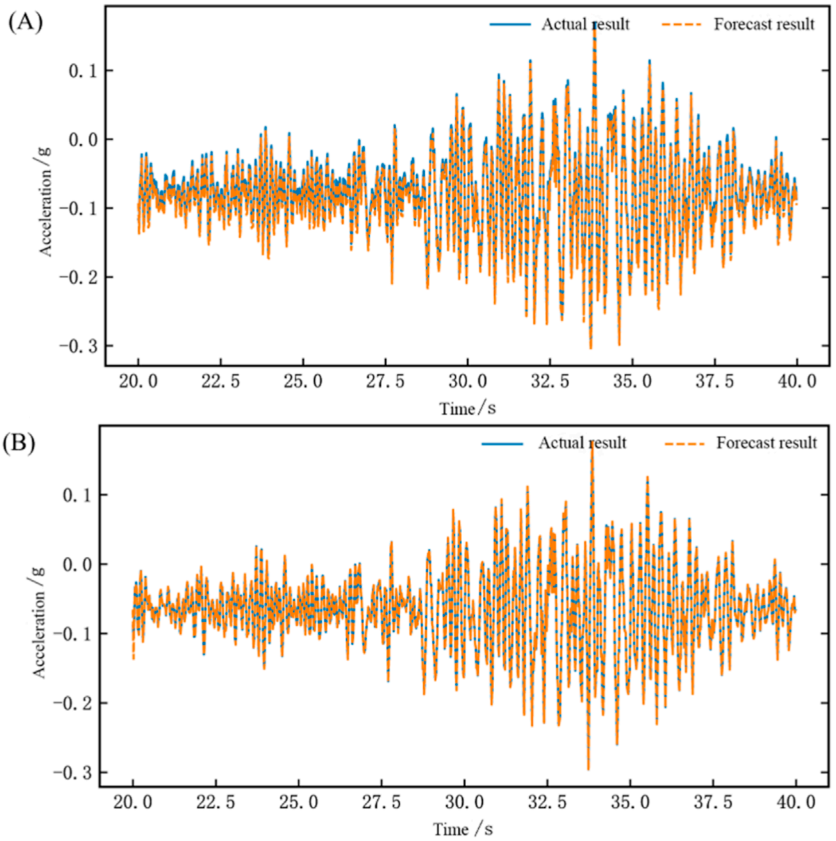

FIGURE 10
Time domain waveform chart of network testing for the dual-array system identification (Wenchuan floor wave) **(A)** Comparison chart of results for Shaking Table 1 **(B)** Comparison chart of results for Shaking Table 2.

In Figure 2, T_D represents the differential time constant, k_a、 k_v、 k_d represents the acceleration, velocity, and displacement feedback gain in the multi-parameter generator, and α and β represent the integral gain.

After applying the multi-parameter control scheme to the two-array system, if G_4 represents the multi-parameter generator transfer function and G_5 represents the multi-parameter feedback transfer function, then the control inputs of the two sub-stations can be written as:

$$\begin{cases} E_1 = G_4 u_1 - G_5 x_1 \\ E_2 = G_4 u_2 - G_5 x_2 \end{cases} \tag{9}$$

Substituting Equation 9 into Equation 8, and further considering the characteristics of the sensors and servo valves, we obtain the control system model. Ultimately, the two-array system model under multi-parameters is obtained Equation 10 as follows:

$$\begin{cases} s^2 x_1 = \dfrac{k_q}{A_p} G_q G_4 \dfrac{\left(G_p G_{fa} s^2 - G_1 G_{p1}^2\right) u_1 + G_1 G_{p1}^2 u_2}{G_p G_{fa}{}^2 s^2 - 2 G_1 G_{p1}^2 G_{fa}} \\ s^2 x_2 = \dfrac{k_q}{A_p} G_q G_4 \dfrac{\left(G_p G_{fa} s^2 - G_1 G_{p1}^2\right) u_2 + G_1 G_{p1}^2 u_1}{G_p G_{fa}{}^2 s^2 - 2 G_1 G_{p1}^2 G_{fa}} \end{cases} \tag{10}$$

Where Equation 11 is:

$$\begin{cases} G_p = M_s s^2 + 2cs + 2k \\ G_{p1} = cs + k \\ G_f = G_1\left(M_t s^2 + cs + k\right) + s + \dfrac{k_q}{A_p} G_5 \\ G_{fa} = \dfrac{1}{s^2} G_f \end{cases} \tag{11}$$

Assume Equation 12 is:

$$\begin{cases} G_{11} = G_{22} = \dfrac{k_q}{A_p} G_q G_4 \dfrac{\left(G_p G_{fa} s^2 - G_1 G_{p1}^2\right)}{G_p G_{fa}{}^2 s^2 - 2 G_1 G_{p1}^2 G_{fa}} \\ G_{12} = G_{21} = \dfrac{k_q}{A_p} G_q G_4 \dfrac{G_1 G_{p1}^2}{G_p G_{fa}{}^2 s^2 - 2 G_1 G_{p1}^2 G_{fa}} \end{cases} \tag{12}$$

Write it in the form of a matrix like Equation 13:

$$\begin{Bmatrix} s^2 x_1 \\ s^2 x_2 \end{Bmatrix} = \begin{Bmatrix} G_{11} & G_{12} \\ G_{21} & G_{22} \end{Bmatrix} \begin{Bmatrix} u_1 \\ u_2 \end{Bmatrix} \tag{13}$$

where: G_{11} is the transfer function of the input signal of shaker 1 to the acceleration $s^2 x_1$ of shaker 1, G_{12} is the transfer function of the input signal of shaker 2 to the acceleration $s^2 x_1$ of shaker 1; G_{21} is the transfer function of the input signal of shaker 1 to the acceleration

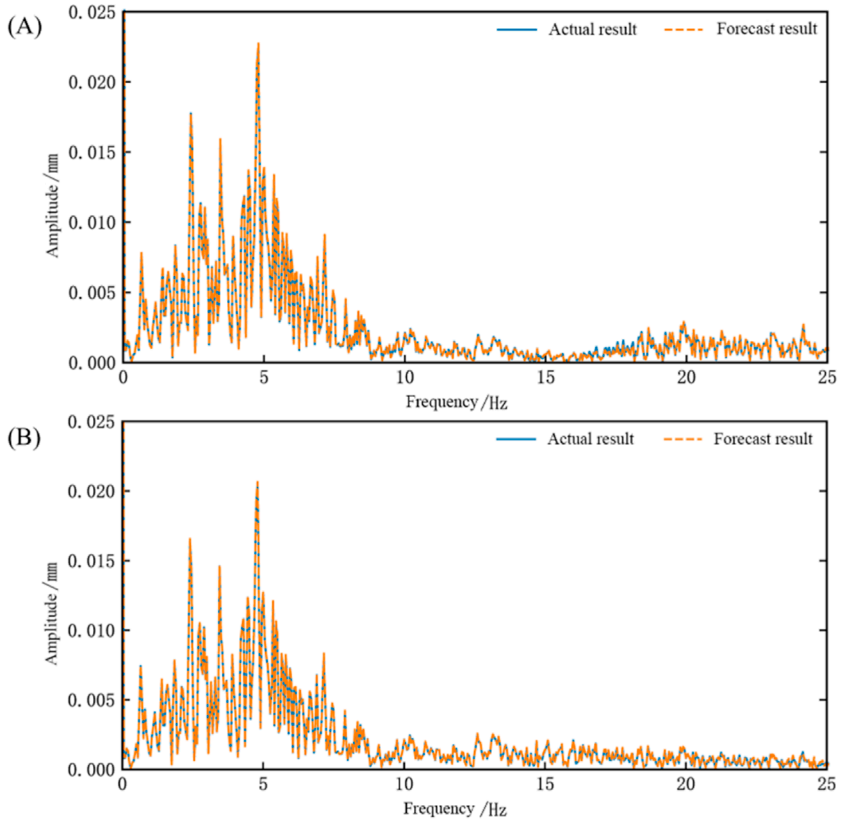

FIGURE 11
Frequency domain waveform chart of network testing for the dual-array system identification (Wenchuan floor wave) **(A)** Comparison chart of results for Shaking Table 1 **(B)** Comparison chart of results for Shaking Table 2.

s^2x_2 of shaker 2, G_{22} is the transfer function from the input signal of Shaker 2 to the acceleration s^2x_2 of Shaker 2.

The basic parameters of the hydraulic and control system of the two-array seismic simulation shaker are shown in Supplementary Table 1, and the relevant parameters of the shaker table are also listed.

3 LSTM neural network system identification principle

3.1 Principles and steps of system identification

The principle of system identification is based on the analysis of system input and output data, with the aim of inferring the intrinsic structure and parameters of the system from this data. Using the Controlled Auto-Regressive (CAR) model as an example, the basic principle of system identification can be explained.

Typically, a single-input single-output CAR model can be represented as Equation 14:

$$A(z^{-1})y(k) = z^{-d}B(z^{-1})u(k) + \xi(k) \tag{14}$$

where, $y(k)$ is the system output, $u(k)$ is the system input, $\xi(k)$ is a random disturbance, d is pure delay, $A(z^{-1})$ and $B(z^{-1})$ can be expressed as Equation 15:

$$\begin{cases} A(z^{-1}) = 1 + a_1z^{-1} + a_2z^{-2} + \ldots + a_pz^{-p} \\ B(z^{-1}) = 1 + b_1z^{-1} + b_2z^{-2} + \ldots + b_qz^{-q} \end{cases} \tag{15}$$

The model structure of the system is shown in Figure 4, which assumes without loss of generality that $C(z^{-1}) = 1$.

Furthermore, the above equation can be written as Equation 16:

$$y(k) = \varphi^T(k)\theta + \xi(k) \tag{16}$$

where, $\phi(k) = [-y(k-1), \ldots, -y(k-p), u(k-d), \ldots, u(k-d-q)]^T$ is a vector constructed from input and output observations, and $\theta = \left[a_0, \ldots, a_p, b_0, \ldots, b_q\right]^T$ is the parameter vector to be solved.

During the experiment, by collecting the input and output data of the system, the input data is the control input signal, and the output data is the system's response signal, that is, obtaining vector $\phi(k)$. For systems that can be modeled, such as the CAR model, the system identification problem can be transformed into a parameter estimation problem, that is, finding the optimal parameter θ estimate by minimizing the error between the model's predicted values and the actual output.

System identification generally includes the following stages:

(1) Experimental Design: According to different practical requirements, clarify the purpose of model identification,

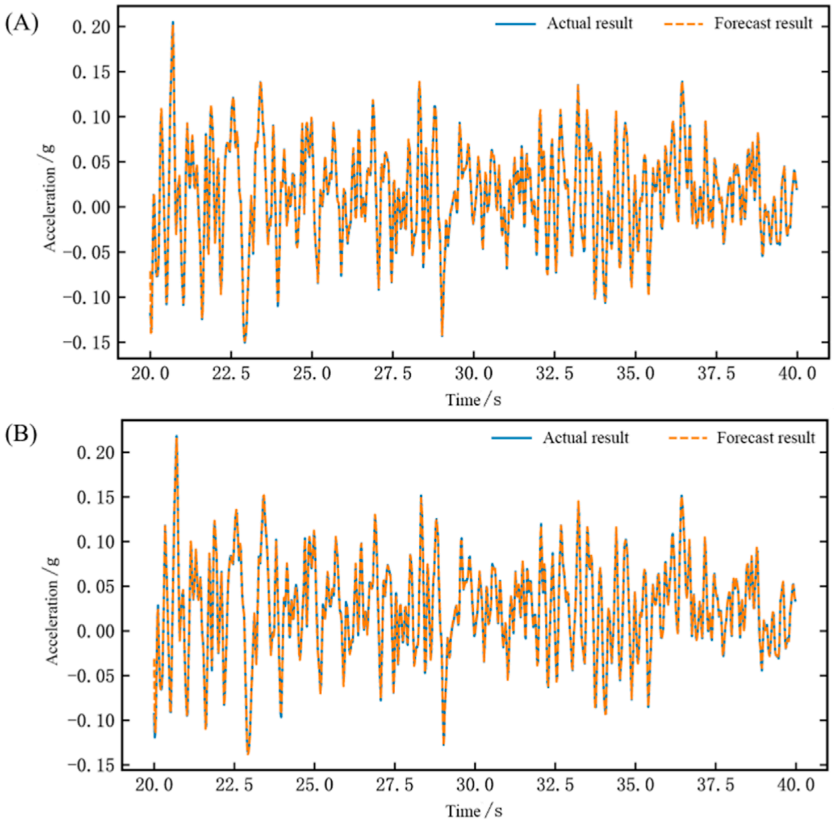

FIGURE 12
Time domain waveform chart of network testing for the dual-array system identification (Traf wave) **(A)** Comparison chart of results for Shaking Table 1 **(B)** Comparison chart of results for Shaking Table 2.

determine the object of system identification, select appropriate input signals, and collect output response data. Generally, suitable input signals should have a certain spectrum and energy distribution to cover the key characteristics of the system and maintain its stability. Moreover, for nonlinear systems, random signals are usually more suitable because they have better excitation performance. The quality of the experimental design directly affects the accuracy of the subsequent model.

(2) Data Collection and Preprocessing: Conduct experiments and collect the input and output data of the system. This includes recording the responses measured by sensors and generating control input signals. Ensure that the experimental environment and measurement errors are considered during data collection. Additionally, preprocess the collected data by performing operations such as denoising, filtering, and sampling to improve the quality and identifiability of the data.
(3) Establish a mathematical model: Use the collected data to create a mathematical model of the system, such as in the form of difference equations, state-space equations, or transfer functions, and estimate the model parameters.
(4) Parameter identification: This typically involves fitting techniques, such as the least squares method, to minimize the error between the model's predictions and the actual observations.
(5) Model validation and optimization: Use data not involved in the identification process for new tests to verify the accuracy and reliability of the obtained model. Ensure that the model can correctly predict the system's response under new input conditions. Additionally, analyze the obtained model to understand the dynamic characteristics of the system. Optimize the model as needed to enhance its performance and adaptability.

3.2 LSTM frame structure and model building

LSTM is a special type of neural network structure that is designed to address the problems of gradient vanishing and gradient explosion encountered by traditional neural networks when handling long-term dependencies. The LSTM unit consists of a cell state and three gating components (input gate, forget gate, and output gate). The forget gate is used to determine which information should be discarded from the cell state; the input gate controls the extent to which the current input affects the cell state; and the output gate decides how the cell state influences the next layer. In the context of controlling a seismic simulation shaking table, the aim is to reproduce the input earthquake waves as accurately as possible, with a one-to-one correspondence between input and output. Therefore,

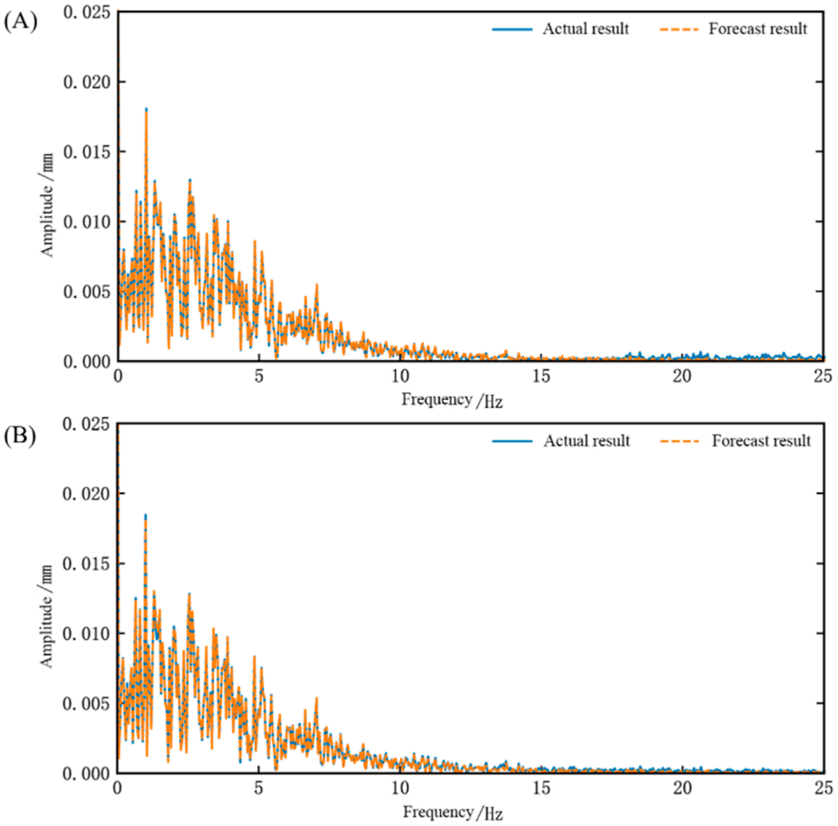

FIGURE 13
Frequency domain waveform chart of network testing for the dual-array system identification (Traf wave) **(A)** Comparison chart of results for Shaking Table 1 **(B)** Comparison chart of results for Shaking Table 2.

a one-to-one LSTM model was ultimately chosen as the controller for the shaking table in this study. The LSTM structure diagram is presented in Figure 5.

In the establishment of the LSTM model, data processing is first conducted to standardize the input seismic wave data to fit the LSTM input format. The dataset is then divided into training and testing sets. Due to the dynamic computation graph utilized in PyTorch, a more intuitive and flexible approach is enabled during the model construction and debugging process. Additionally, the simple and intuitive APIs provided by PyTorch make the construction, training, and evaluation of deep learning models easier. Therefore, the PyTorch framework is employed in this study. In the LSTM used in this research, the model structure is defined using the Sigmoid activation function. The Sigmoid function can independently control the opening and closing states of each gate and possess good gradient propagation characteristics, effectively preventing the problem of gradient vanishing during the training process, thereby achieving selective information transfer.

Then, the Mean Squared Error (MSE) loss function is chosen, and the Adam optimizer is used for backpropagation gradient optimization in this paper. The expression for the MSE loss function is as follows Equation 17:

$$MSE = \frac{1}{m}\sum_{i=1}^{m}(y_i - f(x_i))^2 \tag{17}$$

From the above equation, it can be seen that the loss function MSE represents the sum of the squared differences between the predicted value $f(x)$ of the model and the true value y of the sample. The smaller its value, the smaller the error and the higher the accuracy.

Finally, the input seismic wave dataset is used for model training, and the testing set is employed to evaluate the model's generalization capability. At the same time, the performance of this approach is assessed using the correlation between the actual results and the predicted results, as well as the root mean square error.

Based on the above, the algorithm flowchart for identifying LSTM network is shown in Figure 6:

4 Identification results and analysis of the LSTM dual-array closed-loop system

The LSTM network structure used in this paper specifically includes: an input layer, a hidden layer with 15 neurons, and an output layer. The momentum factor is set to 0.0005, the initial weights of the network are randomly chosen within the range [−1,1], and the learning algorithm employed is the "gradient descent algorithm." The maximum number of training iterations is set to 20,000, and the loss function is calculated using the MSE formula.

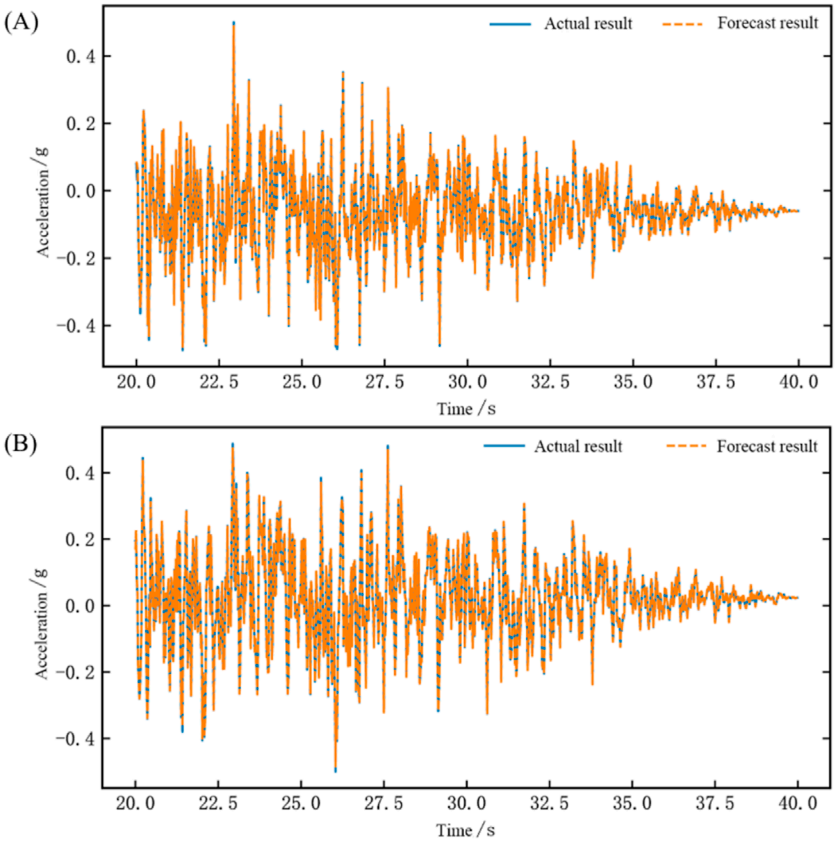

FIGURE 14
Time domain waveform chart of network testing for the dual-array system identification (Artificial wave) **(A)** Comparison chart of results for Shaking Table 1 **(B)** Comparison chart of results for Shaking Table 2.

The training process for system identification is conducted offline. In the results presented below, the curve labeled “Actual Result” represents the output of the shaking table, which serves as the network’s label. The curve labeled “Forecast Result” represents the output of the neural network. The smaller the deviation between the forecast results and the actual results, the better the training performance of the neural network and the higher the accuracy of the system identification. We will first present intuitive result display graphs, and finally evaluate the performance of this method for system identification using the similarity between the actual and forecast waveforms. Assuming the two waveforms are denoted as x and y, their correlation coefficient can be expressed as Equation 18:

$$corr(x,y) = \frac{\sum_{n=1}^{N}(x_n - \bar{x})(y_n - \bar{y})}{\sqrt{\sum_{n=1}^{N}(x_n - \bar{x})^2 \sum_{n=1}^{N}(y_n - \bar{y})^2}} \tag{18}$$

We used different seismic waves as input waveforms, with a sampling time of 0.02 s, corresponding to a sampling frequency of 50 Hz. The simulation time is set to 40 s, resulting in two input datasets each containing 4,000 data points. The first 2000 data points are used as the training set, and the remaining 2000 data points are used as the test set. For the dual-array system, the output data is modeled as a two-dimensional matrix, corresponding to the response waveforms of Shaking Table 1 and Shaking Table 2, respectively. We obtained the output of the dual-array closed-loop system through simulation, which serves as the labels for neural network training. Using the EL Centro wave to analyze the training set, the training results of the dual-array closed-loop system are shown in Figure 7.

Figures 7A, B are comparison charts of the output waveforms and network training results for Shaking Table 1 and Table 2, respectively. After calculation, the root mean square error (RMSE) between the network output waveform and the actual waveform is −52.9 dB for Table 1 and -52.8 dB for Table 2. The correlation coefficients are 0.9998 for Table 1 and 0.9998 for Table 2. The network training results match the actual results very well.

For the test set, we used three different seismic waves and one artificial wave for analysis, performing both time domain and frequency domain analyses. First, we analyzed the EL Centro wave, with the time domain chart shown in Figure 8.

The calculated root mean square error (RMSE) between the network output waveform and the actual waveform is −60.4 dB for Table 1 and -60.9 dB for Table 2. The correlation coefficients are 0.9998 for Table 1 and 0.9998 for Table 2. After performing

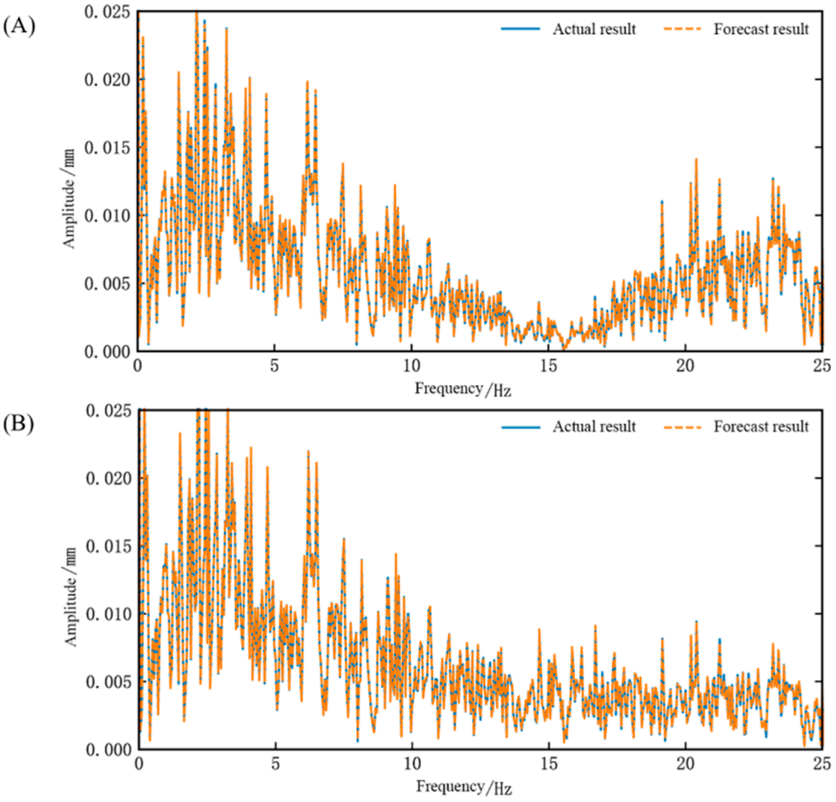

FIGURE 15
Frequency domain waveform chart of network testing for the dual-array system identification (Artificial wave) **(A)** Comparison chart of results for Shaking Table 1 **(B)** Comparison chart of results for Shaking Table 2.

a Fourier transform on the waveform data, the frequency spectrum characteristics of the seismic wave can be obtained, as shown in Figure 9. It can be seen that the frequency domain performance of the network output waveform also almost perfectly replicates the actual frequency domain waveform.

Next, we performed time and frequency domain analyses of the Wenchuan surface wave, as shown in Figures 10, 11. The calculated results indicate that the root mean square error (RMSE) between the network output waveform and the actual waveform is −42.3 dB for Table 1 and -56.2 dB for Table 2. The correlation coefficients are 0.9996 for Table 1 and 0.9997 for Table 2.

Next, we performed time and frequency domain analyses using the Traf wave, as shown in Figures 12, 13. The calculated results indicate that the root mean square error (RMSE) between the network output waveform and the actual waveform is −51.74 dB for Table 1 and -51.20 dB for Table 2. The correlation coefficients are 0.9988 for Table 1 and 0.9986 for Table 2.

Finally, we performed time and frequency domain analyses using the artificial wave, as shown in Figures 14, 15. The calculated results indicate that the root mean square error (RMSE) between the network output waveform and the actual waveform is −49.62 dB for Table 1 and -49.43 dB for Table 2. The correlation coefficients are 0.9996 for Table 1 and 0.9996 for Table 2.

Based on the analysis of these four waveforms, the root mean square error (RMSE) and correlation coefficients between the network output waveforms and the actual time domain waveforms are summarized in Supplementary Table 2. Both the time domain and frequency domain waveform correlations exceed 0.99, indicating that the output closely matches the actual waveforms. This demonstrates that the identification scheme has excellent performance, and the network trained with LSTM can achieve the dual-array system identification task with high accuracy.

5 Conclusion and discussion

This paper primarily designs an identification scheme for a dual-array closed-loop system based on an LSTM network. First, the dual-array system of a seismic simulation shaking table is modeled. Then, a dual-array system identification method based on LSTM is proposed. Using the dataset from the constructed Simulink simulation model, the neural network is trained and tested. The LSTM network is modified to adapt to the system output, considering the characteristics of the dual-array system. This identification scheme is highly applicable, efficient in terms of parameters, and reflects the true characteristics of the system. The main conclusions drawn are as follows:

(1) In training the neural network model, the gradient descent algorithm is highly efficient and adaptable. It effectively handles the nonlinear problems in seismic simulation shaking

tables and has broad application prospects in optimizing control systems.

(2) After identification using the LSTM neural network, the output of the seismic simulation shaking table dual-array closely matches the theoretical output, with a low mean square error and a waveform correlation coefficient exceeding 0.99. This verifies that the identification scheme has high accuracy and good convergence, providing a theoretical basis for performance control of the seismic simulation shaking table.

The research work in this paper is based on closed-loop system and single-degree-of-freedom structure. The subsequent research may consider verifying the applicability of the proposed LSTM neural network identification to open-loop system and multi-degree-of-freedom structure, and further improve the efficiency and accuracy of system identification by combining with other intelligent control algorithms.

Data availability statement

The original contributions presented in the study are included in the article/Supplementary Material, further inquiries can be directed to the corresponding author.

Author contributions

CG: Writing–original draft, Writing–review and editing. MW: Writing–review and editing, Writing–original draft. YS: Writing–review and editing. ZY: Writing–review and editing.

Funding

The author(s) declare that financial support was received for the research, authorship, and/or publication of this article. This work was supported by the Henan Provincial Department of Science and Technology (No.212300410234) and Xinyang Normal University (No. 2024KYJJ110).

Acknowledgments

The author thanks the teachers and classmates of the team for collecting the experimental data.

Conflict of interest

The authors declare that the research was conducted in the absence of any commercial or financial relationships that could be construed as a potential conflict of interest.

Publisher’s note

Supplementary material

The Supplementary Material for this article can be found online at: https://www.frontiersin.org/articles/10.3389/fphy.2024.1475622/full#supplementary-material

References

1. Li P, Liu S, Lu Z, Yang J. Numerical analysis of a shaking table test on dynamic structure-soil-structure interaction under earthquake excitations. *The Struct Des Tall Spec Buildings* (2017) 26:e1382. doi:10.1002/tal.1382

2. Wang S, Gao R, Zhai H, Pang J. Research on synchronous motion control of three shaking tables platform based on EtherCAT. *Machinery Des and Manufacture* (2018) 168–71+176. doi:10.19356/j.cnki.1001-3997.2018.12.042

3. Gao C, Yang Y, Wang J, Qin M, Yuan X. Development and application of a shaking table system. *Arab J Geosci* (2022) 15:1334. doi:10.1007/s12517-022-10604-6

4. Ji J, Li X, Yan W, Li Z, Li H, Cui P, et al. Research on the shaking table array and dynamic model test. *Struct Eng* (2011) 27:31–6. doi:10.15935/j.cnki.jggcs.2011.s1.007

5. Ji J, Li F, Li Z, Sun L. Research and advances on the control technology of the multiple shaking table array system. *Struct Eng* (2012) 28:96–101. doi:10.15935/j.cnki.jggcs.2012.06.024

6. Tao D, Song J, Liu Y, Su Q. Dynamic analysis of double array earthguake simulation shaking table foundation. *Building Sci* (2016) 32:34–8. doi:10.13614/j.cnki.11-1962/tu.2016.11.007

7. Guan G, Xiong W, Wang H. Control of a dual shaking tables vibration test system. *J Of Vibration And Shock* (2017) 36:207–11+217. doi:10.13465/j.cnki.jvs.2017.06.032

8. Enokida R, Ikago K, Guo J, Kajiwara K. Nonlinear signal-based control for shake table experiments with sliding masses. *Earthquake Eng and Struct Dyn* (2023) 52:1908–31. doi:10.1002/eqe.3852

9. Gao C, Li C, Yuan Z, Sima Y, Wang M. Influence and compensation of connection characteristics on shaking table control performance. *Sci Rep* (2024) 14:6860. doi:10.1038/s41598-024-57239-z

10. Zhang X, Wang J. Mechanism study on the interaction effects of shaking table array-test structure. *J Low Frequency Noise, Vibration Active Control* (2024) 43(0):1424–36. doi:10.1177/14613484241259853

11. Wang J, Sun P, Chen L, Yang J, Liu Z, Lian H. Recent advances of deep learning in geological hazard forecasting. *CMES* (2023) 137:1381–418. doi:10.32604/cmes.2023.023693

12. Qu Y, Zhou Z, Chen L, Lian H, Li X, Hu Z, et al. Uncertainty quantification of vibro-acoustic coupling problems for robotic manta ray models based on deep learning. *Ocean Eng* (2024) 299:117388. doi:10.1016/j.oceaneng.2024.117388

13. Chen L, Cheng R, Li S, Lian H, Zheng C, Bordas SPA. A sample-efficient deep learning method for multivariate uncertainty qualification of acoustic–vibration interaction problems. *Computer Methods Appl Mech Eng* (2022) 393:114784. doi:10.1016/j.cma.2022.114784

14. Gao C, Wang J, Yang Y, Qin M. Parameter optimization of shaking table based on later random and nonlinear dynamic particle swarm optimization. *J Xinyang Normal Univ (Natural Sci Edition)* (2023) 36:137–43. doi:10.3969/j.issn.1003-0972.2023.01.023

15. Gao C, Li C, Qin M, Yang Y, Yuan Z. Multi-parameter identification of earthquake simulation shaking table based on BP neural network. *Front Phys* (2024) 12. doi:10.3389/fphy.2024.1309029

16. Yu S, Liu X, Wang J, Liu D, Jin Y. Application of BP neural networks in electro-hydraulic shaking table control system. *Chin Hydraulics and Pneumatics* (2008) 53–5. doi:10.3969/j.issn.1000-4858.2008.07.020

17. Oh BK, Glisic B, Park SW, Park HS. Neural network-based seismic response prediction model for building structures using artificial earthquakes. *J Sound Vibration* (2020) 468:115109. doi:10.1016/j.jsv.2019.115109

18. Zeroual A, Fourar A, Djeddou M. Predictive modeling of static and seismic stability of small homogeneous earth dams using artificial neural network. *Arab J Geosci* (2019) 12:16. doi:10.1007/s12517-018-4162-6

19. Ji J, Hu Z, Yang S. Closed-loop control method of seismic simulation shaking table based on LSTM. *EARTHQUAKE ENGINEERING AND ENGINEERING DYNAMICS* (2022) 42:63–9. doi:10.13197/j.eeed.2022.0507

20. Zhang W, Ji J, Wang D. Parameters tuning of shaking table based on LSTM. *Machine Tool And HydraulicS* (2024) 52:124–30. doi:10.3969/j.issn.1001-3881.2024.05.019

21. Zhang R, Chen Z, Chen S, Zheng J, Büyüköztürk O, Sun H. Deep long short-term memory networks for nonlinear structural seismic response prediction. *Computers and Structures* (2019) 220:55–68. doi:10.1016/j.compstruc.2019.05.006

22. Zhang B, Du H, Zhu F, Wu Y, Rao J, Qiu L. Research on control strategy of random waveform reproduction for single DOF shaking table. *Machine Tool and Hydraulics* (2023) 51:80–5. doi:10.3969/j.issn.1001-3881.2023.23.012

23. Gao C, Yang Y, Qin M, Li C, Yuan Z. Research on parameter identification of shaking table systems based on the RLS method. *PLOS ONE* (2022) 17:e0279092. doi:10.1371/journal.pone.0279092

24. Zhan P, Ji J, Sun L, Wang J, Song L. Research on least souares identification method of shaking table systems. *Industrial Construction* (2014) 44:285–8+301. doi:10.13204/j.gyjz2014.s1.098

25. Ji J, Li W, Wu J. System identification and LSTM network simulation of shaking table open-loop model. *Earthquake Engineering and Engineering* (2022) 42:87–94. doi:10.13197/j.eeed.2022.0309

26. Christudas F, Dhanraj AV. System identification using long short term memory recurrent neural networks for real time conical tank system. *Romanian Journal Of Information Science And Technology* (2020) 23:T57–T77. doi:10.1016/j.jprocont.2020.10.011

27. Guo W, He C, Shao P. A novel system identification method for servo-hydraulic shaking table using physics-guided long short-term memory network. *Mechanical Systems and Signal Processing* (2022) 178:109277. doi:10.1016/j.ymssp.2022.109277

frontiers | Frontiers in Physics

TYPE Original Research
PUBLISHED 10 January 2025
DOI 10.3389/fphy.2024.1466191

OPEN ACCESS

EDITED BY
Yilin Qu,
Northwestern Polytechnical University, China

REVIEWED BY
Dong Lei,
Hohai University, China
Ang Zhao,
Shanghai Civil Aviation College, China

*CORRESPONDENCE
Qidan Xiao,
✉ xiaoqidan253@163.com

RECEIVED 17 July 2024
ACCEPTED 02 December 2024
PUBLISHED 10 January 2025

CITATION
Xiao Q, Gao B, Deng H and Zhao J (2025) Study on the performance of pervious concrete under freeze–thaw cycle based on PFC3D.
Front. Phys. 12:1466191.
doi: 10.3389/fphy.2024.1466191

Study on the performance of pervious concrete under freeze–thaw cycle based on PFC3D

Qidan Xiao[1,2]*, Bo Gao[1,2], Hui Deng[1,2] and Jun Zhao[3]

[1]College of Architecture and Civil Engineering, Xinyang Normal University, Xinyang, China, [2]Henan New Environmentally-Friendly Civil Engineering Materials Engineering Research Center, Xinyang Normal University, Xinyang, China, [3]School of Water Conservancy and Civil Engineering, Zhengzhou University, Zhengzhou, China

Pervious concrete exhibits different freeze–thaw performance compared to conventional concrete owing to its unique porous structure. Therefore, studying its mechanical and durability properties under freeze–thaw conditions has become a pressing issue. A numerical model of pervious concrete was created using the discrete element method based on actual aggregates to evaluate the impact of freeze–thaw cycles (FTCs) on the mechanical properties of pervious concrete. Pore water in the microstructure of pervious concrete was defined using PFC3D software through simulation of the freezing and expansion processes of the pore water, while applying freeze–thaw loading. This study employs the parallel bond model in PFC3D software to account for adhesion between the material particles. The linear ontological relationship of the parallel bond model was modified to a linear curvilinear relationship. The FTCs resulted in strength loss reductions of 0.62%, 2.17%, 4.06%, and 5.87% for corresponding mass losses of 0.66%, 0.89%, 1.21%, and 6.66% compared to the control. The models were monitored for fracture location and uniaxial compressive damage using PFC3D software, and the attenuation constant of the freeze–thaw resistance of pervious concrete was examined with respect to varying porosity and initial uniaxial compressive strength (UCS). The results indicate that the decay constant increases with increasing porosity and modulus of elasticity while decreasing with increasing values of the initial UCS.

KEYWORDS

discrete element method, PFC3D, parallel bond model, freeze–thaw cycles, reality modeling

1 Introduction

The urban “heat island effect” has intensified in recent years, resulting in the development of the concept of a “sponge city.” A sponge city refers to one that can absorb, store, seep, and purify water when it rains, thereby reducing the need to “release” and consume that water [1]. Pervious pavements are an important part of a sponge city; pervious concrete pavements have high porosity, can effectively alleviate the urban heat island effect, and reduce the risk of urban flooding [2]. Pervious concrete contains very little or no fine-aggregate sand, which endows it with a unique porous structure [3]. The porosity of pervious concrete makes it particularly vulnerable to deterioration from freeze–thaw cycle (FTC) loading, which can shorten its overall lifespan [4, 5]. Therefore, evaluation of the mechanical properties and durability of pervious concrete under a freeze–thaw environment is a key problem that needs to be solved at present.

The primary reason for deterioration of the durability of pervious concrete is the leakage of calcium ions during cement hydration; this phenomenon can be successfully inhibited by metakaolin and silica fume [6]. Furthermore, the inclusion of fly ash (FA), rice husk ash, and granulated blast furnace slag can result in more extensive micropore filling [7–10]. This has an important reinforcing effect on the interfacial transition zone and can effectively improve the freeze–thaw cyclic loading resistance of pervious concrete [11–14]. Anderson and Dewoolkar [15] discovered that FA is an effective filler in pervious concrete, but the short curing period may result in insufficient hydration of FA, making pervious concrete with FA more susceptible to deterioration in early freeze–thaw environments. Chindaprasirt et al. [16] found that 10% rice husk ash was effective in increasing the strength of pervious concrete. Cement alone is not as effective as a polymeric cementitious system comprising cement and mineral admixtures.

Some scholars have investigated the effects of cementitious materials containing air-entraining agents (AEAs) on the resilience of pervious concrete to freeze–thaw cycling. Zhong and Wille [5] investigated the effects of the cementitious material type, pore system characteristics, and fiber-reinforcing materials on the freeze–thaw durability of pervious concrete and demonstrated that ultrahigh-strength cementitious materials can greatly enhance such durability. Santos et al. [17] showed that internal blending of appropriate amounts of silane emulsion in cementitious materials enhanced the ability of the concrete containing recycled aggregates to withstand ion penetration, carbonation, and capillary water absorption. Ebrahimi et al. [18] summarized three methods for enhancing the freeze–thaw resistance of concrete, which involved employing AEAs to mitigate the pore water pressure, incorporating fibers or nanotubes to inhibit crack formation, and preparing monolithic waterproof concrete with internal water-repellent agents to minimize water absorption. Vancura et al. [19] and Chen et al. [20–22] found that AEAs are the most commonly used method of introducing air bubbles to improve freeze–thaw durability in plain concrete and that pervious concrete without entrapped air is more susceptible to freeze–thaw damage in cold regions.

Using the normal test procedures meant for conventional concrete owing to the lack of a defined test technique for the freeze–thaw durability of pervious concrete showed that adding 7% sand to coarse aggregates greatly increased the ability of pervious concrete to withstand FTCs. Lund et al. [23] reported that the effects of AEAs on the frost resistance of pervious concrete are mainly through improvement of the workability of the pervious concrete mixture, making it more compact and thereby enhancing the frost resistance rather than by reducing the pore spacing. Yang et al. [14] concluded that AEAs enhance the frost resistance of pervious concrete primarily by boosting its structural strength.

Ethylene vinyl acetate (EVA) emulsion enhances the interfacial bond strength of pervious concrete, while polypropylene (PP) fibers increase the tensile strength, leading to improved frost resistance compared to laboratory-prepared specimens. Giustozzi [24] conducted experiments on the frost resistance of pervious concrete using four different polymer modifiers: cationic styrene-butadiene rubber (SBR) emulsion, polyvinyl acetate (PVAC) emulsion, EVA powder, and anionic SBR emulsion. Their study revealed that these polymer modifiers substantially improved the performances of pervious concrete, especially enhancing its frost resistance, while maintaining permeability. Among these, the PVAC emulsion had the most pronounced enhancement effect on the performance of pervious concrete.

Salt corrosion caused by the FTCs has a universal and direct negative impact on the longevity of pervious concrete. Extensive use of deicing salts and seawater erosion in the coastal areas often accelerates the deterioration rate of pervious concrete, which seriously restricts its promotion and use in cold areas. Feng et al. [25] studied the effects of three different deicing agents on silicate-cement-based pervious concrete using the saturation and drainage methods to illustrate the extent of damage caused; accordingly, the three agents produced effects in the following order: calcium chloride > sodium chloride > magnesium acetate. Sahdeo et al. [26] demonstrated the methods by which the sulfate corrosion resistance, flexural strength, and compressive strength of pervious concrete can be successfully increased through the addition of a tiny quantity of fine sand. Saboo et al. [12] investigated the use of NaCl solution as a freeze–thaw medium to simulate freeze–thaw tests in a deicing salt environment; after 15 FTCs, the concrete specimens showed more than 5% loss of quality, and after 50 FTCs, the concrete specimens showed more than 40% loss of quality. Tsang et al. [27] studied the FTC test results of pervious concrete using calcium chloride solution, urea solution, NaCl solution, magnesium chloride solution, and water as the freeze–thaw media; they found that for a given concentration, NaCl and calcium chloride solutions produced the most serious freeze–thaw damages to pervious concrete. After 50 FTCs, there was a 5% loss of specimen mass, which increased to more than 20% loss of mass after 100 FTCs. Nassiri et al. [28] studied the method by which cured carbon-fiber composite material (CCFCM) affected pervious concrete and discovered that CCFCM greatly increases the ability of pervious concrete to withstand frost. Zou et al. [29] discovered that the use of silanized recycled aggregates would be both environment- and user-friendly; this material creates a hydrophobic silica film on the aggregate surface to inhibit water accumulation, resulting in a compact structure at the aggregate interface through increased C-S-H gel formation and thereby enhancing the frost resistance.

Very few studies are available on the long-term (56 d, 90 d, etc.) performances of modified pervious concretes, and most of these studies concentrate on the early (usually 28 d) performance of the material. Meanwhile, very few studies have been conducted on the fine-scale cracking of pervious concrete following FTCs; indoor tests have only been used to examine the mechanical characteristics and freeze–thaw mechanism, which are insufficient to fully account for the fine-scale structure of pervious concrete following freeze–thaw cycling [30, 31]. In particular, water in the internal pores and micropores of the concrete condenses into ice as the temperature decreases below freezing, expands by roughly 8%, and creates shear strain between the aggregate particles. However, the high permeability of pervious concrete prevents saturation with water so that some of the water pressure is relieved following FTCs. Even when the pervious concrete is not saturated with water, mechanical degradation has been shown to occur [32, 33].

Numerical simulations can be used to explore the mechanical properties of pervious concrete and analyze its behaviors from a fine-scale perspective. By considering pervious concrete as a granular cemented material, we can accurately represent it using the particle flow method, which is a discrete element technique mostly utilized to examine the fine-grained mechanical characteristics of bulk media [34]. Ng and Dai [35] examined the effects of freeze–thaw damage of water ice pressure on the internal microstructure of a cement material and replicated the expansion of cracks in the cement material under a freeze–thaw environment. Zhao et al. [36] simulated the FTC of pervious concrete using discrete parts, created an elastic–plastic parallel-bonded contact model, and analyzed how varying porosity and the initial uniaxial compressive strength (UCS) affect the freeze–thaw decay constants. Xiang et al. [37] used the discrete element method (DEM) to model pervious concrete and accurately simulate the changes in its compression modulus and strength during FTCs. Wu et al. [38] applied a new loading method to obtain the freezing force during FTCs; accordingly, a near-field kinetic model was introduced to compare the damage patterns of experimentally captured cement paste samples.

By taking into account the porosity of the concrete, a randomly distributed predamage was added to imitate the freeze–thaw damage in real macroscopic concrete. To examine the damage of pervious concrete under uniaxial compression, Xie et al. [33] used the DEM and found that the simulation results closely matched the actual data. Xu et al. [39] examined the impacts of aggregate reinforcement on paste migration and pore structure modification by creating a three-dimensional model of recycled aggregate pervious concrete using DEM. Huang et al. [40] concluded that the plasticity near the pore region expands with increasing pressure during freezing; upon thawing, elastic deformation is recovered, yet significant residual deformation persists, resulting in an elastoplastic theoretical model. AlShareedah and Nassiri [32] predicted the hydraulic characteristics of pervious concrete using pore-scale finite volume modeling with the DEM.

Pervious concrete freeze–thaw tests use both rapid and slow freeze–thaw methods. Moradllo et al. [41] used the slow freeze–thaw method to obtain the relationship between the critical pore spacing coefficient and different cooling rates (2, 4, and 6°C/h); they found that a faster cooling rate resulted in a smaller critical pore spacing coefficient. Hosseinzadeh et al. [42] utilized the slow freeze–thaw method and observed notable distinctions in the performances of paste and mortar, with mortar surpassing pastes. Taheri et al. [43] found that for similar fiber compositions, pervious concrete was able to resist 320–360 cycles when subjected to the rapid freeze–thaw method (Standard ASTMC666-0317); however, it could resist only 50–60 cycles when the slow freeze–thaw test (24 h for each cycle) was applied, indicating that the standard freeze–thaw test has slow deterioration even though the rates of freezing and thawing are higher.

Thus, the present study uses simulations and tests to examine the small damage characteristics and fundamental mechanical properties of pervious concrete under repeated FTCs. Based on the analysis of the compressive, flexural, and permeability coefficient data, the ideal mix ratio of pervious concrete was established, and the FTC test was carried out based on the ideal mix ratio. Using actual aggregates, a numerical model of pervious concrete was established for different FTCs using the discrete element software PFC3D. To determine the changes to the mechanical characteristics of the numerical model of pervious concrete, various fine-scale parameters of the model were calibrated. By comparing and analyzing the results from numerical simulations and tests, the numerical model was validated to ascertain the law governing the fine damage characteristics of pervious concrete.

2 Preparation and tests

2.1 Materials

2.1.1 Gelling material

This study utilized P.O 42.5 ordinary Portland cement (OPC) from Tongli Cement Co., Ltd.; FA produced by Henan Yixiang New Material Co., Ltd.; granulated ground blast furnace slag (GGBFS) from Henan Yixiang New Material Co., Ltd.; dispersible emulsion powder (DEP) from Shijiazhuang Chuansheng Building Materials Technology Co., Ltd.; and water reducing agent (WRA) from Hunan Zhongyan Building Materials Technology Co., Ltd. Table 1 displays the chemical compositions of the DEP, FA, GGBFS, and OPC.

2.1.2 Aggregates

In the tests, the natural coarse aggregate (NCA) was composed of 5–10-mm aggregate particles. The NCA was cleaned with tap water prior to usage to remove any muck and was allowed to dry naturally. Table 2 presents the physical attributes of the aggregates.

2.1.3 Test water

Water supplied by the city of Xinyang was used for the preparation, curing, and post-testing of the pervious concrete samples in this study.

2.2 Orthogonal experimental design

2.2.1 Orthogonal test method

In compliance with the guidelines of the Technical Specification for Pervious Cement Concrete Pavement [44], the water–cement ratio (WCR) was designed as per the volumetric method, and the target porosity was adjusted to 15%. By adopting the orthogonal experimental design, samples from the entire test system can be screened more precisely, swiftly, and economically. This method considers various factors and levels to achieve the best results and reflect the actual conditions more accurately.

2.2.2 Orthogonal test grouping

In this study, five different factors were established, including WCR, DEP, WRA, FA, and GGBFS, and four different levels were considered in each group for the orthogonal tests that were then analyzed using analysis of variance to find the optimal fit ratio between the factors. The level factor and orthogonal tables are shown in Tables 3, 4.

2.3 Mixing ratio design

When designing the mix ratio for pervious concrete, the effects of the admixture amount, WCR, and molding technique on water permeability performance should be taken into account. Enhancing the resistance of pervious concrete to frost while preserving its

TABLE 1 Chemical composition chart.

Compositions	SiO_2	Al_2O_3	Fe_2O_3	CaO	MgO	K_2O	PR	Others
OPC	22.21	4.97	2.94	60.22	1.24	2.72	0.56	5.14
FA	59.41	19.51	7.72	4.71	1.72	1.72	0.27	5.71
GGBFS	36.52	12.87	0.72	40.75	9.72	0.27	0.18	0.33
DEP	1.06	2.76	1.74	1.03	1.67	1.57	89.42	3.57

TABLE 2 Physical characteristics of natural coarse aggregate (NCA).

Name	Aggregate size (mm)	Bulk density (kg/m^3)	Apparent density (kg/m^3)	Crushing Value (%)	Water Absorption (%)
NCA	5–10	1,441	2,680	13.9	1.15

TABLE 3 Table of experimental factor levels L16 4^5.

Level factors	WCR(A)	DEP%(B)	WRA%(C)	FA%(C)	GGBFS%(E)
1	0.25 (A1)	0 (B1)	0 (C1)	0 (D1)	0 (E1)
2	0.28 (A2)	4 (B2)	0.1 (C2)	10 (D2)	5 (E2)
3	0.30 (A3)	8 (B3)	0.2 (C3)	20 (D3)	10 (E3)
4	0.32 (A4)	10 (B4)	0.3 (C4)	30 (D4)	15 (E4)

strength is also a crucial consideration. The performance indexes of pervious concrete measured in this test and the specifications of the specimens required are shown in Table 5. Series 1 was prepared according to CJJ/T135-2009 [44], and the quantity of material used in each group is displayed in Table 6.

The optimum compressive strength, effective porosity, and water permeability were determined through the orthogonal test. Series 2 was then prepared according to the optimum ratios. Series 2 is a column specimen with dimensions of 100 mm (length) × 100 mm (width) × 300 mm (height) and is used to analyze the post-freezing and thawing strength losses of pervious concrete along with the change trends in the stress–strain curve. The precise mixing ratio design for the Series 1 test phase is displayed in Table 6. The overall degree of variation for this investigation was determined through 16 sets of orthogonal tests.

2.4 Test methods

2.4.1 Sample preparation and maintenance

The test employed the cement-packed stone method of mixing. Figure 1 depicts the specimen production process. The precise mixing procedure was as follows: the mixer was filled with coarse aggregate and 50% water for 1 min, followed by the addition of cementitious materials for another minute; lastly, the remaining 50% water was added and mixed for another minute. The pervious concrete was loaded into the mold three times through three layers of manual pile insertion and pounding, followed by compaction and leveling. The initial hydration has a major impact on the improved properties of pervious concrete because its WCR is typically low.

Therefore, the surfaces of the specimens were covered with a film as soon as the pervious concrete was loaded into the molds to maintain the moisture content without affecting the initial hydration. Thereafter, the specimens were maintained in a room for a full day at a temperature of 15°C ± 5°C and relative humidity of over 60%. Then, the molds were dismantled. Lastly, the samples were cured for 28 d in a typical constant-temperature curing chamber maintained at 15°C ± 2°C and a relative humidity above 90%.

2.4.2 Compressive strength test

According to the standard GB/T50081-2019 [45], the samples measuring 100 mm × 100 mm × 100 mm underwent cubic compressive testing, whereas the samples measuring 100 mm × 100 mm × 300 mm were subjected to prismatic uniaxial compressive testing at varying ages.

2.4.3 Flexural strength test

According to the standard GB/T50081-2019 [45], the pervious concrete specimens cured for 28 d were subjected to a prismatic flexural test. The prismatic specimens had dimensions of 100 mm × 100 mm × 400 mm.

TABLE 4 Table of experimental factor levels L16 4^5.

Sample	WCR(A)	DEP(B)	WRA(C)	FA(D)	GGBFS(E)
PC-M1	A1	B1	C1	D1	E1
PC-M2	A1	B2	C2	D2	E2
PC-M3	A1	B3	C3	D3	E3
PC-M4	A1	B4	C4	D4	E4
PC-M5	A2	B1	C2	D3	E4
PC-M6	A2	B2	C1	D4	E3
PC-M7	A2	B3	C4	D1	E2
PC-M8	A2	B4	C3	D2	E1
PC-M9	A3	B1	C3	D4	E2
PC-M10	A3	B2	C4	D3	E1
PC-M11	A3	B3	C1	D2	E4
PC-M12	A3	B4	C2	D1	E3
PC-M13	A4	B1	C4	D2	E3
PC-M14	A4	B2	C3	D1	E4
PC-M15	A4	B3	C2	D4	E1
PC-M16	A4	B4	C1	D3	E2

TABLE 5 Performance indicators and corresponding test piece size and quantity table.

Performance	Test piece	Specimen size	Number
28-d compressive strength	Cubic	100 mm × 100 mm × 100 mm	3
28-d prismatic uniaxial compressive strength	Prism	100 mm × 100 mm × 300 mm	3
28-d flexural strength	Prism	100 mm × 100 mm × 400 mm	3
Effective porosity	Cubic	100 mm × 100 mm × 100 mm	3
Permeability	Cubic	100 mm × 100 mm × 100 mm	3

2.4.4 Water permeability test

The permeability coefficient was determined based on Darcy's law in combination with the constant head permeameter method on a cubic specimen of size 100 mm × 100 mm × 100 mm according to the following Equation 1 from [46]:

$$K_T = \frac{L}{H} \times \frac{Q}{A \cdot t} \tag{1}$$

where K_T is the permeability coefficient (mm/s) of the specimen; Q is the quantity of water that seeps out of the model in t seconds (mm^3); L is the sample height (mm); H is the cross-sectional area of the specimen (mm^2); t is the penetration time (s).

2.4.5 Effective porosity test

The effective porosity was computed using the formula below with a cubic specimen of size 100 mm × 100 mm × 100 mm in accordance with Equation 2 the ASTM standard [47]:

$$P = \left(1 - \frac{m_2 - m_1}{V \cdot \rho_w}\right) \tag{2}$$

where P is the specimen porosity; m_2 is the model weight (g) after drying; m_1 is the model weight (g); V is the sample volume cm^3; ρ_w is the density of water (g/cm^3).

TABLE 6 Actual amounts of materials used in each group (kg).

Sample	Concrete	Water	DEP	WRA	FA	GGBFS
PC-M1	9.78	2.45	0.00	0.00	0.00	0.00
PC-M2	7.92	2.45	0.39	0.01	0.98	0.49
PC-M3	6.05	2.45	0.78	0.02	1.96	0.98
PC-M4	4.37	2.45	0.98	0.03	2.94	1.47
PC-M5	6.03	2.60	0.00	0.01	1.86	1.39
PC-M6	5.21	2.60	0.37	0.00	2.79	0.93
PC-M7	8.06	2.60	0.74	0.03	0.00	0.46
PC-M8	7.42	2.60	0.93	0.02	0.93	0.00
PC-M9	5.86	2.72	0.00	0.02	2.72	0.45
PC-M10	6.85	2.72	0.72	0.03	1.81	0.00
PC-M11	6.06	2.72	0.72	0.00	0.91	1.36
PC-M12	7.23	2.72	0.91	0.01	0.00	0.91
PC-M13	6.99	2.81	0.00	0.03	0.88	0.88
PC-M14	7.09	2.81	0.35	0.02	0.00	1.32
PC-M15	5.43	2.81	0.70	0.01	2.63	0.00
PC-M16	5.70	2.81	0.88	0.00	1.75	0.44

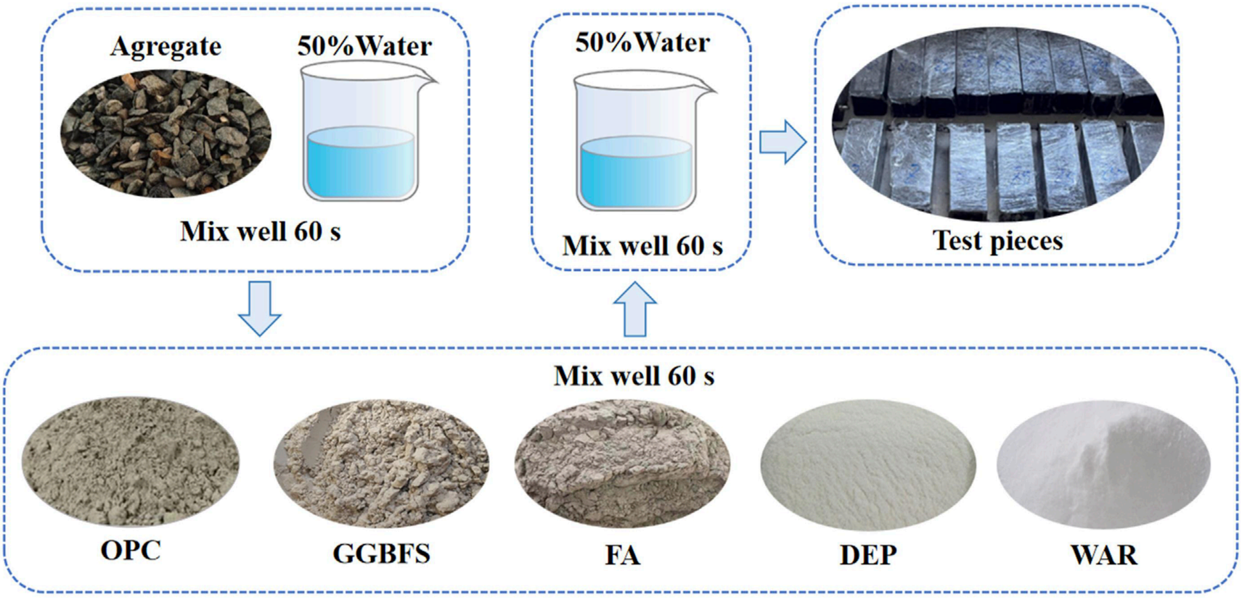

FIGURE 1
Preparation process for pervious concrete.

TABLE 7 Aggregate shape percentages.

Aggregate size	Angular aggregate	Flat aggregate	Elongated aggregate
5 ~ 10 mm	53.1%	32.3%	14.6%

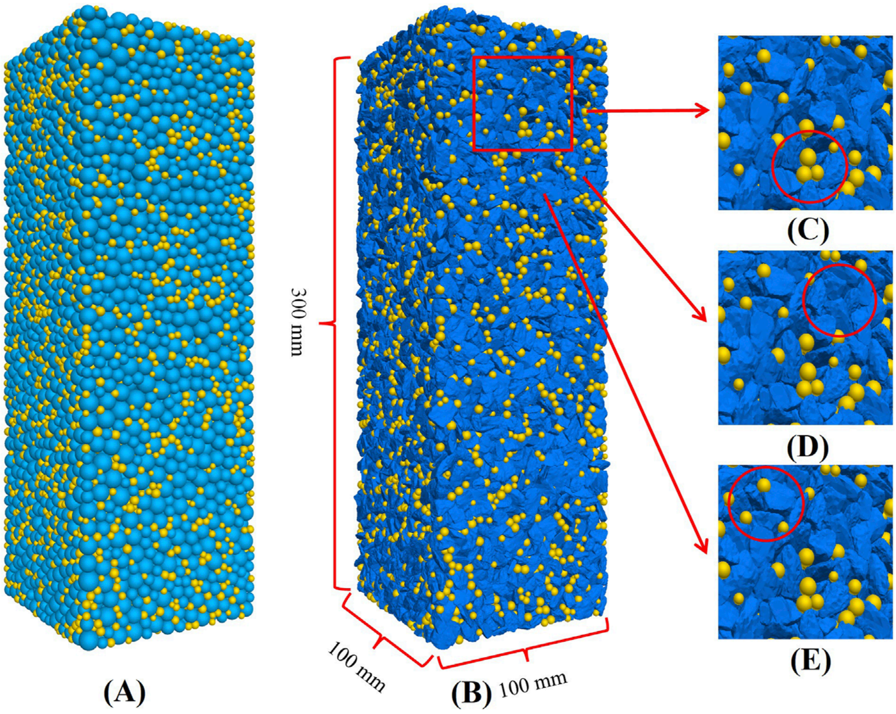

FIGURE 2
(A) Spherical model (aggregates in blue, water in yellow). **(B)** Numerical modeling of pervious concrete after conversion of spherical particles to real aggregates. **(C)** Water in contact with water. **(D)** Aggregate in contact with aggregate. **(E)** Aggregate in contact with water.

2.4.6 Freeze–thaw durability test

The FTC test conforms to the standard GB/T50082-2009 [48]. After 28 d of conventional curing, the specimens were removed from the curing room and immersed in water at 10°C ± 2°C for 4 d. After 28 d of aging, the specimens underwent rapid FTC testing (HDK9/F). The specimens each had a size of 100 mm × 100 mm × 300 mm, with three specimens in each group and 25 FTCs in each test. When the relative dynamic modulus of elasticity of a specimen decreases to 60% or the rate of loss of mass exceeds 5% or the rate of loss of strength exceeds 25%, the FTCs are stopped.

2.5 Model building

2.5.1 Realistic aggregate specimen modeling

Freeze–thaw modeling was developed using the PFC3D software. The real aggregates used in this study were sieved to determine the shapes. Based on the size of the aggregates used in the test, the aggregate model was set to resemble the shape of the real aggregate. The real aggregates were then classified into three types as angular, flat, and elongated aggregates. Table 7 displays the sieved results for each of these aggregate types.

A mold with a height of 300 mm, length of 100 mm, and width of 100 mm was constructed in PFC3D; then, aggregate and water particles were generated with a total porosity of 15%, the water particles in the total porosity were equal to 15%, and the aggregate particles had radii in the range of 2.5–5 mm. The radii of the water particles are in the range of 1.25–2.5 mm. A 3D laser scanner was used to obtain accurate external profile information from the aggregates, save this information as an STL file, and then import it into PFC3D. The corresponding aggregate model was reconstructed in PFC3D, and the rock particles were finally replaced with the actual external profiles of the aggregates. In this manner, the numerical model of pervious concrete was transformed from the sphere model to clump model, as shown in Figure 2.

Because of its high permeability, pervious concrete cannot be saturated with water in practical applications. However, mechanical deterioration occurs under repeated FTCs even if the pervious concrete is not wetted with water. Tests conducted indoors have revealed that during FTCs, the water particles expand along a few internally linked pores. Consequently, the force between the agglomerates is reduced, and the mechanical characteristics are damaged to a greater extent by the closed and microscopic pores than by the connected pores.

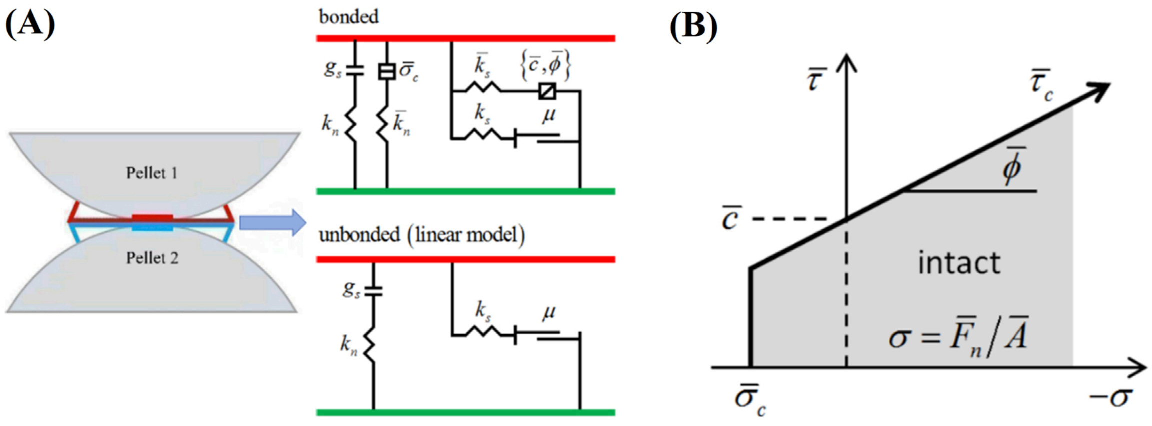

FIGURE 3
(A) Schematic diagram of the parallel bond method and its **(B)** intensity envelope.

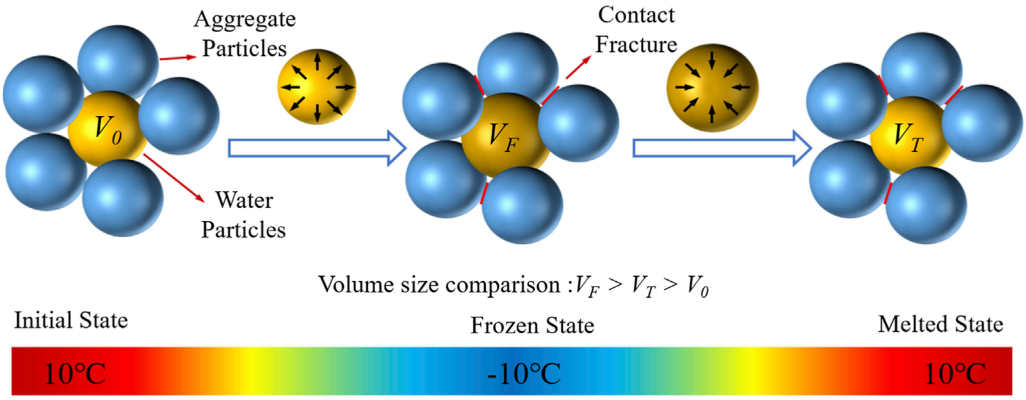

FIGURE 4
Pore water particle state changes.

2.5.2 Internal contact modeling

This model entails (1) contact between neighboring aggregate particles (aggregate–aggregate contact), (2) contact between water particles, and (3) contact between water and aggregate particles.

Using the parallel bond model (PBM), the internal contacts in pervious concrete were examined. The schematic representation of the PBM principle is displayed in Figure 3A.

When the particles are bonded, the linear and parallel bond elements cooperate to resist forces and moments. In contrast, when the bond is broken in the non-bonded state, only the linear element is active, which reduces the PBM to a linear model. The strength envelope of the PBM is depicted in Figure 3B, and the stress expressions (Equations 3, 4) as follows [49]:

$$\bar{\sigma} = \frac{\bar{F}_n}{\bar{A}} + \bar{\beta}\frac{\|\bar{M}_b\|\bar{R}}{\bar{I}} \tag{3}$$

$$\bar{\tau} = \frac{\|\bar{F}_s\|}{\bar{A}} + \bar{\beta}\frac{|\bar{M}_t|\bar{R}}{\bar{J}} \tag{4}$$

where: $\bar{F}_n$ is the normal parallel bond force; $\bar{F}_s$ is the tangential parallel bond force; $\bar{M}_t$ and $\bar{M}_b$ are the rotational and bending moments of the contact plane, respectively; $\bar{R}$ is the radius of the particle; A is the cross-sectional area; $\bar{\beta}$ is the moment contribution coefficient; $\bar{I}$ and $\bar{J}$ are the moment of inertia and polar moment of inertia, respectively. When $\bar{\sigma} \geq \bar{\sigma}_c$, tensile damage occurs and tensile cracks are produced; when $\bar{\tau} \geq \bar{\tau}_c$, shear damage occurs and shear cracks are produced.

2.5.3 FTC simulation

The pore water in the recurring water–ice phase change process that causes volume variations is often responsible for the freeze–thaw damage to pervious concrete. In the frozen state, the water becomes ice with volume expansion, resulting in a certain freezing pressure that squeezes the surrounding aggregate particles to cause interparticle cementation fracture. In the melted state, the ice becomes water and is reabsorbed into the pore space for the next freezing step. This cycling process was implemented through time step integration, with unity time step. The changes in the pore water particle states are shown in Figure 4.

TABLE 8 Compressive and flexural strength results.

Sample	WCR	DEP	WRA	FA	GGBFS	Compressive strength (MPa)	Flexural strength (MPa)
PC-M1	A1	B1	C1	D1	E1	13.61	2.3
PC-M2	A1	B2	C2	D2	E2	15.50	2.4
PC-M3	A1	B3	C3	D3	E3	19.22	2.6
PC-M4	A1	B4	C4	D4	E4	16.91	2.5
PC-M5	A2	B1	C2	D3	E4	18.32	2.6
PC-M6	A2	B2	C1	D4	E3	18.60	2.6
PC-M7	A2	B3	C4	D1	E2	27.32	3.2
PC-M8	A2	B4	C3	D2	E1	21.57	2.8
PC-M9	A3	B1	C3	D4	E2	27.07	3.2
PC-M10	A3	B2	C4	D3	E1	20.72	2.7
PC-M11	A3	B3	C1	D2	E4	16.94	2.3
PC-M12	A3	B4	C2	D1	E3	21.89	2.8
PC-M13	A4	B1	C4	D2	E3	26.70	3.1
PC-M14	A4	B2	C3	D1	E4	18.83	2.4
PC-M15	A4	B3	C2	D4	E1	15.10	2.1
PC-M16	A4	B4	C1	D3	E2	17.82	2.3

TABLE 9 Analysis of extreme differences in compressive strength.

Number	WCR	DEP	WRA	FA	GGBFS
$\overline{K_1}$	16.700	20.668	17.240	20.660	18.248
$\overline{K_2}$	21.448	18.663	18.198	20.678	22.178
$\overline{K_3}$	21.905	21.040	21.568	25.910	21.498
$\overline{K_4}$	19.863	22.545	22.910	19.668	17.993
R	5.205	2.378	5.670	1.7675	4.185

TABLE 10 Analysis of extreme differences in flexural strength.

Number	WCR	DEP	WRA	FA	GGBFS
$\overline{K_1}$	2.475	2.800	2.375	2.675	2.475
$\overline{K_2}$	2.800	2.550	2.500	2.675	2.800
$\overline{K_3}$	2.750	2.550	2.750	3.050	2.775
$\overline{K_4}$	2.475	2.600	2.875	2.600	2.450
R	0.325	0.250	0.500	0.125	0.350

The mechanical properties of pervious concrete diminish as a result of permanent freezing and thawing damage that develops inside the material after several FTCs. A water–ice particle phase-transition-coupled expansion method based on the particle discrete element is proposed from the above analysis of the freeze–thaw damage of pervious concrete. Using the particle flow procedure, the freeze–thaw cycling process of pervious concrete was simulated, and the following assumptions were made:

(1) Pervious concrete specimens were simplified to consist of natural coarse aggregate and pore water particles.
(2) Pervious concrete internal pore moisture seepage was not considered during the freeze–thaw process.
(3) Through temperature changes (warming or cooling), the pore water particles reach the target temperatures consistently. The initial volume V_0 of individual pore water particles during an FTC can be calculated using the following Equation 5:

$$V_0 = \frac{4}{3}\pi r_0^3 \tag{5}$$

TABLE 11 Permeability and porosity results.

Sample	WCR	DEP	WRA	FA	GGBFS	Effective porosity (%)	Permeability (mm/s)
PC-M1	A1	B1	C1	D1	E1	27.98	7.903
PC-M2	A1	B2	C2	D2	E2	29.64	5.653
PC-M3	A1	B3	C3	D3	E3	14.40	3.154
PC-M4	A1	B4	C4	D4	E4	25.74	6.847
PC-M5	A2	B1	C2	D3	E4	23.62	7.425
PC-M6	A2	B2	C1	D4	E3	18.98	3.245
PC-M7	A2	B3	C4	D1	E2	11.50	3.316
PC-M8	A2	B4	C3	D2	E1	15.28	4.537
PC-M9	A3	B1	C3	D4	E2	14.08	4.481
PC-M10	A3	B2	C4	D3	E1	20.86	5.395
PC-M11	A3	B3	C1	D2	E4	22.33	5.923
PC-M12	A3	B4	C2	D1	E3	14.35	4.358
PC-M13	A4	B1	C4	D2	E3	16.97	5.208
PC-M14	A4	B2	C3	D1	E4	21.54	2.932
PC-M15	A4	B3	C2	D4	E1	20.50	4.031
PC-M16	A4	B4	C1	D3	E2	18.90	3.222

TABLE 12 Analysis of extreme differences in porosity.

Number	WCR	DEP	WRA	FA	GGBFS
$\overline{K_1}$	24.44	20.66	22.05	18.84	21.16
$\overline{K_2}$	18.35	22.76	22.53	21.05	18.53
$\overline{K_3}$	17.90	17.18	16.33	19.45	16.17
$\overline{K_4}$	17.48	18.57	18.77	19.83	23.31
R	0.0710	0.0557	0.0572	0.0221	0.0713

TABLE 13 Analysis of extreme differences in permeability coefficients.

Number	WCR	DEP	WRA	FA	GGBFS
$\overline{K_1}$	5.889	6.255	5.073	4.627	5.467
$\overline{K_2}$	4.631	4.306	5.367	5.330	4.168
$\overline{K_3}$	4.039	4.106	3.776	4.799	3.991
$\overline{K_4}$	3.848	4.741	5.192	4.651	5.782
R	2.041	2.149	1.591	0.703	1.791

where r_0 is the initial radius of the water particle, and the volume V_F of individual pore water particles after phase-change freezing can be calculated using the following Equation 6:

$$V_F = \frac{4}{3}\pi(r_0 + u_v)^3 = V_0 + \triangle V_W \tag{6}$$

Here, $\triangle V_W = 4\pi\left(r_0^2 u_v + r_0 u_v + \frac{1}{3u_v^3}\right)$ is the volume change of the pore water particles after freezing; u_v is the radius expansion of the pore water particles and is calculated using the following formulas 7, 8 from [46, 50]:

$$u_v = r_0 \frac{P_i}{E_m} \frac{1 + \nu_m + 2(1 + 2\nu_m)n}{2(1 - n)} \tag{7}$$

$$p_i = \frac{0.029}{\frac{1}{E_m}\frac{1+2n+(1-4n)\nu_m}{2(1-n)} + 1.029\frac{1-2\nu_i}{E_i}} \tag{8}$$

where n is the porosity and p_i is the pore ice pressure; the modulus of elasticity and Poisson's ratio of the pore ice are represented by E_m, ν_m and E_i, ν_i, respectively.

The following expression (Equation 9) can be used to determine the volume change relationship with the unfrozen water

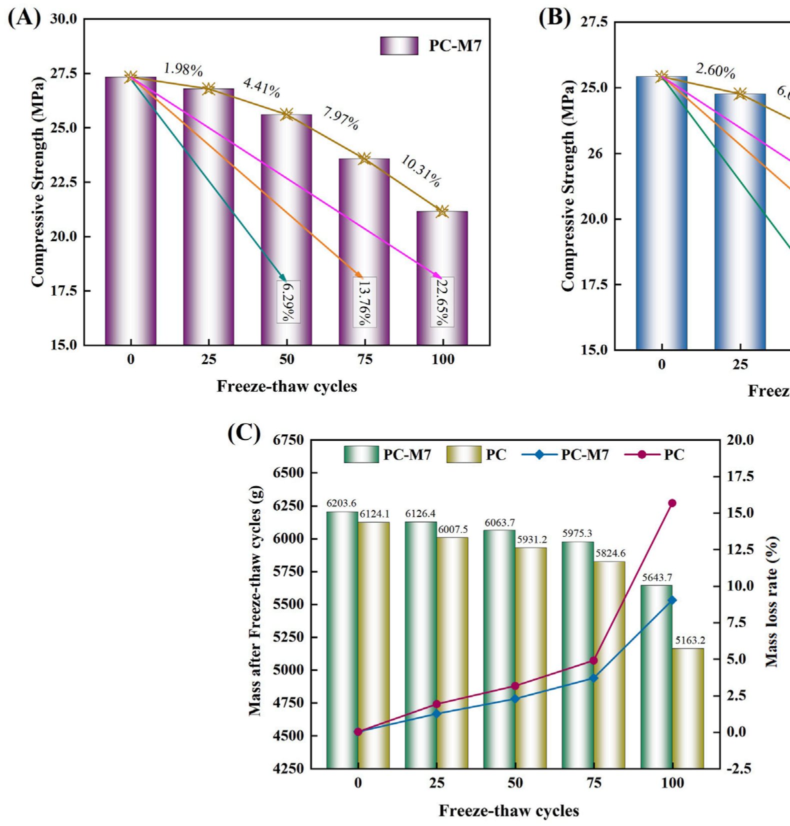

FIGURE 5
Pervious concrete freeze–thaw damage graphic following a typical curing period of 28 d: **(A, B)** compressive strength loss; **(C)** mass loss.

content during freezing and thawing of the individual pore water particles:

$$V = \begin{cases} V_0 + \triangle V_W (1 - w_u) & T \le 0°C \\ V_0 & T \ge 0°C \end{cases} \tag{9}$$

where V is the volume of pore water particles at any temperature; w_u is the unfrozen water content that can be calculated using the following Equation 10:

$$w_u = \begin{cases} 1 - \left[1 + 0.139\left(\frac{1}{\triangle T}\right)^{\frac{1}{3}} In\left(\frac{1 + e^{-0.268\triangle T}}{2}\right)\right]\left(1 - e^{-0.268\triangle T}\right) & (\triangle T > 0) \\ 1 & (\triangle T < 0) \end{cases} \tag{10}$$

where $\triangle T = T_m - T, T_m$ is the freezing point of free-body water accumulation at atmospheric pressure, which is typically equal to 273.15 K; T is the current value of the temperature measurement.

Based on the numerical computations, the pore water particles in the specimen reach the desired temperature when the designated temperature is attained by either warming or cooling. As a result, once the FTCs achieve the desired temperature, the temperature is no longer maintained constant. Thus, the relationship of temperature change with time is expressed by the following cosine function (Equation 11):

$$T = 20cos\left(\frac{\pi t}{30}\right) \tag{11}$$

3 Results and analyses

3.1 Compressive and flexural strengths

The compressive and flexural strengths of the pervious concrete specimens were measured using a universal testing machine (WAW-3000). For each group of tests, three specimens measuring 100 mm × 100 mm × 100 mm were used to determine the compressive strength, and three specimens measuring 100 mm × 100 mm × 400 mm were used to determine the flexural strength. The average value of the test was used as the result, and when the maximum and minimum values exceeded 15% of the median value, the test data were considered invalid. Table 8 shows the compressive and flexural strength results of the pervious concrete samples. The fundamental mechanical characteristics of pervious concrete can be measured using key indices, such as the compressive and flexural strengths. As shown in Table 8, the pervious concrete specimens exhibit significant variations in both compressive and flexural strengths when subjected to various influences. The maximum compressive strength among the tested pervious concrete specimens is 27.32 MPa, while the minimum compressive strength is 13.61 MPa. Similarly, the maximum flexural strength is 3.2 MPa and minimum flexural strength is 2.1 MPa.

To determine the key factors influencing the compressive and flexural strengths, an analysis using the extreme variance method is necessary. The extreme variance analysis results for the compressive

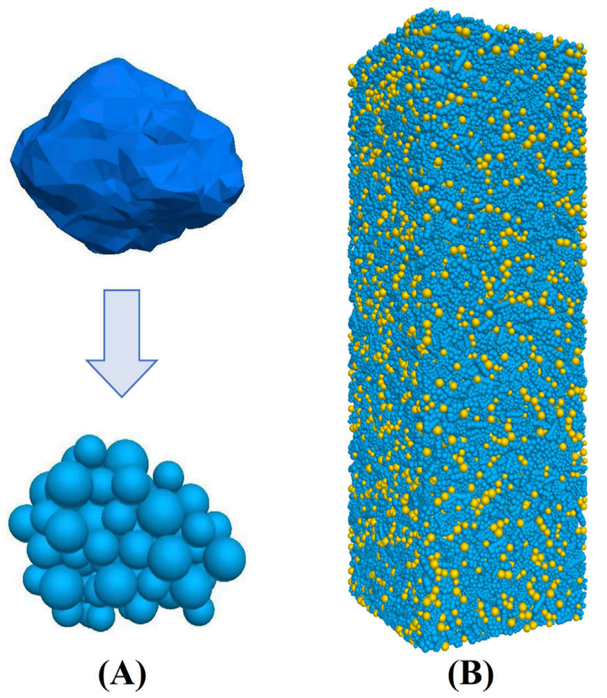

FIGURE 6
Rigid cluster model of aggregates transformed into the flexible cluster model: **(A)** conversion of single rigid rock particles to flexible rock particles; **(B)** conversion of rigid numerical model to flexible numerical model.

TABLE 14 Analysis of extreme differences in permeability coefficients.

Parallel bond model (PBM)	A-A	W-W	W-A
Elastic modulus (GPa)	4.2	4.2	3.0
Plastic modulus (GPa)	3.36	—	—
Tensile strength (MPa)	—	50	50
Cohesion (MPa)	14.5	20	20
Density (kg/m^3)	2,680	1,000	
Friction coefficient	0.70	0.01	

strength are detailed in Table 9, while the results for the flexural strength are presented in Table 10.

As illustrated in Table 9, the factors influencing the compressive strength of pervious concrete in descending order of impact are the WRA dosage, WCR, GGBFS dosage, DEP dosage, and FA dosage. In the absence of other factors or properties, the key conditions for achieving the highest compressive strength in pervious concrete are a WCR of 0.3, DEP dosage of 8%, WRA dosage of 0.3%, FA dosage of 10%, and GGBFS dosage of 5%.

As illustrated in Table 10, the factors influencing the flexural strength of pervious concrete in descending order of impact are WRA dosage, WCR, GGBFS dosage, DEP dosage, and FA dosage. The optimum flexural strength of pervious concrete can be achieved under the following conditions: WCR of 0.28, DEP dosage of 0%, WRA dosage of 0.3%, FA dosage of 20%, and GGBFS dosage of 5%.

3.2 Effective porosity and permeability

The water permeability coefficient of pervious concrete was calculated using the constant head technique, whereas the effective porosity was determined using the mass approach. To ensure accuracy, three specimens measuring 100 mm × 100 mm × 100 mm each were assessed for each group. The average of the test results was then used as the final data for each group. The measurement results of the effective porosity and water permeability coefficient are shown in Table 11.

As seen from Table 11, various factors have different degrees of influence on the effective porosity and permeability coefficient; the effective porosities of most of the specimens meet the designed porosity of 15%, while the permeability coefficients meet the specification of 0.5 mm/s. The pervious concrete specimens exhibited a minimum of 11.5% effective porosity and maximum of 29.64%; similarly, the permeability coefficient ranged from 2.932 mm/s to 7.903 mm/s. To ascertain the principal elements impacting the permeability coefficient and effective porosity of pervious concrete, an analysis was conducted using the extreme variance method. Tables 12, 13 display the results of the extreme variance analysis for effective porosity and permeability coefficient, respectively.

As illustrated in Table 12, the factors influencing the effective porosity of pervious concrete in descending order of impact are GGBFS dosage, WCR, WRA dosage, DEP dosage, and FA dosage. In the absence of other factors or properties, the optimal conditions for minimizing the effective porosity of pervious concrete are a WCR of 0.25, DEP dosage of 4%, WRA dosage of 0%, FA dosage of 10%, and GGBFS dosage of 15%.

As illustrated in Table 13, the factors influencing the permeability coefficient of pervious concrete in descending order of impact are DEP dosage, WCR, GGBFS dosage, WRA dosage, and FA dosage. The optimal conditions for achieving the best permeability coefficient for pervious concrete are a WCR of 0.25, DEP dosage of 0%, WRA dosage of 0.1%, FA dosage of 10%, and GGBFS dosage of 10%.

3.3 Freeze–thaw durability

Series 2 samples (100 mm × 100 mm × 300 mm) were prepared using the best resultant preferred proportion (PC-M7) and were subjected to freeze–thaw durability tests. Figures 5A, B, C illustrate the mass and strength losses following 28 d of freeze–thaw damage maintenance. There were no visible damages to the appearance of the pervious concrete samples after 25 FTCs, suggesting that the impact of 25 FTCs was not substantial. The strength and mass losses of the Series 2 samples after 100 FTCs were lower than those of the control pervious concrete samples (without cementitious materials).

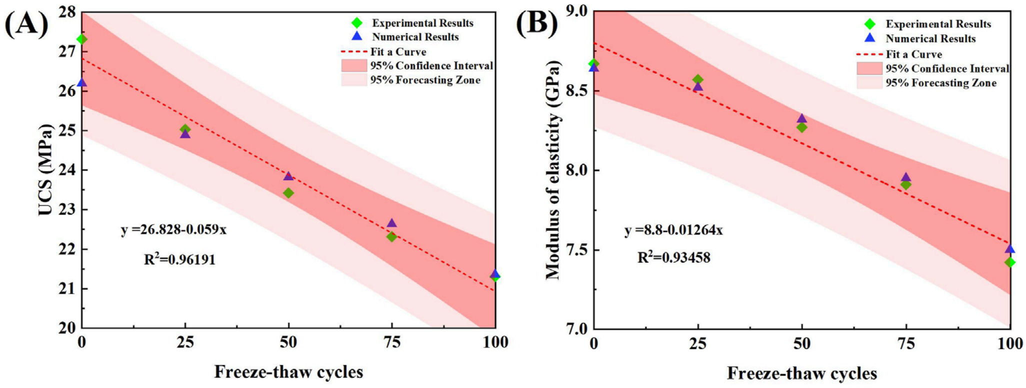

FIGURE 7
(A) Relationship between the uniaxial compressive strength (UCS) and number of freeze–thaw cycles (FTCs); **(B)** relationship between modulus of elasticity and number of FTCs.

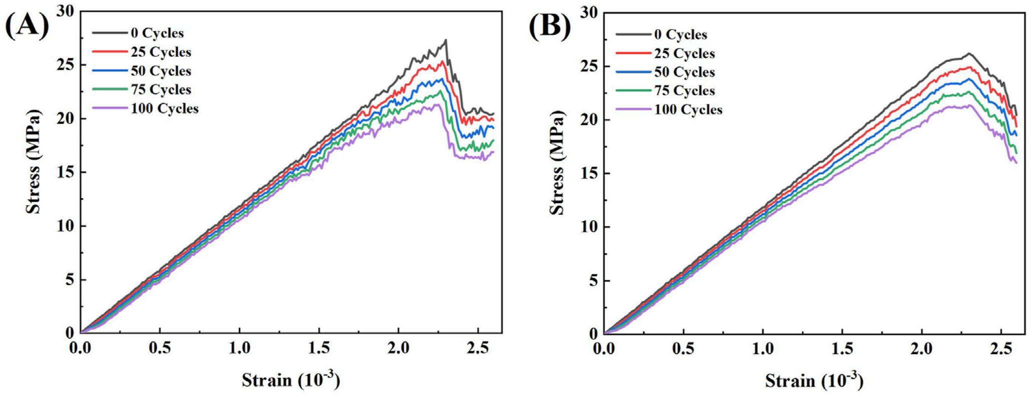

FIGURE 8
(A) Experimental and **(B)** simulation results for the stress–strain curves based on different numbers of FTCs.

4 Discrete element simulation

4.1 Validation and calibration of parameters

4.1.1 Calibration of parameters

Damage to pervious concrete is caused by a combination of the cement paste bond location between the aggregates and damage to the aggregates themselves. To replicate the actual damages to the specimens, the non-flexible clusters must be converted to flexible clusters to realize the actual fracture of the aggregates. The average radius of the discrete metaparticles generated in the ball generation command was controlled using the FISH language. To achieve a compromise between computational efficiency and accuracy, discrete unit particles with an average radius of 1.0 mm were used instead of rigid aggregate clusters in the aggregate DEM developed in this study. Figure 6 shows the generated flexible cluster model.

To reduce the complexity of parameter calibrations, the particle and parallel bond moduli as well as the particle and parallel bond stiffness ratios are usually considered equal. In addition, the actual freeze–thaw damage occurs between aggregate skeletons, so it is necessary to set the strength values of water–water interparticle bonding and aggregate–water interparticle bonding large enough to avoid affecting the results. Along with the indoor test results, the trial-and-error method was used to calibrate the fine-scale parameters, and the model fine-scale parameters were finally obtained as shown in Table 14 [36].

4.1.2 Fine-scale parameter validation

The experimental and numerical simulation results of pervious concrete samples for different numbers of FTCs are displayed in Figure 7. The dashed line in Figure 7 indicates that the UCS and modulus of elasticity of pervious concrete are negatively correlated with the number of FTCs. The stress–strain curves from the simulations and tests are essentially similar, as seen in Figure 8, suggesting that the numerical model is a superior representation of the fundamental mechanical characteristics of pervious concrete.

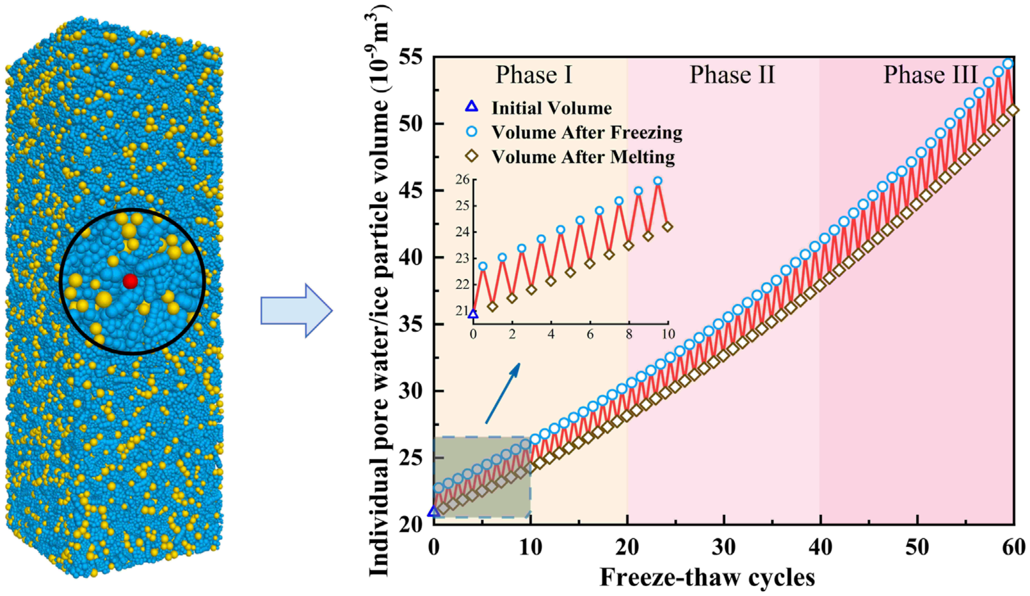

FIGURE 9
Pore water/ice particle volume changes during the FTCs.

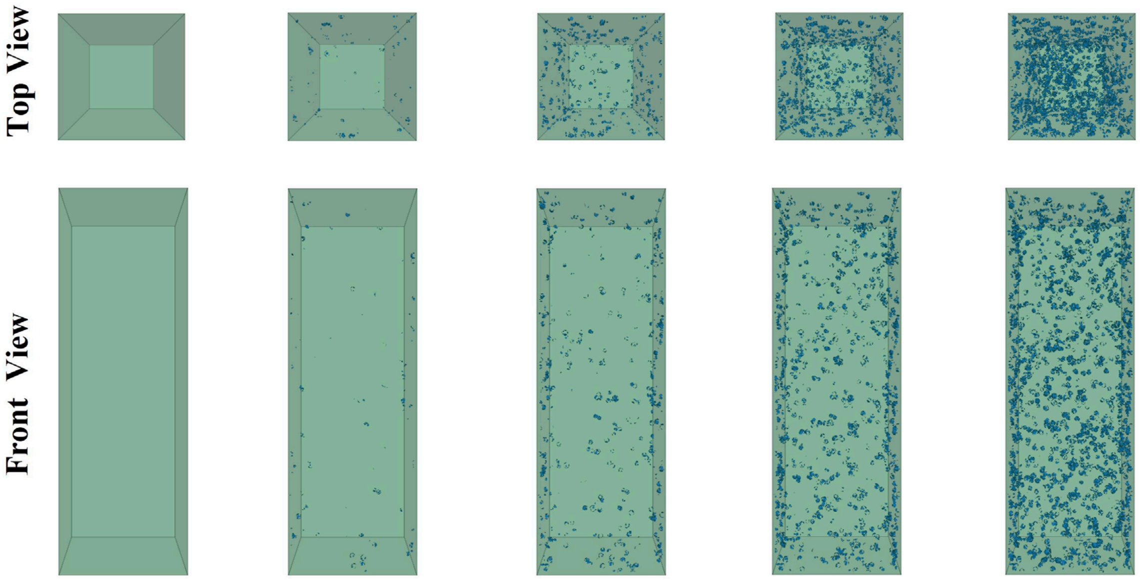

(A) 0 FTCs **(B) 25 FTCs** **(C) 50 FTCs** **(D) 75 FTCs** **(E) 100 FTCs**

FIGURE 10
Expansion process of microcracks for **(A)** 0, **(B)** 25, **(C)** 50, **(D)** 75, and **(E)** 100 FTCs.

4.2 Numerical simulations

4.2.1 Effects of FTCs on pervious concrete

The volume changes of individual water particles were calibrated during the FTC, and the changes in the volume of water particles with temperature after 60 FTCs are plotted in Figure 9; it can be seen that the amount of changes in the volume of the water particles after freezing and thawing are relatively small during the early stages, whereas these change are more obvious in the middle and later stages of freezing and thawing.

The internal pore water in the frozen state undergoes volume expansion, resulting in a freezing pressure due to pore expansion. With each FTC, the pore volume increases, allowing more water to enter during the next freeze. As a result, the volume

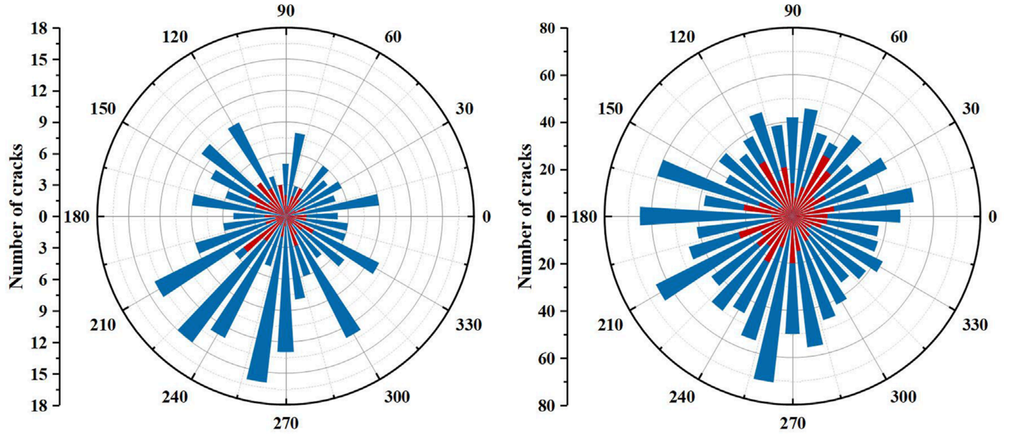

(A) 25 FTCs

(B) 50 FTCs

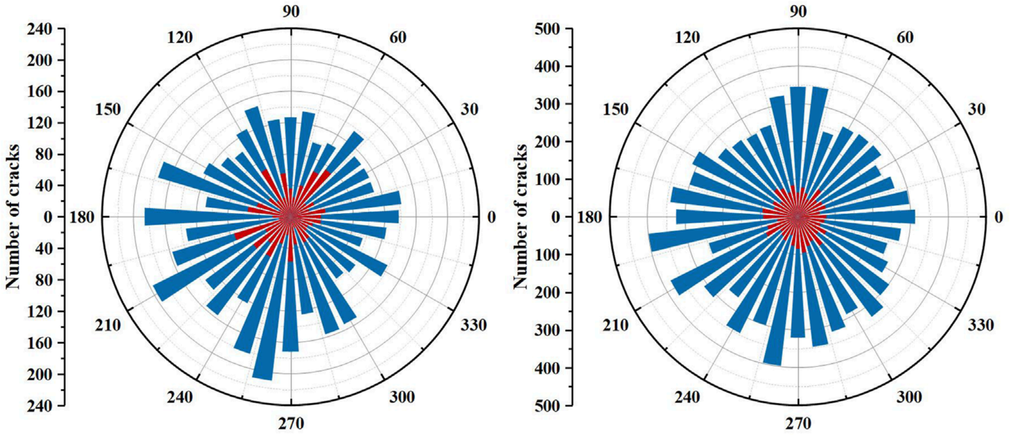

(C) 75 FTCs

(D) 100 FTCs

FIGURE 11
Crack rose diagrams for **(A)** 25, **(B)** 50, **(C)** 75, and **(D)** 100 FTCs (tensile cracks in blue, shear cracks in red).

expansion of pore water increases again, leading to the formation of microcracks. Figure 10 shows the distribution of microcracks in the internal contact fracture after every 25 FTCs, and it can be seen that microcracks are generated from the surface toward the interior.

Figure 11 shows that after 25, 50, 75, and 100 FTCs, more number of tensile microcracks are produced than shear microcracks, indicating that tensile microcracks are dominant during the freezing and thawing cycles. With the freezing and thawing cycle, the tensile microcracks gradually develop and increase in all directions mainly due to the decrease in temperature, whereby the pore water particles become ice particles and expand, causing extrusion of the surrounding rock particles. This is mainly attributable to the volume expansion of the pore water particle phase into ice particles with decrease in temperature, which results in extrusion of the surrounding rock particle skeleton. In terms of the shear microcracks, more disorder is observed while the numbers produced in the prefreezing and thawing stages are small; the development in the later stage is then relatively faster, indicating that deterioration due to damage of the specimen is more significant in the later stages of freezing and thawing.

Supplementary Figure S1 shows the distribution of cracks as well as damage to the aggregates and bond point after uniaxial compressive test of the specimens under different numbers of FTCs. From Figure 10, it can be seen that the FTCs induced cracks around the model and that the number of cracks in the permeable concrete increased abruptly with increasing numbers of FTCs, resulting in a decrease of the UCS. With increasing stress, the cracks were gradually and mostly concentrated around the freeze–thaw cracks, eventually forming the damage pattern shown in Supplementary Figure S1.The model reflects the residual strains generated and captures the cumulative damage of the pervious concrete samples below the cracks through observation of the crack formation process. The modulus of elasticity of pervious concrete decreases as the number of FTCs increases, as shown in Figure 7B. The experimental and simulated strain energies are computed by Equation 12 and the stress-strain curves shown in Figure 8.

$$U = \int \sigma d\varepsilon \tag{12}$$

where U is the strain energy density; σ is the stress; ε is the strain.

Based on the stress–strain data of the specimens for different numbers of FTCs, as shown in Figure 8A, the strain energies were calculated (Supplementary Figure S2). In the absence of FTCs, the strain energy was measured as 70.66 kJ/m^3. With increasing cycle counts, this energy reduces to 67.21 kJ/m^3 for 25 cycles, 22.64 kJ/m^3 for 50 cycles, 12.46 kJ/m^3 for 75 cycles, and 11.25 kJ/m^3 for 100 cycles, marking reductions of 6.30%, 67.96%, 82.37%, and 84.10%, respectively, compared to the absence of FTCs. As a result, the strain energies of the specimens and number of FTCs have an inverse relationship consistent with the patterns seen in UCS and changes in modulus of elasticity with increasing numbers of FTCs.

4.2.2 Impact of porosity on pervious concrete under FTC regulation

Four samples with different porosity levels (10%, 15%, 20%, and 25%) were tested through FTCs to examine the effects of porosity on pervious concrete while maintaining all other microscopic parameters constant. The results showed that samples with higher porosities were more prone to rupture, as shown in Supplementary Figure S3. This indicates that porosity has a direct effect on the mechanical properties of pervious concrete in the presence of FTCs. The axial compressive strength of pervious concrete after 50 FTCs showed that the modulus of elasticity and UCS are closely correlated with porosity. The initial UCS and modulus of elasticity are maximal at 29.86 MPa and 11.21 GPa, respectively, for pervious concrete with 10% porosity. As the porosity increased from 10% to 25%, the UCS and elastic modulus decreased gradually.

Supplementary Figure S4 illustrates the manner in which porosity directly affects the decay constants for the modulus of elasticity and UCS, indicating that porosity directly affects the performance of pervious concrete following repeated FTCs. For instance, after 50 FTCs, the UCS of pervious concrete with 10% porosity was 27.68 MPa; after 50 FTCs, the UCS dropped by 4.12% from the starting value. Following 50 FTCs, the loss rate of the UCS increased with porosity, reaching 7.16%, 12.46%, and 16.35%. The starting UCS, modulus of elasticity, decay constant, and FTC fluctuation pattern for the simulations are in agreement with the experimental findings. The is mainly because large pores are the weak points of stress transfer in pervious concrete, and higher porosity means that the stress concentration is more visible. The integrity of the specimens was severely damaged as a result of more water being pumped into the pores following the FTCs.

5 Conclusion

The present study involved various formulations of pervious concrete, with differences in the amounts of DEP, WRA, FA, and GGBFS used, for assessing the effects of FTCs and measuring the compressive strengths of the samples following a standard 28-day curing period. Next, using PFC3D as the evaluation framework, an actual aggregate model of pervious concrete was created. The damage caused by repeated FTCs to pervious concrete as well as the correlations among initial UCS, porosity, and decay constant were examined using a PBM. The following are the primary conclusions of this study:

(1) Compared to the control group, the addition of 8% DEP, 0.2% WRA, 10% FA, and 5% GGBFS to pervious concrete based on a WCR of 0.28 resulted in strength losses of 0.62%, 2.17%, 4.06%, and 5.87% after 25, 50, 75, and 100 FTCs as well as mass losses of 0.66%, 0.89%, 1.21%, and 6.66%, respectively.

(2) Using PFC3D software, models of pervious concrete were created based on actual aggregates, and the accuracies of these PBM-based models were confirmed by contrasting the outcomes of numerical simulations with experimental data. The mechanical parameters of pervious concrete were numerically calculated after 25 FTCs through uniaxial compressive tests, and the findings showed good agreement with the experimental data. These results provide reference values for practical applications.

(3) By monitoring the locations of cracks and compression failures in the broken samples and by creating a complete record of the damage process, the simulation results of the gradual damage process of pervious concrete were obtained, providing effective and feasible technical references for actual conditions.

(4) Using various porosity and starting UCS values for pervious concrete, the impact on the decay constant was examined. The modulus of elasticity and decay constant of UCS were directly correlated with porosity, suggesting that the FTCs had greater impacts on pervious concrete with higher porosities. Conversely, the initial UCS and its decay constant are inversely related. As a result, the decay constants of UCS and elastic moduli of pervious concrete can be easily calculated following an arbitrary number of FTCs by considering the initial values.

Data availability statement

The original contributions presented in this study are included in the article/Supplementary Material, and any further inquiries may be directed to the corresponding author.

Author contributions

QX: writing–original draft and writing–review and editing. BG: conceptualization, investigation, software, writing–original draft, and writing–review and editing. HD: investigation, methodology, software, supervision, and writing–review and editing. JZ: investigation, methodology, software, supervision, and writing–review and editing.

Funding

The authors declare that financial support was received for the research, authorship, and/or publication of this article. This research was sponsored by the Training Scheme for Young Backbone Teachers in Colleges and Universities in Henan Province (no. 2019-163), Excellent Teaching Case Project of Professional Degree Postgraduates in Henan Province (no. 2022-115), Scientific Research Foundation of Graduate School of Xinyang Normal University (no. 2024KYJJ107), Special Projects of Key R&D and Promotion in Xinyang City (no. 20220055), and Key Scientific and Technological Projects in Henan Province (no. 232102320196).

Conflict of interest

The authors declare that the research was conducted in the absence of any commercial or financial relationships that could be construed as a potential conflict of interest.

Publisher's note

Supplementary material

The Supplementary Material for this article can be found online at: https://www.frontiersin.org/articles/10.3389/fphy.2024.1466191/full#supplementary-material

SUPPLEMENTARY FIGURE 1
Uniaxial compression damage for different numbers of FTCs.

SUPPLEMENTARY FIGURE 2
Peak total strain energy versus number of FTCs.

SUPPLEMENTARY FIGURE 3
Relationships between the elasticity modulus, number of FTCs, and uniaxial compressive strength of the pervious concrete for different porosities.

SUPPLEMENTARY FIGURE 4
Impacts of porosity and attenuation constant on the characteristics of the pervious concrete.

References

1. Guan X, Wang J, Xiao F. Sponge city strategy and application of pavement materials in sponge city. *J Clean Prod* (2021) 303:127022. doi:10.1016/j.jclepro.2021.127022

2. Lund MS, Kevern JT, Schaefer VR, Hansen KK. Mix design for improved strength and freeze-thaw durability of pervious concrete fill in pearl-chain bridges. *Mater Structures* (2017) 50:42–15. doi:10.1617/s11527-016-0907-4

3. Bilal H, Chen T, Ren M, Gao X, Su A. Influence of silica fume, metakaolin and sbr latex on strength and durability performance of pervious concrete. *Construction Building Mater* (2021) 275:122124. doi:10.1016/j.conbuildmat.2020.122124

4. Adil G, Kevern JT, Mann D. Influence of silica fume on mechanical and durability of pervious concrete. *Construction Building Mater* (2020) 247:118453. doi:10.1016/j.conbuildmat.2020.118453

5. Zhong R, Wille K. Material design and characterization of high performance pervious concrete. *Construction Building Mater* (2015) 98:51–60. doi:10.1016/j.conbuildmat.2015.08.027

6. Bonicelli A, Giustozzi F, Crispino M. Experimental study on the effects of fine sand addition on differentially compacted pervious concrete. *Construction Building Mater* (2015) 91:102–10. doi:10.1016/j.conbuildmat.2015.05.012

7. Li H, Xu C, Dong B, Chen Q, Gu L, Yang X. Enhanced performances of cement and powder silane based waterproof mortar modified by nucleation csh seed. *Construction Building Mater* (2020) 246:118511. doi:10.1016/j.conbuildmat.2020.118511

8. Li H, Xue Z, Liang G, Wu K, Dong B, Wang W. Effect of cs-hs-pce and sodium sulfate on the hydration kinetics and mechanical properties of cement paste. *Construction Building Mater* (2021) 266:121096. doi:10.1016/j.conbuildmat.2020.121096

9. Nazeer M, Kapoor K, Singh S. Strength, durability and microstructural investigations on pervious concrete made with fly ash and silica fume as supplementary cementitious materials. *J Building Eng* (2023) 69:106275. doi:10.1016/j.jobe.2023.106275

10. Wu H, Liu Z, Sun B, Yin J. Experimental investigation on freeze–thaw durability of portland cement pervious concrete (pcpc). *Construction Building Mater* (2016) 117:63–71. doi:10.1016/j.conbuildmat.2016.04.130

11. Hesami S, Ahmadi S, Nematzadeh M. Effects of rice husk ash and fiber on mechanical properties of pervious concrete pavement. *Construction Building Mater* (2014) 53:680–91. doi:10.1016/j.conbuildmat.2013.11.070

12. Saboo N, Shivhare S, Kori KK, Chandrappa AK. Effect of fly ash and metakaolin on pervious concrete properties. *Construction Building Mater* (2019) 223:322–8. doi:10.1016/j.conbuildmat.2019.06.185

13. Qin L, Gao X, Su A, Li Q. Effect of carbonation curing on sulfate resistance of cement-coal gangue paste. *J Clean Prod* (2021) 278:123897. doi:10.1016/j.jclepro.2020.123897

14. Yang X, Liu J, Li H, Ren Q. Performance and itz of pervious concrete modified by vinyl acetate and ethylene copolymer dispersible powder. *Construction Building Mater* (2020) 235:117532. doi:10.1016/j.conbuildmat.2019.117532

15. Anderson I, Dewoolkar MM. Laboratory freezing-and-thawing durability of fly ash pervious concrete in a simulated field environment. *ACI Mater J* (2015) 112. doi:10.14359/51687921

16. Chindaprasirt P, Jaturapitakkul C, Sinsiri T. Effect of fly ash fineness on compressive strength and pore size of blended cement paste. *Cement and concrete composites* (2005) 27:425–8. doi:10.1016/j.cemconcomp.2004.07.003

17. Santos WF, Quattrone M, John VM, Angulo SC. Roughness, wettability and water absorption of water repellent treated recycled aggregates. *Construction Building Mater* (2017) 146:502–13. doi:10.1016/j.conbuildmat.2017.04.012

18. Ebrahimi K, Daiezadeh MJ, Zakertabrizi M, Zahmatkesh F, Korayem AH. A review of the impact of micro-and nanoparticles on freeze-thaw durability of hardened concrete: mechanism perspective. *Construction Building Mater* (2018) 186:1105–13. doi:10.1016/j.conbuildmat.2018.08.029

19. Vancura M, MacDonald K, Khazanovich L. Microscopic analysis of paste and aggregate distresses in pervious concrete in a wet, hard freeze climate. *Cement and Concrete Composites* (2011) 33:1080–5. doi:10.1016/j.cemconcomp.2011.05.011

20. Chen L, Li H, Guo Y, Chen P, Atroshchenko E, Lian H. Uncertainty quantification of mechanical property of piezoelectric materials based on isogeometric stochastic fem with generalized n th-order perturbation. *Eng Comput* (2024) 40:257–77. doi:10.1007/s00366-023-01788-w

21. Chen L, Lian H, Xu Y, Li S, Liu Z, Atroshchenko E, et al. Generalized isogeometric boundary element method for uncertainty analysis of time-harmonic wave propagation in infinite domains. *Appl Math Model* (2023) 114:360–78. doi:10.1016/j.apm.2022.09.030

22. Chen L, Wang Z, Lian H, Ma Y, Meng Z, Li P, et al. Reduced order isogeometric boundary element methods for cad-integrated shape optimization in electromagnetic scattering. *Computer Methods Appl Mech Eng* (2024) 419:116654. doi:10.1016/j.cma.2023.116654

23. Lund M, Hansen K, Brincker R, Jensen A, Amador S. Evaluation of freeze-thaw durability of pervious concrete by use of operational modal analysis. *Cement Concrete Res* (2018) 106:57–64. doi:10.1016/j.cemconres.2018.01.021

24. Giustozzi F. Polymer-modified pervious concrete for durable and sustainable transportation infrastructures. *Construction Building Mater* (2016) 111:502–12. doi:10.1016/j.conbuildmat.2016.02.136

25. Feng L, Zhang Y, Wang X, Mery S, Akin M, Li M, et al. Impact of deicing salts on pervious concrete pavement. *Front Mater* (2023) 10:1189114. doi:10.3389/fmats.2023.1189114

26. Sahdeo SK, Ransinchung G, Rahul K, Debbarma S. Effect of mix proportion on the structural and functional properties of pervious concrete paving mixtures. *Construction Building Mater* (2020) 255:119260. doi:10.1016/j.conbuildmat.2020.119260

27. Tsang C, Shehata MH, Lotfy A. Optimizing a test method to evaluate resistance of pervious concrete to cycles of freezing and thawing in the presence of different deicing salts. *Materials* (2016) 9:878. doi:10.3390/ma9110878

28. Nassiri S, AlShareedah O, Rodin III H, Englund K. Mechanical and durability characteristics of pervious concrete reinforced with mechanically recycled carbon fiber composite materials. *Mater Structures* (2021) 54:107. doi:10.1617/s11527-021-01708-8

29. Zou D, Wang Z, Shen M, Liu T, Zhou A. Improvement in freeze-thaw durability of recycled aggregate permeable concrete with silane modification. *Construction Building Mater* (2021) 268:121097. doi:10.1016/j.conbuildmat.2020.121097

30. Nguyen DH, Sebaibi N, Boutouil M, Leleyter L, Baraud F. A modified method for the design of pervious concrete mix. *Construction Building Mater* (2014) 73:271–82. doi:10.1016/j.conbuildmat.2014.09.088

31. Borhan TM, Al Karawi RJ. Experimental investigations on polymer modified pervious concrete. *Case Stud Construction Mater* (2020) 12:e00335. doi:10.1016/j.cscm.2020.e00335

32. AlShareedah O, Nassiri S. Spherical discrete element model for estimating the hydraulic conductivity and pore clogging of pervious concrete. *Construction Building Mater* (2021) 305:124749. doi:10.1016/j.conbuildmat.2021.124749

33. Xie C, Yuan L, Zhao M, Jia Y. Study on failure mechanism of porous concrete based on acoustic emission and discrete element method. *Construction Building Mater* (2020) 235:117409. doi:10.1016/j.conbuildmat.2019.117409

34. Xiao Q, Hu X, Li X, Zhang G, Zhao J. Study on the basic mechanical properties and discrete element method simulation of permeable concrete. *Sustainability* (2023) 15:13310. doi:10.3390/su151813310

35. Ng K, Dai Q. Numerical investigation of internal frost damage of digital cement paste samples with cohesive zone modeling and sem microstructure characterization. *Construction Building Mater* (2014) 50:266–75. doi:10.1016/j.conbuildmat.2013.09.025

36. Zhao H, Geng Q, Liu X. Influence of freeze–thaw cycles on mechanical properties of pervious concrete: from experimental studies to discrete element simulations. *Construction Building Mater* (2023) 409:133988. doi:10.1016/j.conbuildmat.2023.133988

37. Xiang J, Liu H, Lu H, Gui F. Degradation mechanism and numerical simulation of pervious concrete under salt freezing-thawing cycle. *Materials* (2022) 15:3054. doi:10.3390/ma15093054

38. Wu P, Liu Y, Peng X, Chen Z. Peridynamic modeling of freeze-thaw damage in concrete structures. *Mech Adv Mater Structures* (2023) 30:2826–37. doi:10.1080/15376494.2022.2064015

39. Xu F, Li X, Xiong Q, Li Y, Zhu J, Yang F, et al. Influence of aggregate reinforcement treatment on the performance of geopolymer recycled aggregate permeable concrete: from experimental studies to pfc 3d simulations. *Construction Building Mater* (2022) 354:129222. doi:10.1016/j.conbuildmat.2022.129222

40. Huang S, Lu Z, Ye Z, Xin Z. An elastoplastic model of frost deformation for the porous rock under freeze-thaw. *Eng Geology* (2020) 278:105820. doi:10.1016/j.enggeo.2020.105820

41. Moradllo MK, Qiao C, Ghantous RM, Zaw M, Hall H, Ley MT, et al. Quantifying the freeze-thaw performance of air-entrained concrete using the time to reach critical saturation modelling approach. *Cement and Concrete Composites* (2020) 106:103479. doi:10.1016/j.cemconcomp.2019.103479

42. Hosseinzadeh N, Montanari L, Qiao C, Suraneni P. Damage in cement pastes and mortars exposed to cacl2 and low-temperature cycles. *Mater Structures* (2022) 55:105. doi:10.1617/s11527-022-01949-1

43. Taheri BM, Ramezanianpour AM, Sabokpa S, Gapele M. Experimental evaluation of freeze-thaw durability of pervious concrete. *J building Eng* (2021) 33:101617. doi:10.1016/j.jobe.2020.101617

44. CJJ/T135-2009 (2009). *Technical specification for pervious cement concrete pavement*. China: Architecture and Building Press Beijing.

45. GB/T50081-2019 (2019). *Standard for test methods of concrete physical and mechanical properties*. China: Architecture and Building Press Beijing.

46. Zhang Y, Li H, Abdelhady A, Yang J. Comparative laboratory measurement of pervious concrete permeability using constant-head and falling-head permeameter methods. *Construction Building Mater* (2020) 263:120614. doi:10.1016/j.conbuildmat.2020.120614

47. ASTM. Standard test method for density and void content of freshly mixed pervious concrete (2014) Available from: https://www.astm.org/c1688_c1688m-14a.html (Accessed January 10, 2023).

48. GB/T50082-2009 (2009). *The test method of long-term and durability on ordinary concrete*. China: Architecture and Building Press Beijing.

49. Tomac I, Gutierrez M. Coupled hydro-thermo-mechanical modeling of hydraulic fracturing in quasi-brittle rocks using bpm-dem. *J Rock Mech Geotechnical Eng* (2017) 9:92–104. doi:10.1016/j.jrmge.2016.10.001

50. Liu Q-s., Huang S-b., Kang Y-s., Pan Y. Study of unfrozen water content and frost heave model for saturated rock under low temperature. *Chin J Rock Mech Eng* (2016) 35:2000–12. doi:10.13722/j.cnki.jrme.2015.1157

frontiers | Frontiers in Physics

TYPE Original Research
PUBLISHED 29 January 2025
DOI 10.3389/fphy.2024.1522808

OPEN ACCESS

EDITED BY
Yilin Qu,
Northwestern Polytechnical University, China

REVIEWED BY
Heng Zhang,
University of Shanghai for Science and Technology, China
Mengxi Zhang,
Tianjin University, China

*CORRESPONDENCE
Qingxiang Pei,
✉ pqx1112@163.com

RECEIVED 05 November 2024
ACCEPTED 30 December 2024
PUBLISHED 29 January 2025

CITATION
Zhang X, Ai K, Yang S, Pei Q and Lei G (2025) Acoustic interaction of submerged thin-shell structures considering seabed reflection effects.
Front. Phys. 12:1522808.
doi: 10.3389/fphy.2024.1522808

Acoustic interaction of submerged thin-shell structures considering seabed reflection effects

Xin Zhang[1], Kai Ai[2], Sen Yang[1,3], Qingxiang Pei[1,3]* and Guang Lei[1,3]

[1]Henan International Joint Laboratory of Structural Mechanics and Computational Simulation, College of Architectural and Civil Engineering, Huanghuai University, Zhumadian, China, [2]Key Laboratory of Geotechnical Mechanics and Engineering of Ministry of Water Resources, Yangtze River Scientific Research Institute, Wuhan, China, [3]College of Architecture and Civil Engineering, Xinyang Normal University, Xinyang, China

This paper presents a novel approach for simulating acoustic-shell interaction, specifically focusing on seabed reflection effects. The interaction between acoustic waves and shell vibration is crucial in various engineering applications, particularly in underwater acoustics and ocean engineering. The study employs the finite element method (FEM) with Kirchhoff-Love shell elements to numerically analyze thin-shell vibrations. The boundary element method (BEM) is applied to simulate exterior acoustic fields and seabed reflections, using half-space fundamental solutions. The FEM and BEM are coupled to model the interaction between acoustic waves and shell vibration. Furthermore, the FEM-BEM approach is implemented within an isogeometric analysis (IGA) framework, where the basis functions used for geometric modeling also discretize the physical fields. This ensures geometric exactness, eliminates meshing, and enables the use of Kirchhoff-Love shell theory with high-order continuous fields. The coupled FEM-BEM system is accelerated using the fast multipole method (FMM), which reduces computational time and memory storage. Numerical examples demonstrate the effectiveness and efficiency of the proposed algorithm in simulating acoustic-shell interaction with seabed reflection.

KEYWORDS

FEM, BEM, seabed reflection, shell vibration, acoustics

1 Introduction

The management of noise has consistently been a focal point within the field of marine engineering [1, 2]. In the realm of structural design aimed at mitigating noise emissions and reflections from marine structures, numerical simulation is of paramount importance [3, 4]. While the Finite Element Method (FEM) is highly adaptable for structural dynamics, its application in exterior acoustic scenarios is challenging [5-8]. This is because FEM requires the discretization of a vast finite region from an unbounded domain and necessitates the imposition of artificial boundary conditions using specialized techniques, which can be complex and may compromise the accuracy of the simulation. In contrast, the Boundary Element Method (BEM) is often favored for external acoustic issues as it necessitates the discretization of only the structural surfaces, which are the boundaries of the infinite acoustic domain, and inherently satisfies the boundary conditions at infinity [9-12].

Thin-shell structures submerged in water exhibit characteristics through the interplay between structural vibrations and acoustic phenomena, as referenced in various studies [13-17]. Essentially, when an acoustic wave propagates through a fluid, it has the capacity to induce vibrations in surrounding structures. These structural vibrations subsequently generate additional acoustic waves that radiate back into the fluid [18, 19]. A practical method for modeling the interaction between acoustics and shells is through the integration of FEM and BEM. This approach leverages the individual strengths of FEM and BEM in the realms of exterior acoustics, which deals with unbounded domains, and structural dynamics, respectively [20-22]. The coupling of FEM and BEM was pioneered by Everstine and Henderson for the analysis of acoustic-shell interactions [23]. Subsequent developments have expanded its application to encompass shape sensitivity analysis [24], structural optimization [25], and uncertainty quantification [26].

In numerous real-world situations, the reflection of sound waves by the seabed can exert a substantial impact on acoustic fields, particularly in the shallow-water offshore areas [27-30]. This phenomenon is known as the half-space or plane symmetrical acoustic issue [31, 32]. To address this challenge, a variety of boundary element methods that utilize mirroring techniques have been put forward by researchers such as [33, 34], and [35]. However, these methods presuppose that the acoustic waves are scattered by rigid bodies and do not account for the interaction between acoustics and structural elements.

Based on the authors' comprehensive understanding, no existing studies have yet addressed the simulation of acoustic-shell interactions in the context of seabed reflections. This research aims to bridge this gap in the literature. Pioneering an approach, this study couples BEM with half-space fundamental solutions to FEM to assess acoustic-shell interactions, thereby enabling the inclusion of seabed reflection effects. Furthermore, to enhance the computational efficiency of the BEM with half-space fundamental solutions and to minimize its memory usage, we have developed fast multipole expansions for this method.

The layout of the paper is as follows: Section 2 details the coupling scheme of FEM and BEM for simulating acoustic-shell interactions that consider seabed reflections. Section 3 elaborates on the implementation of fast multipole methods to expedite the acoustic simulation process. Section 4 presents a range of numerical examples to illustrate the approach. Finally, Section 5 concludes the paper.

2 Acoustic interaction with shells and seabed reflections

2.1 Defining the problem

Figure 1 depicts a system involving the interaction between acoustic and structural components. An elastic thin-shell occupies the region Ω_s, which is encompassed by an infinite fluid domain Ω_f. The interface where the fluid and the structure meet is denoted by Γ_{sf}, defined as the intersection of Ω_s and Ω_f. The space within the shell is occupied by air, forming the domain Ω_a. Given the significant difference in density between the air and the structural material, it is reasonable to disregard the influence of air pressure on the structural vibrations.

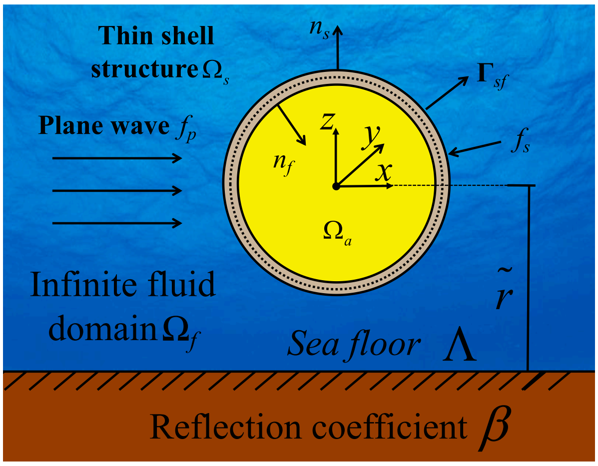

FIGURE 1
System for acoustic-structural interaction. The unit normal vector of the shell structure is denoted as $\vec{n}_s$, while that of the fluid is $\vec{n}_f$. A dashed line indicates the mid-surface of the shell structure. The pressure load from the sound field is $\vec{f}_p$, and the external mechanical load is $\vec{f}_s$.

The mechanical response of the thin-shell is defined by the Kirchhoff-Love shell theory, as detailed in references [36, 37]. Meanwhile, the acoustic fields within the fluid domain are regulated by the Helmholtz equation, which is discussed in [38-41]. The thin-shell structure is actuated by a time-varying force with an angular frequency of ω. Consequently, the equations governing the acoustic-structural interaction system are presented as Equations 1–4.

$$\nabla \cdot \boldsymbol{\sigma}(\mathbf{x}) + \omega^2 \rho_s \mathbf{u}(\mathbf{x}) = 0 \quad \mathbf{x} \in \Omega_s \tag{1}$$

$$\nabla^2 p(\mathbf{x}) + k^2 p(\mathbf{x}) = 0 \quad \mathbf{x} \in \Omega_f \tag{2}$$

$$\boldsymbol{\sigma}(\mathbf{x}) \cdot \mathbf{n}_s(\mathbf{x}) - p(\mathbf{x})\, \mathbf{n}_f(\mathbf{x}) = 0 \quad \mathbf{x} \in \Gamma_{sf} \tag{3}$$

$$-\mathrm{i}\omega \mathbf{u}(\mathbf{x}) \cdot \mathbf{n}_f(\mathbf{x}) = v_f^n(\mathbf{x}) \quad \mathbf{x} \in \Gamma_{sf} \tag{4}$$

Equations 1, 2 serve as the foundational equations that shape the configuration of acoustic fields. Equations 3, 4 delineate the conditions for continuous displacement and balanced forces at the interfaces where the fluid and structure interact. The symbol ∇ denotes the Laplacian operator, $\boldsymbol{\sigma}$ signifies the stress tensor, $\mathbf{u}$ represents the displacement vector, ρ_s is the density of the shell, $p(\mathbf{x})$ denotes the acoustic pressure, $\mathbf{n}_s$ is the outward normal vector to the shell surfaces, $\mathbf{n}_f$ is the inward normal vector to the structural surface, i is the imaginary unit with $\mathrm{i} = \sqrt{-1}$, v_f^n is the normal velocity of the fluid, and k, defined as ω/c, represents the wave number, with c being the speed of sound propagation within the fluid domain.

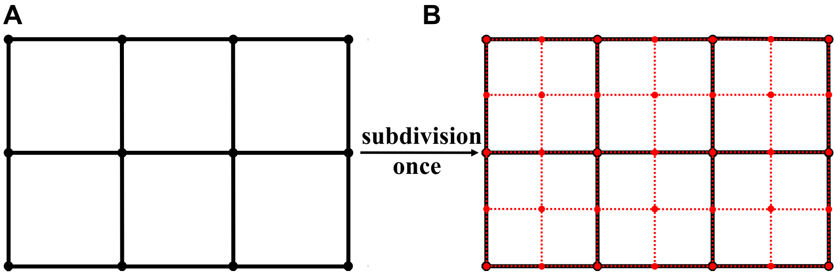

FIGURE 2
Method for generating Catmull-Clark Subdivision Surfaces. The black points represent the control points prior to subdivision, while the red points indicate the positions after subdivision has been applied. **(A)** Initial control mesh. **(B)** One level refined mesh.

2.2 Geometric modeling employing Catmull-Clark subdivision surfaces

The choice of a discretization approach or the selection of basis functions is crucial in numerical simulations. Typically, in traditional FEM and BEM, polynomial functions are the preferred choice for basis functions. In this study, we integrate FEM and BEM within the framework of isogeometric analysis (IGA), as referenced in [42-46]. This integration leverages the same basis functions used for geometric modeling to discretize the physical fields. This approach not only preserves the geometric precision but also eliminates the need for mesh generation. Most significantly, it facilitates the construction of high-order continuous fields, which is essential for the application of the Kirchhoff-Love shell theory, as further elaborated in [47].

Non-Uniform Rational B-splines (NURBS), as discussed in [48- 52], are a prevalent choice for geometric construction in Computer-Aided Design (CAD), with polygonal meshes subsequently derived for numerical analysis. In this research, we embrace the principles of isogeometric analysis, utilizing identical basis functions for both geometric modeling and numerical simulation. We opt for Catmull-Clark subdivision surfaces over NURBS for CAD model construction, as they ensure watertight geometries with support for arbitrary topologies, as described in [53].

Constructing geometry with Catmull-Clark subdivision surfaces begins with the establishment of a control mesh, which is made up of quadrilateral elements. The vertices of this mesh are known as control points. Following the initial setup, the control mesh undergoes subdivision, during which new control points are introduced and the positions of the existing ones are adjusted, as shown in Figure 2. This process of subdivision can be repeated iteratively, adhering to a set of subdivision rules that progress from level k to level $k+1$, as illustrated in Figure 3. However, since continuous subdivision is not feasible, practical implementations of limit subdivision surfaces are assessed through the use of spline basis functions for parameterization.

Subdivision surfaces excel in their capacity to manage singular points while ensuring controlled curvature at these locations. Figure 4A illustrates a regularly colored subdivision surface element, where each vertex within the element has a valence of 4, signifying the lack of extraordinary vertices within the element. A patch is delineated as a collection of all elements that share vertices with a particular target element. A regular patch is composed of nine elements featuring sixteen vertices. The element highlighted in Figure 4B contains an extraordinary vertex, which adds complexity to surface evaluation as it disrupts the tensor-product property. It should be noted that the initial grid might include irregular elements with multiple extraordinary vertices, but after subdivision, each resulting sub-element will contain at most one exceptional vertex. The evaluation of a surface point with parametric coordinates (ξ,η) is conducted through a linear combination of control points and $2\kappa+8$ basis functions, characterized by a valence of κ, as shown in Equation 5.

$$\mathbf{x}(\xi,\eta) = \sum_{\ell=0}^{2\kappa+7} \hat{N}_\ell(\xi,\eta)\,\mathbf{P}_\ell \tag{5}$$

in which $\mathbf{x}$ represents the Cartesian coordinates of the point, $\widehat{N}_\ell$ refers to the basis functions, $\mathbf{P}_\ell$ signifies the control points, and κ indicates the valence of the vertex.

2.3 Analysis of thin-shell vibrations employing IGAFEM

As previously stated, subdivision surfaces are employed for both crafting geometric models and discretizing the physical fields. The collective elements establish the boundary Γ, which is delineated by Equation 6.

$$\Gamma = \bigcup_{e=1}^{N_e} \Gamma_e \tag{6}$$

in which N_e denotes the overall count of elements, with element Γ_e signifying the e-th element. Consequently, the displacement can be articulated as follows by leveraging the basis functions associated with the Catmull-Clark subdivision, as shown in Equation 7.

$$\tilde{\mathbf{u}}^e = \sum_{\ell=0}^{2\kappa+7} \hat{N}_\ell(\xi,\eta)\,\tilde{\mathbf{u}}_\ell^e \tag{7}$$

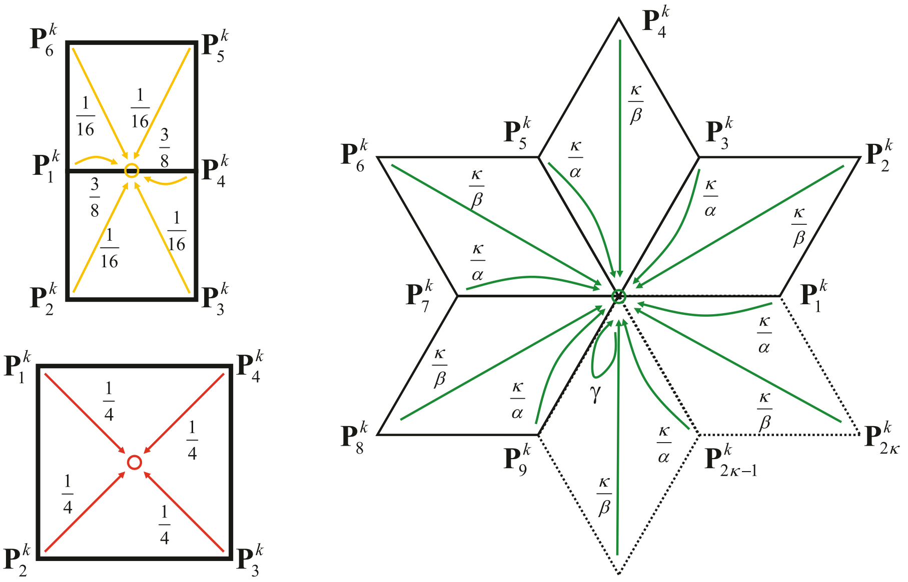

FIGURE 3
Algorithm pertaining to the topology of Catmull-Clark subdivision surfaces.

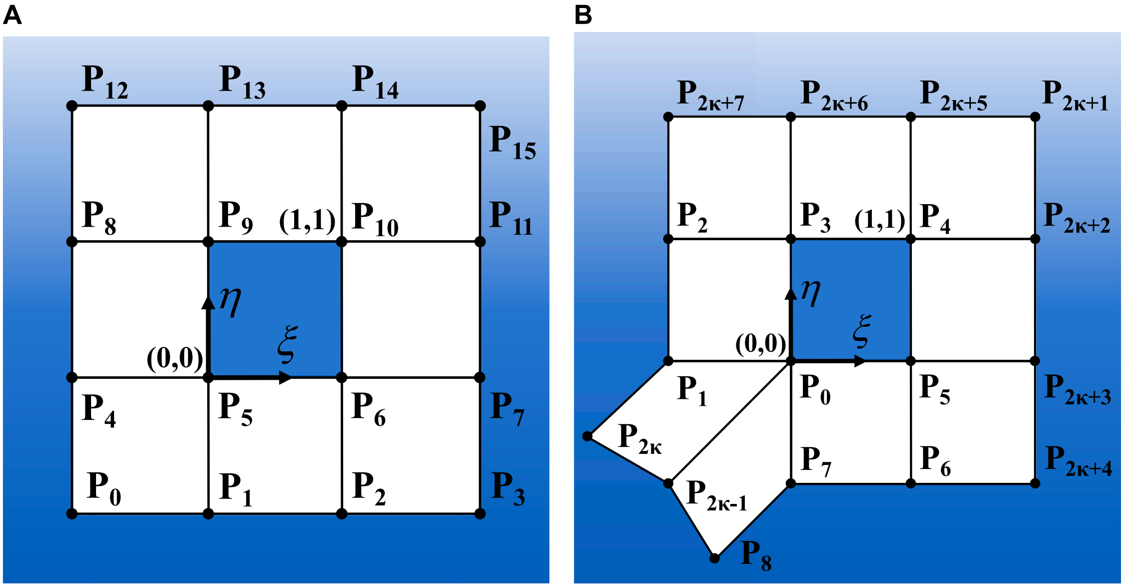

FIGURE 4
Patches associated with elements in a Catmull-Clark subdivision surface. **(A)** For a regular element. **(B)** For an irregular element.

in which $\tilde{\mathbf{u}}_{\ell}^{e}$ denotes the nodal parameter associated with the ℓ-th control point, employed for discretizing the displacements. Combining all the individual element matrices results in the subsequent Equation 8.

$$\mathbf{A}\tilde{\mathbf{u}} = \mathbf{f} \tag{8}$$

in which $\tilde{\mathbf{u}}$ represents the vector of displacements at all vertices, and $\mathbf{f}$ signifies the load vector. Furthermore, the matrix $\mathbf{A}$ can be formulated as Equation 9.

$$\mathbf{A} = \mathbf{K} - \omega^2\mathbf{M}, \quad \mathbf{K} = \bigcup_{e=1}^{N_e}\mathbf{K}^e, \quad \mathbf{M} = \bigcup_{e=1}^{N_e}\mathbf{M}^e \tag{9}$$

in which $\mathbf{K}$ signifies the global stiffness matrix of the structure, while $\mathbf{M}$ represents the global mass matrix. The element stiffness matrix is denoted by $\mathbf{K}^e$ and the element mass matrix by $\mathbf{M}^e$. It should be noted that the load vector $\mathbf{f}$ is the sum of two components, $\mathbf{f}_s$ and $\mathbf{f}_p$, where $\mathbf{f}_s$ corresponds to the external mechanical load, and $\mathbf{f}_p$ corresponds to the load due to acoustic pressure.

2.4 Analysis of acoustic phenomena employing IGABEM

Within the three-dimensional domain $\Omega \subset \mathbb{R}^3$ bounded by Γ, the propagation of acoustic waves is governed by the Helmholtz equation. This equation can be transformed into boundary integral equations. To address the issue of irregular frequencies or spurious modes in exterior acoustic scenarios, we employ the Burton-Miller formulation, which is a linear combination of the conventional boundary integral equation (CBIE) and its derivatives [54-57], as shown in Equation 10.

$$\begin{aligned} C(\mathbf{x})\, p(\mathbf{x}) + \alpha C(\mathbf{x})\, q(\mathbf{x}) = &\int_\Gamma G(\mathbf{x},\mathbf{y})\, q(\mathbf{y})\, \mathrm{d}\Gamma + \alpha \int_\Gamma \frac{\partial G(\mathbf{x},\mathbf{y})}{\partial n_f(\mathbf{x})} q(\mathbf{y})\, \mathrm{d}\Gamma \\ &- \int_\Gamma \frac{\partial G(\mathbf{x},\mathbf{y})}{\partial n_f(\mathbf{y})} p(\mathbf{y})\, \mathrm{d}\Gamma \\ &- \alpha \int_\Gamma \frac{\partial^2 G(\mathbf{x},\mathbf{y})}{\partial n_f(\mathbf{x})\, \partial n_f(\mathbf{y})} p(\mathbf{y})\, \mathrm{d}\Gamma + \tilde{p}_{\mathrm{inc}}(\mathbf{x}) \end{aligned} \tag{10}$$

in which $\mathbf{x}$ and $\mathbf{y}$ correspond to the source and field points, respectively. The term $C(\mathbf{x})$ represents the discontinuity across the boundary, which takes a value of $\frac{1}{2}$ for smooth surfaces. The coupling parameter α is given by $\frac{\mathrm{i}}{k}$ when $k > 1$, and $\alpha = \mathrm{i}$ in other cases. The quantity $q(\mathbf{y}) = \frac{\partial p(\mathbf{y})}{\partial n_f(\mathbf{y})}$ denotes the flux of sound pressure. The term $\tilde{p}_{\mathrm{inc}}(\mathbf{x}) = p_{\mathrm{inc}}(\mathbf{x}) + \frac{\partial p_{\mathrm{inc}}(\mathbf{x})}{\partial n_f(\mathbf{x})}$ encompasses both the incident wave's sound pressure and its normal derivative at point $\mathbf{x}$, with $p_{\mathrm{inc}}(\mathbf{x})$ being the incident wave's sound pressure at that location. The functions $G(\mathbf{x},\mathbf{y})$ and its normal derivative for three-dimensional full-space acoustics are specified as Equations 11, 12.

$$G(\mathbf{x},\mathbf{y}) = \frac{\mathrm{e}^{\mathrm{i}kr}}{4\pi r} \tag{11}$$

$$\frac{\partial G(\mathbf{x},\mathbf{y})}{\partial n_f(\mathbf{y})} = -\frac{\mathrm{e}^{\mathrm{i}kr}}{4\pi r^2} (1 - \mathrm{i}kr) \frac{\partial r}{\partial n_f(\mathbf{y})} \tag{12}$$

in which $r = |\mathbf{x} - \mathbf{y}|$. The fundamental solution for half-space problems is represented by $G^*(\mathbf{x},\mathbf{y})$, as shown in Equation 13.

$$G^*(\mathbf{x},\mathbf{y}) = G(\mathbf{x},\mathbf{y}) + \beta G(\mathbf{x}^*,\mathbf{y}) \tag{13}$$

in which $\mathbf{x}^*$ denotes the reflection of point $\mathbf{x}$ across the infinite plane Γ_h, and β signifies the reflection coefficient. The coefficient β equals one for a rigid boundary and -1 for a soft boundary. By replacing $G(\mathbf{x},\mathbf{y})$ with $G^*(\mathbf{x},\mathbf{y})$, Equation 10 is converted into Equation 14.

$$\begin{aligned} C(\mathbf{x})\, p(\mathbf{x}) + \alpha C(\mathbf{x})\, q(\mathbf{x}) = &\int_\Gamma G^*(\mathbf{x},\mathbf{y})\, q(\mathbf{y})\, \mathrm{d}\Gamma + \alpha \int_\Gamma \frac{\partial G^*(\mathbf{x},\mathbf{y})}{\partial n_f(\mathbf{x})} q(\mathbf{y})\, \mathrm{d}\Gamma \\ &- \int_\Gamma \frac{\partial G^*(\mathbf{x},\mathbf{y})}{\partial n_f(\mathbf{y})} p(\mathbf{y})\, \mathrm{d}\Gamma \\ &- \alpha \int_\Gamma \frac{\partial^2 G^*(\mathbf{x},\mathbf{y})}{\partial n_f(\mathbf{x})\, \partial n_f(\mathbf{y})} p(\mathbf{y})\, \mathrm{d}\Gamma + \tilde{p}^*_{\mathrm{inc}}(\mathbf{x}) \end{aligned} \tag{14}$$

in which $\tilde{p}^*_{\mathrm{inc}}(\mathbf{x}) = p^*_{\mathrm{inc}}(\mathbf{x}) + \frac{\partial p^*_{\mathrm{inc}}(\mathbf{x})}{\partial n_f(\mathbf{x})}$, and the partial derivative of $G^*(x,y)$ is shown in Equations 15–17.

$$\frac{\partial G^*(\mathbf{x},\mathbf{y})}{\partial n_f(\mathbf{y})} = -\frac{\mathrm{e}^{\mathrm{i}kr}}{4\pi r^2} (1 - \mathrm{i}kr) \frac{\partial r}{\partial n_f(\mathbf{y})} - \beta \frac{\mathrm{e}^{\mathrm{i}kr^*}}{4\pi (r^*)^2} (1 - \mathrm{i}kr^*) \frac{\partial r^*}{\partial n_f(\mathbf{y})} \tag{15}$$

$$\frac{\partial G^*(\mathbf{x},\mathbf{y})}{\partial n_f(\mathbf{x})} = -\frac{\mathrm{e}^{\mathrm{i}kr}}{4\pi r^2} (1 - \mathrm{i}kr) \frac{\partial r}{\partial n_f(\mathbf{x})} - \beta \frac{\mathrm{e}^{\mathrm{i}kr^*}}{4\pi (r^*)^2} (1 - \mathrm{i}kr^*) \frac{\partial r^*}{\partial n_f(\mathbf{x})} \tag{16}$$

$$\begin{aligned} \frac{\partial^2 G^*(\mathbf{x},\mathbf{y})}{\partial n_f(\mathbf{x})\, \partial n_f(\mathbf{y})} = &\frac{\mathrm{e}^{\mathrm{i}kr}}{4\pi r^3} \left[\left(3 - 3\mathrm{i}kr - k^2 r^2\right) \frac{\partial r}{\partial n_f(\mathbf{y})} \frac{\partial r}{\partial n_f(\mathbf{x})} + (1 - \mathrm{i}kr)\, n_i(\mathbf{x})\, n_i(\mathbf{y}) \right] \\ &+ \beta \frac{\mathrm{e}^{\mathrm{i}kr^*}}{4\pi (r^*)^3} \left[\left(3 - 3\mathrm{i}kr^* - k^2 (r^*)^2\right) \frac{\partial r}{\partial n_f(\mathbf{y})} \frac{\partial r}{\partial n_f(\mathbf{x})} \right. \\ &\left. + (1 - \mathrm{i}kr^*)\, n_i(\mathbf{x})\, n_i(\mathbf{y}) \right] \end{aligned} \tag{17}$$

In this approach, the physical field is discretized using the basis functions of the subdivision surface that are employed in the geometric construction, as displayed in Equation 18.

$$\begin{aligned} p_e &= \sum_{\ell=0}^{2\kappa+7} \hat{N}_\ell(\xi,\eta)\, \tilde{p}^e_\ell \\ q_e &= \sum_{\ell=0}^{2\kappa+7} \hat{N}_\ell(\xi,\eta)\, \tilde{q}^e_\ell \end{aligned} \tag{18}$$

in which p_e represents the acoustic pressure at the point (ξ,η) within the element Γ_e; q_e signifies the normal flux associated with p_e. Additionally, $\tilde{p}^e_\ell$ refers to the ℓ-th nodal variable associated with the sound pressure, while $\tilde{q}^e_\ell$ represents the normal flux corresponding to $\tilde{p}^e_\ell$. By inserting Equation 18 into Equation 14 and applying these equations at a discrete set of collocation points $\mathbf{x}_j$, Equation 19 can be derived.

$$\begin{aligned} &C(\mathbf{x}_j)\, p(\mathbf{x}_j) + \alpha C(\mathbf{x}_j)\, q(\mathbf{x}_j) + \sum_{e=1}^{N_e} \sum_{\ell=0}^{2\kappa+7} \int_{\Gamma_e} \hat{N}_\ell(\xi,\eta) \frac{\partial G^*\left(\mathbf{x}_j, \mathbf{y}(\xi,\eta)\right)}{\partial n_f(\mathbf{y}(\xi,\eta))} \mathrm{d}\Gamma \tilde{p}^e_\ell \\ &+ \alpha \sum_{e=1}^{N_e} \sum_{\ell=0}^{2\kappa+7} \int_{\Gamma_e} \hat{N}_\ell(\xi,\eta) \frac{\partial^2 G^*\left(\mathbf{x}_j, \mathbf{y}(\xi,\eta)\right)}{\partial n_f(\mathbf{x}_j)\, \partial n_f(\mathbf{y}(\xi,\eta))} \mathrm{d}\Gamma \tilde{p}^e_\ell \\ &= \sum_{e=1}^{N_e} \sum_{\ell=0}^{2\kappa+7} \int_{\Gamma_e} \hat{N}_\ell(\xi,\eta)\, G^*\left(\mathbf{x}_j, \mathbf{y}(\xi,\eta)\right) \mathrm{d}\Gamma \tilde{q}^e_\ell \\ &+ \alpha \sum_{e=1}^{N_e} \sum_{\ell=0}^{2\kappa+7} \int_{\Gamma_e} \hat{N}_\ell(\xi,\eta) \frac{\partial G^*\left(\mathbf{x}_j, \mathbf{y}(\xi,\eta)\right)}{\partial n_f(\mathbf{x}_j)} \mathrm{d}\Gamma \tilde{q}^e_\ell + \tilde{p}^*_{\mathrm{inc}}(\mathbf{x}_j) \end{aligned} \tag{19}$$

in which the subscript j indicates the index of the collocation point. These collocation points are determined by projecting the control points onto the surface. Equation 19 can be expressed in matrix-vector form as Equation 20.

$$\mathbf{H}\tilde{\mathbf{p}} = \mathbf{G}\tilde{\mathbf{q}} + \mathbf{p_i} \tag{20}$$

in whichn $\mathbf{H}$ and $\mathbf{G}$ are the matrices of coefficients, while $\tilde{\mathbf{p}}$ and $\tilde{\mathbf{q}}$ are the column vectors that compile the nodal parameters related to the acoustic pressure and its flux, respectively. $\mathbf{p_i}$ signifies the nodal pressure vector attributed to the incident wave. It is crucial to address the singular integrals present in Equation 10. Numerous methods have been proposed to handle these singular integrals within BEM, as cited in [58-61]. This research adopts the singularity subtraction technique introduced by Guiggiani, recognized for its precision and efficiency, as detailed in [62].

2.5 Integration of IGAFEM and IGABEM

Equations 8, 20, originating from the structure (using FEM) and the acoustic (using BEM) respectively, are tightly interlinked and cannot be resolved in isolation. They are interconnected through the boundary conditions outlined in Equations 3, 4. The sound pressure within the fluid domain can be perceived as a force exerted on the shell surface. Consequently, the nodal force vector $\mathbf{f}_p$ due to the acoustic load can be formulated as Equation 21.

$$\mathbf{f}_p = \tilde{\mathbf{n}}_f \Theta \tilde{\mathbf{p}} \tag{21}$$

in which Θ is defined as the integral over the boundary Γ of the product of the transpose of the subdivision basis functions' global vector $\hat{N}_\ell$ and $\hat{N}_\ell$ itself, multiplied by $d\Gamma$. The vector $\hat{N}_\ell$ denotes the global vector of subdivision basis functions, and $\tilde{\mathbf{n}}_f$ represents the matrix of normal vectors, which is given by Equation 22.

$$\tilde{\mathbf{n}}_f = \begin{Bmatrix} n_{1f}\cdot e_1 & 0 & \cdots \\ n_{1f}\cdot e_2 & 0 & \cdots \\ n_{1f}\cdot e_3 & 0 & \cdots \\ 0 & n_{2f}\cdot e_1 & \cdots \\ 0 & n_{2f}\cdot e_2 & \cdots \\ 0 & n_{2f}\cdot e_3 & \cdots \\ \cdots & \cdots & \cdots \end{Bmatrix} \tag{22}$$

in which e_1, e_2, e_3 denote the three unit normal vectors. By applying Equation 21, we can derive a new expression for the global nodal force vector, which is presented in Equation 23.

$$\mathbf{f} = \mathbf{C}_{sf}\tilde{\mathbf{p}} + \mathbf{f}_s \tag{23}$$

in which $\mathbf{C}_{sf} = \tilde{\mathbf{n}}_f \Theta$.

Next, we will investigate the relationship between the velocities on the shell's mid-surface and the sound pressure. The vector $\mathbf{v}_f^n$ represents the nodal parameters related to the fluid's normal velocity component, while the vector $\mathbf{v}_s^n$ signifies the nodal variables associated with the normal velocity component of the structure. Assuming no energy dissipation occurs at the interface between the fluid and structural domains, we get Equation 24.

$$\mathbf{v}_f^n - \mathbf{v}_s^n = 0 \tag{24}$$

in which $\mathbf{v}_s^n = \mathrm{i}\omega \mathbf{C}_{fs}\tilde{\mathbf{u}}$, and $\mathbf{C}_{fs} = \tilde{\mathbf{n}}_f^{\mathrm{T}}$. Subsequently, the vector $\tilde{\mathbf{q}}$, encompassing the nodal parameters related to the acoustic flux, can be formulated as Equation 25.

$$\tilde{\mathbf{q}} = \frac{\partial \tilde{\mathbf{p}}}{\partial n} = -\mathrm{i}\omega\rho_f \mathbf{v}_f^n = \omega^2 \rho_f \mathbf{C}_{fs}\tilde{\mathbf{u}} \tag{25}$$

in which ρ_f represents the fluid's density.

By inserting Equation 25 into Equation 20, we obtain the following coupled system of equations for the acoustics, as shown in Equation 26.

$$\mathbf{H}\tilde{\mathbf{p}} = \mathbf{G}\omega^2 \rho_f \mathbf{C}_{fs}\tilde{\mathbf{u}} + \mathbf{p}_\mathbf{i} \tag{26}$$

Incorporating Equation 23 into Equation 8 yields the following coupled system of equations for structural dynamics shown in Equation 27.

$$\mathbf{A}\tilde{\mathbf{u}} = \mathbf{C}_{sf}\tilde{\mathbf{p}} + \mathbf{f}_s \tag{27}$$

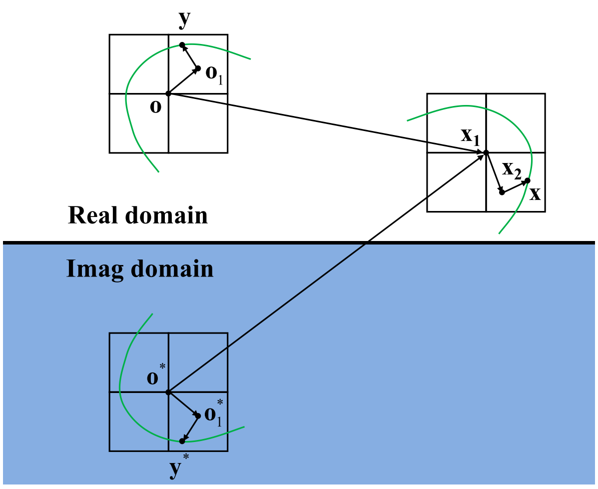

FIGURE 5
Nodes at the boundary and the points for multipole expansion in the half-space Fast Multipole Method (FMM).

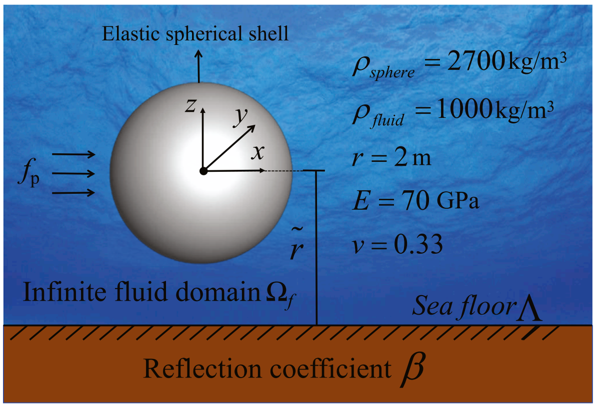

FIGURE 6
System for acoustic-structural interaction involving elastic spherical shells.

By integrating Equation 27 into Equation 26, the indeterminate displacement $\tilde{\mathbf{u}}$ is eliminated, leading to a boundary element formulation that is linked with the finite element equation, as shown in Equation 28.

$$[\mathbf{H} - \mathbf{G}\mathbf{Y}]\,\tilde{\mathbf{p}} = \mathbf{G}\tilde{\mathbf{q}}_s + \mathbf{p}_\mathbf{i} \tag{28}$$

in which $\mathbf{Y}$ denotes the global admittance matrix, and $\tilde{\mathbf{q}}_s$ accounts for the influence of sound speeds originating from the structural domain. These are given by Equation 29.

$$\begin{gathered} \mathbf{Y} = \omega^2 \rho_f \mathbf{C}_{fs}\mathbf{A}^{-1}\mathbf{C}_{sf} \\ \tilde{\mathbf{q}}_s = \omega^2 \rho_f \mathbf{C}_{fs}\mathbf{A}^{-1}\mathbf{f}_s \end{gathered} \tag{29}$$

3 Enhancing computation speed with the fast multipole method

The Fast Multipole Method (FMM) is a highly efficient algorithm designed to accelerate the computation of long-range

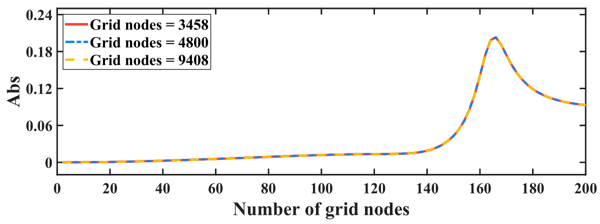

FIGURE 7
The numerical results of the sphere model are verified in the convergence of three mesh node numbers.

interactions in N-body problems. Introduced by [63], FMM reduces the computational complexity from $\mathcal{O}(N^2)$ to $\mathcal{O}(N)$ or $\mathcal{O}(N\log N)$, depending on the implementation. This significant improvement is achieved through hierarchical space decomposition and the use of multipole and local expansions, which approximate interactions between distant clusters of particles. The fundamental solution for the full-space, as introduced in Equation 11, is expanded into the following series shown in Equation 30.

$$G(\mathbf{x},\mathbf{y}) = \frac{ik}{4\pi}\sum_{n=0}^{\infty}\sum_{m=-n}^{n}(2n+1)\,\bar{\mathbf{I}}_n^m(k,\overrightarrow{\mathbf{oy}})\,\mathbf{O}_n^m(k,\overrightarrow{\mathbf{ox}}) \tag{30}$$

in which $\mathbf{O}$ serves as a local expansion point in proximity to $\mathbf{y}$, as shown in Figure 5. The terms $\mathbf{I}_n^m$ and $\mathbf{O}_n^m$ are defined as Equations 31, 32.

$$\mathbf{I}_n^m(k,a) = j_n(kr)\,\mathbf{Y}_n^m(\theta,\phi) \tag{31}$$

$$\mathbf{O}_n^m(k,a) = h_n^{(1)}(kr)\,\mathbf{Y}_n^m(\theta,\phi) \tag{32}$$

The terms $\bar{\mathbf{I}}_n^m$ represent the complex conjugates of $\mathbf{I}_n^m$. The functions j_n and $h_n^{(1)}$ correspond to the n-th order spherical Bessel and Hankel functions of the first kind, respectively, as detailed in [64]. The spherical harmonics are denoted by $\mathbf{Y}_n^m$, which are given by Equation 33.

$$\mathbf{Y}_n^m(\theta,\phi) = c_n^m\mathbf{P}_n^m(\cos\theta)\,e^{im\phi} \tag{33}$$

in which $c_n^m = \sqrt{\frac{(n-m)!}{(n+m)!}}$ and $\mathbf{P}_n^m$ refers to the associated Legendre functions.

To derive a Fast Multipole Method (FMM) scheme tailored for a half-space acoustic problem, we modify the fundamental solution for the half-space into the following form in Equation 34.

$$G^*(\mathbf{x},\mathbf{y}) = G(\mathbf{x},\mathbf{y}) + \beta G(\mathbf{x},\mathbf{y}^*) \tag{34}$$

Subsequently, the boundary integral for the j-th element in Equation 28 can be re-expressed as Equations 35, 36.

$$g^{ij} = \int_{\Gamma_j} G(\mathbf{x},\mathbf{y}) + \beta G(\mathbf{x},\mathbf{y}^*)]\,q(\mathbf{y})\,d\Gamma(\mathbf{y}) \tag{35}$$

$$h^{ij} = \int_{\Gamma_j}\left[\frac{\partial G(\mathbf{x},\mathbf{y})}{\partial n_f(\mathbf{y})} + \beta\frac{\partial G(\mathbf{x},\mathbf{y}^*)}{\partial n_f(\mathbf{y})}\right]p(\mathbf{y})\,d\Gamma(\mathbf{y}) \tag{36}$$

Consequently, employing Equation 13, we can express the boundary integrals over a boundary element Γ_j that is situated at a distance from the source point $\mathbf{x}$ in the following manner in Equations 37, 38.

$$\begin{aligned} g^{ij} = \frac{ik}{4\pi}\sum_{n=0}^{\infty}\sum_{m=-n}^{n}(2n+1)\Big[&\mathbf{M}_n^m\left(k,\overrightarrow{\mathbf{oy}_j}\right)\mathbf{O}_n^m(k,\overrightarrow{\mathbf{ox}}) \\ &+\beta\mathbf{M}_n^m\left(k,\overrightarrow{\mathbf{o}^*\mathbf{y}_j^*}\right)\mathbf{O}_n^m(k,\overrightarrow{\mathbf{o}^*\mathbf{x}})\Big] \end{aligned} \tag{37}$$

$$\begin{aligned} h^{ij} = \frac{ik}{4\pi}\sum_{n=0}^{\infty}\sum_{m=-n}^{n}(2n+1)\Big[&\tilde{\mathbf{M}}_n^m\left(k,\overrightarrow{\mathbf{oy}_j}\right)\mathbf{O}_n^m(k,\overrightarrow{\mathbf{ox}}) \\ &+\beta\tilde{\mathbf{M}}_n^m\left(k,\overrightarrow{\mathbf{o}^*\mathbf{y}_j^*}\right)\mathbf{O}_n^m(k,\overrightarrow{\mathbf{o}^*\mathbf{x}})\Big] \end{aligned} \tag{38}$$

in which $\mathbf{y}_j$ denotes a field point on Γ_j; $\mathbf{M}_n^m(k,\overrightarrow{\mathbf{oy}_j})$ and $\tilde{\mathbf{M}}_n^m(k,\overrightarrow{\mathbf{oy}_j})$ are the multipole moments of the low-frequency FMM techniques in the real domain, respectively, and are defined as Equations 39, 40.

$$\mathbf{M}_n^m\left(k,\overrightarrow{\mathbf{oy}_j}\right) = \int_{\Gamma_j}\bar{\mathbf{I}}_n^m\left(k,\overrightarrow{\mathbf{oy}_j}\right)q(\mathbf{y})\,d\Gamma(\mathbf{y}) \tag{39}$$

$$\tilde{\mathbf{M}}_n^m\left(k,\overrightarrow{\mathbf{oy}_j}\right) = \int_{\Gamma_j}\frac{\partial\bar{\mathbf{I}}_n^m\left(k,\overrightarrow{\mathbf{oy}_j}\right)}{\partial n(\mathbf{y})}p(\mathbf{y})\,d\Gamma(\mathbf{y}) \tag{40}$$

By replacing $\mathbf{o}$ and $\mathbf{y}_j$ with $\mathbf{o}^*$ and $\mathbf{y}_j^*$ in Equations 39, 40, we obtain the expressions for $\mathbf{M}_n^m(k,\overrightarrow{\mathbf{o}^*\mathbf{y}_j^*})$ and $\tilde{\mathbf{M}}_n^m(k,\overrightarrow{\mathbf{o}^*\mathbf{y}_j^*})$ as presented in Equations 37, 38, respectively. To determine the moments of the leaf cell, we aggregate the multipole moments from N_l boundary elements in the vicinity of point $\mathbf{o}$, as shown in Equations 41–44.

$$\mathbf{M}_n^m(k,\mathbf{o}) = \sum_{j=1}^{N_l}\mathbf{M}_n^m\left(k,\overrightarrow{\mathbf{oy}_j}\right) \tag{41}$$

$$\mathbf{M}_n^m(k,\mathbf{o}^*) = \sum_{j=1}^{N_l}\mathbf{M}_n^m\left(k,\overrightarrow{\mathbf{o}^*\mathbf{y}_j^*}\right) \tag{42}$$

$$\tilde{\mathbf{M}}_n^m(k,\mathbf{o}) = \sum_{j=1}^{N_l}\tilde{\mathbf{M}}_n^m\left(k,\overrightarrow{\mathbf{oy}_j}\right) \tag{43}$$

$$\tilde{\mathbf{M}}_n^m(k,\mathbf{o}^*) = \sum_{j=1}^{N_l}\tilde{\mathbf{M}}_n^m\left(k,\overrightarrow{\mathbf{o}^*\mathbf{y}_j^*}\right) \tag{44}$$

When $|\mathbf{o}_1\mathbf{x}| > |\mathbf{o}_1\mathbf{y}|$ and $|\mathbf{o}_1^*\mathbf{x}| > |\mathbf{o}_1^*\mathbf{y}^*|$, the low-frequency Fast Multipole Method (FMM) facilitates the relocation of the moment center from $\mathbf{o}$ and $\mathbf{o}^*$ to $\mathbf{o}_1$ and $\mathbf{o}_1^*$ using the M2M (moments to moments) translation formula, which is expressed as Equations 45, 46.

$$\begin{aligned} \mathbf{M}_n^m(k,\mathbf{o}_1) = \sum_{n_1=0}^{\infty}\sum_{m_1=-n_1}^{n_1}\sum_{l\in\mathfrak{I}}(2n_1+1) \\ -1^{m_1}W_{n,n_1,m,m_1,l}\times I_l^{-m-m_1}(k,\overrightarrow{\mathbf{o_1o}}) \end{aligned} \tag{45}$$

$$\begin{aligned} \mathbf{M}_n^m(k,\mathbf{o}_1^*) = \sum_{n_1=0}^{\infty}\sum_{m_1=-n_1}^{n_1}\sum_{l\in\mathfrak{I}}(2n_1+1) \\ -1^{m_1}W_{n,n_1,m,m_1,l}\times I_l^{-m-m_1}\left(k,\overrightarrow{\mathbf{o_1^*o^*}}\right) \end{aligned} \tag{46}$$

in which $W_{n,n_1,m,m_1,l}$ is expressed in Equation 47.

$$W_{n,n_1,m,m_1,l} = (2l+1)\,\mathrm{i}^{n_1-n+l}\begin{pmatrix} n & n_1 & l \\ 0 & 0 & 0 \end{pmatrix}\begin{pmatrix} n & n_1 & l \\ m & m_1 & -m-m_1 \end{pmatrix} \tag{47}$$

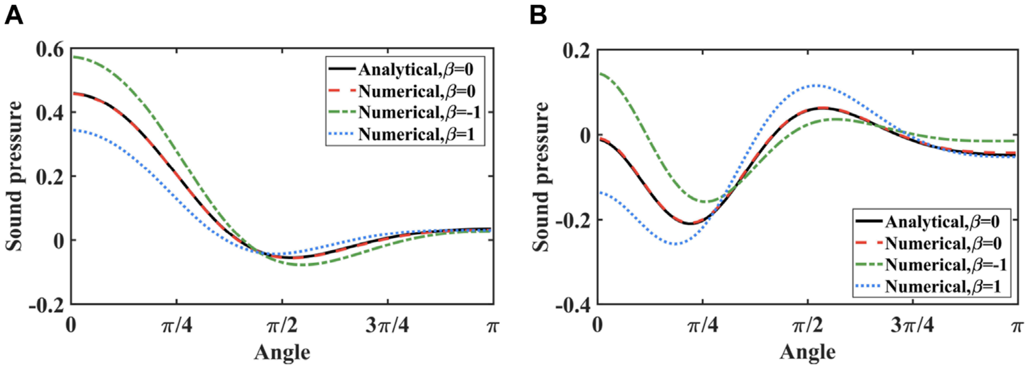

FIGURE 8
Sound pressure at computational points on circles with a 2-m radius across various frequencies. **(A)** 100 Hz. **(B)** 200 Hz.

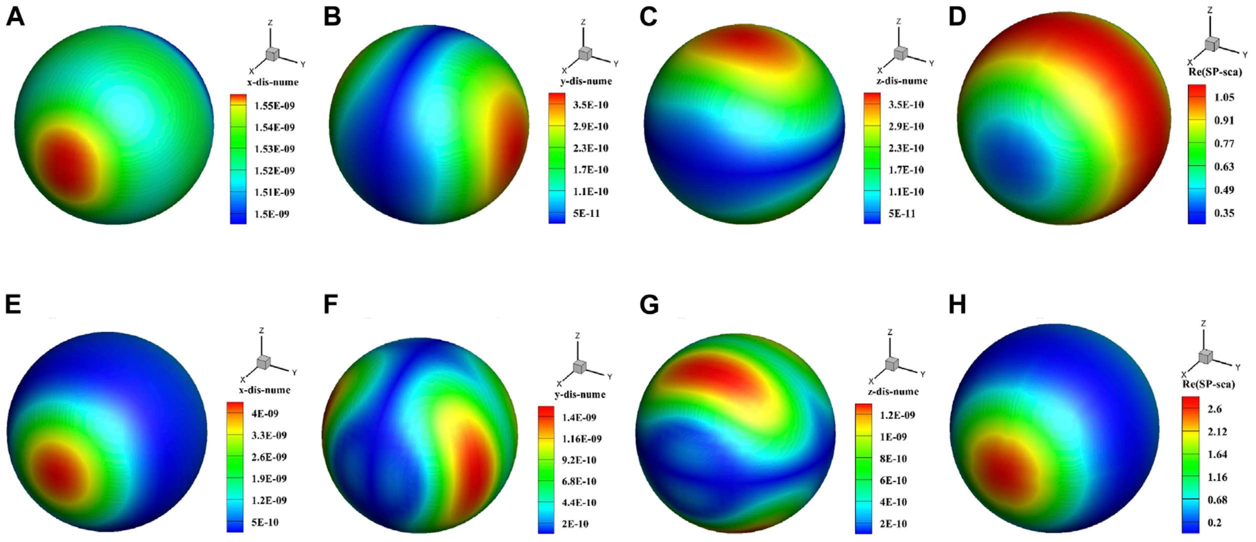

FIGURE 9
Sound pressure and displacement distributions on the surface of a spherical shell: the first three columns depict the three components of displacement, while the fourth column shows the sound pressure. **(A)** 100 Hz, displacement x. **(B)** 100 Hz, displacement y. **(C)** 100 Hz, displacement z. **(D)** 100 Hz, sound pressure. **(E)** 200 Hz, displacement x. **(F)** 200 Hz, displacement y. **(G)** 200 Hz, displacement z. **(H)** 200 Hz, sound pressure.

The symbol $\begin{pmatrix} \cdot \\ \cdot \end{pmatrix}$ represents the Wigner 3j symbol, and the set $\mathfrak{I}$ is defined as Equation 48.

$$\mathfrak{I}(n, n_1, m, m_1) = \left\{ \begin{array}{l} l | l \in \mathbf{Z}, n + n_1 - l\text{:}even, \\ \max\{|m + m_1|, |n - n_1|\} \le l \le n + n_1 \end{array} \right\} \tag{48}$$

Taking into account the influence of the infinite/symmetry plane, we can formulate the M2L (moments to local expansion coefficients) translation formula as shown in Equations 49, 50.

$$L_n^m(k, \mathbf{x}_1) = \sum_{n_1=0}^{\infty} \sum_{m_1=-n_1}^{n_1} \sum_{l \in \mathfrak{I}} (2n_1 + 1)(-1)^{m_1} W_{n,n_1,m,m_1,l} \times \left[\mathbf{O}_l^{m+m_1}(k, \overrightarrow{\mathbf{o}_1 \mathbf{x}_1}) \mathbf{M}_{n_1}^{m_1}(k, \mathbf{o}_1) + \beta \mathbf{O}_l^{m+m_1}(k, \overrightarrow{\mathbf{o}_1 \mathbf{x}_1}) \mathbf{M}_{n_1}^{m_1}(k, \mathbf{o}_1^*) \right] \tag{49}$$

$$\tilde{L}_n^m(k, \mathbf{x}_1) = \sum_{n_1=0}^{\infty} \sum_{m_1=-n_1}^{n_1} \sum_{l \in \mathfrak{I}} (2n_1 + 1)(-1)^{m_1} W_{n,n_1,m,m_1,l} \times \left[\mathbf{O}_l^{m+m_1}(k, \overrightarrow{\mathbf{o}_1 \mathbf{x}_1}) \tilde{M}_{n_1}^{m_1}(k, \mathbf{o}_1) + \beta \mathbf{O}_l^{m+m_1}(k, \overrightarrow{\mathbf{o}_1 \mathbf{x}_1}) \tilde{M}_{n_1}^{m_1}(k, \mathbf{o}_1^*) \right] \tag{50}$$

Following that, the L2L (local expansion to local expansion) translation formula can be employed to shift the center of the local expansion from $\mathbf{x}_1$ to $\mathbf{x}_2$, as shown in Equations 51, 52.

$$L_n^m(k, \mathbf{x}_2) = \sum_{n_1=0}^{\infty} \sum_{m_1=-n_1}^{n_1} \sum_{l \in \mathfrak{I}} (2n_1 + 1)(-1)^{m_1} W_{n,n_1,-m,m_1,l} \times I_l^{m-m_1}(k, \overrightarrow{\mathbf{x}_1 \mathbf{x}_2}) L_{n_1}^{m_1}(k, \mathbf{x}_1) \tag{51}$$

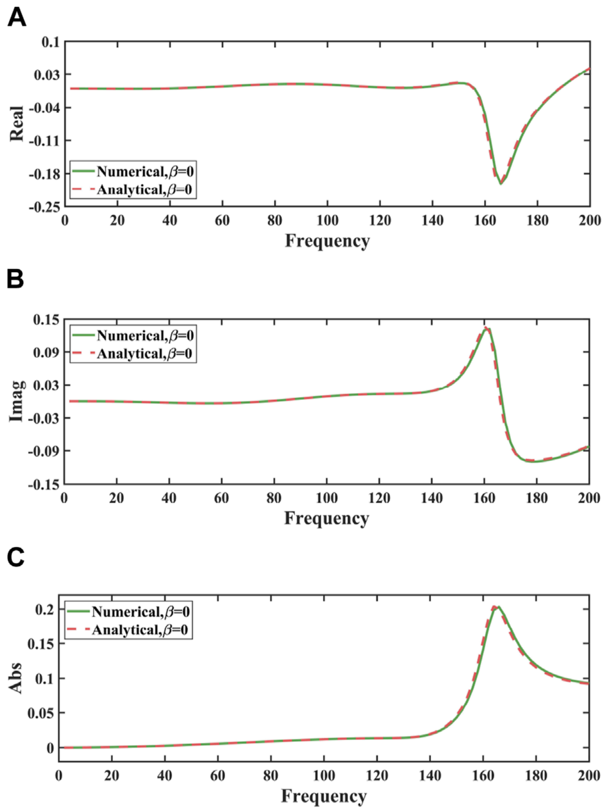

FIGURE 10
Sound pressure of the sphere model across various frequencies with $\beta = 0$, incremented by a frequency step of 1 Hz. **(A)** $\beta = 0$, real part. **(B)** $\beta = 0$, imaginary part. **(C)** $\beta = 0$, sound pressure.

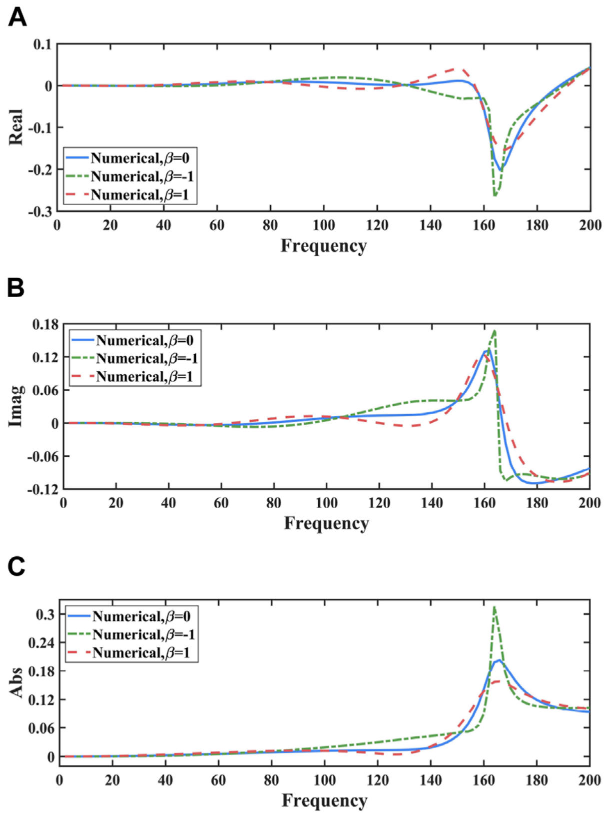

FIGURE 11
Sound pressure of the sphere model across various frequencies with $\beta = 0$, $\beta = -1$, and $\beta = 1$, incremented by a frequency step of 1 Hz. **(A)** Real part. **(B)** Imaginary part. **(C)** Sound pressure.

$$\tilde{L}_n^m(k,\mathbf{x}_2) = \sum_{n_1=0}^{\infty}\sum_{m_1=-n_1}^{n_1}\sum_{l\in\Im}(2n_1+1)(-1)^{m_1}W_{n,n_1,-m,m_1,l} \times I_l^{m-m_1}(k,\overrightarrow{\mathbf{x}_1\mathbf{x}_2})\,\tilde{L}_{n_1}^{m_1}(k,\mathbf{x}_1) \tag{52}$$

For the set of N_l boundary elements that are close to $\mathbf{o}$ but far from the source points $\mathbf{x}$, the sums $\sum_{j=1}^{N_l} h^{ij}$ or $\sum_{j=1}^{N_l} g^{ij}$ can be expressed using the local expansion coefficients shown in Equation 53.

$$\sum_{j=1}^{N_l} g^{ij} = \frac{ik}{4\pi}\sum_{n=0}^{\infty}\sum_{m=-n}^{n}(2n+1)L_n^m(k,\mathbf{x}_2)\,\bar{\mathbf{I}}_n^m(k,\overrightarrow{\mathbf{x}_2\mathbf{x}_1}) \tag{53}$$

$$\sum_{j=1}^{N_l} h^{ij} = \frac{ik}{4\pi}\sum_{n=0}^{\infty}\sum_{m=-n}^{n}(2n+1)\tilde{L}_n^m(k,\mathbf{x}_2)\,\bar{\mathbf{I}}_n^m(k,\overrightarrow{\mathbf{x}_2\mathbf{x}_1}) \tag{54}$$

within the low-frequency FMM. To refine the Burton-Miller formulation, which is a linear combination of the Conventional Boundary Integral Equation (CBIE) and its normal derivative, we simply introduce adjustments to Equations 53, 54, as shown in Equations 55, 56.

$$\sum_{j=1}^{N_l} g^{ij} = \frac{ik}{4\pi}\sum_{n=0}^{\infty}\sum_{m=-n}^{n}(2n+1)L_n^m(k,\mathbf{x}_2)\times\left[\bar{I}_n^m(k,\overrightarrow{\mathbf{x}_2\mathbf{x}_1}) + \alpha\frac{\partial\bar{I}_n^m(k,\overrightarrow{\mathbf{x}_2\mathbf{x}_1})}{\partial n(\mathbf{x})}\right] \tag{55}$$

$$\sum_{j=1}^{N_l} h^{ij} = \frac{ik}{4\pi}\sum_{n=0}^{\infty}\sum_{m=-n}^{n}(2n+1)\tilde{L}_n^m(k,\mathbf{x}_2)\times\left[\bar{I}_n^m(k,\overrightarrow{\mathbf{x}_2\mathbf{x}_1}) + \alpha\frac{\partial\bar{I}_n^m(k,\overrightarrow{\mathbf{x}_2\mathbf{x}_1})}{\partial n(\mathbf{x})}\right] \tag{56}$$

The implementation process involves the following key steps:

1. Hierarchical Tree Construction: The computational domain is partitioned into a hierarchical octree structure, with each node representing a subdomain. Boundary elements are assigned to the appropriate nodes based on their spatial location.
2. Multipole Expansion Calculation: For each leaf node, multipole moments are computed using the source terms within the node. These moments encapsulate the collective influence of sources on distant targets.
3. M2M Translations: Multipole expansions from child nodes are aggregated and translated to their parent nodes, propagating the influence up the hierarchical tree.
4. M2L Translations: At each interaction list, multipole expansions from distant nodes are translated into local expansions at the target nodes. This step leverages the translation operators to approximate interactions efficiently.
5. L2L Translations: Local expansions are propagated down the tree to account for interactions within localized regions.

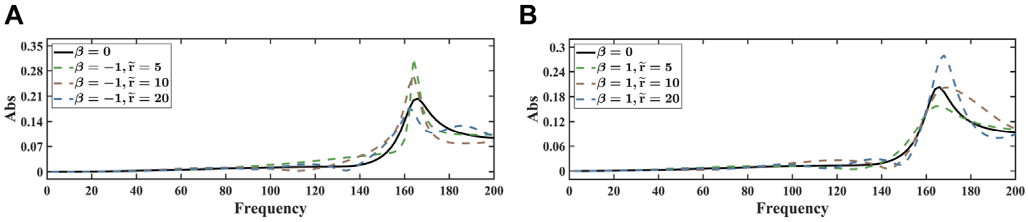

FIGURE 12
Sound pressure in terms of frequencies with different distances from the seabed for the sphere model. **(A)** $\beta = -1$. **(B)** $\beta = 1$.

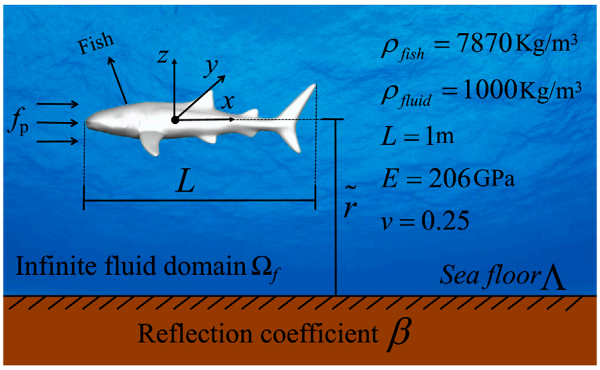

FIGURE 13
Acoustic-structural interaction system for the fish model.

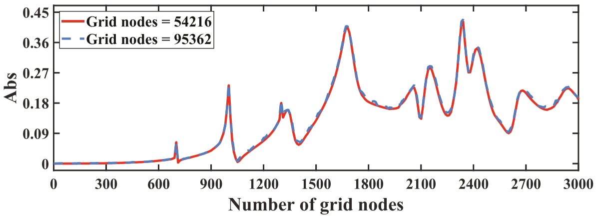

FIGURE 14
The numerical results of the fish model are verified in the convergence of two mesh node numbers.

6. Evaluation of Local Expansions: The final local expansions are evaluated at the target points, providing the approximate contributions from distant sources.

4 Numerical illustrations

In this segment, the primary objective of the elastic spherical shell model is to verify the accuracy of the numerical model by comparing the analytical and numerical solutions. The fish model, with its relatively complex geometry, represents the structural features of real underwater organisms or submersibles. It is intended to demonstrate the applicability and effectiveness of the proposed method in solving underwater acoustic scattering problems. The computations are executed using Fortran 90 on a desktop computer with 128 GB of RAM and an Intel (R) Core (TM) i7-7700 CPU.

4.1 Acoustic scattering by an elastic spherical shell

This section examines the acoustic field scattered by a spherical shell structure when subjected to incident plane waves, taking into account the reflections from the seabed, as depicted in Figure 6. In the diagram, the center of the sphere is at the origin; Λ represents the seabed surface; $\tilde{r}$ is the distance from the origin to the seabed surface; f_p is the incident plane wave; Ω_f signifies the infinite fluid domain. The seabed reflection coefficient is denoted by β, where $\beta = -1$ corresponds to a soft seabed and $\beta = 1$ corresponds to a rigid seabed.The incident plane waves, which have an amplitude of 1, travel along the positive x-axis. Using Catmull-Clark subdivision surfaces, three elastic spherical shells with 3,458, 4,800, and 9,408 mesh points were constructed. Figure 7 presents the variation curves of sound pressure with frequency for the spherical models at 3,458, 4,800, and 9,408 mesh points, respectively. The computation times for a single frequency were 33 s, 56 s, and 85 s for each model. It can be observed from the figure that the differences in the sound pressure curves across the three mesh densities are minimal; however, the computation times differ significantly. Therefore, this study adopts the spherical model with fewer mesh points to balance computational efficiency and accuracy.When analyzing the acoustic scattering of the sphere model, we found that the computation time for the traditional Catmull-Clark subdivision surfaces coupled with the FEM-BEM method was 428 s, whereas the computation time for the Catmull-Clark subdivision surfaces accelerated by FMM and coupled with the FEM-BEM method was only 33 s, demonstrating that the computational efficiency of FMM is significantly higher than that of traditional algorithms.

The sound pressure values at the computed points on the circle for incident wave frequencies of 100 Hz and 200 Hz are depicted in Figure 8, where the circle represents the projection of the sphere model, with a radius of 2 m, onto the yoz plane. As observed in the figure, at a frequency of 200 Hz, the sound pressure curve exhibits more pronounced fluctuations, indicating that the larger the external sound wave impacting the sphere model, the greater the magnitude of sound pressure variation. When $\beta = 0$, the sound pressure curves from numerical and analytical solutions align, confirming the validity and reliability of the algorithm presented in this study. For $\beta = 0, 1, -1$, the numerical solutions vary significantly,

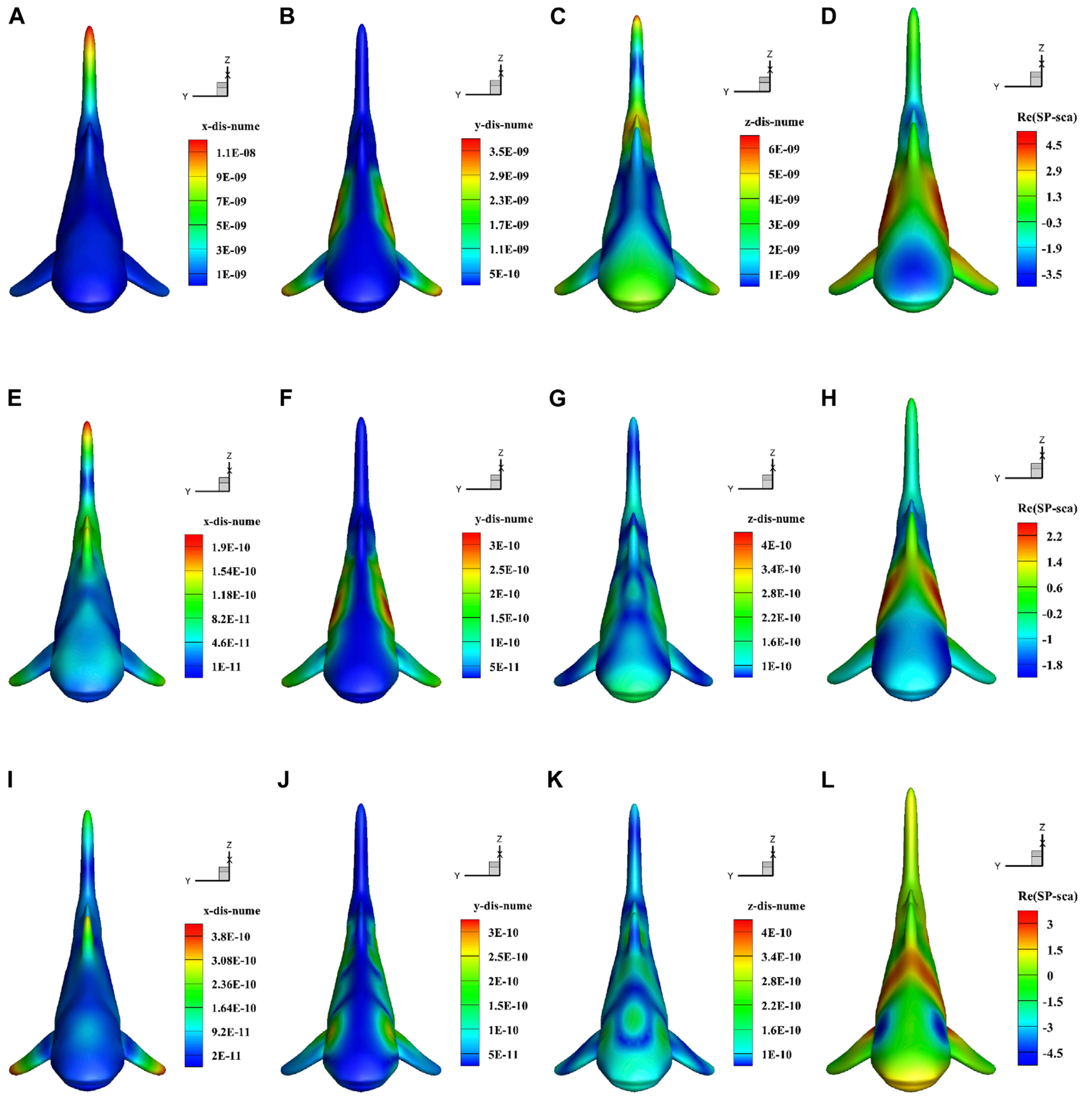

FIGURE 15
Sound pressure and displacement distributions on the surface of a fish model: the first three columns depict the three components of displacement, while the fourth column shows the sound pressure. **(A)** 1000 Hz, displacement x. **(B)** 1000 Hz, displacement y. **(C)** 1000 Hz, displacement z. **(D)** 1000 Hz,sound pressure. **(E)** 2000 Hz, displacement x. **(F)** 2000 Hz, displacement y. **(G)** 2000 Hz, displacement z. **(H)** 2000 Hz, sound pressure. **(I)** 3000 Hz, displacement x. **(J)** 3000 Hz, displacement y. **(K)** 3000 Hz, displacement z. **(L)** 3000 Hz, sound pressure.

demonstrating the importance of considering the seabed reflection effects and highlighting the significance of the seabed's nature.

Figure 9 illustrates the displacement and sound pressure distributions on the sphere model when it is positioned 5 m above the seabed. The first three columns represent the displacement components in the x, y, and z axes, respectively, while the last column indicates the sound pressure. As observed in the figure, the sound pressure pattern exhibits symmetry along the x-axis, and the displacement components also mirror this symmetry. The displacement in the x-direction is the most significant, whereas the y-direction shows the least. The sound pressure on the sphere's surface diminishes as we move in the negative x-axis direction, whereas the x-direction displacement component increases progressively.

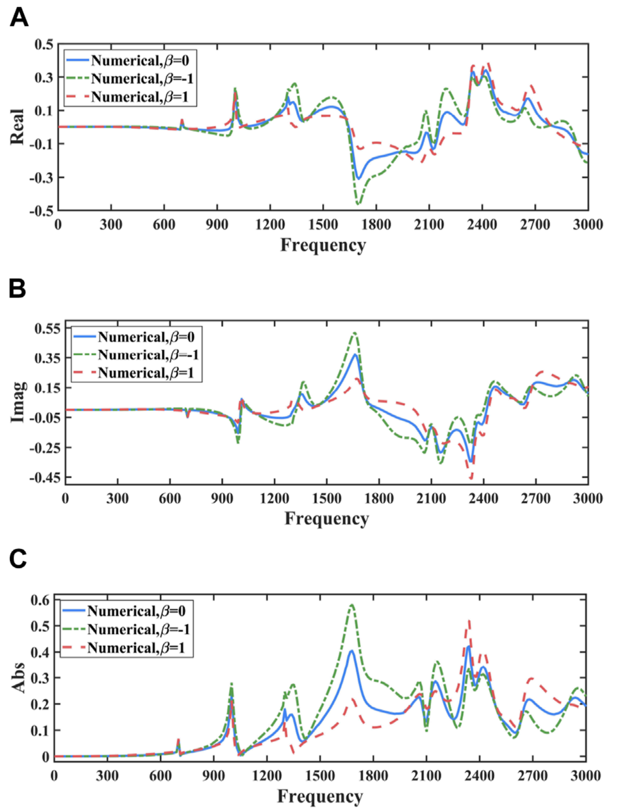

FIGURE 16
Sound pressure in terms of frequencies with different seabed reflection coefficient for the fish model: frequency steps of 10 Hz. **(A)** Real part. **(B)** Imaginary part. **(C)** Sound pressure.

Figure 10 displays the sound pressure of the sphere model across various frequencies with $\beta = 0$. Figures 10A–C depict the real part, imaginary part, and magnitude of the sound pressure, respectively. From the figure, it can be seen that when the frequency is within the range of [0.140]Hz, the analytical solution and numerical solution of the sound pressure on the surface of the sphere model match very well, and the sound pressure changes are very small. When the frequency is within the range of [160,200] Hz, the numerical solution still matches well with the analytical solution, but the sound pressure begins to change dramatically. This phenomenon further validates the reliability of the algorithm presented in this paper and shows that sound scattering is frequency-dependent.

Figure 11 shows the sound pressure of the sphere model at different frequencies when $\beta = 0$, $\beta = -1$, and $\beta = 1$. From the figure, it can be seen that the sound pressure curves for $\beta = 0$, $\beta = -1$, and $\beta = 1$ are distinct, indicating that the impact of seabed reflection on the structural acoustic coupling system response in shallow water environments cannot be ignored. It is noteworthy that the sound pressure curves for $\beta = 1$ and $\beta = -1$ are roughly distributed on either side of the sound pressure curve for $\beta = 0$, and the two curves are essentially symmetric about the sound pressure curve for $\beta = 0$. This phenomenon indicates that the effects of rigid and flexible seabeds on sound waves are opposite.

Figure 12 illustrates the sound pressure of the sphere model at various distances from the seabed, where $\tilde{r}$ denotes the distance from the model's center to the seabed. It can be observed from the figure that when the frequency is less than 60Hz, the sound pressure curves for different $\tilde{r}$ are very close to each other; when the frequency exceeds 60Hz, the differences between the sound pressure curves for different $\tilde{r}$ gradually increase. This phenomenon confirms that the effect of ground reflection is frequency-dependent.

4.2 Acoustic scattering by a fish model

This section analyzes the acoustic field scattering by a fish model under the action of incident plane waves, taking into account the reflection effects of the seabed, as shown in Figure 13. This subsection calculates the sound pressure and displacement under incident plane waves at different frequencies. The incident plane waves propagate along the positive x-axis with a unit amplitude and are scattered by the underwater model.

Using Catmull-Clark subdivision surfaces, two fish models with 54,216 and 222 mesh points were constructed. Figure 14 illustrates the sound pressure curves as a function of frequency for the fish models with 54,216 and 222 mesh points, respectively. The computation times for a single frequency were 483 s and 1,016 s for each model. As shown in the figure, the differences in the sound pressure curves between the two mesh densities are minor, with only slight fluctuations that are acceptable considering the significant disparity in computation times. Therefore, this study selects the fish model with 54,216 mesh points to optimize computational efficiency while maintaining acceptable accuracy.

When analyzing the acoustic scattering of the fish model, we found that the computation time for the traditional Catmull-Clark subdivision surfaces coupled with the FEM-BEM method was 5,143 s, whereas the computation time for the Catmull-Clark subdivision surfaces accelerated by FMM and coupled with the FEM-BEM method was only 483 s.

Figure 15 shows the distribution of displacement and sound pressure for the fish model at a distance of 0.5 m from the seabed. As shown in the figure, the sound pressure and displacement distributions are symmetric along the x-axis. The magnitude order of the various displacement components of the fish model at different frequencies is not the same. For instance, at a frequency of 1,000 Hz, the displacement component in the x-direction is the largest, and the displacement component in the z-direction is the smallest; at a frequency of 3,000 Hz, the displacement component in the z-direction is the largest, and the displacement component in the y-direction is the smallest.

Figure 16 displays the sound pressure of the fish model at different frequencies for $\beta = 0$, $\beta = -1$, and $\beta = 1$, with a frequency range of [03,000]Hz and a frequency step of 10 Hz. As shown in the figure, the sound pressure on the surface of the fish model varies with β. When the frequency is within the range of [0.600]Hz, the sound pressure curves for $\beta = 0$, $\beta = -1$, and $\beta = 1$ match very closely. However, when the frequency exceeds 600Hz, differences begin to emerge among them. This phenomenon once again confirms that the seabed reflection effect is frequency-dependent, not only for spherical models but also for complex models, and it also validates the necessity of considering the seabed reflection effect.

Figure 17 illustrates the sound pressure of the fish model at various distances from the seabed. It can be observed from the

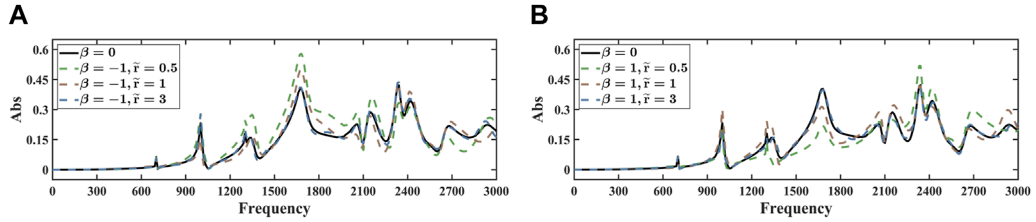

FIGURE 17
Sound pressure in terms of frequencies with different distances from the seabed for the fish model. **(A)** $\beta = -1$. **(B)** $\beta = 1$.

figure that as the distance from the seabed increases, the sound pressure curve gradually aligns with the sound pressure curve for $\beta = 0$. This phenomenon indicates that in shallow sea areas, the seabed reflection effect must be taken into account, while in deep sea areas, the seabed reflection effect can be selectively considered based on needs. This phenomenon is related to the nature of the seabed.

5 Conclusion

This paper presents a novel algorithm for analyzing the interaction between sound wave propagation and the vibration of underwater thin-shell structures, taking into account the effects of seabed reflection. We couple FEM with BEM to solve for shell vibrations and sound wave propagation in an infinite domain. To consider the effects of seabed reflection, the BEM employs a half-space fundamental solution approach. Within the isogeometric framework, geometric modeling is conducted using Catmull-Clark subdivision surfaces, and the same basis functions used for geometric modeling are applied to discretize the physical fields of the coupled FEM/BEM system. The use of isogeometric analysis maintains geometric accuracy, reduces meshing efforts, and produces high-order continuous fields, enabling the application of Kirchhoff-Love shell theory. Additionally, FMM is formulated to accelerate vibro-acoustic simulations. The precision of this algorithm is demonstrated through numerical examples.This study also has certain limitations. The current model's assumption of linear elastic material properties, while suitable for small deformations and stresses, does not capture nonlinear behaviors under extreme conditions. The absence of fluid-structure interactions (FSI) in the present model may overlook critical phenomena such as damping and dynamic loading from fluid flows. Furthermore, the simplified treatment of seabed topographies with predefined reflection coefficients β limits the model's applicability to real-world scenarios.In the future, incorporating nonlinear material models, fluid-structure interaction modeling, and the uncertainty of seabed reflection coefficients into the model will ensure that the proposed algorithm not only maintains high computational efficiency but also delivers accurate and reliable results in complex vibration-acoustic analyses.

Data availability statement

The raw data supporting the conclusions of this article will be made available by the authors, without undue reservation.

Author contributions

XZ: Conceptualization, Formal Analysis, Methodology, Project administration, Resources, Software, Writing–original draft. KA: Conceptualization, Formal Analysis, Writing–original draft. SY: Data curation, Investigation, Resources, Software, Validation, Visualization, Writing–original draft. QP: Conceptualization, Formal Analysis, Funding acquisition, Resources, Software, Supervision, Writing–review and editing. GL: Data curation, Validation, Visualization, Writing–original draft.

Funding

The author(s) declare that financial support was received for the research, authorship, and/or publication of this article. Sponsored by the Henan Provincial Key R&D and Promotion Project under Grant No. 232102220033, the Zhumadian 2023 Major Science and Technology Special Project under Grant No. ZMDSZDZX2023002, and the Postgraduate Education Reform and Quality Improvement Project of Henan Province under Grant No. YJS2023JD52.

Conflict of interest

The authors declare that the research was conducted in the absence of any commercial or financial relationships that could be construed as a potential conflict of interest.

Generative AI statement

The author(s) declare that no Generative AI was used in the creation of this manuscript.

Publisher's note

References

1. Belibassakis K, Prospathopoulos J. A 3D-BEM for underwater propeller noise propagation in the ocean environment including hull scattering effects. *Ocean Eng* (2023) 286:115544. doi:10.1016/j.oceaneng.2023.115544

2. Helal KM, Fragasso J, Moro L. Effectiveness of ocean gliders in monitoring ocean acoustics and anthropogenic noise from ships: a systematic review. *Ocean Eng* (2024) 295:116993. doi:10.1016/j.oceaneng.2024.116993

3. Li Z, Zhang Y, Yang A. Numerical study on the flow-induced noise from waterjet-propelled ship regarding a flexible boundary. *Ocean Eng* (2023) 287:115911. doi:10.1016/j.oceaneng.2023.115911

4. Viitanen V, Hynninen A, Sipilä T. Computational fluid dynamics and hydroacoustics analyses of underwater radiated noise of an ice breaker ship. *Ocean Eng* (2023) 279:114264. doi:10.1016/j.oceaneng.2023.114264

5. Cheng Y, Du W, Dai S, Yuan Z, Incecik A. Wave energy conversion by an array of oscillating water columns deployed along a long-flexible floating breakwater. *Renew Sustainable Energy Rev* (2024) 192:114206. doi:10.1016/j.rser.2023.114206

6. Jiao J, Huang S, Tezdogan T, Terziev M, Soares CG. Slamming and green water loads on a ship sailing in regular waves predicted by a coupled cfd–fea approach. *Ocean Eng* (2021) 241:110107. doi:10.1016/j.oceaneng.2021.110107

7. Shao X, Yao HD, Ringsberg JW, Li Z, Johnson E. Performance analysis of two generations of heaving point absorber wecs in farms of hexagon-shaped array layouts. *Ships and Offshore Structures* (2024) 19:687–98. doi:10.1080/17445302.2024.2317658

8. Shen XW, Du CB, Jiang SY, Zhang P, Chen LL. Multivariate uncertainty analysis of fracture problems through model order reduction accelerated sbfem. *Appl Math Model* (2024) 125:218–40. doi:10.1016/j.apm.2023.08.040

9. Li Z, Bouscasse B, Ducrozet G, Gentaz L, Le Touzé D, Ferrant P. Spectral wave explicit Navier-Stokes equations for wave-structure interactions using two-phase computational fluid dynamics solvers. *Ocean Eng* (2021) 221:108513. doi:10.1016/j.oceaneng.2020.108513

10. Gao Z, Li Z, Liu Y. A time-domain boundary element method using a kernel-function library for 3d acoustic problems. *Eng Anal Boundary Elem* (2024) 161:103–12. doi:10.1016/j.enganabound.2024.01.001

11. Chen L, Huo R, Lian H, Yu B, Zhang M, Natarajan S, et al. Uncertainty quantification of 3d acoustic shape sensitivities with generalized nth-order perturbation boundary element methods. *Computer Methods Appl Mech Eng* (2025) 433:117464. doi:10.1016/j.cma.2024.117464

12. Chen L, Lian H, Liu Z, Chen H, Atroshchenko E, Bordas S. Structural shape optimization of three dimensional acoustic problems with isogeometric boundary element methods. *Computer Methods Appl Mech Eng* (2019) 355:926–51. doi:10.1016/j.cma.2019.06.012

13. Ren Y, Qin Y, Pang F, Wang H, Su Y, Li H. Investigation on the flow-induced structure noise of a submerged cone-cylinder-hemisphere combined shell. *Ocean Eng* (2023) 270:113657. doi:10.1016/j.oceaneng.2023.113657

14. Kha J, Karimi M, Maxit L, Skvortsov A, Kirby R. Forced vibroacoustic response of a cylindrical shell in an underwater acoustic waveguide. *Ocean Eng* (2023) 273:113899. doi:10.1016/j.oceaneng.2023.113899

15. Huang H, Zou MS, Jiang LW. Study on the integrated calculation method of fluid–structure interaction vibration, acoustic radiation, and propagation from an elastic spherical shell in ocean acoustic environments. *Ocean Eng* (2019) 177:29–39. doi:10.1016/j.oceaneng.2019.02.032

16. Chen LL, Lian HJ, Dong HW, Yu P, Jiang SJ, Bordas SPA. Broadband topology optimization of three-dimensional structural-acoustic interaction with reduced order isogeometric FEM/BEM. *J Comput Phys* (2024) 509:113051. doi:10.1016/j.jcp.2024.113051

17. Chen L, Lian H, Pei Q, Meng Z, Jiang S, Dong H, et al. Fem-bem analysis of acoustic interaction with submerged thin-shell structures under seabed reflection conditions. *Ocean Eng* (2024) 309:118554. doi:10.1016/j.oceaneng.2024.118554

18. Choi YM, Bouscasse B, Ducrozet G, Seng S, Ferrant P, Kim ES, et al. An efficient methodology for the simulation of nonlinear irregular waves in computational fluid dynamics solvers based on the high order spectral method with an application with openfoam. *Int J Naval Architecture Ocean Eng* (2023) 15:100510. doi:10.1016/j.ijnaoe.2022.100510

19. Wei Y, Incecik A, Tezdogan T. A hydroelasticity analysis of a damaged ship based on a two-way coupled CFD-DMB method. *Ocean Eng* (2023) 274:114075. doi:10.1016/j.oceaneng.2023.114075

20. Liu D, Havranek Z, Marburg S, Peters H, Kessissoglou N. Non-negative intensity and back-calculated non-negative intensity for analysis of directional structure-borne sound. *The J Acoust Soc America* (2017) 142:117–23. doi:10.1121/1.4990374

21. Wilkes DR, Peters H, Croaker P, Marburg S, Duncan AJ, Kessissoglou N. Non-negative intensity for coupled fluid-structure interaction problems using the fast multipole method. *The J Acoust Soc America* (2017) 141:4278–88. doi:10.1121/1.4983686

22. Faugeras B, Heumann H. FEM-BEM coupling methods for tokamak plasma axisymmetric free-boundary equilibrium computations in unbounded domains. *The J Acoust Soc America* (2017) 343:201–16. doi:10.1016/j.jcp.2017.04.047

23. Everstine GC, Henderson FM. Coupled finite element/boundary element approach for fluid-structure interaction. *The J Acoust Soc America* (1990) 87:1938–47. doi:10.1121/1.399320

24. Chen LL, Lian HJ, Liu ZW, Gong Y, Zheng CJ, Bordas SPA. Bi-material topology optimization for fully coupled structural-acoustic systems with isogeometric FEM–BEM. *Eng Anal Boundary Elem* (2022) 135:182–95. doi:10.1016/j.enganabound.2021.11.005

25. Xu J, Wang L, Yuan J, Luo Z, Wang Z, Zhang B, et al. Dlfsi: a deep learning static fluid-structure interaction model for hydrodynamic-structural optimization of composite tidal turbine blade. *Renew Energy* (2024) 224:120179. doi:10.1016/j.renene.2024.120179

26. Chen LL, Cheng RH, Li SZ, Lian HJ, Zheng CJ, Bordas SPA. A sample-efficient deep learning method for multivariate uncertainty qualification of acoustic-vibration interaction problems. *Computer Methods Appl Mech Eng* (2022) 393:114784. doi:10.1016/j.cma.2022.114784

27. Zou MS, Wu YS, Liu SX. A three-dimensional sono-elastic method of ships in finite depth water with experimental validation. *Ocean Eng* (2018) 164:238–47. doi:10.1016/j.oceaneng.2018.06.052

28. Jiang LW, Zou MS, Liu SX, Huang H. Calculation method of acoustic radiation for floating bodies in shallow sea considering complex ocean acoustic environments. *J Sound Vibration* (2020) 476:115330. doi:10.1016/j.jsv.2020.115330

29. Qi LB, Yu Y, Tang HC, Zou MS. Study of the influence of added water and contained water on structural vibrations and acoustic radiation using different dynamic modeling methods. *J Hydrodynamics* (2023) 35:1157–67. doi:10.1007/s42241-024-0087-6

30. Huang H, Zou MS, Jiang LW. Study on the integrated calculation method of fluid-structure interaction vibration, acoustic radiation, and propagation from an elastic spherical shell in ocean acoustic environments. *Ocean Eng* (2019) 177:29–39. doi:10.1016/j.oceaneng.2019.02.032

31. Liu XL, Wu HJ, Sun RH, Jiang WK. A fast multipole boundary element method for half-space acoustic problems in a subsonic uniform flow. *Eng Anal Boundary Elem* (2022) 137:16–28. doi:10.1016/j.enganabound.2022.01.008

32. Messaoudi A, Cottereau R, Gomez C. Boundary effects in radiative transfer of acoustic waves in a randomly fluctuating half-space. *Multiscale Model and Simulation* (2023) 21:1299–321. doi:10.1137/22m1537795

33. Yasuda Y, Higuchi K, Oshima T, Sakuma T. An efficient technique for plane-symmetrical acoustic problems in low-frequency FMBEM. *INTER-NOISE NOISE-CON Congress Conf Proc (Institute Noise Control Engineering)* (2011) 593–601.

34. Yasuda Y, Sakuma T. A technique for plane-symmetric sound field analysis in the fast multipole boundary element method. *J Comput Acoust* (2005) 13:71–85. doi:10.1142/s0218396x05002591

35. Brunner D, Of G, Junge M, Steinbach O, Gaul L. A fast BE-FE coupling scheme for partly immersed bodies. *Int J Numer Methods Eng* (2010) 81:28–47. doi:10.1002/nme.2672

36. Magisano D, Corrado A, Leonetti L, Kiendl J, Garcea G. Large deformation Kirchhoff–Love shell hierarchically enriched with warping: isogeometric formulation and modeling of alternating stiff/soft layups. *Computer Methods Appl Mech Eng* (2024) 418:116556. doi:10.1016/j.cma.2023.116556

37. Zhang R, Zhao G, Wang W, Du X. Large deformation frictional contact formulations for isogeometric Kirchhoff–Love shell. *Int J Mech Sci* (2023) 249:108253. doi:10.1016/j.ijmecsci.2023.108253

38. Duan J, Zhang L, Sun X, Chen W, Da L. An equivalent source CVIS method and its application in predicting structural vibration and acoustic radiation in ocean acoustic channe. *Ocean Eng* (2021) 222:108570. doi:10.1016/j.oceaneng.2021.108570

39. Chen LL, Lian HJ, Natarajan S, Zhao W, Chen XY, Bordas SPA. Multi-frequency acoustic topology optimization of sound-absorption materials with isogeometric boundary element methods accelerated by frequency-decoupling and model order reduction techniques. *Computer Methods Appl Mech Eng* (2022) 395:114997. doi:10.1016/j.cma.2022.114997

40. Xie K, Chen M, Zhang L, Li W, Dong W. A unified semi-analytic method for vibro-acoustic analysis of submerged shells of revolution. *Ocean Eng* (2019) 189:106345. doi:10.1016/j.oceaneng.2019.106345

41. Li R, Liu Y, Ye W. A fast direct boundary element method for 3d acoustic problems based on hierarchical matrices. *Eng Anal Boundary Elem* (2023) 147:171–80. doi:10.1016/j.enganabound.2022.11.035

42. Hughes TJR, Cottrell JA, Bazilevs Y. Isogeometric analysis: CAD, finite elements, NURBS, exact geometry and mesh refinement. *Computer Methods Appl Mech Eng* (2005) 194:4135–95. doi:10.1016/j.cma.2004.10.008

43. Chen LL, Wang ZW, Lian HJ, Ma YJ, Meng ZX, Li P, et al. Reduced order isogeometric boundary element methods for CAD-integrated shape optimization in electromagnetic scattering. *Computer Methods Appl Mech Eng* (2024) 419:116654. doi:10.1016/j.cma.2023.116654

44. Yang HS, Dong CY, Wu YH. Non-conforming interface coupling and symmetric iterative solution in isogeometric fe-be analysis. *Computer Methods Appl Mech Eng* (2021) 373:113561. doi:10.1016/j.cma.2020.113561

45. Qu YL, Zhou ZB, Chen LL, Lian HJ, Li XD, Hu ZM, et al. Uncertainty quantification of vibro-acoustic coupling problems for robotic manta ray models based on deep learning. *Ocean Eng* (2024) 299:117388. doi:10.1016/j.oceaneng.2024.117388

46. Chen L, Liu L, Zhao W, Liu C. An isogeometric approach of two dimensional acoustic design sensitivity analysis and topology optimization analysis for absorbing material distribution. *Computer Methods Appl Mech Eng* (2018) 336:507–32. doi:10.1016/j.cma.2018.03.025

47. Zhang S, Li T, Zhu X, Yin C, Li Q. Far field acoustic radiation and vibration analysis of combined shells submerged at finite depth from free surface. *Ocean Eng* (2022) 252:111198. doi:10.1016/j.oceaneng.2022.111198

48. Chen LL, Lian HJ, Xu YM, Li SZ, Liu ZW, Atroshchenko E, et al. Generalized isogeometric boundary element method for uncertainty analysis of time-harmonic wave propagation in infinite domains. *Appl Math Model* (2023) 114:360–78. doi:10.1016/j.apm.2022.09.030

49. Wu YH, Dong CY, Yang HS, Sun FL. Isogeometric symmetric FE-BE coupling method for acoustic-structural interaction. *Appl Mathematics Comput* (2021) 393:125758. doi:10.1016/j.amc.2020.125758

50. Liu ZW, Bian PL, Qu YL, Huang WC, Chen LL, Chen JB A galerkin approach for analysing coupling effects in the piezoelectric semiconducting beams. *Eur J Mechanics-A/Solids* (2024) 103:105145. doi:10.1016/j.euromechsol.2023.105145

51. Cao G, Yu B, Chen L, Yao W. Isogeometric dual reciprocity BEM for solving non-fourier transient heat transfer problems in FGMs with uncertainty analysis. *Int J Heat Mass Transfer* (2023) 203:123783. doi:10.1016/j.ijheatmasstransfer.2022.123783

52. Zhang S, Yu B, Chen L. Non-iterative reconstruction of time-domain sound pressure and rapid prediction of large-scale sound field based on IG-DRBEM and POD-RBF. *J Sound Vibration* (2024) 573:118226. doi:10.1016/j.jsv.2023.118226

53. Catmull E, Clark J. Recursively generated B-spline surfaces on arbitrary topological meshes. *Computer-Aided Des* (1978) 10:350–5. doi:10.1016/0010-4485(78)90110-0

54. Wu S, Xiang Y, Liu B, Li G. A weak-form interpolation meshfree method for computing underwater acoustic radiation. *Ocean Eng* (2021) 233:109105. doi:10.1016/j.oceaneng.2021.109105

55. Kirkup SM. The boundary element method in acoustics (Integrated sound software) (2007).

56. Wu TW, Ochmann M. Boundary element acoustics fundamentals and computer codes. *The J Acoust Soc America* (2002) 111:1507–8. doi:10.1121/1.1456929

57. Chen L, Lu C, Lian H, Liu Z, Zhao W, Li S, et al. Acoustic topology optimization of sound absorbing materials directly from subdivision surfaces with isogeometric boundary element methods. *Computer Methods Appl Mech Eng* (2020) 362:112806. doi:10.1016/j.cma.2019.112806

58. Gao XW, Yang K, Wang J. An adaptive element subdivision technique for evaluation of various 2D singular boundary integrals. *Eng Anal Boundary Elem* (2008) 32:692–6. doi:10.1016/j.enganabound.2007.12.004

59. Chen J, Hong H. Review of dual boundary element methods with emphasis on hypersingular integrals and divergent series. *Appl Mech Rev* (1999) 52:17–33. doi:10.1115/1.3098922

60. Zhong Y, Zhang J, Dong Y, Yuan L, Lin W, Tang J. A serendipity triangular patch for evaluating weakly singular boundary integrals. *Eng Anal Boundary Elem* (2016) 69:86–92. doi:10.1016/j.enganabound.2016.05.003

61. Zhang J, Qin X, Xu H, Li G. A boundary face method for potential problems in three dimensions. *Int J Numer Methods Eng* (2009) 80:320–37. doi:10.1002/nme.2633

62. Rong J, Wen L, Xiao J. Efficiency improvement of the polar coordinate transformation for evaluating BEM singular integrals on curved elements. *Eng Anal Boundary Elem* (2014) 38:83–93. doi:10.1016/j.enganabound.2013.10.014

63. Greengard L, Rokhlin V. A fast algorithm for particle simulations. *J Comput Phys* (1987) 73:325–48. doi:10.1016/0021-9991(87)90140-9

64. Chen LL, Zhao J, Lian HJ, Yu B, Atroshchenko E, Li P. A BEM broadband topology optimization strategy based on taylor expansion and soar method-application to 2d acoustic scattering problems. *Int J Numer Methods Eng* (2023) 124:5151–82. doi:10.1002/nme.7345

frontiers | Frontiers in Physics

TYPE Original Research
PUBLISHED 25 February 2025
DOI 10.3389/fphy.2025.1496451

OPEN ACCESS

EDITED BY
Elena Atroshchenko,
University of New South Wales, Australia

REVIEWED BY
Carmelo Scuro,
University of Calabria, Italy
Himanshu Mittal,
Ministry of Earth Sciences, India

*CORRESPONDENCE
Elena Serea,
✉ edanila@tuiasi.ro

RECEIVED 14 September 2024
ACCEPTED 16 January 2025
PUBLISHED 25 February 2025

CITATION
Donciu C, Serea E and Temneanu MC (2025) Frequency domain estimation method of the characteristic period of the P wave of earthquakes.
Front. Phys. 13:1496451.
doi: 10.3389/fphy.2025.1496451

Frequency domain estimation method of the characteristic period of the P wave of earthquakes

Codrin Donciu[1], Elena Serea[2]* and Marinel Costel Temneanu[1]

[1]Laboratory Electrical Measurements, Department of Electrical Measurements, "Gheorghe Asachi" Technical University of Iași, Iași, Romania, [2]Laboratory Energy Utilization, Department of Energy Utilization, Electrical Drives and Industrial Automation, "Gheorghe Asachi" Technical University of Iași, Iași, Romania

Early warning system earthquake alerts exploit the time delay that the surface waves have in reference to the P waves and estimate the magnitude based on the interpretation of the specific parameters of the P waves. One of the most commonly used parameters for estimating the moment magnitude of an earthquake is the characteristic period measured in the first 3 s after the appearance of the P wave. The classic method determines the characteristic period in the time domain by using the velocity and displacement waves of the acquired samples. In this paper, we present a new method for estimating the characteristic period through its corresponding frequency. This method includes zero padding of the P-wave sequence, conversion of the extended sequence from the time domain to the frequency domain, identification of local frequency maxima, and calculation of the weighted average of the frequency based on the identified maxima. Tests conducted on synthetic signals, as well as standard deviation evaluation tests for simultaneous recordings at several seismic stations, revealed better performance than the classic method in terms of noise immunity and number of false alarms.

KEYWORDS

earthquake, P wave, characteristic period, frequency domain, zero padding

1 Introduction

The intense ground motions caused by an earthquake pose a major hazard to the population living near the epicenter and can cause substantial damage to roads, buildings, and other infrastructure. Among natural disasters, earthquakes account for approximately one-fifth of economic losses and are responsible for approximately 20,000 deaths per year. A destructive earthquake cannot be predicted accurately at the moment or place of its occurrence. However, earthquake early warning systems (EEWS) can provide an estimation of the approaching event. EEWS can trigger anticipative alarms because the onset of an earthquake is achieved by non-destructive primary P waves and continues with destructive surface waves. P waves have a higher travel speed; they will reach the destination first and can be a source of information regarding the destructive waves that will reach the destination later. Moreover, P-wave-based EEWS can work in tandem with seismicity indicator-based systems that make use of the

Gutenberg–Richter law to increase the probability of detection of major earthquakes [1–3].

After several decades of development, EEWS are currently operational and provide alerts to populations (Japan [4, 5], Taiwan [6, 7], Mexico [8], and South Korea [9]), institutions, or limited users (India [10], Romania [11], Turkey [12], and the West Coast of the United States [13]), or are under development or testing (Italy [14], Chile, Costa Rica, EI Salvador, Nicaragua, Switzerland, Israel, Beijing, and the Fujian region of China) [15].

The main component of an EEW system is the algorithm that estimates the magnitude of an earthquake. The assessment is performed using the velocity and displacement waveforms and must contain as much of the low-frequency component of the frequency spectrum as possible to avoid magnitude saturation [16].

Among the first P-wave parameters used for magnitude estimation is the predominant period, defined as the period corresponding to the maximum amplitude in the frequency spectrum of displacement [17, 18]. An approach to the predominant period based on the velocity wave known as the τp method is presented in [19]. Because this method contains numerous limitations related to the sampling frequency and signal processing, an improved version was proposed in [20], where the predominant period is continuously calculated, and its maximum value (τp max) can be determined. Another magnitude estimation parameter is the characteristic period τc. This refers to both velocity and displacement waves, which are much more stable than τp max [21]. In current studies, the characteristic period is the most commonly used parameter for magnitude estimation with regard to the peak of the displacement wave (Pd) [22, 23] or alongside other geophysical parameters as input data for neural networks [24, 25].

However, the characteristic period of a specific earthquake, computed from different recording stations, exhibits large dispersion in terms of standard deviation due to local conditions, noise, and artifacts and thus may trigger false alarms or mute real ones. In order to evaluate the characteristic period of the P wave, we propose a new method based on the accurate determination of local maxima within the displacement wave's frequency spectrum. Its performance is evaluated using both synthesized and recorded waveforms, yielding better results than the standard approaches.

2 Methods

To define the characteristic period [21], the vertical components of the ground displacement wave $u(t)$ and velocity $\dot{u}$ (t) were used, with the ratio r being

$$r = \frac{\int_0^{t_0} \dot{u}^2(t)dt}{\int_0^{t_0} u^2(t)dt}, \tag{1}$$

where the integration is over the time interval (0, t_0) after the onset of the P wave. In most of the existing EEWS, t_0 is set to 3 s, and any straightforward implementation of Equation 1 belongs to the time domain methods used to evaluate the characteristic period. They have been adopted by the scientific community as a benchmark and as a standard specification in most of the existing EEWS [22, 26]. Using Parseval's theorem, according to which the energy of an aperiodic signal or the power of a periodic signal in the time domain is equal to the energy or power in the frequency domain, the results of Equation 2 are obtained and further exploited to develop frequency-domain methods.

$$r = \frac{4\pi^2 \int_0^{\infty} f^2 |\hat{u}(f)|^2 df}{\int_0^{\infty} |\hat{u}(f)|^2 df} = 4\pi^2 \langle f^2 \rangle, \tag{2}$$

where f is the frequency, $\hat{u}(f)$ is the frequency spectrum of the displacement wave $u(t)$, and $\langle f^2 \rangle$ is the average of f^2 weighted by $|\hat{u}(f)|^2$, hereafter denoted by $f_C.^2$

The characteristic period is defined according to Equation 3:

$$\tau_c = \frac{1}{\sqrt{f_c^2}} = \frac{2\pi}{\sqrt{r}}. \tag{3}$$

Although the characteristic period of the P wave is calculated based on the ratio r, as can be seen in Equation 3, the characteristic period can also be expressed based on the frequency spectrum of the displacement. More precisely, the squared characteristic frequency is the average of the squared frequencies weighted by the square of the amplitudes in the frequency spectrum.

$$f_c^2 = \frac{A_1^2 \cdot f_1^2 + A_2^2 \cdot f_2^2 + \cdots + A_n^2 \cdot f_n^2}{A_1^2 + A_2^2 + \cdots + A_n^2}, \tag{4}$$

where $A_1 \ldots A_n$ are the amplitudes of the spectral components, and $f_1 \ldots f_n$ are the frequencies of the spectral components. These values of the spectral components are obtained by applying a fast Fourier transform (FFT) to the displacement sequence in the time domain. There are many reported results in using FFT to differentiate seismic signals from ambient signals or those produced by explosions because the generated spectra can be distinguished [27, 28], but to date, no straightforward implementation of Equation 4 in EEWS makes use of the τc parameter.

Furthermore, the proposed development implies a better localization of the local maxima points in the discrete-time Fourier transform (DTFT)-associated function and thus minimizes the picket fence effect [29].

Three methods for increasing frequency resolution were considered: zero padding [30], FFT interpolation [31], and windowing [32]. Due to the specific nature of the seismic signals, a short analysis qualifies the zero-padding technique as the best candidate because:

- interpolation techniques are inefficient when the analyzed signal is a multi-frequency one, with massive overlap of adjacent energy bands;
- except for a rectangular window that is similar in the frequency domain with zero padding, the remaining windowing techniques reduce the signal's amplitude toward the edges, and thus, the first points in the earthquake spectrum (the ones with the most important information) are affected;
- there are no computational or timing constraints that could impact the practical deployment of the zero-padding technique because the FFT algorithm is highly efficient, and the time required to calculate frequency spectrum, even with sequences of zeros ten times larger than signal length, is of the order of milliseconds.

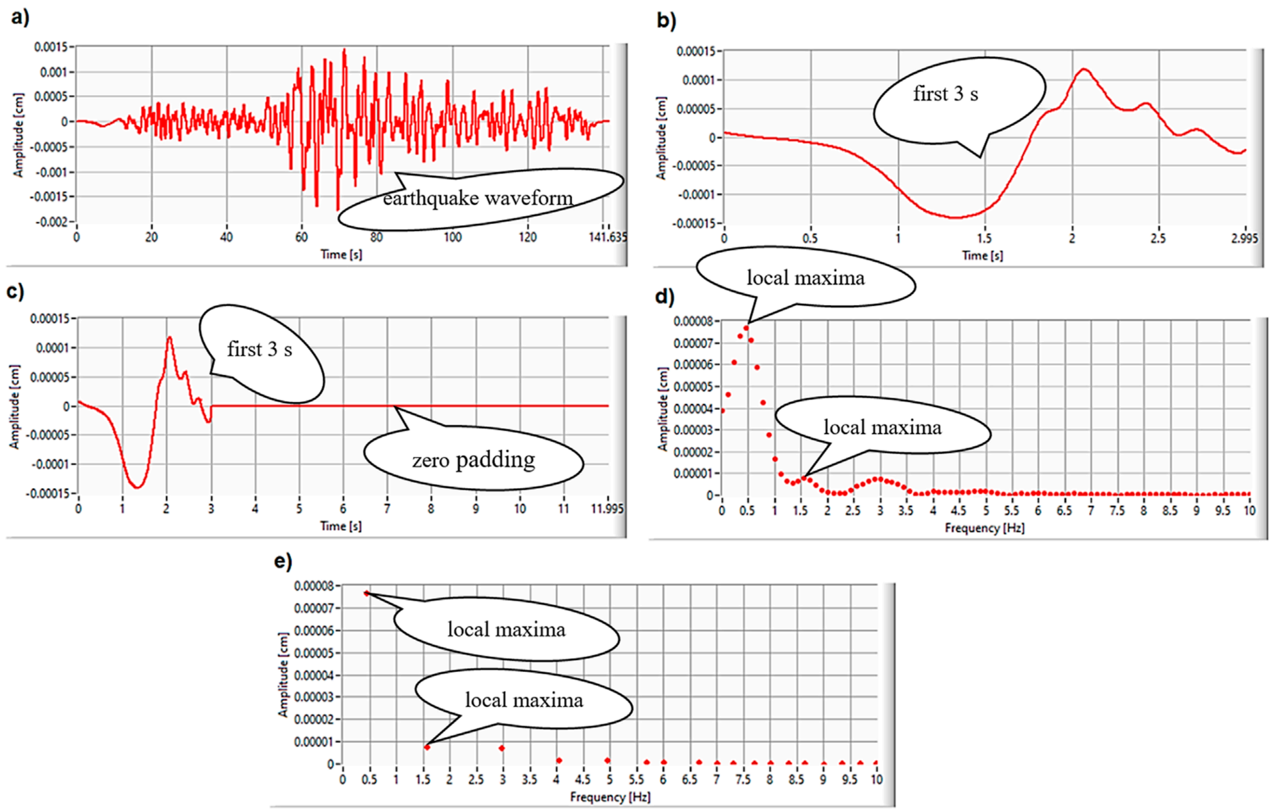

FIGURE 1
Attainment of the characteristic period of the seismic P-wave estimation in the frequency domain: **(A)** Display a recorded seismic waveform; **(B)** Extract the first 3 s of the signal; **(C)** Pad the sequence with zeros; **(D)** Apply FFT; **(E)** Identify the local maxima.

For the presented method, zero padding is the solution used to reduce the distance between bins in frequency by increasing the sequence of the investigated signal by adding zeros to its end before the FFT is applied. The extension of the seismic signal with null samples will not negatively influence the application of the method because it is only desired to obtain a specific length of the signal. Studies prove that this is a viable alternative method that improves the readability of the signal frequency [33, 34]. The increased length of the signal has the consequence of decreasing the width between consecutive spectral lines, resulting in a finer frequency resolution.

After applying zero padding, the local maxima in the frequency spectrum are identified, and the characteristic frequency is evaluated as

$$f_c^2 = \frac{A_1^2 \cdot f_1^2 + A_2^2 \cdot f_2^2 + \ldots + A_k^2 \cdot f_k^2}{A_1^2 + A_2^2 + \ldots + A_k^2}, \tag{5}$$

where k, A_k, and f_k are the number of identified maxima, the amplitude, and the frequency, respectively.

Structurally, as can be seen in Figure 1, the method of calculating the characteristic period in the frequency spectrum includes the following steps: from the earthquake displacement waveform (a), the first 3 s of the signal are extracted (b), the retrieved sequence is padded with zeros (c), and FFT is applied to obtain the frequency spectrum (d). At the level of the frequency spectrum, the local maxima (e) are identified, through which the weighted average of the characteristic frequency is calculated (Equation 5), and implicitly, its inverse is also calculated.

To test the proposed method, a comparative study was carried out between the classic method, from the time domain that uses the ratio between speed and displacement (M1), the method from the frequency domain based on Equation 4 to calculate the characteristic frequency (M2), and the proposed method (M3) based on Equation 5. The test signals used to calculate the characteristic frequency and characteristic period were synthesized by summing sinusoidal signals with imposed frequencies and amplitudes. The reference frequency against which the absolute error was calculated was obtained using the signal synthesis values (the amplitudes and frequencies of the sinusoidal signals were summed to obtain the test signals). The framework of signal acquisition is similar to the physical one used in the acquisition of seismic signals: sampling frequency, 200 Hz; acquisition time, 3 s; total number of acquired points, 600.

3 Results

A method for calculating the characteristic period of the P wave of earthquakes based on the frequency spectrum

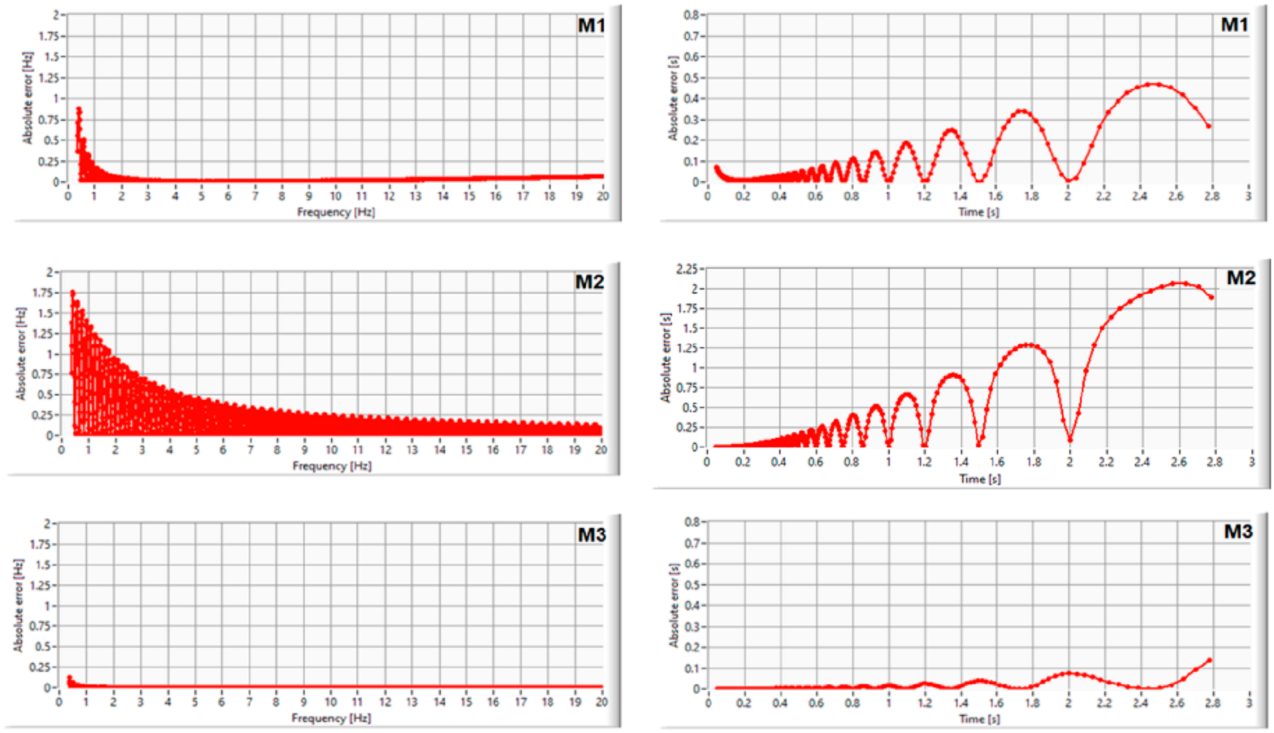

FIGURE 2
Absolute error graph of the three compared methods, in frequency-domain (left) and time-domain (right) calculations, for a singular spectrum signal.

of the displacement wave was developed. Three types of validation tests were carried out: one with signals containing a single spectral component (a pure sinusoidal signal), one with signals with two spectral components, and one with three spectral components with different frequency and amplitude values.

3.1 Testing using a signal with a single spectral component

A set of sinusoidal signals of 3 units amplitude was used, for which the frequency was varied between 0.3 Hz and 20 Hz, the range covering the area of interest for EEW systems (Figure 2). The variation step is 0.1 Hz. For each signal, the characteristic frequency and the characteristic period were calculated by three methods (time-domain classic method M1, frequency-domain method M2, and proposed method M3), and the absolute errors compared to the reference were determined. The column of graphs on the left in Figure 2 shows the absolute errors for the characteristic frequency, and the column on the right shows the results for the characteristic period for the three methods M1, M2, and M3.

It can be observed that for all methods, the errors increase with a decrease in the frequency and implicitly with an increase in the period. The M2 method presents almost twice as many absolute errors as the classical method M1, whereas the proposed method M3 presents errors reduced to at least one-third of the number presented by the classical method.

3.2 Testing using a signal having two spectral components

A set of synthetic signals from a sinusoidal signal of 8 units amplitude and 0.9 Hz frequency was used, as was a sinusoidal signal of 3 units amplitude, for which the frequency was varied between 0.3 and 20 Hz (Figure 3). For each signal, the characteristic frequency and the characteristic period were determined by the three methods, and the absolute errors were then compared to the reference (parameters imposed on the signal synthesis) and plotted in Figure 3. Within this test for all methods, the errors increase with decreasing frequency and increasing period. The M2 method presents almost twice as many errors as the classical method M1, whereas the errors of the proposed method M3 were reduced to at least one-third of the number presented by the classical method.

3.3 Testing using a signal having three spectral components

A set of synthetic signals from a sinusoidal signal of 8 units amplitude and 0.9 Hz frequency, a sinusoidal signal of 2.7 units amplitude and 1.3 Hz frequency, and a sinusoidal signal of 3 units amplitude, for which the frequency was varied between 0.3 and 20 Hz, was used (Figure 4). Similarly, the frequencies and characteristic periods were calculated using the three methods. Comparing the absolute errors from Figures 3, 4 in the corresponding domain, it is found that there is no change in the ratio between the errors of the three

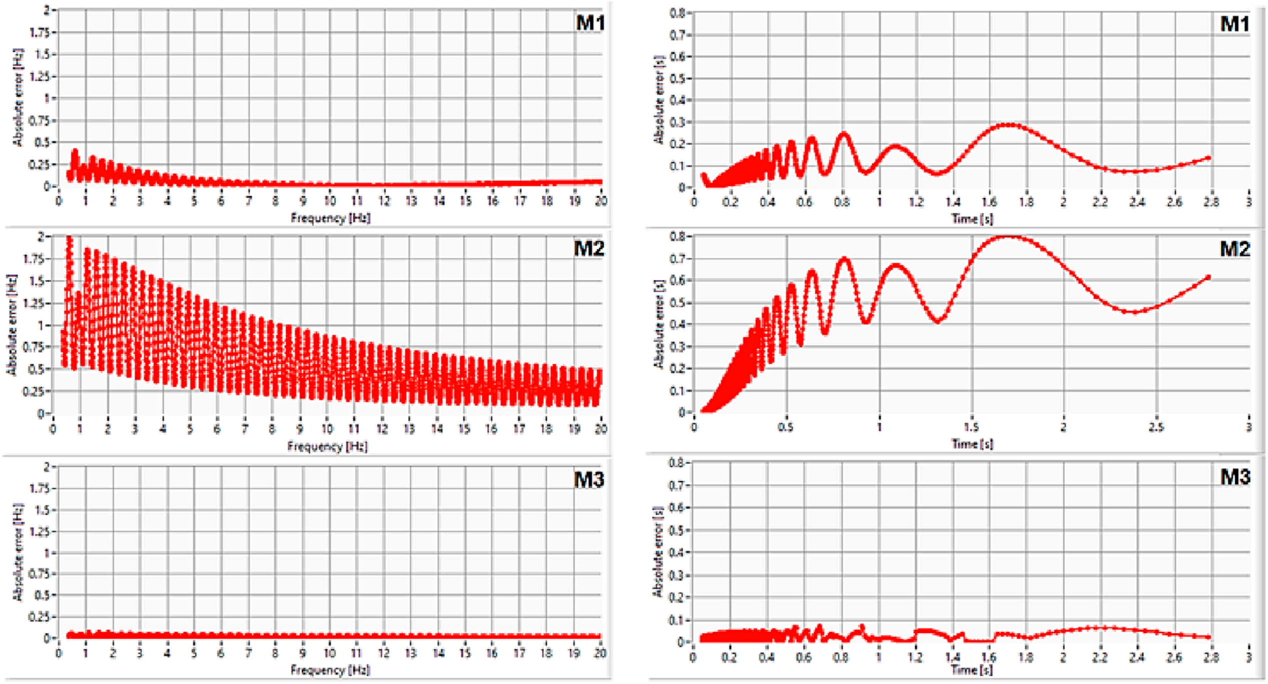

FIGURE 3
Absolute error graph of the three compared methods, in frequency-domain (left) and time-domain (right) calculations, for a multicomponent signal with two spectra.

methods with an increase in the number of harmonics. This asserts that the proposed method leads to a reduced standard deviation compared to the classical method, as well as for multicomponent waveforms.

3.4 Performance under noisy conditions

In seismic monitoring, accurate data are essential for understanding the behavior of structures under stress or seismic activity. Noise can interfere with measurements, leading to false readings or missed events. A high signal-to-noise ratio (SNR) ensures that seismic signals and vibrations are captured clearly, providing reliable data for analysis.

- An SNR below 10 dB indicates poor signal quality, requiring significant noise reduction.
- An SNR between 10 dB and 20 dB is useable but may need some filtering.
- An SNR above 20 dB ensures reliable data with minimal noise interference.

A sinusoidal signal of 3V amplitude was used for the comparative evaluation of methods M1 and M3 in the presence of noise, over which an additional white noise of 1V amplitude was added, as represented in Figure 5. For this case, the signal/noise ratio is 9.5 dB.

FFT performs averaging operations in calculation by its nature. Moreover, the proposed method M3 uses only the distinct peaks obtained after zero padding. Considering the fact that the time-domain energy of the noise is distributed in frequency over the entire spectrum, M3 obtains superior results to the M1 method in the presence of high noise. The results of applying FFT on the signal with noise after zero padding are represented in Figure 6.

Figure 7 presents a comparative analysis of the absolute error in determining the τ_c parameter for a sinusoidal signal frequency variation of up to 20 Hz.

3.5 Standard deviation evaluation

A comparison was made between the classical method and the proposed method, subjected to the dispersion of the values of the characteristic period of an earthquake when several stations that simultaneously record an event are considered. Thus, the average value of the characteristic period and the standard deviation were calculated for a given earthquake characterized by the seismic waves recorded at N different stations. This reasoning was applied to the vertical waves of ten earthquakes that occurred in 2021, 2022, and 2023, with the main parameters listed in Table 1, whose records at 200 Hz were taken from the ESM Database [35].

D_{max} represents the distance between the epicenter and the farthest station from which the recording of the considered earthquake was used. N is the number of stations from which records of a certain earthquake were taken. The average characteristic period was calculated as shown in Equation 6:

$$\overline{\tau_c} = \frac{\sum_1^N \tau_{ci}}{N}. \tag{6}$$

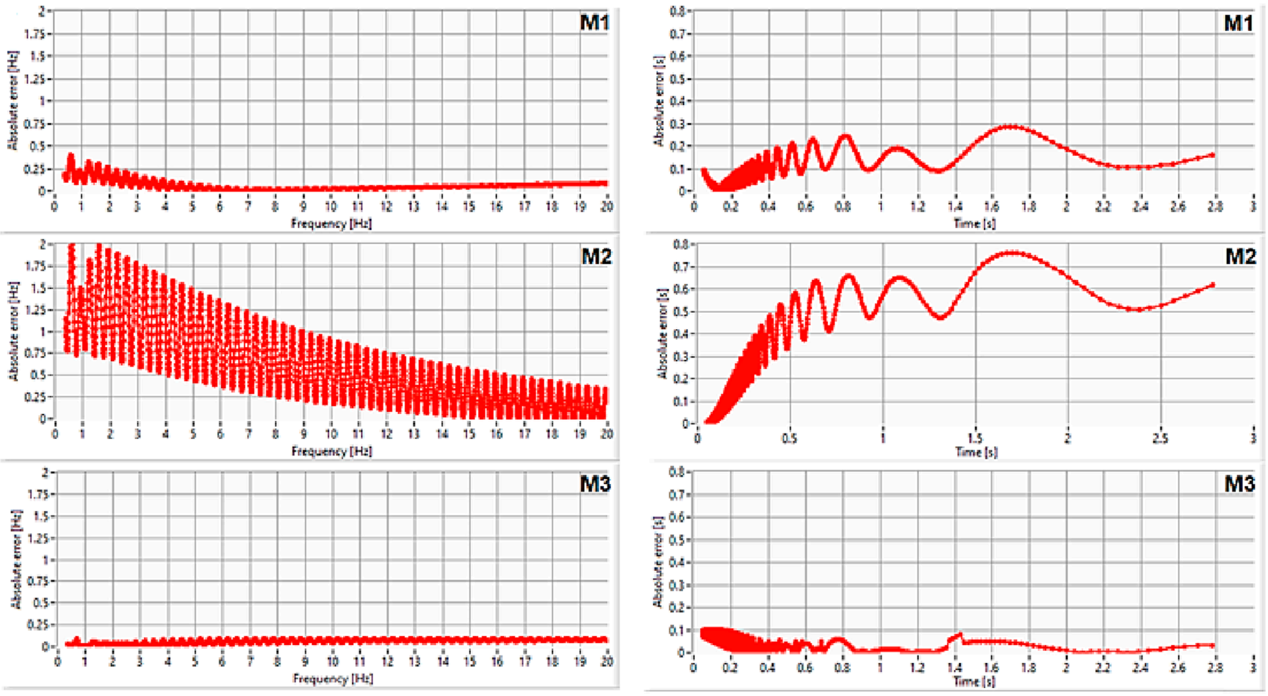

FIGURE 4
Absolute error graph of the three compared methods, in frequency-domain (left) and time-domain (right) calculations, for a multicomponent signal with three spectra.

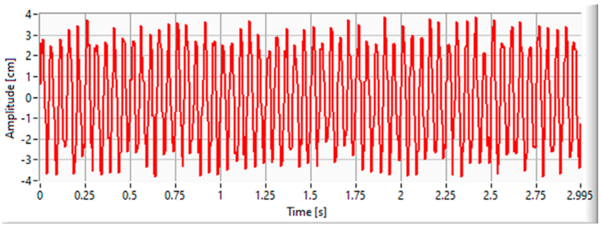

FIGURE 5
Sinusoidal signal summed with white noise.

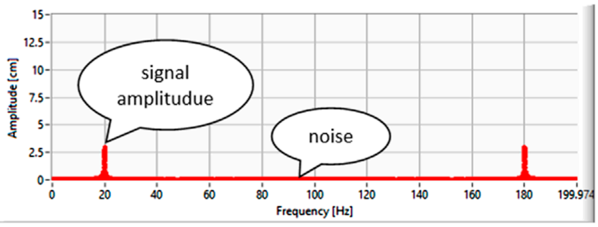

FIGURE 6
Applying FFT to a signal with noise after zero padding.

The standard deviation was determined using Equation 7:

$$s(\tau_c) = \frac{\sum_1^N (\overline{\tau_c} - \tau_{ci})^2}{N-1}. \tag{7}$$

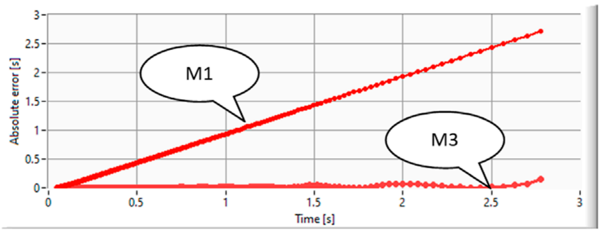

FIGURE 7
Absolute error comparison for M1 and M3 applied on a signal with a frequency up to 20 Hz.

The results in Table 1 show that using the proposed method (M3) leads to a smaller dispersion for each earthquake than the classic method (M1).

Accuracy of EEWS alerts. It is not yet possible to absolutely and rapidly determine the final effects of an earthquake rupture based on the data recorded at the beginning of the earthquake. Hence, EEWS seldom provide false alarms or miss alerts [36]. A false alarm arises when parameter estimation exceeds the alert threshold, although the ground movement after the completed rupture does not reach the evaluated effect. Similarly, a missed alert arises when parameter estimation does not reach the alert threshold, although the ground movement after the completed rupture exceeds the evaluated effect [37]. Even if it is considered that EEWS can perfectly determine the average value of ground motion, the accuracy of EEWS is determined by the variation

TABLE 1 Standard deviation of the seismic characteristic period calculated with the time-domain method (M1) and the proposed method (M3).

Date_event	Magnitude [mw]	Dmax [km]	No. of stations (N)	Classic method (M1)		Proposed method (M3)	
				Mean [s] $\overline{\tau_c}$	Standard deviation [s] $s(\tau_c)$	Mean [s] $\overline{\tau_c}$	Standard deviation [s] $s(\tau_c)$
2023.06.21_0000149	4.1	113	7	0.31	±0.13	0.28	±0.11
2023.06.06_0000145	4.7	293	13	0.63	±0.28	0.52	±0.15
2023.02.14_0000139	5.5	269	24	0.98	±0.31	1.11	±0.22
2021.08.01_0000049	5.7	260	22	1.14	±0.82	1.13	±0.43
2022.11.23_0000008	6.1	315	30	1.05	±0.94	1.21	±0.48
2023.02.20_0000197	6.3	335	34	1.30	±0.95	1.28	±0.39
2023.02.06_0000011	6.7	430	40	1.45	±0.45	1.52	±0.42
2020.10.30_0000082	7.0	450	40	2.15	±0.50	2.08	±0.49
2023.02.06_0000222	7.5	480	40	3.42	±0.43	3.55	±0.46
2023.02.06_0000008	7.8	620	40	4.27	±1.24	4.36	±1.22

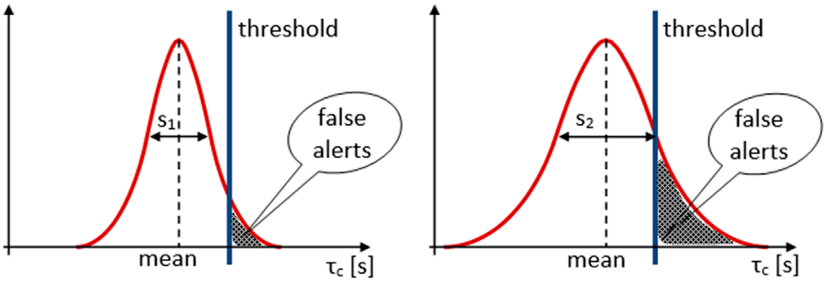

FIGURE 8
Cause–effect relationship between EEW false alarms, threshold values, and standard deviations.

from the average value of the ground motion metrics that the EEW system uses to evaluate ground motion [38]. Under these conditions, if two methods for evaluating ground motion metrics are considered to have the same mean value for an earthquake but different standard deviations s_1 and s_2, as shown in Figure 8, the number of false alarms, given by the area of the shaded surface, is higher for the higher standard deviation. It results in one of the major advantages of using the proposed method (M3) instead of the classic one (M1).

4 Discussion

The proposed method was tested to determine the characteristic period by calculating the characteristic frequency from the frequency spectrum of the signal. Testing was carried out in two ways: by simulation and by calculation of real P-wave signals obtained from earthquake recordings.

4.1 Testing the method by simulation

Synthesized signals with precisely known frequency/periods were used for testing. For these signals, the frequency/period was calculated using the classical method M1 from the time domain, which uses the ratio between speed and displacement; the method M2 based on Equation 4, which is derived directly from the classical method by correspondence in frequency; and the proposed method, M3.

Method M1 provides results in terms of time, and M2 and M3 provide results in terms of frequency. To make comparisons from the point of view of absolute errors both as characteristic period and characteristic frequency, the characteristic period obtained by M1 was converted into characteristic frequency, and the characteristic frequencies obtained by M2 and M3 were converted into characteristic periods.

Tests were carried out with pure sinusoidal signals and with sinusoidal signals with harmonics, and graphs of the absolute errors obtained for the three methods were plotted. The following observations were made:

- Switching to the frequency domain (M2) did not provide better results than the classical method.
- The application of the M3 method leads to a reduction in the relative errors for all test variants with synthesized signals, regardless of the number or frequency values of the harmonics.
- Because P-wave sequences are limited to 3 s, signals with frequencies below 0.3 Hz or periods of more than 3 s will contain less than one period of the useful signal.

Thus, for all methods, the errors increase at low frequencies and implicitly at long periods and represent the area where saturation occurs for large earthquakes.

4.2 Testing the method with real P waves

Because this work refers to a method of estimating the characteristic period of the P wave of earthquakes, testing with real P waves was carried out only for the purpose of estimating the period and validating the simulation testing. Forecasting the magnitude based on the P wave is dependent on the soil structure in the direction of earthquake propagation from the epicenter to the seismic station where the wave is recorded, which is geophysically dependent. For the test, 290 seismic recordings from 10 different earthquakes recorded at different stations were used. For each recording, the characteristic period was determined using M1 and M3. The periods were grouped by the ten earthquake events, and the average value and standard deviation were calculated for each event. As shown in Table 1, the standard deviation calculated for the proposed method has lower values than the classical method of up to 6.3 Mw, corresponding to a characteristic period of 1.30 s, with no other specific conditions where the performance differs. For earthquakes above this value, no improvements were observed compared to the classical method.

EEW systems use a threshold for both the characteristic period and maximum amplitude. For the characteristic period, the threshold was set to 1 s. The alarm is sent if the threshold imposed for the characteristic period is exceeded, along with the threshold for the maximum amplitude. Given that the EEW alarm is triggered for a threshold of 1 s corresponding to 5.5–5.7 Mw, which is the interval in which the proposed method provides a better standard deviation, we consider that this method can be used to increase the EEW performance.

5 Conclusion

Most earthquake early warning systems are used to predict the event magnitude and the peak ground acceleration parameters attained from the initial P waves recorded at close seismic stations. Commonly, the peak amplitudes of displacement, along with the characteristic period and integral of the squared velocity, are used in specific algorithms to compute the level of danger and the necessity for EEWS to trigger an emergency alarm. Estimating the characteristic period τc involves inputs such as velocity and acceleration from multiple P waves that are similarly recorded at several seismic stations. As τc increases with the magnitude of an earthquake and is independent of the distance between the earthquake epicenter and an observation station up to a few hundred kilometers away, it is a key factor in EWS regional seismic prediction.

The proposed method for calculating the characteristic period of the seismic P wave in the frequency domain has a lower standard deviation than the classical method. Tests carried out using synthetic signals, with a single tone or with harmonic content, reveal that the determination errors of the characteristic period are smaller when using this method. Statistical tests to evaluate the standard deviation, in which earthquake records from several stations were interpreted, also revealed the superior behavior of the proposed method up to 6.3 Mw, with direct consequences in reducing the number of false alarms. Thus, it is suited for EEWS systems that use the τc parameter in alarm decision algorithms. In this context, we consider that this method can be used with good results in magnitude prediction applications based on the characteristic period of the initial wave.

Data availability statement

The raw data supporting the conclusions of this article will be made available by the authors, without undue reservation.

Author contributions

CD: writing–original draft. ES: writing–review and editing. MT: writing–original draft.

Funding

The author(s) declare that financial support was received for the research, authorship, and/or publication of this article. This research was funded by the European Regional Development Fund, grant number 7227/19.11.2021 (SMIS code 137414) — “Seismic warning system with automatic unlocking of entrance doors with interphone.” The article publishing charge was funded by “Gheorghe Asachi” Technical University of Iași, România.

Conflict of interest

The authors declare that the research was conducted in the absence of any commercial or financial relationships that could be construed as a potential conflict of interest.

Publisher’s note

References

1. Iwata D, Nanjo KZ. Adaptive estimation of the Gutenberg–Richter b value using a state space model and particle filtering. *Scientific Rep* (2024) 14(1):4630. doi:10.1038/s41598-024-54576-x

2. Taroni M, Vocalelli G, De Polis A. Gutenberg–Richter B-value time series forecasting: a weighted likelihood approach. *Forecasting* (2021) 3(3):561–9. doi:10.3390/forecast3030035

3. Rafiei MH, Adeli H. NEEWS: a novel earthquake early warning model using neural dynamic classification and neural dynamic optimization. *Soil Dyn Earthquake Eng* (2017) 100:417–27. doi:10.1016/j.soildyn.2017.05.013

4. Kodera Y, Hayashimoto N, Tamaribuchi K, Noguchi K, Moriwaki K, Takahashi R, et al. Developments of the nationwide earthquake early warning system in Japan after the 2011 M w 9.0 Tohoku-Oki earthquake. *Front Earth Sci* (2021) 9. doi:10.3389/feart.2021.726045

5. Goltz JD, Evelyn R. Imminent warning communication: earthquake early warning and short-term forecasting in Japan and the US. In: *Disaster risk communication: a challenge from a social psychological perspective* (2020). p. 121–53.

6. Wu Y-M, Mittal H, Chen D-Y, Hsu T-Y, Lin P-Y. Earthquake early warning systems in Taiwan: current status. *J Geol Soc India* (2021) 97:1525–32. doi:10.1007/s12594-021-1909-6

7. Kumar R, Mittal H, Sharma B. Earthquake genesis and earthquake early warning systems: challenges and a way forward. *Surv Geophys* (2022) 43(4):1143–68. doi:10.1007/s10712-022-09710-7

8. Cuéllar A, Espinosa-Aranda JM, Suárez R, Ibarrola G, Uribe A, Rodríguez FH, et al. The Mexican Seismic Alert System (SASMEX): its alert signals, broadcast results and performance during the M 7.4 Punta Maldonado earthquake of March 20th. In: *Early warning for geological disasters: scientific methods and current practice* (2012). p. 71–87.

9. Sheen D-H, Park J-H, Chi H-C, Hwang E-H, Lim I-S, Jeong Seong Y, et al. The first stage of an earthquake early warning system in South Korea. *Seismological Res Lett* (2017) 88(6):1491–8. doi:10.1785/0220170062

10. Mittal H, Wu Y-M, Sharma ML, Yang BM, Gupta S. Testing the performance of earthquake early warning system in northern India. *Acta Geophysica* (2019) 67:59–75. doi:10.1007/s11600-018-0210-6

11. Ionescu C, Marmureanu A, Marmureanu G. Rapid earthquake early warning (REWS) in Romania: application in real time for governmental authority and critical infrastructures. In: *The 1940 vrancea earthquake. Issues, insights and lessons learnt: proceedings of the symposium commemorating 75 Years from november 10, 1940 vrancea earthquake*. Springer International Publishing (2016).

12. Erdik M, Fahjan Y, Ozel O, Alcik H, Mert A, Gul M. Istanbul earthquake rapid response and the early warning system. *Bull earthquake Eng* (2003) 1:157–63. doi:10.1023/A:1024813612271

13. Patel SC, Allen RM. The MyShake App: user experience of early warning delivery and earthquake shaking. *Seismological Soc America* (2022) 93(6):3324–36. doi:10.1785/0220220062

14. Valbonesi C. Between necessity and legal responsibility: the development of EEWS in Italy and its international framework. *Front Earth Sci* (2021) 9:685153. doi:10.3389/feart.2021.685153

15. Wang Y, Li S, Song J. Threshold-based evolutionary magnitude estimation for an earthquake early warning system in the Sichuan–Yunnan region, China. *Scientific Rep* (2020) 10(1):21055. doi:10.1038/s41598-020-78046-2

16. Lior I, Rivet D, Ampuero J-P, Sladen A, Barrientos S, Sánchez-Olavarría R, et al. Magnitude estimation and ground motion prediction to harness fiber optic distributed acoustic sensing for earthquake early warning. *Scientific Rep* (2023) 13(1):424. doi:10.1038/s41598-023-27444-3

17. Furuya I. Predominant period and magnitude. *J Phys Earth* (1969) 17(2):119–26. doi:10.4294/jpe1952.17.119

18. Kanai K. 3. On the spectrum of strong earthquake motions. *Bull Earthq Res Inst* (1961) 39:85–95.

19. Nakamura Y. On the urgent earthquake detection and alarm system (UrEDAS). *Proc 9th World Conference Earthquake Engineering* (1988) 7:673–8.

20. Allen RM, Hiroo K. The potential for earthquake early warning in southern California. *Science* (2003) 300(5620):786–9. doi:10.1126/science.1080912

21. Kanamori H. Real-time seismology and earthquake damage mitigation. *Annu Rev Earth Planet Sci* (2005) 33(1):195–214. doi:10.1146/annurev.earth.33.092203.122626

22. Cheng Z, Peng C, Chen M. Real-time seismic intensity measurements prediction for earthquake early warning: a systematic literature review. *Sensors* (2023) 23(11):5052. doi:10.3390/s23115052

23. Skarlatoudis AA, Thio HK, Somerville PG. Estimating shallow shear-wave velocity profiles in Alaska using the initial portion of P waves from local earthquakes. *Earthquake Spectra* (2022) 38(2):1076–102. doi:10.1177/87552930211061589

24. Hsu T-Y, Wu R-T, Liang C-W, Kuo C-H, Lin C-M. Peak ground acceleration estimation using P-wave parameters and horizontal-to-vertical spectral ratios. *Terr Atmos Ocean Sci* (2020) 31(1):1–8. doi:10.3319/tao.2019.07.04.01

25. Zlydenko O, Elidan G, Hassidim A, Kukliansky D, Matias Y, Meade B, et al. A neural encoder for earthquake rate forecasting. *Scientific Rep* (2023) 13(1):12350. doi:10.1038/s41598-023-38033-9

26. Chandrakumar C, Prasanna R, Stephens M, Tan ML. Earthquake early warning systems based on low-cost ground motion sensors: a systematic literature review. *Front Sensors* (2022) 3:1020202. doi:10.3389/fsens.2022.1020202

27. Korrat IM, Lethy A, ElGabry MN, Hussein HM, Othman AS. Discrimination between small earthquakes and quarry blasts in Egypt using spectral source characteristics. *Pure Appl Geophys* (2022) 179(2):599–618. doi:10.1007/s00024-022-02953-w

28. Mariani MC, Gonzalez-Huizar H, Md AMB, Tweneboah OK. Using dynamic Fourier analysis to discriminate between seismic signals from natural earthquakes and mining explosions. *aims geosciences* (2017) 3(3):438–49. doi:10.3934/ms.2017.3.438

29. Donciu C, Temneanu M. An alternative method to zero-padded DFT. *Measurement* (2015) 70:14–20. doi:10.1016/j.measurement.2015.03.015

30. Alazzawi O, Wang D. A novel structural damage identification method based on the acceleration responses under ambient vibration and an optimized deep residual algorithm. *Struct Health Monit* (2022) 21(6):2587–617. doi:10.1177/14759217211065009

31. Naghizadeh M, Innanen KA. Two-dimensional fast generalized Fourier interpolation of seismic records. *Geophys Prospecting* (2013) 61:62–76. doi:10.1111/j.1365-2478.2012.01089.x

32. Marcelo Hidalgo R, Fernández G, Rivera RR, Larrondo H. A simple adjustable window algorithm to improve FFT measurements. *IEEE Trans Instrumentation Meas* (2002) 51(1):31–6. doi:10.1109/19.989893

33. Van DN, Basu B. Zero-pad effects on conditional simulation and application of spatially-varying earthquake motions. In: *6th European workshop on structural health monitoring-tu*, 3 (2012).

34. Chen Y, He Y, Li S, Wu H, Peng Z. Seismic spectrum decomposition based on sparse time-frequency analysis. *J Appl Geophys* (2020) 177:104031. doi:10.1016/j.jappgeo.2020.104031

35. Luzi L, Lanzano G, Felicetta C, et al. *Engineering strong motion Database (ESM) (version 2.0)*. Rome, Italy: Istituto Nazionale di Geofisica e Vulcanologia (2020). Available from: https://esm-db.eu/#/event/search Accessed October 8, 2023.

36. Minson SE, Meier M-A, Baltay AS, Hanks TC, Cochran ES. The limits of earthquake early warning: timeliness of ground motion estimates. *Sci Adv* (2018) 4(3):eaaq0504. doi:10.1126/sciadv.aaq0504

37. Festa G, Picozzi M, Caruso A, Colombelli S, Cattaneo M, Chiaraluce L, et al. Performance of earthquake early warning systems during the 2016–2017 Mw 5–6.5 Central Italy sequence. *Seismological Res Lett* (2018) 89(1):1–12. doi:10.1785/0220170150

38. Minson SE, Baltay AS, Cochran ES, Hanks TC, Page MT, McBride SK, et al. Men-Andrin Meier. The limits of earthquake early warning accuracy and best alerting strategy. *Scientific Rep* (2019) 9(1):2478. doi:10.1038/s41598-019-39384-y

Frontiers in Physics

TYPE Original Research
PUBLISHED 31 March 2025
DOI 10.3389/fphy.2025.1539545

EDITED BY
Yilin Qu,
Northwestern Polytechnical University, China

REVIEWED BY
Ali Mehri,
Babol Noshirvani University of Technology, Iran
Ang Zhao,
Shanghai Civil Aviation College, China

*CORRESPONDENCE
Ziyu Cui,
✉ 13939099786@163.com

RECEIVED 04 December 2024
ACCEPTED 05 March 2025
PUBLISHED 31 March 2025

CITATION
Hu Q, Cui Z, Liu H and Zhong S (2025) Research on noise prediction methods for sound barriers based on the integration of conditional generative adversarial networks and numerical methods.
Front. Phys. 13:1539545.
doi: 10.3389/fphy.2025.1539545

Research on noise prediction methods for sound barriers based on the integration of conditional generative adversarial networks and numerical methods

Qian Hu[1], Ziyu Cui[2]*, Hongxue Liu[1] and Senhao Zhong[3]

[1]School of Architectural Engineering, Huanghuai University, Zhumadian, China, [2]College of Architecture and Civil Engineering, Xinyang Normal University, Xinyang, China, [3]Solux College of Architecture and Design, University of South China, Hengyang, China

This study proposes a novel approach utilizing Conditional Generative Adversarial Networks (CGANs) to accelerate wideband acoustic state analysis, addressing the computational challenges in traditional Boundary Element Method (BEM) approaches. Traditional BEM-based acoustic analysis requires repeated computation of frequency-dependent system matrices across multiple frequencies, leading to significant computational costs. The asymmetry and full-rank nature of the BEM coefficient matrices further increase computational demands, particularly in large-scale problems. To overcome these challenges, this paper introduces a CGAN-based modeling framework that significantly reduces computation time while maintaining high predictive accuracy. The framework demonstrates exceptional adaptability when handling datasets with varying characteristics, effectively capturing underlying patterns within the data. Numerical experiments validate the effectiveness of the proposed method, highlighting its advantages in both accuracy and computational efficiency. This CGAN-based approach provides a promising alternative for efficient wideband acoustic analysis, significantly reducing computation time while ensuring accuracy.

KEYWORDS

boundary element method, CGAN, sound barrier, acoustic scattering, machine learning

1 Introduction

In the field of acoustics, the simulation and analysis of sound wave propagation through complex structures [1, 2] are of paramount importance. Frequency sweep calculations [3] are crucial for understanding the behavior of sound waves across a range of frequencies, which is essential for designing effective acoustic barriers and noise reduction devices. Traditional computational methods typically employ the Finite Element Method (FEM) [4–6] or the Boundary Element Method (BEM) [7–10]. Among these, BEM [11]is widely recognized for its superior accuracy and simplicity in mesh generation [12–14], making it a preferred method for addressing acoustic problems. Its natural compliance with the

Sommerfeld radiation condition at infinity further solidifies its utility in external acoustic analyses [15], [9].

Conventional sound pressure calculations are typically optimized for specific frequencies, limiting their application across broader frequency ranges. To address this limitation, broadband analysis [16] has been introduced, enabling the computation of results over a wider frequency spectrum. However, in broadband analysis [17–19], the frequency band is divided into segments, necessitating the recalculation of the coefficient matrix and boundary element system [20, 21], equations for each frequency. This process imposes a significant computational burden. Recent advancements in computational power and data-driven methods have spurred the development of neural networks [22–25], presenting promising opportunities for accelerating complex acoustic analyses. For example, [26] proposed a noise prediction model for wing structures, while [27] utilized Deep Neural Networks (DNN) to expedite uncertainty quantification in vibro-acoustic coupling analysis. These studies underscore the potential of neural networks in acoustic modeling and analysis.

This paper introduces an efficient method for accelerating frequency sweep calculations in broadband acoustics using Conditional Generative Adversarial Networks (CGANs) [28]. By employing CGANs, the computational overhead inherent in broadband analysis is significantly reduced. Generative Adversarial Networks (GANs) [29–32], initially proposed as a framework for training generative models, offer several advantages: eliminating the need for Markov chains, relying solely on backpropagation for gradient computation, avoiding inference during learning, and easily integrating various factors and interactions. However, a major limitation of GANs is their inability to control the modes of generated data in an unconditional model.

In contrast, Conditional Generative Adversarial Networks (CGANs) incorporate a conditioning variable, enabling control over the generative process and constraining outputs to a user-defined distribution. This enhancement improves model stability. The adversarial training mechanism in CGANs not only ensures accurate and realistic data generation but also uncovers the underlying relationships within the data [33–36]. These capabilities make CGANs particularly suitable for acoustic scattering problems characterized by complex distribution features. This study focuses on integrating CGANs with traditional numerical methods to predict the acoustic scattering characteristics of barriers, thereby reducing computational complexity, accelerating computations, and establishing new surrogate models for acoustic scattering analysis [37, 38].

Neural network-based prediction methods are widely adopted across various fields due to their dynamic capabilities [39–42]. These methods leverage learning algorithms that achieve high prediction accuracy by iterative training on simulated sound pressure and sensitivity data. A key advantage of this approach is its ability to construct highly nonlinear models [43–45], making it particularly effective for complex noise analysis. Additionally, these methods reduce computational workloads, provide high-precision predictions, and meet the demands of rapid analysis in engineering applications. As technology continues to advance, neural network-based methods have evolved rapidly, finding applications across numerous disciplines.

Significant research progress in machine learning-driven sound pressure [46] prediction has been made in recent years, both domestically and internationally. Applications such as robotic fish, noise barrier models, and submarines demonstrate the engineering relevance of these advancements. In 2023, [47] applied deep neural networks and Catmull-Clark subdivision surfaces [48, 49] to perform vibro-acoustic analysis on various geometric models, achieving sound pressure responses across multiple parameters and dimensions. That same year, [50] used Loop subdivision surfaces to model the robotic fish “Manta” and predicted the effects of geometric and material parameters on sound pressure.

To improve the efficiency of broadband optimization and apply CGANs to 2D acoustic problems, this paper presents the following contributions:

- Development of a CGAN-based network for predicting data, such as sound pressure.
- Validation of the CGAN network’s performance through an infinitely long rigid model and an acoustic barrier model.

The structure of this paper is as follows: Section 2 outlines the boundary element integral equations, while Section 3 details the theory of CGAN networks and their loss functions. Section 4.1 validates the accuracy and efficiency of CGAN predictions using the infinitely long rigid cylinder model, and Section 4.2 demonstrates the feasibility of CGAN networks as surrogate models for acoustic scattering analysis through an acoustic barrier model.

2 Acoustic boundary element method

Consider the Helmholtz equation for a 2D acoustic problem, given as Equation 1.

$$\nabla^2 p(\mathbf{x}) + k^2 p(\mathbf{x}) = 0, \forall \mathbf{x} \in \Omega \tag{1}$$

The Helmholtz half-space problem can be represented by the following BIE and normal derivative boundary integral equation (HBIE).

$$C(\mathbf{x}) p(\mathbf{x}) + \int_S F(\mathbf{x},\mathbf{y}) p(\mathbf{y}) \,\mathrm{d}S(\mathbf{y}) = \int_S G(\mathbf{x},\mathbf{y}) q(\mathbf{y}) \,\mathrm{d}S(\mathbf{y}) + p_{\mathrm{inc}}(\mathbf{x}) \tag{2}$$

and

$$C(\mathbf{x}) q(\mathbf{x}) + \int_S H(\mathbf{x},\mathbf{y}) p(\mathbf{y}) \,\mathrm{d}S(\mathbf{y}) = \int_S K(\mathbf{x},\mathbf{y}) q(\mathbf{y}) \,\mathrm{d}S(\mathbf{y}) + \frac{\partial p_{\mathrm{inc}}(\mathbf{x})}{\partial n(\mathbf{x})} \tag{3}$$

where $\mathbf{y}$ signifies the field point, $\mathbf{x}$ denotes the source point, and q is the normal derivative of the sound pressure p: $q(\mathbf{x}) = \partial p(\mathbf{x})/\partial n(\mathbf{x})$. When $\mathbf{x}$ is located on a border that is smooth S, $C(\mathbf{x}) = 1/2$. Acoustic pressure incident at position $\mathbf{x}$ is given by $p_{inc}(\mathbf{x})$. Green’s function $G(\mathbf{x},\mathbf{y})$ and its derivative in Equation 2 and Equation 3 are presented as follows

$$\begin{cases} G(\mathbf{x},\mathbf{y}) = \dfrac{\mathrm{i}}{4} H_0^{(1)}(kr) \\ F(\mathbf{x},\mathbf{y}) = \dfrac{\partial G(\mathbf{x},\mathbf{y})}{\partial n(\mathbf{y})} = -\dfrac{\mathrm{i}k}{4} H_1^{(1)}(kr) \dfrac{\partial r}{\partial n(\mathbf{y})} \\ K(\mathbf{x},\mathbf{y}) = \dfrac{\partial G(\mathbf{x},\mathbf{y})}{\partial n(\mathbf{x})} = -\dfrac{\mathrm{i}k}{4} H_1^{(1)}(kr) \dfrac{\partial r}{\partial n(\mathbf{x})} \\ H(\mathbf{x},\mathbf{y}) = \dfrac{\partial^2 G(\mathbf{x},\mathbf{y})}{\partial n(\mathbf{x}) \partial n(\mathbf{y})} = \dfrac{\mathrm{i}k}{4r} H_1^{(1)}(kr) n_j(\mathbf{x}) n_j(\mathbf{y}) - \dfrac{\mathrm{i}k^2}{4} H_2^{(1)}(kr) \dfrac{\partial r}{\partial n(\mathbf{x})} \dfrac{\partial r}{\partial n(\mathbf{y})} \end{cases} \tag{4}$$

where the nth order first kind Hankel function is indicated by $H_n^{(1)}$, k denotes by the wave number, $\mathrm{i} = \sqrt{-1}$, n_j is the Cartesian component of $n(\mathbf{x})$ or $n(\mathbf{y})$ and the distance between the field and source locations is represented by the formula $r = |\mathbf{x} - \mathbf{y}|$.

For exterior acoustic problems, using either Equation 2 or Equation 3 alone can lead to non-uniqueness of the solution at certain imaginary frequencies. According to the Burton-Miller idea, a linear combination of Equation2 and Equation 3 can effectively resolve this issue. The Burton-Miller formulation is expressed as follows

$$\begin{aligned} C(\mathbf{x})\left[p(\mathbf{x}) + \alpha q(\mathbf{x})\right] + \int_S \left[F(\mathbf{x},\mathbf{y}) + \alpha H(\mathbf{x},\mathbf{y})\right] p(\mathbf{y})\,\mathrm{d}S(\mathbf{y}) \\ = \int_S \left[G(\mathbf{x},\mathbf{y}) + \alpha K(\mathbf{x},\mathbf{y})\right] q(\mathbf{y})\,\mathrm{d}S(\mathbf{y}) + p_{\mathrm{inc}}(\mathbf{x}) + \alpha \frac{\partial p_{\mathrm{inc}}(\mathbf{x})}{\partial n(\mathbf{x})} \end{aligned} \tag{5}$$

in which α represents the coupling parameter: defined as $\alpha = \mathrm{i}/k$ where $k > 1$ and $\alpha = \mathrm{i}$ in other cases.

By discretizing the structural boundary into several elements using constant elements and introducing the coefficient matrix, Equation 5 can be reformulated as follows

$$\mathbf{H}\mathbf{p} - \mathbf{G}\mathbf{q} = \mathbf{p}_f^{\mathrm{inc}} \tag{6}$$

where $\mathbf{H}$ and $\mathbf{G}$ $\in \mathbb{C}^{N\times N}$ (N indicates the number of degrees of freedom.) are the coefficient matrices. They are asymmetric, fully populated, and frequency-related. The column vectors $\mathbf{p}$ and $\mathbf{q}$, respectively, represent the sound pressure and the acoustic flux at the collocation locations. $\mathbf{p}_f^{\mathrm{inc}}$ is the vector of the incident wave. To determine the sound pressure values at the boundary surface nodes, Equation 6 needs to be solved. Subsequently, the sound pressure can be computed at any point within the acoustic domain by using Equation 5 with $\alpha = 0$ and $C(\mathbf{x}) = 1$.

Its sound pressure, $\mathbf{p}_f$, can be written as follows if the computation takes into account the external acoustic field.

$$\mathbf{p}_f = -\left|\mathbf{H}_f\mathbf{p} - \mathbf{G}_f\mathbf{q}\right| + \mathbf{p}_f^{inc} \tag{7}$$

where the matrices $\mathbf{H}_f$ and $\mathbf{G}_f$ as well as the vector $\mathbf{p}_f^{inc}$ are similar to those in Equation 6, except that the source point $\mathbf{x}$ is outside the structure domain.

2.1 BEM formulas for shape sensitivity analysis of acoustics

To derive the general formula for acoustic sensitivity analysis by the direct differentiation method, we first differentiate Equation 5 to obtain.

$$\begin{aligned} C(\mathbf{x})\left[\dot{p}(\mathbf{x}) + \alpha \dot{q}(\mathbf{x})\right] &+ \int_S \left[\dot{F}(\mathbf{x},\mathbf{y}) + \alpha \dot{H}(\mathbf{x},\mathbf{y})\right] p(\mathbf{y})\,\mathrm{d}S(\mathbf{y}) \\ &+ \int_S \left[F(\mathbf{x},\mathbf{y}) + \alpha H(\mathbf{x},\mathbf{y})\right] \dot{p}(\mathbf{y})\,\mathrm{d}S(\mathbf{y}) \\ &+ \int_S \left[F(\mathbf{x},\mathbf{y}) + \alpha H(\mathbf{x},\mathbf{y})\right] p(\mathbf{y})\,\mathrm{d}\dot{S}(\mathbf{y}) \\ &= \int_S \left[\dot{G}(\mathbf{x},\mathbf{y}) + \alpha \dot{K}(\mathbf{x},\mathbf{y})\right] q(\mathbf{y})\,\mathrm{d}S(\mathbf{y}) \\ &+ \int_S \left[G(\mathbf{x},\mathbf{y}) + \alpha K(\mathbf{x},\mathbf{y})\right] \dot{q}(\mathbf{y})\,\mathrm{d}S(\mathbf{y}) \\ &+ \int_S \left[G(\mathbf{x},\mathbf{y}) + \alpha K(\mathbf{x},\mathbf{y})\right] q(\mathbf{y})\,\mathrm{d}\dot{S}(\mathbf{y}) \\ &+ \dot{p}_{\mathrm{inc}}(\mathbf{x}) + \alpha \frac{\partial \dot{p}_{\mathrm{inc}}(\mathbf{x})}{\partial n(\mathbf{x})} \end{aligned} \tag{8}$$

The basic solution and its derivatives are determined by the coordinates of the field and source points. Therefore, under continuous shape modification, their values might be impacted by a change in a form design variable. In general, the sensitivities of the coordinates can be used to express $\dot{G}$, $\dot{F}$, $\dot{K}$, $\dot{H}$, $\dot{p}$ and $\dot{q}$.

$$\begin{cases} \dot{G}(\mathbf{x},\mathbf{y}) = -\dfrac{\mathrm{i}k}{4} H_1^{(1)}(kr)\,\dot{r} \\[2ex] \dot{F}(\mathbf{x},\mathbf{y}) = -\dfrac{\mathrm{i}k}{4} H_1^{(1)}(kr) \left[\dfrac{\left(\dot{\mathbf{y}}_j - \dot{\mathbf{x}}_j\right) n_j(\mathbf{y})}{r} + r_{,j}\dot{n}_j(\mathbf{y})\right] \\ \qquad + \dfrac{\mathrm{i}k^2}{4} H_2^{(1)}(kr)\,\dot{r} r_{,j} n_j(\mathbf{y}) \\[2ex] \dot{K}(\mathbf{x},\mathbf{y}) = -\dfrac{\mathrm{i}k}{4} H_1^{(1)}(kr) \left[\dfrac{\left(\dot{\mathbf{y}}_j - \dot{\mathbf{x}}_j\right) n_j(\mathbf{x})}{r} + r_{,j}\dot{n}_j(\mathbf{x})\right] \\ \qquad + \dfrac{\mathrm{i}k^2}{4} H_2^{(1)}(kr)\,\dot{r} r_{,j} n_j(\mathbf{x}) \\[2ex] \dot{H}(\mathbf{x},\mathbf{y}) = \dfrac{\mathrm{i}k}{4r} H_1^{(1)}(kr) \left[\dot{n}_j(\mathbf{x}) n_j(\mathbf{y}) + n_j(\mathbf{x}) \dot{n}_j(\mathbf{y})\right] \\ \qquad + \dfrac{\mathrm{i}k^3}{4} H_3^{(1)}(kr)\,\dot{r} r_{,j} n_j(\mathbf{x}) r_{,l} n_l(\mathbf{y}) \\ \qquad - \dfrac{\mathrm{i}k^2}{4} H_2^{(1)}(kr) \dfrac{n_j(\mathbf{x}) n_j(\mathbf{y})\,\dot{r}}{r} \\ \qquad - \dfrac{\mathrm{i}k^2}{4} H_2^{(1)}(kr)\, r_{,j} n_j(\mathbf{x}) \left[\dot{r}_{,l} n_l(\mathbf{y}) + r_{,l}\dot{n}_l(\mathbf{y})\right] \\ \qquad - \dfrac{\mathrm{i}k^2}{4} H_2^{(1)}(kr)\, r_{,l} n_l(\mathbf{y}) \left[\dot{r}_{,l} n_j(\mathbf{x}) + r_{,l}\dot{n}_j(\mathbf{x})\right] \\ \qquad - \dfrac{\mathrm{i}k^2}{4} H_2^{(1)}(kr) \dfrac{2\dot{r} r_{,j} n_j(\mathbf{x}) r_{,l} n_l(\mathbf{y})}{r} \end{cases} \tag{9}$$

where Equations 10, 11 express the details of Equations 9.

$$\dot{r} = r_{,j}\left(\dot{\mathbf{y}}_j - \dot{\mathbf{x}}_j\right) \tag{10}$$

$$\dot{r}_{,l} n_l(\mathbf{y}) + r_{,l}\dot{n}_l(\mathbf{y}) = \frac{\left(\dot{\mathbf{y}}_l - \dot{\mathbf{x}}_l\right) n_l(\mathbf{y})}{r} - \frac{\dot{r} r_{,l} n_l(\mathbf{y})}{r} + r_{,j}\dot{n}_l(\mathbf{y}) \tag{11}$$

where $\dot{()}$ indicates differentiation concerning the design variables. Once the form design variable has fully parameterized the border of the studied domain, $\dot{\mathbf{x}}_j$ and $\dot{\mathbf{y}}_j$ will be assessed. $\dot{n}_l(\mathbf{y})$ and $\mathrm{d}\dot{S}(\mathbf{y})$ can be written as Equations 12, 13

$$\dot{n}_l(\mathbf{y}) = -\dot{\mathbf{y}}_{j,l} n_j(\mathbf{y}) + \dot{\mathbf{y}}_{j,m} n_j(\mathbf{y}) n_m(\mathbf{y}) n_l(\mathbf{y}) \tag{12}$$

and

$$\mathrm{d}\dot{S}(\mathbf{y}) = \left[\dot{\mathbf{y}}_{l,l} - \dot{\mathbf{y}}_{l,j} n_l(\mathbf{y}) n_j(\mathbf{y})\right] \mathrm{d}S(\mathbf{y}) \tag{13}$$

where the partial derivatives concerning the coordinate component are indicated by an index following a comma, such as $\dot{\mathbf{y}}_{j,m} = \partial\dot{\mathbf{y}}_j/\partial\mathbf{y}_m$.

The following matrix-form linear algebraic equations are obtained by discretizing Equation 8 using the constant boundary element and gathering the equations for each collocation point.

$$\mathbf{H}\dot{\mathbf{p}} + \dot{\mathbf{H}}\mathbf{p} - \mathbf{G}\dot{\mathbf{q}} - \dot{\mathbf{G}}\mathbf{q} = \dot{\mathbf{p}}_{\mathrm{inc}} \tag{14}$$

where $\dot{\mathbf{H}}$ and $\dot{\mathbf{G}}$ $\in \mathbb{C}^{N\times N}$ (The number of degrees of freedom is indicated by N.) are the coefficient matrices. They are fully

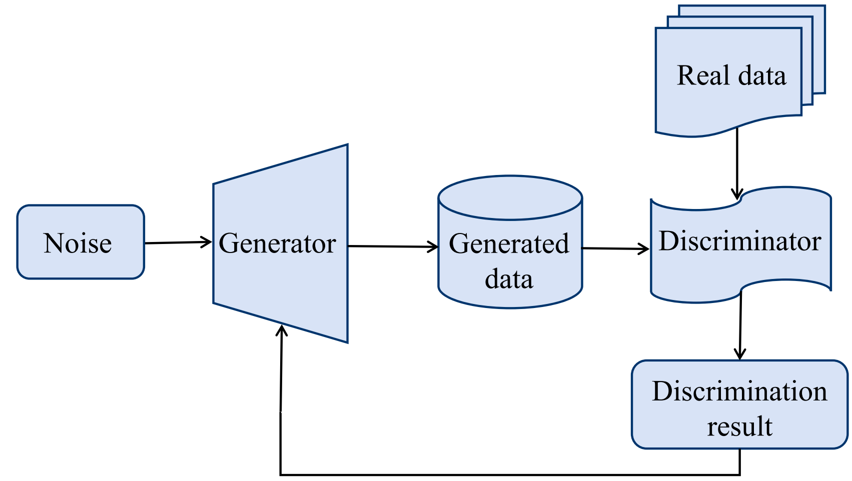

FIGURE 1
GAN network structure diagram.

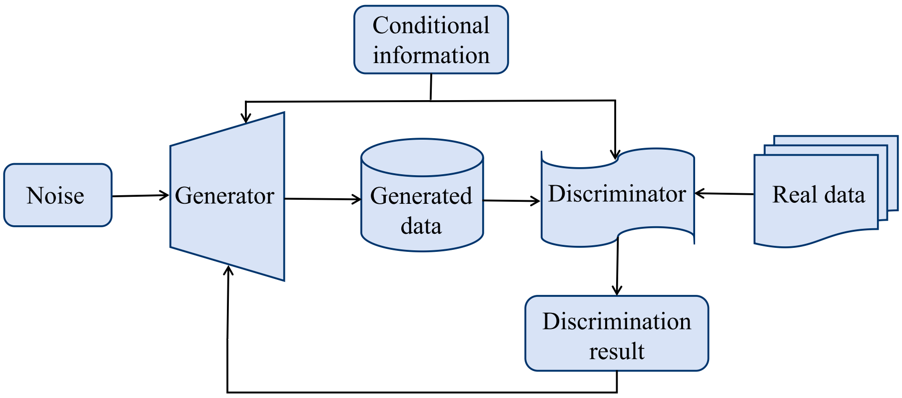

FIGURE 2
CGAN network structure diagram.

populated, asymmetric, and dependent on frequency. The column vectors $\dot{\mathbf{p}}$ and $\dot{\mathbf{q}}$ represent the sensitivity of the acoustic flux and the sound pressure, respectively. $\dot{\mathbf{p}}_{\text{inc}}$ represents the sensitivity vector of incident waves.

To determine all the unknown boundary state values for the analysis of shape sensitivity, solve Equation 6 and use all the values at the boundaries and known boundary sensitivity values to solve Equation 14. By Equation 8, the value for any point $\mathbf{x}$ in the problem domain can be computed with $\alpha = 0$ and $C(\mathbf{x}) = 1$. In the end, the sensitivities of the objective function presented at certain computing points in the fluid domain concerning shape design variables could be calculated.

Since the Hankel function in Equation 4 and its derivative in Equation 9 depend on the wave number k, Equation 6, Equation 7 and Equation 14 are all dependent on frequency. The computation of the system equation and coefficient matrix of the BEM for 2D acoustic state and sensitivity analysis at each discrete frequency point within a frequency band is necessary, which results in a significant computational cost for tackling multifrequency problems.

3 Theory of conditional generative adversarial networks

3.1 Generate adversarial neural networks

The innovation of Generative Adversarial Networks (GANs) lies in their combination of deep learning and probability theory. They are made up of two rival neural networks that are capable of autonomous learning and are intended to use unsupervised learning to replicate the distribution of actual data [51, 52]. The generator and discriminator engage in an iterative training process that resembles a game, where the generator aims to produce data that closely resembles real data, while the discriminator continuously improves its ability to distinguish between real and generated data. Together, they form the fundamental architecture of GANs. The

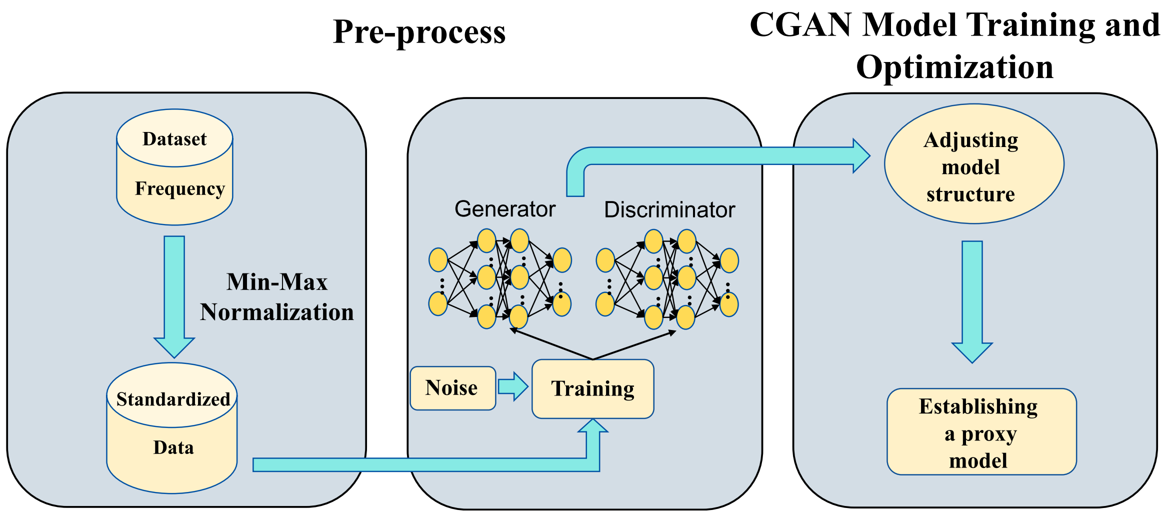

FIGURE 3
CGAN network structure diagram.

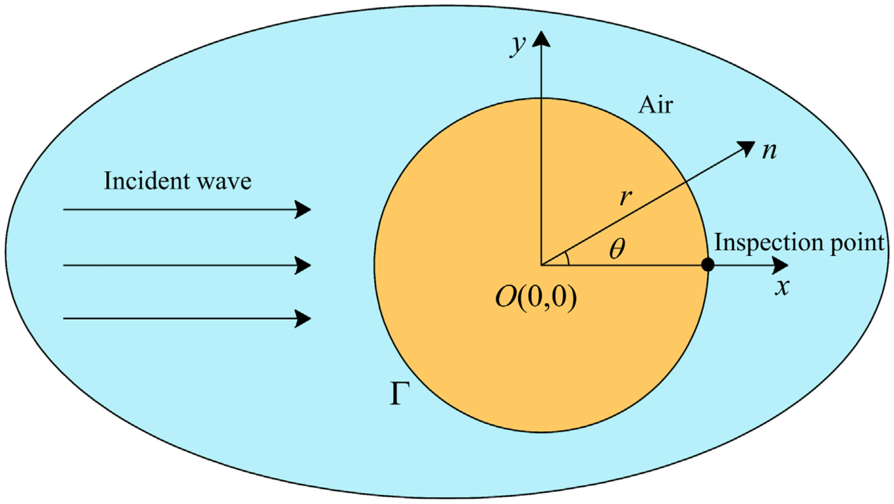

FIGURE 4
The infinite cylinder serves as the design domain for sound scattering.

TABLE 1 Parameters used in the simulations.

Parameter	Symbol	Value	Unit
The density of the air medium	ρ_f	1.21	kg/m^3
The speed of the sound	c_{air}	343	m/s
The step size of frequency	f_{step}	1.0	Hz

goal is to make the generated data as similar as possible to the characteristics of the actual data [53]. The generator aims to create data that closely resembles real data to deceive the discriminator, while the discriminator's role is to distinguish between real data and the fake data produced by the generator. As they strive toward achieving a Nash equilibrium in game theory-where the produced data is indistinguishable from actual data-both networks are always learning and improving. Figure 1 displays the GAN's process flowchart.

The generator takes random noise as input and generates samples resembling the distribution of real data [54]. The discriminator receives either real data or fake data produced by the generator. When the input is real data, the discriminator outputs 1; when the input is generated data, it outputs 0. Both the discriminator's and the generator's capabilities are continually enhanced by iterative training, leading to a balanced state where the discriminator is unable to discriminate between the two input data categories. This indicates that the generator has successfully

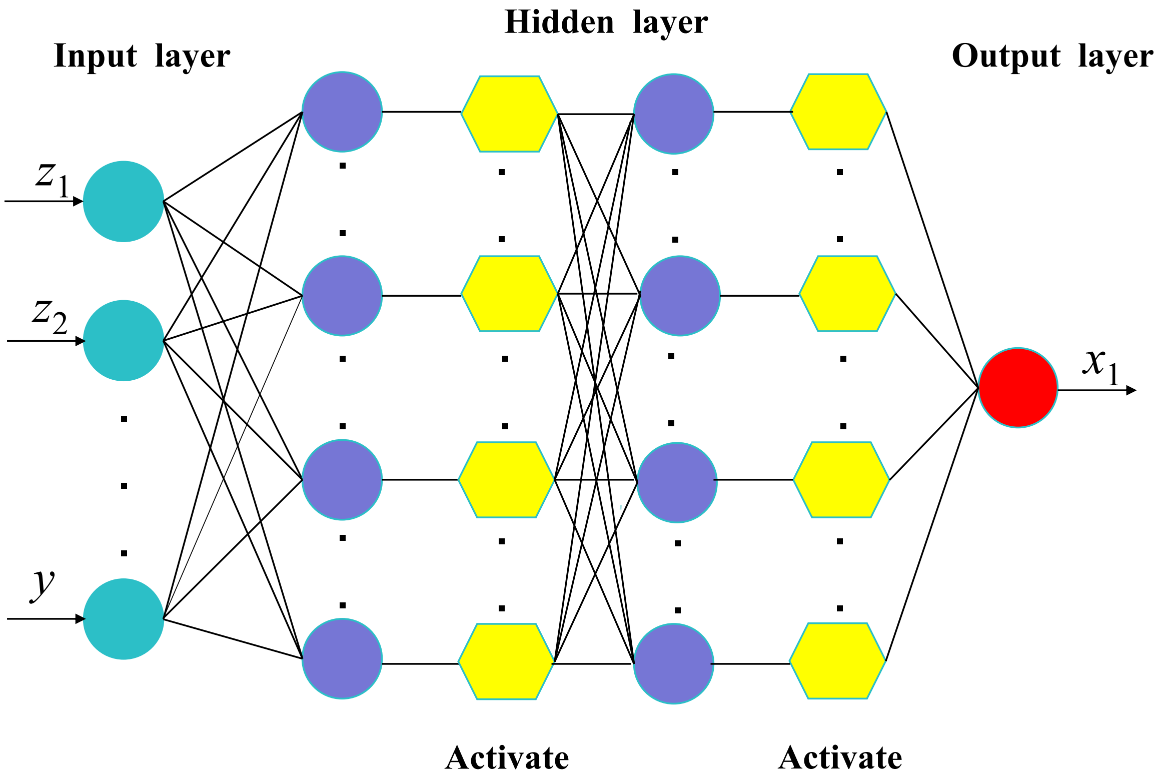

FIGURE 5
The Generator's network structure of CGAN.

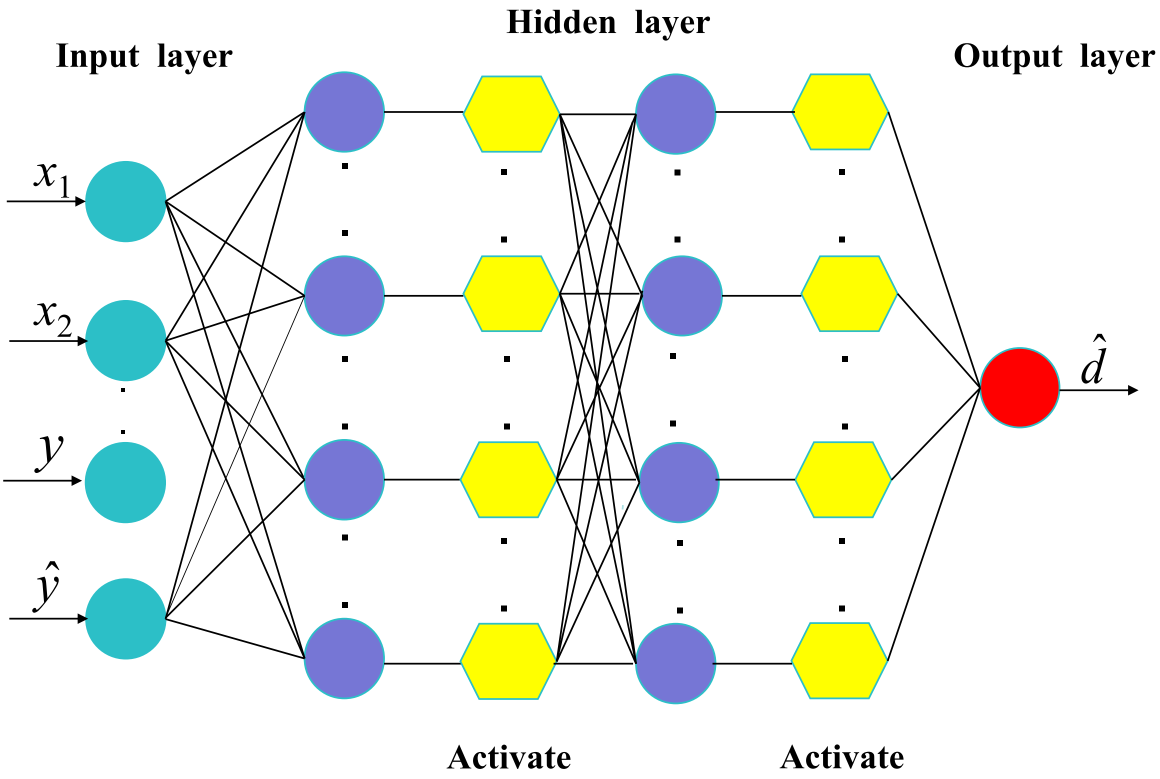

FIGURE 6
The Discriminator's network structure of CGAN.

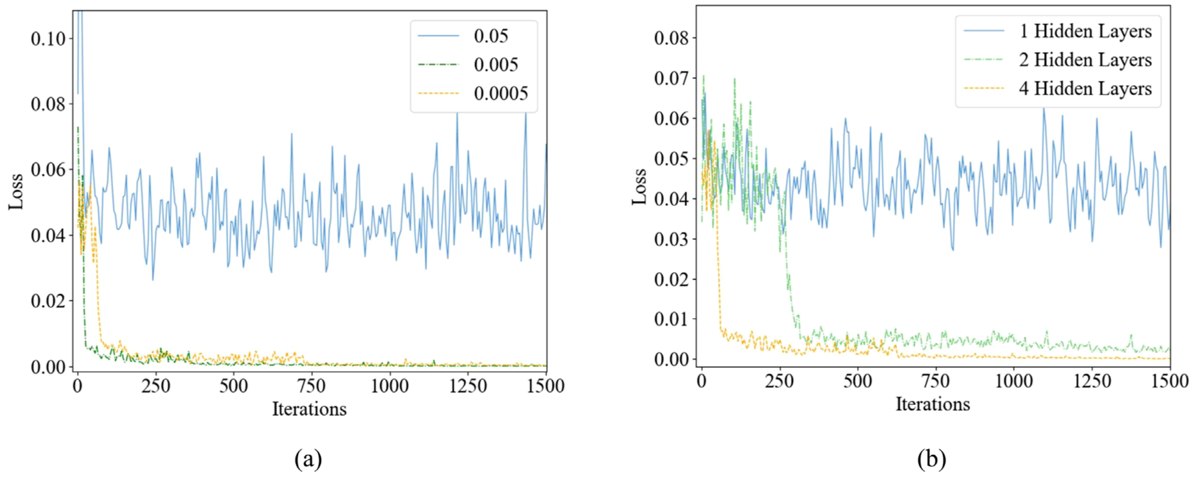

FIGURE 7
Training loss varies with different hyperparameters: **(a)** Different learning rates; **(b)** Different number of hidden layers.

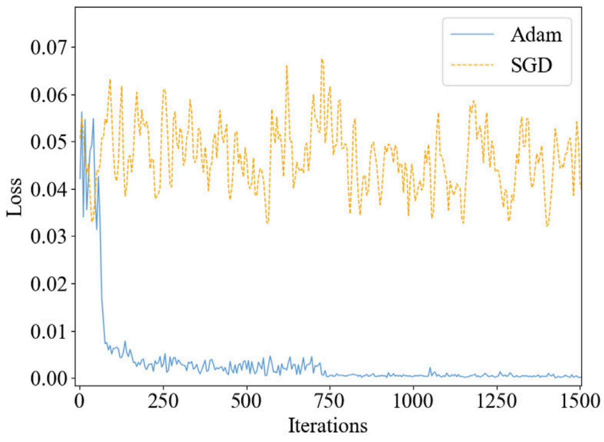

FIGURE 8
Training loss varies with different optimizers.

simulated the distribution of real data. The loss value of a GAN is closely tied to the loss values of both the generator and the discriminator, and its loss function can be expressed as Equation 15.

$$\min_G \max_D V(D,G) = E_{x\sim P_{\text{data}}(x)}[\log D(x)] + E_{z\sim P_z(z)}[\log(1 - D(G(z)))] \quad (15)$$

In this context, $P_{\text{data}}(\cdot)$ and $P_z(\cdot)$ represent the distributions of the sample data and noise data, respectively. However, GANs still have a number of difficulties, though, such as non-synchronous training between the discriminator and generator, poor data accuracy, high sample variability, and trouble reaching a level of stability. The CGAN architecture is used in this study to overcome these constraints. A thorough overview of CGAN will be given in the sections that follow.

3.2 Conditional generation adversarial neural network

By adding conditional information, the Conditional Generative Adversarial Network (CGAN) [55] improves on the classic GAN architecture and successfully converts it from an unsupervised learning model to a model with supervised learning. CGAN constrains the data production process by adding conditional variables, which allows for the targeted and accurate generation of desired outputs. The CGAN's design is quite similar to that of a typical GAN, as seen in Figure 2, but it incorporates extra conditional variables in the discriminator and generator. Because of this improvement, CGAN can function as a supervised, regulated network model.

In Equation 16, the CGAN's goal function is shown, where conditional probability is introduced to form a constrained maximization-minimization function.

$$\min_G \max_D V(D,G) = E_{x\sim P_{\text{data}}(x)}[\log D(x|y)] + E_{z\sim P_z(z)}[\log(1 - D(G(z|y)))] \quad (16)$$

After incorporating conditional variables, the discriminator and generator in CGAN are tasked with two key responsibilities: the discriminator must distinguish between real and generated data under specified conditions, while the generator aims to produce data that aligns with the real data distribution under those same conditions. Random noise and the associated conditional information are inputs to the generative model, generating samples that mimic the distribution of real data. Conversely, the discriminator receives real data, conditional information, and the generated sample $G(y,z)$ as input, outputting either 0 or 1 to classify the input as real or generated. Fundamentally, the discriminator functions as a binary classification model. This structured approach effectively addresses the limitations of GANs.

During the adversarial optimization process, the generator and discriminator continuously refine their performance, ultimately achieving a state of equilibrium where the discriminator can no

TABLE 2 CGAN's network architecture and training parameter configurations.

Network	Hidden layers	Loss function	Activation function	Optimizer	Learning rate
Generator	4	MSE	Sigmoid	Adam	0.0005
Discriminator	4	MSE	Sigmoid	Adam	0.0005

TABLE 3 Development environment.

Operating system	Framework	Language	Memory	GPU
Windows 11	TensorFlow 2.6.0	Python 3.7	16 GB	NVIDIA GeForce GTX 1650

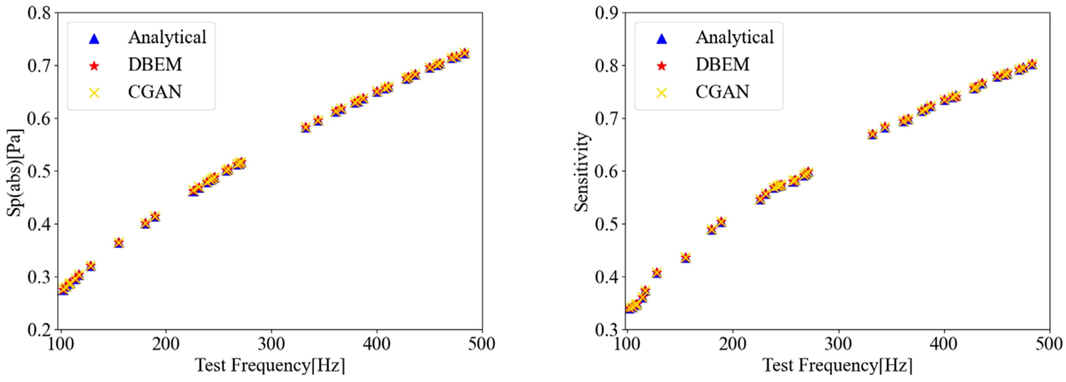

(a) (b)

FIGURE 9
Comparison of CGAN Prediction Results Under Unknown Conditions (Training set:361, Test set: 40): **(a)** Sound Pressure; **(b)** Sensitivity.

longer differentiate between real and generated data. The training process for CGAN alternates between updating the generator and the discriminator, linking the overall loss function to the individual loss functions of both components. This relationship is represented in Equation 17:

$$L(G,D) = E_{x,y,P_{data}(x,y)}\left[\log D(x,y)\right] + E_{y,p_y(y),z,p_z(z)}\left[\log\left(1 - D\left(G(y,z),y\right)\right)\right] \tag{17}$$

In this context, x represents the real data, y denotes the conditional information, and $P_{data}(x,y)$ indicates the distribution of the input data. The functions $D(\cdot)$ and $G(\cdot)$ represent the outputs of the discriminator D and the generator G, respectively, while z denotes the random noise. The loss functions for D and G can be expressed as Equation 18 and Equation 19:

$$L_D = -E_{x,y,P_{data}(x,y)}\left[\log D(x,y)\right] - E_{z,p_z,y,p_y(z,y)}\left[\log\left(1 - D\left(G(z,y)\right),y\right)\right] \tag{18}$$

$$L_G = E_{z,p_z,y,p_y(z,y)}\left[\log\left(1 - D\left(G(z,y)\right),y\right)\right] \tag{19}$$

It is important to note that, due to its generative nature, CGAN has the ability to produce a wide range of data. This generated data also contributes to the training process of the network, which significantly reduces the amount of data required for modeling. As a result, the CGAN network is well-suited to address the issues examined in this paper. Compared to other neural networks, CGAN can be applied to small-scale data problems. However, the training time is slightly longer than that of other neural network models.

4 Numerical example

This section presents two computational examples to evaluate the performance of the proposed algorithm. The acoustic scattering data were generated using numerical simulations implemented in the Fortran 90 programming language. The dataset was subsequently divided into training and testing sets for the CGAN. Figure 3 illustrates the training process of the entire CGAN network, which can be systematically divided into two primary stages. All computations were conducted on a laptop equipped with 16 GB of RAM and an Intel(R) Core(TM) i5-9300H Central Processing Unit (CPU).

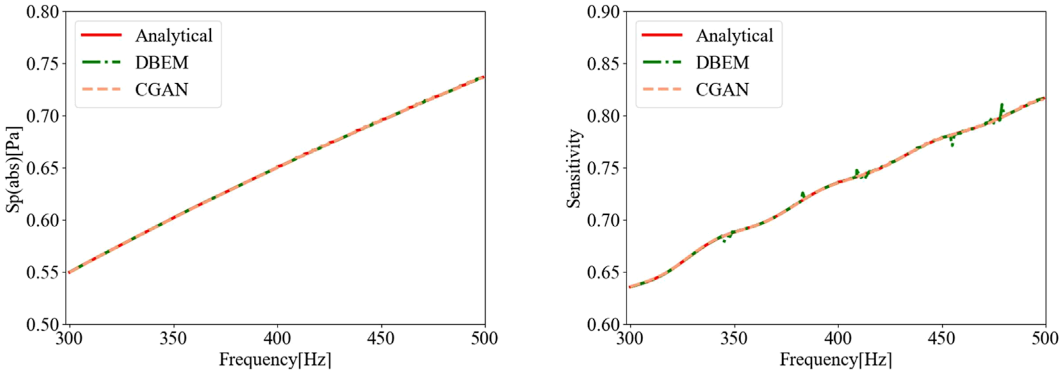

(a) (b)

FIGURE 10
Comparison Between CGAN and DBEM(Training set:361, Test set: 40): **(a)** Sound Pressure; **(b)** Sensitivity.

TABLE 4 Comparison of DBEM and CGAN results across different Frequencies (Sound pressure).

Frequency	Sound Pressure with		Sound Pressure with Analytical	Error with (%)		Computation Time (s)	
	DBEM	CGAN		DBEM	CGAN	DBEM	CGAN
300	0.63559	0.63565	0.63556	0.005	0.015	189.2725	1.3589(Prediction) 227.003 (Training)
320	0.65251	0.65258	0.65247	0.006	0.018		
340	0.67979	0.68011	0.67982	0.003	0.042		
360	0.69433	0.69438	0.69429	0.006	0.013		
380	0.71508	0.71504	0.71485	0.032	0.026		
400	0.73545	0.73516	0.73541	0.005	0.034		
420	0.74895	0.74889	0.74896	0.001	0.009		
440	0.76985	0.76987	0.76975	0.013	0.016		
460	0.78442	0.78451	0.78512	0.089	0.077		
480	0.79936	0.79917	0.80024	0.11	0.133		
500	0.81642	0.81523	0.81628	0.017	0.129		

4.1 Infinite-length rigid cylinder model

The acoustic scattering from a cylinder can be simplified to a two-dimensional problem by assuming that a plane wave beam strikes an infinitely rigid cylinder (see Figure 4). The plane wave propagates along the positive x-axis. The cylinder is centered at (0 m, 0 m) with a radius of 1 m, and its circumference is discretized using 720 constant boundary elements. Additionally, the coordinates of the calculation points are (10 m, 0 m) (see Figure 4). Other parameters for the numerical simulation are provided in Table 1. The problem of acoustic scattering by an infinitely rigid cylinder has the analytical solution, which is represented as Equation 20.

$$p(r,\theta) = -\sum_{n=0}^{\infty} \varepsilon_n \mathrm{i}^n \frac{nJ_n(kr_0) - kr_0 J_{n+1}(kr_0)}{nH_n^{(1)}(kr_0) - kr_0 H_{n+1}^{(1)}(kr_0)} H_n^{(1)}(kr)\cos(n\theta) \quad (20)$$

In the above equation, $\varepsilon_0 = 1$ for $n = 0$, and $\varepsilon_n = 2$ otherwise, where ε_n represents the Neumann symbols. The expansion consists of 50 terms, and at the detection point, $\theta = 0$. To assess the accuracy of the proposed method, the relative error between the traditional Boundary Element Method (DBEM) and the analytical solution, and that between the CGAN-predicted results and the analytical solution, have been calculated. The relative error is

TABLE 5 Comparison of DBEM and CGAN results across different Frequencies (Sensitivity).

Frequency	Sensitivity with		Sensitivity with Analytical	Error with (%)		Computation Time (s)	
	DBEM	CGAN		DBEM	CGAN	DBEM	CGAN
300	0.54974	0.54967	0.54973	0.001	0.011	378.1168	1.5467(Prediction) 215.483 (Training)
320	0.57099	0.57094	0.57098	0.001	0.007		
340	0.59166	0.59161	0.59165	0.002	0.006		
360	0.61179	0.61164	0.61178	0.002	0.022		
380	0.63110	0.63101	0.63092	0.003	0.012		
400	0.65007	0.65011	0.65005	0.003	0.008		
420	0.66843	0.66839	0.66841	0.004	0.002		
440	0.68628	0.68644	0.68625	0.004	0.027		
460	0.70379	0.70379	0.70375	0.006	0.006		
480	0.72075	0.72078	0.72070	0.007	0.010		
500	0.73655	0.73601	0.73651	0.006	0.069		

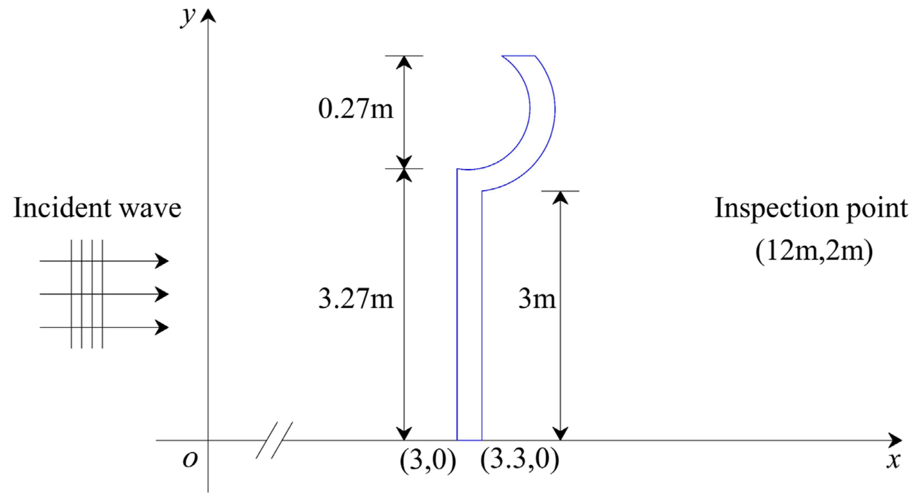

FIGURE 11
The design domain of the semi-curved sound barrier model.

determined using Equation 21:

$$\text{Relative} \quad \text{Error} = \frac{\left|X_{output} - X_{analytical}\right|}{\left|X_{analytical}\right|} \times 100\% \tag{21}$$

Here, X_{output} represents the results obtained from DBEM-CGAN, and $X_{\text{analytical}}$ represents the results of the analytical solution. Before training the neural network, data preprocessing is essential. First, a portion of the dataset is randomly selected as the test set to evaluate the model post-training. Additionally, to enhance training efficiency and prediction accuracy by addressing the scale differences among features, data standardization is a critical step. Standardization not only improves the model's adaptability across different datasets but also increases its sensitivity to feature variations, thereby improving its generalization capability. The standardization process can be implemented using Equation 22:

$$x' = \frac{x - x_{\min}}{x_{\max} - x_{\min}} \tag{22}$$

In this context, x' represents the value of a single data point, $x_{\min}$ is the minimum value in the corresponding column, and $x_{\max}$ is the maximum value in that column. After standardization, all features in the dataset are rescaled to a uniform range, ensuring that differences in feature magnitudes do not affect model

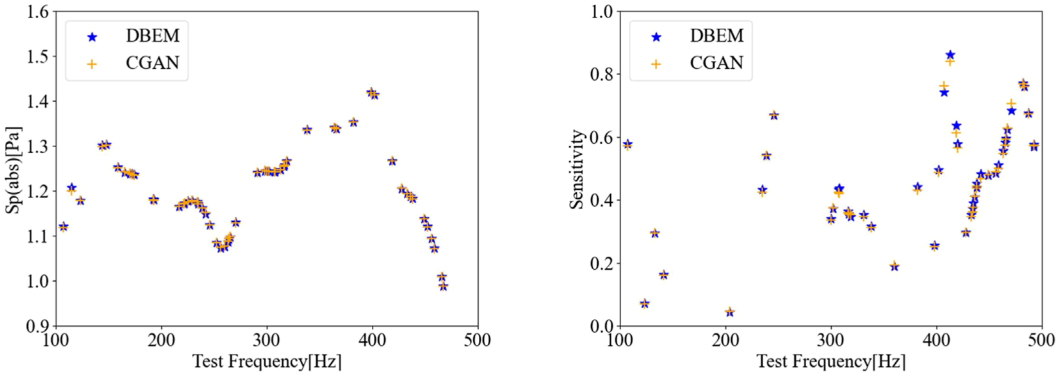

(a) (b)

FIGURE 12
Comparison of CGANâ€™s Prediction Results on the Test Set with DBEM Results (Training set:361, Test set: 40): **(a)** Sound Pressure; **(b)** Sensitivity.

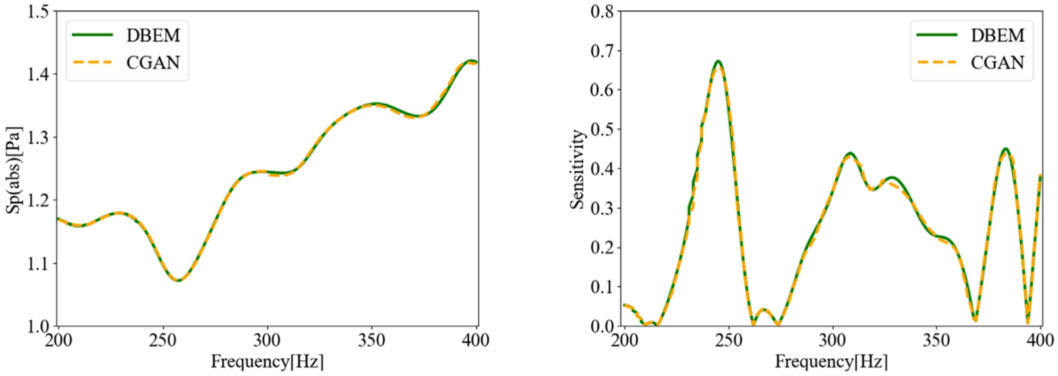

(a) (b)

FIGURE 13
Comparison of CGANâ€™s Prediction Results with DBEM Results (Training set:361, Test set: 40): **(a)** Sound Pressure; **(b)** Sensitivity.

training and prediction. The standardized dataset is then divided into two subsets: the training set, used to train the model, and the test set, employed to evaluate its performance. Following evaluation, the predicted outputs are post-processed as described in Equation 23.

$$x = x' \cdot (x_{\max} - x_{\min}) + x_{\min} \tag{23}$$

Based on the acquired dataset (sound pressure and sensitivity from 100Hz to 500 Hz), the data is input into the CGAN model for training. Figures 5, 6 present a simplified diagram of the CGAN structure, illustrating the discriminator's and generator's training procedure. Z_1 and Z_2 represent the random noise inputs to the generator, and y denotes the label information corresponding to the frequency information of the real data. The generated data x_1 symbolizes the sensitivity and sound pressure at the observing point. In the discriminator, x_2 represents the real data, $\hat{y}$ represents the label information of the generated data corresponding to its frequency information, and $\widehat{d}$ represents the discrimination result, stating if the data is fake or true.

For the tasks of sound pressure and sensitivity prediction, these can be considered a regression problem. Thus, the mean squared error (MSE) function is employed as the loss function, as shown in Equation 24. Since the discriminator operates as a binary classifier, the Sigmoid function is used as the activation function. To ensure balanced performance between the generator and discriminator, the same activation function is applied to both. Additionally, the parameter dimensions are kept within a compact range to enhance the model's efficiency.

Figure 7 illustrates the variation in the generator's training loss under different learning rates and optimizers, while Figure 8 demonstrates the impact of the number of hidden layers on the training loss.

$$\mathrm{MSE} = \frac{1}{n}\sum_{i=1}^{n}(\hat{y}_i - y_i)^2 \tag{24}$$

As the learning rate decreases, the model loss decreases. When the learning rates are set to 0.005 and 0.0005, the losses are similar, but the model accuracy is higher at a learning rate

TABLE 6 CGAN testing input parameters and results.

Sound pressure	CGAN	Relative error (%)	Sensitivity	CGAN	Relative error (%)
1.178	1.180	0.19	0.294	0.295	0.36
1.164	1.165	0.04	0.159	0.161	1.33
1.171	1.172	0.04	0.045	0.043	3.08
1.176	1.177	0.03	0.346	0.352	1.60
1.179	1.179	0.03	0.192	0.188	2.55
1.176	1.176	0.02	0.251	0.255	1.51
1.151	1.149	0.20	0.761	0.743	2.52
1.075	1.073	0.21	0.840	0.862	2.50
1.077	1.076	0.09	0.565	0.578	2.36
1.087	1.087	0.03	0.361	0.372	2.90
1.093	1.092	0.12	0.377	0.391	3.62
1.099	1.098	0.09	0.443	0.453	2.03
1.241	1.241	0.00	0.467	0.482	3.03
1.245	1.245	0.01	0.499	0.511	2.25
1.338	1.338	0.01	0.548	0.556	1.53

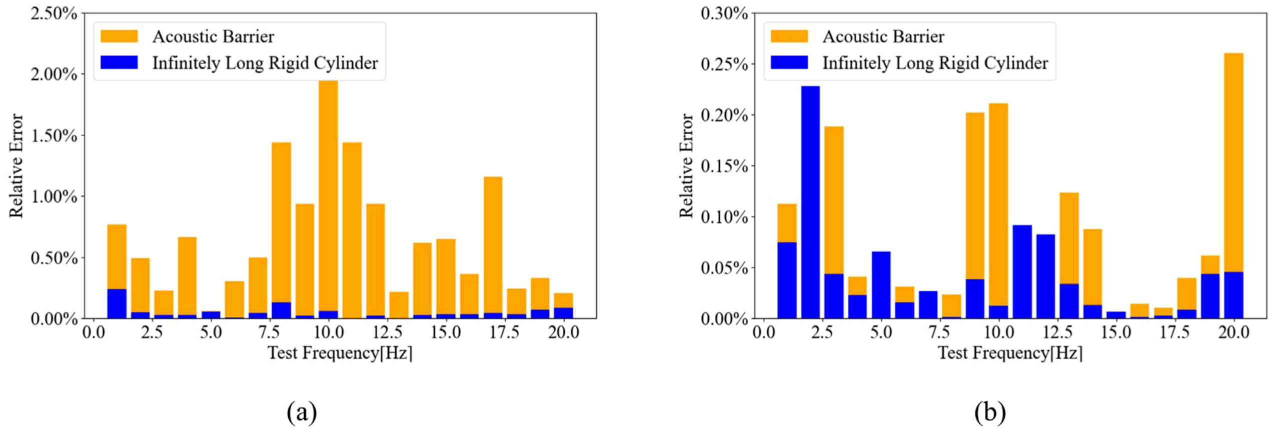

FIGURE 14
The relative errors between DBEM and CGAN under different models: **(a)** Sound pressure; **(b)** Sensitivity.

of 0.0005. Furthermore, when comparing different activation functions, Adam significantly outperforms SGD. The effect of varying the number of hidden layers was tested, and by comparing the loss to actual results, it was determined that a configuration with four hidden layers yields the best performance. Finally, Table 2 displays the CGAN model's network framework configuration, with the detailed configuration parameters provided in Table 3.

To evaluate the predictive accuracy of the CGAN network, the classical infinite-length rigid cylinder model was selected as the benchmark. By splitting the data, a portion is selected as the test set, while the remaining data is used as the training set for training. The total number of sound pressure and sensitivity data is 401, with 10% of the dataset (i.e., 40 data points) selected as the test set, and the remaining data used as the training set. Figure 9a presents the sound pressure prediction results on

TABLE 7 Development environment.

Variables	RMSE	MAE	R^2
Sound Pressure	0.00146	0.000891	0.998
Sensitivity	0.00926	0.00688	0.997

the test dataset, while Figure 9b provides a comparative analysis of sensitivity predictions on the test dataset. In this context, Unknown Conditions refers to the test set, as the data patterns in the test set are unknown to the trained model. The results demonstrate that the CGAN model consistently achieves a high level of agreement with analytical solutions in both sound pressure predictions and sensitivity analyses. This indicates that the CGAN model effectively captures the underlying patterns within the data, even under unknown operating conditions, showcasing exceptional predictive accuracy and reliability. In addition, the sound pressure sensitivities were calculated using both the DBEM method and the CGAN model, with the results compared to the analytical solution, as shown in Figure 10. The figure clearly demonstrates that the CGAN model significantly outperforms the DBEM method in terms of accuracy, producing predictions that exhibit neither oscillatory behavior nor spurious frequency points. Furthermore, the CGAN model offers a substantial advantage in computational efficiency over the DBEM method. A detailed comparison of the results and corresponding computation times is provided in Tables 4, 5.

The data in the table indicate that DBEM and CGAN exhibit similar error performance. While DBEM demonstrates a slight edge in accuracy, CGAN significantly surpasses DBEM in computational time, achieving a notable reduction in the time required. This underscores the clear superiority of CGAN in computational efficiency. Thus, despite the minimal difference in error, CGAN offers a substantial advantage in time efficiency, making it the preferred choice for applications where computational speed is paramount.

4.2 Sound barrier model

As urbanization accelerates and the use of transportation vehicles becomes more widespread, traffic noise has become an increasingly severe issue, causing numerous inconveniences and hazards to peopleâ€™s daily lives and work. Consequently, mitigating the harm caused by traffic noise is essential. Sound barriers are widely used in acoustic and noise control engineering as structures or devices designed to block or reduce the transmission of sound waves.

To evaluate the effectiveness of sound barriers, the accuracy and efficiency of the CGAN model were first validated using the infinitely long rigid cylinder model. In this section, a more complex noise barrier model is considered to comprehensively assess the CGAN modelâ€™s performance in terms of both precision and computational efficiency. The sound pressure and related data are generated from a plane wave incident parallel to the x-axis, which is scattered by the sound barrier. The sound barrier model is discretized into 1,118 elements, and the sound pressure at the point (12 m, 2 m) is calculated using the DBEM. From the obtained sound pressure and sensitivity data, the frequency range of 100â€"500 Hz is selected as the training dataset for the CGAN model. The sound barrier model is illustrated in Figure 11.

The data processing method and the relative error calculation are consistent with those used in the infinitely long rigid cylinder model. The prediction results on the predefined test set are shown in Figure 12. As illustrated in the figure, the sound pressure and sensitivity predicted by the CGAN model exhibit the high degrees of consistency with the actual data, demonstrating excellent agreement. These findings highlight the generalization capability of the CGAN model when applied to unseen datasets. Furthermore, a comparative analysis between DBEM and CGAN was conducted within the frequency range of 200â€"400 Hz, with the results presented in Figure 13.

Table 6 presents the relative errors for several test points. It can be observed that all relative errors fall within a narrow range, with the maximum error not exceeding 3.62%. Unlike the infinite-length rigid cylinder model, the sound barrier model lacks analytical solutions and features more complex geometrical configurations. As a result, both DBEM and CGAN exhibit certain deviations. Nevertheless, the overall error remains within a small range, further validating the CGAN model's ability to accurately learn patterns embedded in the data and deliver high-precision predictions.

In particular, the CGAN model demonstrates exceptional consistency and accuracy in sound pressure predictions. Figure 14 illustrates the relative error between the predicted values of the CGAN model and the calculated values of DBEM under different model configurations. For sensitivity predictions, although the data is inherently more complex and exhibits slightly higher errors compared to sound pressure, the CGAN model still maintains remarkably high prediction accuracy. This highlights the modelâ€™s capability to handle diverse data types while demonstrating robust performance and reliability. The regression model evaluation metrics were calculated using the specified formula, and the detailed statistical results are presented in Table 7.

Overall, these results comprehensively highlight the CGAN model's outstanding capabilities and exceptional performance in sound barrier data prediction, reaffirming its effectiveness in addressing complex computational challenges. In the face of more complex models in the future, DBEM will require more time. The accuracy of the CGAN model has been demonstrated through the numerical example. Therefore, when calculating other models, it is sufficient to use the DBEM method to compute a portion of the data, and the remaining data can be generated using CGAN, which significantly reduces the computation time compared to the DBEM method.

5 Conclusion

This paper proposes a method to enhance computational efficiency by utilizing the CGAN network for the rapid and accurate prediction of sound pressure and sensitivity:

1. The integration of the Boundary Element Method (BEM) with CGAN is investigated to evaluate the applicability of CGAN in solving such problems.
2. The predictive model developed through CGAN demonstrates a significant reduction in computation time, thereby improving the efficiency of sound scattering analysis.
3. Adjustments to specific parameters and structures of CGAN have proven effective in addressing the regression challenges were encountered in this study.

Future research will aim to extend the application of CGAN to the structural optimization of sound barriers.

Data availability statement

The raw data supporting the conclusions of this article will be made available by the authors, without undue reservation.

Author contributions

QH: Conceptualization, Funding acquisition, Methodology, Software, Writing–review and editing. ZC: Data curation, Methodology, Software, Writing–original draft. HL: Data curation, Methodology, Software, Writing–original draft. SZ: Conceptualization, Methodology, Software, Supervision, Writing–original draft.

Funding

The author(s) declare that financial support was received for the research, authorship, and/or publication of this article. The authors appreciate the financial support of the Henan Provincial Department of Science and TechnologyResearch Project (No.222102230113).

Conflict of interest

The authors declare that the research was conducted in the absence of any commercial or financial relationships that could be construed as a potential conflict of interest.

Generative AI statement

The author(s) declare that no Generative AI was used in the creation of this manuscript.

Publisher's note

References

1. Chen L, Lian H, Pei Q, Meng Z, Jiang S, Dong H-W, et al. Fem-bem analysis of acoustic interaction with submerged thin-shell structures under seabed reflection conditions. *Ocean Eng* (2024) 309:118554. doi:10.1016/j.oceaneng.2024.118554

2. Xu Y, Yang S. Sensitivity analysis of non-uniform rational b-splines–based finite element/boundary element coupling in structural-acoustic design. *Front Phys* (2024) 12:1428875. doi:10.3389/fphy.2024.1428875

3. Chen L, Lian H, Xu Y, Li S, Liu Z, Atroshchenko E, et al. Generalized isogeometric boundary element method for uncertainty analysis of time-harmonic wave propagation in infinite domains. *Appl Math Model* (2023) 114:360–78. doi:10.1016/j.apm.2022.09.030

4. Vuong CD, Yu T, Rungamornrat J, Bui TQ. A smoothing gradient thermo-mechanical damage model for thermal shock crack propagation: theory and fe implementation. *Int J Non-Linear Mech* (2024) 163:104755. doi:10.1016/j.ijnonlinmec.2024.104755

5. Mahrous E, Valéry Roy R, Jarauta A, Secanell M. A three-dimensional numerical model for the motion of liquid drops by the particle finite element method. *Phys Fluids* (2022) 34. doi:10.1063/5.0091699

6. Liu Z, Sheng L, Liu X, Chang Y, Chen G, Guo X. Mechanical analysis for deepwater drilling riser system with structural parameters uncertainty. *Ocean Eng* (2024) 305:118049. doi:10.1016/j.oceaneng.2024.118049

7. Chen L, Liu C, Lian H, Gu W. Electromagnetic scattering sensitivity analysis for perfectly conducting objects in tm polarization with isogeometric bem. *Eng Anal Boundary Elem* (2025) 172:106126. doi:10.1016/j.enganabound.2025.106126

8. Liu C, Pei Q, Cui Z, Song Z, Zhao G, Yang Y. Isogeometric boundary element method analysis for dielectric target shape optimization in electromagnetic scattering. *Sci Prog* (2024) 107:00368504241294114. doi:10.1177/00368504241294114

9. Padrino JC, Sprittles JE, Lockerby DA. Efficient simulation of rarefied gas flow past a particle: a boundary element method for the linearized g13 equations. *Phys Fluids* (2022) 34. doi:10.1063/5.0091041

10. Langins A, Stikuts AP, Cēbers A. A three-dimensional boundary element method algorithm for simulations of magnetic fluid droplet dynamics. *Phys Fluids* (2022) 34. doi:10.1063/5.0092532

11. Chen L, Lian H, Liu Z, Chen H, Atroshchenko E, Bordas S. Structural shape optimization of three dimensional acoustic problems with isogeometric boundary element methods. *Computer Methods Appl Mech Eng* (2019) 355:926–51. doi:10.1016/j.cma.2019.06.012

12. [Dataset] Zhong S, Jiang X, Du J, Liu J. A reduced-order boundary element method for two-dimensional acoustic scattering. *Front Phys* (2024) 12. doi:10.3389/fphy.2024.1464716

13. Marburg S. Six boundary elements per wavelength: is that enough? *J Comput Acoust* (2002) 10:25–51. doi:10.1142/s0218396x02001401

14. Marburg S, Schneider S. Influence of element types on numeric error for acoustic boundary elements. *J Comput Acoust* (2003) 11:363–86. doi:10.1142/s0218396x03001985

15. Arnold S (1949). Partial differential equations in physics

16. Sobolev A. Wide-band sound-absorbing structures for aircraft engine ducts. *Acoust Phys* (2000) 46:466–73. doi:10.1134/1.29911

17. Willmann E, Boll B, Mikaelyan G, Wittich H, Meißner RH, Fiedler B. Vibro-acoustic modulation based measurements in cfrp laminates for damage detection in open-hole structures. *Composites Commun* (2023) 42:101659. doi:10.1016/j.coco.2023.101659

18. Xiao Q, Zhang G, Chen Z, Wu G, Xu Y. A hybrid csrpim/sea method for the analysis of vibro-acoustic problems in mid-frequency range. *Eng Anal Boundary Elem* (2023) 146:146–54. doi:10.1016/j.enganabound.2022.10.004

19. Zhao K, Li H, Zha Z, Zhai M, Wu J. Detection of sub-healthy apples with moldy core using deep-shallow learning for vibro-acoustic multi-domain features. *Meas Food* (2022) 8:100068. doi:10.1016/j.meafoo.2022.100068

20. Chen L, Huo R, Lian H, Yu B, Zhang M, Natarajan S, et al. Uncertainty quantification of 3d acoustic shape sensitivities with generalized nth-order perturbation

boundary element methods. *Computer Methods Appl Mech Eng* (2025) 433:117464. doi:10.1016/j.cma.2024.117464

21. Chen L, Lian H, Liu C, Li Y, Natarajan S. Sensitivity analysis of transverse electric polarized electromagnetic scattering with isogeometric boundary elements accelerated by a fast multipole method. *Appl Math Model* (2025) 141:115956. doi:10.1016/j.apm.2025.115956

22. Chen L, Pei Q, Fei Z, Zhou Z, Hu Z. Deep-neural-network-based framework for the accelerating uncertainty quantification of a structural–acoustic fully coupled system in a shallow sea. *Eng Anal Boundary Elem* (2025) 171:106112. doi:10.1016/j.enganabound.2024.106112

23. Biancoli A, Fancher CM, Jones JL, Damjanovic D. Breaking of macroscopic centric symmetry in paraelectric phases of ferroelectric materials and implications for flexoelectricity. *Nat Mater* (2015) 14:224–9. doi:10.1038/nmat4139

24. Wang C, Hong L, Qiang X, Xu M. Novel numerical method for uncertainty analysis of coupled vibro-acoustic problem considering thermal stress. *Computer Methods Appl Mech Eng* (2024) 420:116727. doi:10.1016/j.cma.2023.116727

25. Lian H, Li X, Qu Y, Du J, Meng Z, Liu J, et al.Bayesian uncertainty analysis for underwater 3d reconstruction with neural radiance fields. *Appl Math Model* (2024) 138:115806. doi:10.1016/j.apm.2024.115806

26. Jiang S, Liang Y, Cheng Y, Gao L. Research on the prediction method of wing structure noise based on the combination of conditional generative adversarial neural network and numerical methods. *Front Phys* (2024) 12:1452876. doi:10.3389/fphy.2024.1452876

27. Chen L, Cheng R, Li S, Lian H, Zheng C, Bordas SP. A sample-efficient deep learning method for multivariate uncertainty qualification of acoustic–vibration interaction problems. *Computer Methods Appl Mech Eng* (2022) 393:114784. doi:10.1016/j.cma.2022.114784

28. Carazo A, Roger M, Omais M. Analytical prediction of wake-interaction noise in counter-rotating open rotors. In: *17th AIAA/CEAS aeroacoustics conference (32nd AIAA aeroacoustics conference)* (2011). p. 2758.

29. Samaniego E, Anitescu C, Goswami S, Nguyen-Thanh VM, Guo H, Hamdia K, et al. An energy approach to the solution of partial differential equations in computational mechanics via machine learning: concepts, implementation and applications. *Computer Methods Appl Mech Eng* (2020) 362:112790. doi:10.1016/j.cma.2019.112790

30. Zhang J, Zhang W, Zhu J, Xia L. Integrated layout design of multi-component systems using xfem and analytical sensitivity analysis. *Computer Methods Appl Mech Eng* (2012) 245:75–89. doi:10.1016/j.cma.2012.06.022

31. Dühring MB, Jensen JS, Sigmund O. Acoustic design by topology optimization. *J sound vibration* (2008) 317:557–75. doi:10.1016/j.jsv.2008.03.042

32. Chen L, Lu C, Lian H, Liu Z, Zhao W, Li S, et al. Acoustic topology optimization of sound absorbing materials directly from subdivision surfaces with isogeometric boundary element methods. *Computer Methods Appl Mech Eng* (2020) 362:112806. doi:10.1016/j.cma.2019.112806

33. Hombal V, Mahadevan S. Bias minimization in Gaussian process surrogate modeling for uncertainty quantification. *Visualization Mech Process An Int Online J* (2011) 1:321–49. doi:10.1615/int.j.uncertaintyquantification.2011003343

34. Olofsson S, Deisenroth MP, Misener R. Design of experiments for model discrimination using Gaussian process surrogate models. *Computer Aided Chem Eng (Elsevier)* (2018) 44:847–52. doi:10.1016/B978-0-444-64241-7.50136-1

35. Li MY, Grant E, Griffiths TL. Gaussian process surrogate models for neural networks. *Uncertainty Artif Intelligence (Pmlr)* (2023) 1241–52.

36. Bilionis I, Zabaras N. Multidimensional adaptive relevance vector machines for uncertainty quantification. *SIAM J Scientific Comput* (2012) 34:B881–B908. doi:10.1137/120861345

37. Chen L, Zhao J, Lian H, Yu B, Atroshchenko E, Li P. A bem broadband topology optimization strategy based on taylor expansion and soar method-application to 2d acoustic scattering problems. *Int J Numer Methods Eng* (2023) 124:5151–82. doi:10.1002/nme.7345

38. Lakshminarayanan B, Pritzel A, Blundell C. Simple and scalable predictive uncertainty estimation using deep ensembles. *Adv Neural Inf Process Syst* (2017) 30.

39. Sriboriboon P, Qiao H, Kwon O, Vasudevan RK, Jesse S, Kim Y. Deep learning for exploring ultra-thin ferroelectrics with highly improved sensitivity of piezoresponse force microscopy. *npj Comput Mater* (2023) 9:28. doi:10.1038/s41524-023-00982-0

40. He J, Wang C, Li J, Liu C, Xue D, Cao J, et al. Machine learning assisted prediction of dielectric temperature spectrum of ferroelectrics. *J Adv Ceramics* (2023) 12:1793–804. doi:10.26599/jac.2023.9220788

41. Wang Y, Liao Z, Shi S, Wang Z, Poh LH. Data-driven structural design optimization for petal-shaped auxetics using isogeometric analysis. *Computer Model Eng and Sci* (2020) 122:433–58. doi:10.32604/cmes.2020.08680

42. Oishi A, Yagawa G. Computational mechanics enhanced by deep learning. *Computer Methods Appl Mech Eng* (2017) 327:327–51. doi:10.1016/j.cma.2017.08.040

43. Chen L, Wang Z, Lian H, Ma Y, Meng Z, Li P, et al. Reduced order isogeometric boundary element methods for cad-integrated shape optimization in electromagnetic scattering. *Computer Methods Appl Mech Eng* (2024) 419:116654. doi:10.1016/j.cma.2023.116654

44. Levine Y, Wies N, Sharir O, Cohen N, Shashua A. Tensors for deep learning theory: analyzing deep learning architectures via tensorization. In: *Tensors for data processing*. Elsevier (2022). p. 215–48.

45. Huang G, Wu G, Yang Z, Chen X, Wei W. Development of surrogate models for evaluating energy transfer quality of high-speed railway pantograph-catenary system using physics-based model and machine learning. *Appl Energy* (2023) 333:120608. doi:10.1016/j.apenergy.2022.120608

46. Chen L, Lian H, Natarajan S, Zhao W, Chen X, Bordas S. Multi-frequency acoustic topology optimization of sound-absorption materials with isogeometric boundary element methods accelerated by frequency-decoupling and model order reduction techniques. *Computer Methods Appl Mech Eng* (2022) 395:114997. doi:10.1016/j.cma.2022.114997

47. Zhou Z, Gao Y, Cheng Y, Ma Y, Wen X, Sun P, et al. Uncertainty quantification of vibroacoustics with deep neural networks and catmull–clark subdivision surfaces. *Shock and Vibration* (2024) 2024:7926619. doi:10.1155/2024/7926619

48. Chen L, Lian H, Liu Z, Gong Y, Zheng C, Bordas S. Bi-material topology optimization for fully coupled structural-acoustic systems with isogeometric fem–bem. *Eng Anal Boundary Elem* (2022) 135:182–95. doi:10.1016/j.enganabound.2021.11.005

49. Stam J. Exact evaluation of catmull-clark subdivision surfaces at arbitrary parameter values. *Seminal Graphics Pap Pushing Boundaries* (2023) 2:139–48. doi:10.1145/3596711.3596728

50. Qu Y, Zhou Z, Chen L, Lian H, Li X, Hu Z, et al. Uncertainty quantification of vibro-acoustic coupling problems for robotic manta ray models based on deep learning. *Ocean Eng* (2024) 299:117388. doi:10.1016/j.oceaneng.2024.117388

51. Chen L, Lian H, Dong H-W, Yu P, Jiang S, Bordas SP. Broadband topology optimization of three-dimensional structural-acoustic interaction with reduced order isogeometric fem/bem. *J Comput Phys* (2024) 509:113051. doi:10.1016/j.jcp.2024.113051

52. Wang S, Cao J, Philip SY. Deep learning for spatio-temporal data mining: a survey. *IEEE Trans knowledge Data Eng* (2020) 34:3681–700. doi:10.1109/TKDE.2020.3025580

53. Burton A, Miller G. The application of integral equation methods to the numerical solution of some exterior boundary-value problems. *Proc R Soc Lond A. Math Phys Sci* (1971) 323:201–10. doi:10.1098/rspa.1971.0097

54. Gauthier J. Conditional generative adversarial nets for convolutional face generation. 2 (2014).*Class project Stanford CS231N: convolutional Neural networks Vis recognition*

55. Mirza M. Conditional generative adversarial nets. *arXiv preprint arXiv:1411.1784* (2014). doi:10.48550/arXiv.1411.1784

frontiers | Frontiers in Physics

TYPE Original Research
PUBLISHED 07 April 2025
DOI 10.3389/fphy.2025.1540732

OPEN ACCESS

EDITED BY
Leilei Chen,
Huanghuai University, China

REVIEWED BY
Emad Awad,
Alexandria University, Egypt
Liguo Jin,
China Earthquake Administration, China

*CORRESPONDENCE
Lijun Qiu,
✉ qiuljun@126.com

RECEIVED 06 December 2024
ACCEPTED 28 February 2025
PUBLISHED 07 April 2025

CITATION
Zhang B and Qiu L (2025) Reflection of P_1-wave incident obliquely at the free surface of a fluid-saturated half-space: a comprehensive study via the model of soil mechanics.
Front. Phys. 13:1540732.
doi: 10.3389/fphy.2025.1540732

Reflection of P_1-wave incident obliquely at the free surface of a fluid-saturated half-space: a comprehensive study via the model of soil mechanics

Bo Zhang[1] and Lijun Qiu[1,2]*

[1]School of Civil Engineering, Hebei University of Architecture, Zhangjiakou, China, [2]Hebei Innovation Center of Transportation Infrastructure in Cold Region, Hebei University of Architecture, Zhangjiakou, China

Introduction: Elastic wave propagation in fluid-saturated porous media is of great significance in various fields. Based on the soil mechanics model of a two-phase medium, the reflection problem of an obliquely incident plane P_1-wave at the free surface is systematically explored, which aims to reveal the physical mechanism of wave propagation in saturated semi-infinite space.

Methods: The dispersion characteristic equations of body waves are obtained by using the Helmholtz decomposition method. The theoretical formulas of reflection coefficients and surface displacements are derived and verified for correctness by simplifying. Finally, numerical investigations are carried out on the variations of the displacement reflection coefficients and surface displacements with the incident angle for different boundary conditions, wave frequencies f, porosities n, Poisson's ratios ν, and modulus ratios E_w/μ.

Results: It is shown that the surface response of half-space is somewhat affected by the boundary conditions while little influenced by the wave frequency. It is also found that the effects of material properties on the surface response cannot be ignored.

Discussion: These conclusions provide a theoretical basis for wave survey technology of seismic engineering and site seismic response analysis.

KEYWORDS

saturated two-phase medium, model of soil mechanics, dispersion equation, boundary conditions, reflection coefficients, surface displacement

1 Introduction

Elastic wave propagation in fluid-saturated porous media has been studied for many years. It is of theoretical and practical significance in various fields such as soil dynamics, geotechnical engineering, earthquake engineering, geophysics, acoustics, petroleum engineering, etc. The reflection of elastic waves in saturated two-phase media is one of the important branches. Due to the existence of pore water in the soil skeleton, the mechanical properties of two-phase media become very complex, which results in the problem of wave propagation being much more complicated than that of a single-phase medium [1, 2]. Therefore, when the seismic wave propagates to the free surface of two-phase media, it will show complex reflection characteristics.

It is well known that Biot first predicted the existence of three body waves in a two-phase medium, namely, the fast P_1-wave, the slow P_2-wave, and the S-wave. The three body waves are dispersed and attenuated, the speed and attenuation of which are related to the frequency and the properties of saturated soil materials [3, 4]. All these laid the foundation for the theoretical study of wave propagation in a fluid-saturated porous medium. After that, many scholars studied the various aspects of wave propagation in such medium. The P_2-wave with strong dispersion and high attenuation characteristics was successively confirmed through experiments by Plona and Berryman in 1980 [5, 6]. Following the Biot model, different two-phase medium models, including the Zienkiewicz model [7, 8], the Men Fu-lu model [9–11], the model of soil mechanics [12], and the theory of mixture [13], were proposed by different researchers. Chen and Liao [14] compared the first four models in detail and pointed out the essential differences between them. They also theoretically explained that the soil mechanics model is a special case of the Biot model, which has the advantage of a clear physical meaning of modeling parameters. At the same time, more and more scholars used the Biot model to study the reflection of elastic waves at the boundary of the fluid-saturated medium. For example, Deresiewicz [15] deduced theoretical formulas for the reflection coefficient of plane waves incident on a free interface of a non-dissipative liquid-filled porous solid. Deresiewicz and Rice [16] derived analytical formulas for the reflection coefficients and reflection angles of body waves (P_1-, P_2-, and SV-waves) incident upon a free interface because of the dissipation. Xu et al. [17] presented analytical expressions of reflection coefficients when P_1-wave incident obliquely at four kinds of plane interfaces of saturated soil (i.e., free drainable/undrainable boundary, fixed drainable/undrainable boundary) and analyzed the effect of incident frequency, incident angle, and interface conditions on reflection coefficients. Lin et al. [18–20] investigated the dynamic response (e.g., surface displacement, surface strain, rocking strains, and energy partitions) of a half-space saturated with inviscid fluid subjected to obliquely incident P_1- or SV-wave in the case of free draining boundary, and he also adopted the linear porosity-modulus relation. Unlike Lin et al. [20], Rjoub [21, 22] presented the dynamic response (same as Lin et al., but without surface displacement) of a half-space saturated with viscous fluid, considering the oblique incidence of P_1- and SV-waves. Tajuddin and Hussaini [23] studied the reflection of body waves at free permeable and impermeable boundaries and rigid permeable and impermeable boundaries. Xia et al. [24] developed the secular equation of the Rayleigh surface wave and discussed its dispersion characteristic in a poroelastic half-space. You [25] discussed the free-surface motion caused by incident P_1- or SV- wave in drained or undrained boundary conditions based on the exact dynamic-stiffness matrix of half-space. Nie and Xu [26] deduced the wave field solutions by using the Wave Based Method and the boundary conditions (i.e., permeable and impermeable conditions) of saturated half-space when incident P- and SV-waves, and they also showed the effects of permeability coefficient, angle, and frequency on them. Yang [27] introduced the concept of homogeneous pore fluid into Biot's theory to analyze the saturation effects of subsoil on ground motions when an inclined SV-wave incident on the free surface of a partially saturated half-space. Later, based on governing equations of a three-phase medium, Chen [28] explained that a special wave mode conversion occurred when the fast P_1-wave incident at a certain angle on the nearly saturated soil. Zhou [29] investigated the dynamic response of P_1- and SV- waves incident at the interface of partially saturated soil and discussed the effects of boundary conditions, water saturation, frequency, Poisson's ratio, and modulus ratio (i.e., shear modulus of soil frame to bulk modulus of fluid) on it. Xue et al. [30] explored the phenomenon of wave mode conversion for a P_1-wave incident on the surface of a partially saturated half-space, and the critical saturation degree and angle of wave mode conversion were found for a specific nearly saturated soil. Afterward, wave propagation in the semi-infinite space was further enriched to the reflection and refraction of waves at different interfaces [31–37] and extended to wave propagation in the distinct media [38–43].

Since Chinese scholar Men proposed the soil mechanics model, quite a few researchers have also used it to study the wave propagation characteristics in a two-phase medium from theoretical [44–50] and practical views [51–54]. Among them, it is worth mentioning that Chen and Men [52] and Cui [51] presented a new method to understand the mechanism of soil liquefaction. Chen [44] and Chen et al. [45] analyzed the near-field wave motions combing the transmitting boundary. Recently, Xiao et al. [49] investigated the propagation and attenuation characteristics of Rayleigh waves in ocean sites. A preliminary analysis of the wave propagation characteristics in the infinite saturated medium based on the model of soil mechanics has been conducted by Zhang et al. [50]. The results showed that the frequency and soil properties may have a significant influence on the velocity and attenuation coefficient of the three body waves. For this reason, these parameters are bound to affect the reflection of each wave incident upon a free plane boundary.

Among the existing literature, the velocity of plane P_1-wave is the fastest, and the attenuation of it is slow in the saturated infinite space. Therefore, it is of great interest to study the propagation characteristic of P_1-wave under different boundary conditions in a fluid-saturated half-space. However, it is rare to use the model of soil mechanics to study the propagation of elastic waves in the semi-infinite field. As mentioned above, the model of soil mechanics is introduced to discuss the reflection of P_1-wave on the free surface of saturated two-phase media in this paper. By Fortran software, numerical analysis is conducted to study the effects of boundary drainage, wave frequency, porosity, Poisson's ratio, and modulus ratio on the displacement reflection coefficients and surface displacements.

2 The propagation theory of elastic wave based on the model of soil mechanics

2.1 The equations of motion

The model of soil mechanics for a fluid-saturated medium in which the liquid phase is assumed to be ideal, the solid phase is isotropic elastic, and the compression modulus of solid particles in point contact tends to infinity, can be expressed as [12, 44, 49, 50].

$$\begin{cases} \mu\Delta\boldsymbol{u} + (\lambda+\mu)\nabla(\nabla\cdot\boldsymbol{u}) + (1-n)\nabla p_f + [B](\dot{\boldsymbol{U}} - \dot{\boldsymbol{u}}) = \rho_1\ddot{\boldsymbol{u}} \\ n\nabla p_f - [B](\dot{\boldsymbol{U}} - \dot{\boldsymbol{u}}) = \rho_2\ddot{\boldsymbol{U}} \\ (1-n)\nabla\cdot\boldsymbol{u} + n\nabla\cdot\boldsymbol{U} - \dfrac{n}{E_{\mathrm{w}}}p_f = 0 \end{cases} \tag{1}$$

Where, Δ $(=\nabla^2)$ is the Laplace operator in the Cartesian Coordinate, ∇ is the Hamiltonian operator. $\boldsymbol{u}$, $\dot{\boldsymbol{u}}$, and $\ddot{\boldsymbol{u}}$ denote the solid phase's displacement, velocity, and acceleration vector, respectively. $\boldsymbol{U}$, $\dot{\boldsymbol{U}}$ and $\ddot{\boldsymbol{U}}$ represent the absolute displacement, velocity, and acceleration vector of the liquid phase separately. λ and μ are the classical Lame constants, which are functions of the Poisson's ratio v and the elastic modulus of the solid phase E, $\lambda = Ev/((1+v)(1-2v))$ and $\mu = E/2(1+v)$. n is the porosity. ρ_1 and ρ_2 are defined to describe the solid and liquid density per unit volume, in which $\rho_1 = (1-n)\rho_{\mathrm{s}}$ and $\rho_2 = n\rho_{\mathrm{w}}$, ρ_{s} and ρ_{w} are the solid and fluid mass densities separately. p_f is the true pore pressure. E_{w} refers to the bulk modulus of liquid. k $(=K/\rho_{\mathrm{w}}g)$ is the dynamic permeability coefficient of the solid skeleton, in which K (m/s) is the permeability coefficient that satisfies Darcy's law, and g is the gravitation acceleration. $[B]$ represents the dissipation coefficient, which is a third-order diagonal matrix. $[B] = diag(b_x, b_y, b_z)$, and $b_x = b_y = b_z = n^2/k$ in the isotropic medium.

2.2 Solutions of the equations

Considering Helmholtz's resolution, we introduce scalar potential functions (ϕ_{s}, ϕ_{w}) and vector potential functions ($\boldsymbol{\psi}_{\mathbf{s}}$, $\boldsymbol{\psi}_{\mathbf{w}}$) to describe the displacements of solid- and liquid-phase, which can be written as follows [11, 50, 55].

$$\begin{cases} \boldsymbol{u} = \nabla\phi_{\mathrm{s}} + \nabla\times\boldsymbol{\psi}_{\mathrm{s}} \\ \boldsymbol{U} = \nabla\phi_{\mathrm{w}} + \nabla\times\boldsymbol{\psi}_{\mathrm{w}} \end{cases} \tag{2}$$

Insertion of Equation 2 in Equation 1 yields the wave equation expressed by potential function, as can be shown in the following form [50].

$$\begin{cases} \rho_1\ddot{\phi}_{\mathrm{s}} - (\lambda+2\mu)\Delta\phi_{\mathrm{s}} = p_f - \rho_2\ddot{\phi}_{\mathrm{w}} \\ \rho_1\ddot{\boldsymbol{\psi}}_{\mathrm{s}} - \mu\Delta\boldsymbol{\psi}_{\mathrm{s}} = -\rho_2\ddot{\boldsymbol{\psi}}_{\mathrm{w}} \\ np_f - [B](\dot{\phi}_{\mathrm{w}} - \dot{\phi}_{\mathrm{s}}) - \rho_2\ddot{\phi}_{\mathrm{w}} = 0 \\ \rho_2\ddot{\boldsymbol{\psi}}_{\mathrm{w}} + [B](\dot{\boldsymbol{\psi}}_{\mathrm{w}} - \dot{\boldsymbol{\psi}}_{\mathrm{s}}) = 0 \\ (1-n)\Delta\phi_{\mathrm{s}} + n\Delta\phi_{\mathrm{w}} - \dfrac{n}{E_{\mathrm{w}}}p_f = 0 \end{cases} \tag{3}$$

The in-plane wave problem in a fluid-saturated medium is a P-SV wave problem in the xoz plane. Assuming the displacements $\boldsymbol{u}$ and $\boldsymbol{U}$ are independent of the coordinate y. The scalar potential functions $\phi_{\mathrm{s}} = \phi_{\mathrm{s}}(x,z,t)$, and $\phi_{\mathrm{w}} = \phi_{\mathrm{w}}(x,z,t)$ in the xoz plane. The vector potential functions $\boldsymbol{\psi}_{\mathbf{s}} = (0, \psi_{\mathrm{s}}(x,z,t), 0)$, and $\boldsymbol{\psi}_{\mathbf{w}} = (0, \psi_{\mathrm{w}}(x,z,t), 0)$. The components of solid-phase displacement (u_x, u_z) and the components of liquid-phase displacement (U_x, U_z) can be written in the form of potential functions, as shown in Equations 4a, 4b; [1, 20]. The potential function expressions of normal stress (σ_{zz}) and shear stress (σ_{xz}) are written in Equation 4c by the plane strain character. From the fifth of Equation 3, the potential function expression of pore fluid pressure (p_f) can be given by the third of Equation 4c.

$$\begin{cases} u_x = \dfrac{\partial\phi_{\mathrm{s}}}{\partial x} - \dfrac{\partial\psi_{\mathrm{s}}}{\partial z} \\ u_z = \dfrac{\partial\phi_{\mathrm{s}}}{\partial z} + \dfrac{\partial\psi_{\mathrm{s}}}{\partial x} \end{cases} \tag{4a}$$

$$\begin{cases} U_x = \dfrac{\partial\phi_{\mathrm{w}}}{\partial x} - \dfrac{\partial\psi_{\mathrm{w}}}{\partial z} \\ U_z = \dfrac{\partial\phi_{\mathrm{w}}}{\partial z} + \dfrac{\partial\psi_{\mathrm{w}}}{\partial x} \end{cases} \tag{4b}$$

$$\begin{cases} \sigma_{zz} = \left(\lambda + \dfrac{1-n}{n}E_{\mathrm{w}}\right)\nabla^2\phi_{\mathrm{s}} + 2\mu\left(\dfrac{\partial^2\phi_{\mathrm{s}}}{\partial z^2} + \dfrac{\partial^2\psi_{\mathrm{s}}}{\partial x\partial z}\right) + E_{\mathrm{w}}\nabla^2\phi_{\mathrm{w}} \\ \sigma_{xz} = 2\mu\dfrac{\partial^2\phi_{\mathrm{s}}}{\partial x\partial z} + \mu\left(\dfrac{\partial^2\psi_{\mathrm{s}}}{\partial x^2} - \dfrac{\partial^2\psi_{\mathrm{s}}}{\partial z^2}\right) \\ p_f = \dfrac{1-n}{n}E_{\mathrm{w}}\nabla^2\phi_{\mathrm{s}} + E_{\mathrm{w}}\nabla^2\phi_{\mathrm{w}} \end{cases} \tag{4c}$$

Assuming the plane harmonic wave solutions of the potential functions in the following forms [11].

$$\begin{cases} \phi_{\mathrm{s}} = A_{\mathrm{s}}e^{i(\omega t - \boldsymbol{k}_{\mathbf{P}}\cdot\boldsymbol{r})} \\ \phi_{\mathrm{w}} = A_{\mathrm{w}}e^{i(\omega t - \boldsymbol{k}_{\mathbf{P}}\cdot\boldsymbol{r})} \\ \psi_{\mathrm{s}} = B_{\mathrm{s}}e^{i(\omega t - \boldsymbol{k}_{\mathbf{S}}\cdot\boldsymbol{r})} \\ \psi_{\mathrm{w}} = B_{\mathrm{w}}e^{i(\omega t - \boldsymbol{k}_{\mathbf{S}}\cdot\boldsymbol{r})} \end{cases} \tag{5}$$

Where, A_{s} and A_{w} are the potential function amplitudes of solid- and liquid-phases for P-wave, respectively. B_{s} and B_{w} represent the potential function amplitudes of solid- and liquid-phases for S-wave separately. $\boldsymbol{k}_{\mathbf{P}}$ and $\boldsymbol{k}_{\mathbf{S}}$ denote the propagation directions of P- and S-waves (wave vector). k_{P} and k_{S} are the values of vectors ($\boldsymbol{k}_{\mathbf{P}}$ and $\boldsymbol{k}_{\mathbf{S}}$), with k_{P} and k_{S} representing the wave numbers of P- and S-waves, respectively. $\boldsymbol{r}$ denotes the position vector. $i = \sqrt{-1}$. ω is the circular frequency of a wave.

Substituting Equation 5 into Equation 3, we can obtain the dispersion equations of P- and S-waves.

$$\begin{aligned} &\frac{(\lambda+2\mu)nE_{\mathrm{w}}}{\rho_1\rho_2}\left(\frac{k_{\mathrm{P}}}{\omega}\right)^4 - \left\{\left(\frac{\lambda+2\mu}{\rho_1} + \frac{nE_{\mathrm{w}}}{\rho_2} + \frac{(1-n)^2E_{\mathrm{w}}}{n\rho_1}\right)\right. \\ &\left. -\frac{ib}{\omega\rho_1\rho_2}\left(\lambda+2\mu+\frac{E_{\mathrm{w}}}{n}\right)\right\}\left(\frac{k_{\mathrm{P}}}{\omega}\right)^2 + 1 - \frac{ib}{\omega}\left(\frac{1}{\rho_1}+\frac{1}{\rho_2}\right) = 0 \end{aligned} \tag{6a}$$

$$\left(\frac{ib\mu}{\omega\rho_1\rho_2} - \frac{\mu}{\rho_1}\right)\left(\frac{k_{\mathrm{S}}}{\omega}\right)^2 + 1 - \frac{ib}{\omega}\left(\frac{1}{\rho_1}+\frac{1}{\rho_2}\right) = 0 \tag{6b}$$

It can be seen from Equations 6a, 6b that the velocities and attenuation coefficients for two kinds of compressional waves (P_1- and P_2- waves) and one shear wave (S- wave) in an unbounded saturated medium are calculated. All three body waves are dispersed and attenuated, which are related to the properties of medium and wave frequency.

3 Reflection of P_1-wave in a semi-infinite saturated medium

The obliquely incident P_1-wave at the free surface of a semi-infinite saturated medium is a free field problem and also an important part of the site response analysis. In this case, the stresses on the free surface are zero. The upper medium is air without

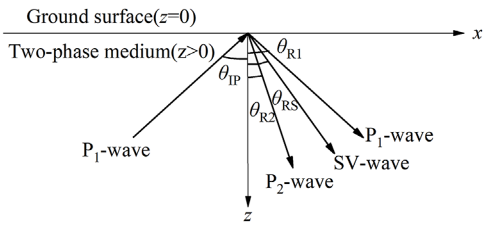

FIGURE 1
Fluid-saturated half-space subjected to an incident P_1-wave.

density, and the lower medium is saturated soil. We now introduce a rectangular coordinate system, with x as the horizontal axis and z as the vertical axis. The z-axis points downward vertically, which is directed into the interior of the two-phase medium. The half-space is bounded by a horizontal plane ($z = 0$). The plane P_1-wave with angular frequency ω is incident from the bottom to the free surface at an angle θ_{IP}. Then the reflected P_1-, P_2-, and SV-waves are generated in the saturated medium (i.e., $z > 0$), whose angles of reflection are θ_{R1}, θ_{R2}, and θ_{RS}. All the reflected waves travel at the incident wave frequency (ω). The geometry considered in this paper is shown in Figure 1.

According to Snell's law, the relations between the angles of the reflected and incident waves are given by [55, 56].

$$\frac{V_{\mathrm{P1}}}{\sin\theta_{\mathrm{IP}}} = \frac{V_{\mathrm{P1}}}{\sin\theta_{\mathrm{R1}}} = \frac{V_{\mathrm{P2}}}{\sin\theta_{\mathrm{R2}}} = \frac{V_{\mathrm{S}}}{\sin\theta_{\mathrm{RS}}} \tag{7}$$

Where, V_{P1}, V_{P2}, and V_{S} are the wave velocities. As is shown in Equation 7, the reflection angles of each reflected wave can be determined when the wave velocity and incident angle are known. Moreover, the reflection angle (θ_{R1}) of the P_1 wave is the same as its incident angle (θ_{IP}).

3.1 Potential functions of elastic wave

In the two-phase medium (i.e., the half-space $z > 0$), the incident P_1-wave gives rise to reflected waves of all three types, i.e., P_1-, P_2-, and SV- waves. The expressions for solid- and liquid-phases potential functions of P-wave (ϕ_{s}, ϕ_{w}) and SV-wave (ψ_{s}, ψ_{w}) are shown in Equation 8; [27]. The plane harmonic solutions of potential functions for different waves are shown in Equations 9a-9d; [27].

$$\begin{cases} \phi_{\mathrm{s}} = \phi_{\mathrm{s1}}^{\mathrm{I}} + \phi_{\mathrm{s1}}^{\mathrm{R}} + \phi_{\mathrm{s2}}^{\mathrm{R}} \\ \phi_{\mathrm{w}} = \phi_{\mathrm{w1}}^{\mathrm{I}} + \phi_{\mathrm{w1}}^{\mathrm{R}} + \phi_{\mathrm{w2}}^{\mathrm{R}} \\ \psi_{\mathrm{s}} = \psi_{\mathrm{s}}^{\mathrm{R}} \\ \psi_{\mathrm{w}} = \psi_{\mathrm{w}}^{\mathrm{R}} \end{cases} \tag{8}$$

$$\begin{cases} \phi_{\mathrm{s1}}^{\mathrm{I}} = A_{\mathrm{s1}}^{\mathrm{I}} \exp\left[i\left(\omega t - k_{1x}^{\mathrm{I}} x + k_{1z}^{\mathrm{I}} z\right)\right] \\ \phi_{\mathrm{w1}}^{\mathrm{I}} = A_{\mathrm{w1}}^{\mathrm{I}} \exp\left[i\left(\omega t - k_{1x}^{\mathrm{I}} x + k_{1z}^{\mathrm{I}} z\right)\right] \end{cases} \tag{9a}$$

$$\begin{cases} \phi_{\mathrm{s1}}^{\mathrm{R}} = A_{\mathrm{s1}}^{\mathrm{R}} \exp\left[i\left(\omega t - k_{1x}^{\mathrm{R}} x - k_{1z}^{\mathrm{R}} z\right)\right] \\ \phi_{\mathrm{w1}}^{\mathrm{R}} = A_{\mathrm{w1}}^{\mathrm{R}} \exp\left[i\left(\omega t - k_{1x}^{\mathrm{R}} x - k_{1z}^{\mathrm{R}} z\right)\right] \end{cases} \tag{9b}$$

$$\begin{cases} \phi_{\mathrm{s2}}^{\mathrm{R}} = A_{\mathrm{s2}}^{\mathrm{R}} \exp\left[i\left(\omega t - k_{2x}^{\mathrm{R}} x - k_{2z}^{\mathrm{R}} z\right)\right] \\ \phi_{\mathrm{w2}}^{\mathrm{R}} = A_{\mathrm{w2}}^{\mathrm{R}} \exp\left[i\left(\omega t - k_{2x}^{\mathrm{R}} x - k_{2z}^{\mathrm{R}} z\right)\right] \end{cases} \tag{9c}$$

$$\begin{cases} \psi_{\mathrm{s}}^{\mathrm{R}} = B_{\mathrm{s}}^{\mathrm{R}} \exp\left[i\left(\omega t - k_{\mathrm{s}x}^{\mathrm{R}} x - k_{\mathrm{s}z}^{\mathrm{R}} z\right)\right] \\ \psi_{\mathrm{w}}^{\mathrm{R}} = B_{\mathrm{w}}^{\mathrm{R}} \exp\left[i\left(\omega t - k_{\mathrm{s}x}^{\mathrm{R}} x - k_{\mathrm{s}x}^{\mathrm{R}} z\right)\right] \end{cases} \tag{9d}$$

Where, $\phi_{\mathrm{s1}}^{\mathrm{I}}$ ($\phi_{\mathrm{w1}}^{\mathrm{I}}$) is a potential function in the solid (liquid) of incident P_1-wave. $A_{\mathrm{s1}}^{\mathrm{I}}$ and $A_{\mathrm{w1}}^{\mathrm{I}}$ are the amplitudes of the corresponding potential functions. Similarly, $\phi_{\mathrm{s1}}^{\mathrm{R}}$, $\phi_{\mathrm{s2}}^{\mathrm{R}}$, and $\psi_{\mathrm{s}}^{\mathrm{R}}$ are the solid-phase potential functions of the reflected P_1-, P_2-, and SV-waves, respectively. $A_{\mathrm{s1}}^{\mathrm{R}}$, $A_{\mathrm{s2}}^{\mathrm{R}}$ and $B_{\mathrm{s}}^{\mathrm{R}}$ correspond to the solid-phase potential amplitudes. $\phi_{\mathrm{w1}}^{\mathrm{R}}$, $\phi_{\mathrm{w2}}^{\mathrm{R}}$ and $\psi_{\mathrm{w}}^{\mathrm{R}}$ denote the liquid-phase potential functions of the reflected P_1-, P_2-, and SV-waves, separately. $A_{\mathrm{w1}}^{\mathrm{R}}$, $A_{\mathrm{w2}}^{\mathrm{R}}$ and $B_{\mathrm{w}}^{\mathrm{R}}$ are the liquid-phase potential amplitudes. k_{1x}^{I} and k_{1z}^{I} represent the components of the incident P_1-wave vector in the x and z directions. k_{1x}^{R} and k_{1z}^{R} are the components of the reflected P_1-wave vector in the x and z directions. Similarly, k_{2x}^{R}, k_{2z}^{R}, $k_{\mathrm{s}x}^{\mathrm{R}}$ and $k_{\mathrm{s}z}^{\mathrm{R}}$ are the components of the reflected P_2- and SV- wave vectors of the corresponding directions.

Following the geometric relationship of wave vectors, it can be seen that the wave vectors and their components of all waves satisfy the equalities Equation 10. Moreover, by Snell's law, the x-components of the wave numbers for the incident and reflected waves are the same, as shown in Equation 11; [55, 56].

$$\begin{cases} \left(k_{1x}^{\mathrm{I}}\right)^2 + \left(k_{1z}^{\mathrm{I}}\right)^2 = \left(k_1^{\mathrm{I}}\right)^2 \\ \left(k_{1x}^{\mathrm{R}}\right)^2 + \left(k_{1z}^{\mathrm{R}}\right)^2 = \left(k_1^{\mathrm{R}}\right)^2 \\ \left(k_{2x}^{\mathrm{R}}\right)^2 + \left(k_{2z}^{\mathrm{R}}\right)^2 = \left(k_2^{\mathrm{R}}\right)^2 \\ \left(k_{\mathrm{s}x}^{\mathrm{R}}\right)^2 + \left(k_{\mathrm{s}z}^{\mathrm{R}}\right)^2 = \left(k_{\mathrm{s}}^{\mathrm{R}}\right)^2 \end{cases} \tag{10}$$

$$k_{1x}^{\mathrm{I}} = k_{1x}^{\mathrm{R}} = k_{2x}^{\mathrm{R}} = k_{\mathrm{s}x}^{\mathrm{R}} \tag{11}$$

From Equations 6a, 6b, the relations between the various amplitudes in Equations 9 can be obtained as follows.

$$\delta_1 = \frac{A_{\mathrm{w1}}^{\beta}}{A_{\mathrm{s1}}^{\beta}} = \frac{\left(\lambda + 2\mu + \frac{1-n}{n} E_{\mathrm{w}}\right)\left(k_1^{\beta}\right)^2 - \rho_1 \omega^2}{\rho_2 \omega^2 - E_{\mathrm{w}}\left(k_1^{\beta}\right)^2}, \beta = \mathrm{I}, \mathrm{R} \tag{12a}$$

$$\delta_2 = \frac{A_{\mathrm{w2}}^{\mathrm{R}}}{A_{\mathrm{s2}}^{\mathrm{R}}} = \frac{\left(\lambda + 2\mu + \frac{1-n}{n} E_{\mathrm{w}}\right)\left(k_2^{\mathrm{R}}\right)^2 - \rho_1 \omega^2}{\rho_2 \omega^2 - E_{\mathrm{w}}\left(k_2^{\mathrm{R}}\right)^2} \tag{12b}$$

$$\delta_{\mathrm{s}} = \frac{B_{\mathrm{w}}^{\mathrm{R}}}{B_{\mathrm{s}}^{\mathrm{R}}} = \frac{\mu\left(k_{\mathrm{s}}^{\mathrm{R}}\right)^2 - \rho_1 \omega^2}{\rho_2 \omega^2} \tag{12c}$$

Where, δ_1, δ_2, and δ_{s} are the amplitude ratios of potentials related to liquid and solid phases for P_1-, P_2-, and SV-waves, respectively.

3.2 Boundary conditions and solutions

3.2.1 Boundary conditions of the free surface

When P_1-wave is obliquely incident on the free surface of the saturated medium, the boundary conditions can be completely permeable or impermeable, i.e., (a) Open-pore boundary and (b) Sealed-pore boundary [15, 57]. In case (a), the pore fluid can flow freely, so the normal and shear stresses of the soil skeleton and the pore pressure are zeros. Under condition (b), the pore fluid is enclosed in a porous medium, so the normal and shear stresses of the soil skeleton and the displacement of solid related to liquid are zeros. Then, the drained and undrained conditions can be expressed as [17].

$$\begin{cases} \sigma_{ij|z=0^+} = 0 \\ p_{f|z=0^+} = 0 \end{cases} \tag{13a}$$

$$\begin{cases} \sigma_{ij|z=0^+} = 0 \\ u_{z|z=0^+} - U_{z|z=0^+} = 0 \end{cases} \tag{13b}$$

In which the subscripts (i, $j = x$, z) represent the components in both x and z directions. $\sigma_{ij|z=0^+}$ denotes the total stress of a saturated two-phase medium. $p_{f|z=0^+}$ is the pore pressure of the boundary.

On inserting Equations 4a–4c, together with Equation 12a, 12b, 12c, into Equations 13a, 13b, and taking account of Equation 10 and Equation 11, we find the analytical formulas of amplitude ratios under permeable and impermeable boundaries, i.e., $A_{\mathrm{s1}}^{\mathrm{R}}/A_{\mathrm{s1}}^{\mathrm{I}}$, $A_{\mathrm{s2}}^{\mathrm{R}}/A_{\mathrm{s1}}^{\mathrm{I}}$, and $B_{\mathrm{s}}^{\mathrm{R}}/A_{\mathrm{s1}}^{\mathrm{I}}$. The formulas in the form of the matrix are through

$$[S_{\mathrm{P-SV}}]_f \{A_{\mathrm{s1}}^{\mathrm{R}}, A_{\mathrm{s2}}^{\mathrm{R}}, B_{\mathrm{s}}^{\mathrm{R}}\}^{\mathrm{T}} = \{F\}^{\mathrm{T}} A_{\mathrm{s1}}^{\mathrm{I}} \tag{14a}$$

$$[\overline{S}_{\mathrm{P-SV}}]_f \{A_{\mathrm{s1}}^{\mathrm{R}}, A_{\mathrm{s2}}^{\mathrm{R}}, B_{\mathrm{s}}^{\mathrm{R}}\}^{\mathrm{T}} = \{\overline{F}\}^{\mathrm{T}} A_{\mathrm{s1}}^{\mathrm{I}} \tag{14b}$$

Where, the superscript - denotes the impermeable boundary. $\{F\}$ and $\{\overline{F}\}$ are the matrixes related to the incident P_1-wave. $[S_{\mathrm{P-SV}}]_f$ and $[\overline{S}_{\mathrm{P-SV}}]_f$ are the 3-order matrixes corresponding to the reflected waves. The elements of $\{F\}$, $\{\overline{F}\}$, $[S_{\mathrm{P-SV}}]_f$, and $[\overline{S}_{\mathrm{P-SV}}]_f$ are given in the Appendix.

3.2.2 Surface response of saturated half-space

Without loss of generality, we assume the potential function amplitude of the incident wave equals unity, i.e., $A_{\mathrm{s1}}^{\mathrm{I}} = 1$ [1]. Substituting Equations 11, 12a–c into Equations 14a, b, we can obtain the potential function amplitudes of the reflected waves $A_{\mathrm{s1}}^{\mathrm{R}}$, $A_{\mathrm{s2}}^{\mathrm{R}}$, and $B_{\mathrm{s}}^{\mathrm{R}}$ (i.e., the amplitude reflection coefficients of P_1-, P_2-, and SV-waves). Then inserting $A_{\mathrm{s1}}^{\mathrm{R}}$, $A_{\mathrm{s2}}^{\mathrm{R}}$, and $B_{\mathrm{s}}^{\mathrm{R}}$ into Equation 4a, the solid-phase displacement reflection coefficients of each reflected wave are given through the expressions

$$\begin{cases} R_{\mathrm{s1}}^{\mathrm{R}} = A_{\mathrm{s1}}^{\mathrm{R}} \\ R_{\mathrm{s2}}^{\mathrm{R}} = \dfrac{k_2^{\mathrm{R}}}{k_1^{\mathrm{I}}} A_{\mathrm{s2}}^{\mathrm{R}} \\ R_{\mathrm{ss}}^{\mathrm{R}} = \dfrac{k_{\mathrm{s}}^{\mathrm{R}}}{k_1^{\mathrm{I}}} B_{\mathrm{s}}^{\mathrm{R}} \end{cases} \tag{15}$$

Where, $R_{\mathrm{s1}}^{\mathrm{R}}$, $R_{\mathrm{s2}}^{\mathrm{R}}$, and $R_{\mathrm{ss}}^{\mathrm{R}}$ are employed to denote the displacement reflection coefficients of P_1-, P_2-, and SV-waves in the solid phase, respectively.

Insertion of Equations 8, 9 in Equation 4a yields the surface displacement components (e.g., the horizontal and vertical displacements u_x and u_z) of the solid phase corresponding to the sum of one incident and three reflected waves may be written

$$\begin{cases} u_x = k_{1x}^{\mathrm{I}} A_{\mathrm{s1}}^{\mathrm{I}} + k_{1x}^{\mathrm{R}} A_{\mathrm{s1}}^{\mathrm{R}} + k_{2x}^{\mathrm{R}} A_{\mathrm{s2}}^{\mathrm{R}} - k_{sz}^{\mathrm{R}} B_{\mathrm{s}}^{\mathrm{R}} \\ u_z = -k_{1z}^{\mathrm{I}} A_{\mathrm{s1}}^{\mathrm{I}} + k_{1z}^{\mathrm{R}} A_{\mathrm{s1}}^{\mathrm{R}} + k_{2z}^{\mathrm{R}} A_{\mathrm{s2}}^{\mathrm{R}} + k_{sx}^{\mathrm{R}} B_{\mathrm{s}}^{\mathrm{R}} \end{cases} \tag{16}$$

4 Degenerate validation of solutions

4.1 Validation of degenerate formulas

Let the liquid density $\rho_{\mathrm{w}} = 0$, and the bulk modulus of liquid $E_{\mathrm{w}} = 0$. Then, the solution in this paper can degenerate into the case of a P-wave incident on the free interface of a single-phase medium. Now, the potential amplitude ratios of the liquid-solid phase in the two-phase medium $\delta_1 = 0$, $\delta_2 = 0$, and $\delta_{\mathrm{s}} = 0$. And the wave vector of the reflected P_1-wave is the same as that of the P_2-wave, i.e., $k_1^{\mathrm{R}} = k_2^{\mathrm{R}}$, $k_{1z}^{\mathrm{R}} = k_{2z}^{\mathrm{R}}$. When the two-phase medium is reduced to a single-phase medium, the velocity of P-wave $V_{\mathrm{P}} = \sqrt{(\lambda + 2\mu)/\rho_{\mathrm{s}}}$, the velocity of SV-wave $V_{\mathrm{S}} = \sqrt{\mu/\rho_{\mathrm{s}}}$, which can be derived from the dispersion Equations 6a, 6b. The potential amplitude of the reflected P-wave $A_{\mathrm{s}}^{\mathrm{R}} = A_{\mathrm{s1}}^{\mathrm{R}} + A_{\mathrm{s2}}^{\mathrm{R}}$. Accordingly, Equation 14a, 14b can be simplified as

$$\begin{cases} \mu\left(\dfrac{V_{\mathrm{P}}^2}{V_{\mathrm{S}}^2}\left(k_1^{\mathrm{I}}\right)^2 - 2\left(k_{1x}^{\mathrm{I}}\right)^2\right)\left(A_{\mathrm{s}}^{\mathrm{I}} + A_{\mathrm{s}}^{\mathrm{R}}\right) + 2\mu k_{\mathrm{s}x}^{\mathrm{R}} k_{\mathrm{s}z}^{\mathrm{R}} B_{\mathrm{s}}^{\mathrm{R}} = 0 \\ 2\mu k_{1x}^{\mathrm{I}} k_{1z}^{\mathrm{I}}\left(A_{\mathrm{s}}^{\mathrm{R}} - A_{\mathrm{s}}^{\mathrm{I}}\right) + \mu\left(\left(k_{\mathrm{s}x}^{\mathrm{R}}\right)^2 - \left(k_{\mathrm{s}z}^{\mathrm{R}}\right)^2\right) B_{\mathrm{s}}^{\mathrm{R}} = 0 \end{cases} \tag{17}$$

Equation 17 is further simplified to obtain a new expression, which is the same as the Equations of a single-phase medium in Stein and Wysession [56]. It can be seen that the reflection of the P-wave on the free surface of a single-phase medium is a special case in this paper.

4.2 Validation of numerical analysis

To further verify the correctness of the formulas for reflection coefficient and surface displacement, Equation 17 is compared with the curve of P-wave incident on the free surface of a single-phase medium in Pujol [55]. The parameters for single-phase media are taken from Pujol [55], namely, $V_{\mathrm{P}}/V_{\mathrm{S}} = 1.732$ and $\upsilon = 0.25$. The variations of amplitude ratios and surface displacements with the incident angle are shown in Figure 2 when the P-wave is incident on the interface. It is noted that the displacement components u_x and u_z in Figure 2b are normalized by a factor k_1^{I}, which represents the displacement intensity of the incident P-wave. If not specified, the surface displacements in the following figures are all normalized.

It can be seen from Figure 2 that the calculated results of Equation 17 are consistent with those of Pujol [55]. This is sufficient to demonstrate the correctness of the formula derived in this paper.

5 Numerical analysis

In this section, we use the formulas derived above to compute the displacement reflection coefficients and surface displacements when the plane P_1-wave is incident obliquely on the free boundary of a fluid-saturated half-space. Numerical examples are conducted in Fortran to explore the influence of boundary conditions, wave frequency, and characteristics of saturated soil materials (the porosity n, the Poisson's ratio υ, the fluid bulk modulus to the stiffness of soil E_{w}/μ) on the

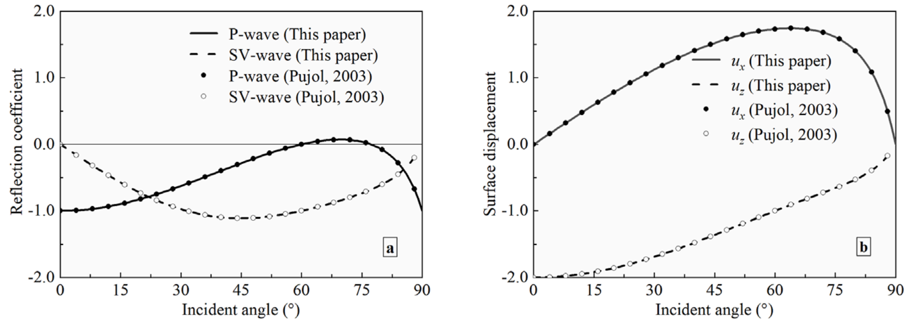

FIGURE 2
Surface response versus P-wave incident angle for an elastic half-space. **(a)** Amplitude reflection coefficient; **(b)** Surface displacement.

surface response of saturated half-space. Some soil parameters of the two-phase medium used in the calculation are taken from Ref. [21] and listed as follows: $\rho_s = 2650\,\text{kg.m}^{-3}$, $\rho_w = 1000\,\text{kg.m}^{-3}$, $E_w = 2.0 \times 10^9\text{Pa}$, and $k = 1.0 \times 10^{-7}\ \text{m}^3\text{.s/kg}$. The other soil parameters, i.e., the porosity n, the Poisson's ratio υ, and the modulus ratio E_w/μ, will be given in the analysis of each section below.

Figure 3 through Figure 7 present the variations of the displacement reflection coefficients and surface displacements as described in Equations 15, 16 with incident angles under different conditions, i.e., boundary conditions, wave frequencies, porosities, Poisson's, and modulus ratios. It can be seen that the displacement reflection coefficients and surface displacements vary smoothly with the incident angle of the P_1-wave. The displacement reflection coefficient of the P_2-wave is one order of magnitude smaller than those of the other reflected waves (P_1- and SV-waves). When the P_1-wave is at normal or grazing incidence, i.e., the incident angle equals zero or 90°, only the incident wave is reflected, and the reflected P_2- and SV-waves vanish. At this time, the displacement reflection coefficient of the reflected P_1-wave is −1.0, of which the phase is opposite to that of the incident P_1-wave. This is consistent with the reflection characteristics of compressive P-wave on the surface of an elastic medium [56]. Furthermore, when the incident P_1-wave strikes the interface perpendicularly, the surface displacements $u_x = 0$, $u_z = -2.0$. When the incident angle is 90°, the surface displacements $u_x = 0.0$, $u_z = 0.0$, which implies that the reflected P_1-wave annihilates the incident P_1-wave at the free surface. And the phase difference between u_x and u_z is 180° [51]. This holds for a single-phase medium as well [55]. In addition, with increasing incident angle, the vertical displacement u_z decreases, while the horizontal displacement u_x increases before reaching its peak value (near $\theta_{IP} = 60°$) and has a reverse tendency thereafter.

5.1 Influence of boundary conditions

When P_1-wave propagates in a saturated half-space, specific solutions can be obtained using appropriate boundary conditions. The single control variable method is introduced to analyze the influence of boundary drainage on the surface response of half space. The values of the physical parameters of the saturated poroelastic half-space are selected from Section 5, and the other parameters are as follows: $n = 0.1$, $\upsilon = 0.2$, and $E_w/\mu = 0.1$. The frequency of incident wave $f = 100$ Hz. The curves in Figure 3 represent the displacement reflection coefficients and surface displacements with distinct boundaries.

It can be seen from Figure 3a that the displacement reflection coefficient of P_1-wave decreases with an increase in the incident angle before reaching its minimum value near 65°under different conditions. Moreover, when the incident angle θ_{IP} is greater than 36°, the displacement reflection coefficient under the impermeable interface is more than that of the permeable interface. Figure 3b shows that the displacement reflection coefficient of the P_2-wave is much less than those of other reflected P_1- and SV-waves, and the coefficient under a permeable interface is greater than that under an impermeable boundary. From Figure 3c, for the reflected SV-wave, the displacement reflection coefficient increases with a rise in the incident angle before attaining its maximum value near 45°. Also, the displacement reflection coefficient at an impermeable interface is more than that at a permeable interface if the θ_{IP} is within the range of 16°-90°. Given Figure 3d, u_x reaches its peak value at approximately 60°, while u_z reaches its peak value at 0°, and the peak value of u_z is larger than that of u_x. If $\theta_{IP} < 30°$, the vertical and horizontal displacements (e.g., u_x and u_z) under two boundary conditions are the same. However, if $\theta_{IP} > 30°$, both displacements u_x and u_z (absolute values) increase slightly under the impervious interface. Accordingly, the boundary conditions have a certain effect on the surface response of half-space, and this effect manifests a considerable dependence on the incident angle.

5.2 Influence of wave frequency

As analyzed in Refs. [2, 50], all three body waves are dispersive and attenuated, and the velocities and attenuation are frequency-dependent. To illustrate the effects of wave frequency on the reflection, four different values of wave frequency are considered in this paper, i.e., $f = 1$, 10, 100, and 1000 Hz. The four typical frequencies are within the common frequency range used in engineering and experimental testing [58]. The soil parameters remain invariable, as described in Section 5.1. The boundary is completely permeable. Figure 4 shows the variations of displacement

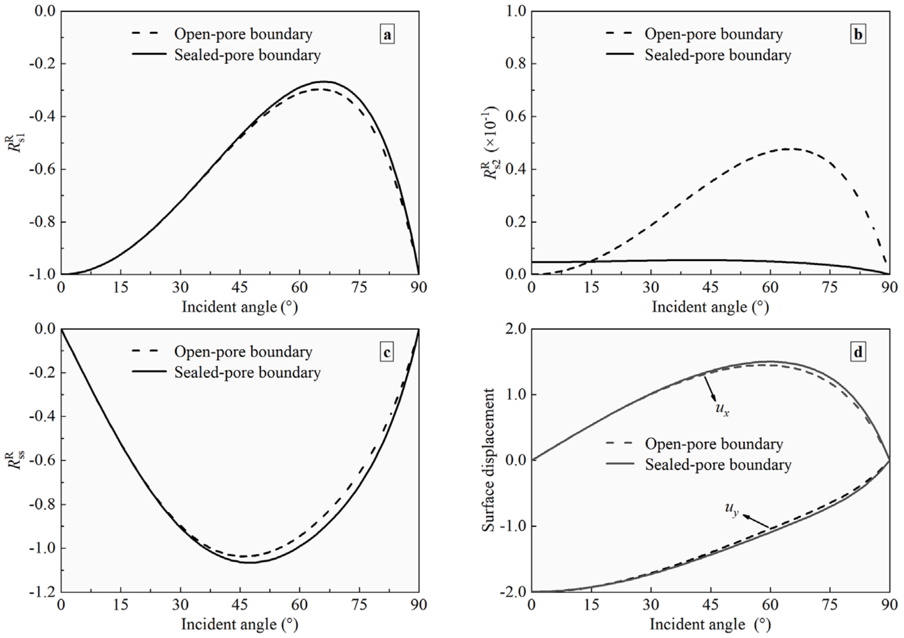

FIGURE 3
The displacement reflection coefficients and surface displacements versus incident angle with different permeable boundaries. **(a)** P_1-wave; **(b)** P_2-wave; **(c)** SV-wave; **(d)** Surface displacement.

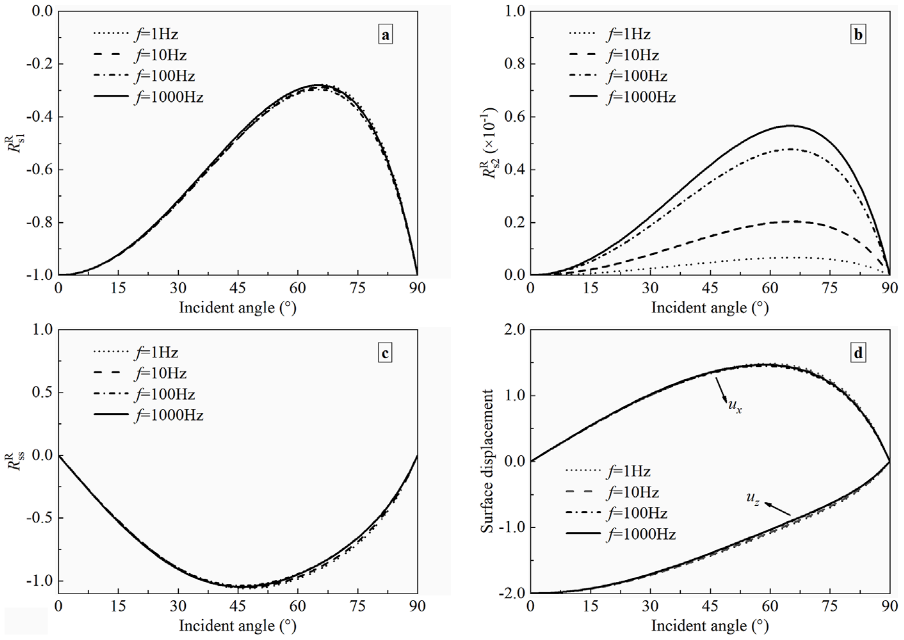

FIGURE 4
The displacement reflection coefficients and surface displacements versus incident angle with different frequencies. **(a)** P_1-wave; **(b)** P_2-wave; **(c)** SV-wave; **(d)** Surface displacement.

coefficients and surface displacements with the incident angle for different frequencies.

It is clear from Figure 4 that the surface response is not sensitive to wave frequency. However, the displacement reflection coefficient of P_2-wave decreases as the frequency is reduced. This result matches the case of Rjoub [21]. So, the frequency is assumed to be 100 Hz when analyzing the effect of soil parameters on surface response next.

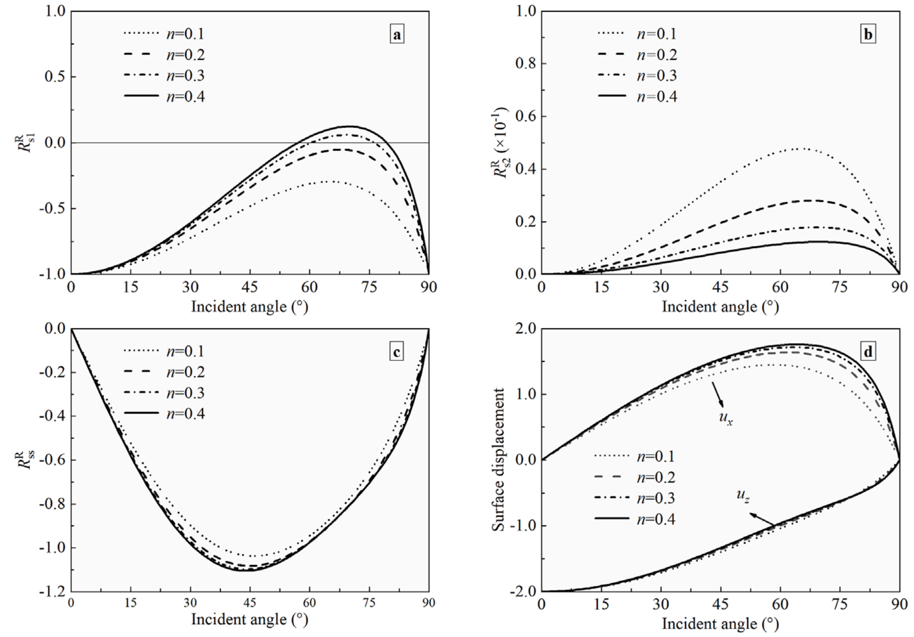

FIGURE 5
The displacement reflection coefficients and surface displacements versus incident angle with different porosities. **(a)** P_1-wave; **(b)** P_2-wave; **(c)** SV-wave; **(d)** Surface displacement.

5.3 Influence of porosity

Since porosity mainly affects the loose degree of soil, it is instructive to investigate the effect of porosity on the displacement reflection coefficients and surface displacements. Except for the porosity, the soil parameters remain invariable, as described in Section 5.1. The frequency of the incident plane P_1-wave is also taken to be 100 Hz. The boundary is completely permeable. The variations with the incident angle of displacement coefficients and surface displacements are shown in Figure 5 in the case that the porosity $n = 0.1$, 0.2, 0.3, and 0.4, respectively.

It is shown in Figure 5a that the variations of displacement reflection coefficient for reflected P_1-wave with porosity are very complex. When the porosity $n = 0.3$ and 0.4, a special wave mode conversion occurs, namely, only P_2-and SV- waves are reflected, and the reflected P_1-wave is not generated. Under the case that $n = 0.3$, the displacement reflection coefficient of P_1-wave exhibits zero values at incident angles of 60° and 77°. The angles for incidence corresponding to wave mode conversion are 57°and 79° with the instance that $n = 0.4$. If the porosity $n = 0.1$ and 0.2, this phenomenon disappears. Moreover, the displacement reflection coefficient for P_1-wave decreases with the increase of porosity when the incident angles $\theta_{\mathrm{IP}} < 57^\circ$or $\theta_{\mathrm{IP}} > 79^\circ$. From Figures 5b, c, the displacement reflection coefficient for SV-wave (P_2-wave) increases (decreases) with the increase in porosity, and that for P_2-wave is the smallest of all three reflected waves as described in Section 5.1. It is noticed from Figure 5d that the horizontal displacement u_x increases with a rise in porosity. However, the porosity considered in this study has little impact on vertical displacement u_z. The effect of porosity on the surface response depends on the incident angle to a large extent.

5.4 Influence of Poisson's ratio

The Poisson's ratio mainly affects Lame constants (λ and μ), which reflect the consolidation status of the soil. To investigate the effects of Poisson's ratio on the displacement reflection coefficients and surface displacements, the soil parameters remain constants as described in Section 5.1, except for Poisson's ratio. The frequency of the incident plane P_1-wave $f = 100$ Hz. The boundary is completely permeable. Figure 6 shows the effects of Poisson's ratio on the displacement reflection coefficients and surface displacements. In calculations, the Poisson's ratio (υ) is taken to be 0.1, 0.2, 0.3, and 0.4.

It can be found from Figures 6a–c that the displacement reflection coefficient of P_1-wave increases with the increasing Poisson's ratio at the same incident angle, while those of P_2- and SV-waves diminish with a rise of Poisson's ratio. For all three reflected waves, the amplitude of variation is related to the incident angle. As observed in Figure 6d, the horizontal displacement u_x (the vertical displacement u_z) decreases (increases) with the rise of Poisson's ratio. When the Poisson's ratio increases, the variation range of horizontal displacement is larger than that of vertical displacement, and the variation range depends on the incident angle.

5.5 Influence of modulus ratio

The modulus ratio mainly affects the stiffness of the soil layer in the saturated half-space. The larger the modulus ratio is, the softer the soil layer is. For this reason, there is a need to study the effects of the modulus ratio on the displacement reflection coefficients and surface displacements. Except for the modulus ratio, the soil parameters are taken according to Section 5.1. The

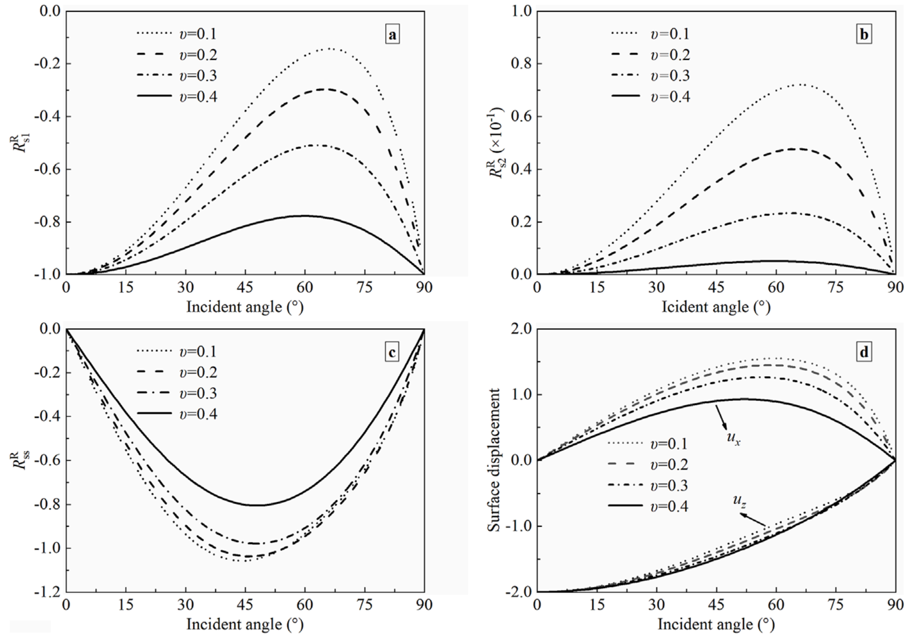

FIGURE 6
The displacement reflection coefficients and surface displacements versus incident angle with different Poisson's ratios **(a)** P_1-wave; **(b)** P_2-wave; **(c)** SV-wave; **(d)** Surface displacement.

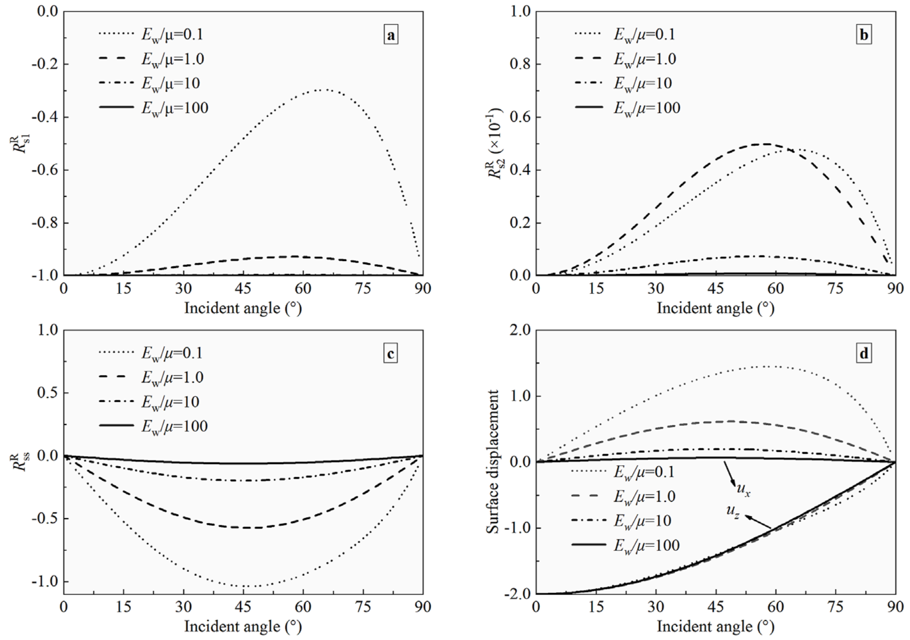

FIGURE 7
The displacement reflection coefficients and surface displacements versus incident angles with different modulus ratios **(a)** P_1-wave; **(b)** P_2-wave; **(c)** SV-wave; **(d)** Surface displacement.

frequency f of the incident plane P_1-wave is taken as 100 Hz. The boundary is completely permeable. The modulus ratio E_w/μ = 0.1, 1.0, 10, and 100. Figure 7 depicts the displacement reflection coefficients and surface displacements as a function of incident angle for the above four values of modulus ratio.

It can be revealed from Figure 7 that the displacement reflection coefficients and surface displacements vary with the modulus ratio. As can be seen from Figures 7a–c, the displacement reflection coefficient of P_1-wave (P_2- or SV-wave) increases (decreases) with the increasing modulus ratio at the same incident angle. The variation amplitude is related to the incident angle. Moreover, when the modulus ratio $E_w/\mu = 100$, the displacement reflection coefficient of P_1-wave increases towards −1.0, and that of SV-wave reduces to nearly 0, indicating that soft soil mainly transmits compression waves. All in all, the effect of incident angle on the reflection coefficients of P_2 and SV waves diminishes with the increase of the modulus ratio. Figure 7d shows us that the horizontal displacement u_x decreases with a rise in modulus ratio, while the vertical displacement u_z is less affected. For $E_w/\mu = 100$, the peak displacement u_x decreases to 0.063. The extent of influence is decided by the incident angle.

6 Conclusion

Based on the soil mechanics model in a fluid-saturated medium, the dispersion equation of elastic waves is established. When the P_1-wave travels toward the free ground of a two-phase medium, the theoretical formulas of displacement reflection coefficient and surface displacement for all reflected waves are also obtained by combining the boundary conditions. Thereafter, the analytical expressions mentioned above degenerate to the reflection problem of a single-phase half-space to verify correctness. At last, when the boundary conditions, wave frequency, porosity, Poisson's ratio, and modulus ratio are taken to be different values, the variation of the surface response of saturated half-space with the incident angle of P_1-wave is numerically analyzed. In light of the previous discussion, some main conclusions can be summarized as follows.

(1) The displacement reflection coefficient and surface displacement are angle-dependent. When the incident angle θ_{IP} equals 0°or 90°, only reflected P_1-wave occurs.
(2) The boundary conditions have a certain effect on the surface response of half-space. The surface displacements in the impermeable interface are slightly larger than those in the permeable interface, and the magnitude of the increase is related to the incident angle.
(3) For all frequencies being considered, its influence on surface response is insignificant.
(4) The effect of material properties (i.e., porosity, Poisson's ratio, and modulus ratio) on the surface response is discussed in detail. The wave mode conversion will occur when the porosity $n = 0.3, 0.4$. The displacement component u_x (u_z) decreases (increases) with a rise in Poisson's ratio. The effect of the modulus ratio can not be ignored. The impacts of all soil parameters strongly depend on the incident angle.

In addition, the conclusions drawn in this paper not only theoretically reveal that more attention should be paid to the influence exerted by the incident angle of elastic waves in soil dynamics research but also have practical engineering significance for the commonly used seismic reflection wave method and well-logging data processing in the field of engineering seismic exploration.

Data availability statement

The original contributions presented in the study are included in the article/supplementary material, further inquiries can be directed to the corresponding author.

Author contributions

BZ: Funding acquisition, Investigation, Methodology, Writing–original draft, Writing–review and editing. LQ: Project administration, Software, Supervision, Validation, Writing–review and editing.

Funding

The author(s) declare that financial support was received for the research and/or publication of this article. This research work was funded by the Science Research Project of Hebei Education Department, QN2025419, BZ.

Acknowledgments

The authors would like to thank the Science Research Project of Hebei Education Department (Grant No. QN2025419) for funding the work presented in this paper.

Conflict of interest

The authors declare that the research was conducted in the absence of any commercial or financial relationships that could be construed as a potential conflict of interest.

Generative AI statement

The author(s) declare that no Generative AI was used in the creation of this manuscript.

Publisher's note

References

1. Wu S. *Wave propagation in soils*. Beijing: Science Press (1997). p. 62–89.

2. Yang J, Wu S, Cai Y. Characteristics of propagation of elastic waves in saturated soils. *J Vib Eng* (1996)(02) 128–37.doi:10.16385/j.cnki.issn.1004-4523.1996.02.011

3. Biot MA. Theory of propagation of elastic waves in a fluid-saturated porous solid. I. Low-frequency range. *J Acoust Soc Am* (1956) 28(2):168–78. doi:10.1121/1.1908239

4. Biot MA. Theory of propagation of elastic waves in a fluid-saturated porous solid: II. Higher frequency range. *J Acoust Soc Am* (1956) 28(2):179–91. doi:10.1121/1.1908241

5. Plona TJ. Observation of a second bulk compressional wave in a porous medium at ultrasonic frequencies. *Appl Phys Lett* (1980) 36:259–61. doi:10.1063/1.91445

6. Berryman JG. Confirmation of Biot's theory. *Appl Phys Lett* (1980) 37:382–4. doi:10.1063/1.91951

7. Zienkiewicz OC, Chang CT, Bettess P. Drained, undrained, consolidating and dynamic behaviour assumptions in soils. *Geotechnique* (1980) 30(4):385–95. doi:10.1680/geot.1980.30.4.385

8. Zienkiewicz OC, Shiomi T. Dynamic behaviour of saturated porous media; the generalized Biot formulation and its numerical solution. *Int J Numer Anal Met* (1984) 8(1):71–96. doi:10.1002/nag.1610080106

9. Men F. Wave propagation in a porous, saturated elastic medium. *Acta Geophys Sinica* (1965) 14(02):107–14. (in Chinese).

10. Men F. Problems of wave propagation in porous fluid-saturated media. *Acta Geophys Sinica* (1981) 24(01):65–76. (in Chinese).

11. Men F. Dissipation and dispersion of seismic waves in water-saturated strata. *Acta Geophys Sinica* (1984) 27(1):64–73. (in Chinese).

12. Men F. On wave propagation in fluid-saturated porous media. *Conf Soil Dyn Earthquake Eng* (1982)(1) 225–38.

13. Bowen RM, Reinicke KM. Plane progressive waves in a binary mixture of linear elastic materials. *J Appl Mech* (1978) 45(3):493–9. doi:10.1115/1.3424351

14. Chen S, Liao Z. Study on mechanic models of two-phase media. *Earthquake Eng Eng Vibration* (2002) 22(04):1–8. doi:10.13197/j.eeev.2002.04.001

15. Deresiewicz H. The effect of boundaries on wave propagation in a liquid-filled porous solid: I. Reflection of plane waves at a free plane boundary (non-dissipative case). *B Seismol Soc Am* (1960) 50(4):599–607. doi:10.1785/BSSA0500040599

16. Deresiewicz H, Rice JT. The effect of boundaries on wave propagation in a liquid-filled porous solid: III. Reflection of plane waves at a free plane boundary (general case). *B Seismol Soc Am* (1962) 52(3):595–625. doi:10.1785/BSSA0520030595

17. Xu C, Wu S, Cai Y, Chen Y. Wave reflection at the plane interface of saturated soil. *Explo Shock Waves* (1998)(01) 9–15. (in Chinese).

18. Lin CH, Lee VW, Trifunac MD. On the reflection of elastic waves in a poroelastic half-space saturated with non-viscous fluid. In: *Department of civil engineering*. Los Angeles, CA: University of Southern California (2001). Report No. CE01-04.

19. Lin CH. *Wave propagation in a poroelastic half-space saturated with inviscid fluid [dissertation thesis]*. Los Angeles: University of Southern California (2002).

20. Lin CH, Lee VW, Trifunac MD. The reflection of plane waves in a poroelastic half-space saturated with inviscid fluid. *Soil Dyn Earthq Eng* (2005) 25(3):205–23. doi:10.1016/j.soildyn.2004.10.009

21. Al Rjoub YS. The reflection of P-waves in a poroelastic half-space saturated with viscous fluid. *Soil Dyn Earthq Eng* (2013) 49:218–30. doi:10.1016/j.soildyn.2013.02.016

22. Al Rjoub YS. The Reflection of SV-waves in a poroelastic half-space saturated with viscous fluid. In: *13th international conference*. Italy, Pisa (2013). doi:10.1016/j.soildyn.2013.07.001

23. Tajuddin M, Hussaini S. Reflection of plane waves at boundaries of a liquid filled poroelastic half-space. *J Appl Geophys* (2005) 58(1):59–86. doi:10.1016/j.jappgeo.2005.04.003

24. Xia T, Chen L, Wu S. Characteristics of Rayleigh waves in a saturated half-space soil. *J Hydraul Eng* (1998)(02) 48–54. (in Chinese).

25. You H. *Elastic wave scattering by a canyon or tunnel in layered saturated half space [dissertation thesis]*. Tianjin: Tianjin University (2005).

26. Nie W, Xu X. The wave fields solution of half space saturated porous medium when incident P, SV waves. *Site Invest Sci Tech* (2007)(02) 18–20+53. doi:10.3969/j.issn.1001-3946.2007.02.005

27. Yang J. Saturation effects of soils on ground motion at free surface due to incident SV waves. *J Eng Mech* (2002) 128(12):1295–303. doi:10.1061/(ASCE)0733-9399(2002)128:12(1295)

28. Chen J. *Wave propagation in unsaturated and partially saturated soils [dissertation thesis]*. Shanghai: Tongji University (2000).

29. Zhou X. *Study on wave characteristic and dynamic response of partially saturated soils [dissertation thesis]*. Hangzhou: Zhejiang University (2006).

30. Xue S, Chen S, Chen R, Sun X, Wang Y. Analysis on wave mode conversion of incident P_1 wave in nearly saturated soil. *Chin Quart Mech.* (2005)(01) 128–33. doi:10.3969/j.issn.0254-0053.2005.01.019

31. Kumar R, Kumar S, Miglani A. Reflection and transmission of plane waves between two different fluid-saturated porous half-spaces. *J Appl Mech Tech Ph* (2011) 52:773–82. doi:10.1134/S0021894411050129

32. Singh P, Chattopadhyay A, Srivastava A, Singh AK. Reflection and transmission of P-waves in an intermediate layer lying between two semi-infinite media. *Pure Appl Geophys* (2018) 75(12):4305–19. doi:10.1007/s00024-018-1896-8

33. Zhou D, Yin X, Zong Z. The characteristics of reflection and transmission coefficients of porous medium saturated with an ideal fluid. *Ann Geophys-italy* (2019) 62(5). doi:10.4401/ag-7815

34. Wang E, Carcione José M, Ba J, Liu Y. Reflection and transmission of plane elastic waves at an interface between two double-porosity media: effect of local fluid flow. *Surv Geophys* (2020) 41(2):283–322. doi:10.1007/s10712-019-09572-6

35. Kumar M, Singh A, Kumari M, Barak MS. Reflection and refraction of elastic waves at the interface of an elastic solid and partially saturated soils. *Acta Mech* (2020) 232:33–55. doi:10.1007/s00707-020-02819-z

36. Kumari M, Barak M, Singh A, Kumar M. Effect of various physical properties on the reflection coefficients of inhomogeneous waves at the stress-free surface of partially saturated soils induced by obliquely incident fast P-wave. *J Ocean Eng Sci* (2022) 7(3):225–36. doi:10.1016/j.joes.2021.08.003

37. Zhang J, Ma Q, Jiang H. Study on the transmission and reflection of P_1 wave at the interface between saturated soil and saturated frozen soil medium. *Rock Soil Mech* (2024) 45(10):3139–52. doi:10.16285/j.rsm.2023.1801

38. Kumar R, Deswal S. Wave propagation in micropolar liquid-saturated porous solid. *Indian J Pure Ap Mat* (2000) 31(10):1317–38.

39. Dai Z. *Research on wave propagation in double porosity media [dissertation thesis]*. Shanghai: Shanghai Jiaotong University (2006).

40. Chen W, Xia T, Huang R, Zhou X. Reflection characteristics of P_1 waves at the free boundary of unsaturated soil. *Eng Mech* (2013) 30(9):56–62. doi:10.6052/j.issn.1000-4750.2012.04.0269

41. Qiu H. *Research on propagation characteristics of elastic waves in Biot-type three-phase medium [dissertation thesis]*. Hangzhou: Zhejiang University (2019).

42. Awad E, Dai W, Sobolev S. Thermal oscillations and resonance in electron-phonon interaction process. *Z Angew Math Phys* (2024) 75(4):143. doi:10.1007/s00033-024-02277-w

43. Awad E. Modeling of anomalous thermal conduction in thermoelectric magnetohydrodynamics: Couette formulation with a multiphase pressure gradient. *Phys Fluids* (2024) 36(3). doi:10.1063/5.0190970

44. Chen S. *Numerical simulation for near-field wave motion in two-phase media [dissertation thesis]*. Harbin: China Earthquake Administration, Institute of Engineering Mechanics (2002).

45. Chen S, Liao Z, Chen J. A decoupling FEM for simulating near-field wave motions in two-phase media. *Chin J Geophys.* (2005) 48(4):909–17. doi:10.3321/j.issn:0001-5733.2005.04.025

46. Jing L, Zhuo X, Wang X. Effect of complex site on seismic wave propagation. *Earthq Eng Eng Vib* (2005) 25(6):16–23. doi:10.13197/j.eeev.2005.06.004

47. Jing L, Zhuo X, Wang X. The effect of complex media on seismic wave propagation. *Chin J Geotech Eng.* (2005) 27(4):393–7. doi:10.3321/j.issn:1000-4548.2005.04.006

48. Wang X. *Analysis on wave propagation in two-dimensional saturated media [master's thesis]. Harbin: China Earthquake Administration*. Institute of Engineering Mechanics (2003).

49. Xiao M, Cui J, Li Y, Jiang J, Shan Y, Duhee P. Propagation characteristics of Rayleigh waves and their influence on seabed dynamics in ocean sites. *J Hunan Univ (Natural Sciences)* (2023) 50(05):191–203. doi:10.16339/j.cnki.hdxbzkb.2023069

50. Zhang B, Chen X, Qiu L, Dong J, Zhou Z, Ji Z, et al. (2023). Characteristic of elastic wave propagation in fluid-saturated porous media based on the model of soil mechanics. *Pure Appl Geophys.* 180(6): 2309–26. doi:10.1007/s00024-023-03269-z

51. Cui J. *The wave propagation in saturated soil layer and sand liquefaction [dissertation thesis]. Harbin: China Earthquake Administration*. Institute of Engineering Mechanics (2002).

52. Chen W, Men F. Study on FEM to simulate slip and seismic liquefaction of slope-field by theory of two-phased dynamics. *Earthq Eng Eng Vib* (2002) 22(01):132–40. doi:10.13197/j.eeev.2002.01.023

53. Chen W. A direct differential method for nonlinear dynamic response of sand layer under water. *Rock Soil Mech* (2007) 28(s1):698–702. doi:10.16285/j.rsm.2007.s1.152

54. Li Y. *Analysis on nonlinear ground response in one dimension based on the theory of wave propagation in two-phase media [master's thesis]. Harbin: China Earthquake Administration*. Institute of Engineering Mechanics (2008).

55. Pujol J. Elastic wave propagation and generation in seismology. New York: Cambridge University Press. (2003).

56. Stein S, Wysession M. An introduction to seismology, earthquakes, and earth structure. Oxford: Blackwell Publishing (2003).

57. Deresiewicz H, Skalak R. On uniqueness in dynamic poroelasticity. *B Seismol Soc Am* (1963) 53(4):783–8. doi:10.1785/BSSA0530040783

58. Chen W, Xia T, Chen W, Zhai C. Propagation of plane P-waves at interface between elastic solid and unsaturated poroelastic medium. *Appl Math Mech* (2012) 33(7):829–44. doi:10.1007/s10483-012-1589-6

Appendix

Let $q_1 = \frac{1-n}{n} + \delta_1$ and $q_2 = \frac{1-n}{n} + \delta_2$, then the elements of $\{F\}$, $\{\overline{F}\}$, $[S_{\text{P-SV}}]_f$, and $[\overline{S}_{\text{P-SV}}]_f$ are shown as follows.

1. The amplitude coefficients of the incident P_1-wave

$$\{F\} = \left\{-(\lambda + q_1 E_{\text{w}})\left(k_1^{\text{I}}\right)^2 - 2\mu\left(k_{1z}^{\text{I}}\right)^2, 2\mu k_{1x}^{\text{I}} k_{1z}^{\text{I}}, -q_1 E_{\text{w}}\left(k_1^{\text{I}}\right)^2\right\}$$

$$\left\{\overline{F}\right\} = \left\{-(\lambda + q_1 E_{\text{w}})\left(k_1^{\text{I}}\right)^2 - 2\mu\left(k_{1z}^{\text{I}}\right)^2, 2\mu k_{1x}^{\text{I}} k_{1z}^{\text{I}}, (1-\delta_1) k_{1z}^{\text{I}}\right\}$$

2. The amplitude coefficients of all the reflected waves

$$[S_{\text{P-SV}}]_f = \begin{bmatrix} d_{11} & d_{12} & d_{13} \\ d_{21} & d_{22} & d_{23} \\ d_{31} & d_{32} & d_{33} \end{bmatrix}, \left[\overline{S}_{\text{P-SV}}\right]_f = \begin{bmatrix} d_{11} & d_{12} & d_{13} \\ d_{21} & d_{22} & d_{23} \\ \overline{d}_{31} & \overline{d}_{32} & \overline{d}_{33} \end{bmatrix};$$

$$d_{11} = (\lambda + q_1 E_w)\left(k_1^{\text{I}}\right)^2 + 2\mu\left(k_{1z}^{\text{I}}\right)^2, d_{12} = (\lambda + q_2 E_w)\left(k_2^{\text{R}}\right)^2 + 2\mu\left(k_{2z}^{\text{R}}\right)^2, d_{13} = 2\mu k_{\text{s}x}^{\text{R}} k_{\text{s}z}^{\text{R}};$$

$$d_{21} = 2\mu k_{1x}^{\text{I}} k_{1z}^{\text{I}}, d_{22} = 2\mu k_{2x}^{\text{R}} k_{2z}^{\text{R}}, d_{23} = \mu\left(\left(k_{\text{s}x}^{\text{R}}\right)^2 - \left(k_{\text{s}z}^{\text{R}}\right)^2\right);$$

$$d_{31} = q_1 E_w\left(k_1^{\text{I}}\right)^2, d_{32} = q_2 E_w\left(k_2^{\text{R}}\right)^2, d_{33} = 0;$$

$$\overline{d}_{31} = (1-\delta_1) k_{1z}^{\text{I}}, \overline{d}_{32} = (1-\delta_2) k_{2z}^{\text{R}}, \overline{d}_{33} = (1-\delta_{\text{s}}) k_{\text{s}x}^{\text{R}}.$$

Nomenclature

Symbols:

E_w	bulk modulus of pore water (unit: Pa)
K	permeability coefficient (unit: m/s)
k	dynamic permeability coefficient (unit: $m^3.s/kg$)
n	porosity
v	Poisson's ratio
λ, μ	Lame's constants of solid phase (unit: Pa)
E	elastic modulus of the solid phase (unit: Pa)
ρ_w	pore fluid mass density (unit: Kg/m^3)
ρ_s	solid mass density (unit: Kg/m^3)
ρ	total density (unit: Kg/m^3)
p_f	true pore pressure (unit: Pa)
ω	angular frequency
$\mathbf{u}, \dot{\mathbf{u}}, \ddot{\mathbf{u}}$	displacement, velocity, and acceleration vectors of the solid phase (unit: m, m/s, m/s^2)
$\mathbf{U}, \dot{\mathbf{U}}, \ddot{\mathbf{U}}$	displacement, velocity, and acceleration vectors of fluid phase (unit: m, m/s, m/s^2)
ϕ_s, ψ_s	potential functions associated with solid phase
ϕ_w, ψ_w	potential functions associated with pore fluid.

frontiers | Frontiers in Physics

TYPE Original Research
PUBLISHED 05 June 2025
DOI 10.3389/fphy.2025.1510629

OPEN ACCESS

EDITED BY
Elena Atroshchenko,
University of New South Wales, Australia

REVIEWED BY
Ali Mehri,
Babol Noshirvani University of Technology, Iran
Mohamed S. Abdalzaher,
National Research Institute of Astronomy and Geophysics, Egypt

*CORRESPONDENCE
Zhaoyang Yan,
✉ 916056875@qq.com

RECEIVED 13 October 2024
ACCEPTED 28 April 2025
PUBLISHED 05 June 2025

CITATION
Wang C, Zhang X, Gao W, Wang F, Lu J and Yan Z (2025) Accurate earthquake and mining tremor identification via a CEEMDAN-LSTM framework.
Front. Phys. 13:1510629.
doi: 10.3389/fphy.2025.1510629

Accurate earthquake and mining tremor identification via a CEEMDAN-LSTM framework

Chao Wang[1], Xiufeng Zhang[1], Weiming Gao[1], Fangfang Wang[1], Jianqi Lu[2,3] and Zhaoyang Yan[2,3]*

[1]Yankuang Energy Group Company Limited, Zoucheng, Shandong, China, [2]Key Laboratory of Earthquake Engineering and Engineering Vibration, Institute of Engineering Mechanics, China Earthquake Administration, Harbin, Heilongjiang, China, [3]Key Laboratory of Earthquake Disaster Mitigation, Ministry of Emergency Management, Harbin, Heilongjiang, China

The accurate identification of mining tremors and earthquakes is important for establishing a comprehensive mining tremor catalog that can aid in providing regulatory oversight for mining activities. Moreover, using a catalog purely consisting of earthquakes allows for more advanced seismological studies, such as active fault delineation, strong earthquake prediction, and stress field calculations, to be conducted. We focus on the spectral characteristics of mining tremors and earthquakes. By identifying short-period surface waves in the given data and utilizing an improved complete ensemble empirical mode decomposition method with adaptive noise (CEEMDAN) in combination with long short-term memory (LSTM) networks, we conduct a discriminative analysis of seismic events in Liaoning, China, and Japan. After completing basic preprocessing steps for both mining tremors and earthquakes, CEEMDAN is used to decompose the data into different intrinsic mode functions (IMFs). The variance contribution rates of the IMFs are extracted as features, which distinctly identify the short-period surface wave components of mining tremors. These features are subsequently input into an LSTM model for classification training, resulting in an accurate classification model. The results demonstrate that CEEMDAN-LSTM effectively addresses the noise and short-period surface wave aliasing issues encountered within the modes, yielding significantly enhanced classification accuracy. The classification success rate has been significantly improved to 96.5%. Additionally, this study explores the advantages and limitations of various classification features and models, providing effective technical support and new perspectives for the automatic identification of seismic events in the future. This research provides not only an understanding of the characteristics of mining tremors and earthquakes but also a scientific basis for earthquake early warning and disaster prevention. This study suggests that future research can further optimize the model in terms of speed and apply the model to classify more nonnatural seismic events.

KEYWORDS

mining tremor, complete ensemble empirical mode decomposition with adaptive noise, earthquake early warning, long short-term memory, wave identification

1 Introduction

Mining tremors refer to earthquakes caused by geological structural changes resulting from mining activities such as blasting and collapses in mines. Mining tremors typically occur in and around mining areas, especially during large-scale underground mining operations. On the one hand, using a pure earthquake catalog can facilitate in-depth seismological research, such as active fault delineation, strong earthquake prediction, and stress field calculations. On the other hand, owing to the potential threat of mining tremors to miner safety and the surrounding environment, a comprehensive catalog of mining tremors and other nonnatural seismic events also benefits regulatory activities in the mining sector. According to the current theories for identifying earthquakes and mining tremors, earthquakes are primarily tectonic earthquakes that occur when stress concentrations exceed the elastic limits of rocks, causing rock fractures and displacements, with the initial P-wave moving upward within a certain azimuth range and downward in other azimuths. In contrast, the seismic sources of most mining tremors mainly impose tension on external media, generating expansive waves, which are characterized by downward vertical initial P-waves [1]. There are many differences in geophysics between natural earthquakes and mining tremors collapses. Natural earthquakes are caused by crustal plate movements and other factors. Their seismic wave spectra are wide, with well-developed surface waves. The hypocenters are deep, and the seismic source mechanisms are related to plate interactions. The seismic activity has periodicity, and the changes in the geophysical field cover a wide range. In contrast, mine-induced seismic collapses are triggered by the failure and collapse of rock masses caused by mining activities. Their seismic wave spectra are narrow with prominent high frequencies, and the hypocenters are shallow. The seismic source mechanisms are related to the changes in stress of the goaf and rock masses. Their seismic activities are related to the mining process, and the changes in the geophysical field are concentrated in the local area of the mining area, with a relatively small range and amplitude [1].

Sha et al. [2] classified earthquakes and mining tremors based on time-domain features such as the direction of the initial P-wave, the development trends of surface waves, and the P/S wave amplitude ratio. Feng et al. [1] classified earthquakes based on the direction of the initial P-wave and amplitude attenuation. Dong et al. [3] effectively distinguished mining explosions and microseismic events by selecting the energy, seismic moment, ratio of the longitudinal and transverse wave energies, corner frequency, and static stress drop as stable discrimination indicators. Zheng et al. [4] conducted a time-frequency analysis on mining tremor waveforms via the S-transform. These multiparameter combined analysis methods provide different research approaches and techniques for classifying earthquakes and mining tremors. However, these characteristic parameters are artificially designed through specific methods, and their definitions are relatively cumbersome, requiring various postprocessing methods, making rapid differentiation through computer programs impossible and indicating that signals cannot be automatically distinguished as earthquakes or mining tremors [5]. Therefore, more scholars have adopted short-period surface wave classification for earthquakes and mining tremors. Xuesong et al. [6] proposed that short-period surface waves are distinct features for distinguishing mining tremors from earthquakes. Bi et al. [7] used the Hilbert–Huang transform (HHT) to extract the maximum amplitude corresponding to the mode component period and the average cepstral value as effective features for distinguishing earthquakes and mining explosions, and Jinlong et al. [8] used the HHT in combination with ensemble empirical mode decomposition (EEMD) to extract surface waves and classify mining tremors and earthquakes in the Hegang region, reaching an accuracy rate of over 90%. However, the mode mixing problem encountered when EEMD is used for processing has not been effectively solved. When facing seismic and mining tremor waveforms in different regions, the frequency ranges of short-period surface waves and environmental noise partially overlap, leading to difficulty in terms of effectively separating surface waves during the decomposition process with EEMD, resulting in poorer classification effectiveness.

With the advancement of computer technology, artificial intelligence has been increasingly incorporated into earthquake event identification research. Ming et al. [9] applied convolutional neural networks (CNNs) to automatically classify and identify the aftershock waveforms of the Wenchuan earthquake in the Beijing-Tianjin-Hebei metropolitan region, achieving training and detection accuracies exceeding 95%. Mousavi et al. [10] implemented a precise method for extracting earthquake P-wave and S-wave phases via the earthquake transformer (EQ transformer). Zhu et al. [11] successively used support vector machines (SVMs) and deep CNNs (DCNNs) to accurately estimate earthquake magnitudes [12], Liu et al. [13] used a generative adversarial network (GAN) to classify microseismic events and noise, and Zhou et al. [14] used a CNN model (SW-CNN) to process waveforms from 2 s before to 5 s after the corresponding P-waves arrive to classify earthquakes, explosions, and mining tremors. Chen et al. [15] combined the K-means algorithm and a CNN to classify earthquake waveforms and demonstrated that the K-CNN model could accurately classify earthquake waveforms by analyzing synthetic microseismic data with different noise levels and microseismic field data applications. Abdalzaher et al. [16] developed a machine learning framework integrating XGBoost and other classifiers to discriminate between tectonic earthquakes and quarry blasts, achieving a classification accuracy of 97.21% based on spatio-magnitude features. In a subsequent study [17], the authors introduced the 2S1C1S model for real-time seismic intensity estimation using single-component seismogram data from the initial 2-s post-P-wave window, demonstrating 99.05% accuracy. Their most recent work [18] employed an optimized quadratic discriminant analysis (QDA) model to distinguish small-magnitude earthquakes ($M \leq 3$) from quarry blasts using eight waveform-derived features, yielding 99.4% classification accuracy. These methodologies demonstrate substantial improvements over conventional discriminative approaches, with performance metrics (R^2, F1-score, MCC) indicating robust generalization capabilities and practical utility for seismic hazard mitigation. Zhang et al. [19] employed EEMD and a CNN to classify earthquake signals, achieving classification results as high as 93.85%. The above studies have proven that the use of artificial intelligence methods for

---

Abbreviations: (CEEMDAN), complete ensemble empirical mode decomposition with adaptive noise; (LSTM), long short-term memory.

earthquake identification and detection can yield significantly improved efficiency.

In terms of microseismic event identification, Fan et al. [20] used wavelet scattering decomposition to identify microseismic signals in coal mines and noise. Chen et al. [21] proposed an improved method for identifying microseismic mine events through a combination of wavelet decomposition and an extreme learning machine (ELM), successfully distinguishing microseismic mine events from noise with a success rate of 91.1%. Qin et al. [22]used modal decomposition and deep learning methods to predict the evolution trends of microseismic events, demonstrating good predictive and generalization performance. Gu et al. [23] employed backpropagation (BP) networks to classify five types of microseismic signals acquired from rockburst mines, achieving a classification model accuracy rate of 88.3%. Li [24] proposed a method for extracting features and classifying microseismic mine signals on the basis of local mean decomposition (LMD) and pattern recognition, attaining a classification accuracy rate of 93.0%. These studies have validated the excellence of deep learning in terms of identifying seismic events and noise, highlighting the notion that starting the microseismic event identification process from the frequency domain can be a more efficient strategy. However, the current focus in microseismic event identification research mainly involves classifying noise and mining tremors, with fewer classification methods developed for distinguishing earthquakes from mining tremors.

Therefore, this study selects many records of mining tremors and seismic events to explore a more efficient short-period surface wave classification method and integrates it with artificial intelligence, proposing the complete ensemble empirical mode decomposition with adaptive noise-long short-term memory (CEEMDAN-LSTM) method. First, on the basis of the developmental characteristics of short-period surface waves, an improved version of the CEEMDAN method [25] is used to decompose the input data to obtain a series of intrinsic mode functions (IMFs), and the variance contribution rate of each IMF is extracted. By inputting the variance contribution rates into an LSTM network [26] for training, a corresponding classification model is obtained. Additionally, compared with directly inputting waveform data into traditional neural networks after analyzing the features extracted by CEEMDAN, this model is validated to have superior classification capabilities. Compared with traditional EEMD, the CEEMDAN-LSTM model solves the modal aliasing problem faced when utilizing low-frequency data and can accurately classify earthquakes and mining tremors, providing strong technical support for seismological research and practical applications.

2 Data

The observational data used in this study are obtained from stations in Liaoning Province, and some seismic data are obtained from Japan. The employed mining tremor data are all selected from Liaoning Province between 2013 and 2023, totaling 14,577 records with a magnitude range of 2-4, different epicentral distances, and source depths ranging from 4 to 50 km. The earthquake data were acquired from Liaoning Province between 2020 and 2023 and include 13,548 records. Additionally, data acquired from the K-NET of Japan between 2022 and 2023 are selected after performing screening, totaling 5,329 records with a magnitude range of 3-8, epicentral distances from 0 to 200 km, and source depths ranging from 4 to 120 km. The data from Liaoning are velocity records with a sampling frequency of 100 Hz, whereas the data from Japan are acceleration records with the same sampling frequency.

Before conducting data processing, the following steps are implemented for preprocessing [1]: baseline correction [2]; 0.3-Hz Butterworth high-pass filtering [3]; converting acceleration records into velocity records via integration [4]; extracting P-wave arrival times via the STA/LTA method [27] and selecting data from 1 s before to 100 s after a P-wave arrives as analysis samples; and [5] normalizing all the data to the same scale. Figure 1 illustrates the technical roadmap of this paper.

After the above processing steps, this study selects a total of 262 mining tremors, comprising 7,012 records, and 508 earthquakes, forming 8,610 records, including 3,281 from Liaoning and 5,329 from Japan. The earthquake epicenter distribution is shown in Figure 2. Figure 3 shows the station map, where the ratio of the training set to the test set is 8:2. These data are selected to ensure independence, with data concerning the same earthquake event obtained from different stations not simultaneously included in the test and training sets. Initially, earthquake event classification is performed on the test and training sets, followed by reading data from each station into the dataset. Figures 4a–c illustrates the epicentral distance distribution. In theory, the main goal of this study is to identify the components of short-period surface waves in waveform data, as their degree of attenuation during propagation is smaller than that of high-frequency waves. Therefore, the impact of attenuation on the ability to distinguish earthquakes from mining tremors is relatively minor. Figures 4d,e displays the magnitude distribution of the data. In contrast, the source mechanism of earthquakes is relatively complex, consisting of several small fractures that form the source, each with a certain process, and occur at greater depths.

3 Materials and methods

The research approach of this article is as follows. First, CEEMDAN is used to decompose the signals of earthquakes and mining tremors, the variance contribution rates of the decomposed IMFs are calculated, and then the features of each IMF are input into LSTM for learning and obtaining classification results.

3.1 Complete ensemble empirical mode decomposition with adaptive noise

For analyzing the spectral characteristics of a signal, the traditional fast Fourier transform (FFT) method is widely used. However, during the process of transferring a signal from the time domain to the frequency domain, temporal information is lost, making it impossible to accurately determine the appearance and disappearance moments of frequencies. To address this limitation, time-frequency analysis techniques, which can effectively track the spectrum changes over time, have been developed.

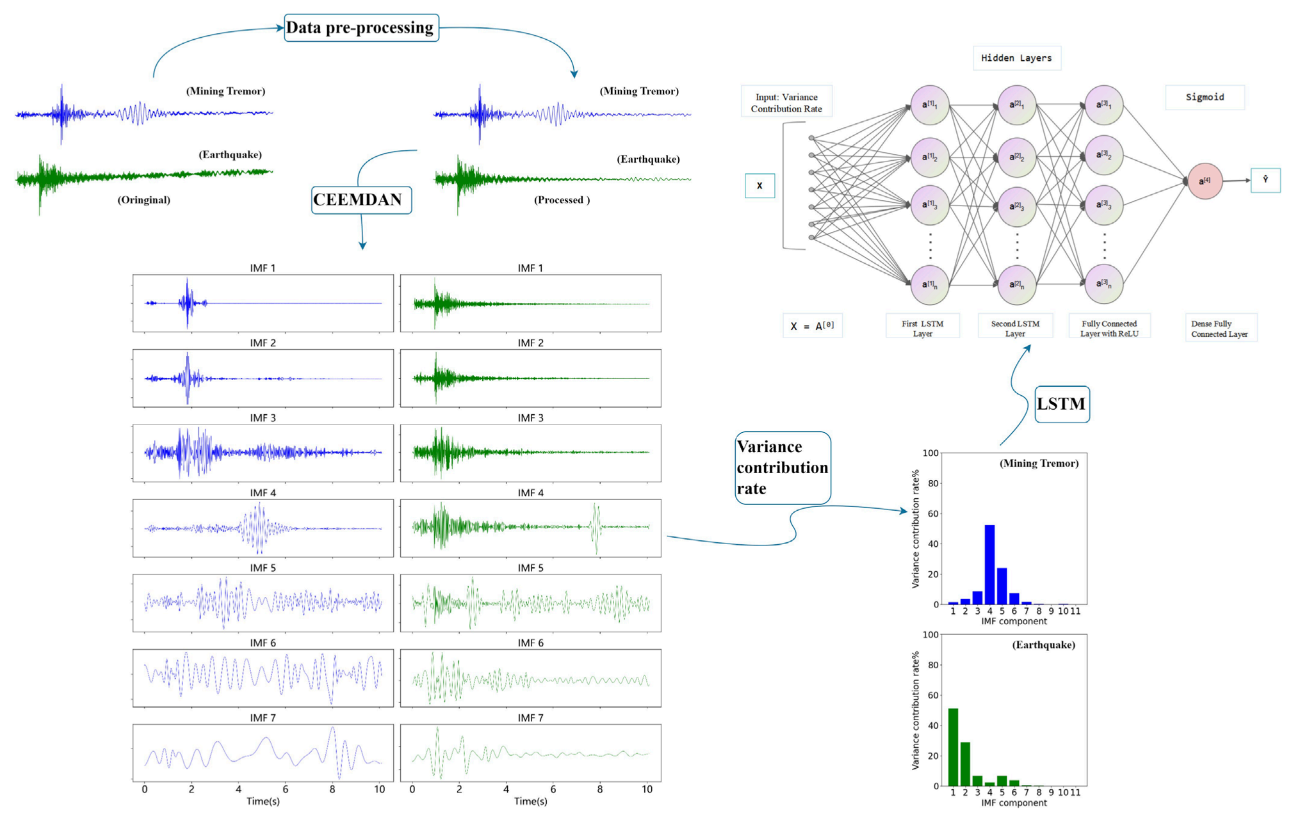

FIGURE 1
Figure shows the overall architecture flowchart of this paper, where blue represents mine earthquakes and green represents natural earthquakes.

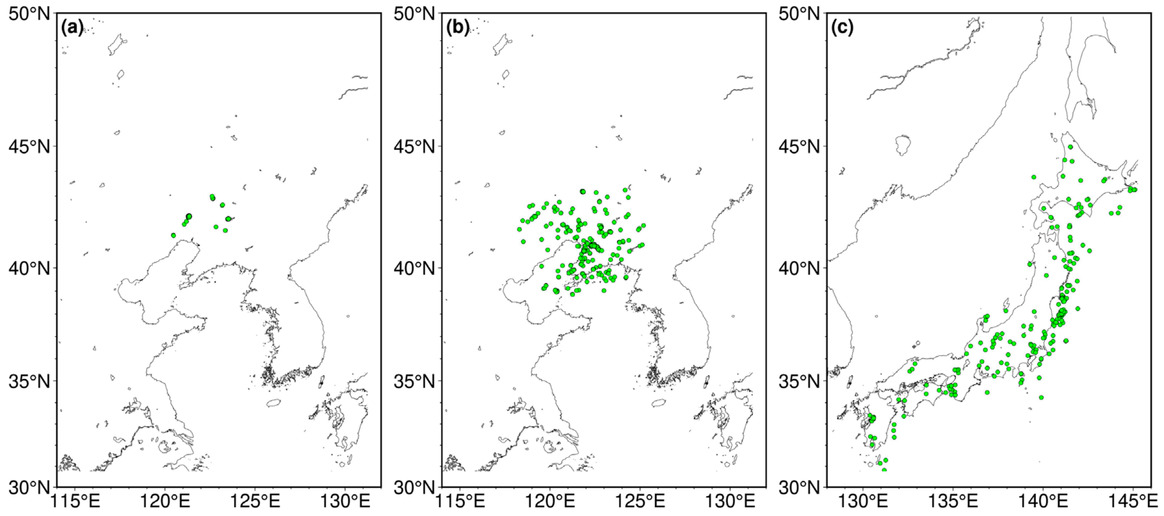

FIGURE 2
(a) Map of earthquake epicenters in Liaoning. **(b)** Map of mining tremor epicenters in Liaoning. **(c)** Map of earthquake epicenters monitored by the K-NET of Japan.

Common time-frequency analysis methods include the short-time Fourier transform (STFT), the Gabor transform, and the Wigner-Ville distribution, among others. Although these methods can theoretically handle nonlinear and nonstationary signals, limitations remain in practical applications. In contrast with the aforementioned traditional methods, the HHT completely eliminates the dependencies on linearity and stationarity, making it especially suitable for analyzing nonlinear and nonstationary signals

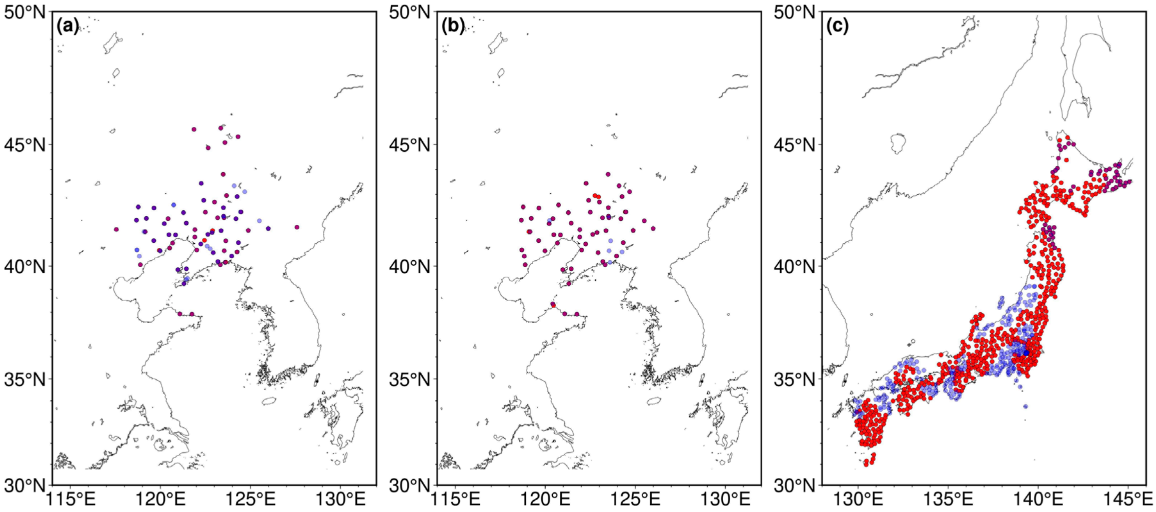

FIGURE 3
Schematic representation of the locations of seismic stations. Yellow indicates the training set, and blue indicates the validation set. **(a)** Locations of seismic stations in Liaoning. **(b)** Locations of mining tremor stations in Liaoning. **(c)** Locations of seismic stations in the K-NET of Japan.

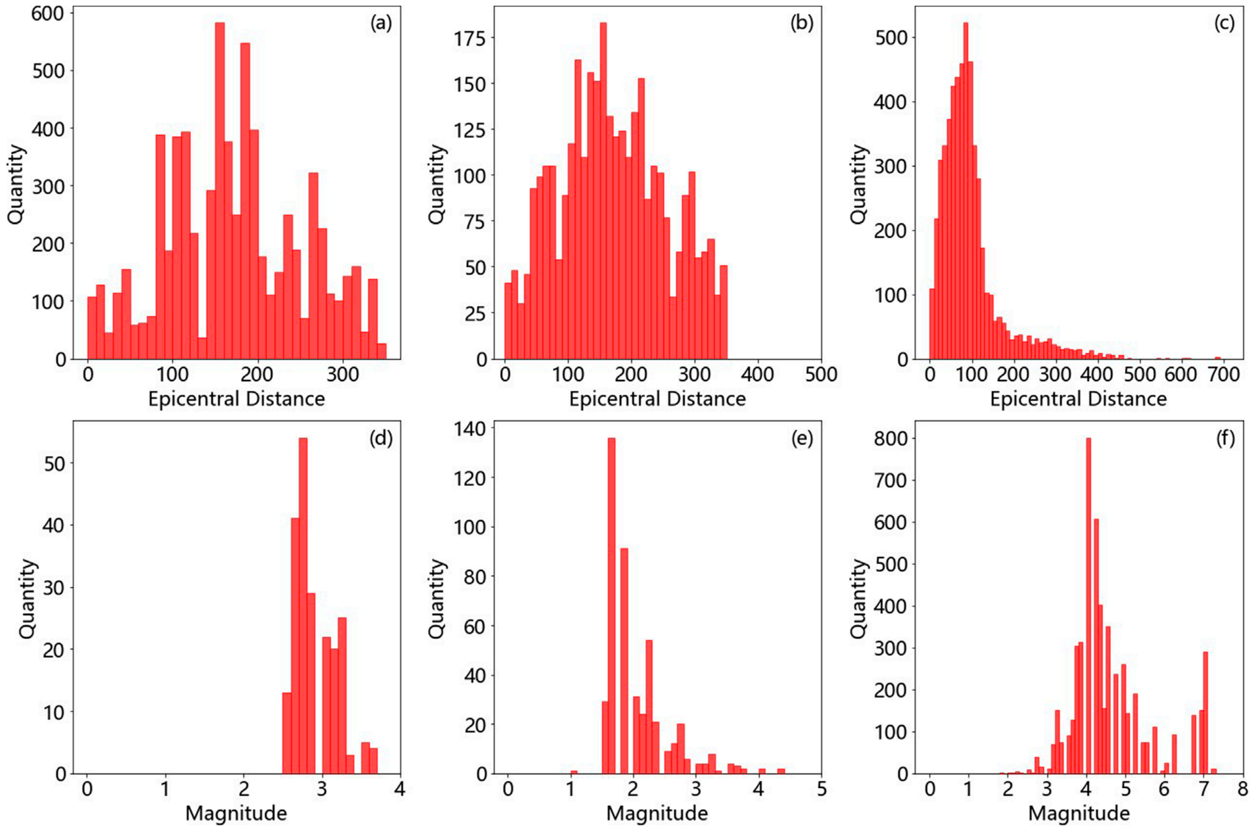

FIGURE 4
(a) Distribution of the epicentral distances for mining tremors in Liaoning. **(b)** Distribution of the epicentral distances for earthquakes in Liaoning. **(c)** Distribution of the epicentral distances for earthquakes in Japan. **(d)** Magnitude distribution of the hypocenters for mining tremors in Liaoning. **(e)** Magnitude distribution of the hypocenters for earthquakes in Liaoning. **(f)** Magnitude distribution of the hypocenters for earthquakes in Japan.

such as seismic waves. EEMD is an improved version of empirical mode decomposition (EMD) and is used to decompose nonlinear and nonstationary signals. EEMD enables the decomposition of a signal based on the given data themselves rather than predefined base functions. However, it still faces challenges such as mode mixing and incomplete mode decomposition. To address this issue, EEMD introduces a strategy of adding white noise at different time scales to compensate for potential frequency band losses. Nonetheless, in practical applications, especially when addressing signals with similar frequencies, mode mixing is still common.

To further improve upon EEMD, CEEMDAN was proposed. It is an advanced signal processing technique that is aimed at decomposing complex signals into simpler components known as IMFs. CEEMDAN inherits the basic principles of EMD and its EEMD variant and has been improved to overcome the mode mixing problem, providing a more robust decomposition method. Through this method, each step in the signal decomposition process becomes more precise, effectively reducing the degree of mode mixing and enhancing the reliability of the conducted analysis. The principle of this approach is as follows.

Given an original signal $x(t)$, N white noise sequences, $\{w_i(t)\}_{i=1}^{N}$ are added to generate N new signal sequences, as in Equation 1:

$$x_i(t) = x(t) + w_i(t), i = 1, 2, \ldots, N \tag{1}$$

For each noisy signal $x_i(t)$, the following steps are performed to extract the corresponding IMFs. First, all local maxima and minima are found, the local maxima are used to interpolate and form the upper envelope $e_{on}(t)$, and the local minima are used to interpolate and form the lower envelope $e_{low}(t)$. The means of the upper and lower envelopes are calculated to obtain $m(t)$, as in Equation 2:

$$m(t) = \frac{e_{low}(t) + e_{on}(t)}{2} \tag{2}$$

The mean envelope is subtracted from the signal to extract a detail $d(t)$, as in Equation 3:

$$d(t) = x(t) - m(t) \tag{3}$$

If $d(t)$ satisfies the conditions of an IMF, it is taken as an IMF; otherwise, $d(t)$ is used to replace $x(t)$, and the sifting process is repeated. After each IMF is extracted, the added noise level is adaptively adjusted based on the characteristics of the residual signal (the signal remaining after the IMFs are removed). This process is repeated on the residual signal using the adjusted noise levels to extract subsequent IMFs. For each IMF, the ensemble average is calculated from all iterations; i.e., the corresponding IMFs obtained from all noise-added versions of the original signal are averaged. This step can eliminate the added noise, leaving a more accurate representation of the intrinsic oscillatory mode. This process is repeated until the residual signal becomes a monotonic function, and no more IMFs can be extracted. The final set of IMFs and the residual represent the complete decomposition result of the original signal. Variance is defined as the mean of the squares minus the square of the mean, reflecting the proportion of signal energy contained in each mode. The variance contribution rate of each mode α_k [28] is given by Equation 4:

$$\alpha_k = \frac{\overline{x}_k^2 - (\overline{x}_k)^2}{\sum_{k=1}^{N} \left(\overline{x}_k^2 - (\overline{x}_k)^2\right)} \tag{4}$$

In this equation, k is the k-th mode, N is the total number of modes, and x_k is the amplitude of the seismic wave for the k-th mode.

3.2 Construction of the LSTM model

3.2.1 Overview of the LSTM model

Long short-term memory (LSTM), a specialized architecture of artificial neural networks (ANNs), addresses the limitations of traditional recurrent neural networks (RNNs) in handling long-range temporal dependencies by incorporating a memory cell regulated by three adaptive gates (input, forgetting, output). This innovation mitigates gradient vanishing/exploding issues inherent in standard RNNs, enabling precise control over information retention and forgetting [26]. Compared to feedforward neural networks (FNNs), LSTM's temporal memory mechanism and dynamic gating allow adaptive sequential processing critical for seismic signal analysis [29]. Recent studies demonstrate its efficacy in early earthquake warning systems, underground mining tremor classification, and real-time anomaly detection in sensor networks [30], highlighting its stability optimization and context-aware capabilities in geophysical applications. In a classic LSTM model, the update equations at step t are as follows (Equations 5–10):

$$i_t = \sigma\left(W_i x_t + U_i h_{t-1} + b_i\right) \tag{5}$$

$$f_t = \sigma\left(W_f x_t + U_f h_{t-1} + b_f\right) \tag{6}$$

$$o_t = \sigma\left(W_o x_t + U_o h_{t-1} + b_o\right) \tag{7}$$

$$\tilde{c}_t = \tanh\left(W_c x_t + U_c h_{t-1}\right) \tag{8}$$

$$c_t = f_t \odot c_{t-1} + i_t \odot \tilde{c}_t \tag{9}$$

$$h_t = o_t \odot \tanh\left(c_t\right) \tag{10}$$

In this equation, i_t is obtained through a linear transformation of the input x_t and the previous hidden layer output h_{t-1}, followed by an activation function σ. The result of the input gate i_t is a vector where each element is a real number between 0 and 1, which is used to control the amount of information flowing through the gate for each dimension. The matrices W_i and U_i, and the vector b_i are the parameters of the input gate, which are learned during training. The forgetting gate f_c and the output gate o_c are computed similarly, each with its own parameters W, U and b. Unlike traditional RNNs, in LSTM, the transition from the state of the previous memory cell c_{t-1} to the current state c_t is not solely determined by the state calculated from the activation function but also jointly controlled by the input gate and the forgetting gate.

In a trained network, LSTM has the ability to handle sequential data through its gating mechanism, thus achieving long-term memory functionality. Specifically, when the input sequence lacks critical information, the forgetting gate value of the LSTM model approaches 1, and the input gate value approaches 0, allowing past memories to be retained. Conversely, when important information appears in the input sequence, the input gate value increases to nearly one to store this information in the internal memory

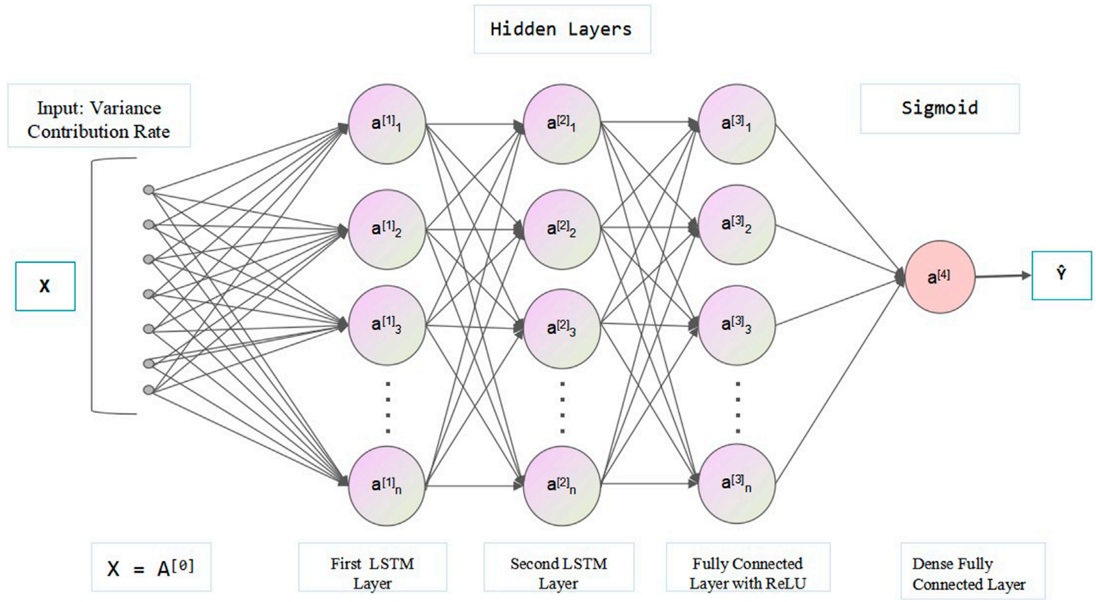

FIGURE 5
Structural diagram of an LSTM unit.

cell. Furthermore, when the important information in the input sequence indicates that the prior memory is no longer relevant, the input gate value increases to nearly 1, whereas the forgetting gate value decreases to nearly 0. This mechanism clears old memories and stores new key information. Figure 5 shows the structure of an LSTM unit.

3.2.2 Model architecture

In this study, we design a neural network architecture consisting of multiple layers specifically for handling binary classification problems. The input layer of the network receives sequential data with 11 time steps. This is followed by two LSTM layers, each containing 32 LSTM units, which can capture the long-term dependencies in time series. To reduce overfitting, three dropout layers are incorporated into the network, with dropout rates of 40% for the first two layers and an increased dropout rate of 40% for the final layer before the output layer. Additionally, the network includes a fully connected layer with 32 neurons, utilizing the rectified linear unit (ReLU) activation function to enhance the nonlinear expression capabilities of the model and applying L2 regularization to further mitigate the risk of overfitting. The final output layer is a fully connected layer that uses the sigmoid activation function to output probabilities for the two classes. The model was trained using the Adam optimizer and binary cross-entropy loss—specifically designed for binary classification tasks where outputs are probabilities between 0 and 1. A training-validation split of 8:2 was applied to ensure robust generalization to unseen data. The initial learning rate was set to 0.05—a value commonly adopted in deep learning practice [31]—and dynamically adjusted using a step scheduler that reduces the learning rate by a factor of 10 every 10 epochs. This strategy was implemented to balance rapid convergence during early training and parameter refinement in later stages, as supported by studies on optimization stability [32]. Using TensorFlow distributed training, LSTM model parameters are stored in fragments and multi-node parallel processing is used to reduce scaling effect when processing large-scale data This network architecture not only adapts to complex binary classification tasks but also effectively balances the learning ability and generalizability of the model.

4 Results

4.1 Decomposition results produced by CEEMDAN for earthquakes and mining tremors

In this study, both mining tremors and earthquake signals are decomposed into 11 IMFs, with these components arranged in frequency order from high to low across different time scales. Specifically, IMF1 represents the component with the highest frequency and the shortest wavelength. As the decomposition process progresses, the frequency decreases, and the wavelength increases for each subsequent IMF component until the final residual component is reached. For mining tremors, short-period surface wave components can typically be identified in the fourth or fifth IMF component, whereas these components are absent from the IMFs of earthquakes, highlighting a significant distinction between mining tremors and earthquakes. By selecting two typical records of mining tremors and earthquakes, the variance contribution rates of different IMF components are calculated after using CEEMDAN for decomposition purposes and presented as histograms. Figures 6a,b visually display the prominent IMF components and their growth trends for mining tremors and earthquakes, respectively. Additionally, Figure 6c, d show the average variance contribution rates of all mining tremor and earthquake records processed by CEEMDAN, respectively. The analysis results indicate that the energy is primarily concentrated in the initial IMFs for both mining tremors and earthquakes. However, for mining tremors, a significant variance contribution rate increase occurs around the fourth IMF component due to the presence of short-period surface waves, indicating a higher amplitude and suggesting that surface waves encompass a major portion of the signal energy. Figures 7, 8 illustrate the decomposed results obtained for mining tremor and earthquake signals, with part (a) representing the components of each IMF for which the presence and separation of surface waves can be observed, while part (b) displays the Fourier spectral analysis corresponding to each component, highlighting the dominant frequency distribution of each IMF component. The waveform characteristics of mining tremors and earthquakes exhibit noticeable differences in their time-frequency features. The frequency values of mining tremors are typically concentrated in the low-frequency range, indicating a shallow seismic source with developed surface waves and high energy in the low-frequency band. In contrast, the frequency values of earthquakes are distributed more widely in the time-frequency plot, with longer durations and slower decay processes. This distinction reflects the complexity of the seismic source mechanism for earthquakes, which comprises multiple small ruptures, each with a certain duration process, originating from deeper sources where seismic waves propagate through dense, hard rock formations, resulting in lower energy losses and higher-frequency components, leading to longer-lasting waveforms in the records.

4.2 Comparison between the EEMD and CEEMDAN methods

Compared with the other methods, CEEMDAN has the following advantages. First, it is more effective at reducing the degree of mode mixing, providing clearer and more accurate mode decomposition results. Second, by adaptively adjusting the level of noise added, CEEMDAN not only reduces its computational complexity but also improves its decomposition efficiency. Moreover, CEEMDAN better controls the impact of noise during the decomposition process, effectively reducing the false modes introduced by noise. Finally, the adaptive noise addition strategy of CEEMDAN provides greater flexibility and adaptability for handling different types of signals. Figures 9, 10 show that EEMD performs poorly in terms of data mode separation when the white noise level is low, typically only decomposing 1-2 IMFs and struggling to accurately identify surface waves. In contrast, even at low noise levels, CEEMDAN can clearly identify surface waves in the fifth IMF. When the white noise level is too high, the EEMD method is affected by the introduction of too many false modes due to noise, which impacts its ability to effectively calculate variance contribution rates. Additionally, owing to the inconsistent surface wave frequencies contained in seismic waveforms derived from different regions, the ability of EEMD to separate modes when handling data acquired from different regions varies, resulting in ineffective surface wave identification capabilities. In comparison, CEEMDAN, through its improved noise management scheme and adaptive algorithm, exhibits superior mode separation capabilities when handling a large amount of data obtained from different regions, demonstrating greater generality and adaptability.

4.3 LSTM results analysis

LSTM evaluates the input data via the following metrics: accuracy, which is the proportion of correctly predicted samples out of the total number of samples; the number of true positives (TP), which is the number of positive cases correctly predicted as positive; the number of true negatives (TN), which is the number of negative cases correctly predicted as negative; the number of false positives (FP), which is the number of negative cases incorrectly predicted as positive; and the number of false negatives (FN), which is the number of positive cases incorrectly predicted as negative, as Equation 11.

$$Accuracy = \frac{TP + TN}{TP + TN + FP + FN} \tag{11}$$

Loss: This is the difference between the values predicted by a model and the true values, which is usually represented as a numerical value. For this study, the binary cross-entropy loss is used. N is the number of samples. y_i is the true label of sample i. $\hat{y}_i$ is the predicted probability of sample i, as Equation 12.

$$Loss = -\frac{1}{N}\sum_{i=1}^{N}\left[y_i \log\left(\hat{y}_i\right) + \left(1 - y_i\right)\log\left(1 - \hat{y}_i\right)\right] \tag{12}$$

Precision: This is the proportion of correctly predicted positive samples out of all samples predicted as positive by the model. It is a metric that measures the accuracy of a model in terms of predicting positive cases, as Equation 13.

$$Precision = \frac{TP}{TP + FP} \tag{13}$$

Recall: This is the proportion of correctly predicted positive samples out of all actual positive samples. It measures the ability of a model to capture positive cases, as Equation 14.

$$Recall = \frac{TP}{TP + FN} \tag{14}$$

F1 Score: This is the harmonic mean of precision and recall, which is used to measure the balance between the precision and recall of a model. A higher F1 score indicates better model performance, as Equation 15.

$$F1 = 2 \times \frac{Precision \times Recall}{Precision + Recall} \tag{15}$$

After calculating the variance contribution rates of the IMFs decomposed by CEEMDAN, they are input into a three-layer LSTM model. The analysis results are shown in Table 1.

During training, the following parameters are selected. The batch size is 12, representing the number of data instances contained in each training batch; the number of epochs is 300, indicating the number of complete passes made by the training data through the neural network; and early stopping is implemented to halt the training process when the performance attained on the validation set does not improve in consecutive epochs or begins to decline. The accuracy function and loss function results are shown in Figures 11, 12. (A) shows the ROC curve, and (B) shows the confusion matrix.

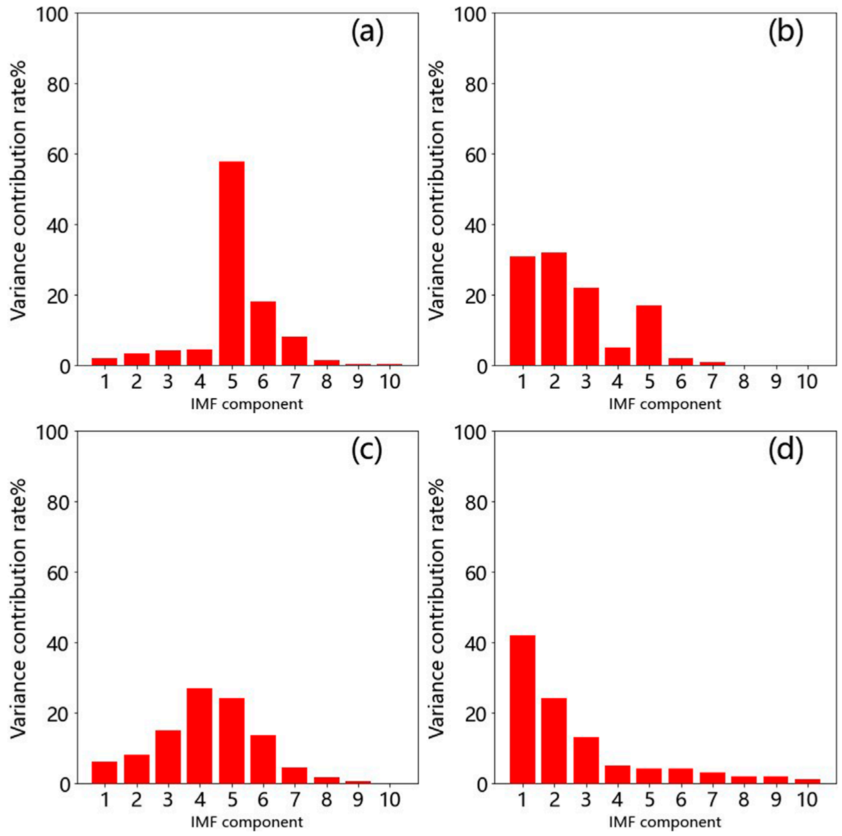

FIGURE 6
(a) Histogram of the variance contribution rates for mining tremors. **(b)** Histogram of the variance contribution rates for earthquakes. **(c)** Histogram of the average variance contribution rates for mining tremors. **(d)** Histogram of the average variance contribution rates for earthquakes.

4.4 Comparisons conducted under different data and different models

4.4.1 Comparison among the variance contribution rate inputs of different models

To compare the efficiency of LSTM in terms of classifying earthquakes and mining tremors via variance contribution rates, this study selects a CNN,ViT 2D model and an SVM as baseline methods. The variance contribution rates obtained from the CEEMDAN decomposition process are input into the CNN and SVM for comparison purposes. The ViT-2D (Vision Transformer) model is mainly composed of three parts: patch + position + cls embedding layer, Transformer encoder layer and MLP classification layer, full connection layer [-1,16,128], discard layer and Transformer layer [-1,16,128]. 17,128], identity mapping layer [-1, 128], normalization layer [-1, 128], full connection layer [-1,2]. A CNN is a deep learning algorithm that consists of convolutional layers, pooling layers, fully connected layers, etc., effectively extracting features from data; CNNs are widely used in image recognition and video analysis tasks. An SVM is a supervised learning model used for data classification and regression analysis. It distinguishes different data points by finding an optimal hyperplane. An SVM uses kernel techniques to handle linearly inseparable data and can maintain high accuracy in situations with small samples. The CNN utilizes a two-layer network + a fully connected layer, with 16, 32, and 64 neurons, a convolution kernel size of (2.1), a rate dropout set to 0.5, and an ReLU activation function. The SVM penalty parameter C is set to 0.5, and the employed kernel function is the polynomial kernel. As shown in Table 2 (validation set), LSTM has a significant advantage in terms of handling these data.

After 500 experiments, the 95% confidence interval of the model is (0.9583, 0.9717). Assuming the null hypothesis H_0: the true accuracy rate of this study $\pi = 0.9$ (here, 0.9 is referred to the literature of Shen Jie [30]), and the alternative hypothesis H_1: the true accuracy rate of this study $\pi \neq 0.9$. For a two-sided test, when the significance level $\alpha = 0.05$, the critical value $z = 1.96$. Since the calculated $z = 6.84 > 1.96$, we reject the null hypothesis H_0 and conclude that there is a significant difference between the accuracy rate of this study and the assumed benchmark accuracy rate of 0.9. That is to say, the accuracy rate of this study is statistically significantly higher than 0.9.

4.4.2 Comparison among LSTM and CNN models with different parameter inputs

To verify the superior identification capability of CEEMDAN, different data for identifying mining tremors are input into LSTM for identification purposes, including [1] waveform data from 1 s before and 3 s after the arrival time of a P-wave [2]; waveform data from 1 s before and 14 s after the arrival time of the P-wave [3]; the variance contribution rates of the IMFs decomposed via EEMD; and [4] the

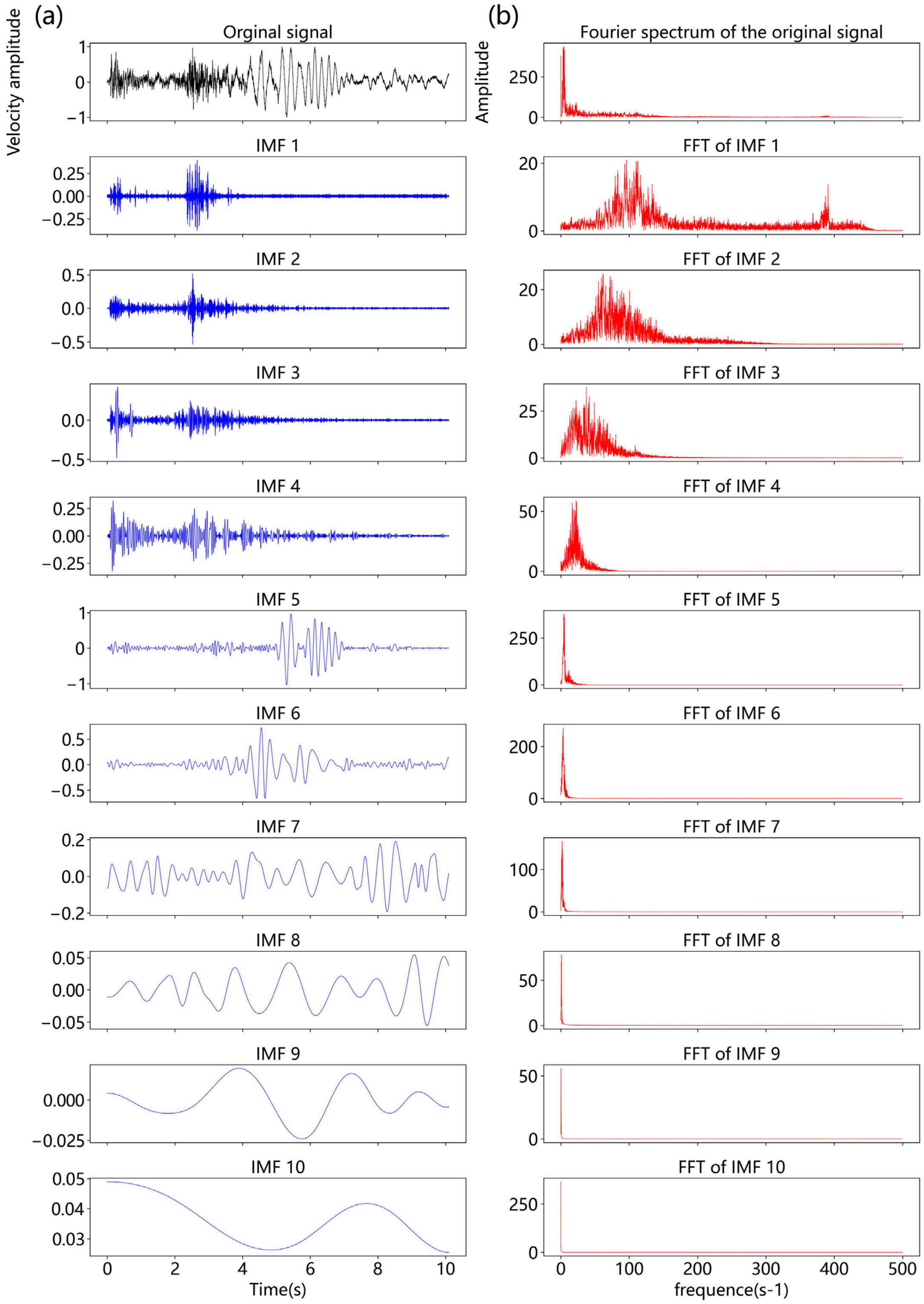

FIGURE 7
(a) Various IMF components of mining tremors and **(b)** their corresponding Fourier spectra.

dominant frequency. The model selection process is similar to that described above, with accuracy serving as the comparison indicator. The results, as shown in Table 3, indicate that the success rate achieved via CEEMDAN with LSTM is the highest. The accuracy rate of this study was 96.5%, which was higher than the accuracy rate of 91% for classification of natural earthquake and mine earthquake

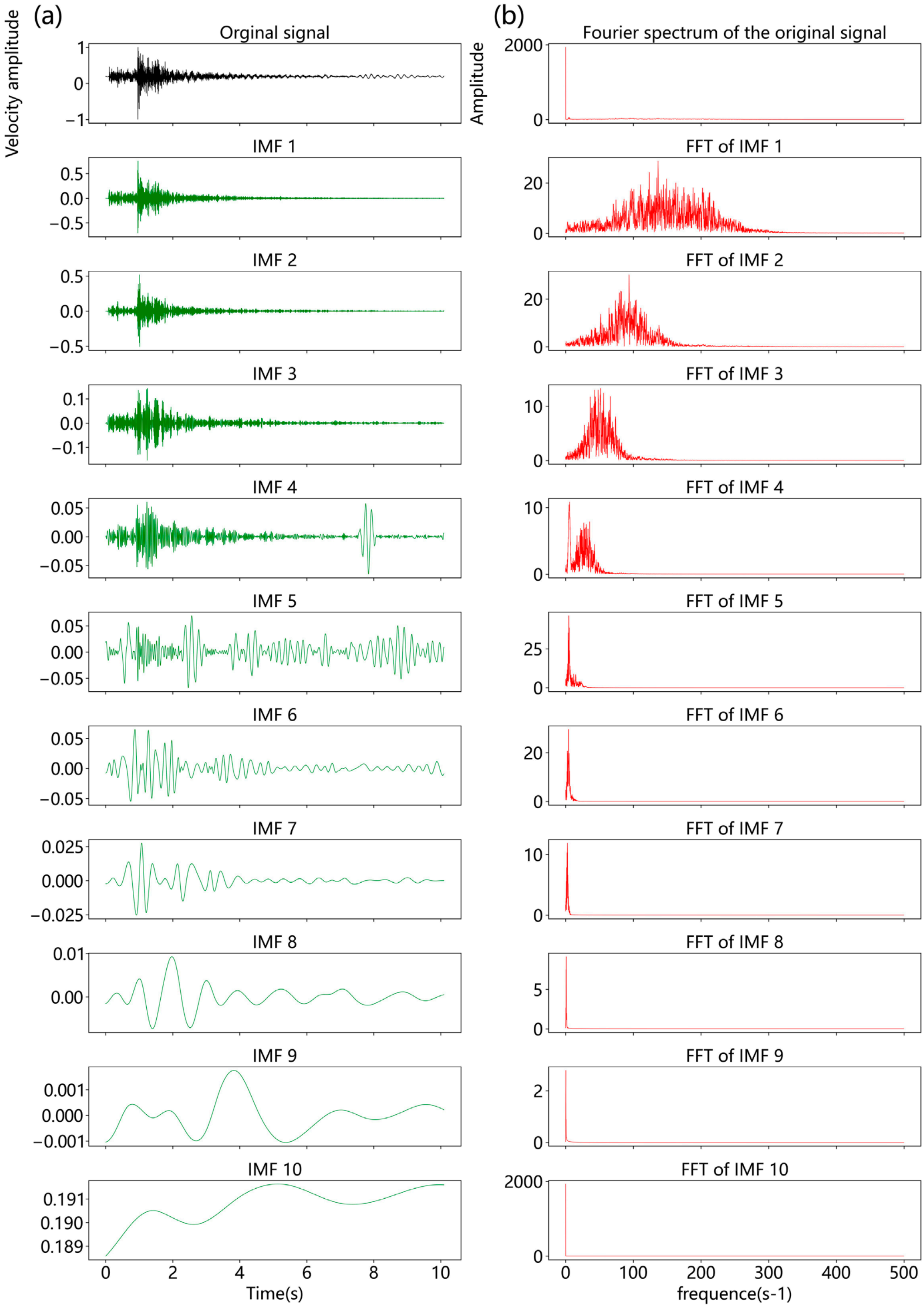

FIGURE 8
(a) Various IMF components of earthquakes and **(b)** their corresponding Fourier spectra.

based on ViT 2D model by Shen Jie [33]. Figure 13 shows the classification accuracy of different models with different inputs. From this, it can be clearly seen that ViT-2D can achieve an effect of 91.2% on the data from −1–3 s. However, this is based on the premise of more complete preprocessing of the data and the removal of noise. This step requires a large amount of manual intervention to remove the unavailable data. On the other hand, for the data screened by CEEMDAN features, since it acts on the short-period surface

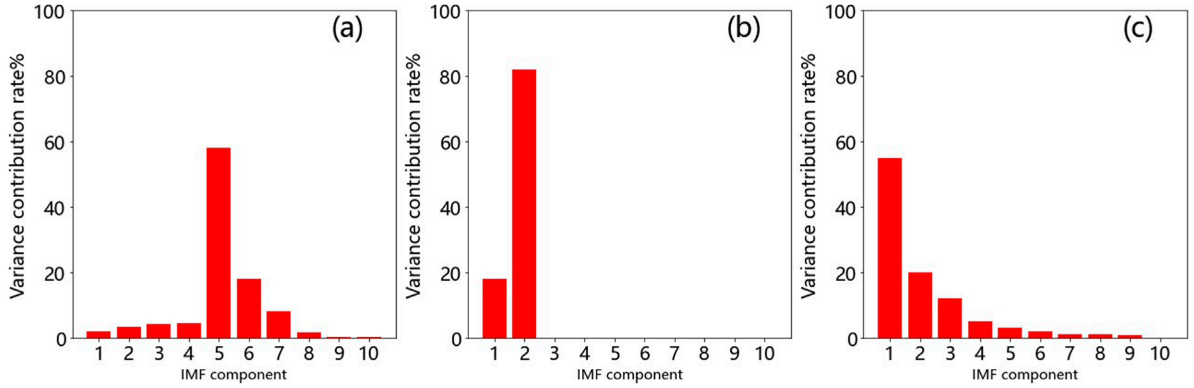

FIGURE 9
Mining tremors. **(a)** CEEMDAN decomposition diagram. **(b)** EEMD decomposition results produced with the noise level controlled at 0.01. **(c)** EEMD results produced with the noise level controlled at 0.5.

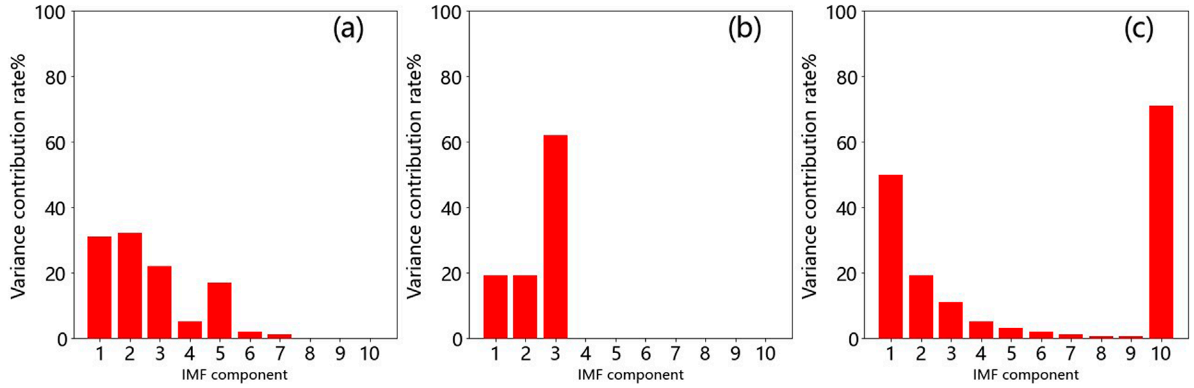

FIGURE 10
Earthquakes. **(a)** CEEMDAN decomposition diagram. **(b)** EEMD results produced with the noise level controlled at 0.01. **(c)** EEMD results produced with the noise level controlled at 0.5.

TABLE 1 Results obtained on the training and validation sets with LSTM.

Metrics	Training set	Validation set
Accuracy	96.1%	96.5%
Loss	13.1%	11.0%
Precision	96.1%	98.2%
Recall	97.1%	99.3%
F1 Score	97.1%	N/A

waves for identifying mining tremors, after actual measurement, only simple preprocessing such as baseline calibration and filtering of the original data is needed to complete the identification of mining tremors, and it can also actively remove the unavailable data. In this regard, LSTM has more advantages. The reason is that LSTM has better advantages in exploring the general temporal sequence problems (that is, there is a causal relationship in the development of the sequence), and the variance contribution rates of IMFs are sequences with distinct causal relationships between the preceding and the following. The CEEMDAN-LSTM method has a better prospect for real-time monitoring and classification.

5 Conclusion and discussion

5.1 Conclusion

This study selected recorded data from different mining tremors and earthquakes that occurred in the Liaoning region and applied the CEEMDAN-LSTM method to classify these events, achieving a high success rate. The following conclusions were drawn from the research.

Previous studies have provided numerous criteria for distinguishing between mining tremors and earthquakes, including the initial directions of P-waves and the dominant frequency. Utilizing only the initial direction of a P-wave as a discriminant

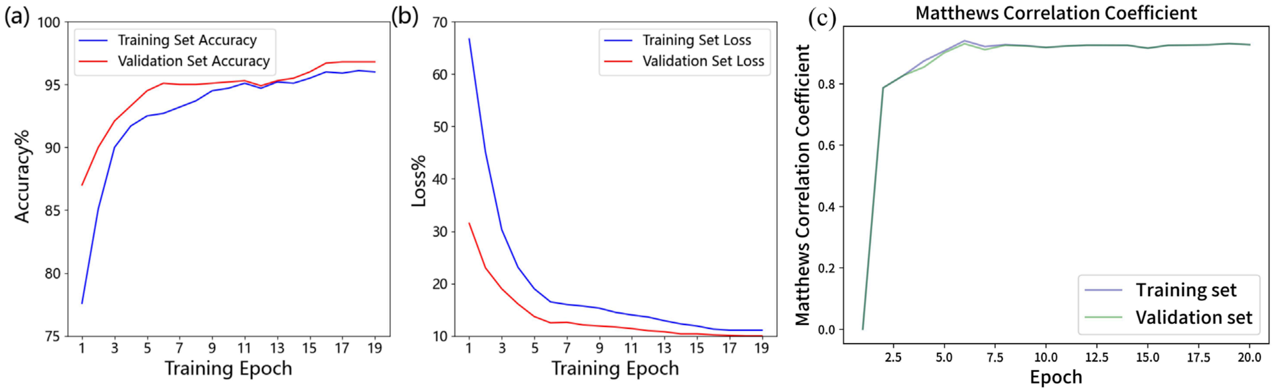

FIGURE 11
(a) Represents the training accuracy function; **(b)** Rep-resents the training loss function; **(c)** Represents the Matthews Correlation Coefficient.

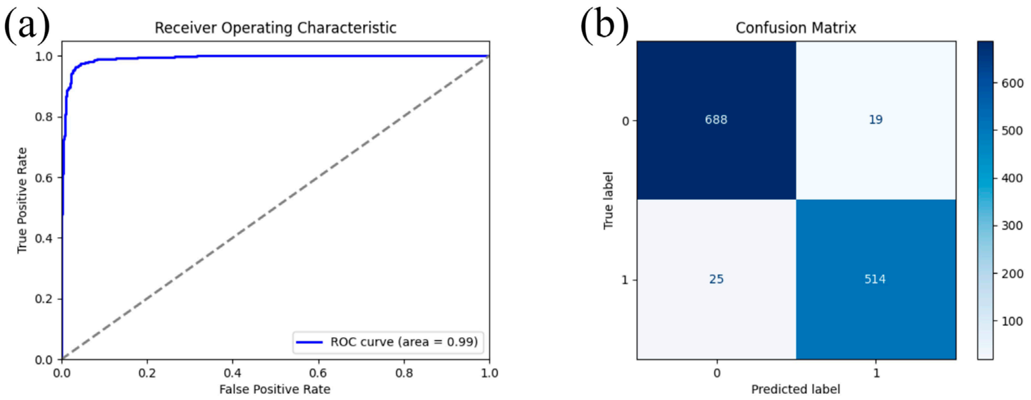

FIGURE 12
(a) shows the ROC curve, and **(b)** shows the confusion matrix.

TABLE 2 Comparative results of the four tested models.

Metrics	SVM	CNN	LSTM	ViT-2D
Accuracy	91.3%	93.2%	96.5%	94.2%
Precision	94.7%	95.1%	98.1%	96.7%
Recall	93.1%	95.2%	99.1%	97.1%
Loss	19.7%	17.5%	10.9%	15.1%

indicator makes it difficult to eliminate noise interference in data with high noise levels; similarly, the dominant frequency overlaps with the frequencies of noise when processing data derived from various regions, making it difficult to address the noise interference issue. The method of identifying short-period surface waves through CEEMDAN not only resolves the issue of ambiguous identification criteria but also overcomes the difficulties caused by overlapping noise and surface wave frequencies, significantly improving the success rate achieved when classifying earthquakes and mining tremors.

Mining tremor records are relatively rare, and previous studies have focused mostly on analyzing single events. When addressing a large amount of general, extensive data, the frequency range of surface waves induced by mining tremors significantly fluctuates and overlaps with the frequency range of noise. When the EEMD method is used, effectively separating mining tremor surface waves from noise is difficult. In comparison, the CEEMDAN method can more effectively remove noise and accurately identify surface wave frequencies.

5.2 Discussion and future work

This study demonstrates the efficacy of the CEEMDAN-LSTM model in discriminating mining tremors from tectonic earthquakes. To advance this framework, several avenues merit further investigation. First, enhancing computational efficiency of CEEMDAN decomposition requires integrating advanced spline interpolation techniques and parallelized GPU acceleration via CUDA/OpenCL frameworks, as validated in XGBoost-based seismic classification [16]. This optimization would expedite the extraction of intrinsic mode functions (IMFs), reducing latency

TABLE 3 Comparison among the results produced with different inputs.

Input	Three-layer CNN	LSTM	SVM	ViT-2D
1 Second Before and 3 Seconds After a P-Wave	56.7%	58.1%	—	91.2%
1 Second Before and 14 Seconds After a P-Wave	69.1%	61.7%	—	85.1%
Variance Contribution Rate of EEMD	74.3%	76.7%	73.1%	79.3%
Excellence Frequency	78.15%	78.1%	84.3%	85.1%
Variance Contribution Rate of CEEMDAN	93.2%	96.5%	91.3%	94.2%

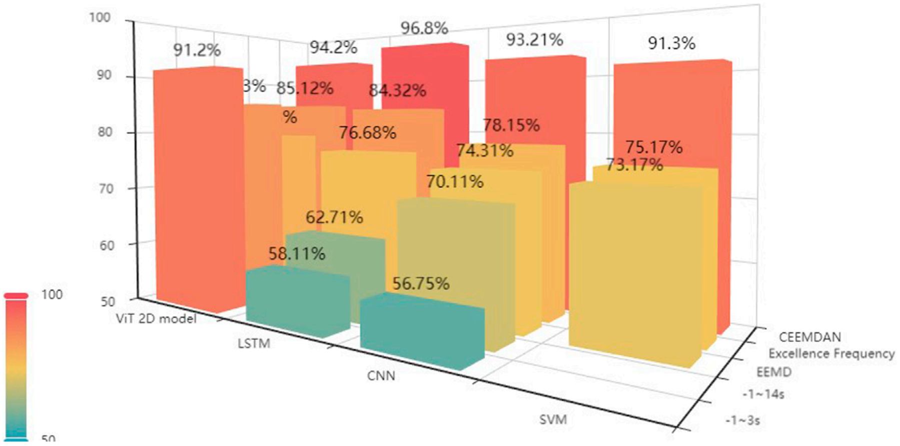

FIGURE 13
shows the classification accuracy of different models with different inputs.

in real-time applications. Second, expanding the dataset scope to include multi-source seismic records would improve model generalization, aligning with recent efforts in hybrid data fusion for earthquake early warning [17].

For feature engineering, integrating machine learning algorithms—such as support vector machines (SVM) or random forest (RF)—to exploit CEEMDAN-derived frequency components can enhance discriminative power. Specifically, combining traditional variance contribution rates with time-frequency metrics (Teager energy operator, wavelet packet entropy) and domain-specific indices (P/S amplitude ratios) would enable multi-scale analysis, as demonstrated in hybrid models for microseismic event classification [23]. Additionally, applying adaptive noise reduction techniques (Wiener filtering, wavelet thresholding) during CEEMDAN decomposition could mitigate artifacts from low signal-to-noise ratio (SNR) datasets, improving the fidelity of reconstructed waveforms.

To address scalability challenges, distributed GPU computing frameworks should be adopted to parallelize LSTM training, enabling linear scaling with dataset size. This approach mirrors successful implementations in large-scale seismic intensity estimation [18]. Furthermore, exploring lightweight LSTM variants (e.g., bidirectional LSTM with attention mechanisms) could balance temporal modeling capabilities and computational efficiency, as previously shown in rockburst-prone mine monitoring [23].

Data availability statement

The Japanese waveform data can be downloaded from http://www.kyoshin.bosai.go.jp/. NIED K-NET, KiK-net, National Research Institute for Earth Science and Disaster Resilience, doi: 10.17598/NIED.0004. Requests to access the mining seismic data of Liaoning province should be directed to the corresponding author.

Author contributions

CW: Data curation, Writing – original draft. XZ: Formal analysis, Funding acquisition, Writing – review and editing. WG: Formal Analysis, Project administration, Writing – original draft. FW: Data curation, Writing – original draft. JL: Conceptualization, Data curation, Methodology, Writing – review and editing. ZY: Formal Analysis, Methodology, Software, Supervision, Visualization, Writing – review and editing.

Funding

The author(s) declare that financial support was received for the research and/or publication of this article. This research was financially supported by the Taishan Industrial Experts

Program (NO.tscx202408130), Shandong Energy Group (NO. SNKJ2023A18-R02).

Conflict of interest

Authors CW, XZ, WG and FW were employed by Yankuang Energy Group Company Limited.

The remaining authors declare that the research was conducted in the absence of any commercial or financial relationships that could be construed as a potential conflict of interest.

The authors declare that this study received funding from Shandong Energy Group. The funder had the following involvement in the study: data collection and analysis, decision to publish, preparation of the manuscript.

Generative AI statement

The author(s) declare that no Generative AI was used in the creation of this manuscript.

Publisher's note

References

1. Feng W, Zhen L, Bing L, et al. Characteristics analysis of mining tremors, blasts and (natural) seismic events in Zoucheng area. *Seismol Geomagn Obs Res* (2013) 34:82–6. doi:10.3969/j.issn.1003-3246.2013.01/02.016

2. Sha L, Jiansi Y, Baofeng T, et al. Study on the identification of blasts, mine collapses, and earthquakes in the Capital Region. *Acta Seismol Sin* (2012) 34:202–14. doi:10.3969/j.issn.0253-3782.2012.02.007

3. Dong LJ, Wesseloo J, Potvin Y, Li XB. Discriminant models of blasts and seismic events in mine seismology. *Int J Rock Mech Min Sci* (2016) 86:282–91. doi:10.1016/j.ijrmms.2016.04.021

4. Jianchang Z, Changpeng X, Jinhua Z, et al. Time-frequency analysis of seismic waveforms in mining areas based on S-transform. *Seismol Geomagn Obs Res* (2014) 35:8–14. doi:10.3969/j.issn.1003-3246.2014.05/06.002

5. Zhang J, Jiang R, Li B, Xu N. An automatic recognition method of microseismic signals based on EEMD-SVD and ELM. *Comput Geosci* (2019) 133:104318. doi:10.1016/j.cageo.2019.104318

6. Xuesong H, Shiyu L, Ping S, et al. Identification of earthquakes and mining tremors using wavelet packets. *China Earthq* (2006) 22:425–34. doi:10.3969/j.issn.1001-4683.2006.04.010

7. Bi MX, Huang HM, Bian YJ, Zhou HJ, Chen YY, Zhao J. Study on seismic signal features extraction based on EMD. *Prog Geophys* (2012) 27:1890–6. doi:10.6038/j.issn.1004-2903.2012.05.008

8. Jinlong C, Shujie L, Donghui G, et al. Spectral characteristics analysis of mining tremors and earthquakes recorded by Hegang Seismic Array. *Seismol Geomagn Obs Res* (2020) 41:15–26.

9. Ming Z, Shi C, Dave Y. Waveform classification and seismic recognition by convolution neural network. *Acta Geophys Sin* (2019) 62:374–82. doi:10.6038/cjg2019M0151

10. Mousavi SM, Ellsworth WL, Zhu W, Chuang LY, Beroza GC. Earthquake transformer-an attentive deep-learning model for simultaneous earthquake detection and phase picking. *Nat Commun* (2020) 11:3952. doi:10.1038/s41467-020-17591-w

11. Zhu J, Li S, Song J, Wang Y. Magnitude estimation for earthquake early warning using a deep convolutional neural network. *Front Earth Sci* (2021) 9:9. doi:10.3389/feart.2021.653226

12. Zhu J, Li S, Song J. Magnitude estimation for earthquake early warning with multiple parameter inputs and a support vector machine. *Seismol Res Lett* (2021) 93:126–36. doi:10.1785/0220210144

13. Liu H, Li S, Song J. Discrimination between earthquake P waves and microtremors via a generative adversarial network. *Bull Seismol Soc Am* (2022) 112:669–79. doi:10.1785/0120210231

14. Zhou Z, Binhua L, Xing J, et al. Study on intelligent recognition of seismic waveforms based on convolutional neural networks. *World Earthq Eng* (2023) 39:148–57. doi:10.19994/j.cnki.WEE.2023.0038

15. Chen Y, Zhang G, Bai M, Zu S, Guan Z, Zhang M. Automatic waveform classification and arrival picking based on convolutional neural network. *Earth Space Sci* (2019) 6:1244–61. doi:10.1029/2018EA000466

16. Abdalzaher MS, Krichen M, Fouda MM. Enhancing earthquakes and quarry blasts discrimination using machine learning based on three seismic parameters. *Ain Shams Eng J* (2024) 15:102925. doi:10.1016/j.asej.2024.102925

17. Abdalzaher MS, Soliman MS, Krichen M, Alamro MA, Fouda MM. Employing machine learning for seismic intensity estimation using a single station for earthquake early warning. *Remote Sens* (2024) 16(12):2159. doi:10.3390/rs16122159

18. Abdalzaher MS, Moustafa SSR, Farid W, Salim MM. Enhancing analyst decisions for seismic source discrimination with an optimized learning model. *Geoenvironmental Disasters* (2024) 11:23. doi:10.1186/s40677-024-00284-7

19. Zhang G, Lin C, Chen Y. Convolutional neural networks for microseismic waveform classification and arrival picking. *Geophysics* (2020) 85:227–40. doi:10.1190/geo2019-0267.1

20. Fan X, Cheng J, Wang Y, Li S, Duan J, Wang P. Intelligent recognition of coal mine microseismic signal based on wavelet scattering decomposition transform. *J China Coal Soc* (2022) 47:2722–31. doi:10.13225/j.cnki.jccs.2021.1382

21. Chen Z, Ding L, Luo H A method for identifying microseismic events in mines based on improved wavelet decomposition and ELM. *J China Coal Soc* (2020) 45:637–48. doi:10.13225/j.cnki.jccs.2020.0373

22. Qin C, Zhao W, Jia H, Gao W, Chen Y, Yu W, et al. Microseismic time series prediction method in coal mines based on modal decomposition and deep learning. *J China Coal Soc* (2024). 1–16. doi:10.13225/j.cnki.jccs.2023.1151

23. Gu X, Zhang C, Guo W, et al. Research on the characteristics and identification of typical microseismic signals in rockburst-prone mines. *J China Coal Soc* (2024) 1–19. doi:10.13225/j.cnki.jccs.2023.1237

24. Li W. Feature extraction and classification method of mine microseismic signals based on LMD and pattern recognition. *J China Coal Soc* (2017) 42:1156–64. doi:10.13225/j.cnki.jccs.2016.0888

25. Wu Z, Huang N. Ensemble empirical mode decomposition: a noise-assisted data analysis method. *Adv Adapt Data Anal* (2009) 01(1):1–41. doi:10.1142/S1793536909000047

26. Hochreiter S, Schmidhuber J. Long short-term memory. *Neural Comput* (1997) 9:1735–80. doi:10.1162/neco.1997.9.8.1735

27. Allen RV. Automatic earthquake recognition and timing from single traces. *Bull Seismol Soc Am* (1978) 68:1521–32. doi:10.1785/bssa0680051521

28. Shi R, Yang Z. Feature extraction of multi-rope friction hoist load information based on improved EMD, J. *China Coal Soc* (2014) 39:782–8. doi:10.13225/j.cnki.jccs.2013.1502

29. Bilal MA, Ji Y, Wang Y, Akhter MP, Yaqub M. An early warning system for earthquake prediction from seismic data using batch normalized graph convolutional neural network with attention mechanism (BNGCNNATT). *Sensors (Basel)* (2022) 22:6482. doi:10.3390/s22176482

30. Zhang X, Zhang M, Tian X. Real-time earthquake early warning with deep learning: application to the 2016 M 6.0 central Apennines, Italy earthquake. *Geophys Res Lett* (2021) 48:e2020GL089394. doi:10.1029/2020GL089394

31. Kingma DP, Ba JL. Adam: a method for stochastic optimization. arXiv preprint arXiv:1412.6980. (2015)

32. Loshchilov I, Hutter F. SGDW: stochastic gradient descent with warm restarts. In: *International conference on learning representations* (2016).

33. Shen J. Classification of natural and unnatural earthquakes based on deep learning [D]. *Inst Eng Mech China Earthquake Adm* (2024). doi:10.13197/j.eeed.2024.0502

Frontiers in
Physics

Investigates complex questions in physics to understand the nature of the physical world

Addresses the biggest questions in physics, from macro to micro, and from theoretical to experimental and applied physics.

Discover the latest Research Topics

See more →

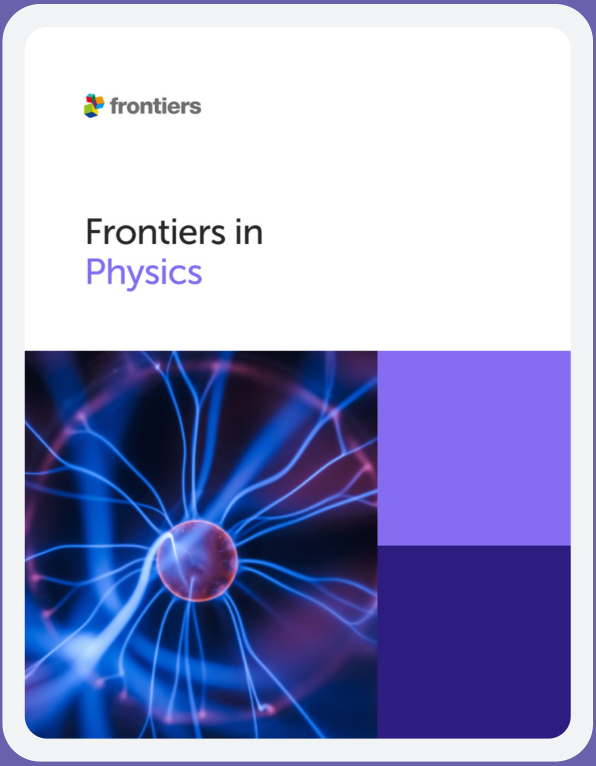

Frontiers

Avenue du Tribunal-Fédéral 34
1005 Lausanne, Switzerland
frontiersin.org

Contact us

+41 (0)21 510 17 00
frontiersin.org/about/contact

frontiers | Research Topics